

Assuming:

$$B = \frac{1}{\sqrt{s_{mn}s_{mn}}} \lambda(s_{pq}\delta_{pq}) + \sqrt{\frac{2}{27}}k(3\lambda + 2\mu) \quad (104.549)$$

Plastic parameter can be written as:

$$d\lambda = \frac{n_{ij}E_{ijpq}d\epsilon_{pq}}{n_{ij}E_{ijpq}m_{kl}} = \frac{\lambda_{nominator}}{\lambda_{denominator}} \quad (104.550)$$

$$\lambda_{nominator} = n_{ij}E_{ijpq}d\epsilon_{pq} = n_{ij}d\sigma_{ij} \quad (104.551)$$

$$\begin{aligned} \lambda_{denominator} &= n_{ij}E_{ijpq}m_{kl} = n_{ij}Hq_{ij} \\ &= \left\{ \frac{1}{\sqrt{s_{ij}s_{ij}}}s_{ij} + \sqrt{\frac{2}{27}}k\delta_{ij} \right\} \left\{ 2\mu \frac{1}{\sqrt{s_{mn}s_{mn}}}s_{ij} + B\delta_{ij} \right\} \\ &= 2\mu + \frac{1}{\sqrt{s_{mn}s_{mn}}}(B + 2\mu\sqrt{\frac{2}{27}}k)(s_{ij}\delta_{ij}) + 3B\sqrt{\frac{2}{27}}k \end{aligned} \quad (104.552)$$

Finally plastic tensor can be expressed as:

$$E_{pqmn}^{pl} = \frac{E_{pqkl}n_{kl}m_{ij}E_{ijmn}}{n_{ab}E_{abcd}m_{cd}} = \frac{Hq_{pq}Hq_{mn}}{\lambda_{denominator}} \quad (104.553)$$

where:

$$\begin{aligned} Hq_{pq}Hq_{mn} &= \left\{ \frac{2\mu}{\sqrt{s_{ij}s_{ij}}}s_{pq} + B\delta_{pq} \right\} \left\{ \frac{2\mu}{\sqrt{s_{ij}s_{ij}}}s_{mn} + B\delta_{mn} \right\} \\ &= 4\mu^2 \frac{1}{s_{ij}s_{ij}}s_{pq}s_{mn} + 4\mu \frac{1}{\sqrt{s_{ij}s_{ij}}}Bs_{pq}\delta_{mn} + B^2\delta_{pq}\delta_{mn} \end{aligned} \quad (104.554)$$

When isotropic hardening is considered for Drucker-Prager model,  $\xi$  and  $h$  are not zero. These parameters can be obtained using following equations:

$$\xi = -p\sqrt{\frac{2}{3}} \quad (104.555)$$

$$h = \sqrt{\frac{2}{3}m_{ij}m_{ij}}k = \sqrt{\frac{2}{3}(1 + \frac{2}{9}k^2)k} \quad (104.556)$$

Plastic parameter ( $d\lambda$ ) and plastic modulus ( $E_{pqmn}^{pl}$ ) can be written as:

$$\lambda_{denominator} = n_{ij}E_{ijpq}m_{kl} - \xi h = n_{ij}Hq_{ij} - \xi h \quad (104.557)$$

$$E_{pqmn}^{pl} = \frac{E_{pqkl}n_{kl}m_{ij}E_{ijmn}}{n_{ab}E_{abcd}m_{cd}} = \frac{Hq_{pq}Hq_{mn}}{\lambda_{denominator}} \quad (104.558)$$

$k$  is the scalar internal variable to be updated at each step of analysis using following equation:

$$\begin{aligned} k^{updated} &= k + dk = k + hd\lambda \\ &= k + \sqrt{\frac{2}{3}(1 + \frac{2}{9}k^2)kd\lambda} = k(1 + \sqrt{\frac{2}{3}(1 + \frac{2}{9}k^2)d\lambda}) \end{aligned} \quad (104.559)$$

By considering kinematic hardening for Drucker-Prager material model, tensorial internal variable ( $\alpha_{ij}$ ) is introduced and has to be updated at each step of analysis. The stress derivatives of yield function and plastic potential function can be written as:

$$n_{ij} = m_{ij} = \frac{1}{\sqrt{(s_{ij} - p\alpha_{ij})(s_{ij} - p\alpha_{ij})}}(s_{ij} - p\alpha_{ij}) + \sqrt{\frac{2}{27}}k\delta_{ij} \quad (104.560)$$

Tensorial parameters of  $\xi_{ij}$  and  $h_{ij}$  can be calculated using Armstrong-Frederick saturation-type kinematic hardening rule ([Armstrong and Frederick \(1966\)](#)):

$$\xi_{ij} = -\frac{p}{\sqrt{(s_{ij} - p\alpha_{ij})(s_{ij} - p\alpha_{ij})}}(s_{ij} - p\alpha_{ij}) \quad (104.561)$$

$$h_{ij} = \frac{2}{3}h_am_{ij} - \alpha_{ij}c_r\sqrt{\frac{2}{3}m_{ij}m_{ij}} \quad (104.562)$$

Plastic parameter ( $d\lambda$ ) and plastic modulus ( $E_{pqmn}^{pl}$ ) are obtained from following equations:

$$d\lambda = \frac{n_{ij}E_{ijpq}d\epsilon_{pq}}{n_{ij}E_{ijkl}m_{kl} - \xi_{ij}h_{ij}} = \frac{n_{ij}d\sigma_{ij}}{2\mu - \xi_{ij}h_{ij}} \quad (104.563)$$

$$E_{pqmn}^{pl} = \frac{E_{pqkl} n_{kl} m_{ij} E_{ijmn}}{n_{ab} E_{abcd} m_{cd} - \xi_{ij} h_{ij}} \quad (104.564)$$

Tensorial internal variable ( $\alpha_{ij}$ ) can be updated using following equation:

$$\begin{aligned} \alpha_{ij}^{updated} &= \alpha_{ij} + d\alpha_{ij} = \alpha_{ij} + h_{ij}d\lambda \\ &= \alpha_{ij} + \left( \frac{2}{3}h_{am}m_{ij} - \alpha_{ij}c_r \sqrt{\frac{2}{3}m_{ij}m_{ij}} \right) d\lambda \end{aligned} \quad (104.565)$$

#### 104.6.18.6 Modified Cam-Clay Model

The critical state line for Cam-Clay can be written as

$$e_c = e_{c,r} - \lambda_c \ln p_c \quad (104.566)$$

where  $e_c$  is the critical void ratio at critical mean stress ( $p_c$ ),  $e_{c,r}$  is the reference critical void ratio, and  $\lambda_c$  is the normal consolidation slope. In general it is assumed that the normal consolidation line (NCL) is parallel to CSL, which is defined as:

$$e = e_\lambda - \lambda \ln p \quad (104.567)$$

where  $e_\lambda$  is the intercept on the NCL at  $p = 1$ .  $\lambda$  is the normal consolidation slope or the elasto-plastic slope of  $e - \ln p$  relation. The same relation is used for unloading-reloading line (URL) with different slope as:

$$e = e_\kappa - \kappa \ln p \quad (104.568)$$

where  $e_\kappa$  is the intercept on the URL at  $p = 1$ . The yield function for Cam-Clay model can be defined as

$$f = q^2 - M^2[p(p_0 - p)] = 0 \quad (104.569)$$

where  $M$  is the critical state stress ration in  $q-p$  space and  $p_0$  is the initial internal scalar variable which will be changed by change in plastic volumetric strain.

Cam-Clay model is one of the associated flow rule models which means the same function is used for both yield and plastic potential surfaces ( $f = g$ ). The plastic flow of the Cam-Clay model is associated

with its yield function, in other words, the plastic flow is defined by the potential function ( $g$ ), which is assumed the same as the yield function ( $f$ ).

The evolution law of for Cam-Clay model is a scalar one which can be expressed by:

$$\dot{p}_0 = \frac{(1+e)p_0}{\lambda - \kappa} \dot{\epsilon}_v^p \quad (104.570)$$

where  $e$  is the void ratio,  $\lambda$  is the normal consolidation slope or the elasto-plastic slope of  $e-\ln p$  relation, and  $\kappa$  is the slope of unloading-reloading line. This equation proves that the change of  $p_0$  is controlled by change of plastic volumetric strain. By considering the yield function expressed in Equation (104.569) and considering the associated flow rule, stress derivatives can be evaluated as:

$$n_{ij} = m_{ij} = 3s_{ij} + \frac{1}{3}M^2(p_0 - 2p)\delta_{ij} \quad (104.571)$$

Elastic modulus in terms of shear modulus ( $G$ ) and bulk modulus ( $K$ ) can be expressed as:

$$E_{ijkl} = (K - \frac{2}{3}G)\delta_{ij}\delta_{kl} + G(\delta_{ik}\delta_{jl} + \delta_{il}\delta_{jk}) \quad (104.572)$$

$$\begin{aligned} Hq_{ij} &= E_{ijkl}m_{kl} \\ &= \{(K - \frac{2}{3}G)\delta_{ij}\delta_{kl} + G(\delta_{ik}\delta_{jl} + \delta_{il}\delta_{jk})\}\{3s_{ij} + \frac{1}{3}M^2(p_0 - 2p)\delta_{ij}\} \\ &= 6Gs_{ij} + \{(K - \frac{2}{3}G)M^2(p_0 - 2p) + \frac{2}{3}M^2(p_0 - 2p)G\}\delta_{ij} \end{aligned} \quad (104.573)$$

Defining  $D$  as:

$$D = (K - \frac{2}{3}G)M^2(p_0 - 2p) + \frac{2}{3}M^2(p_0 - 2p)G \quad (104.574)$$

$\xi$  and  $h$  in case of using Cam-Clay constitutive model can be expressed as following equations:

$$\xi = M^2p \quad (104.575)$$

$$h = (1+e_0)p_0 \frac{d\epsilon_v}{\lambda - \kappa} \quad (104.576)$$

where  $d\epsilon_v = M^2(2p - p_0)$ . Plastic parameter can be written as:

$$d\lambda = \frac{n_{ij}E_{ijpq}d\epsilon_{pq}}{n_{ij}E_{ijpq}m_{kl} - \xi h} = \frac{\lambda_{nominator}}{\lambda_{denominator}} \quad (104.577)$$

$$\lambda_{nominator} = n_{ij}E_{ijpq}d\epsilon_{pq} = n_{ij}d\sigma_{ij} \quad (104.578)$$

$$\begin{aligned} \lambda_{denominator} &= n_{ij}E_{ijpq}m_{kl} - \xi h = n_{ij}Hq_{ij} - \xi h \\ &= \{3s_{ij} + \frac{1}{3}M^2(p_0 - 2p)\delta_{ij}\}\{6Gs_{ij} + D\delta_{ij}\} - \xi h \\ &= 18Gs_{ij}s_{ij} + DM^2(p_0 - 2p) - \xi h \end{aligned} \quad (104.579)$$

Then the plastic tensor can be expressed as:

$$\begin{aligned} E_{pqmn}^{pl} &= \frac{E_{pqkl}n_{kl}m_{ij}E_{ijmn}}{n_{ab}E_{abcd}m_{cd} - \xi h} \\ &= \frac{Hq_{pq}Hq_{mn}}{\lambda_{denominator}} \end{aligned} \quad (104.580)$$

where:

$$\begin{aligned} Hq_{pq}Hq_{mn} &= \{6Gs_{ij} + D\delta_{ij}\}\{6Gs_{ij} + D\delta_{ij}\} \\ &= D^2\delta_{pq}\delta_{mn} + 6GD\delta_{pq}s_{mn} + 6GDs_{pq}\delta_{mn} + 36G^2s_{pq}s_{mn} \end{aligned} \quad (104.581)$$

$p_0$  is the scalar internal variable to be updated at each step of analysis using the following equation:

$$p_0^{updated} = p_0 + dp_0 = p_0 + hd\lambda \quad (104.582)$$

#### 104.6.18.7 Comparison of Computational Time of Accelerated Constitutive Models with NewTemplate3Dep

In order to compare the computational time of accelerated constitutive models with the ones available in NewTemplate3Dep, cyclic simulations are done in constitutive level using explicit integration method. Simulations are done for all the mentioned cases of von Mises, Drucker-Prager, and Cam-Clay constitutive models. The ratios of computational time of NewTemplate3Dep ( $t_N$ ) to accelerated constitutive models ( $t_{Acc}$ ) are summarized in Table (104.1). As it is observed, there are improvements in range of 2 to 3 times in computational time which can lead to reducing the computational time of soil-structure systems.

Table 104.1: Comparison of computational time of accelerated constitutive models with NewTemplate3Dep

Constitutive Model	$t_N/t_{Acc}$	Constitutive Model	$t_N/t_{Acc}$
von Mises Perfectly Plastic	3.1	Drucker-Prager Perfectly Plastic	2.9
von Mises Isotropic Hardening	2.6	Drucker-Prager Isotropic Hardening	2.5
von Mises Kinematic Hardening	2.3	Drucker-Prager Kinematic Hardening	1.9
Cam-Clay	2.2	—	—

## 104.7 Elastic-Plastic Models for Contacts, Joints and Interfaces

This section is based on [Sinha and Jeremić \(2017\)](#).

### 104.7.1 Experimental Data

The response of the interface plays a very important role on the behavior of deep and shallow foundations, retaining walls, geo-membranes, submerged structures and soil-structure interaction. The load transfer mechanism from structure to the soil acts at the interface. The soil-structure interface comprise of a very thin small shearing band. The initial investigation by [Yoshimi and Kishida \(1981\)](#) indicated the thickness of the shear band as nine times the mean grain size diameter  $D_{50}$ . [Tejchman and Wu \(1995\)](#) conducted several tests on sand-steel interface and concluded that the thickness of the interface for rough interface is 30-40  $D_{50}$  and for smooth interface is 6-10  $D_{50}$ . [DeJong et al. \(2006\)](#); [DeJong and Westgate \(2009\)](#) investigated the shear-zone thickness to be 5-10 times the mean particle diameter  $D_{50}$ . [Martinez et al. \(2015\)](#) conducted several axial and torsional shear experiments on sand-steel interface to understand the micro mechanics involved at interface. The micro-mechanical hypothesis proposed by [Martinez et al. \(2015\)](#) is shown in Figure 104.28. The thickness of the interface zone formed by the particle in axial shearing migrates along the interface whereas for torsional shearing it migrates away from the interface. Similar mechanical hypothesis was observed by [DeJong et al. \(2006\)](#). It was also observed that for torsional shear the shear band zone was 2-3 times larger than the purely axial shearing. It also depends upon the characteristics of the soil beneath and the surface structural material and its roughness.

Since 1960's, researchers have been carrying out experiments to understand the interface behavior. The initial works have been contributed by [Potyondy \(1961\)](#); [Brumund and Leonards \(1973\)](#); [Littleton](#)

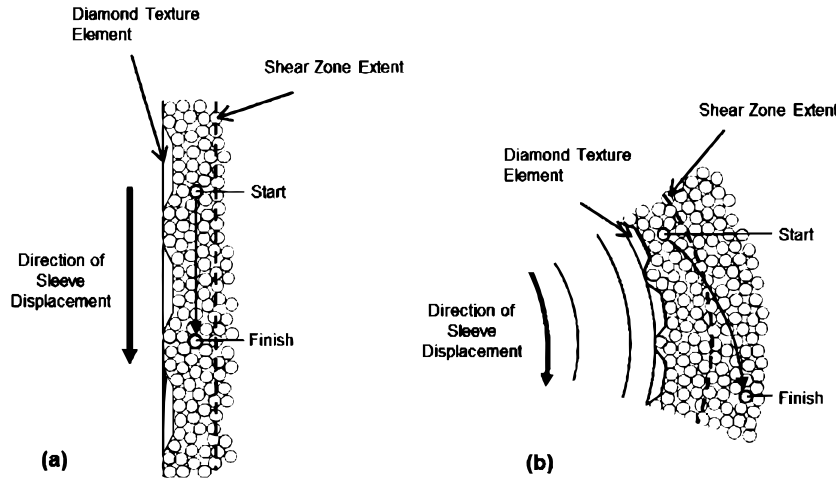


Figure 104.28: Hypothesis for a particle movement under (a) axial and (b) torsional loading ([Martinez et al. \(2015\)](#))

(1976). Potyondy (1961) studied the effect of soil-moisture content, structural surface roughness, soil-composition and normal load intensity on the skin-friction of the soil-structure interface. Brumund and Leonards (1973) investigated the static and dynamic friction angle between sand steel interface. Littleton (1976) performed drained and undrained tests on clay-steel interface and found that the shear stress response was steeper than the usual clay-clay interface. Based on the normal confinement  $\sigma_n$ , an initial hardening was observed until the peak shear strength  $\tau_p$  is reached. After that softening to residual  $\tau_r$  was observed. Later Desai (1981) emphasized on the importance of modeling of interface behavior for real soil-structure interactions. He also pointed out the lack of existing experimental data which could be used to develop constitutive models defining the interface behavior. Yoshimi and Kishida (1981) used a ring torsion apparatus to find the friction angle between dry sand and steel surface over a wide variation of surface roughness and sand density. Uesugi and Kishida (1986a,b); Kishida and Uesugi (1987) carried a series of laboratory experiments between steel and air-dried sands using simple shear apparatus shown in Figure 104.29 and Figure 104.30. It was found that the interface behavior is highly influenced by the sand type and surface roughness  $R_{max}$  while the effect of normal stress  $\sigma_n$  and mean grain size  $D_{50}$  are of poor significance. Thus, Kishida and Uesugi (1987) proposed a normalized roughness  $R_n$  to evaluate the relative coefficient of friction  $\mu_y$  of sand-steel interface as shown in Figure ??.

$$R_{max}(L = D_{50})/D_{50} \quad (104.583)$$

where,  $R_{max}(L = D_{50})$  is the  $R_{max}$  value of the steel surface with gauge length  $L = D_{50}$ .

Desai and Nagaraj (1988) performed a cyclic normal and shear tests on dry sand and concrete interface in translational shear box. Monotonic and cyclic normal loads along with cyclic shear loads

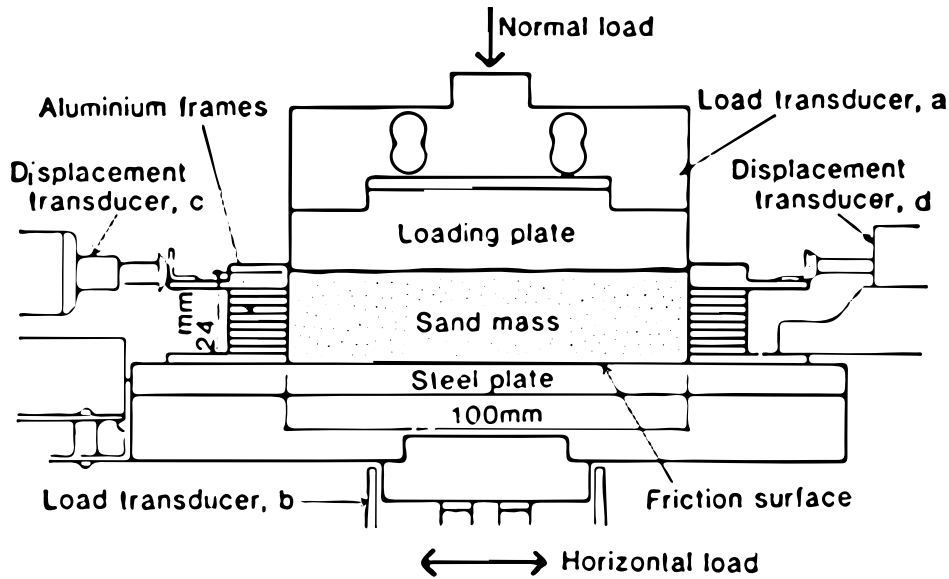


Figure 104.29: Section of friction test apparatus (Uesugi and Kishida (1986b)).

were applied. The shear behavior was modeled with a modified form of Ramberg-Osgood (R-O) model. Although Desai and Nagaraj (1988) did not show any experimental results, he idealized the normal interface behavior to be composed of (1) Virgin loading; (2) unloading; (3) reloading; 4 tensile condition; (5) partial debonding; and 6 rebonding as shown in Figure 104.32. Uesugi et al. (1989, 1990) studied the frictional behavior of sand-steel interface subject to repeated shearing under one-way or two-way loadings. It was found that under repeated loading conditions the coefficient of friction  $\mu$  converged close to the residual coefficient of friction  $\mu_r$  as could be observed in Figure ?? Boulon (1989) performed a lot of experiments on piles in sand. Direct simple shear tests were carried out to investigate the shear behavior between the granular soil and rough construction material. Based on the experimental results obtained later Boulon and Nova (1990) proposed a mathematical model and constitutive integration to model the interface behavior in finite element method (FEM). Aubry et al. (1990) proposed a dilatancy based cyclic elastic-plastic constitutive model for the interface. Cyclic loading functions with memory of last loading reversal was used to model subsequent loadings and unloading. The yield function was defined using simple Mohr Coulomb with additional parameter  $F$  as a function of normal stress  $\sigma_n$  and plastic compressibility  $\beta$  to account for curvature and dilation of the yield surface.

Fakharian and Evgin (1995) developed a 3-D apparatus capable of performing direct and simple shear type testing of interfaces between soil and structure. The developed apparatus was subsequently used to perform numerous experiments Fakharian and Evgin (1996); Evgin and Fakharian (1997); Fakharian and Evgin (1997); Fakharian (1996); Fakharian et al. (2002) over sand-steel interface for different stress paths for different relative densities  $D_r$  of sand. The 3-D apparatus made it possible to conduct 2-D

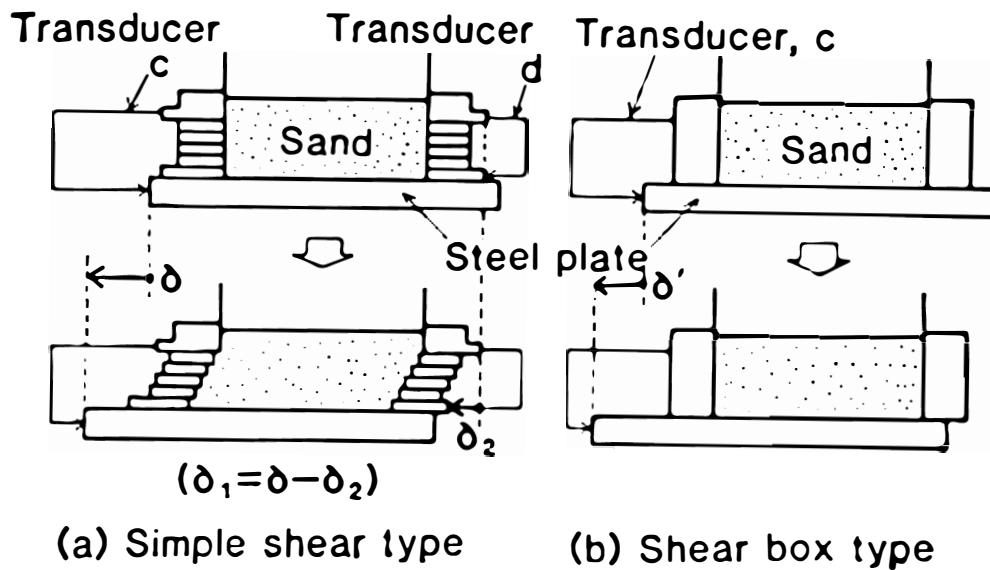


Figure 104.30: Measurement of tangential displacement (Uesugi and Kishida (1986b)).

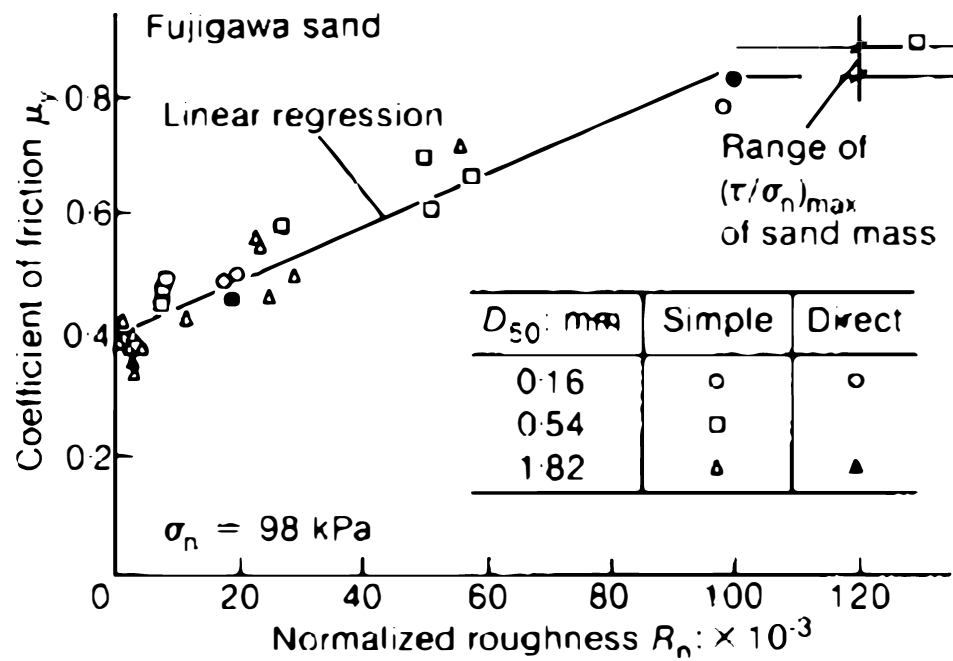


Figure 104.31: Coefficient of friction at yield  $\mu_y$  and normalized roughness (after Kishida and Uesugi (1987)).

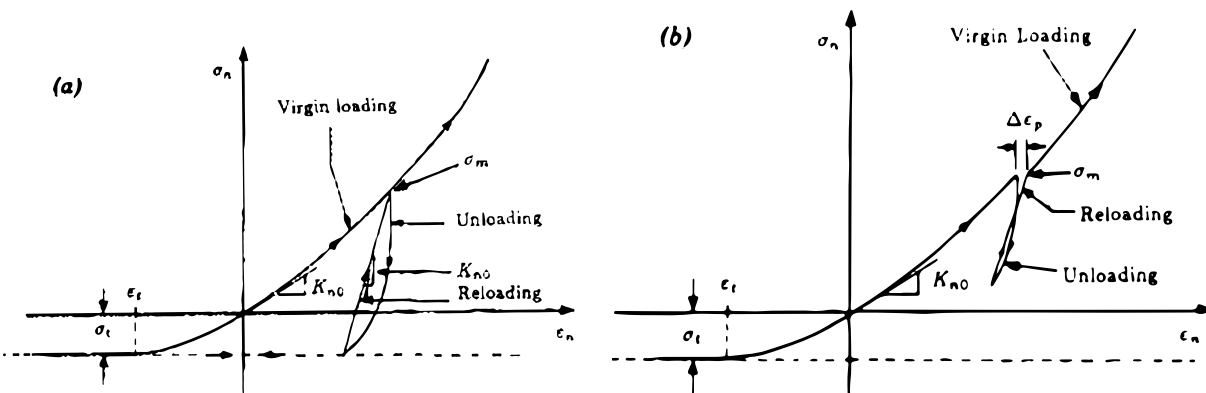


Figure 104.32: Schematic of Stress-Strain Response for Normal Behavior ([Desai and Nagaraj \(1988\)](#)) : (a) Virgin Loading and unloading with Tensile stress Condition; (b) Partial Loading.

shear test with constant normal stress  $\sigma_n$ . Monotonic and cyclic test results are shown in Figure 104.34 and Figure 104.34. The experiment results in Figure 104.34 clearly shows a peak shear stress ratio  $(\tau/\sigma_n)_p$  and a residual stress ratio  $(\tau/\sigma_n)_r$ . Initial hardening and then softening depends upon the relative density  $D_r$  of the sand was observed. A higher relative density  $D_r = 80\%$  sand shows dilation for lower confinement and thus a peak behavior whereas a low relative density  $D_r = 25\%$  sand shows no dilation. For cyclic shear tests, the loose soil  $D_r = 25\%$  shown in Figure 104.35(b) showed gain in strength due to densification resulting from particle breakage. While for soil with high relative density  $D_r = 80\%$  almost no gain in shear strength was observed during cyclic shearing. The 3-D tests performed showed that the shear stress  $\tau$  is almost isotropic for different shear stress paths.

[Shahrour and Rezaie \(1997\)](#) performed a series of monotonic and cyclic tests on Hostun Sand with rough and smooth surface with constant normal load condition. The results obtained were used to propose an elasto-plastic bounding surface based constitutive model for the interface behavior. The monotonic and cyclic test are shown in Figure 104.36 for rough and smooth interface surface. From Figure 104.36, it could be observed that for smooth interface, the shear stress  $\tau$  increases only upto the critical shear stress  $\tau_c$ . Whereas for rough soil, the shear stress  $\tau$  hardens to a peak strength  $\tau_p$  and then softens to the critical shear strength  $\tau_c$ . The behavior observed for rough and smooth interface is similar to dense and loose soil as observed in tests by [Fakharian and Evgin \(1996\)](#). The cyclic test shown in Figure 104.36(c) showed similar response as was observed by [Fakharian and Evgin \(1996\)](#).

[DeJong et al. \(2006\)](#) performed laboratory soil-structure investigation under constant normal stiffness using particle image velocimetry (PIV)method. Cyclic shearing was carried out to simulate and understand the the shear behavior at pile interface. Cyclic degradation exponential model was proposed of model the change in void ratio. Later [Mortara et al. \(2007\)](#) also performed cyclic shear tests on sand

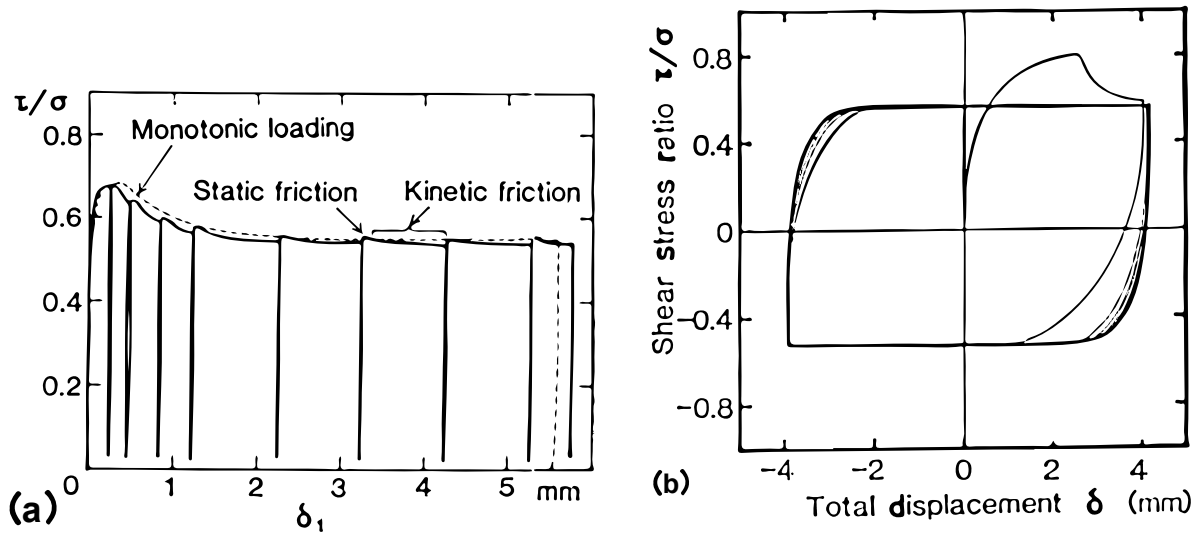


Figure 104.33: (a) Monotonic and (b) cyclic response of Toyora sand with steel interface (Uesugi et al. (1989)) ( $D_r = 90\%$ ,  $\sigma_n = 98 kPa$ ,  $R_n = 150 e^{-3}$ ).

steel interfaces. DeJong and Westgate (2009) quantified the soil-structure interface behavior to the shearing on the factor like relative density  $D_r$ , particle angularity, particle hardness, surface roughness, normal stress and normal stiffness. Local as well as global load displacement response was recorded to understand the load-transfer mechanism.

## 104.7.2 Axial Contact, Joint, Interface

The contact/joint/interface behavior in the normal direction is modeled as penalty stiffness function as described in the Section 104.7.2.1. The penalty function can be chosen as linear with fixed stiffness also known as Hard Contact/Joint/Interface (Section 104.7.2.2), or it can be assumed to be a non-linear function with stiffness increasing exponentially with penetration. This type of normal behavior is called as Soft Contact/Joint/Interface (Section 104.7.2.3). Soft Contact/Joint/Interface represents more realistic soil-structure interface behavior. The soil becomes stiff as the penetration increases and gets relaxed upon unloading.

### 104.7.2.1 Penalty Method

At the interface of the soil-foundation system, an impenetrability constraint exists as shown in Equation ?? to ???. The contacting/interfacing bodies cannot penetrate into each other. The impenetrability leads to an inequality constraint, which requires special methods such as penalty method, Lagrange, barrier,

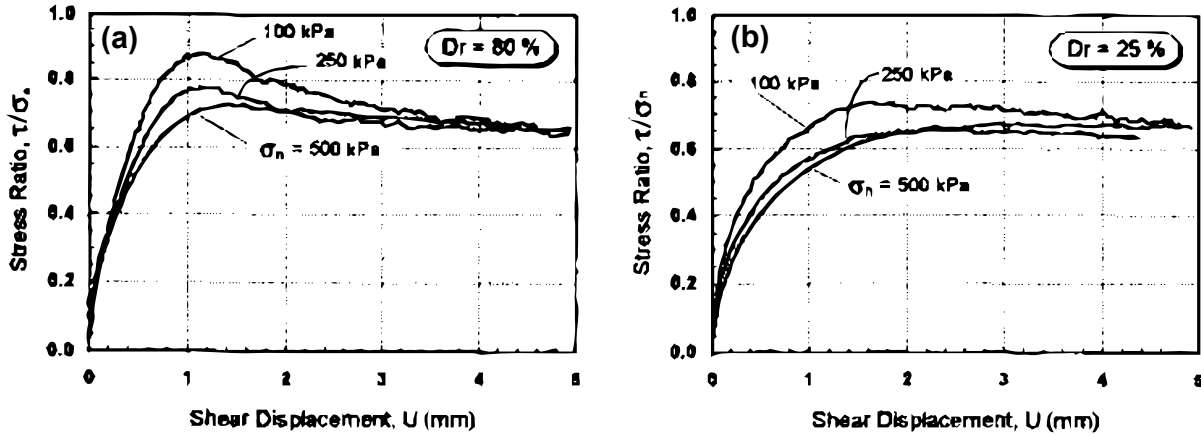


Figure 104.34: Stress ratio versus shear displacement for  $\sigma_n = 100, 200, 500 \text{ kPa}$ : (a) rough surface-dense sand ( $D_r = 80\%$ ); (b) rough surface loose sand ( $D_r = 25\%$ ) (Fakharian and Evgin (1996)).

augmented Lagrangian, etc. as described in (Wriggers, 2002). Penalty method is a common approach used for solving constrained minimization (or maximization) problems involving inequalities as described in section ?? and Section ???. In this approach, a large penalty term is added to the minimizing functional to prevent the solution from escaping the constrained space.

Figure 104.37 shows a two contact/interface node pairs initially separated by a small distance of  $g$  in the contact/interface normal direction. During pure contact/interface/joint, the two node penetrates against each other by  $\Delta_n$ . The instantaneous relative distance between the two contact/interface surfaces is  $u$ . Thus, if  $u < g$  there is no contact/interface and normal force  $N = 0$  otherwise there is contact/interface and a normal force  $N$  will act.

In the penalty stiffness formulation, a small penetration  $\Delta_n$  is allowed between the mass and the floor having stiffness  $k_n$  such that during contact the normal force  $N$  is defined as

$$N = k_n \Delta_n \text{ if } \Delta_n \geq 0 \quad (104.584)$$

where  $k_n$  can be thought of the normal contact/interface stiffness and  $\Delta_n$  is the relative displacement between the two contact/interface surfaces with respect to the initial gap  $g$  in contact/interface normal direction. It is defined as the following

$$\Delta_n = u_n^r - g_n = u - g \quad (104.585)$$

where  $u_n^r$  is the relative displacement in the contact/interface normal direction and  $g_n$  is the initial gap in contact/interface normal direction. Theoretically, for rigid contact/interface case, the penalty stiffness  $k_n$  is assumed to infinite resulting in  $\Delta_n = 0$ . However, for numerical reasons, infinity is not possible, and

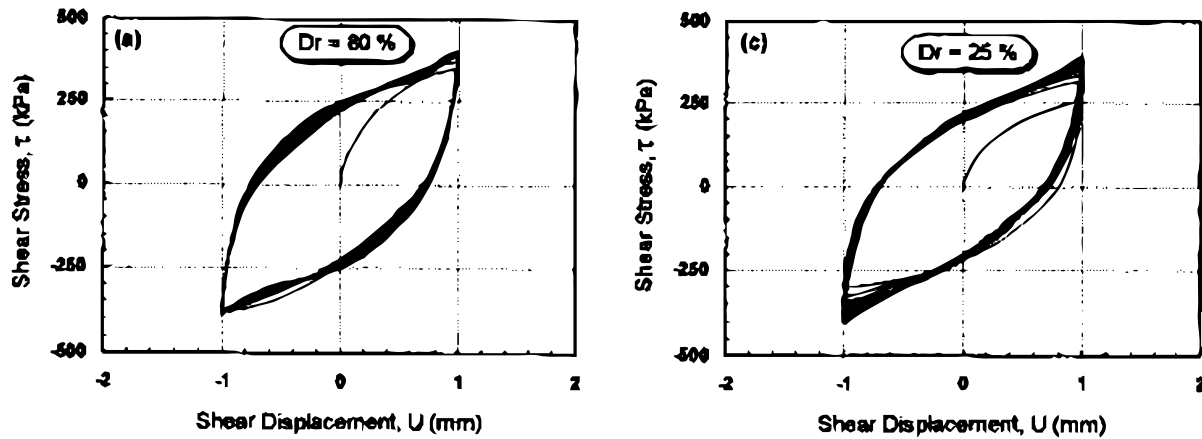


Figure 104.35: Cyclic test results, shear stress versus shear displacement for  $\sigma_n = 500\text{kPa}$ : (a) rough surface, dense sand ( $D_r = 80\%$ ); (b) rough surface, loose sand ( $D_r = 25\%$ ) (Fakharian and Evgin (1996)).

thus  $\Delta_n = 0$  is never enforced. This results in small penetration at contact/interface surfaces resulting in  $\Delta_n < 0$  during contact. For penalty method, the term penetration is thus normally referred to  $\Delta_n$  defining the two possible states as:

- *No Contact/Joint/Interface* (Penetration  $\Delta_n > 0$ )
- *Contact/Joint/Interface State* (Penetration  $\Delta_n \leq 0$ )

In equation 104.584, if the penalty stiffness parameter  $k_n$  is assumed to be constant and independent of penetration ( $\Delta_n$ ), it is referred as a hard contact. This type of contact/interface is more physical for interactions between two rigid surfaces or bodies. However, to model interaction between soft-soil and rigid foundation, a soft contact/interface with penalty stiffness increasing with penetration is preferred. The following Section 104.7.2.2 and 104.7.2.3 describes hard and soft contact/interface respectively.

For coupled contact/interface problems described in Section ??, in order to enforce the no-drainage condition in contact/interface normal direction between  $U$  (soil) and  $u$  (foundation) degrees of freedom, an additional penalty stiffness parameter  $k_p$  is required. Section ?? describes how penalty stiffness  $k_p$  is used to enforce the undrained condition.

It must be noted that in the penalty or any other method (Lagrange, barrier .. etc.) as described in (Wriggers, 2002), to get to the solution it has to take into account of whether the contact/interface is active or not. Thus, the inequality constraint has to be changed to the active (closed gap) or inactive (open gap) based on the state of contact. As a result, the topology of the structure changes due to

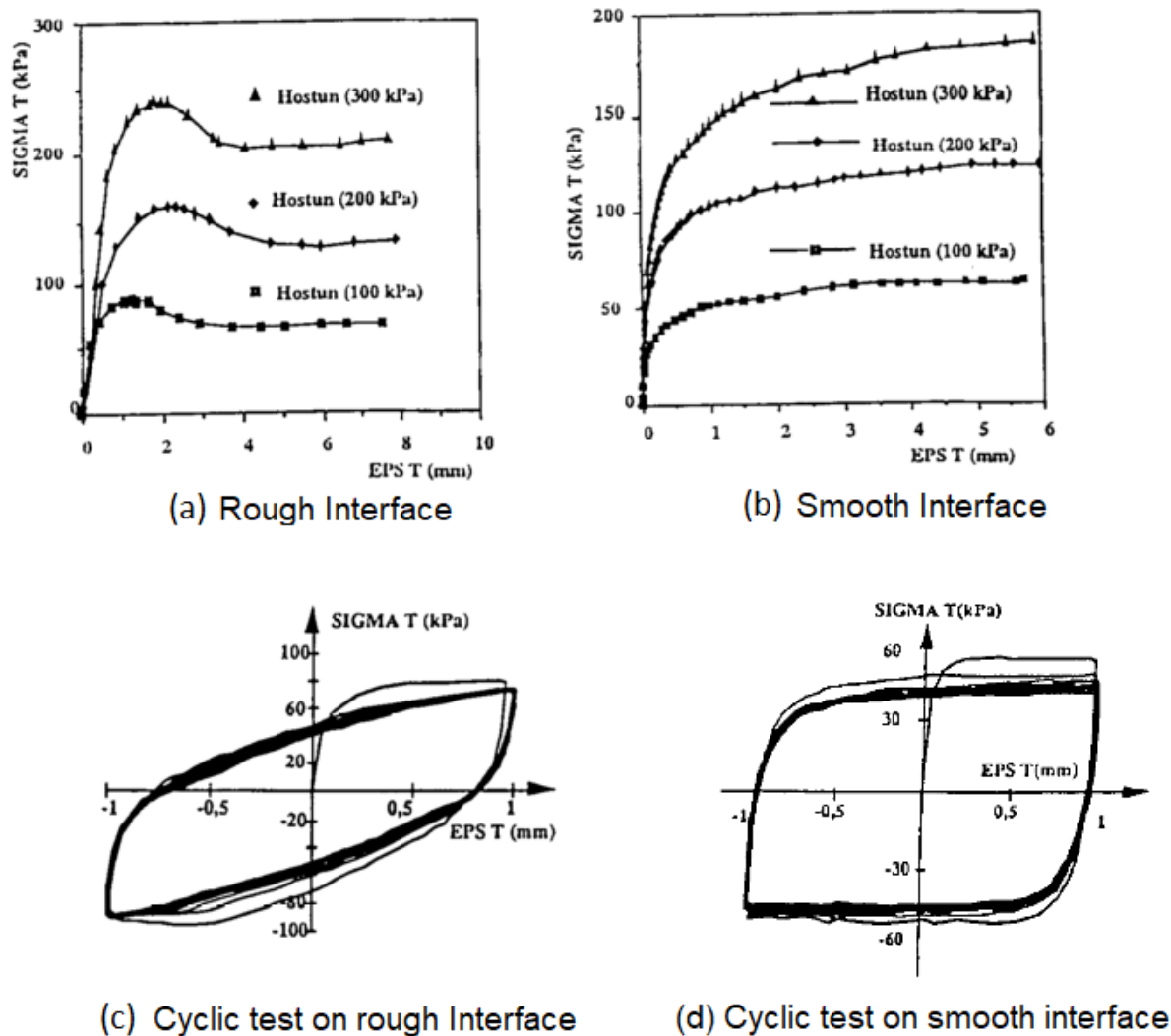


Figure 104.36: (a) and (b) Monotonic and (c) and (d) cyclic test on dense Hostun sand and steel interface(Shahrour and Rezaie (1997)).

contact. This points out one of the difficulties while solving the contact/interface problem i.e. the stiffness matrix changes with active or inactive constraint equations.

As compared to one of the popular Lagrange method, the penalty method leads to non-physical penetration but does not create any additional variables. However, the non-physical penetration could be utilized to model more complicated normal contact/interface force function as such for soft contact/interface shown in Figure ?? and non-linear shear interface models as described in section ??.

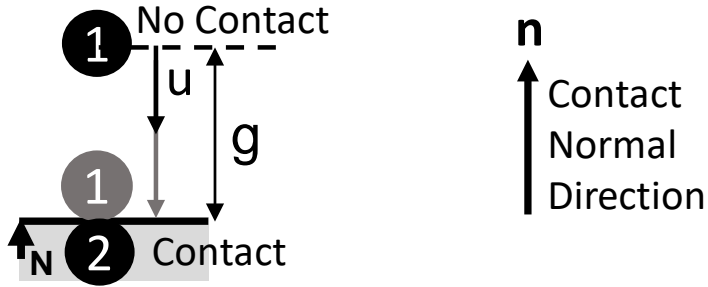


Figure 104.37: Contact/Interface/Joint Node Pairs.

#### 104.7.2.2 Hard Contact/Joint/Interface

In hard contact, the normal penalty stiffness  $k_n$  is assumed to be constant with penetration  $\Delta_n$ . As a result, the normal contact/interface force  $F_n$  or stress  $\sigma_n$  varies linearly with penetration.

$$\begin{aligned} F_n &= k_n \Delta_n \\ \sigma_n &= k_n \epsilon \end{aligned} \tag{104.586}$$

where  $k_n$  represents the normal stiffness between soil-structure interface and  $\Delta_n$  is the penetration in contact/interface normal direction.

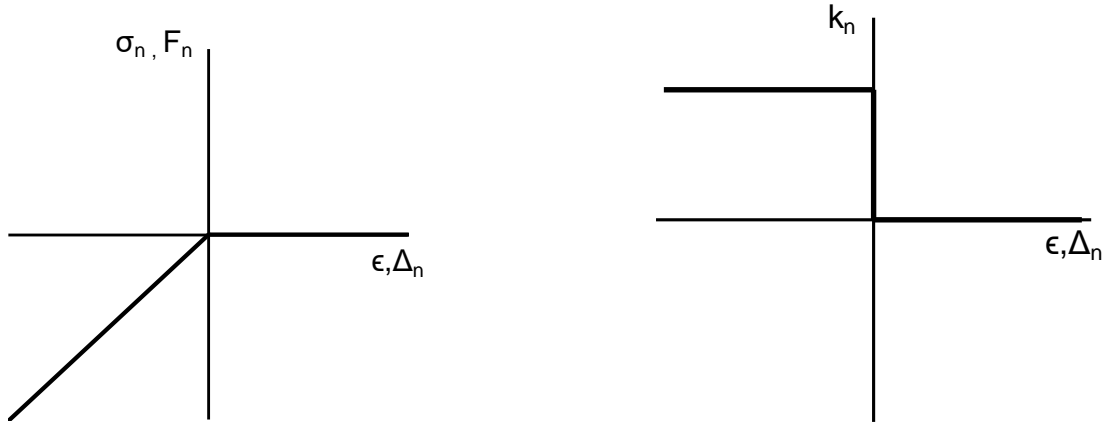
Figure 104.38: Hard contact/interface normal (a) force and (b) stiffness function with penetration  $\Delta_n$ 

Figure 104.38 shows the normal force  $F_n$  or stress  $\sigma_n$  and stiffness  $k_n$  as a function of penetration  $\Delta_n$  or normal strain  $\epsilon$  respectively. The normal stiffness  $k_n$  is assumed to be constant and thus has an abrupt jump or discontinuity at  $\Delta_n = 0$  leading to  $C^0$  continuity. The abrupt change of stiffness could often lead to numerical convergence problems.

### 104.7.2.3 Soft Contact/Joint/Interface

For rocks, (Gens et al., 1990) presented a nonlinear (hyperbolic) function of elastic normal stress with penetration. The function had different stiffness for loading and unloading up-to a permanent deformation  $u_{mc}$ . The hyperbolic function  $u/(u - u_{mc})$  has a singularity at  $u = u_{mc}$ . It does not increase monotonically and does not possess continuous derivatives for  $u \geq 0$ . In FEM since, the stiffness cannot be infinite at  $u = u_{mc}$  and the displacement  $u$  can be greater than  $u \geq u_{mc}$ , which can lead to numerical instability and convergence problems. As per authors knowledge, there has not been enough experimental investigation to understand the normal contact/interface behavior of the soil-structure interface. Desai and Nagaraj (1988) claim to have performed cyclic normal tests on a concrete-soil interface on a shear box but did not show any experimental results. Desai and Nagaraj (1988) idealized the normal behavior based on the critical state soil mechanics as shown in Figure 104.32. (Bandis et al., 1983) investigated the response of fresh and weathered rock. It could be observed that after some (2–4) cycles, the loading and unloading curve fairly overlaps and could be approximated by the same function. More recently, Lei and Barton (2022) presented a very nice set of experiments with data for proper choice of interface parameters.

The normal behavior at the interface being modeled here using penalty stiffness approach, a non-linear exponential elastic function is assumed for the soft contact. The parameters include an initial stiffness  $k_i$  and a stiffening rate  $S_r$  to control the normal stress  $\sigma_n$  function with penetration  $\Delta_n$ . In comparison

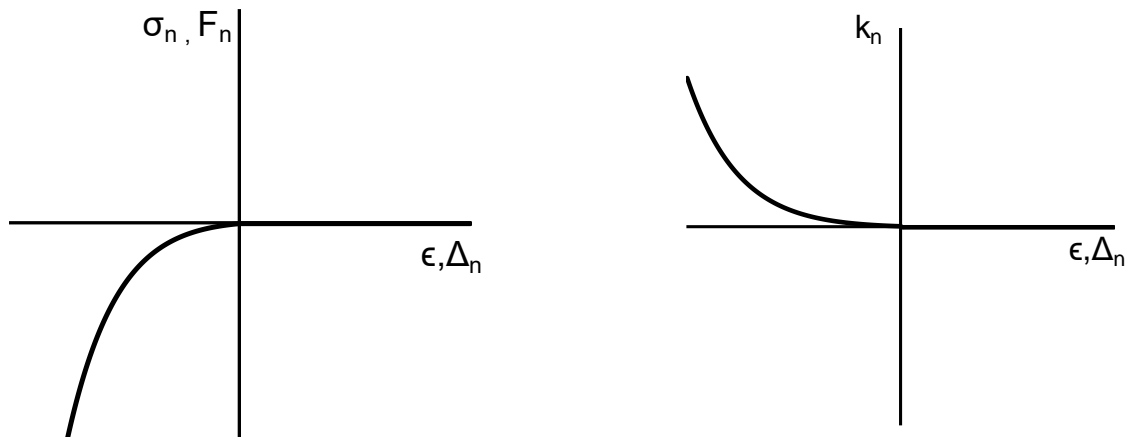


Figure 104.39: Soft contact/interface normal (a) force and (b) stiffness function with penetration  $\Delta_n$

to hard contact, soft contact/interface thus has a smooth exponential, normal contact/interface force function with penetration as shown in Figure ???. The exponential variation is expected to match the realistic increasing contact force with penetration as shown in Figure 104.32. As stated earlier, it must

be noted that in this model the response is assumed to be fully non-linear elastic with no tensile region. As a result, the loading and unloading stiffness and response is the same.

The non-linear normal force  $F_n$  or stress  $\sigma_n$  is defined as:

$$\begin{aligned} F_n &= k_i \exp(-S_r \Delta_n) \Delta_n \\ \sigma_n &= k_i \exp(-S_r \epsilon) \epsilon \end{aligned} \quad (104.587)$$

where  $k_i$  represents the initial normal stiffness between soil-structure interface and  $S_r$  represents the stiffening (or hardening) rate with penetration  $\Delta_n$  or normal strain  $\epsilon$ . Equation 104.587 represents the normal force  $F_n$  and stress  $\sigma_n$  for force based and stress based contact respectively. At soil-foundation interface, as the foundation penetrates more, the soil becomes harder resulting in an increase of interface normal stiffness  $k_n$  and normal stress  $\sigma_n$ . The stiffening rate leads to an exponential increment of contact/interface stress per unit of penetration  $\Delta_n$ . From the above formulation it must be noted that for the stress based contact, the penetration  $\Delta_n$  is replaced with normal strain  $\epsilon$ . Subsequently, the parameters initial normal stiffness  $k_i$  and stiffening rate  $S_r$  should also be calibrated accordingly. Similarly, the stiffness and other derivatives could be obtained by replacing penetration  $\Delta_n$  with normal strain  $\epsilon$ . The normal stiffness  $k_n$  has unit of  $n/m$  for the force based contact/interface and  $Pa$  for the stress based contact.

Equation 104.587 could be differentiated to get the stiffness  $k_n$  as:

$$\begin{aligned} k_n &= k_i \exp(-S_r \Delta_n) (1 - S_r \Delta_n) \\ k_n &= k_i \exp(-S_r \epsilon) (1 - S_r \epsilon) \end{aligned} \quad (104.588)$$

It can be observed from equation 104.588 that putting  $\Delta_n = 0$ , the normal stiffness  $k_n$  becomes equal to initial normal stiffness  $k_i$  i.e.  $k_n = k_i$ . When  $\Delta_n \geq 0$ , the stiffness grows exponentially. Extending Equation 104.587 and 104.588 to uplift (no-contact) ( $\Delta_n \geq 0$ ), with the assumption of small initial stiffness  $k_i$ , the force and stiffness function would lead to  $C^1$  continuity. The  $C^1$  continuity thus would lead to a smooth stiffness function even at the border of contact/interface and non-contact region resulting in quadratic convergence at global FEM level for the Newton-Raphson method. However the non-linear behavior would lead to comparatively larger number of iterations than hard contact,

It is also interesting to note that by setting the stiffening rate  $S_r = 0$ , hard contact/interface can be recovered i.e.  $k_n = k_i$  and  $\sigma_n = k_n \epsilon$ . This demonstrates the generality of soft contact/interface formulation.

The exponential growth of stiffness in finite element method (FEM) can lead to numerical instability for large values. To avoid this, a maximum normal stiffness  $k_n^{max}$  is applied to restrict its further growth. Figure 104.40 shows the stiffness  $k_n$  function with and without a cap. The stiffness function thus can

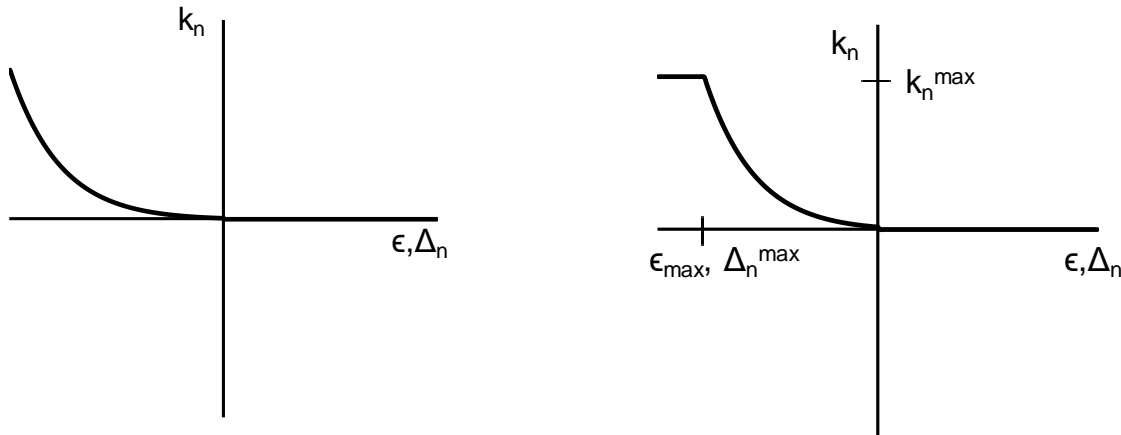


Figure 104.40: Soft Contact Stiffness function (a) without any limit and (b) with limit

be written as:

$$\begin{aligned} k_n &= \max(k_i \exp(-S_r \Delta_n)(1 - S_r \Delta_n), k_n^{max}) \\ k_n^{max} &= k_i \exp(-S_r \Delta_n^{max})(1 - S_r \Delta_n^{max}) \end{aligned} \quad (104.589)$$

For implementing the above Equation 104.589 in FEM, there would be a need to find  $\Delta_n^{max}$  corresponding to maximum allowable normal stiffness  $k_n^{max}$  in order to integrate the stiffness function  $k_n$ . An efficient method to get  $\Delta_n^{max}$  is described in Section 104.7.2.3 below.

**Iterative Method To Find  $\Delta_n^{max}$** . For soft contact/interface implementation in FEM, it would be required to find out  $\Delta_n^{max}$  for a given initial normal stiffness  $k_i$ , stiffening rate  $S_r$  and maximum normal stiffness  $k_n^{max}$ . Since Equation 104.589 is a nonlinear function, an iterative method is needed to get to the solution. One of the best solution search methods is the bisection method, which repeatedly bisects an assumed solution interval, choosing only one of the branches where the solution might exist. In this method, an initial guess of solution space is required.

Theoretically, a large solution space could be given but would not be computationally feasible and optimal. For the given problem, it is often desired to predict solution space to get in as fewer iterations as possible. To reach the solution optimally and efficiently, an initial guess of solution range for penetration  $\Delta_n$  was found to be  $[k_n^{max}/k_i, 0.5k_n^{max}/k_i]$ .

### 104.7.3 Shear Contact/Joint/Interface

#### 104.7.3.1 Interface Shear Zone

At the soil-structure interface, there exists a thin shearing zone of 5-20 times the  $D_{50}$  [Yoshimi and Kishida \(1981\)](#); [Martinez et al. \(2015\)](#); [DeJong et al. \(2006\)](#); [DeJong and Westgate \(2009\)](#) as shown in Figure 104.41. Since the interface constitutive models are defined in stress-strain space, the applied displacements must be converted to strains. Based on the shear zone thickness  $SZ_h$ , the total shear

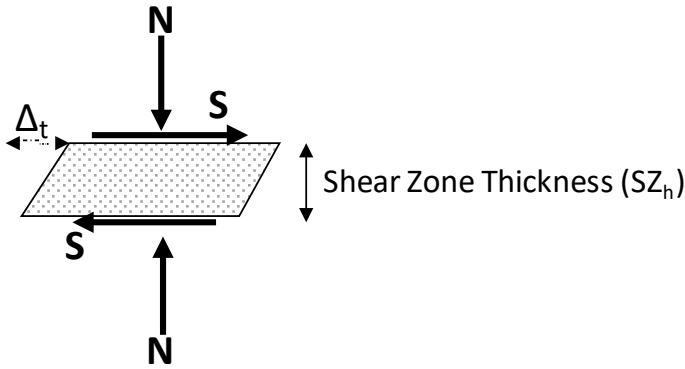


Figure 104.41: Thin shear zone at soil-structure interface

strain  $\gamma$  and incremental shear strain  $\Delta\gamma$  can be calculated as

$$\begin{aligned}\gamma &= \Delta_t/SZ_h \\ \Delta\gamma &= \delta\Delta_t/SZ_h\end{aligned}\tag{104.590}$$

where  $\Delta_t$  and  $\delta\Delta_t$  are the total and incremental shear displacement at the interface between the two soil-structure contact/interface surface.

Similarly, the normal strain  $\epsilon$  and incremental normal strain  $\Delta\epsilon$  can be calculated as

$$\begin{aligned}\epsilon &= \Delta_n/SZ_h \\ \Delta\epsilon &= \delta\Delta_n/SZ_h\end{aligned}\tag{104.591}$$

where  $\Delta_n$  and  $\delta\Delta_n$  are the total and incremental penetration in contact/interface normal direction. In the interface constitutive models, the normal strain  $\epsilon$  is generally also referred as volumetric strain  $\epsilon_v$  [Stutz \(2016\)](#). The normal stress is assumed to offer confinement to the interface shear band. It must be noted that although a shear band of thickness  $SZ_h$  is assumed, the interface element itself has zero thickness. The shear zone thickness  $SZ_h$  is a material parameter for the interface models. The shear zone thickness can vary based on the roughness of the soil-structure interface but could be generally assumed to be around 5-20 mean particle size diameter  $D_{50}$ .

**Shear Contact/Joint/Interface Models.** This section describes three models to describe the non-linear shear interface behavior which is intended to capture some of the actual soil-structure interface response.

Apart from the traditional Mohr-Coulomb i.e. Elastic-Perfectly Plastic Shear (EPPS) model, two additional non-linear models have been proposed. The Non-Linear Hardening Shear (NLHS) is a non-linear Armstrong-Frederick type hardening model where the normalized shear stress parameter  $\mu = \tau/\sigma_n$  increases non-linearly from 0 to residual normalized shear stress  $\mu_r = \tau_r/\sigma_n$ . Non-Linear Hardening Softening Shear (NLHSS) adds one more level of sophistication. It can model the softening of normalized shear stress parameter  $\mu$ . Once the peak normalized shear stress  $\mu_p = \tau_p/\sigma_n$  is attained, it starts to decrease to the residual normalized shear stress  $\mu_r$ . Figure 104.42 shows a typical monotonic response of the three models for a constant normal stress  $\sigma_n$ :

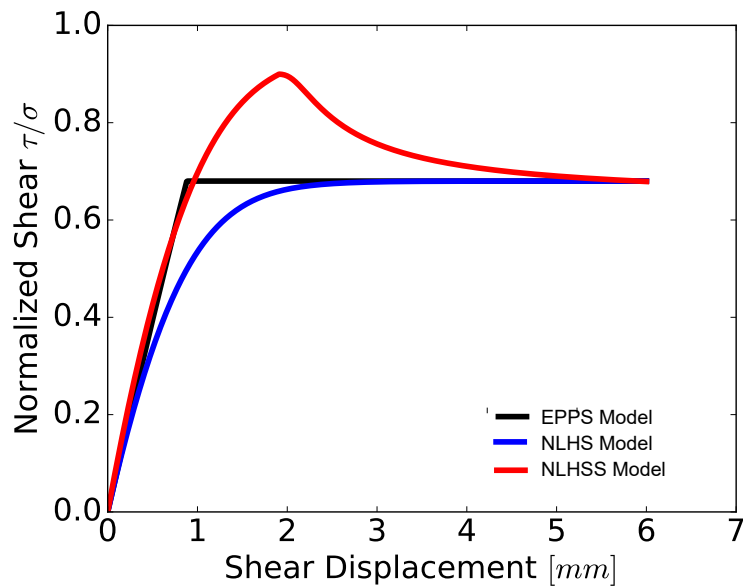


Figure 104.42: Comparison of the interface models with monotonic response

From the Figure 104.42, it can be observed that the models behave quite differently. The EPPS model reaches the residual state at very small shear strain  $\gamma = \Delta_u/SZ_h$  level where as because of non-linear hardening both NLHS and NLHSS reach at larger shear strains  $\gamma$ . EPPS and NLHS do not show any peak behavior whereas NLHSS shows a peak followed by softening to residual strength. The models are explained in detail in the next section. NLHS and NLHSS model assume to have negligible to no elastic region and follow the elasto-plasticity theory. And since, the linear Armstrong-Frederick hardening parameter  $H_a$  is assumed to be equal to the elastic stiffness  $k_t$ , resulting in the overall elasto-plastic stiffness equal to  $0.5k_t$ . The thin shear zone at the soil-structure interface starts to develop plastic deformation as soon as a small shear stress  $\tau$  is applied. It must also be noted in Figure 104.42 that

the elastic shear stiffness  $k_t$  depends upon the normal stress  $\sigma_n$ . Thus, for a given normal stress  $\sigma_n$ , the shear stiffness  $k_t$  is defined as

$$k_t = k_t^{\sigma_n} = (k_t)^{\sigma_{p0}} \frac{\sigma_n}{\sigma_{p0}} \quad (104.592)$$

where  $\sigma_{p0}$  is the constant stress of  $101.3\text{kPa}$  and  $(k_t)^{\sigma_{p0}}$  is the shear stiffness for a normal stress of  $\sigma_n = \sigma_{p0} = 100\text{kPa}$ . The models are thus developed using kinematic hardening plasticity with initial kinematic hardening stiffness  $H_a$  equal to the elastic stiffness  $k_t$ . As stated above, this leads to initial elastic-plastic stiffness equal to  $0.5k_t$  and also results in incremental elastic strain energy equal to the incremental plastic free energy as described in Section ??.

#### 104.7.3.2 Elastic Perfectly Plastic Shear (EPPS) Model

The simplest shear interface model is the Mohr Coulomb interface model with an elastic stiffness under no slippage and zero stiffness when it slips. The material behavior is of type elastic-perfectly plastic type. The yield function ( $f$ ) is thus given as

$$f := \tau - \mu\sigma_n \leq 0 \quad (104.593)$$

where  $\mu$  is a constant coefficient of friction,  $\tau$  is the shear stress and  $\sigma_n$  is the normal stress.

Figure 104.43 shows the performance of EPPS model for different loading conditions. Since it is a elastic perfectly-plastic model, the shear stiffness  $k_t$  is constant with shear strain  $\gamma$  or displacement  $\Delta_t$  and becomes zero (perfectly-plastic state) when it reaches its residual friction coefficient  $\mu_r$ . Figure 104.43(a) and 104.43(c) shows the monotonic and full cyclic response with elastic perfectly-plastic behavior respectively. Figure 104.43(b) and 104.43(d) shows the monotonic cyclic behavior before and after reaching the residual friction coefficient  $\mu_r$ . This kind of interface behavior is mostly observed between rigid surfaces in contact. For more realistic soil-structure interface non-linear yield function should be used as described in the coming sections.

#### 104.7.3.3 Nonlinear Hardening Shear (NLHS) Model

In this model, the normalized shear stress hardening variable  $\mu$  increases from 0 to critical or residual normalized shear stress  $\mu_r$  using the non-linear Armstrong Frederick type hardening law. The evolution rule for frictional hardening variable  $\mu$  is given as

$$\Delta\mu = k_t \Delta\gamma^p - \frac{k_t}{\mu_r} |\Delta\gamma^p| \mu \quad (104.594)$$

where  $k_t$  is the non-linear elastic hardening variable and  $\Delta\gamma^p$  is the plastic part of the shear strain  $\Delta\gamma$ . The material behavior is thus of type non-linear hardening type.

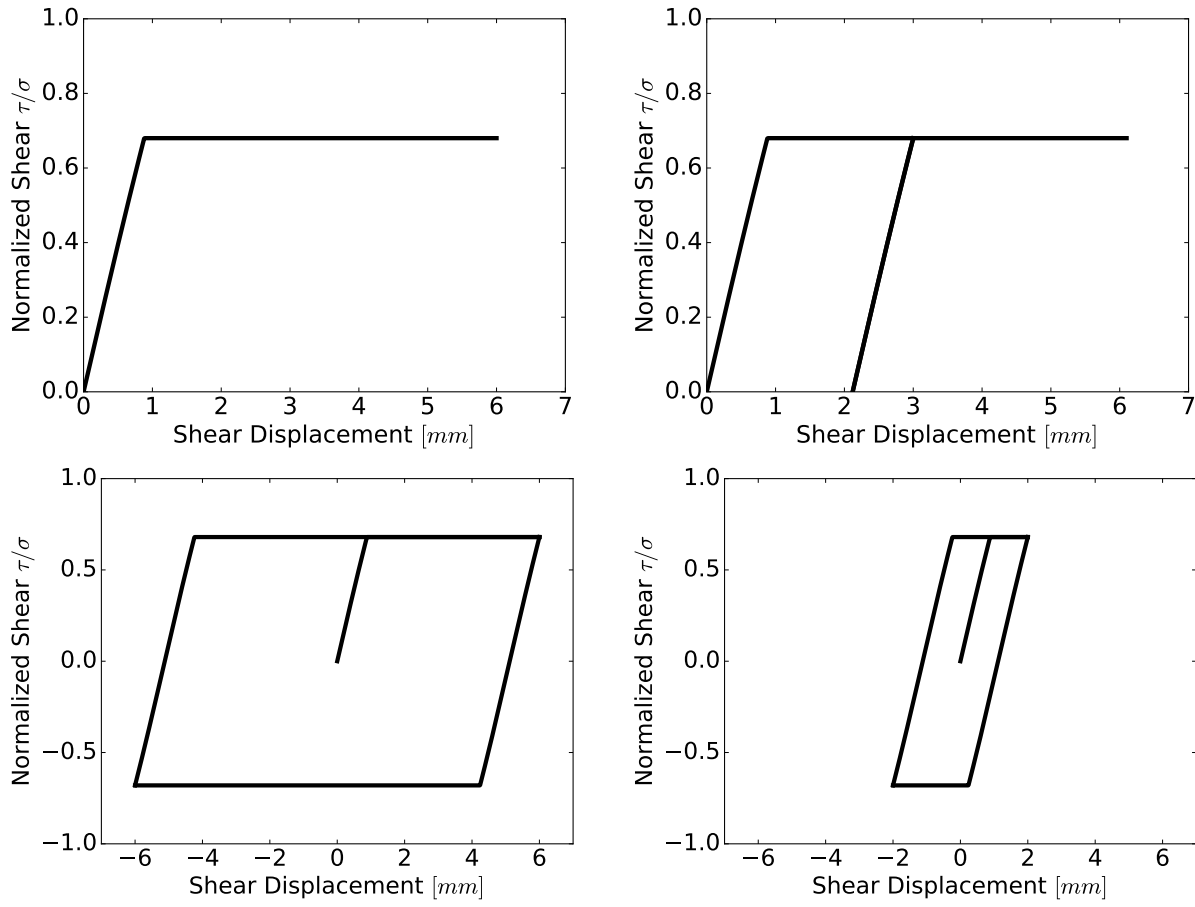


Figure 104.43: Response of Linear Elastic Perfectly Plastic Shear (EPPS) Model with normal stress of  $100kPa$ , residual coefficient of friction  $\mu_r = 0.68$ , shear stiffness  $k_t = 200kPa$  and shear zone length  $SZ_h = 5mm$ .

The yield function ( $f$ ) is still given as

$$f := \tau - \mu\sigma_n \leq 0 \quad (104.595)$$

where the normalized shear stress hardening variable  $\mu$  evolves by Equation 104.594,  $\tau$  is the shear stress and  $\sigma_n$  is the normal stress.

Figure 104.44 shows the performance of NLHS model for different loading conditions. It can be observed that the hardening variable  $\mu$  increases non-linearly from 0 to residual normalized shear stress ratio  $\mu_r$  at large shear displacements. As compared to the EPPS models, it is more realistic as the soil-structure interface develops the shear strength gradually with increments of shear strain  $\Delta\gamma$  or shear displacements  $\Delta_t$ .

For loose or low relative density  $D_r$  soil at soil-structure interface Fakharian and Evgen (1996);

Shahrour and Rezaie (1997) as shown in Figure 104.34(b) and 104.36(b), this model could be calibrated to model the non-linear hardening response. The monotonic and full cyclic response of this model shown in Figure 104.44(b) can be seen to match the interface behavior investigated by Uesugi et al. (1989) and is shown in Figure ???. Figure 104.44(d) shows the response of the model subject to cyclic shearing before reaching the residual strength. It could be observed that it is able to model the non-linear interface behavior as investigated by Fakharian and Evgin (1996); Shahrour and Rezaie (1997) which is shown in Figure 104.35 and Figure 104.36(c) respectively.

For dense soil with higher relative density  $D_r$ , it is important to model the peak normalized shear stress  $\mu_p$ , followed by the softening behavior until the residual shear stress  $\mu_r$  is reached. The NLHSS model proposed in next section can be used to model both hardening and softening.

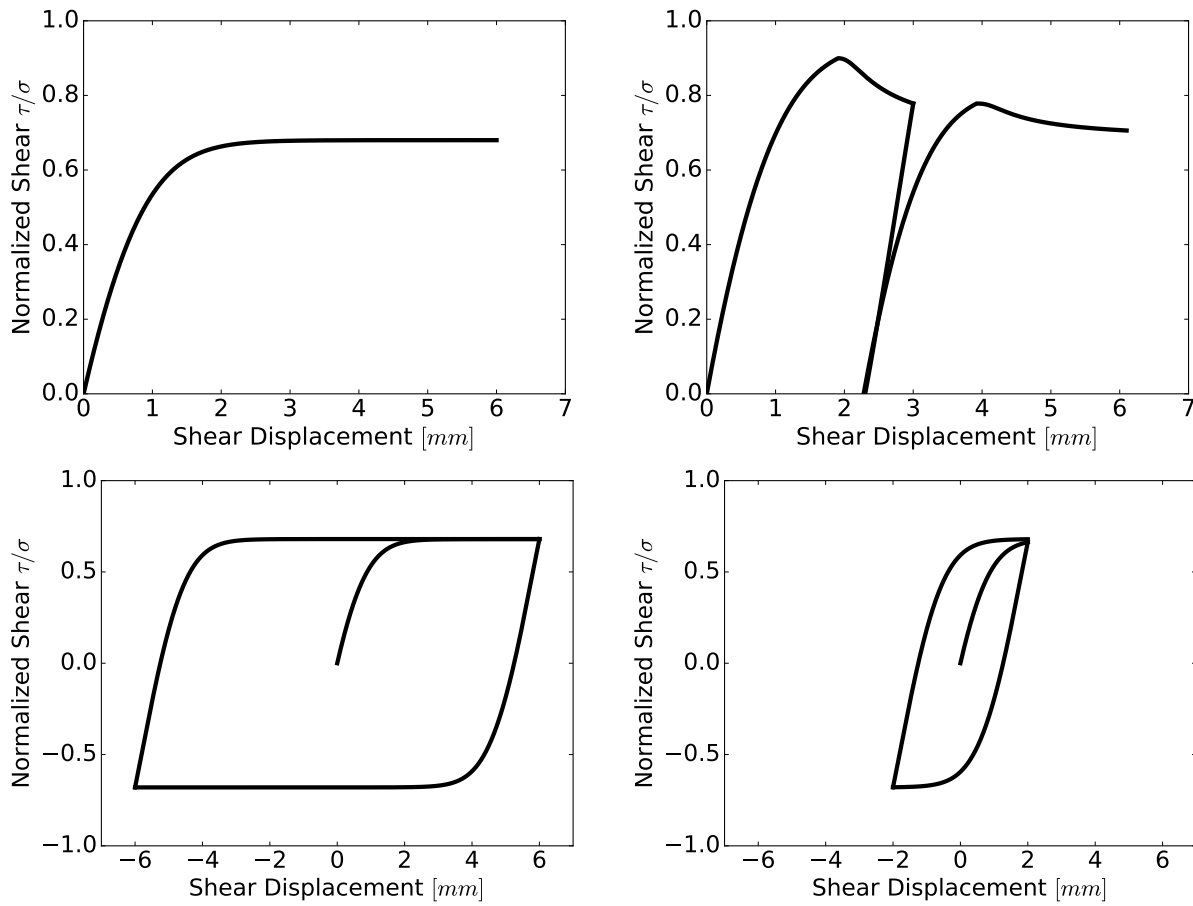


Figure 104.44: Response of Non-Linear Hardening Plastic Contact/Joint/Interface (NLHS) model with normal stress of  $100kPa$ , residual normalized shear stress of  $\mu_r = 0.68$ , shear stiffness  $k_t = 400kPa$  and shear zone length  $SZ_h = 5mm$ .

#### 104.7.3.4 Nonlinear Hardening Softening Shear (NLHSS) Model

In this model, the normalized shear stress hardening/softening variable  $\mu$  increases from 0 to its peak limit  $\mu_p$  and then with more shear displacement reaches to the residual normalized shear stress of  $\mu_r$  using a non-linear Armstrong Frederick type hardening/softening law. The evolution of the hardening/softening variable  $\mu$  during hardening phase is given as

$$\Delta\mu = k_t \Delta\gamma^P - \frac{k_t}{\mu_p} |\Delta\gamma^P| \mu \quad (104.596)$$

where  $k_t$  is the non-linear hardening variable and  $\Delta\gamma^P$  is the the plastic part of incremental shear strain  $\Delta\gamma$ . Once the peak normalized shear stress is attained, the material starts to soften. The softening behavior is modeled as reduction of normalized shear stress ratio  $\mu$  as

$$\Delta\mu = -\frac{n * b(\mu_p - \mu_r)}{(\pi/2)^n \theta^{1/n-1}} * \cos^2 \theta \Delta\gamma^P \quad (104.597)$$

$$\theta = \frac{\mu_p - \mu}{\mu_p - \mu_r} (\pi/2)^n \quad (104.598)$$

where  $b$  is the softening rate,  $\Delta\gamma^P$  is the incremental plastic shear strain and  $n$  represents the size of the peak plateau as shown in Figure 104.45. This incremental form of softening phase is derived from the inverse tangent function raised to power  $n$  as

$$f = a * (\arctan(b * \gamma^P))^n \quad (104.599)$$

where  $a$  is a constant parameter of the function and in Equation 104.598 is equal to  $(\mu_p - \mu)/(\mu_p - \mu_r)$ . The softening rate parameter  $b$  represents the rate at which the normalized shear stress  $\mu_p$  decreases with further application of shear displacement  $\Delta_t$  as shown in Figure 104.45. A larger value of  $b$  would result in faster decay. The size of peak plateau parameter  $n$  determines the size of the plateau formed at the peak as shown in Figure 104.45. A larger value of  $n$  would result in a larger plateau. It must be noted that the peak plateau size parameter  $n$  also influences the overall rate of softening as could be seen from the derived incremental Equation 104.598. The parameters  $n$  and  $b$  can be calibrated from monotonic shearing tests. Figure 104.46 shows the response of the model with the peak plateau size parameter  $n = 4$  and softening rate parameter  $b = 40$ .

The yield function ( $f$ ) is again given as

$$f := \tau - \mu \sigma_n \leq 0 \quad (104.600)$$

where  $\mu$  is a normalized shear stress hardening/softening variable evolved by Equation 205.17 and 104.598,  $\tau$  is the shear stress and  $\sigma_n$  is the normal stress.

Since in the model, the hardening law is defined as Armstrong-Frederick type, the peak shear stress ratio  $\mu_p$  is defined as only 95% of the asymptotic limit of the Equation 205.17. Thus, the asymptotic

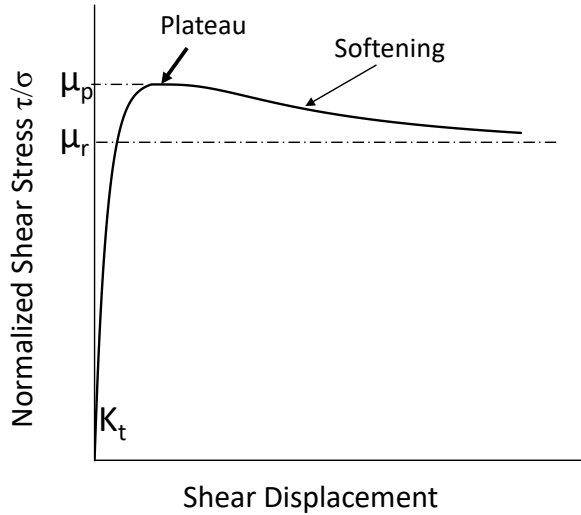


Figure 104.45: Non-Linear Hardening Softening Shear model parameters

limit of Armstrong-Frederick type hardening is raised by a factor of 1/0.95 times the peak shear stress ratio  $\mu_p$ .

In this model during cyclic shearing, it is assumed that once the peak strength is passed, the material would not be able to again attain the peak strength during cyclic loading. It is based on the assumption that as the material passes the peak strength, particle breakage and smoothening of the surface takes place which cannot be recovered back by any process. Thus as the material softens, the peak coefficient of friction  $\mu_p$  is iteratively redefined to the coefficient of friction  $\mu$  in the softening phase. This effect can also be observed from the tests performed by Uesugi et al. (1989) as shown in Figure ??(b). As soon as the peak shear stress ratio  $\mu_p$  degrades to residual strength in the first cycle, other cycles follow the residual shear stress ratio  $\mu_r$ .

Figure 104.44 shows the performance of NLHSS model for different loading conditions. The response of the model is very close to the realistic interface behavior observed by Uesugi et al. (1989) as shown in Figure ??(b) . During cyclic shearing shown in Figure 104.44(c), the model predicts the peak behavior only in the first cycle. After that, the response is governed by the residual normalized shear stress  $\mu_r$ . Figure 104.44(c) shows the cyclic shearing behavior when the residual normalized shear stress  $\mu_r$  is not attained in the first cycle. As a result of unloading and reloading, it again attains the last peak normalized shear stress  $\mu_p$  that it had attained during the softening phase.

NLHSM can be extended further to model the variation of peak normalized shear stress  $\mu_p$  for different normal stress  $\sigma_n$  conditions as observed in tests by Fakharian and Evgin (1996); Shahrou and Rezaie (1997); Evgin and Fakharian (1997); Fakharian and Evgin (1997); Fakharian (1996); Fakharian

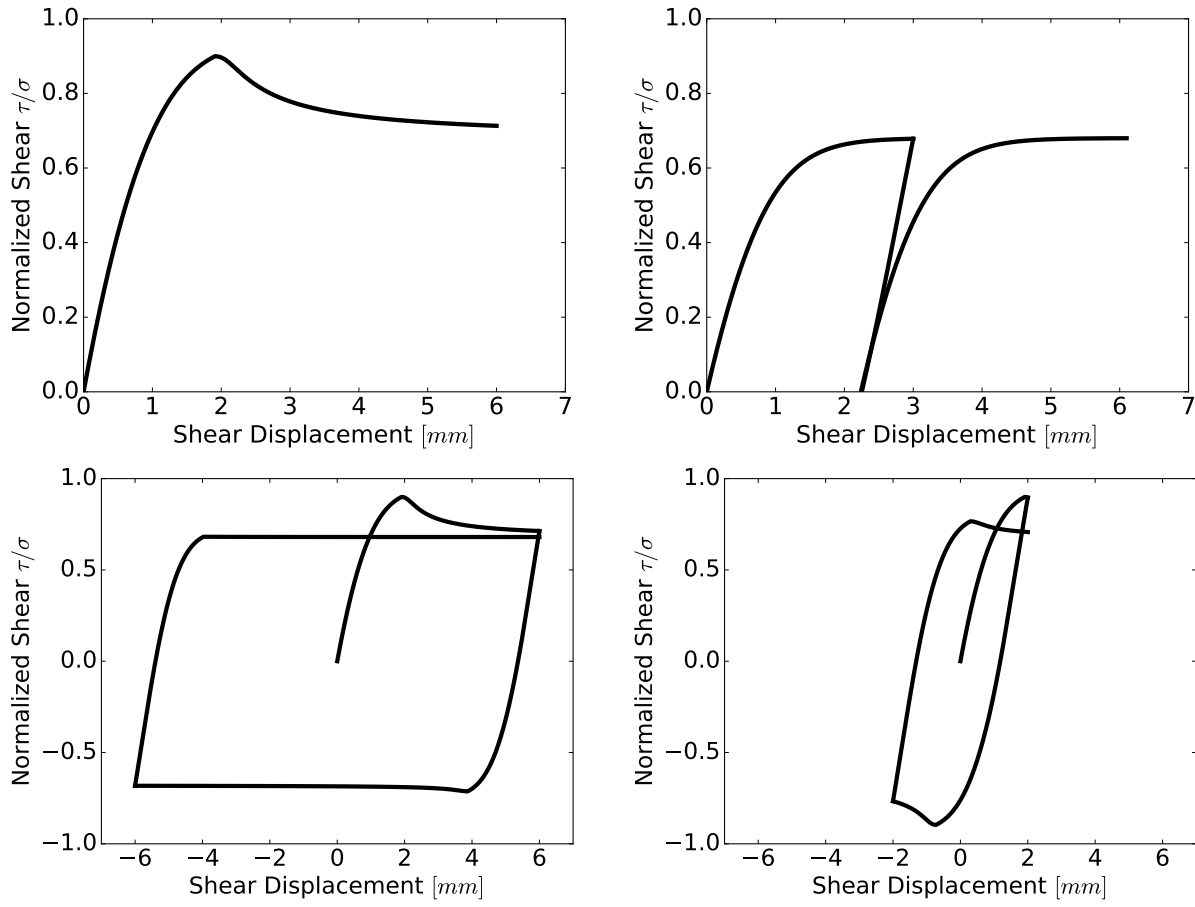


Figure 104.46: Response of Non-Linear Hardening Softening Shear (NLHSS) model with normal stress of  $100kPa$ , residual normalized shear stress  $\mu_r = 0.68$ , peak normalized shear stress  $\mu_p = 0.9$ , shear stiffness  $k_t = 800kPa$ , peak-plateau parameter  $n = 4$ , softening rate parameter  $b = 40$  and shear zone length  $SZ_h = 5mm$ .

et al. (2002). For a given relative density  $D_r$  of soil in the sheared zone, the peak normalized shear stress  $\mu_p$  can be generalized to be a logarithmic function of normal stress  $\sigma_n$  as

$$\mu_p = \mu_{p0} - k * \log(\sigma_n/P_0) \quad (104.601)$$

where  $\mu_{p0}$  is the peak normalized shear stress at normal stress of  $\sigma_n = P_0$ ,  $k$  is the peak normalized shear stress rate of decrease and  $P_0$  is the reference stress of  $P_0 = 100kPa$ . This is similar to the Bolton (1986) stress-dilatancy relationship observed in sands. In the above Equation 104.601, for the normal stress of  $\sigma_n \leq P_0$ , the peak normalized shear stress  $\mu_p$  would become greater than  $\mu_{p0}$  as the term  $\log(\sigma_n/P_0)$  becomes negative. This would result in high peak normalized shear stress  $\mu_p$  for low confining stress  $\sigma_n$ . As a result, the peak normalized shear stress  $\mu_p$  needs to be restricted to a value. In this model,

it is assumed that  $\mu_{p0}$  would also act as the maximum possible peak normalized shear stress  $\mu_p$  for low normal stresses or confinement. Thus the above Equation 104.601 can be re-written with the limit on peak normalized shear stress  $\mu_p$  as

$$\mu_p = \max(\mu_{p0}, \mu_{p0} - k * \log(\sigma_n/P_0)) \quad (104.602)$$

where  $\mu_{p0}$  also represents the maximum peak normalized shear stress  $\mu_p^{max}$ , that the sheared zone soil could attain. Thus, with experiments conduction for different normal stress  $\sigma_n$ , the peak normalized shear stress  $\mu_p$  can be calibrated as the function of normal stress  $\sigma_n$  with peak normalized shear stress limit  $\mu_{p0}$  and peak normalized shear stress rate of decrease  $k$ . Figure ?? shows the response of the model for different normal loads of 100kPa, 250kPa and 500kPa and also validates the model with the experimental results from [Fakharian and Evgin \(1996\)](#) as shown in Figure 104.34.

Extending The Models to 3D . Section ?? described the model in 2-D in  $\tau - \sigma_n$  space, to make the reader understand the basics of the model. The model can be easily extended to 3-D using the back stress variable  $\alpha$  instead of the normalized shear stress  $\mu$  for NLHS and NLHSS models. In 3-D, there would be normal stress component  $\sigma_n$  in contact/interface normal direction  $n$  and two tangential stress components  $\tau_1$  and  $\tau_2$  in tangential contact/interface plane in directions 1 and 2 respectively. Similarly, the shear strain  $\gamma$  has two components as  $\gamma_1$  and  $\gamma_2$  in the two tangential directions 1 and 2 respectively. As stated earlier, since normal interface behavior is assumed to be non-linear elastic, the plastic strains are only developed in shear. Thus the incremental plastic strain  $\Delta\gamma^p$  and its magnitude  $|\Delta\gamma^p|$  in these models is defined as

$$|\Delta\gamma^p| = \sqrt{\Delta\gamma_1^p \Delta\gamma_2^p} \quad (104.603)$$

$$\Delta\gamma^p = [\Delta\gamma_1^p, \Delta\gamma_2^p] \quad (104.604)$$

where  $\Delta\gamma_1^p$  and  $\Delta\gamma_2^p$  represents the incremental plastic shear strain components in contact/interface tangential (shear) direction 1 and 2 respectively. The plastic flow direction  $m$  is defined as the direction of incremental plastic shear strain  $\delta\gamma^p$  and thus is defined as  $m = \delta\gamma^p / |\Delta\gamma^p|$

#### 104.7.3.5 EPPS Model

EPPS Model described in Section 104.7.3.2, is the simplest Mohr Coulomb type elastic perfectly-plastic model. The yield function ( $f$ ) is defined as

$$f := (\tau_1/\sigma_n - \mu_r)^2 + (\tau_2/\sigma_n - \mu_r)^2 = 0 \quad (104.605)$$

where  $\sigma_n$  is the normal stress,  $\tau_1, \tau_2$  are the shear stress and  $\mu_r$  is the residual friction coefficient. Being an elastic-perfectly plastic model with no internal variables, there is no hardening/softening evolution rule.

#### 104.7.3.6 NLHS Model

The non-linear hardening shear model described in Section 104.7.3.3 is modeled in 3-D using the back stress internal variable  $\alpha$ . The yield function ( $f$ ), is defined as

$$f := (\tau_1/\sigma_n - \alpha_1)^2 + (\tau_2/\sigma_n - \alpha_2)^2 = 0 \quad (104.606)$$

where  $\sigma_n$  is the normal stress,  $\tau_1, \tau_2$  are the shear stress and  $\alpha_1, \alpha_2$  are the back stress components in contact/interface tangential direction 1 and 2 respectively on the contact-interface plane. The hardening law would be then defined as

$$\Delta\alpha = k_t \Delta\gamma^p - \frac{k_t}{\mu_p} |\Delta\gamma^p| \alpha \quad (104.607)$$

$$\Delta\alpha = H_m |\Delta\gamma^p| \quad (104.608)$$

$$H_m = k_t m - \frac{k_t}{\mu_p} \alpha \quad (104.609)$$

where  $\mu_p$  is the peak normalized shear stress, which depends upon the normal stress  $\sigma_n$  as stated in Equation 104.601 and  $k_t$  represents the initial elastic shear stiffness of soil-structure interface.  $H_m$  represents the non-linear Armstrong-Frederick type hardening modulus and  $m$  represents the plastic flow direction.

#### 104.7.3.7 NLHSS Model

The non-linear hardening softening shear model described in Section 104.7.3.4 is also modeled in 3D using the back stress internal variable  $\alpha$ . The yield function ( $f$ ) is defined as Equation 104.606. The hardening evolution law for the back stress  $\alpha$  is defined by Equation 104.609. The softening law is defined as Von-Mises type as

$$\Delta\alpha = -\frac{n * b(\mu_p - \mu_r)}{(\pi/2)^n \theta^{1/n-1}} * \cos^2 \theta \Delta\gamma^p \quad (104.610)$$

$$\theta = \frac{\mu_p - |\alpha|}{\mu_p - \mu_r} (\pi/2)^n \quad (104.611)$$

$$\Delta\alpha = S_m \Delta\gamma^p \quad (104.612)$$

$$S_m = -\frac{n * b(\mu_p - \mu_r)}{(\pi/2)^n \theta^{1/n-1}} * \cos^2 \theta \quad (104.613)$$

where  $\mu_r$  is the residual normalized shear stress that is constant and depends upon the soil and structure material,  $\mu_p$  is the peak normalized shear stress at the start of softening phase and  $S_m$  represents the softening modulus.

As stated in Section 104.7.3.4, for NLHSS model, the peak normalized shear stress  $\mu_p$  of the material is iteratively defined to the back stress  $\mu_p = |\alpha|$  in softening phase. This means that the dilatancy surface squeezes towards the critical surface as the sheared zone soil at interface continues to shear.

Using the incremental Equation 104.609 Equation 104.613 presented for both hardening and softening phase respectively, the 3-D model can be integrated. using the elastic-plastic theory Hill (1950); Temam (1985); Wu Tai (1966); Lubliner (1990); de Borst and Fennstra (1990); de Borst (1987). The elastic-plastic stiffness or consistent tangent stiffness Jeremić (1994); Crisfield (1987) can then be computed easily at each loading increment or iteration. Section ?? presents the elastic-plastic integration for the interface models.

## 104.8 Inelastic Behavior and Models for Rock

### 104.8.1 Overview of Intact Rock Behavior

(Stavrogin et al., 2001), (Fairhurst, 2003), (Mogi, 2006)

Rock, and other geomaterials, feature a distinct set of material behavior that separates them from other natural and/or man made materials. Rock material subjected to shock waves in particular shows a variety of response regimes and behavior that warrant further discussion. Of particular interest are the following specifics of rock behavior: pressure sensitivity, dilative and compactive response, inherent and induced anisotropy, full coupling of porous rock solid with pore fluid and temperature fields and bifurcation response, resulting in shear and compaction bands. Each of these aspects of rock behavior will be described in sections below.

It is also very important to note that this study will focus on behavior of intact rock material, while main focus of research in rock mechanics is on behavior of jointed rock masses. While behavior of discontinuous, jointed rock mass is very important for construction in rock (tunnels, dams, foundations...), behavior of intact rock mass becomes very important for any modeling and simulation of deeper rock structures, particularly where strong shock waves are involved. This is emphasized by the fact that rock blocks do behave like solid for high pressures. For example, during shock loading blocks might fuse at contact/interface and behave like a solid, in which case the inelastic (elastic-plastic) behavior of intact rock mass has major impact on overall rock mass response.

This section uses selection of published results to emphasize distinct features of mechanical response of rock that are considered important for proper modeling of shock wave propagation. While there exist

a significant body of published work on behavior of intact rock (which is still much smaller than body of published work on behavior of rock as discrete media), chosen here are publications and results that provide important results used to emphasize distinct features of mechanical behavior of rock. Emphasizing these distinct feature of rock behavior is important for a number of reasons. Two main reasons are that while the shock wave theory was developed over last two centuries (see brief overview in section 104.8.3) main focus was on ideal domains (linear elastic solids or fluids), rock features many distinct modes of mechanical response that demand use of high fidelity numerical modeling. In addition to that, even when shock wave theories were developed for inelastic (elastic-plastic) solids, this was done for metals, elastic-plastic response of which lacks many features found in rock (geomaterial) response (pressure sensitivity, anisotropy, dilative and compactive response...)

### 104.8.1.1 Pressure Sensitivity

Rock material response shows strong pressure sensitivity. Both initial yielding response, inelastic response and ultimate strength strongly depend on confinement pressure experienced by rock material. Confinement pressure acting on rock can be inherent, coming from location of rock mass (depth) and from geologic factors (tectonics). [Fairhurst \(2003\)](#) details initial stress determination procedures. Initial stress determination (stress level from previous, historical loading stages, tectonics, erosion) is very important in view of pressure sensitivity and elastic-plastic response of rock. Depending on the type of rock material, the effects of confinement pressure on response vary. Figures [104.47 – 104.55](#)) show test data for a full elastic-plastic response of various rock specimens for varying confinement pressures. Both axial ( $\epsilon_1$ ) and radial ( $\epsilon_2$ ) strains are shown versus axial stress ( $\Delta\sigma_1$ ). It is very important to recognize a number of distinct features of rock behavior that these test show:

- Varying confinement pressure influences yield stress, that is an increase of yield stress is observed with the increase in confinement pressure,
- Elastic stiffness increases with increase in confinement pressure,
- Ductility increases with increase in confinement pressure,
- Increase in confinement pressure significantly influences final strain level achieved
- Volume change (dilation, as observed from radial strain results ( $\epsilon_2$ ) is significant, however, in some cases it increases and in some decreases with confinement pressure increase (as observed in Figures [104.47 – 104.52](#))
- Elastic degradation/damage is increasing with cycles of loading (Fig. [104.54](#) for example, reduction of loading-unloading-reloading slope signifies elastic damage)
- Presence of energy dissipation in rock for various confinement pressures (area of hysteresis loops, see for example Fig. [104.53 – 104.55](#))

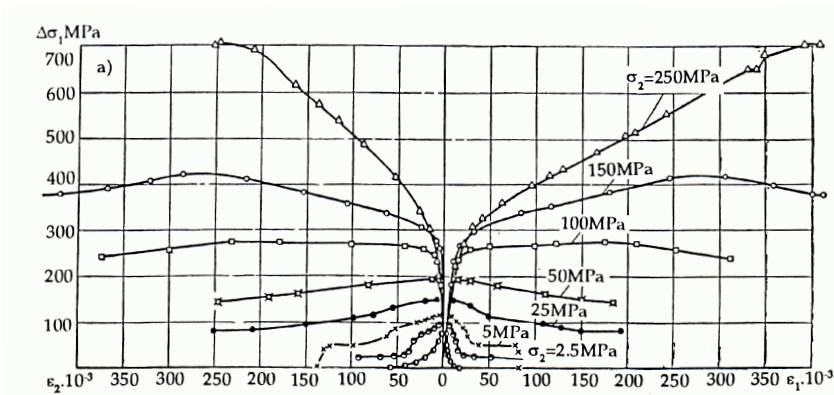


Figure 104.47: Full elastic-plastic response of marble specimens for varying confinement pressures. Shown are axial ( $\epsilon_1$ ) and radial ( $\epsilon_2$ ) strains versus axial stress ( $\Delta\sigma_1$ ) for triaxial loading of 3D samples (Stavrogin et al., 2001).

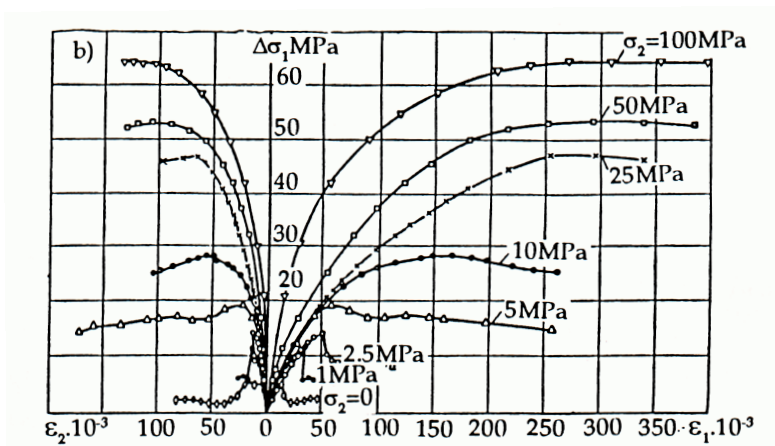


Figure 104.48: Full elastic-plastic response of lignite specimens for varying confinement pressures. Shown are axial ( $\epsilon_1$ ) and radial ( $\epsilon_2$ ) strains versus axial stress ( $\Delta\sigma_1$ ) for triaxial loading of 3D samples (Stavrogin et al., 2001).

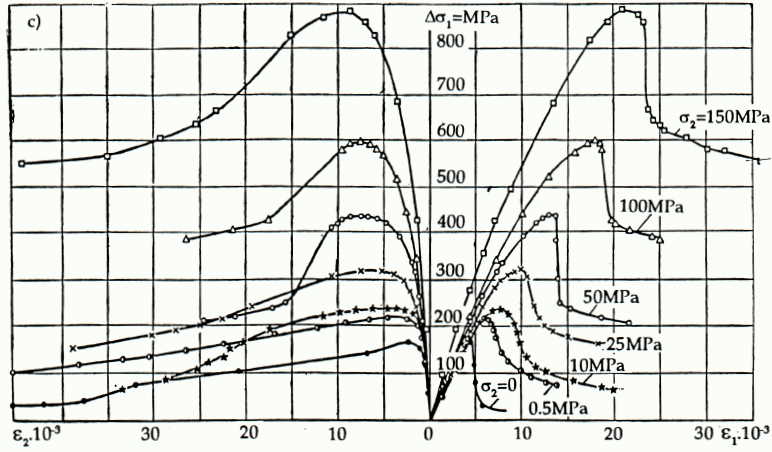


Figure 104.49: Full elastic-plastic response of granite specimens for varying confinement pressures. Shown are axial ( $\epsilon_1$ ) and radial ( $\epsilon_2$ ) strains versus axial stress ( $\Delta\sigma_1$ ) for triaxial loading of 3D samples (Stavrogin et al., 2001)

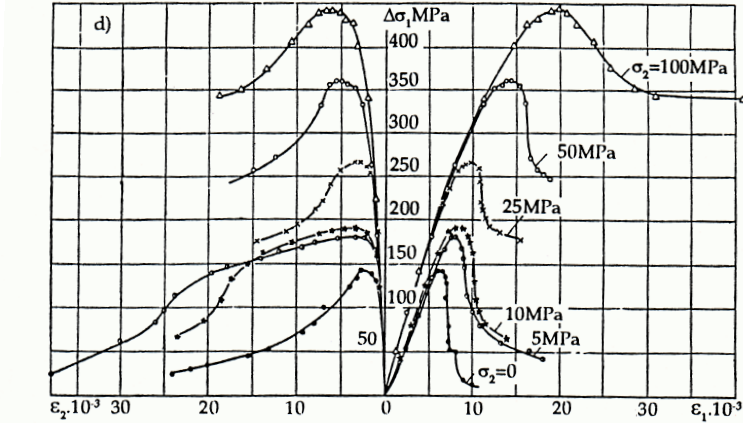


Figure 104.50: Full elastic-plastic response of sandstone (non-burst prone) specimens for varying confinement pressures. Shown are axial ( $\epsilon_1$ ) and radial ( $\epsilon_2$ ) strains versus axial stress ( $\Delta\sigma_1$ ) for triaxial loading of 3D samples (Stavrogin et al., 2001).

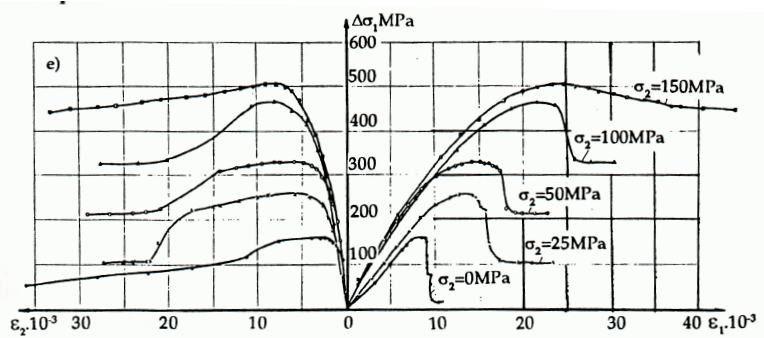


Figure 104.51: Full elastic-plastic response of sandstone (burst prone) specimens for varying confinement pressures. Shown are axial ( $\epsilon_1$ ) and radial ( $\epsilon_2$ ) strains versus axial stress ( $\Delta\sigma_1$ ) for triaxial loading of 3D samples (Stavrogin et al., 2001).

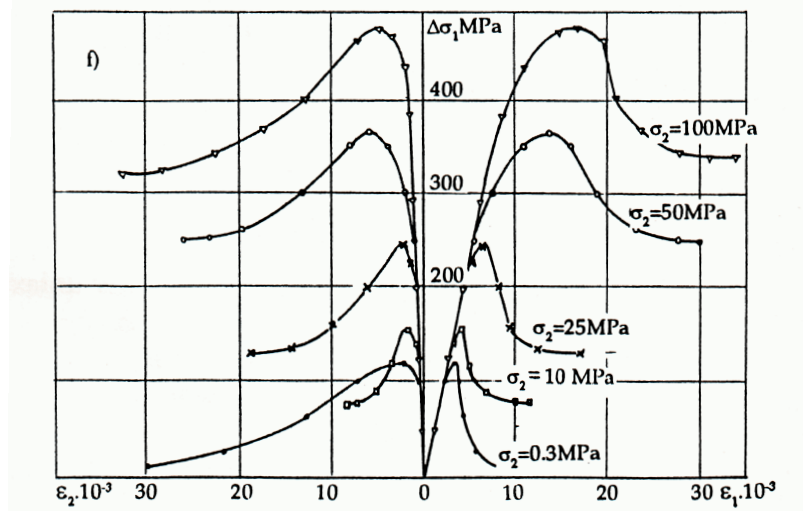


Figure 104.52: Full elastic-plastic response of sulphidic ore specimens for varying confinement pressures. Shown are axial ( $\epsilon_1$ ) and radial ( $\epsilon_2$ ) strains versus axial stress ( $\Delta\sigma_1$ ) for triaxial loading of 3D samples (Stavrogin et al., 2001).

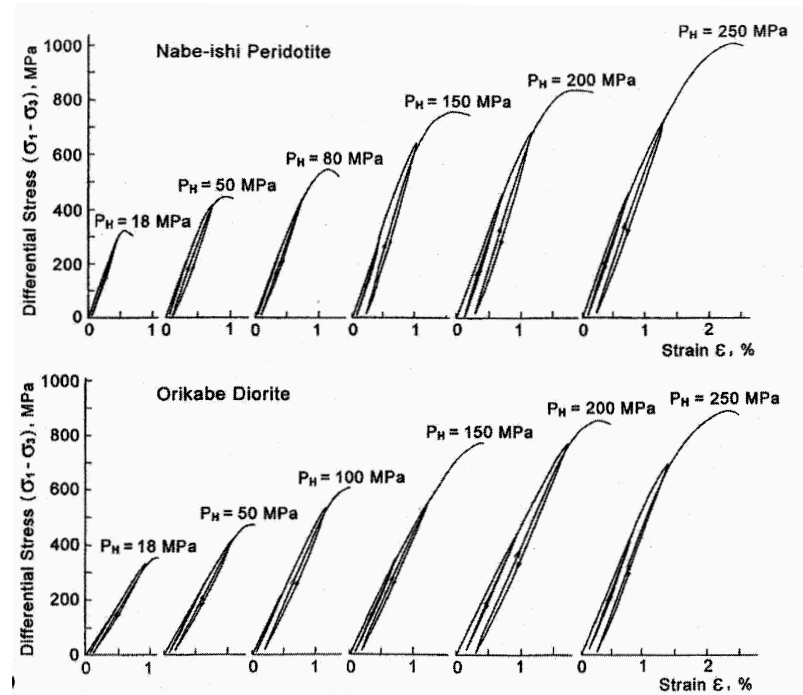


Figure 104.53: Full elastic-plastic response, with loading-reloading cycles of Periodite (upper) and Diorite (lower) specimens for varying confinement pressures. Shown are axial ( $\epsilon_1$ ) strains versus differential stresses ( $\sigma_1 - \sigma_3$ ) for triaxial loading of 3D samples (Mogi, 2006).

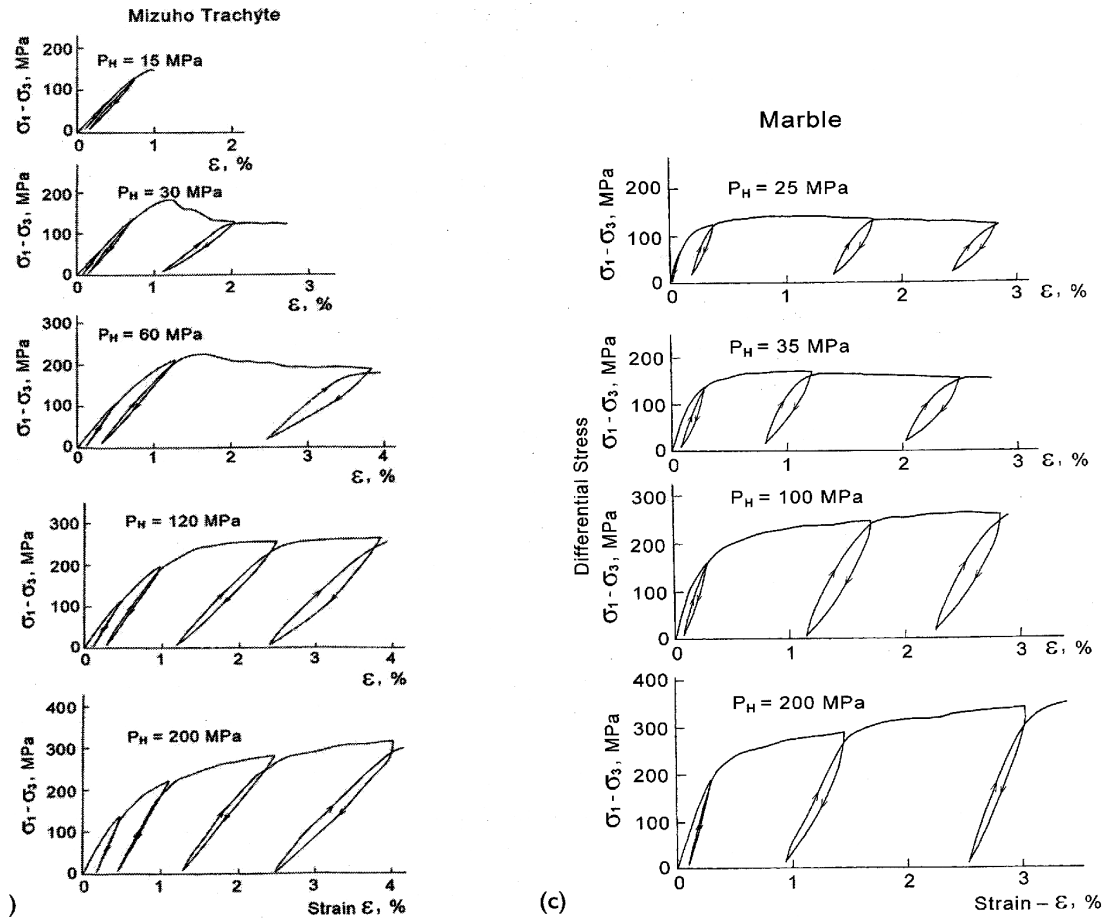


Figure 104.54: Full elastic-plastic response, with loading-reloading cycles of Trachite (left) and Marble (right) specimens for varying confinement pressures. Shown are axial ( $\epsilon_1$ ) strains versus differential stresses ( $\sigma_1 - \sigma_3$ ) for triaxial loading of 3D samples (Mogi, 2006).

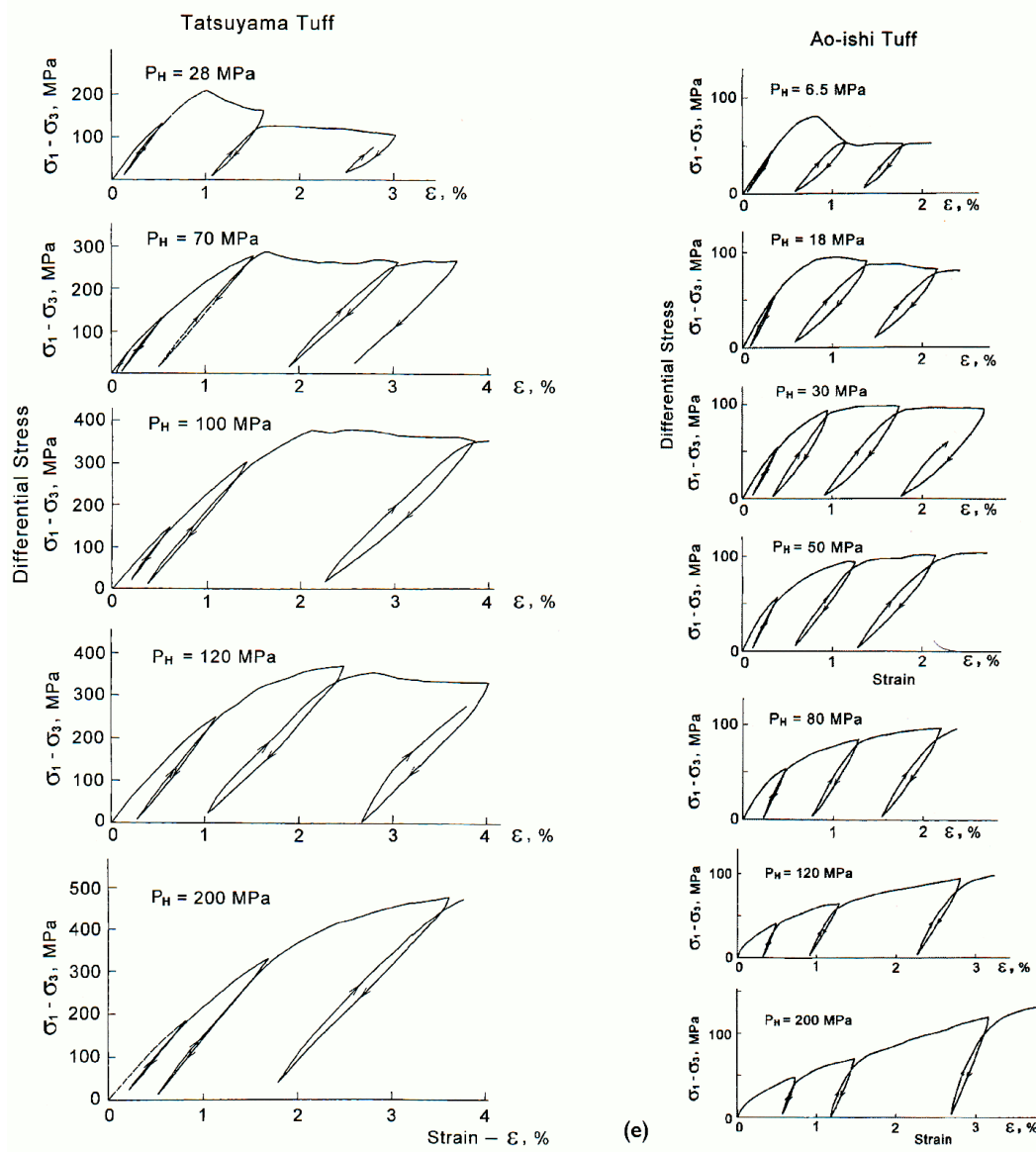


Figure 104.55: Full elastic-plastic response, with loading-reloading cycles of Tuff specimens (two different rock sources) for varying confinement pressures. Shown are axial ( $\epsilon_1$ ) strains versus differential stresses ( $\sigma_1 - \sigma_3$ ) for triaxial loading of 3D samples (Mogi, 2006).

### 104.8.1.2 Dilative and Compactive Response

Rock (similar to other geomaterials) feature dilative (increase in volume) and compactive (decrease in volume) response for both hydrostatic confinement as well as for deviatoric loading (shear stresses). Lockner and Stanchits (2002) performed a number of tests on (initially isotropic) sandstone and measured the undrained poroelastic response for changes in mean (hydrostatic, normal) and deviatoric (shear) stress. While change in pore pressure was found to result from changes in mean (hydrostatic) stress, it was also resulting from changes in deviatoric stress. This dependence of pore pressure, and consequently pore volume, on deviatoric stress is called dilatancy and is a feature found in most geomaterials. Figure 104.56 shows measured dependence of a coefficient  $\eta$ , defined as a ratio of change in pore pressure due to change in deviatoric stress ( $\Delta p = -\eta \Delta \sigma_{deviatoric}$ ).

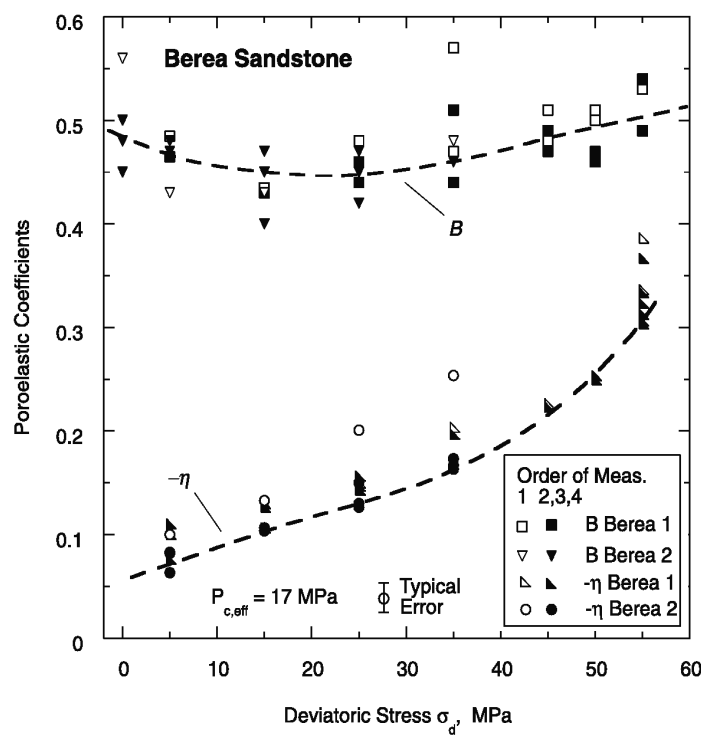


Figure 104.56: Measured poroelastic (Skempton's) coefficient  $B$  and  $\eta$  for Berea Sandstone. (Lockner and Stanchits, 2002).

Figure 104.56 also shows measured values for coefficient  $B$ , which defines a ratio of change in pore pressures due to change in mean stress ( $\Delta p = -\eta \Delta \sigma_{mean}$ ). Coefficient  $B$  and  $\eta$  are also known as Skempton's coefficients (Skempton, 1954). Hamiel et al. (2005) developed a model based on data provided by Lockner and Stanchits (2002) that captures dilatancy in poroelastic regime. In addition to

that, one of their models allows for variability in Skempton's coefficients and seems to capture test data quite well. While presented development focuses on seismic pore fluid pressure development (positive and negative) it has modeling and simulation implications for other dynamic, rock events where pores are filled with fluid and dilatancy is involved (which is always the case).

Dilatant response in elastic-plastic regime can be observed in Figures 104.47 – 104.52. In particular, volumetric strain calculations ( $\epsilon_{volumetric} = \epsilon_{ii} = \epsilon_1 + 2\epsilon_2$ ) reveal that dilatant response is present during elastic phase of loading (before yielding), significant dilation occurs after plastic limit. Thus we can conclude that while dilatancy is present in elastic phase of loading (as concluded by [Lockner and Stanchits \(2002\)](#)) dilatancy is even more pronounced in elastic-plastic loading regime.

In the limit of compactive and dilative response is the localized compactive/explosive deformation. [Olsson \(1999, 2001\)](#) details recent findings of compaction bands. They are thin zones of pure compressional deformation with very low permeability and porosity. porosity drop for such zones is on the order of ten times ( $10\times$ ) when compared to porosity of surrounding rock ([Olsson, 1999](#)). In addition to that, compaction zones (bands) growth is described in terms of shock wave analysis. [Issen and Rudnicki \(2001\)](#) developed a more general theory of compaction band formation, particularly in view of plasticity models with cap. Plasticity models with cap are necessary if realistic behavior of rock is to be modeled, covering a wide range of stress states, from tension, shear to compression. [Borja \(2006\)](#) reviews analytical conditions for appearance of volume implosion/explosion (diffuse process) and compaction bands (localized process). He shows that general conditions for localization of deformation can be used for both shear as well as for compaction and dilative localization of deformation.

### 104.8.1.3 Anisotropy

Various rock types feature directional features (bedding, foliation, flow structures) which are reflected in anisotropic elastic and plastic properties. Anisotropy of rock behavior can be inherent and/or induced. Inherent anisotropy is present before the current loading is applied and is most likely resulting from past geological processes in rock (past loading). Induced anisotropy results from current loading processes and can significantly change orientation and value of elastic constants from inherent values ([Amadei and Goodman, 1982; Amadei, 1983](#)). Anisotropy can also be apparent, when bedding planes obvious and hidden when bedding planes not directly observable. Measurements of anisotropy are not readily available in literature as such tests are quite involved and complex. For example [Pariseau \(2006\)](#) reports that measurements indicate that Young's modulus is parallel to bedding plane is often about twice as large as Young's modulus perpendicular to bedding plane. Figure 104.57 shows usual test setup when rock cores are extracted with different orientations to the test loading. For such anisotropic test setups, variations of axial Young's modulus are shown in Figure 104.58.

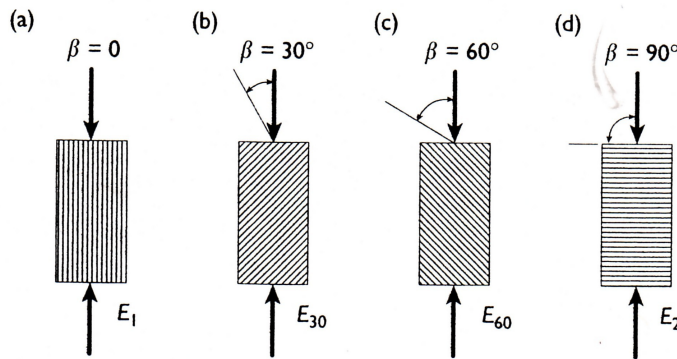


Figure 104.57: Test setup for measuring elastic anisotropy for rock cores extracted at different orientations ([Pariseau, 2006](#)).

In addition to influence of anisotropy on elastic constants, permeability is significant influenced by anisotropy of rock. [A.Angabini \(2003\)](#) shows significant influence of rock anisotropy on both elastic properties and on anisotropic permeability. He used 438 samples with distinct orientations to measure isotropic and anisotropic material properties out of research wells in The Netherlands along of 2.6 km test section and going to depths of up to 1.6 km. His measurements indicate that in addition elastic anisotropy, permeability anisotropy is significant. Figure 104.59 shows differences (variation) in measured specific permeabilities at different depths for wells in The Netherlands.

In addition to significant anisotropy in permeability (for example at depth 345m permeability in

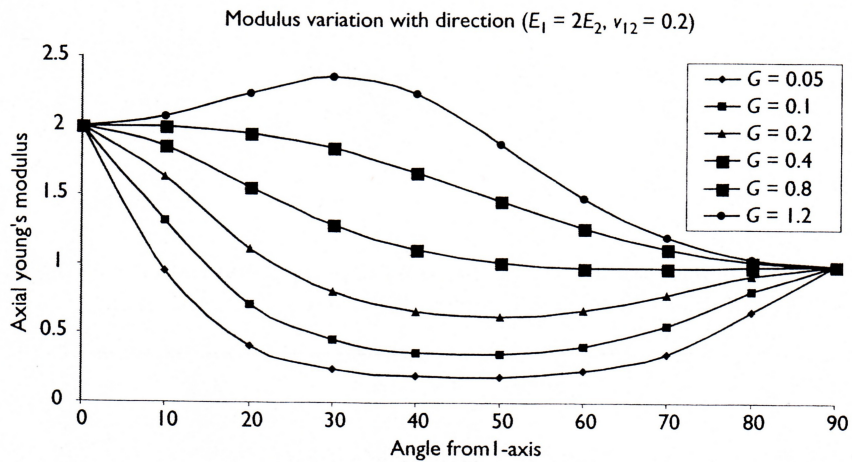


Figure 104.58: Anisotropic variations of axial Young's moduli for different orientation of core samples (Pariseau, 2006).

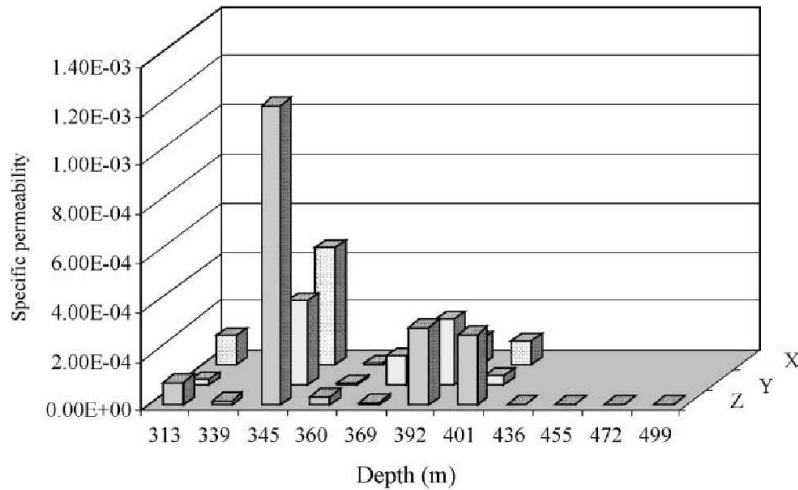


Figure 104.59: Measured specific permeabilities at different depths for wells in The Netherlands, parallel to bedding ( $x, y$ ) and perpendicular to bedding ( $z$ ) (A. Angabini, 2003).

vertical direction ( $Z$ ) is three times higher than the one in  $X$  and 5 times higher than permeability in  $Y$  direction), significant spatial variation of permeability is present. For example, within 6 meters (between depth of 339m and 345m difference is two orders of magnitude!

Measured anisotropy of elastic and elastic-plastic properties is also significant. For example, Figure 104.60 shows directional elastic moduli (obtained using either static or dynamic tests, for dry and saturated conditions) for mudstone and sandstone.

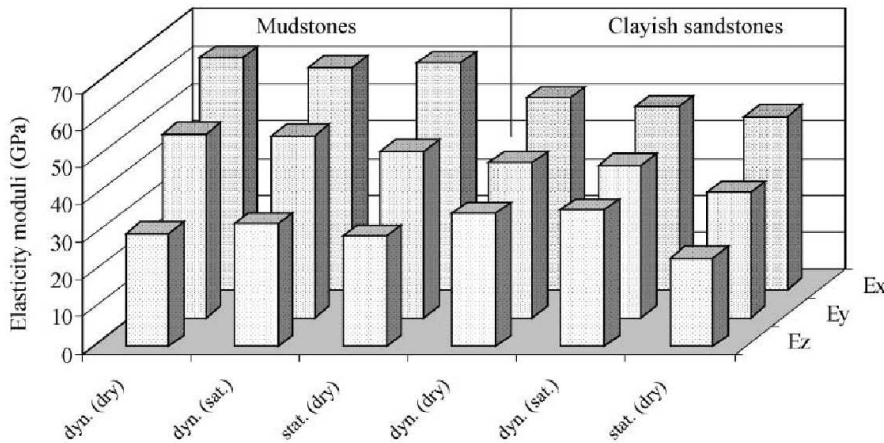


Figure 104.60: Measured anisotropic elastic moduli for different rock samples (Mudstone and Clayish sandstone) for wells in The Netherlands. Young's modulus parallel to bedding ( $x, y$ ) and perpendicular to bedding ( $z$ ) (A. Angabini, 2003).

Differences between elastic moduli in different directions of two or more are obvious. In addition to that, since elastic moduli in all three directions are different, rock exhibits general anisotropy (as opposed to cross anisotropy, where two elastic moduli would be the same).

Similar to elastic moduli (Young's moduli), Poisson's ratios do show significant anisotropy as shown in Figure 104.61.

In addition to elastic anisotropy (as shown in Figures 104.60 and 104.61) uniaxial strength also shows very strong directional dependence as shown in Figure 104.62.

Anisotropy of rock is not localized to one region of the domain, rather it is present in every level. Figure 104.63 shows elastic anisotropic moduli for wells in the Netherlands test area for a full depth of 1.7km. It is important to note that in addition to anisotropy that extends throughout depth, inherent uncertainty on measured moduli is present as well. This uncertainty (spread of data points for same depth) will be discussed in some more details in section 104.8.2.

In view of importance of anisotropy on rock response, determination of anisotropy is very important if simulations are to be used in predicting rock behavior. This is particularly true for modeling and simulation of shock wave propagation as anisotropy (both in elasticity and permeability) can significantly influence results.

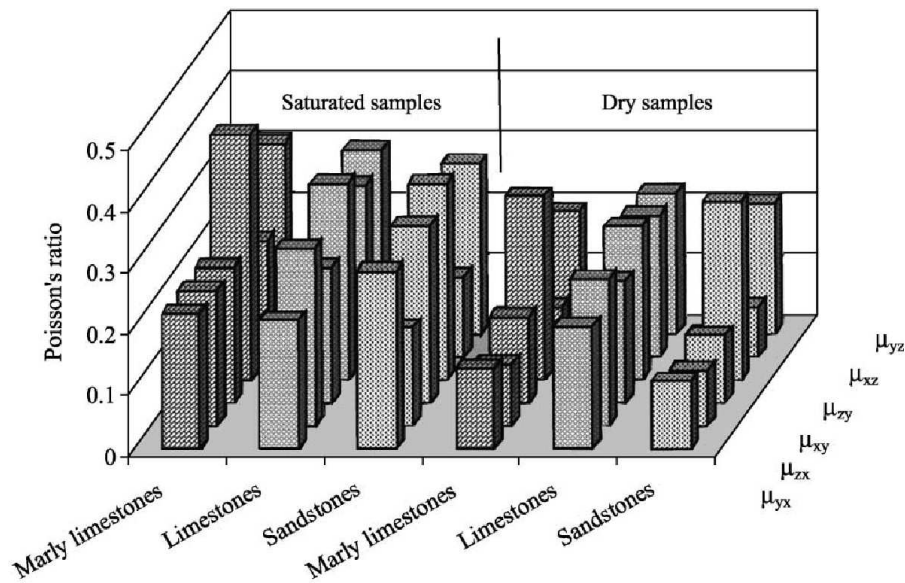


Figure 104.61: Dynamic Poisson's ratios for different rock samples (limestone and sandstone) in dry and saturated conditions, for wells in The Netherlands, ([A.Angabini, 2003](#)).

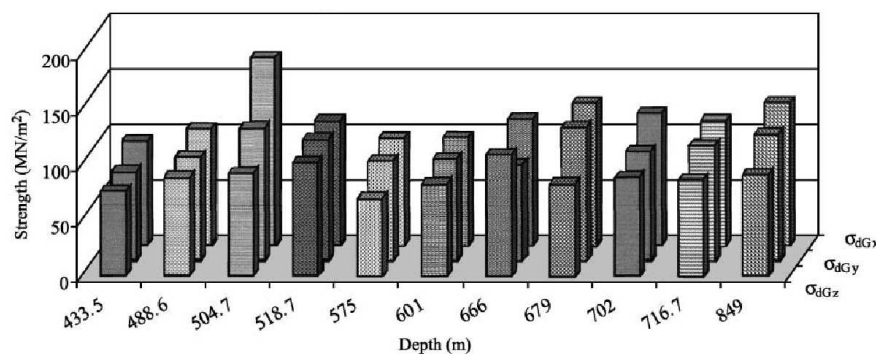


Figure 104.62: Uniaxial strength of mudstone for three different orientations of core sample, for various sampling depths, for wells in The Netherlands, ([A.Angabini, 2003](#)).

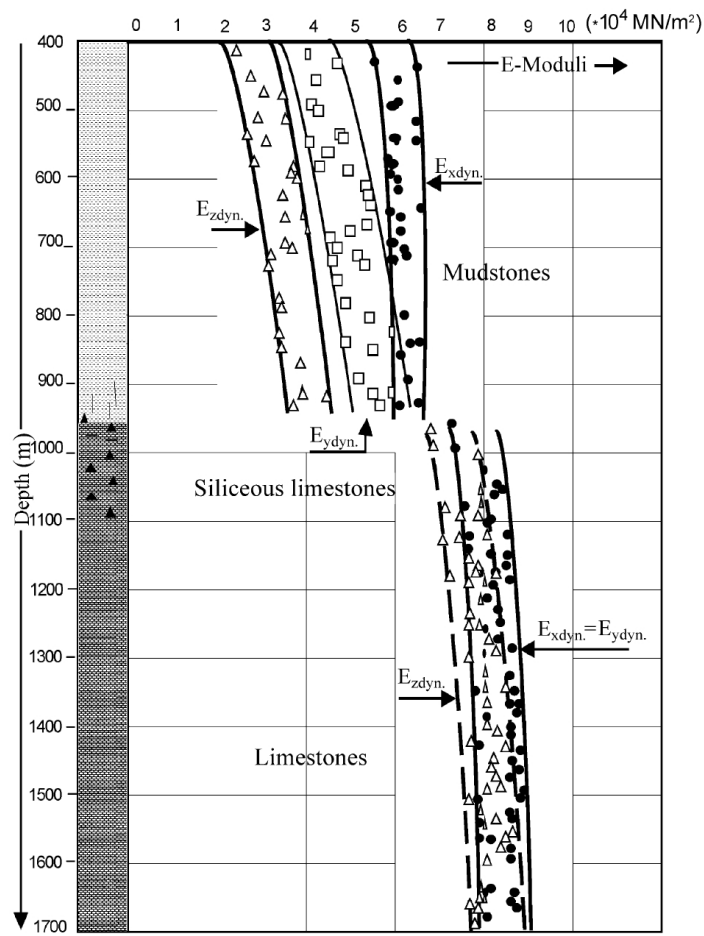


Figure 104.63: Anisotropic properties of mudstone and limestone at three directions at different depths (full depth profile), for wells in The Netherlands, (A.Angabini, 2003).

#### 104.8.1.4 High Rate Elastic-Plastic Loading

Experimental data presenting (controlled) high rate elastic-plastic loading is fairly limited compared to the abundance of low rate data. It is very important to note that high rate controlled tests are of much value as they allow separation of high rate constitutive response from shock loading tests that are accomplished using high energy shock application to rock samples, which then initiate many other facets of multi-physics of rock behavior (described in more detail in section 104.8.3 on page 354). One of the best controlled high loading rate data sets were published by Stavrogin and Protosenya (1983); Stavrogin and Pevzner (1983); Stavrogin et al. (2001). A wide range of loading rates (strain rates, ranging over 12 orders of magnitude), presented (Stavrogin and Protosenya, 1983; Stavrogin and Pevzner, 1983; Stavrogin et al., 2001), allows development of qualitative understanding and development of quantitative model parameters for rock material. Figures 104.64, 104.65 and 104.66 show the influence of rate of loading on peak strength and elastic limit (yield stress) for rock samples (marble, diabase and sandstone respectively) confined to different pressures,

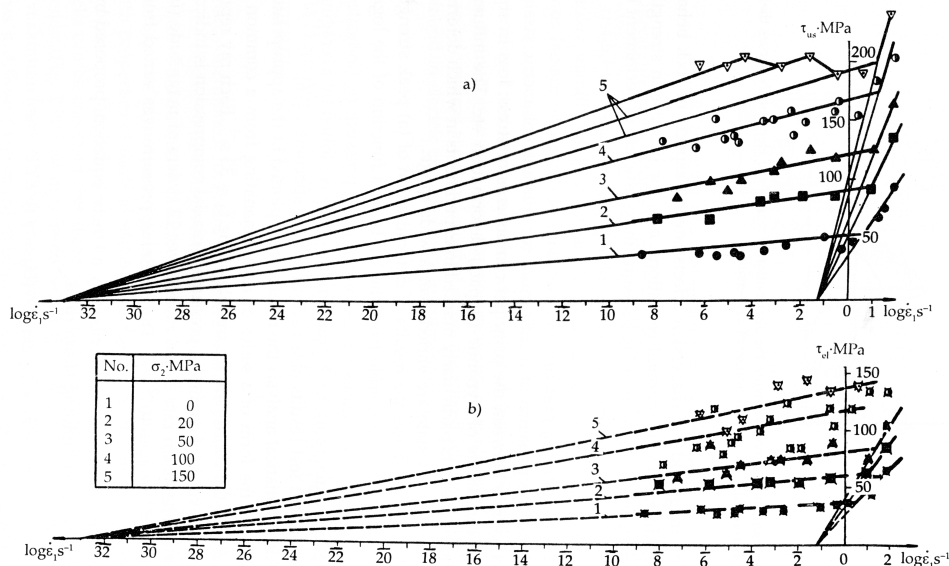


Figure 104.64: Marble: dependence of peak strength ( a ) upper) and elastic limit (yield stress) ( b ) on loading rate ( $\dot{\epsilon}$ ) for different confining stresses (1 –  $\sigma_2$  = 0 Mpa; 2 –  $\sigma_2$  = 20 Mpa; 3 –  $\sigma_2$  = 50 Mpa; 4 –  $\sigma_2$  = 100 Mpa; 5 –  $\sigma_2$  = 150 Mpa) (Stavrogin and Protosenya, 1983).

While highest loading (strain) rates are on the order of  $\dot{\epsilon} = 10^2$  1/s which is lower than shock loading rates (estimated to be over  $\dot{\epsilon} = 10^5$  1/s) this data is still very useful as it can be used to calibrated models where strength and elastic limits are dependent on loading rate, and then use those models

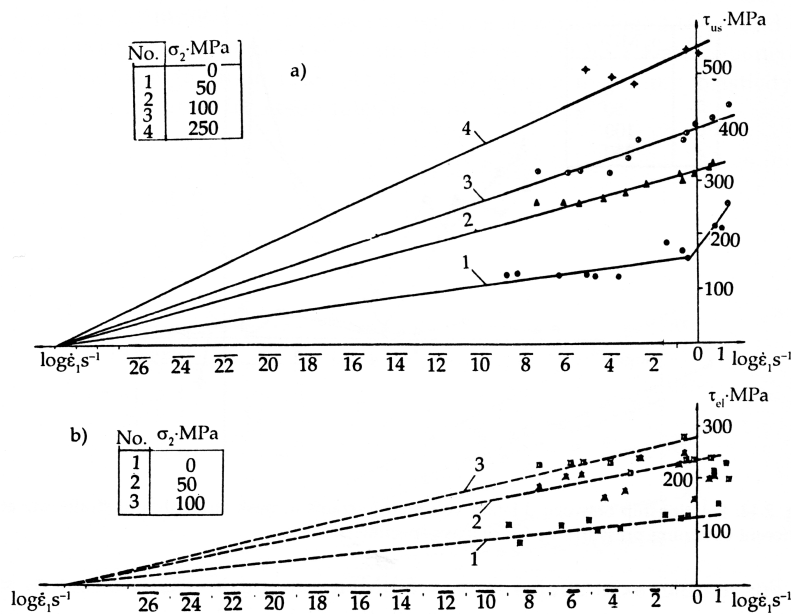


Figure 104.65: Diabase: dependence of peak strength ( a) upper) and elastic limit (yield stress) ( b) lower) on loading rate ( $\dot{\epsilon}$ ) for different confining stresses (1 –  $\sigma_2$  = 0 MPa; 2 –  $\sigma_2$  = 50 MPa; 3 –  $\sigma_2$  = 100 MPa; 4 –  $\sigma_2$  = 150 MPa) (Stavrogin et al., 2001).

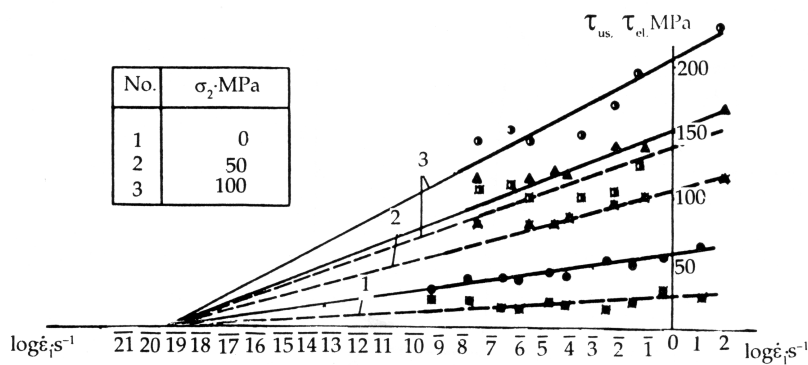


Figure 104.66: Sandstone: dependence of peak strength ( full lines) and elastic limit (dashed lines) on loading rate ( $\dot{\epsilon}$ ) for different confining stresses (1 –  $\sigma_2$  = 0 MPa; 2 –  $\sigma_2$  = 50 MPa; 3 –  $\sigma_2$  = 100 MPa) (Stavrogin et al., 2001).

to predict (in the sense of true prediction (Oberkampf et al., 2002)) shock wave propagation. Data presented in above Figures suggests that both peak strength and elastic limit increase with confinement pressures (pressure sensitive material, as discussed in section 104.8.1.1 on page 331). Presented data also suggest that both peak strength and elastic limit increase (linearly!) with the increase of rate of loading. Dependence of peak strength and elastic limits is proportional to loading rate increase, although such factor of proportionality is not very high. This is more evident from Figures 104.67 and 104.68 where full stress strain curves are shown for marble and granite respectively.

While data shown in Figures 104.67 and 104.68 does not cover such wide range of loading strain rates, it still leads to similar conclusion, that is increase in strain rate will lead to proportional increase in elastic limit and peak strength. Similar conclusion was drawn by Zhao et al. (1999), however, their results show much larger variation and weaker factor of proportionality.

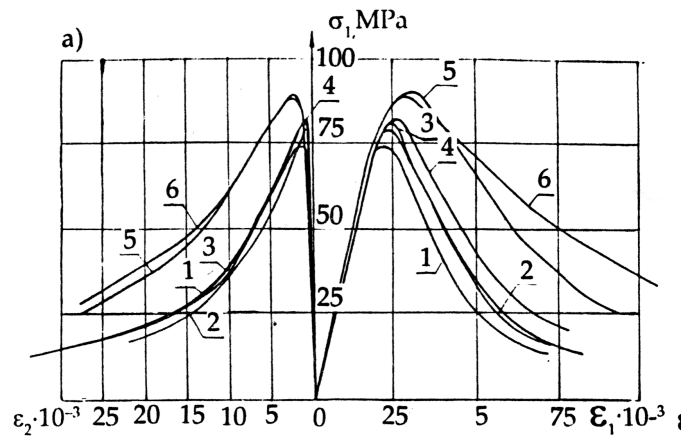


Figure 104.67: Marble: stress-strain response for different strain rates ( $\dot{\epsilon}_1$ ) 1 –  $\dot{\epsilon}_1 = 2 \times 10^{-6} 1/s$ ; 2 –  $\dot{\epsilon}_1 = 2 \times 10^{-5} 1/s$ ; 3 –  $\dot{\epsilon}_1 = 2 \times 10^{-4} 1/s$ ; 4 –  $\dot{\epsilon}_1 = 2 \times 10^{-3} 1/s$ ; 5 –  $\dot{\epsilon}_1 = 2 \times 10^{-2} 1/s$ ; 6 –  $\dot{\epsilon}_1 = 2 \times 10^{-1} 1/s$ ; (Stavrogin et al., 2001).

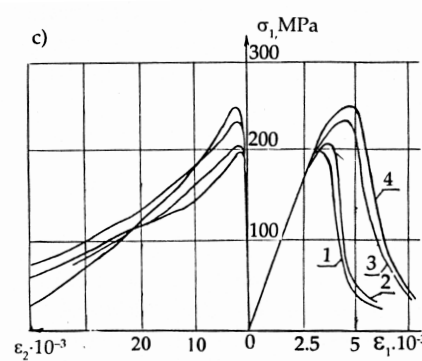


Figure 104.68: Granite: stress-strain response for different strain rates ( $\dot{\epsilon}_1$ ) 1 –  $\dot{\epsilon}_1 = 10^{-5} 1/s$ ; 2 –  $\dot{\epsilon}_1 = 2 \times 10^{-4} 1/s$ ; 3 –  $\dot{\epsilon}_1 = 5 \times 10^{-2} 1/s$ ; 4 –  $\dot{\epsilon}_1 = 2 \times 10^{-1} 1/s$ ; (Stavrogin et al., 2001).

### 104.8.1.5 Coupling with Pore Fluid Pressure and Temperature

In addition to constitutive response of elastic, plastic and damaged matrix (solid porous skeleton) pore fluid and temperature fields have large influence on behavior of rock. Pore pressure directly influences mechanical response of solid skeleton through effective stress principle (see section 104.8.6). In addition to that, changes in temperature field will affect both pore fluid and elastic-plastic-damage characteristics of the porous solid (rock skeleton).

For example, Figure 104.69 shows dependence of stress at failure for sandstone. In particular, Figure 104.69(a) (left) shows clear dependence of failure stress on pore pressure, where increase in pore fluid pressure reduces the failure limit (stress). This is the case for different confining stresses,

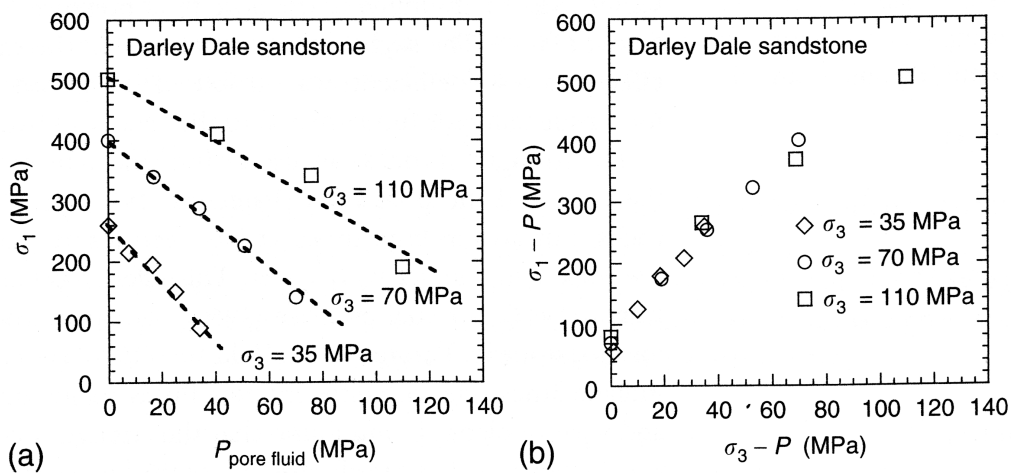


Figure 104.69: Sandstone: ultimate stresses (full capacity mobilized) as a function of ( a) left) pore fluid pressure; ( b) right) effective principal stress (Jaeger et al., 2007).

and the dependence is linear, which nicely follows equations that will be given in section 104.8.6. If the dependence is plotted in somewhat different form, as a function of effective stress, as shown in Figure 104.69(b) (right) all the points fall into (almost) same line. Present variation is inherent to all geomaterials and is discussed in some detail in section 104.8.2.

In addition to a full saturation, where effective stress principle is fully valid, partial saturation plays a very important role in behavior of porous rock. Partial saturation will affect response of porous rock matrix through increase in pore fluid (mix or water and air) pressures as loading is applied and rock undergoes compactive or dilatant response. Such interaction of pore fluid (mix or air and water) will also be affected by the rate of load application as the fluid viscosity starts having effects on pore pressure

advection and diffusion. For example, Figures 104.70 and 104.71 shows effects of moisture content<sup>68</sup> on peak strength, elastic limit and coefficient of cohesion for sandstone and limestone (cohesion only).

Full saturation of sandstone samples was achieved at moisture content of 3 % while for limestone it

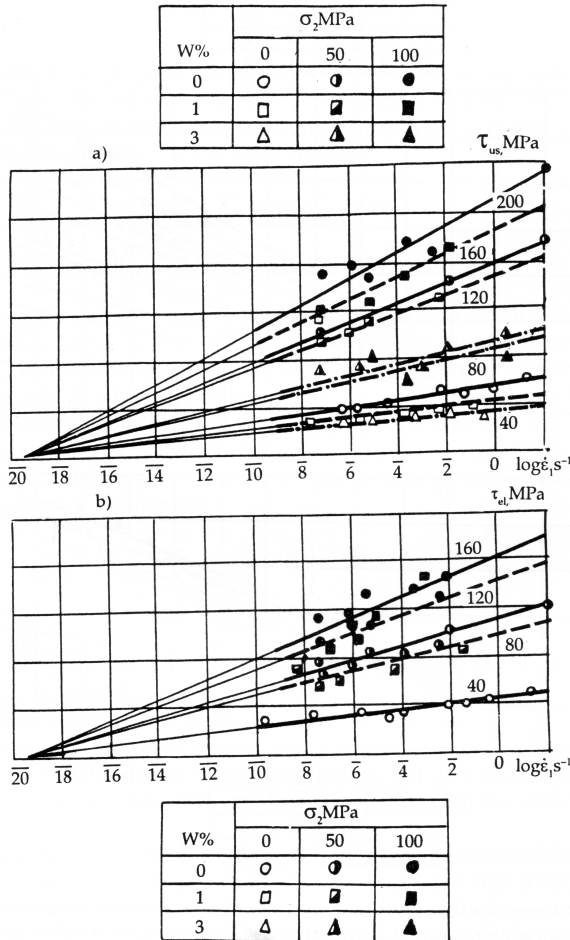


Figure 104.70: Sandstone: dependence of peak strength (a) upper and elastic limit (yield stress) (b) lower on loading rate ( $\dot{\epsilon}$ ) for different confining stresses ( $1 - \sigma_2 = 0$  MPa;  $2 - \sigma_2 = 50$  MPa;  $3 - \sigma_2 = 100$  MPa;  $4 - \sigma_2 = 150$  MPa) and moisture content ( $W$ ) (Stavrogin et al., 2001).

was 8 %. Results show that steady decrease of peak strength, elastic limit and coefficient of cohesion with increase in moisture content. It is very interesting to note that an increase in loading rate still increases the peak strength, elastic limit and coefficient of cohesion (as concluded in section 104.8.1.4 for dry samples), even with increase in influence of pore fluid (water and air) pressures, that now has to advect and diffuse. This type of interaction of pore fluid with loading rate and response of rock skeleton is somewhat counter-intuitive as it was expected that increase in saturation with increase in loading rate

<sup>68</sup>Moisture content is here defined as weight percentage of the water content compared to the weight of the sample.

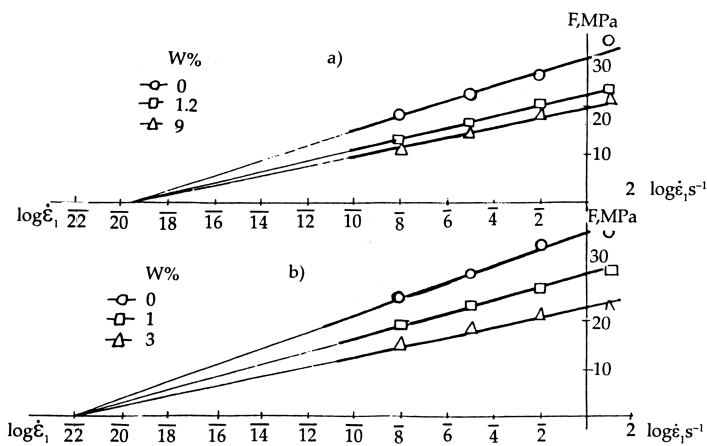


Figure 104.71: Dependence of the coefficient of cohesion for sandstone (a, upper) and limestone (b, lower) on strain rate ( $\dot{\epsilon}$ ) for different levels of moisture content ( $W$ ) (Stavrogin et al., 2001).

will lead to an increase in pore fluid pressures during high loading rate events, and thus reduce peak strength, elastic limit and coefficient of cohesion.

The influence of pore fluid on response can also be followed on full stress strain curves, as shown in Figure 104.72 for limestone. While increase in water (moisture) content leads to a decrease in stiffness and elastic-plastic strength, increase in strain (loading) rate leads to an increase in stiffness and elastic-plastic strength (stress-strain curves are "higher" for faster loading). This seemingly counter-intuitive response might need to be explored in more depth.

While previously shown results assume that pore space within rock is mostly connected, Curran (1994) uses simple micromechanical models to predict that at high confinement, the behavior of fully water-saturated rock changes from a classical effective stress response (see more about effective stresses in section 104.8.6) to a much stronger and stiffer material. This transition happens at different confining pressures, depending primarily on solids bulk modulus and the pore morphology/fabric. For example, Curran (1994) note that hard rock with small ratio of crack volume to pore volume, the transition begins at 0.2 GPa, while for soft rock (or rock with high ratios of crack volume to pore volume), the transition happens at much higher confinements, of 1 – 2 GPa. This change in rock skeleton needs to be taken into account for any modeling and simulations where such threshold compressive values are reached or exceeded. In addition to that, a very important observation was made by (Larson and Anderson, 1979), in that under high confining pressures, liquid water will turn into ice VI<sup>69</sup> thus significantly changing the nature of coupling of pore fluid with porous solid.

Changes in temperature will affect both the pore fluid (by changing the volume and reactivity with

<sup>69</sup>Ice VI is a tetragonal crystalline form of ice formed by cooling water to 270 K at 1.1 GPa.

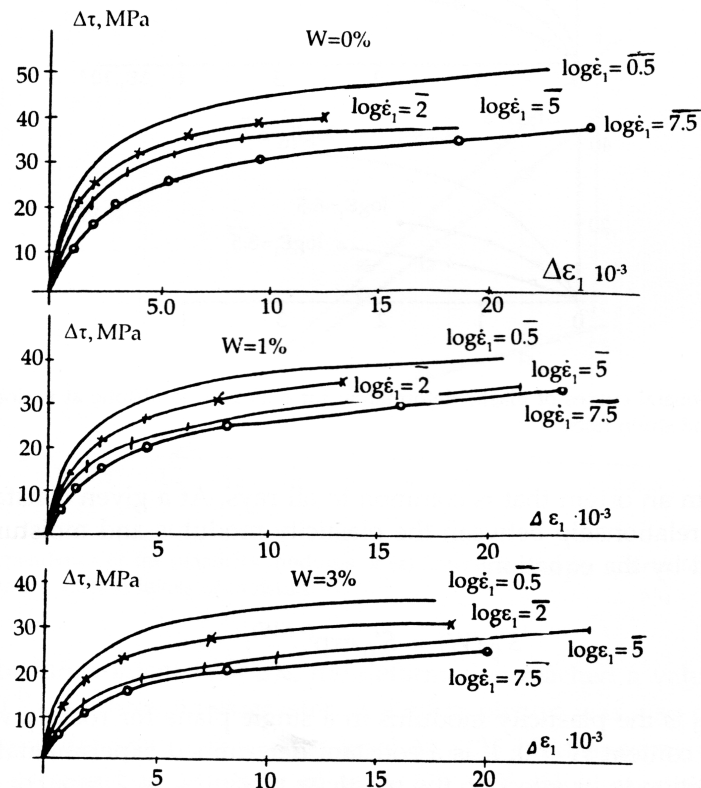


Figure 104.72: Limestone: stress-strain ( $\tau - \epsilon_1$ ) curves for different strain rates ( $\dot{\epsilon}$ ) and different levels of moisture content ( $W$ ) (Stavrogin et al., 2001).

rock minerals), as well as the behavior of the solid (porous) matrix. With an increase in temperature, rock becomes softer but much more ductile. Inada et al. (1992) performed a number of tests on granite, andesite and sandstone, with changes of temperature from  $-160^{\circ}\text{ C}$  ( $-256^{\circ}\text{ F}$ ) to  $+100.00^{\circ}\text{ C}$  ( $212^{\circ}\text{ F}$ ) for both dry and wet (saturated) rock samples. Figure 104.73 shows stress-strain curves resulting from those tests. While the influence of saturation and temperature varies for different types of rock, general trend is that with increased temperature response becomes softer (lower stiffness, lower peak strength) with higher ductility. Temperature range presented does not cover completely application area for shock loading (where temperatures might reach and exceed melting point for rock), however softening and increase in ductility trend will continue as the temperatures increase until close to melting point. At such high temperatures, rock behavior will gradually change from solid to heavy fluid with significant changes in viscosity. Holyoke and Rushmer (2002) did a number of tests on muscovite-biotite metapelite and a biotite gneiss with very high temperatures (from  $650^{\circ}\text{ C}$  ( $1202^{\circ}\text{ F}$ ) to  $950^{\circ}\text{ C}$  ( $1742^{\circ}\text{ F}$ )) and reported dilatancy effects and highly ductile response, with strains extending over 15 % and reaching peak strength at 5 – essentially represents a new material that has to be properly modeled.

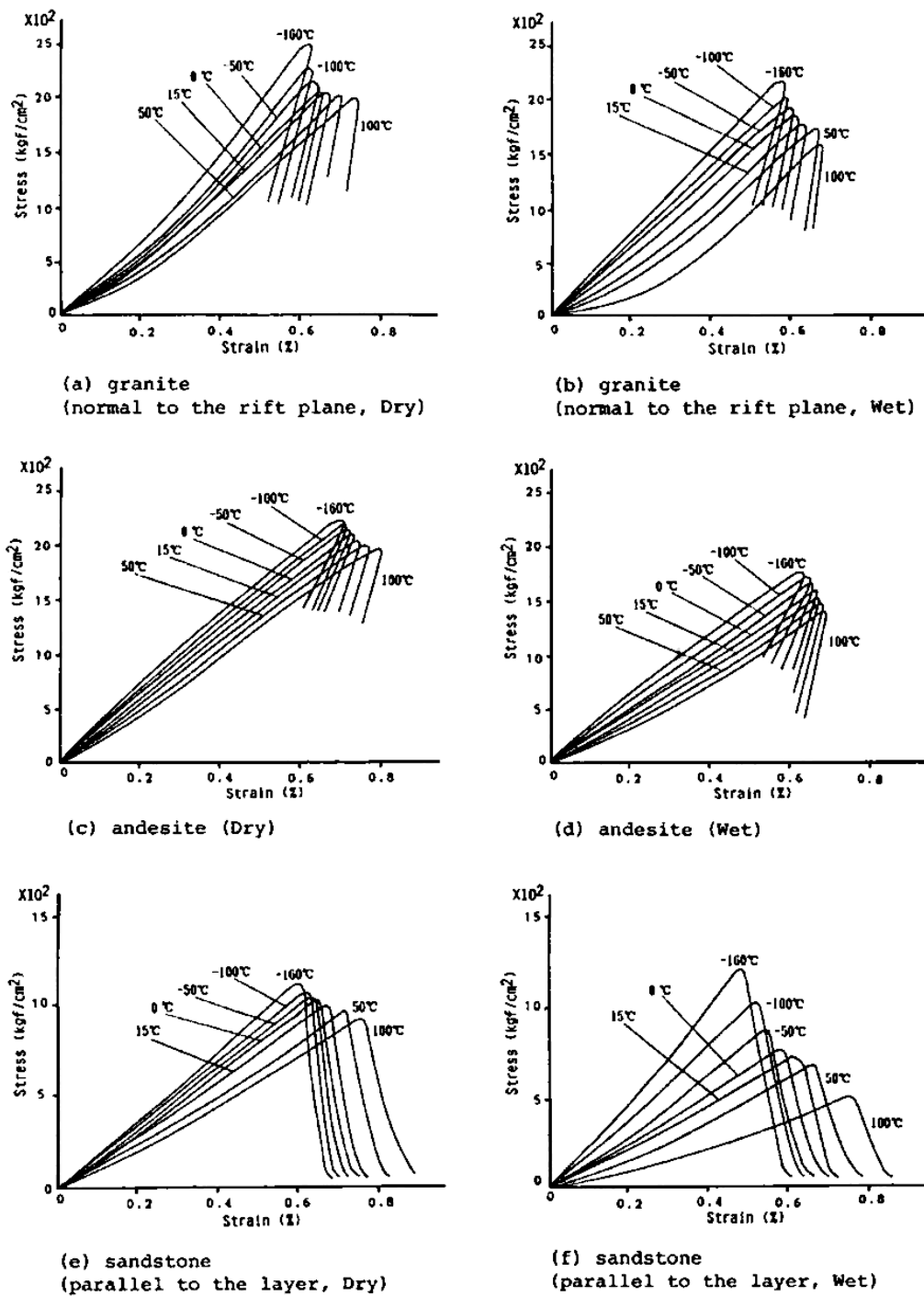


Figure 104.73: Stress-strain curves for dry and wet samples of granite, andesite and sandstone with varying temperature (Inada et al., 1992).

### 104.8.2 Uncertainty and Variability of Rock Behavior

Rock material behavior is characterized by point wise uncertainty and spatial variability. While this topic is covered in much more detail in section 506.6, given here is a brief account of experimental data that supports above statement. Test data shown in previous sections exhibits variation. This variation is present in any set of test data were more than one sample was used to determine material properties. For example, Figure 104.74 from [Pariseau \(2006\)](#), shows values for shear modulus for a variety of rock types. It is noted that the variability is quite large, yet this is nothing unusual and is rather

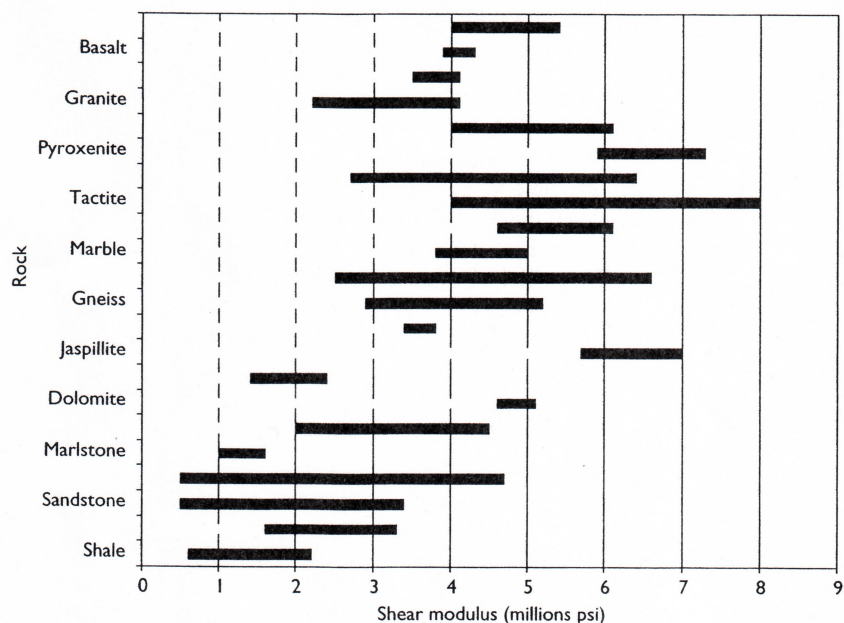


Figure 104.74: Variation of shear modulus for different rock types ([Pariseau, 2006](#)).

characteristic of rock material. In addition to that, variability of rock material parameters is apparent in any other set of test data. For example larger and/or smaller variability is present in data presented in Figures 104.56, 104.59–104.63, 104.64–104.66, 104.69–104.71. This variability is always present (see discussion in section 506.6) and need to be taken into account in order to have higher confidence in modeling and simulation of rock behavior. One possible approach to fully incorporating uncertainty into modeling and simulation is given in section 506.6 on page 2649.

### 104.8.3 Effects of Shock Loading on Intact Rock Behavior

In previous sections I have attempted to present main features of intact rock behavior for a variety of loading conditions, loading rates, temperatures... Select set of publications were used to describe specifics of rock behavior, including pressure sensitivity, dilative and compactive response, anisotropy, effects of high rate of loading and effects of pore fluid pressures and temperatures and finally the uncertainty of such data. In this section, select publications on shock loading in rock are reviewed with the main aim of synthesizing previous findings and showing that all of the previous specifics of intact rock behavior influence response to shock loading.

It is very important to note that the history of development of modern theory of shock waves is long and quite interesting. [Salas \(2006\)](#) describes many (unsuccessful) attempts by the greatest mechanics minds of last two centuries to develop a consistent theory of shock waves. Such historic are invaluable in having the right prospective in developing consistent approaches for multi-physics modeling of shock waves in intact rock.

A very interesting set of experimental results and findings for rocks of both high porosity (tuff and limestone) ([Larson and Anderson, 1979](#)) and low porosity (granite and sandstone) ([Larson and Anderson, 1980](#)) are available in literature. For low porosity tests a number of important observation are made. Relationship of shock wave velocity versus particle velocity shows a discontinuity. It is suggested that this is due to the shear initiated pore collapse, which relates to dilatancy and compactive/shear localized deformation bands. This is indeed more appropriate, in Authors opinion, and in view of recent research on compressive localization ([Olsson, 1999, 2001; Issen and Rudnicki, 2001; Borja, 2006](#)) that such pore collapse is due to the initiation of diffusive, implosive and localized, compaction bands. In addition to that [Larson and Anderson \(1980\)](#) show that uniaxial strain data for low strain rates can be used to model high strain rate events, for dry rocks. This is a very important findings as it allows calibration of material models using low rate experiments for prediction of shock wave events. In addition to that, it was found that for very low porosity rock where pore are not in contact, the effective stress principle does indeed need to be used in its original form (Biot and not Terzaghi form) as given in equation [104.616](#) in section [104.8.6](#) on page [363](#), with  $\alpha$  having a very low value. This is consistent with findings from micromodels mentioned in section [104.8.1.5](#) ([Curran, 1994](#)). Test result date for highly porous rock (tuff and limestone) ([Larson and Anderson, 1979](#)) show that porosity plays a major role in behavior of rock. For example, the irreversible process of compaction and elastic unloading leads to a large hysteresis, dissipating significant amounts of wave energy, effectively damping the wave out. In addition to that, an increase of strength with strain rate is observed, reinforcing experimental observations be [Stavrogin and Protosenya \(1983\); Stavrogin and Pevzner \(1983\); Stavrogin et al. \(2001\)](#), described in section [104.8.1.4](#)

on page 344.

Dynamic compaction behavior of intact rock material was and still is of considerable interest. Lysne (1970) did a number of experiments on dry and water saturated tuff. The main conclusion he was able to draw was that the compaction of porous rock material is a process that is slower than the shock wave propagation and that it takes longer time (than for the compressive wave to pass) to complete such compaction process. In addition to that, Lysne (1970) was able to show, that at least for stresses in water below 2.5 GPa, the influence of heating on volume change can be neglected in porous rock saturated with water. D. Erskine and Weir (1994) presents data on dry and wet tuff, which exhibits quite complex behavior. Both pore crushing and phase change (liquefaction) are observed and are responsible for complex compression behavior. Heterogeneity of rock also plays a major role in the observed response. Another very important conclusion is that Gruneisen model (aka Debye-Grüneisen model) does not perform well, indicating that there a likely phase transition is happening and needs to be accounted for.

Hiltl et al. (1999) present interesting set of shock-recovery tests results on dry and fully saturated sandstone. Principle of effective stress is again playing important role as it is observed that water saturated samples had much smaller compaction due to distribution of confining pressures between pore water and porous solid. In addition to that, reduction of porosity due to high pressure of shock waves was much smaller for saturated samples, again proving that pore fluid carries quite a bit of load due to slow drainage, as present during shock wave loading. It is also observed that as the shock pulse duration increases, so does the damage, implying that as the pore fluid gains time to drain, effective stresses in porous solid increase and causes the damage and compaction.

#### 104.8.3.1 Shock Waves of First and Second Kind

The dynamic behavior of saturated porous media was studied at length by M.A.Biot (1956); Biot (1962, 1972). In one of his studies (M.A.Biot, 1956) he concluded that there exist three kinds of coupling between pore fluid and porous solid (inertial, viscous and mechanical). He also concluded that the viscous coupling plays a key role and determines response of a coupled system to dynamic excitation, while making wave propagation dispersive. He demonstrated (analytically) the existence of two kinds of compressional waves corresponding to the mechanical and inertial coupling, while the viscous coupling is responsible for a pure wave. For high viscous coupling, the relative movements between the two phases are prevented, so there is only one compressional wave and the total mass behaves as a single-phase medium.

Recent paper by Lomov et al. (2001), actually shows an experimental proof of such coupling. Figure 104.8.3.1 shows two test results for dry and wet samples. It is important to recognize that these

test results can also be used to validate shock wave propagation modeling and simulation as described in section 104.8.6 on page ??.

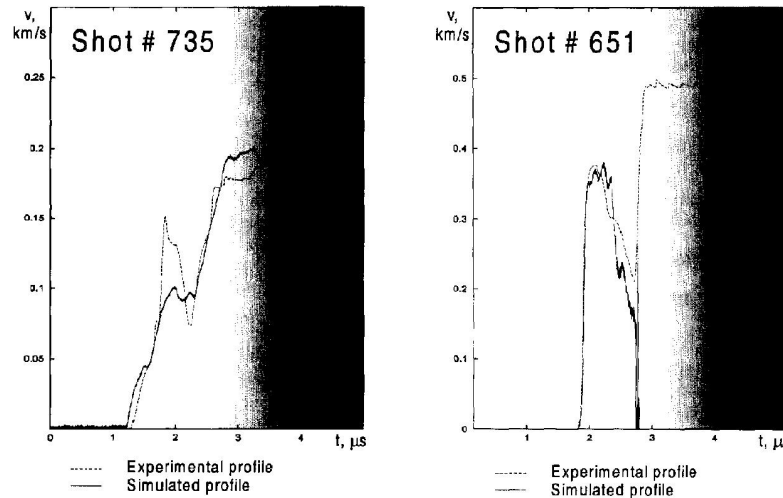


Figure 104.75: Test results for a 1D wave propagation in dry (high coupling) and wet (low coupling) sandstone (Lomov et al., 2001).

For example, for high coupling case (dry sandstone, pore fluid is air), the velocity profile shown in Figure 104.8.3.1 is increasing and when integrated (to get displacements), profile corresponds (at least qualitatively) to high coupling case ( $K = 10^{-6}$  cm/s) presented in Figure 310.14. Similarly, low coupling case (wet sandstone, pore fluid is water) the velocity profile increases, then drops to almost zero and then increases again. Upon integration to get displacement, this will correspond (qualitatively) to low coupling case ( $K = 10^{-2}$  cm/s) presented in Figure 310.14. Permeabilities are here used qualitatively for both water and air and signify ease with which fluid (water or air) moves past porous solid. While, results presented in Figure 310.14 correspond to a linear elastic case, at least qualitatively, they follow test results, which of course correspond to elastic-plastic behavior of rock material. Such elastic-plastic behavior will affect results in many ways (slow the wave propagation speed for one), but at least it is reassuring that an elastic solution can be used to help gain understanding of the basic mechanics.

Analytical solutions for shock wave propagation, even with many simplifying assumptions, are valuable as candidates for verification and validation. Two such solutions are mentioned below. Vasilev et al. (1980) discusses interaction of gas, liquid and porous medium during and after an underground explosion. A complex interaction is described which eventually leads to the implosion of explosion cavity. Although the analysis presented is based on elastic behavior of the porous medium, it provides excellent basis for understanding phenomena involved as well as for verification. Nikolaevskiy et al. (2006) presents

more sophisticated analysis of similar phenomena, using finite difference method ([Wilkins, 1999](#)), and an elastic-plastic material model. However, Authors neglect the dilatancy of the material in order to simplify their solutions. Neglecting dilatancy certainly affects results Compaction related to coupling of pore fluid and porous solid. Moreover, influence of temperature fields is also neglected (isothermal process) which might hinder fidelity of modeling where large temperature changes are present and where temperature change influences behavior of pore fluid and porous solid.

#### 104.8.3.2 Hugoniots

The Hugoniot curves (also known as Rankine-Hugoniot) for material present important data about material state. Material compression state defined by initial pressure, density and energy, can be used, to determine new state upon applying shock loads. Such curves prove important in material modeling for rock subjected to shock loading. Early on [Afanasenkov et al. \(1969\)](#) showed that it is possible to predict shock Hugoniots of any substance up to compression ratio of two with the knowledge of initial density and initial compressibility. [Shipman et al. \(1971\)](#) used a number of experiments to determine Hugoniots for Sandstone. In addition to that they used measured data and developed curves to show that phase boundaries do shift significantly compared to those determined using static means. This important conclusion affects development of elastic-plastic modeling for intact rock where high temperature effects cannot be neglected.

## 104.8.4 Material Modeling of Rock

### 104.8.4.1 Lawrence Livermore National Laboratory Models

A number of models originating from researchers from Lawrence Livermore National Laboratory have been developed over the years. While they do not represent a single line of development (and might have been produced by different research groups from different departments) they are summarized in this LLNL section.

[Glenn \(1995\)](#) presents a simple, yet effective total stress model that depends on mean confinement (pressure), temperature and on a damage parameter that serves as an internal variable and depends on degradation due to tensile and shear failure.

$$\sqrt{3s_{ij}s_{ij}} \leq Y = (1 - D)\bar{Y} + \beta D\bar{Y} \quad (104.614)$$

where  $s_{ij}$  is the deviatoric stress,  $\beta$  is a constant, and  $D$  is a scalar function of the volumetric components of void and equivalent plastic strain tensors. The generalized compressive strength  $\bar{Y}$  is a function of unconfined compressive strength, the ultimate compressive strength, the melting temperature, the mean pressure, the cohesion and an material additional constant.

More recently [Lomov et al. \(2001\)](#); [Antoun et al. \(2003\)](#), presented an elastic viscoplastic material model that takes into the account various influences on rock yielding behavior. For example, taken into the account are the effects of scaling, hardening, damage and melting. In addition to that, compaction is modeled using analytic porous compaction model, while also included are the effects of dilatancy. Model is set in a proper thermodynamic framework. However, it should be noted that strictly following thermodynamics for geomaterial behavior, can have negative effects on modeling proper volumetric response (dilatancy and compaction), with alternative material model formulation spaces being suggested by [Collins and Housby \(1997\)](#). This is an area which certainly deserves much attention, namely the apparent small disconnect between sound thermodynamic framework for modeling (which nicely applies to metal plasticity) and observed behavior of geomaterials (rock included).

### 104.8.4.2 Hoek and Brown Model

One of the most often used material models for rock is Hoek and Brown. It is important to note that this model is actually a failure criterion, delineating elastic and failure states of stress, lacking usual plasticity features, such as hardening and/or softening. The most recent edition of the model ([Hoek et al., 2002](#)) fixes some earlier observed problems with friction angle determination. This is a valuable model for practical work for rock with low confinement stresses, where behavior is brittle and failure indeed occurs as soon as the failure state of stress is reached. However, in view of shock loading modeling, this model

does not hold much promise, as it lacks, as mentioned above, basic elastic-plastic features.

#### 104.8.4.3 Other Models

A number of other material models have been developed for modeling of elastic-plastic-damage behavior of rock. Small selection is presented below. It should be noted that most of those developed models inherit most of their features from models described in previous sections.

[Benz and Schwabb \(2008\)](#) provide comparison for six most commonly used failure criteria for rock. While failure is emphasized, as opposed to full elastic-plastic behavior, the data presented is very telling in view of uncertainty of rock behavior. For example, six deterministic models are calibrated using statistical fitting techniques, and deterministic parameters are developed for a deterministic elastic-plastic (failure) models. The information about the uncertainty of response is thus completely lost.

[Das and Basudhar \(2009\)](#) perform similar exercise with four deterministic models. Moreover, they label some of the test data as outliers thus negatively influencing date regression (removal of statistical moments).

[G. W. Ma and Zhou \(1998\)](#) present an isotropic elastic-plastic model that includes rate dependence, damage development and plasticity of rock. Isotropic damage was used where the elastic constitutive tensor was related to scalar damage parameter  $D$

$$E_{ijkl} = E_{ijkl}(1 - D) \quad (104.615)$$

This is a standard way of incorporating scalar damage ([Carol et al., 1995](#)). Of course, anisotropic damage ([Rizzi, 1993; Carol et al., 2001a,b; Loret and Rizzi, 1997](#)) is more accurate in modeling realistic materials and should be used whenever possible, however in this case, scalar damage was identified as sufficiently accurate for modeling. In this model, yield strength is controlled by accumulated damage, through a simple linear, isotropic relationship. In addition to that, a non-associated plastic flow is employed. However, plastic flow is limited to deviatoric plane (there is no volumetric component) which reduces accuracy of modeling, since rock material does undergo plastic volumetric change upon plastification ([Borja, 2006](#)). Comparison of simulation and experimental data shows somewhat satisfactory similarity, however, bias is present in attenuation plots (similar to results obtained by [Wei et al. \(2009\)](#)).

[Bart et al. \(2000\)](#) presents an interesting approach where an anisotropic poroelastic damage model is used to model slow behavior of rock samples (sandstone). Model is able to predict effects of damage induced by micro-cracking, such as deterioration of elastic and poroelastic properties, induced anisotropy and dilatancy. Model does not feature any plastic deformation, rather inelasticity is completely managed through damage.

Chen et al. (2010) develop an elastic-plastic-damage model which can handle inherent and induced anisotropy. Calibration and application to shale is presented, with main focus on behavior of strongly anisotropic samples. Fabric tensor (not unlike fabric tensor developed for SANISAND family of models described in section 104.6.12) presents an effective modeling tool for modeling anisotropy. However, in their model, Chen and Phoon (2009) simplified modeling of induced anisotropy to isotropic damage (citing complexity of doing it otherwise). This might be unfortunate as induced anisotropy (resulting from anisotropic damage) might be more important than inherent anisotropic, particularly for cases where reversal of loading plays an important role, for example in modeling of shock wave propagation.

### 104.8.5 Model Calibration / Testing Devices

While a number of material models have been developed over years to model rock behavior, calibration of such models has to be done with great care. Rock is fairly stiff material and as such, stiffness of testing equipment can have significant effects on test results. For example, [Labuz and Biolzi \(2007\)](#) discusses such influence in great detail. Figure 104.8.5 shows how inappropriate stiffness of testing equipment can affect (mask) the real rock response.

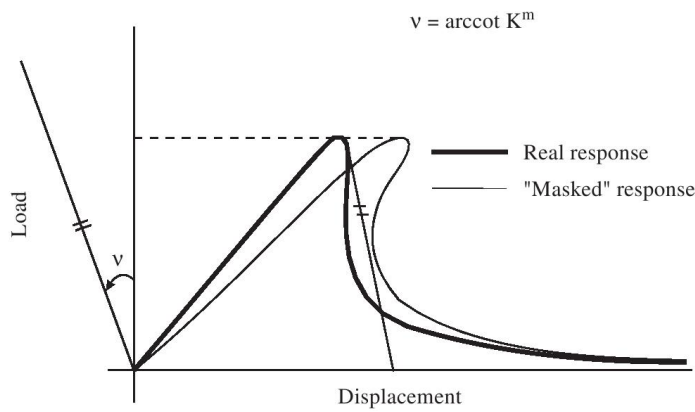


Figure 104.76: Influence of testing machine stiffness on observed and real test specimen behavior ([Labuz and Biolzi, 2007](#)).

In addition to that, elastic-plastic models assume intact rock, so that any influence of discontinuities is removed from test results. This is where scaling of samples plays a very important role. For example [Lo et al. \(1987\)](#) show how variation in test specimen volume (see Figure 104.8.5) can affects (bias) measurements of dynamic elastic modulus, by simply including, within the tested volume, discontinuities and not accounting for them.

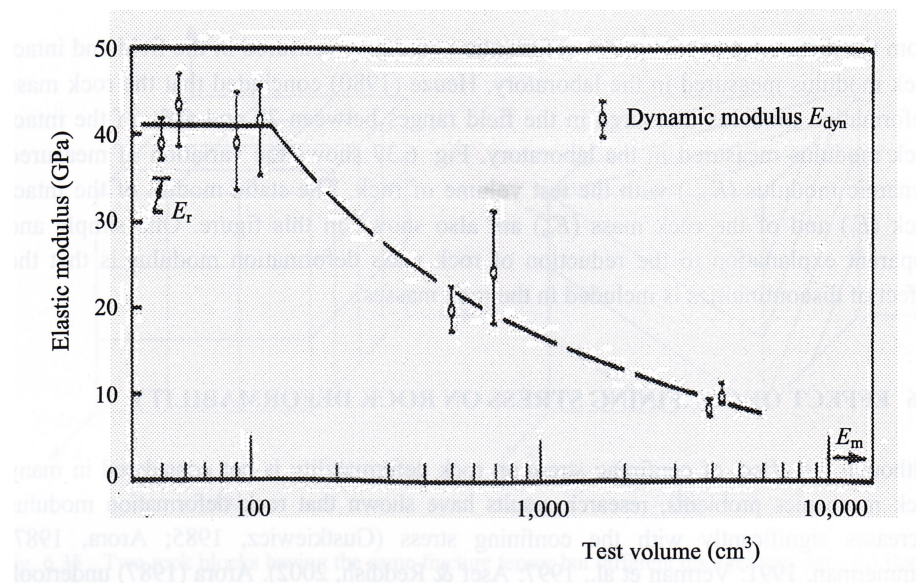


Figure 104.77: Influence of volume of test specimen elastic modulus of rock (([Lo et al., 1987](#))).

### 104.8.6 Influence of Pore Fluid Pressure and Temperature on Rock Response

One of the main features of geomaterials is the coupling of pore fluid with the porous solid. Such coupling is taken into account through the effective stress principle. The relationship between effective stress, total stress and pore pressure is (assuming tensile components of stress as positive and compressive pressure,  $p$  is positive) (Zienkiewicz et al., 1999a)

$$\sigma_{ij}'' = \sigma_{ij} + \alpha \delta_{ij} p \quad (104.616)$$

where  $\sigma_{ij}''$  is effective stress tensor,  $\sigma_{ij}$  is total stress tensor,  $\delta_{ij}$  is Kronecker delta.  $\delta_{ij} = 1$ , when  $i=j$ , and  $\delta_{ij} = 0$ , when  $i \neq j$ . For isotropic materials,  $\alpha = 1 - K_T/K_S$  (Bouteca and Gueguen, 1999), and  $K_T$  is the total bulk modulus of the solid matrix,  $K_S$  is the bulk modulus of the solid particle/grains. For most of the geomechanics problems, as the bulk modulus  $K_S$  of the solid particles is much larger than that of the whole material,  $\alpha \approx 1$  can be assumed. However, in case of rock (as well as for concrete, bone material...), such assumption does not hold all the time so  $\alpha$  needs to be kept throughout derivations (Bouteca and Gueguen, 1999).

## 104.9 Inelastic Behavior and Models for Concrete Beams, Walls and Shells

### 104.9.1 Uniaxial Material Model for Steel

The uniaxial steel material model used in this study was developed by Menegotto and Pinto (1973) and extended by Filippou et al. (1983). Model is capable of capturing the nonlinear hysteretic behavior and isotropic strain-hardening effect of steel for uniaxial state of stress and strain (1D). The stress-strain response of rebar steel material is shown in Figure 104.93. The model, as presented in Menegotto and Pinto (1973), takes on the form:

$$\sigma^* = b\epsilon^* + \frac{(1-b)\epsilon^*}{(1+\epsilon^*R)^{1/R}} \quad (104.617)$$

with

$$\epsilon^* = \frac{\epsilon - \epsilon_r}{\epsilon_0 - \epsilon_r}; \quad \sigma^* = \frac{\sigma - \sigma_r}{\sigma_0 - \sigma_r} \quad (104.618)$$

where  $b$  is the strain-hardening ratio,  $\epsilon_r$  and  $\sigma_r$  are the strain and stress at the point of strain reversal,  $\epsilon_0$  and  $\sigma_0$  are the strain and stress at the point of intersection of the two asymptotes,  $R$  is the curvature parameter that governs the shape of the transition curve between the two asymptotes. It is noted that this model is for uniaxial material behavior, in which the stresses and strains are scalars instead of tensors.

The expression for the curvature parameter  $R$  is suggested by Menegotto and Pinto (1973) as:

$$R = R_0 - \frac{c_{R_1}\xi}{c_{R_2} + \xi} \quad (104.619)$$

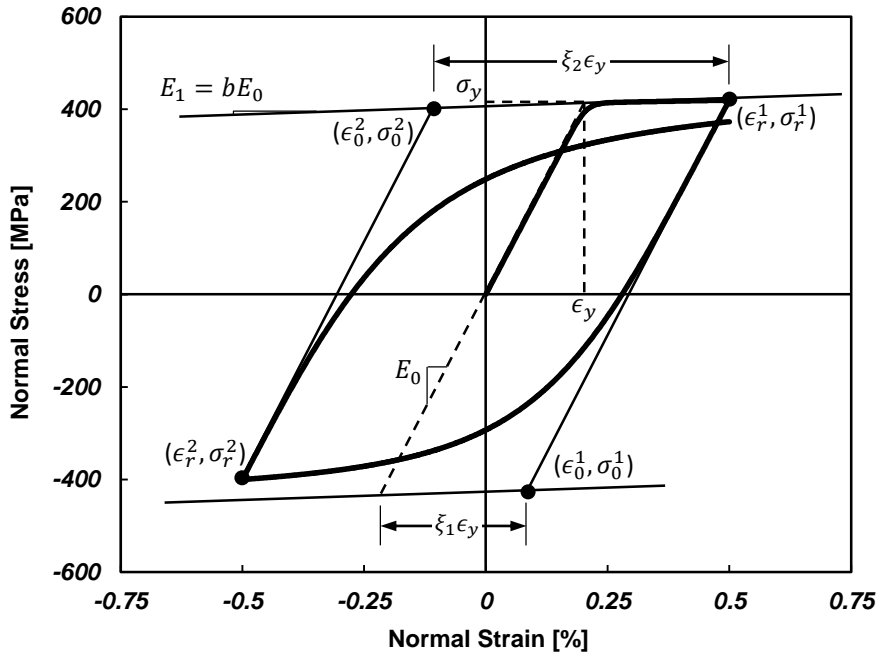


Figure 104.78: Constitutive model for uniaxial steel fiber ([Menegotto and Pinto \(1973\)](#)).

where  $R_0$  is the value of the curvature parameter  $R$  during initial loading,  $c_{R_1}$  and  $c_{R_2}$  are degradation parameters that need to be experimentally determined. The parameter  $\xi$ , which is updated after strain reversal, is defined as:

$$\xi = \left| \frac{(\epsilon_m - \epsilon_0)}{\epsilon_y} \right| \quad (104.620)$$

where  $\epsilon_m$  is the maximum (or minimum) strain at the previous strain reversal point, depending on the loading direction of the material. If the current incremental strain is positive, the parameter  $\epsilon_m$  takes the value of the maximum reversal strain. Parameter  $\epsilon_y$  is the monotonic yield strain.

In order to capture isotropic hardening behavior, [Filippou et al. \(1983\)](#) introduced stress shift mechanism into the original model by [Menegotto and Pinto \(1973\)](#). Note that the hardening rate in compression and tension can be different by choosing different hardening parameters for compression and tension. The proposed relation takes the form:

$$\frac{\sigma_{st}}{\sigma_y} = a_1 \left( \frac{\epsilon_{max}}{\epsilon_y} - a_2 \right) \quad (104.621)$$

where  $\sigma_{st}$  is the shift stress that determines the shift of yield asymptote,  $\epsilon_{max}$  is the absolute maximum strain at strain reversal, and  $a_1$  and  $a_2$  are hardening parameters in compression which are experimentally determined. In the case of tension, the hardening parameters  $a_1$  and  $a_2$  in Equation 104.621 are changed to  $a_3$  and  $a_4$ , that are also determined experimentally or from previous studies for given steel.

### 104.9.2 3D Plastic Damage Concrete Material Model, Faria-Oliver-Cervera

The concrete material model used in this study was developed by [Faria et al. \(1998\)](#). Model features:

- distinct stress-strain envelopes obtained under compression or under tension
- stiffness recovery after loading reversal
- higher concrete strength under 2D or 3D compression test, compared to 1D loading
- plastic deformations discernible after some compressive stress limit is reached

The material model, as presented in [Faria et al. \(1998\)](#), takes on the form:

$$\sigma_{ij} = (1 - d^+) \bar{\sigma}_{ij}^+ + (1 - d^-) \bar{\sigma}_{ij}^- \quad (104.622)$$

where,  $d^+$  and  $d^-$  are scalar damage variables corresponding to tensile and compressive degradation. Cauchy stress tensor  $\sigma_{ij}$  involves effective stress components  $\bar{\sigma}_{ij}^+$  and  $\bar{\sigma}_{ij}^-$ , that are related to the total effective stress ( $\bar{\sigma}_{ij} = \bar{\sigma}_{ij}^+ + \bar{\sigma}_{ij}^-$ ), defined as follows:

$$\bar{\sigma}_{ij} = D_{ijkl}(\varepsilon_{kl} - \varepsilon_{kl}^p) \quad (104.623)$$

In the previous equation,  $D_{ijkl}$  is the fourth order isotropic linear elastic constitutive tensor,  $\varepsilon_{kl}$  the small strain tensor and  $\varepsilon_{kl}^p$  is the plastic strain tensor. Damage variables together with the plastic strain constitute the internal variable set. Tensile part of the effective stress tensor can be written using principal stresses ( $\bar{\sigma}_i$ ) and principal directions ( $p_i$ ):

$$\bar{\sigma}^+ = \sum_i \langle \bar{\sigma}_i \rangle p_i \otimes p_i \quad (104.624)$$

Compressive components of the effective stress can be written as:

$$\bar{\sigma}_{ij}^- = \bar{\sigma}_{ij} - \bar{\sigma}_{ij}^+ \quad (104.625)$$

Following adopted stress split, a tensile equivalent stress  $\bar{\tau}^+$  and a compressive equivalent stress  $\bar{\tau}^-$  are considered. According to [Simo and Ju \(1987\)](#):

$$\bar{\tau}^+ = (\bar{\sigma}_{ij}^+ D_{ijkl} \bar{\sigma}_{kl}^+)^{1/2} \quad (104.626)$$

$$\bar{\tau}^- = (\sqrt{3}(K\bar{\sigma}_{oct}^- + \bar{\tau}_{oct}^-))^{1/2} \quad (104.627)$$

In the last equation,  $\bar{\sigma}_{oct}^-$  and  $\bar{\tau}_{oct}^-$  are the octahedral normal and shear stress, respectively, obtained from  $\bar{\sigma}^-$ .  $K$  is a material characteristic, adjusted so that 2D and 1D compressive strength ratio can match

ratio of 1.16-1.2 (Kupfer et al., 1969). Two separate damage criteria, functions,  $g^+$  for tension and  $g^-$  for compression, are introduced:

$$g^+(\bar{\tau}^+, r^+) = \tau^+ - r^+ \leq 0 \quad (104.628)$$

$$g^-(\bar{\tau}^-, r^-) = \tau^- - r^- \leq 0 \quad (104.629)$$

Variables  $r^+$  and  $r^-$  represent current damage thresholds. Their role is to control the size of expanding damage surfaces. Quadrant ( $\bar{\sigma}_2 = 0, \bar{\sigma}_1, \bar{\sigma}_3 \geq 0$ ) shows 2D representation for this surface, when  $\bar{\tau}^+ = r^+$ , Fig 104.79. The bounding surface associated to the principal effective compressive stresses resembles Drucker-Prager cone. It is obvious that the elastic domain under 2D compression is bounded by stresses greater than the 1D elastic compressive stress, denoted by  $f_0^-$ .

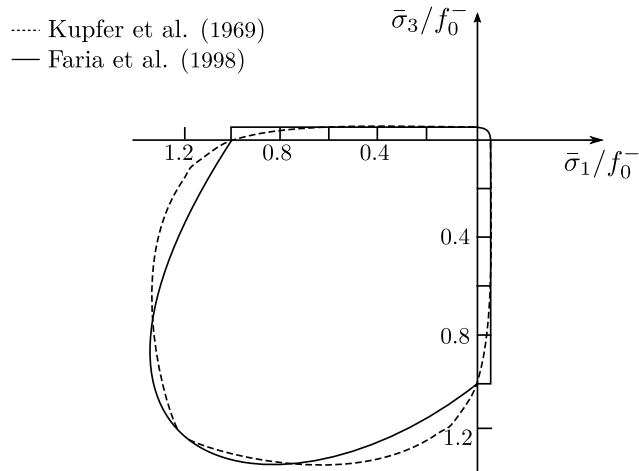


Figure 104.79: Initial 2D elastic domain

For the plastic flow of the tensor  $\dot{\varepsilon}_{ij}^P$  the following is proposed in Faria et al. (1998):

$$\dot{\varepsilon}_{ij}^P = \beta E H(\dot{d}^-) \frac{\langle \bar{\sigma}_{ij} \dot{\varepsilon}_{ij} \rangle}{\bar{\sigma}_{ij} \bar{\sigma}_{ij}} D_{ijkl}^{-1} \bar{\sigma}_{kl} \quad (104.630)$$

where  $\beta$  is the coefficient which controls the rate of intensity of plastic deformation,  $E$  is Young's modulus,  $H(\dot{d}^-)$  denotes the Heaviside step function for the compressive damage rate. Proposed model assumes that plastic strain has the direction of the elastic strain tensor  $D_{ijkl}^{-1} \bar{\sigma}_{kl}$ . It should be noted that the model cannot account for plastic strains for a pure tension test.

Kinematics of damage, internal variables is defined based on the following rate equations:

$$\dot{d}^+ = \dot{\theta}^+ \frac{\partial G^+(r^+)}{\partial r^+} \quad (104.631)$$

$$\dot{r}^+ = \dot{\theta}^+ (\geq 0) \quad (104.632)$$

where  $G^+$  and  $G^-$  are monotonically increasing functions for tension and compression, that are experimentally determined, and  $\dot{\theta}^+$  and  $\dot{\theta}^-$  are damage consistency parameters. Karush-Kuhn-Tucker conditions implies the following (Jeremić et al., 1989-2025):

$$g^+ \leq 0 \quad \text{damage/plastic function} \quad (104.633)$$

$$\dot{\theta}^+ \geq 0 \quad \text{consistency parameter} \quad (104.634)$$

$$g^+ \dot{\theta}^+ = 0 \quad (104.635)$$

which leads to the following conclusions:

- when damage/plasticity function is smaller then zero,  $g^+ < 0$ , consistency parameter must be zero,  $\dot{\theta}^+ = 0$ , implying that no damage occurs,
- when consistency parameter is greater than zero,  $\dot{\theta}^+ > 0$ , damage/plastic function is zero,  $g^+ = 0$  implying the presence of damage.

It is now possible to define consistency parameter  $\dot{\theta}^+$  from the damage consistency condition:

$$\dot{g}^+(\bar{r}^+, r^+) = 0 \implies \dot{r}^+ = \dot{\tau}^+ = \dot{\theta}^+, \quad \dot{\theta}^+ \geq 0 \quad (104.636)$$

Introducing equation (104.636) into (104.631) the flow rule for the tensile damage variable can be expressed as:

$$\dot{d}^+ = \frac{\partial G^+(r^+)}{\partial r^+} \dot{r}^+ = \dot{G}^+(r^+) \geq 0 \quad (104.637)$$

The compression damage variable is then:

$$\dot{d}^- = \frac{\partial G^-(r^-)}{\partial r^-} \dot{r}^- = \dot{G}^-(r^-) \geq 0 \quad (104.638)$$

## 104.10 Calibration of Elastic-Plastic Material Models

- 104.10.1 Calibration of Elastic-Plastic Material Models, Soil
- 104.10.2 Calibration of Elastic-Plastic Material Models, Rock
- 104.10.3 Calibration of Elastic-Plastic Material Models, Contact/Joint/Interface
- 104.10.4 Calibration of Elastic-Plastic Material Models, Concrete
- 104.10.5 Calibration of Elastic-Plastic Material Models, Steel

## 104.11 Energy Dissipation Calculations for Solids

This section is based on [Yang et al. \(2018\)](#)

### 104.11.1 Introduction

Energy dissipation in elastic plastic solids and structures is the result of an irreversible dissipative process in which energy is transformed from one form to another and entropy is produced. The transformation and dissipation of energy is related to permanent deformation and damage within an elastic-plastic material. Of particular interest here is the dissipation of mechanical energy that is input into elastic-plastic solids by static or dynamic excitations.

Early work on plastic dissipation was done by [Farren and Taylor \(1925\)](#) and [Taylor and Quinney \(1934\)](#). They performed experiments on metals and proved that a large part, but not all, of the input mechanical energy is converted into heat. The remaining part of the non-recoverable plastic work is known as the stored energy of cold work. The ratio of plastic work converted into heating (Quinney–Taylor coefficient), usually denoted as  $\beta$ , has been used in most later work on this topic. Based on large amount of experimental data, this ratio was determined to be a constant between 0.6 to 1.0 ([Clifton et al., 1984](#); [Belytschko et al., 1991](#); [Zhou et al., 1996](#); [Dolinski et al., 2010](#); [Ren and Li, 2010](#); [Osovski et al., 2013](#)).

More recently Rittel ([Rittel, 2000](#); [Rittel and Rabin, 2000](#); [Rittel et al., 2003](#)) published several insightful papers on the energy dissipation (heat generation) of polymers during cyclic loading, presenting both experimental and theoretical works. Rosakis et al. [Rosakis et al. \(2000\)](#) presented a constitutive model for metals based on thermoplasticity that is able to calculate the evolution of energy dissipation. Follow up papers ([Hodowany et al., 2000](#); [Ravichandran et al., 2002](#)) present assumptions to simplify the problem. One direct application of plastic dissipation to geotechnical engineering is presented by Veveakis et al. ([Veveakis et al., 2007, 2012](#)), using thermoporomechanics to model the heating and pore

pressure increase in large landslides, like the 1963 Vajont slide in Italy.

In the past few decades, extensive studies have been conducted on energy dissipation in structures and foundations. Work by [Uang and Bertero \(1990\)](#) has been considered a source and a reference for many recent publications dealing with energy as a measure of structural demand. [Uang and Bertero \(1990\)](#) developed an energy analysis methodology based on absolute input energy (or energy demand). Numerical analysis results were compared with experiments on a multi-story building. In work by [Uang and Bertero \(1990\)](#), hysteretic energy is calculated indirectly by taking the difference of absorbed energy and elastic strain energy. The term absorbed energy of each time step is simply defined as restoring force times incremental displacement. It is also stated that hysteretic energy is irrecoverable, which indicates that this parameter was considered the same as hysteretic dissipation or plastic dissipation. An equation for energy balance, is given by ([Uang and Bertero \(1990\)](#)) as:

$$E_i = E_k + E_\xi + E_a = E_k + E_\xi + E_s + E_h \quad (104.639)$$

where  $E_i$  is the (absolute) input energy,  $E_k$  is the (absolute) kinetic energy,  $E_\xi$  is the viscous damping energy,  $E_a$  is the absorbed energy, which is composed of elastic strain energy  $E_s$  and hysteretic energy  $E_h$ .

The problem with this approach is the absence of plastic free energy, which is necessary to correctly evaluate energy dissipation of elastic-plastic materials and to uphold the second law of thermodynamics. While there is no direct plot of plastic dissipation (hysteretic energy) in [Uang and Bertero \(1990\)](#), since it was not defined directly, there are plots of other energy components. Plastic dissipation can be easily calculated from these plots. After doing this, indications of negative incremental energy dissipation, which violates the basic principles of thermodynamics, were found in various sections of the paper.

This misconception could be clarified by renaming hysteretic energy as plastic work, a sum of plastic dissipation and plastic free energy. Both plastic work and plastic free energy can be incrementally negative, but plastic dissipation (defined as the difference of plastic work and plastic free energy) must be incrementally non-negative during any time period. Unfortunately, this misconception has been inherited (if not magnified) by many following studies on energy analysis of earthquake soils and structures (hundreds of papers).

Even [Chopra \(2000\)](#) used similar set of equations in section 7.9, and equation 7.9.6 is clearly wrong!

The basic principles of thermodynamics are frequently used to derive new constitutive models, for example by [Dafalias and Popov \(1975\)](#), [Ziegler and Wehrli \(1987\)](#), [Collins and Houlsby \(1997\)](#), [Houlsby and Puzrin \(2000\)](#), [Collins \(2002\)](#), [Collins and Kelly \(2002\)](#), [Collins \(2003\)](#) and [Feigenbaum and Dafalias \(2007\)](#). The concept of plastic free energy is introduced to enforce the second law of thermodynamics for developed constitutive models. It is important to distinguish between energy dissipation due to plasticity

and plastic work, which is often a source of a confusion. Plastic work is the combination of plastic free energy and plastic energy dissipation, which is defined as the amount of heat (and other forms of energy) transformed from mechanical energy during an irreversible dissipative process. The physical nature of plastic free energy is illustrated later in this section through a conceptual example that is analyzed on particle scale. Essentially, development of plastic free energy is caused by particle rearrangement in granular assembly under external loading.

Specific formulation of free energy depends on whether the elastic and plastic behavior of the material is coupled. According to Collins et al. [Collins and Houlsby \(1997\)](#), [Collins \(2002\)](#), [Collins \(2003\)](#), material coupling behavior can be divided into modulus coupling, where the instantaneous elastic stiffness (or compliance) moduli depend on the plastic strain, and dissipative coupling, where the rate of dissipation function depends not only on the plastic strains and their rates of change but also on the stresses (or equivalently the elastic strains). The modulus coupling describes the degradation of stiffness as in for rock and concrete, and is usually modeled by employing a coupled elastic-plastic constitutive model or by introducing damage variables. The dissipative coupling is considered to be one of the main reasons for non-associative behavior in geomaterials [Collins and Houlsby \(1997\)](#), [Ziegler \(1981\)](#).

A number of stability postulates are commonly used to prevent violation of principles of thermodynamics. Stability postulates include Drucker's stability condition [Drucker \(1956\)](#), [Drucker \(1957\)](#), Hill's stability condition [Bishop and Hill \(1951\)](#), [Hill \(1958\)](#), and Il'lushin's stability postulate [Il'lushin \(1961\)](#), [Lubliner \(1990\)](#). As summarized in a paper by Lade [Lade \(2002\)](#), theoretical considerations by Nemat-Nasser (1983) and Runesson and Mróz (1989) have suggested that they are sufficient but not necessary conditions for stability. These stability postulates can indeed ensure the admissibility of the constitutive models by assuming certain restrictions on incremental plastic work. As demonstrated by [Collins \(2002\)](#), if the plastic strain rate is replaced by the irreversible stain rate in Drucker's postulate, then all the standard interpretations of the classical theory still apply for coupled materials. Dafalias (1977) also modified Il'lushin's postulate in a similar way and applied it to both coupled and uncoupled materials.

It is important to note that development of inelastic deformation in geomaterials involves large changes in entropy, and significant energy dissipation. It is thus useful to perform energy dissipation (balance) analysis for all models with inelastic deformation. In section we focus on energy dissipation on material level. Focus is on proper modeling that follows thermodynamics. Comparison is made between accumulated plastic dissipation and accumulated plastic work, since these quantities can be quite different in most cases. As a way of verification, the input work, which is introduced by applying external forces, is compared with the stored energy and dissipation in the entire system. Finally, conclusions on plastic energy dissipation are drawn from the verified results.

## 104.11.2 Theoretical and Computational Formulations

### 104.11.2.1 Thermo-Mechanical Theory

For energy analysis of elastic-plastic materials undergoing isothermal process, it is beneficial to start from the statement of the first and second laws of thermodynamics:

$$\hat{W} = \dot{\Psi} + \Phi \quad (104.640)$$

where  $\Phi \geq 0$  and  $\hat{W} \equiv \sigma : \dot{\epsilon} = \sigma_{ij}\dot{\epsilon}_{ij}$  is the rate of work per unit volume. The function  $\Psi$  is the Helmholtz free energy, and  $\Phi$  is the rate of dissipation; both defined per volume. The free energy  $\Psi$  is a function of the state variables (also known as internal variables), but  $\Phi$  and  $\hat{W}$  are not the time derivatives of the state functions. The choice of state variables depends on the complexity of constitutive model that is being used, as cyclic loading with certain hardening behaviors usually requires more state variables. This will be elaborated in the following sections as we discuss specific elastic-plastic material models.

For general elastic-plastic materials, the free energy depends on both the elastic and plastic strains. In most material models, it can be assumed that the free energy  $\Psi$  can be decomposed into elastic and plastic parts:

$$\Psi = \Psi_{el} + \Psi_{pl} \quad (104.641)$$

The total rate of work associated with the effective stress can be written as the sum of an elastic and plastic component:

$$\hat{W}^{el} \equiv \sigma_{ij}\dot{\epsilon}_{ij}^{el} = \dot{\Psi}_{el} \quad (104.642)$$

and

$$\hat{W}^{pl} \equiv \sigma_{ij}\dot{\epsilon}_{ij}^{pl} = \dot{\Psi}_{pl} + \Phi \quad (104.643)$$

Note that the focus of this section is the energy dissipation caused by material plasticity, which should be distinguished from viscous coupling and other sources of energy dissipation. So the effects of solid-fluid interaction are neglected and all stresses are defined as effective stresses in further derivations. In order to avoid confusion, the common notation ( $\sigma'_{ij}$ ) will not be used. Standard definition of stress from mechanics of materials, i.e. positive in tension, is used.

In the case of a decoupled material, the elastic free energy  $\Psi_{el}$  depends only on the elastic strains, and the plastic free energy  $\Psi_{pl}$  depends only on the plastic strains, as shown by [Collins and Housby \(1997\)](#):

$$\Psi = \Psi_{el}(\epsilon_{ij}^{el}) + \Psi_{pl}(\epsilon_{ij}^{pl}) \quad (104.644)$$

The effective stress can also be decomposed into two parts:

$$\sigma_{ij} = \alpha_{ij} + \chi_{ij} \quad (104.645)$$

where  $\chi_{ij}$  is a stress-like variable that is related to the dissipative behavior of elastic-plastic material. The difference between the actual stress  $\sigma_{ij}$  and the stress-like variable  $\chi_{ij}$  is another stress-like term  $\alpha_{ij}$ , which is defined from the plastic free energy function  $\Psi_{pl}$ . In simple kinematic hardening models, this variable  $\alpha_{ij}$  controls the shift behavior of stress under cyclic loading, and thus usually referred to as shift or back stress.

Ziegler's orthogonal postulate [Ziegler and Wehrli \(1987\)](#) ensures the validity of Equation 104.645. It is equivalent to the maximum entropy production criterion, which is necessary to obtain unique formulation. Also, this is a weak assumption so that all the major continuum models of thermo-mechanics are included. Equation 104.643 of plastic work rate can hence be rewritten as:

$$\hat{W}^{pl} \equiv \sigma_{ij} \dot{\epsilon}_{ij}^{pl} = \dot{\Psi}_{pl} + \Phi = \alpha_{ij} \dot{\epsilon}_{ij}^{pl} + \chi_{ij} \dot{\epsilon}_{ij}^{pl} \quad (104.646)$$

The plastic work  $\hat{W}^{pl}$  is the product of the actual Cauchy stress  $\sigma_{ij}$  with the plastic strain rate  $\dot{\epsilon}_{ij}^{pl}$ , while the dissipation rate  $\Phi$  is the product of the stress variable  $\chi_{ij}$  with the plastic strain rate  $\dot{\epsilon}_{ij}^{pl}$ . They are only equal if the rate of plastic free energy  $\dot{\Psi}_{pl}$  is zero, or equivalently, if the free energy depends only on the elastic strains.

In kinematic hardening models, where the back stress describes the translation (or rotation) of the yield surface, the decomposition of the true stress (sum of back stress and dissipative stress) is a default assumption. Although such a shift stress is important for anisotropic material models, [Collins and Kelly \(2002\)](#) have pointed out that it is also necessary in isotropic models of geomaterials with different strength in tension and compression.

#### 104.11.2.2 Plastic Free Energy

A popular conceptual model, which focused on particulate materials and demonstrated the physical occurrence of shift stresses, was described by [Besseling and Van Der Giessen \(1994\)](#) and [Collins and Kelly \(2002\)](#). On macro (continuum) scale, every point in a given element is at yield state and deforms plastically. But on meso-scale, only part of this element is undergoing plastic deformations, the remaining part is still within yield surface and respond elastically. The elastic strain energy stored in the elastic part of a plastically deformed macro-continuum element is considered to be locked into the macro-deformation, giving rise to the plastic free energy function  $\Psi_{pl}$  and its associated back stress  $\alpha_{ij}$ . This energy can be released only when the plastic strains are reversed.

For better explanation, the nature of plastic free energy in particulate materials is illustrated through a finite element simulation combined with considerations of particle rearrangement on mesoscopic scale. Figure 104.80 shows stress-strain response of Drucker-Prager with nonlinear Armstrong-Frederick kinematic hardening, a typical elastic-plastic model for metals and geomaterials. Six states during shear are chosen to represent evolution of micro fabric of the numerical sample. Correspondingly, Figure 104.81 shows the process of particle rearrangement of the 2D granular assembly under cyclic shearing from microscopic level. The square window can be roughly considered as a representative volume (a constitutive level or a finite element) in FEM.

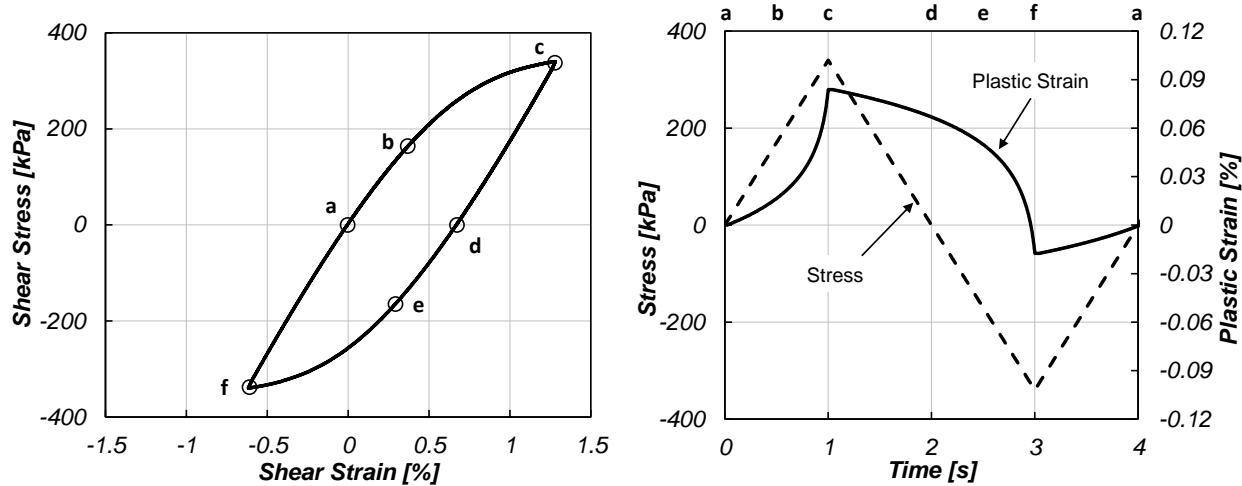


Figure 104.80: Elastic-plastic material modeled with Drucker-Prager yield function and Armstrong-Frederick kinematic hardening under cyclic shear loading: (a) Stress-strain curve; (b) stress and plastic strain versus time.

By discussing movement and energy of particle A in Figure 104.81, the physical nature of plastic free energy is illustrated. At state (a), which is the beginning of deformation, particle A does not bear any load other than its self weight. State (b) is in middle of loading, when particle B pushes downwards to particle A until it makes contact with particle D and E. Load reaches peak at state (c), and there's no space for particle A to move. Then the sample is unloaded to state (d). Particle A is now stuck between particles C, D, and F, which means that certain amount of elastic energy is stored due to particle elastic deformation. Compared with state (a), this part of elastic energy is not released when the sample is unloaded, which indicates that it's not classic strain energy. This part of elastic energy on particle level which can't be released by unloading is defined as the plastic free energy in granular materials. Reverse loading starts at state (e), where particle D pushes particle A upwards, making it squeeze through particle C and F. Elastic energy on particle level, which is now defined as plastic free energy, is released during

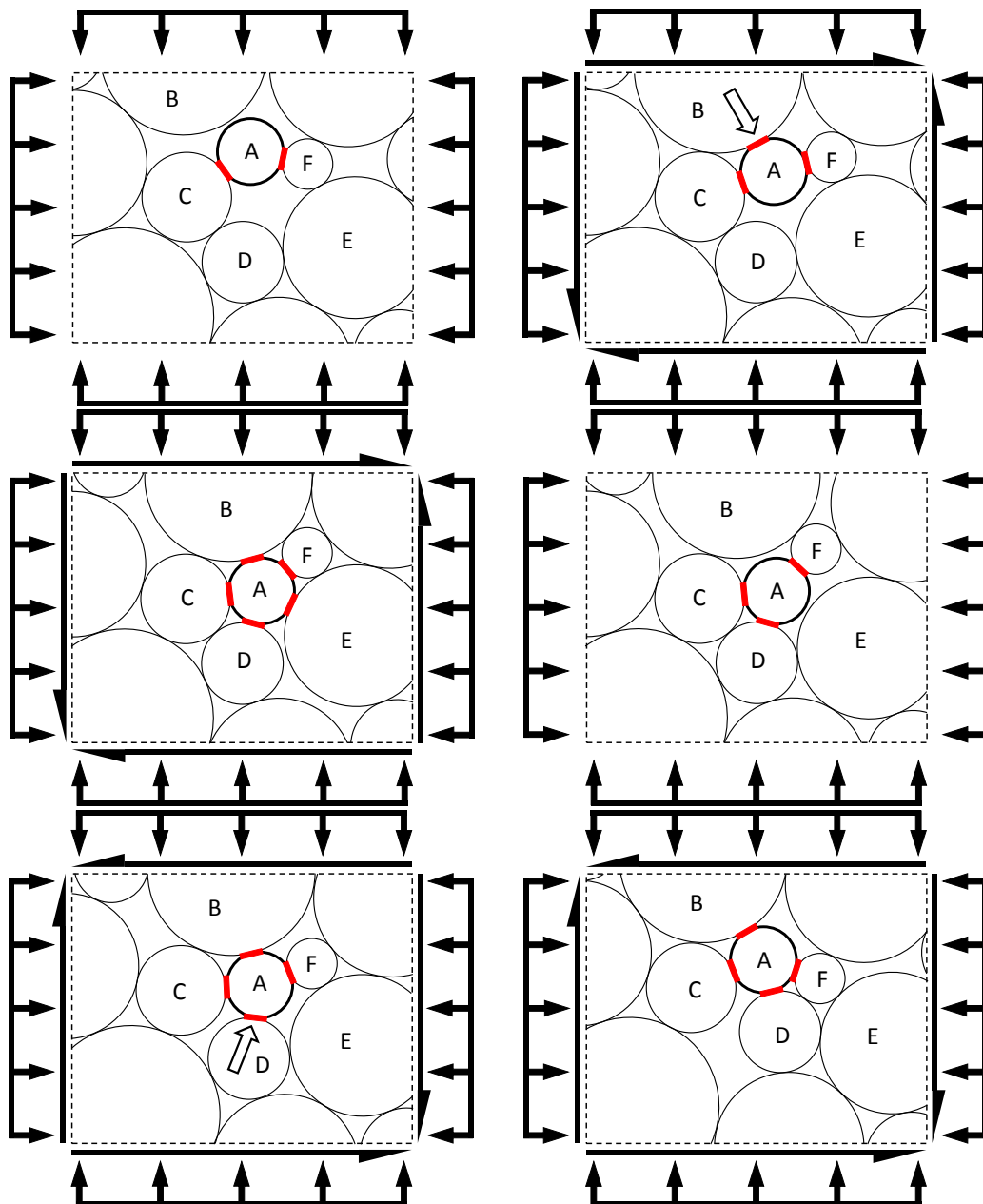


Figure 104.81: Particle rearrangement of a 2D granular assembly under cyclic shearing: (a) Initial state; (b) Loading (accumulating plastic free energy); (c) End of loading (maximum plastic free energy); (d) Unloading (plastic free energy unchanged); (e) Reverse loading (releasing plastic free energy); (f) End of reverse loading (plastic free energy released).

reverse loading.

By analyzing this example, an explanation on particle scale is provided for the origin of plastic free energy in granular materials. It is important to note that the concept of plastic free energy also exists in metals and other materials, as studied by [Dafalias et al. \(2002\)](#) and [Feigenbaum and Dafalias \(2007\)](#). The physical nature of plastic free energy in these materials can be different and probably should be studied on molecular and/or crystalline level.

[Collins Collins and Kelly \(2002\)](#), [Collins \(2003\)](#) suggested that in the case of granular materials, the particle-level plastic energy dissipation during normal compaction, arises from the plastic deformations occurring at the inter-granular contacts on the strong force chains, that are bearing the bulk of the applied loads. Collins also suggested that the locked-in elastic energy is produced in the weak force networks, where the local stresses are not large enough to produce plastic deformation at the grain contacts. The plastic strains can be associated with the irreversible rearrangement of the particles, whilst the elastic energy arises from the elastic compression of the particle contacts. Part of this elastic strain energy will be released during unloading, however other part of this energy will be trapped as a result of the irreversible changes in the particle configuration.

#### 104.11.2.3 Plastic Dissipation

As pointed out, plastic work and energy dissipation are not the same physical quantity. The confusion of these two concepts often leads to incorrect results and conclusions, especially in seismic energy dissipation analysis. Of major concern in this section is the computation of plastic dissipation, as elaborated in this section.

With the decoupling assumption (Equation 104.644), the second law of thermodynamics (positive entropy production) directly leads to the dissipation inequality, which states that the energy dissipated due to the difference of the plastic work rate and the rate of the plastic part of the free energy must be non-negative:

$$\Phi = \sigma_{ij}\dot{\epsilon}_{ij}^{pl} - \dot{\Psi}_{pl} = \sigma_{ij}\dot{\epsilon}_{ij}^{pl} - \rho\dot{\psi}_{pl} \geq 0 \quad (104.647)$$

where  $\dot{\psi}_{pl}$  is the rate of plastic free energy, per unit mass, and  $\rho$  is the mass density. In addition,  $\psi_{pl}$  denotes plastic free energy density, which is generally not constant at different locations in a body. This expression is closer to physics and makes it convenient for further derivations.

Now we proceed to consider how to calculate plastic free energy, which can then be used to calculate dissipation. According to [Feigenbaum and Dafalias \(2007\)](#), plastic free energy density  $\psi_{pl}$  is assumed to be additively decomposed into parts which correspond to the isotropic, kinematic and distortional

hardening mechanisms as follows:

$$\psi_{pl} = \psi_{pl}^{iso} + \psi_{pl}^{ani}; \quad \psi_{pl}^{ani} = \psi_{pl}^{kin} - \psi_{pl}^{dis} \quad (104.648)$$

where  $\psi_{pl}^{iso}$ ,  $\psi_{pl}^{ani}$ ,  $\psi_{pl}^{kin}$ , and  $\psi_{pl}^{dis}$  are the isotropic, anisotropic, kinematic, and distortional parts of the plastic free energy, respectively. The anisotropic part is assumed to decompose into kinematic and distortional parts, which correspond to different hardening models. The subtraction, instead of addition, of  $\psi_{pl}^{dis}$  from  $\psi_{pl}^{kin}$ , to obtain the overall anisotropic part  $\psi_{pl}^{ani}$  of the plastic free energy, is a new concept proposed by Feigenbaum and Dafalias (2007). This expression can better fit experimental data, as well as satisfy the plausible expectations for a limitation of anisotropy development. The distortional part of the plastic free energy  $\psi_{pl}^{dis}$  is related to the directional distortion of yield surface and will only be present if the material model incorporates distortional strain hardening, which is not considered in the formulations and examples of this study.

As pointed out by Dafalias et al. (2002), the thermodynamic conjugates to each of the internal variables exist and each part of the plastic free energy can be assumed to be only a function of these conjugates. The explicit expressions for the isotropic and kinematic components of the plastic free energy are:

$$\psi_{pl}^{iso} = \psi_{pl}^{iso}(\bar{k}) = \frac{\kappa_1}{2\rho} \bar{k}^2; \quad \psi_{pl}^{kin} = \psi_{pl}^{kin}(\bar{\alpha}_{ij}) = \frac{a_1}{2\rho} \bar{\alpha}_{ij} \bar{\alpha}_{ij} \quad (104.649)$$

where  $\bar{k}$  and  $\bar{\alpha}_{ij}$  are the thermodynamic conjugates to  $k$  (size of the yield surface) and  $\alpha_{ij}$  (deviatoric back stress tensor representing the center of the yield surface), respectively. Material constants  $\kappa_1$  and  $a_1$  are non-negative material constants whose values depend on the choice of elastic-plastic material models.

According to definition, the thermodynamic conjugates are related to the corresponding internal variables by:

$$k = \rho \frac{\partial \psi_{pl}^{iso}}{\partial \bar{k}} = \kappa_1 \bar{k}; \quad \alpha_{ij} = \rho \frac{\partial \psi_{pl}^{kin}}{\partial \bar{\alpha}_{ij}} = a_1 \bar{\alpha}_{ij} \quad (104.650)$$

By substituting Equation 104.650 back into Equation 104.649, the plastic free energy can be expressed in terms of the internal variables:

$$\psi_{pl}^{iso} = \frac{1}{2\rho\kappa_1} k^2; \quad \psi_{pl}^{kin} = \frac{1}{2\rho a_1} \alpha_{ij} \alpha_{ij} \quad (104.651)$$

With Equation 104.651, the components of plastic free energy can be computed, as long as the internal variables are provided. Combining Equation 104.647 with 104.651, the plastic dissipation in a given elastic-plastic material can be accurately obtained at any location, at any time. This approach allows engineers and designers to correctly identify energy dissipation in time and space and make appropriate conclusions on material behavior.

#### 104.11.2.4 Energy Computation in Finite Elements

Formulations from the previous section are applied to FEM analysis in order to follow energy dissipation. Energy density is chosen as the physical parameter for energy analysis. Energy density in this study is defined as the amount of energy stored in a given region of space per unit volume.

For FEM simulations, both external forces and displacements can be prescribed. The finite element program accepts either (or both) forces and/or displacements as input and solves for the other. Either way, the rate of input work can be calculated by simply multiplying force and displacement within a time step. Therefor input work of a finite element model is:

$$W_{Input}(t) = \int_0^t \dot{W}_{Input}(T)dT = \int_0^t \sum_i F_i^{ex}(\mathbf{x}, T)\dot{u}_i(\mathbf{x}, T)dT \quad (104.652)$$

where  $F_i^{ex}$  is the external force and  $u_i$  is the displacement computed at the location of the applied load, at given time step, for a load controlled analysis. The external load can have many forms, including nodal loads, surface loads, and body loads. All of them are ultimately transformed into nodal forces. As shown in Equation 104.652, input work is computed incrementally at each time step, in order to obtain the evolution of total input work at certain time.

As shown in Figure 104.82, when loads and/or displacements are introduced into a finite element model, the input energy will be converted in a number of different forms as it propagates through the system. Input energy will be converted into kinetic energy, free energy, and dissipation. As mentioned before, free energy can be further separated into elastic part, which is traditionally defined as strain energy, and plastic part, which is defined as the plastic free energy. Kinetic energy and strain energy can be considered as the recoverable portion of the total energy since they are transforming from one to another. Plastic free energy is more complicated in the sense that it is conditionally recoverable during reverse loading, as has been discussed in detail in previous sections. Other than kinetic energy and free energy, the rest of the input energy is dissipated, transformed into heat or other forms of energy that are irrecoverable.

Calculation of kinetic energy and strain energy is rather straight forward:

$$U_K(\mathbf{x}, t) = \frac{1}{2} \rho \dot{u}_{ij}(\mathbf{x}, t) \dot{u}_{ij}(\mathbf{x}, t) \quad (104.653)$$

$$U_S(\mathbf{x}, t) = \int_0^t \dot{U}_S(\mathbf{x}, T)dT = \int_0^t \sigma_{ij}(\mathbf{x}, T) \dot{\epsilon}_{ij}^{el}(\mathbf{x}, T)dT \quad (104.654)$$

where  $U_K$  and  $U_S$  are the kinetic energy density and strain energy density, respectively.

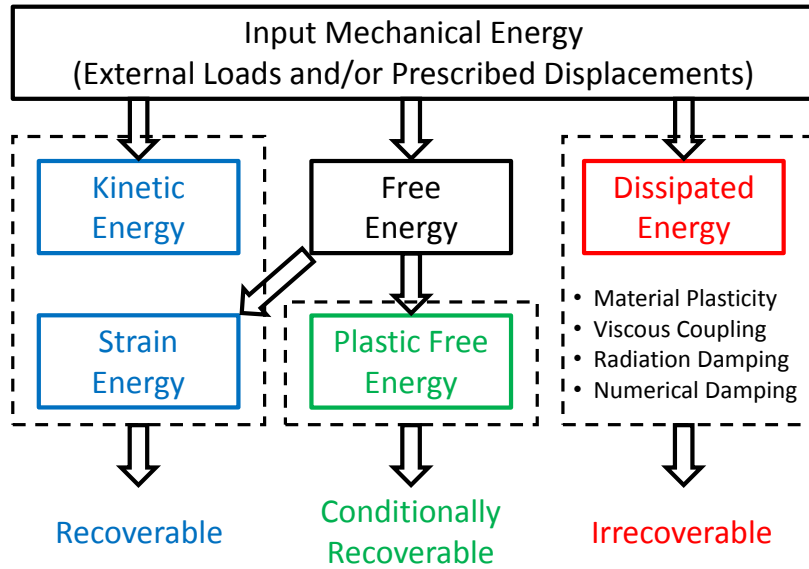


Figure 104.82: Different forms of energy in a dynamic soil-structure system.

Similar to the input energy, strain energy density and plastic free energy are also computed incrementally. Integrating energy density over the entire model, corresponding energy quantities are expressed as:

$$E_K(t) = \int_V U_K(\mathbf{x}, t) dV \quad (104.655)$$

$$E_S(t) = \int_V U_S(\mathbf{x}, t) dV \quad (104.656)$$

$$E_P(t) = \int_V \Psi_{pl}(\mathbf{x}, t) dV \quad (104.657)$$

where  $E_K$ ,  $E_S$ , and  $E_P$  are the kinetic energy, strain energy, and plastic free energy of the entire model, respectively. Energy densities, defined in Equations 104.653 and 104.654 are functions of both time and space, while energy components, defined in the above equations (Equation 104.655, 104.656, and 104.657) are only functions of time, since they are integrated over the whole model.

Although the plastic free energy is conditionally recoverable, it is still considered to be stored in the system, rather than dissipated. Summing up all the stored energy  $E_{Stored}$ , one obtains:

$$E_{Stored} = E_K + E_S + E_P \quad (104.658)$$

Rate of plastic dissipation, given by Equation 104.647, can be integrated over time and space:

$$D_P(t) = \int_V \int_0^t \Phi(\mathbf{x}, T) dT dV \quad (104.659)$$

where  $D_P$  is the dissipation due to plasticity of the entire model at certain time.

Finally the energy balance of a finite element model is given by:

$$W_{Input} = E_{Stored} + D_P = E_K + E_S + E_P + D_P \quad (104.660)$$

### 104.11.3 Numerical Studies

Numerical simulation results presented in this section are performed using the Real-ESSI (Jeremić et al., 1988-2025). Examples in this section focus on constitutive behavior of elastic-plastic material from the perspective of energy dissipation.

All cases are assumed to be static problems. External loads are applied incrementally using load- or displacement-control scheme. System equations are solved using Newton-Raphson iteration algorithm and UMFPACK solver. Standard 8-node-brick elements are used in all cases, in order to eliminate the variation in energy computation caused by different element types.

#### 104.11.3.1 Elastic Material

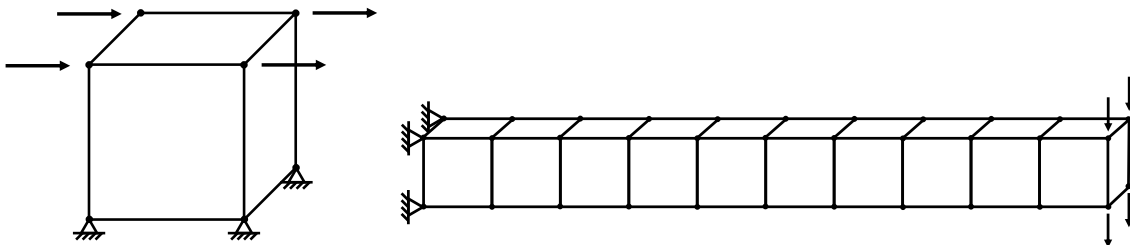


Figure 104.83: Numerical models used in this section: (a) Single brick element; (b) Cantilever with 10 brick elements.

Initial investigation of energy dissipation is focused on linear elastic material. It is noted that linear elastic material does not dissipate energy. Use of linear elastic material model is suitable for preliminary verification of the newly developed energy analysis methodology. In this section, energy balance in a single brick element and a cantilever beam is studied, as shown in Figure 104.83.

It should be mentioned that the bending deformations of cantilever are not accurate due to the use of a single layer of 8-node-brick elements in the direction of stress and strain variation. However, the focus

of this example is energy transformation and balance, which are not affected by inaccurate deformations in this example.

The simplest case is a single element model under uniform shear load. The model is constrained appropriately to simulate simple shear test. In order to show the influence of different material parameters and loads, a set of simulations are performed and the results are presented in Table 104.2 and Figure 104.84.

Table 104.2: Energy analysis results for linear elastic materials (single element).

Material Property		Simulation Results						
$E$ (GPa)	$\nu$	$u$ (m)	$W_{Input}$ (J)	$E_K$ (J)	$E_S$ (J)	$E_P$ (J)	$E_{Stored}$ (J)	$D_P$ (J)
100	0.30	2.60E-5	13.00	0.00	13.00	0.00	13.00	0.00
150	0.30	1.73E-5	8.67	0.00	8.67	0.00	8.67	0.00
200	0.30	1.30E-5	6.50	0.00	6.50	0.00	6.50	0.00
250	0.30	1.04E-5	5.20	0.00	5.20	0.00	5.20	0.00
300	0.30	8.67E-6	4.33	0.00	4.33	0.00	4.33	0.00
200	0.20	1.20E-5	6.00	0.00	6.00	0.00	6.00	0.00
200	0.25	1.25E-5	6.25	0.00	6.25	0.00	6.25	0.00
200	0.30	1.30E-5	6.50	0.00	6.50	0.00	6.50	0.00
200	0.35	1.35E-5	6.75	0.00	6.75	0.00	6.75	0.00
200	0.40	1.40E-5	7.00	0.00	7.00	0.00	7.00	0.00

Since linear elastic material is used with static algorithm, energy components related to dynamics (kinetic energy) and plasticity (plastic free energy and plastic dissipation) are equal to zero. This means that all input work is stored in the system, as observed in all cases.

Figure 104.84 shows that energy stored in the system is inversely proportional to Young's moduli  $E$  and proportional to one plus Poisson's ratio ( $1 + \nu$ ). This is expected because of the following equations for strain energy under static shear loading:

$$E_S = \frac{1}{2}\tau\gamma = \frac{1}{2G}\tau^2 = \frac{1+\nu}{E}\tau^2 \quad (104.661)$$

Note that these relationships are only valid at constitutive level. For models with more finite elements, stress and strain are generally not uniform. The computation of energy depends on the distribution of energy density, and nonuniform stress/strain distribution will result in nonuniform energy density distribution.

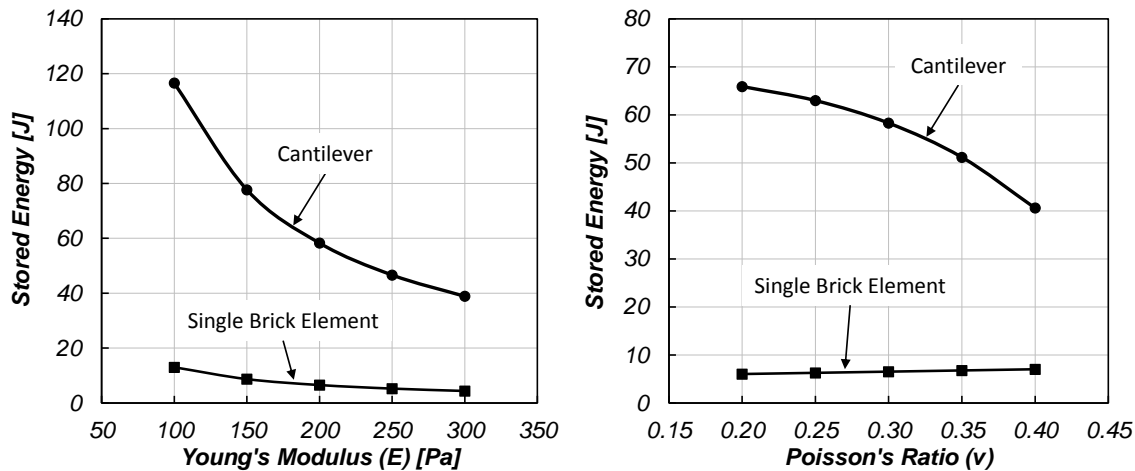


Figure 104.84: Relationships between energy storage and different simulation parameters (single element model): (a) Young's modulus; (b) Poisson's ratio.

In order to study the influence of simulation parameters in larger models, another set of simulations with cantilever model (Figure 104.83b) are performed. Vertical loads are applied to the nodes of the free end. In this case, both shearing and bending occurs, which means that in general a full 3D state of stress and strain is present. The results are presented in Table 104.3 and Figure 104.84. As expected, energy behavior of cantilever is different than the single-element/constitutive example.

For all cases, the energy balance between input and storage is maintained, which gives us confidence on the energy calculation methodology for elastic material. According to results in Figure 104.84, energy stored in the system is still inversely proportional to Young's modulus. This is because the general equation for elastic strain energy density is:

$$E_S = \frac{1}{2E} \left( \sigma_{xx}^2 + \sigma_{yy}^2 + \sigma_{zz}^2 + 2(1+\nu)(\sigma_{xy}^2 + \sigma_{yz}^2 + \sigma_{zx}^2) \right) \quad (104.662)$$

So as long as all the elements have the same Young's modulus, the relationship between stored energy and Young's modulus will remain valid.

### 104.11.3.2 von Mises Plasticity

Elastic-plastic modeling using von Mises material model has been proven to be effective in modeling pressure-independent materials like steel or other metals. In this section, the energy behavior of models using von Mises plasticity with various hardening rules are examined using the proposed method. The material model parameters used in this section are summarized in Table 104.4.

Note that associated plasticity is used in all models in this section, which means that the plastic flow

Table 104.3: Energy analysis results for linear elastic materials (cantilever model).

Material Property		Simulation Results						
$E$ (GPa)	$\nu$	$u$ (m)	$W_{Input}$ (J)	$E_K$ (J)	$E_S$ (J)	$E_P$ (J)	$E_{Stored}$ (J)	$D_P$ (J)
100	0.30	2.33E-3	116.57	0.00	116.57	0.00	116.57	0.00
150	0.30	1.55E-3	77.71	0.00	77.71	0.00	77.71	0.00
200	0.30	1.17E-3	58.28	0.00	58.28	0.00	58.28	0.00
250	0.30	9.33E-4	46.63	0.00	46.63	0.00	46.63	0.00
300	0.30	7.77E-4	38.86	0.00	38.86	0.00	38.86	0.00
200	0.20	1.20E-5	65.89	0.00	65.89	0.00	65.89	0.00
200	0.25	1.26E-3	62.97	0.00	62.97	0.00	62.97	0.00
200	0.30	1.17E-3	58.28	0.00	58.28	0.00	58.28	0.00
200	0.35	1.02E-3	51.17	0.00	51.17	0.00	51.17	0.00
200	0.40	8.12E-4	40.60	0.00	40.60	0.00	40.60	0.00

direction  $m_{ij}$  is equal to the gradient of the yield surface  $n_{ij}(= \partial f/\partial \sigma_{ij})$ . Since the yield function is of von Mises type, associated plasticity leads to the result that only deviatoric plastic flow will appear in all cases.

No Hardening (Elastic-Perfectly Plastic). In this example, elastic-perfectly plastic material is used. Equations 104.647 and 104.651 indicate that in the case of no hardening the rate of plastic free energy is zero. Then the incremental plastic work is equal to incremental plastic dissipation. Note that this is one of the rare cases where plastic dissipation equals to plastic work.

Figure 104.85 shows stress-strain curve (left) and energy calculated for elastic-perfectly plastic constitutive model (right) used here.

In this case, the plastic dissipation is equal to the plastic work. This means that the plastic free energy does not develop at all during loading and unloading. Zero plastic free energy points out the absence of fabric evolution of a particulate, elastic-plastic material, as all the input work is dissipated through particle to particle friction. Since there is no plastic free energy  $E_P$  in this case, the stored energy equals to mechanical energy, which is the combination of strain energy  $E_S$  and kinetic energy  $E_K$ . Total stored energy  $E_{Stored}$  develops nonlinearly and always has the same value at the beginning of every loop after the first one. Plastic dissipation  $D_P$  increases linearly when the material yields. This can be

Table 104.4: Model parameters for cases using von Mises plasticity

Parameter	Unit	Hardening Type			
		No Hardening	Linear Isotropic	Linear Kinematic	A–F Kinematic
mass_density	kg/m <sup>3</sup>	8050	8050	8050	8050
elastic_modulus	GPa	200	200	200	200
poisson_ratio		0.3	0.3	0.3	0.3
von_mises_radius	MPa	250	250	250	250
isotropic_hardening_rate	GPa		20	0	
kinematic_hardening_rate	GPa		0	50	
armstrong_fredrick_ha	GPa				200
armstrong_fredrick_cr					100

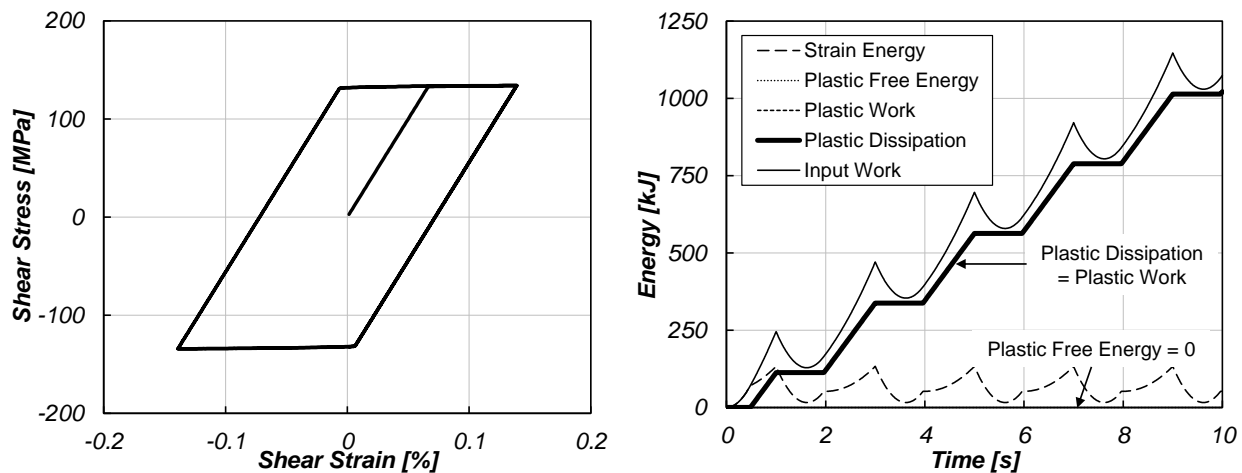


Figure 104.85: Energy analysis of elastic-plastic material modeled using von Mises plasticity with no hardening: (a) Stress–strain curve; (b) Input work, plastic dissipation, strain energy and plastic work.

explained by rewriting Equation 104.647 with  $\Psi_{pl} = 0$ :

$$\Phi = \sigma_{ij}\dot{\epsilon}_{ij}^{pl} \quad (104.663)$$

where stress  $\sigma_{ij}$  is constant after elastic perfectly plastic material yields, and rate plastic deformation  $\dot{\epsilon}_{ij}^{pl}$  is also constant. Then the rate of plastic dissipation is constant which makes the plastic dissipation  $D_p$  increase linearly.

Linear Isotropic Hardening. Next material model used is von Mises plasticity with linear isotropic hardening. First used to model monotonic behavior of elastic-plastic materials, isotropic hardening assumes that the yield surface maintains shape, while isotropically (proportionally) changing its size. Figure 104.86 illustrates the stress-strain response as well as energy balance for elastic-plastic material with isotropic hardening.

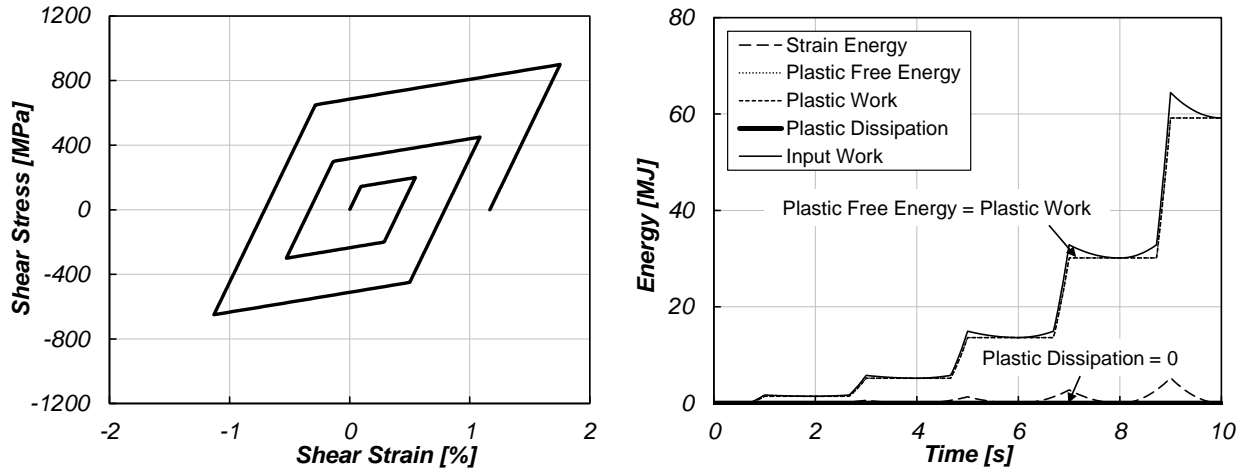


Figure 104.86: Energy analysis of elastic-plastic material modeled using von Mises plasticity with linear isotropic hardening: (a) Stress-strain curve; (b) Input work, plastic dissipation, strain energy, and plastic work.

As can be observed from Figure 104.86, plastic free energy is equal to the plastic work, which means that the plastic dissipation is zero during cycles of loading. Even though this might sound surprising, it can be explained using basic thermodynamics. Linear isotropic hardening, used in this case, can be described through a rate of the internal variable (size of the yield surface)  $\dot{k}$  as:

$$\dot{k} = \kappa_1 |\dot{\epsilon}_{ij}^{pl}| \quad (104.664)$$

where  $|\dot{\epsilon}_{ij}^{pl}|$  is the magnitude of the rate of plastic strain while  $\kappa_1$  is a hardening constant. The hardening constant  $\kappa_1$  is denoted as `isotropic_hardening_rate` in Table 104.4. Substituting previous equation into Equation 104.651 yields:

$$\psi_{pl} = \psi_{pl}^{iso} = \frac{\kappa_1}{2\rho} \epsilon_{ij}^{pl} \dot{\epsilon}_{ij}^{pl} \quad (104.665)$$

Take the time derivative of the above equation:

$$\dot{\psi}_{pl} = \frac{\kappa_1}{\rho} \epsilon_{ij}^{pl} \dot{\epsilon}_{ij}^{pl} \quad (104.666)$$

Then the rate of dissipation due to plasticity can be expressed as:

$$\Phi = \sigma_{ij}\dot{\epsilon}_{ij}^{pl} - \rho\dot{\psi}_{pl} = (\sigma_{ij} - \kappa_1\dot{\epsilon}_{ij}^{pl})\dot{\epsilon}_{ij}^{pl} = (\sigma_{ij} - km_{ij})\dot{\epsilon}_{ij}^{pl} \quad (104.667)$$

where  $m_{ij}$  is the plastic flow direction. The plastic flow direction defines the direction of incremental plastic strain, which can be different from the direction of total plastic strain. But in the case of associated von Mises plasticity with only isotropic hardening, the plastic flow direction  $m_{ij}$  is the same as the direction of the total plastic strain  $\dot{\epsilon}_{ij}^{pl}$ . Thus we have  $\kappa_1\dot{\epsilon}_{ij}^{pl} = km_{ij}$  in the above equation.

Substitute the plastic flow direction  $m_{ij}$  with the gradient of yield surface  $n_{ij}$ , and also note that  $\sigma_{ij}\dot{\epsilon}_{ij}^{pl} = s_{ij}\dot{\epsilon}_{ij}^{pl}$ , where  $s_{ij}(= \sigma_{ij} - 1/3\delta_{ij}\sigma_{kk})$  is the deviatoric part of the stress tensor, the rate of plastic dissipation can be rewritten as:

$$\Phi = (s_{ij} - kn_{ij})\dot{\epsilon}_{ij}^{pl} = \alpha_{ij}\dot{\epsilon}_{ij}^{pl} \quad (104.668)$$

Realizing that the back stress  $\alpha_{ij}$  is always zero since we assume no kinematic hardening, then the rate of plastic dissipation becomes zero, which means there is no energy dissipation during cycles of loading for isotropically hardening material. Obviously, the observed response is not physical from the perspective of energy dissipation. Therefore, isotropic hardening material models cannot properly model energy dissipation, even for monotonic loading.

**Prager Linear Kinematic Hardening.** Compared with isotropic hardening, kinematic hardening can better describe the constitutive, stress-strain behavior of elastic-plastic materials, particularly for cyclic loading. Elastic-plastic material that relies on kinematic hardening is used to analyze energy dissipation. Both linear and nonlinear kinematic hardening rules are investigated in relation to energy dissipation.

Prager's linear kinematic hardening rule is given as:

$$\dot{\alpha}_{ij} = a_1\dot{\epsilon}_{ij}^{pl} \quad (104.669)$$

where  $a_1$  is a hardening constant. The hardening constant  $a_1$  is denoted as `kinematic_hardening_rate` in Table 104.4.

If only linear kinematic hardening (Equation 104.669) is assumed, the back stress  $\alpha_{ij}$  is expressed explicitly, and can be substituted into Equation 104.651 yielding:

$$\psi_{pl} = \psi_{pl}^{kin} = \frac{a_1}{2\rho}\dot{\epsilon}_{ij}^{pl}\dot{\epsilon}_{ij}^{pl} \quad (104.670)$$

Take the time derivative of the above equation:

$$\dot{\psi}_{pl} = \frac{a_1}{\rho}\dot{\epsilon}_{ij}^{pl}\dot{\epsilon}_{ij}^{pl} \quad (104.671)$$

Then the rate of dissipation due to plasticity can be rewritten as:

$$\Phi = \sigma_{ij}\dot{\epsilon}_{ij}^{pl} - \rho\dot{\psi}_{pl} = (s_{ij} - \alpha_{ij})\dot{\epsilon}_{ij}^{pl} = km_{ij}\dot{\epsilon}_{ij}^{pl} \quad (104.672)$$

Notice that the term  $m_{ij}\dot{\epsilon}_{ij}^{pl}$  denotes the magnitude of the rate of plastic strain. Since only linear kinematic hardening is assumed, the internal variable  $k$  will remain constant. So if loads are applied in such a way that the rate of plastic strain is constant, then the rate of dissipation will also remain constant. In other words, the accumulated dissipation will be linearly increasing under the assumption of linear kinematic hardening.

Figure 104.87 shows stress-strain response (left) and energy computation results (right) of an elastic-plastic material modeled using von Mises plasticity with linear kinematic hardening.

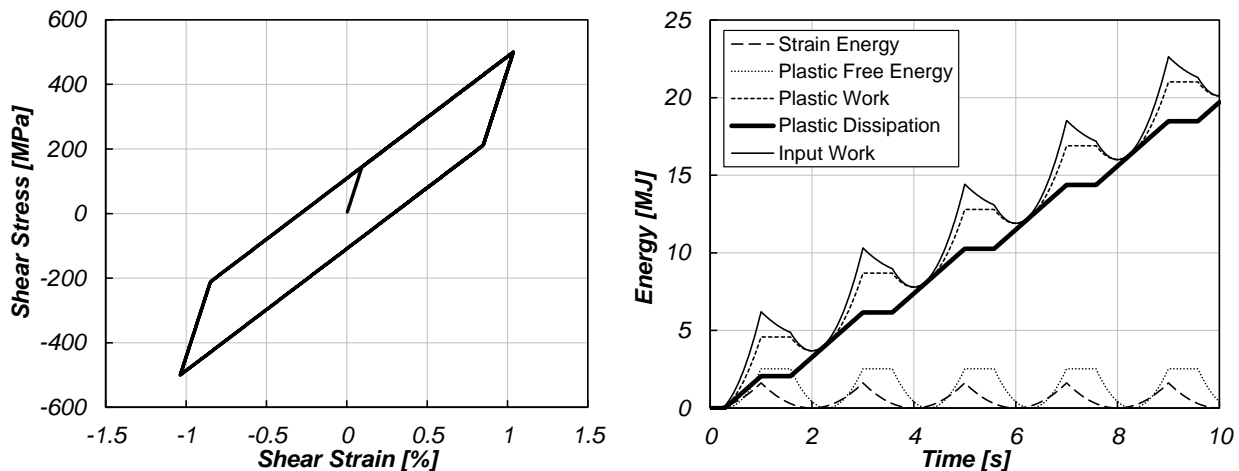


Figure 104.87: Energy analysis of elastic-plastic material modeled using von Mises plasticity with linear kinematic hardening: (a) Stress-strain curve; (b) Input work, plastic dissipation strain energy and plastic work.

As expected, the plastic dissipation increases linearly once the material yields. In contrast to the isotropic hardening case, a significant amount of the input work is dissipated due to material plasticity. The ratio of dissipated energy to input work is largely influenced by the material parameters. However, in general, energy dissipation will be observed if kinematic hardening model is used.

Another important observation is that the plastic work decreases during certain phases of reverse loading, while the actual rate of energy dissipation is always nonnegative. It is important to distinguish plastic work from plastic energy dissipation. Otherwise, one might argue that accumulated energy dissipation can increase or decrease, which is a common mistake observed in a number of publications that violates the second law of thermodynamics.

Armstrong-Frederick Kinematic Hardening. Armstrong-Frederick kinematic hardening model [Armstrong and Frederick \(1966\)](#) is often used to simulate elastic-plastic material behavior under cyclic loading. Material parameters of the Armstrong-Frederick kinematic hardening rule can be derived from basic thermodynamics. The following equation is a general expression for Armstrong-Frederick kinematic hardening rule:

$$\dot{\alpha}_{ij} = a_1 \dot{\epsilon}_{ij}^{pl} - a_2 \dot{\lambda} \alpha_{ij} \quad (104.673)$$

where  $\dot{\lambda}$  is a non-negative scalar plastic multiplier and  $a_2$  is a non-negative material hardening constant. It can be proven that  $a_1/a_2$  is related to the limit of back stress magnitude  $|\alpha_{ij}|$ . In Table 104.4, the hardening constants  $a_1$  and  $a_2$  correspond to parameters `armstrong_fredrik_ha` and `armstrong_fredrik_cr`.

Taking the time derivative of the kinematic part of plastic free energy (Equation 104.671), and substituting the expression of back stress  $\alpha_{ij}$  (Equation 104.673) gives:

$$\dot{\psi}_{pl}^{kin} = \frac{1}{\rho a_1} \alpha_{ij} \dot{\alpha}_{ij} = \frac{1}{\rho} \alpha_{ij} (\dot{\epsilon}_{ij}^{pl} - \frac{a_2}{a_1} \dot{\lambda} \alpha_{ij}) \quad (104.674)$$

Then the rate of plastic energy dissipation of an Armstrong-Frederick kinematic hardening elastic-plastic material is given by:

$$\Phi = \sigma_{ij} \dot{\epsilon}_{ij}^{pl} - \rho \dot{\psi}_{pl} = s_{ij} \dot{\epsilon}_{ij}^{pl} - \alpha_{ij} \dot{\epsilon}_{ij}^{pl} + \frac{a_2}{a_1} \dot{\lambda} \alpha_{ij} \alpha_{ij} = k m_{ij} \dot{\epsilon}_{ij}^{pl} + \frac{a_2}{a_1} \dot{\lambda} \alpha_{ij} \alpha_{ij} \quad (104.675)$$

Compared with Equation 104.672, the above expression has an additional term which makes the rate of plastic dissipation non-constant even if the rate of plastic strain is constant. As the back stress  $\alpha_{ij}$  becomes larger when load increases, the rate of plastic dissipation also increases. This indicates a nonlinear result of total plastic dissipation, which is exactly what we have observed in our computations.

Figure 104.88 shows the energy computation results of an elastic-plastic material modeled using von Mises plasticity with Armstrong-Frederick kinematic hardening. Compared to all previous cases, the material response of this model is more sophisticated and more realistic. Decrease of plastic work is observed, again, while the plastic dissipation is always nonnegative during the entire simulation. For both linear and nonlinear kinematic hardening cases, the plastic free energy is relatively small compared to the plastic dissipation.

#### 104.11.3.3 Drucker–Prager Plasticity

It has been proven that von Mises plasticity generally performs poorly in modeling pressure-sensitive materials like soils. In this section, the thermomechanical formulations presented in earlier sections are

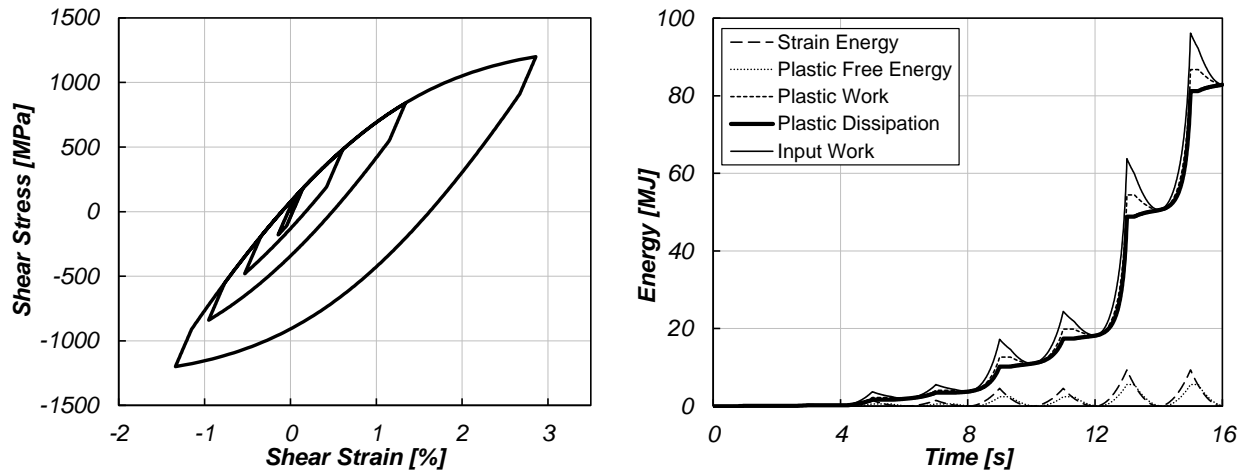


Figure 104.88: Energy analysis of elastic-plastic material modeled using von Mises plasticity with Armstrong–Frederick kinematic hardening: (a) Stress–strain curve; (b) Input work, plastic dissipation, strain energy, and plastic work.

Table 104.5: Model parameters for cases using Drucker–Prager plasticity

Parameter	Unit	Hardening Type				
		Linear Isotropic	Linear Kinematic	A–F Kinematic		
mass_density	$kg/m^3$	2000	2000	2000	2000	2000
elastic_modulus	MPa	150	150	200	200	200
poisson_ratio		0.3	0.3	0.3	0.3	0.3
druckerprager_k		0.25	0.5	0.1	0.1	0.1
confining_stress	kPa	100	100	100	300	500
isotropic_hardening_rate		50	0			
kinematic_hardening_rate		0	50			
armstrong_frederick_ha	MPa			20	20	20
armstrong_frederick_cr				100	100	100

applied to models using Drucker–Prager yield criteria with different hardening types. The material model parameters used in this section are summarized in Table 104.5.

The yield function of Drucker–Prager plasticity is:

$$f = [(s_{ij} - p\alpha_{ij})(s_{ij} - p\alpha_{ij})]^{0.5} - \sqrt{\frac{2}{3}}kp \quad (104.676)$$

where  $p = (1/3)\delta_{ij}\sigma_{kk}$  is the mean stress (or hydrostatic pressure). Note that in this form of Drucker–Prager plasticity, the internal variables  $\alpha_{ij}$  and  $k$ , as well as the hardening constants  $\kappa_1$  and  $a_1$ , are dimensionless.

For the computation of plastic free energy in Drucker–Prager plasticity models, Equation 104.651 is modified:

$$\psi_{pl}^{iso} = \frac{1}{2\rho(\kappa_1 p)}(kp)^2 = \frac{1}{2\rho\kappa_1}k^2p \quad (104.677)$$

$$\psi_{pl}^{kin} = \frac{1}{2\rho(a_1 p)}(\alpha_{ij}p)(\alpha_{ij}p) = \frac{1}{2\rho a_1}\alpha_{ij}\alpha_{ij}p \quad (104.678)$$

All examples presented in this section are using non-associated Drucker–Prager plasticity. The plastic potential function is of von Mises type so that only deviatoric plastic flow exists. In addition, all cases are loaded with constant hydrostatic pressure, which means that the plastic flow direction  $m_{ij}$  is the same as the direction of the total plastic strain  $\epsilon_{ij}^{pl}$ . With the above conditions, Equation 104.663, 104.668, and 104.672 are all still valid for the following examples, as will be observed in their results.

It should be noted that the proposed energy computation approach can also be applied to associated Drucker–Prager plasticity and non-associated Drucker–Prager plasticity with different plastic potential functions. The loading condition can be arbitrary, even with evolving hydrostatic pressures.

**Linear Isotropic Hardening.** Figure 104.89 shows the stress–strain response and energy computation results of an elastic-plastic material modeled using Drucker–Prager plasticity with linear kinematic hardening.

No plastic dissipation is observed in this case, which have been theoretically proven in Equation 104.668. This example again indicates that isotropic hardening is not capable of proper modeling of energy dissipation in elastic-plastic materials.

**Prager Linear Kinematic Hardening.** Figure 104.90 shows the stress–strain response and energy computation results of an elastic-plastic material modeled using Drucker–Prager plasticity with linear kinematic hardening.

Plastic dissipation increases linearly when the material yields, while the plastic work decreases during certain phases of reverse loading. This observation is consistent with the theoretical conclusion drawn from Equation 104.672.

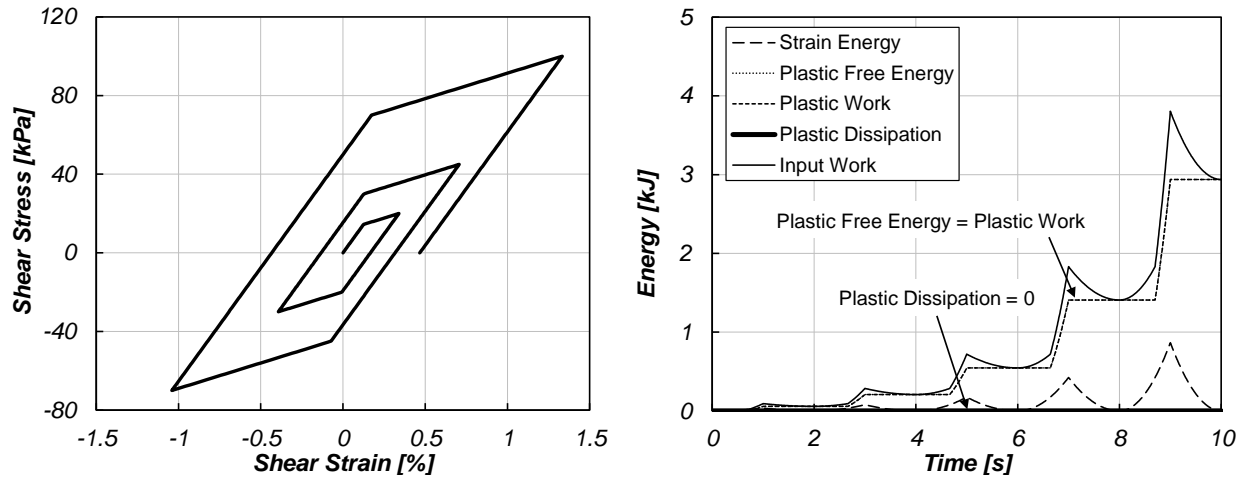


Figure 104.89: Energy analysis of elastic-plastic material modeled using Drucker–Prager plasticity with linear isotropic hardening: (a) Stress–strain curve; (b) Input work, plastic dissipation strain energy and plastic work.

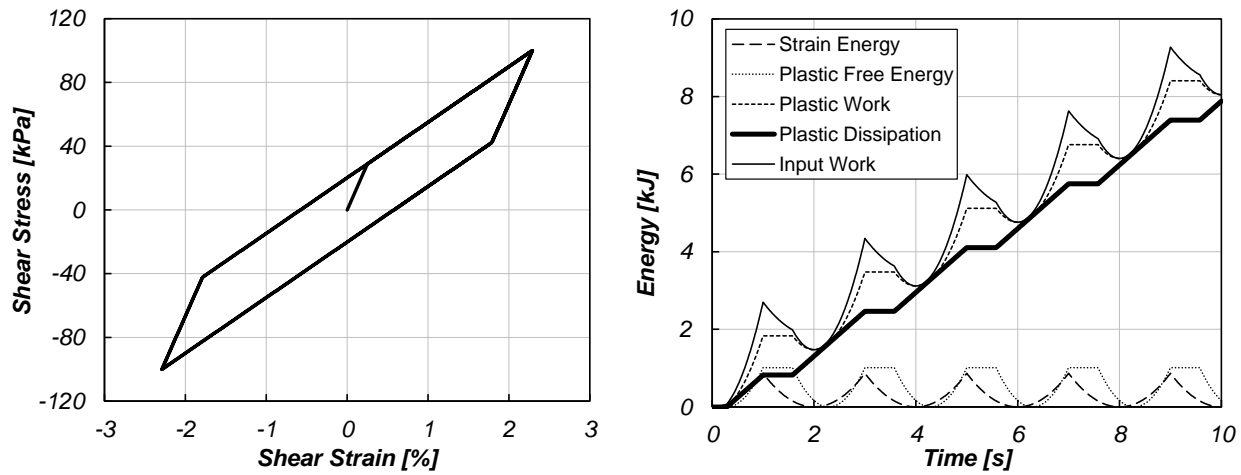


Figure 104.90: Energy analysis of elastic-plastic material modeled using Drucker–Prager plasticity with linear kinematic hardening: (a) Stress–strain curve; (b) Input work, plastic dissipation strain energy and plastic work.

Note that the results of the above two examples share high similarity with those of the cases modeled with associated von Mises plasticity. This is because the hydrostatic pressures were constant during shearing, which makes the pressure-dependent feature of Drucker–Prager plasticity not observed. The energy computation results are expected to be more complicated with different loading conditions. However, the difference between plastic work and plastic dissipation will be observed. And the incremental plastic dissipation should always be nonnegative.

Armstrong–Frederick Kinematic Hardening. In order to illustrate the influence of hydrostatic pressure to the energy dissipation in Drucker–Prager models, three cases with different confining pressures are studied. Armstrong–Frederick kinematic hardening is used here to model the nonlinear hardening response of pressure-dependent material, like soils. Figure 104.91 shows the stress–strain response and energy computation results of these three cases.

As can be observed from Figure 104.91, the slope of stress–strain loop increases, which means the material becomes stiffer, as the confining stress increases. Also, the size of elastic region becomes larger when the confining stress is bigger.

Plastic dissipation and plastic free energy starts to evolve as soon as the material yields. The pattern of evolution of energy components are the same for all three cases, while the value of plastic dissipation decreases as the confining stress increases. This is expected since the material becomes stiffer and harder to plastify with a higher confining stress.

#### 104.11.4 Conclusions

Presented was a methodology for (correct) computation of energy dissipation in elastic-plastic materials based on the second law of thermodynamics. A very important role of plastic free energy was analyzed, with highlights on its physical nature and theoretical formulations. The proposed methodology has been illustrated using a number of elasto-plastic material models.

An analysis of a common misconception that equates plastic work and dissipation, which leads to the violation of the basic principles of thermodynamics, was addressed. A conceptual example, for granular materials, was used to explain the physical meaning of plastic free energy. It was also shown that plastic free energy is responsible for the evolution of internal variables.

It was shown that energy balance is ensured by taking into consideration all energy components, including kinetic and strain energy. Input work was balanced with the stored and dissipated energy, expressed as the summation of all possible components.

Presented approach was illustrated and tested using several elastic-plastic constitutive models with various hardening rules. Elastic materials showed no energy dissipation (as expected), leading to the

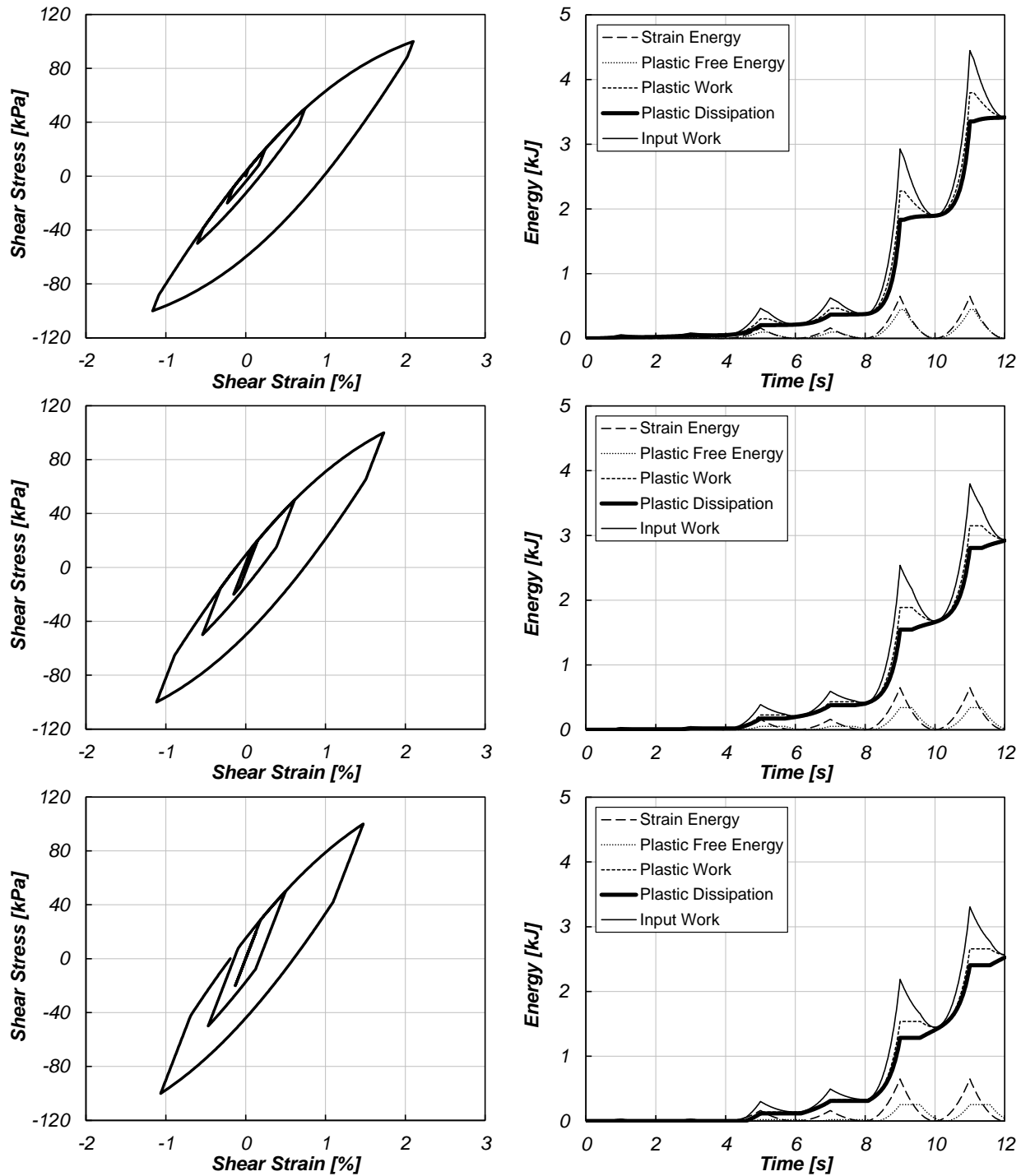


Figure 104.91: Energy analysis of elastic-plastic material modeled using Drucker-Prager plasticity with Armstrong-Frederick kinematic hardening: (a) Confining stress = 100 kPa; (b) Confining stress = 300 kPa; (c) Confining stress = 500 kPa;

input work being equal to the stored energy. Elastic-perfectly plastic materials had no change in plastic free energy, which led to the equality of plastic work and plastic dissipation and indicated no evolution of particle arrangements. The plastic dissipation, in that case, was observed to be increasing linearly. Isotropic hardening materials experienced zero dissipation even after yielding. This observation was surprising, but verified by further derivation of energy equations. This observation also serves as a reminder that the isotropic hardening rules can be used, but only with observed lack of energy dissipation. Prager's linear and Armstrong-Frederick nonlinear kinematic hardening materials both gave significant dissipations, with large fluctuation of plastic free energy as well. In the case with linear kinematic hardening, linear increase of dissipation was derived and observed, while energy was dissipated nonlinearly in the case of nonlinear kinematic hardening. Although the plastic free energy was not significant for some materials, it is noted that it should always be recognized and considered during energy analysis, so that the basic principles of thermodynamics are maintained.

## 104.12 Energy Dissipation Calculations for Structures

This section is based on [Yang et al. \(2019a\)](#)

### 104.12.1 Introduction

Mechanical energy in soil structure interaction (SSI) systems are dissipated during the irreversible dissipative process of energy transformation in which entropy of the system increases. Energy dissipation has been used, directly or indirectly, as a key parameter to evaluate damage in elastic-plastic materials. A common misconception of plastic work and energy dissipation due to plasticity has been noticed in a number of publications [Uang and Bertero \(1990\)](#), [Léger and Dussault \(1992\)](#), [Symans and Constantinou \(1998\)](#), [Soong and Spencer \(2002\)](#), [Symans et al. \(2008\)](#), [Wong \(2008\)](#), [Nehdi et al. \(2010\)](#) in which violations of the second law of thermodynamics were observed. As presented in an earlier section (and also by [Yang et al. \(2018\)](#)), the correct formulation for energy analysis on elastic-plastic solids has been derived from the second law of thermodynamics. The theoretical and computational framework has been verified through system energy balance in a series of numerical studies on elastic and elastic-plastic material models. The purpose of this section is to present a methodology of correctly evaluating energy dissipation in structural elements, which is crucial in determining the safety and economy of a SSI system.

It has been shown [Dafalias et al. \(2002\)](#), [Feigenbaum and Dafalias \(2007\)](#), [Yang et al. \(2018\)](#) that the difference between plastic work and plastic dissipation is the plastic free energy, or cold work, which can be calculated from material internal variables (or state variables), like radius of yield surface or back stress. This computation can be easily performed on solids modeled with classic elasticity/plasticity

constitutive relationships in which internal variables are computed and obtained at every time step. On the other hand, constitutive relationships used to model nonlinear structural elements were proposed mainly based on experimental results Spacone et al. (1996a), Spacone et al. (1996b), Lee and Fenves (1998), Popovics (1973), Mander et al. (1988), Chang and Mander (1994), Waugh (2009), Kolozvari et al. (2015). The internal variables used in these models are different than those used in classic constitutive models for solids. Therefore, a new methodology that can correctly evaluate energy storage and dissipation in structural elements is required.

During the recent few decades, a number of studies have been conducted with focus on energy analysis of SSI systems Uang and Bertero (1990), Léger and Dussault (1992), Kalkan and Kunnath (2007), Kalkan and Kunnath (2008), Symans et al. (2008), Gajan and Saravanathiiban (2011), Moustafa (2011), Moustafa and Mahmoud (2014), Mezgebo and Lui (2017), Deniz et al. (2017). Despite different formulations used, the calculations of energy dissipation due to hysteretic damping (material elasto-plasticity) in these publications were all performed without consideration of plastic free energy, which lead to violations of principles of thermodynamics. It is worth pointing out that such oversight is not rare, especially in literature of civil and geotechnical engineering.

Early work reported by Farren and Taylor (1925) and Taylor and Quinney (1934) showed that plastic free energy could be significant in metals, thus should not be neglected without reasoning. The ratio of plastic work converted into heat, usually referred to as the Quinney–Taylor coefficient, was measured to be between 0.6 to 1.0 Belytschko et al. (1991), Zhou et al. (1996), Dolinski et al. (2010), Osovski et al. (2013). Mason Mason et al. (1994) pointed out that the the Quinney–Taylor coefficient is both strain and strain rate dependent but could be assumed to be a constant in most cases. A constitutive model for metals was presented by Rosakis et al. Rosakis et al. (2000), Hodowany et al. (2000), Ravichandran et al. (2002) based on thermoplasticity, which can model the evolution of energy dissipation and has been validated through experiments. Semnani et al. (2016) presented a thermoplastic framework that could predict strain localization in transversely isotropic materials.

Despite of the existence of sophisticated theories that are capable of modeling the evolution of energy dissipation, including those mentioned earlier, most constitutive relationships used to model structural elements do not involve thermodynamics or thermoplasticity. One commonly used finite element (FE) technique of modeling frame structures is fiber section, in which beams and columns are divided into multiple uniaxial fibers with various constitutive models. This model have been proved to be able to capture nonlinear stress–strain behaviors of structural elements under axial loading and/or bending.

Problems arise when such elements are used to calculate energy dissipation. As observed in many publications Kwan and Billington (2001), Zhu et al. (2006), Gajan and Saravanathiiban (2011), Wang et al. (2012), Zhang et al. (2013), Nikbakht et al. (2014) energy analysis were performed based on the

hysteretic stress-strain or force-displacement response of the elements. This indicates that plastic work was confused with plastic energy dissipation, which is the common misconception pointed out earlier. It is also important to point out that various damage indices derived from energy dissipation are used widely to evaluate damage in structures. Such parameters will not be valid if the fundamental formulation of energy dissipation is incorrect.

In order to correctly evaluate energy dissipation in structural elements modeled with fiber sections, the framework of thermo-mechanics must be enforced on the uniaxial constitutive models. Focus of this section is on proper modeling of different forms of energy (storage and dissipation) in uniaxial materials that follows the second law of thermodynamics. Theoretical and computational formulations of energy dissipation in uniaxial concrete and steel fibers are presented. A series of FE simulations are carried out using the Real-ESSI ([Jeremić et al., 1988-2025](#)) to illustrate the energy behavior of structural systems. The method is verified by comparing the input work and the energy storage and dissipation in the system. The difference between accumulated plastic work and accumulated plastic dissipation, which can be significant in many cases, is addressed. Finally, conclusions on plastic energy dissipation in structural elements are drawn from the verified results.

## 104.12.2 Theoretical and Computational Formulations

### 104.12.2.1 Thermomechanical Framework

The theories of continuum thermo-mechanics have been discussed in a number of earlier publications [Lubliner \(1972\)](#), [Rosakis et al. \(2000\)](#), from which the fundamental framework of this study is derived. General equations of elastoplasticity and thermodynamics are modified with a few plausible assumptions to accommodate the scope of this study. Small deformation theory is assumed, so that the small strain tensor  $\epsilon_{ij}$  is used to describe deformation of the material body. All equations in this section are expressed in index notation.

The general thermomechanical process is governed by momentum balance and the first and second law of thermodynamics. The localized version of the first law of thermodynamics (energy balance equation) is given in the form:

$$\sigma_{ij}\dot{\epsilon}_{ij} + q_{i,i} + \rho r = \rho\dot{e} \quad (104.679)$$

where the term  $\sigma_{ij}\dot{\epsilon}_{ij}$  is called the stress power,  $q_i$  are the components of the heat flux vector,  $\rho$  is the mass density of the material,  $r$  is the heat supply per unit volume, and  $e$  is the internal energy per unit volume. Note that in this section all stresses are defined as effective stresses. In order to avoid confusion, the common notation  $(\sigma'_{ij})$  will not be used. Standard definition of stress from mechanics of materials, i.e. positive in tension, is used.

The localized version of the second law of thermodynamics (Clausius–Duhem inequality) is expressed as:

$$\rho\dot{\eta} - \left(\frac{q_i}{\theta}\right)_{,i} - \frac{1}{\theta}\rho r \geq 0 \quad (104.680)$$

where  $\eta$  is the entropy per unit volume and  $\theta$  is the absolute temperature.

Substituting the heat supply per unit volume  $r$  in Equation 104.680 with the expression from Equation 104.679, and introducing the rate of change of internal dissipation per unit volume  $\Phi$  gives:

$$\rho\theta\dot{\eta} - \rho\dot{\psi} + \sigma_{ij}\dot{\epsilon}_{ij} + \frac{1}{\theta}q_i\theta_{,i} = \Phi + \frac{1}{\theta}q_i\theta_{,i} \geq 0 \quad (104.681)$$

Note that the internal dissipation can have many sources, including material plasticity, viscous coupling, radiation damping, and other forms of energy dissipation.

The Helmholtz free energy per unit volume  $\psi$ , which is referred to as free energy in this section, is defined as:

$$\psi = e - \theta\eta \quad (104.682)$$

The second law of thermodynamics can be expressed in terms of free energy  $\psi$  as:

$$\Phi + \frac{1}{\theta}q_i\theta_{,i} = -\rho\dot{\psi} - \rho\dot{\theta}\eta + \sigma_{ij}\dot{\epsilon}_{ij} + \frac{1}{\theta}q_i\theta_{,i} \geq 0 \quad (104.683)$$

The rate of internal dissipation per unit volume  $\Phi$  can be written as:

$$\Phi = \sigma_{ij}\dot{\epsilon}_{ij} - \rho\dot{\psi} - \rho\dot{\theta}\eta \quad (104.684)$$

At this point, a few assumptions are introduced to simplify the governing equations. According to Feigenbaum and Dafalias (2007), Collins and Housby (1997), Collins (2002), Collins and Kelly (2002), it can be assumed that the deformation of soil and structural elements under earthquake loading is approximately isothermal, which indicates that the temperature field  $\theta$  is constant and uniform. This approximation is reasonable considering the fact that seismic energy is mostly carried by the low-frequency components of earthquake ground motion, which allows the heat generated in the materials to be largely dissipated. With this assumption, the rate of internal dissipation  $\Phi$  is simplified into the form:

$$\Phi = \sigma_{ij}\dot{\epsilon}_{ij} - \rho\dot{\psi} \geq 0 \quad (104.685)$$

Next, all material models studied in this section is assumed to be decoupled, which means that the (small) strain tensor can be additively decomposed into elastic and plastic parts:

$$\epsilon_{ij} = \epsilon_{ij}^{el} + \epsilon_{ij}^{pl} \quad (104.686)$$

Lubliner (1972) and Collins and Houlsby (1997) showed that this assumption can be deduced if the instantaneous elastic moduli of a material are independent of the internal variables. Under the assumption of decoupled material, the free energy  $\psi$  can also be decomposed into elastic and plastic parts as follows:

$$\psi = \psi_{el} + \psi_{pl} \quad (104.687)$$

where the elastic part of the free energy  $\psi_{el}$  is also known as the elastic strain energy, which is defined in incremental form as:

$$\dot{\psi}_{el} = \sigma_{ij}\dot{\epsilon}_{ij}^{el} \quad (104.688)$$

By substituting Equation 104.686, Equation 104.687, and Equation 104.688 into Equation 104.685, the rate of internal dissipation  $\Phi$  can be expressed in terms of the rate of plastic free energy  $\dot{\psi}_{pl}$ :

$$\Phi = \sigma_{ij}\dot{\epsilon}_{ij} - \sigma_{ij}\dot{\epsilon}_{ij}^{el} - \rho\dot{\psi}_{pl} \geq 0 \quad (104.689)$$

Equation 504.8 represents two basic principles that should always be upheld in any energy analysis for decoupled material undergoing isothermal process:

- The stress power that is input into a material body by external loading is transformed into elastic strain energy, plastic free energy, and material internal dissipation. All forms of energy must be considered to maintain energy balance of the material body. This principle ensures the first law of thermodynamics.
- The rate of change of material internal dissipation (plastic dissipation) is nonnegative at any time. In other words, accumulated internal dissipation can not decrease during any time period. This principle ensures the second law of thermodynamics.

Note that material internal dissipation can have many sources. Our interest is the energy dissipation caused by material plasticity, so the term plastic dissipation will be used instead, which indicates no other source of energy dissipation is present in the examples that are being analyzed in the remaining part of this section.

#### 104.12.2.2 Plastic Free Energy

The physical nature of plastic free energy is associated with the material micro-structure. For particulate material, like soil, plastic free energy will be accumulated or released if there is evolution of particle arrangement (micro-fabric), which generally happens as soon as the material body is loaded. For other

structural and geotechnical materials, like metals, their micro-structures are represented by the shape and arrangement of the crystals, whose evolution will result in change in plastic free energy. Detailed explanations of the evolution of plastic free energy can be found in publications by [Besseling and Van Der Giessen \(1994\)](#), [Collins and Kelly \(2002\)](#), and [Yang et al. \(2018\)](#).

Using Equation 504.8, the energy dissipation of any elastic-plastic material under isothermal loading process can be calculated, if all the terms on the right hand side of the equation is known. For most elastic-plastic constitutive models, the stress tensor  $\sigma_{ij}$  and the elastic strain tensor  $e_{ij}^{el}$  are being calculated as simulation progresses. The challenging task is to evaluate the plastic free energy term  $\psi_{pl}$ , whose formulation depends on the internal variables used in the constitutive model.

For a decoupled elastic-plastic material model that exhibits both isotropic and kinematic hardening, the plastic free energy is decomposed into isotropic and kinematic parts, which are calculated individually and then added up. The formulation of plastic free energy in this type of material was given by [Feigenbaum and Dafalias \(2007\)](#):

$$\psi_{pl} = \psi_{pl}^{iso} + \psi_{pl}^{kin} = \frac{1}{2\rho\kappa_1}k^2 + \frac{1}{2\rho a_1}\alpha_{ij}\alpha_{ij} \quad (104.690)$$

where  $\psi_{pl}^{iso}$  and  $\psi_{pl}^{kin}$  are the isotropic and kinematic parts of the plastic free energy, respectively,  $k$  is the radius of yield surface,  $\alpha$  is the back stress,  $\kappa_1$  and  $a_1$  are non-negative material constants. Note that Equation 104.690 can be used for a wide range of constitutive models with various yield functions, including von Mises and Drucker-Prager yield criteria whose energy behaviors has been studied and presented by [Yang et al. \(2018\)](#). Such materials are usually used to model soils and parts of the structure that need to be modeled with solid elements in SSI system.

However, frame structures are generally modeled with beam-column elements in combination with fiber sections and uniaxial material models, where Equation 104.690 does not apply. It should be realized that most uniaxial constitutive relationships are capable of modeling the stress-strain behavior but not the energy dissipation features of the material. Therefore, an approach that follows our thermomechanical framework is presented to correctly evaluate energy storage and dissipation in these material models.

#### 104.12.2.3 Energy Dissipation in Beam-Column Element

Beams and columns are modeled with nonlinear displacement-based beam element, which is implemented in the Real-ESSI Simulator. In order to incorporate confined/unconfined concrete and steel reinforcement bars into beam elements, fiber sections are constructed with corresponding uniaxial fibers. A bottom-fixed reinforced concrete column model is shown in Figure 104.92, along with the constitutive relationships used for the concrete and steel fibers.

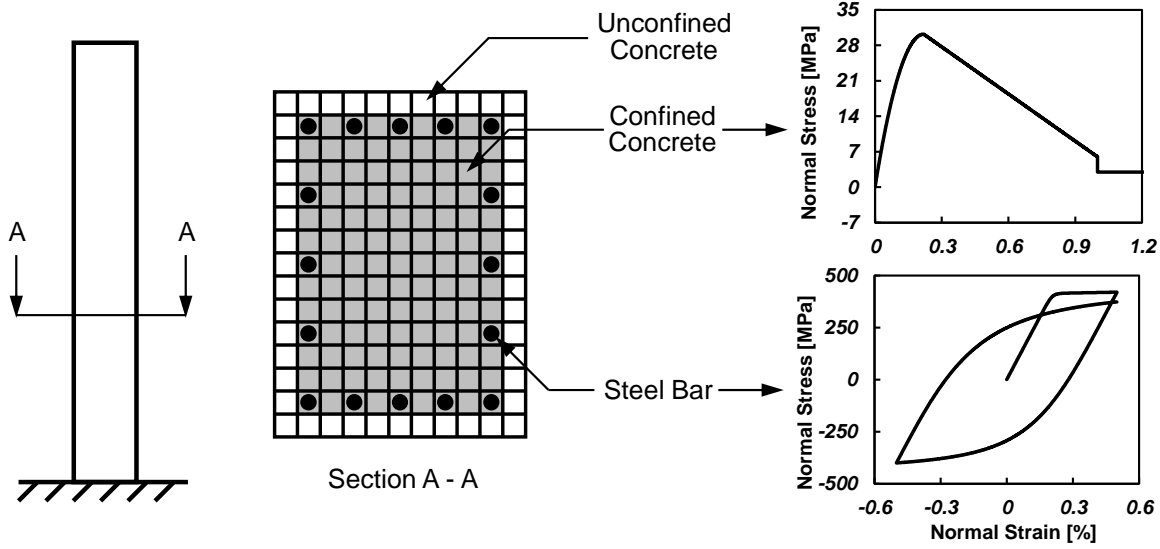


Figure 104.92: Schematic of a bottom-fixed column modeled with concrete and steel fibers.

**Uniaxial Steel Fiber.** The uniaxial steel material model examined in this study was developed by Menegotto and Pinto (1973) and extended by Filippou et al. (1983), and is capable of capturing the nonlinear hysteretic behavior and isotropic strain-hardening effect of steel. The stress-strain response of this material is shown in Figure 104.93, along with some of the material parameters. The model, as presented in Menegotto and Pinto (1973), takes on the form:

$$\sigma^* = b\epsilon^* + \frac{(1-b)\epsilon^*}{(1+\epsilon^*R)^{1/R}} \quad (104.691)$$

with

$$\epsilon^* = \frac{\epsilon - \epsilon_r}{\epsilon_0 - \epsilon_r}; \quad \sigma^* = \frac{\sigma - \sigma_r}{\sigma_0 - \sigma_r} \quad (104.692)$$

where  $b$  is the strain-hardening ratio,  $\epsilon_r$  and  $\sigma_r$  are the strain and stress at the point of strain reversal,  $\epsilon_0$  and  $\sigma_0$  are the strain and stress at the point of intersection of the two asymptotes,  $R$  is the curvature parameter that governs the shape of the transition curve between the two asymptotes. Note that this model is for uniaxial materials, in which the stresses and strains are scalars instead of tensors.

The expression for the curvature parameter  $R$  is suggested by Menegotto and Pinto (1973):

$$R = R_0 - \frac{c_{R_1}\xi}{c_{R_2} + \xi} \quad (104.693)$$

where  $R_0$  is the value of the curvature parameter  $R$  during initial loading,  $c_{R_1}$  and  $c_{R_2}$  are degradation parameters that need to be experimentally determined. The parameter  $\xi$ , that is updated after strain

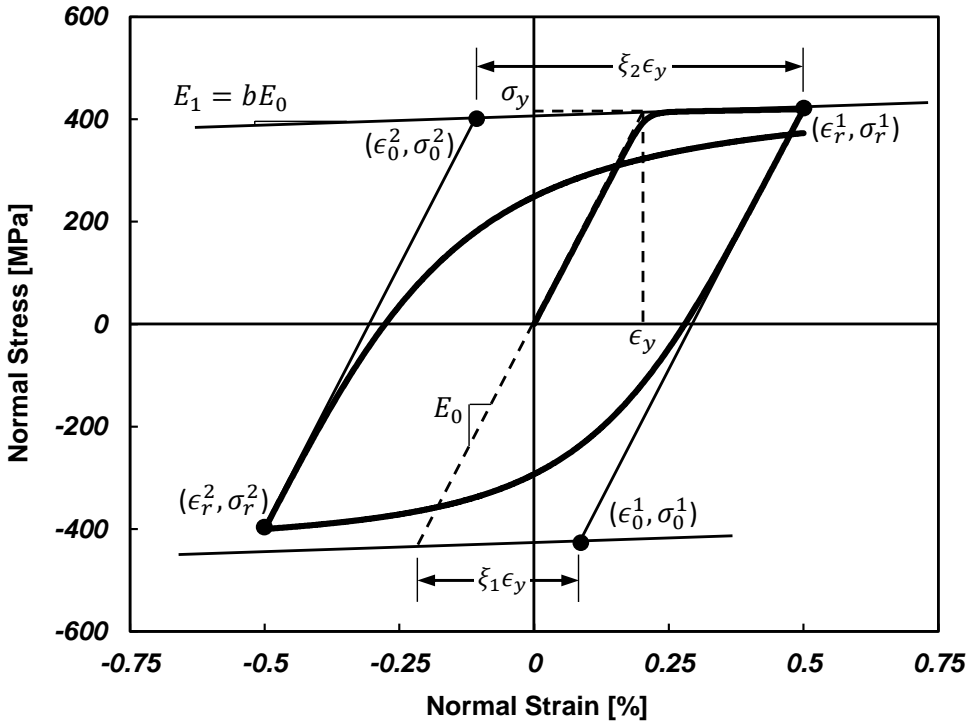


Figure 104.93: Constitutive model for uniaxial steel fiber ([Menegotto and Pinto \(1973\)](#)).

reversal, is defined as:

$$\xi = \left| \frac{(\epsilon_m - \epsilon_0)}{\epsilon_y} \right| \quad (104.694)$$

where  $\epsilon_m$  is the maximum (or minimum) strain at the previous strain reversal point, depending on the loading direction of the material. If the current incremental strain is positive, the parameter  $\epsilon_m$  takes the value of the maximum reversal strain. Parameter  $\epsilon_y$  is the monotonic yield strain.

In order to capture isotropic hardening behavior, [Filippou et al. \(1983\)](#) introduced stress shift mechanism into the original model by [Menegotto and Pinto \(1973\)](#). Note that the hardening rate in compression and tension can be different by choosing different hardening parameters for compression and tension. The proposed relation takes the form:

$$\frac{\sigma_{st}}{\sigma_y} = a_1 \left( \frac{\epsilon_{max}}{\epsilon_y} - a_2 \right) \quad (104.695)$$

where  $\sigma_{st}$  is the shift stress that determines the shift of yield asymptote,  $\epsilon_{max}$  is the absolute maximum strain at strain reversal, and  $a_1$  and  $a_2$  are hardening parameters in compression that are experimentally determined. In the case of tension, the hardening parameters  $a_1$  and  $a_2$  in Equation 104.695 are changed to  $a_3$  and  $a_4$  that are also determined by experiment or obtained from the literature.

The energy computation procedure for this uniaxial steel model is shown in Figure 507.4, and it follows the thermomechanical framework established earlier in this section.

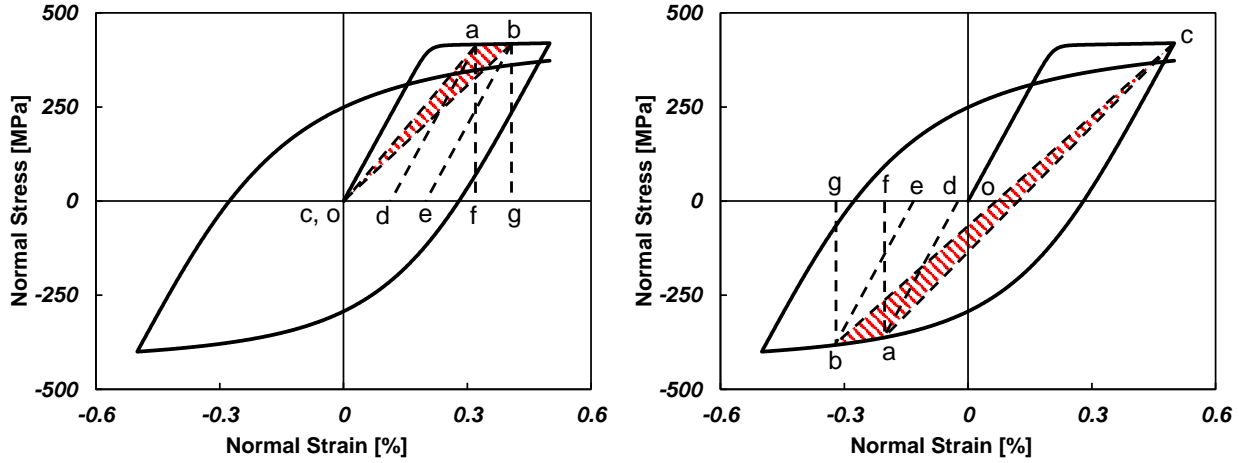


Figure 104.94: Energy computation of uniaxial steel fiber: (a) Monotonic loading branch; (b) Cyclic loading branch.

Note that the only difference between the monotonic loading branch (Figure 507.4(a)) and the cyclic loading branch (Figure 507.4(b)) is that the strain reversal point *c* is at the origin *o* in the monotonic case. So the following explanation of the proposed energy computation method applies to both monotonic and cyclic loading scenarios.

Firstly, the elastic strain energy density  $E_S$  is defined in accordance with the classic assumption that it is only a function of current stress state of the material, which yields:

$$E_S = E_S(\sigma) = \frac{1}{2E_0}\sigma^2 \quad (104.696)$$

Graphically, the elastic strain energy density of the material shown in Figure 507.4 at states *a* and *b* are the triangular areas *afd* and *bge*. Then the incremental form of Equation 507.9 is simply:

$$dE_S = \frac{1}{E_0}\sigma d\sigma \quad (104.697)$$

Next, the incremental plastic dissipation density  $D_P$  from state *a* to *b* is assumed to be the triangular area *abc*:

$$dD_P = \frac{1}{2}[(\sigma - \sigma_r)d\epsilon - (\epsilon - \epsilon_r)d\sigma] \quad (104.698)$$

This assumption ensures that the incremental plastic dissipation is nonnegative, which is one of the two basic principles of our thermomechanical framework. One special case is when the material exhibits

no cyclic softening, which means that perfectly overlapping stress-strain loops will be observed, the energy dissipation calculated using Equation 507.11 for one cyclic is the area of the hysteresis loop. In the proposed thermomechanical framework, the area of hysteresis loop should be equal to the plastic work, rather than plastic dissipation, done in one loading cycle. But in this special case of no cyclic softening, which means no evolution of material state and thus no development of plastic free energy after a complete loading cycle, the plastic work equals to the plastic dissipation in the material in one loading cycle.

For general case where the material does exhibit cyclic softening, plastic free energy density  $E_P$  is graphically denoted by the areas *adoc* and *beoc* at states *a* and *b*, respectively. The formulation representing this assumption is given by:

$$E_P = \frac{1}{2} \left[ \sigma \left( \epsilon - \frac{\sigma}{E_0} - \epsilon_r \right) + \sigma_r \epsilon \right] \quad (104.699)$$

The incremental form of Equation 507.12 is:

$$dE_P = \frac{1}{2} \left[ (\sigma + \sigma_r) d\epsilon + \left( \epsilon - \frac{1}{E_0} \sigma - \epsilon_r \right) d\sigma \right] \quad (104.700)$$

Adding Equation 507.10, 507.11, and 507.13, the incremental form of energy balance is achieved:

$$dE_S + dE_P + dD_P = \sigma d\epsilon \quad (104.701)$$

where the increment of three energy components add up to the increment of stress power during any loading step.

**Uniaxial Concrete Fiber.** The uniaxial concrete material model used in this study is based on the model proposed by Yassin (1994), which is capable of modeling the nonlinear hysteretic behavior and damage effect of concrete. The material parameters and stress-strain response of this material are shown in Figure 104.95.

The monotonic envelope curve of this model in compression is based on the model of Kent and Park (1971) and later generalized by Scott et al. (1982). For a given strain  $\epsilon_c$ , the compressive stress  $\sigma_c$  and corresponding tangent stiffness  $E$  are given by:

$$\epsilon_c \leq \epsilon_{cs} \quad \sigma_c = f_{cs} \left[ 2 \left( \frac{\epsilon_c}{\epsilon_{cs}} \right) - \left( \frac{\epsilon_c}{\epsilon_{cs}} \right)^2 \right] \quad E = E_c \left( 1 - \frac{\epsilon_c}{\epsilon_{cs}} \right) \quad (104.702)$$

$$\epsilon_{cs} < \epsilon_c \leq \epsilon_{cu} \quad \sigma_c = \frac{\epsilon_c - \epsilon_{cs}}{\epsilon_{cu} - \epsilon_{cs}} (f_{cu} - f_{cs}) + f_{cs} \quad E = \frac{f_{cu} - f_{cs}}{\epsilon_{cu} - \epsilon_{cs}} \quad (104.703)$$

$$\epsilon_c > \epsilon_{cu} \quad \sigma_c = f_{cu} \quad E = 0 \quad (104.704)$$

where  $f_{cs}$  is the maximum compressive strength of the concrete material,  $\epsilon_{cs}$  is the concrete strain at compressive strength,  $f_{cu}$  is the ultimate (crushing) strength of the concrete material,  $\epsilon_{cu}$  is the concrete

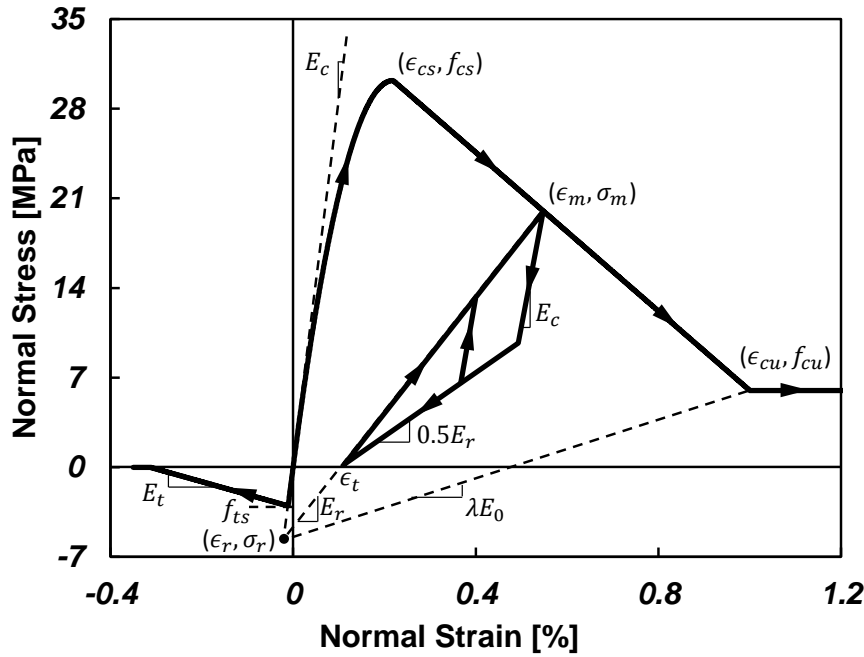


Figure 104.95: Constitutive model for uniaxial concrete fiber (Yassin (1994)).

strain at ultimate strength, and  $E_c$  is the initial concrete tangent stiffness that can be calculated using the equation:

$$E_c = \frac{2f_{cs}}{\epsilon_{cs}} \quad (104.705)$$

All material parameters should be determined by experiment or related literature data.

The cyclic behavior of this concrete model in compression is shown in Figure 104.95. One assumption of this model is that all reloading lines intersect at a common point, where the stress  $\sigma_r$  and strain  $\epsilon_r$  are given by the following expressions:

$$\epsilon_r = \frac{f_{cu} - \lambda E_c \epsilon_{cu}}{E_c(1 - \lambda)} \quad (104.706)$$

$$\sigma_r = E_c \epsilon_r \quad (104.707)$$

After unloading from a point on the compressive monotonic envelope, the model response is bounded by two lines that are defined by:

$$\sigma_{max} = \sigma_m + E_r(\epsilon_c - \epsilon_m) \quad (104.708)$$

$$\sigma_{min} = 0.5E_r(\epsilon_c - \epsilon_t) \quad (104.709)$$

where

$$E_r = \frac{\sigma_m - \sigma_r}{\epsilon_m - \epsilon_r} \quad (104.710)$$

$$\epsilon_t = \epsilon_m - \frac{\sigma_m}{E_r} \quad (104.711)$$

where  $\sigma_m$  and  $\epsilon_m$  are the stress and strain at the unloading point on the compressive monotonic envelope, respectively. If the unloading-reloading cycle is incomplete, the material response will be a straight line with slope  $E_c$ , as shown in Figure 104.95.

The tensile behavior of this concrete model considers tension stiffening and the effects of initial cracking. Details of the monotonic and cyclic behavior of this model under tensile stress can be found in Yassin (1994).

Since there are different loading/unloading branches in this model, the energy computation needs to be considered separately for each branch. One energy component that remains the same in all loading cases is the elastic strain energy density  $E_S$ , which is only a function of current stress:

$$E_S = E_S(\sigma) = \frac{1}{2E_c}\sigma^2 \quad (104.712)$$

And the incremental form of Equation 104.712 is:

$$dE_S = \frac{1}{E_c}\sigma d\sigma \quad (104.713)$$

In order to calculate plastic dissipation, a few assumptions are made that ensures the energy behavior of the concrete material to follow the proposed thermomechanical framework:

- Majority of energy is dissipated during first monotonic load.
- Subsequent cycles of loading, on an already damaged concrete, do not dissipate much energy.
- No energy is dissipated during unloading in both compressive and tensile conditions.
- When the material is cyclically loaded under compression, energy dissipation only happens when the stress reaches the upper bound  $\sigma_{max}$ .
- No energy is dissipated during cyclic loading when the material is under tension.

For a single loading step from stress state  $a$  to  $b$  in each subplot of Figure 104.96, the energy dissipation is represented by the shaded area.

If the material is under compression (Figure 104.96 (a), (b), and (c)), the amount of energy dissipated in the concrete fiber  $D_P$  is calculated by taking the area  $abcdef$ , which is generally a hexagon formed by the two unloading paths originated from stress state  $a$  and  $b$ :

$$dD_P = \frac{1}{2}[(\sigma - \sigma_c)d\epsilon + (\epsilon_c - \epsilon)d\sigma + (\epsilon_c - \epsilon_f)\sigma + (\sigma_f - \sigma_c)(\epsilon - \epsilon_t) + \sigma_c d\epsilon_t] \quad (104.714)$$

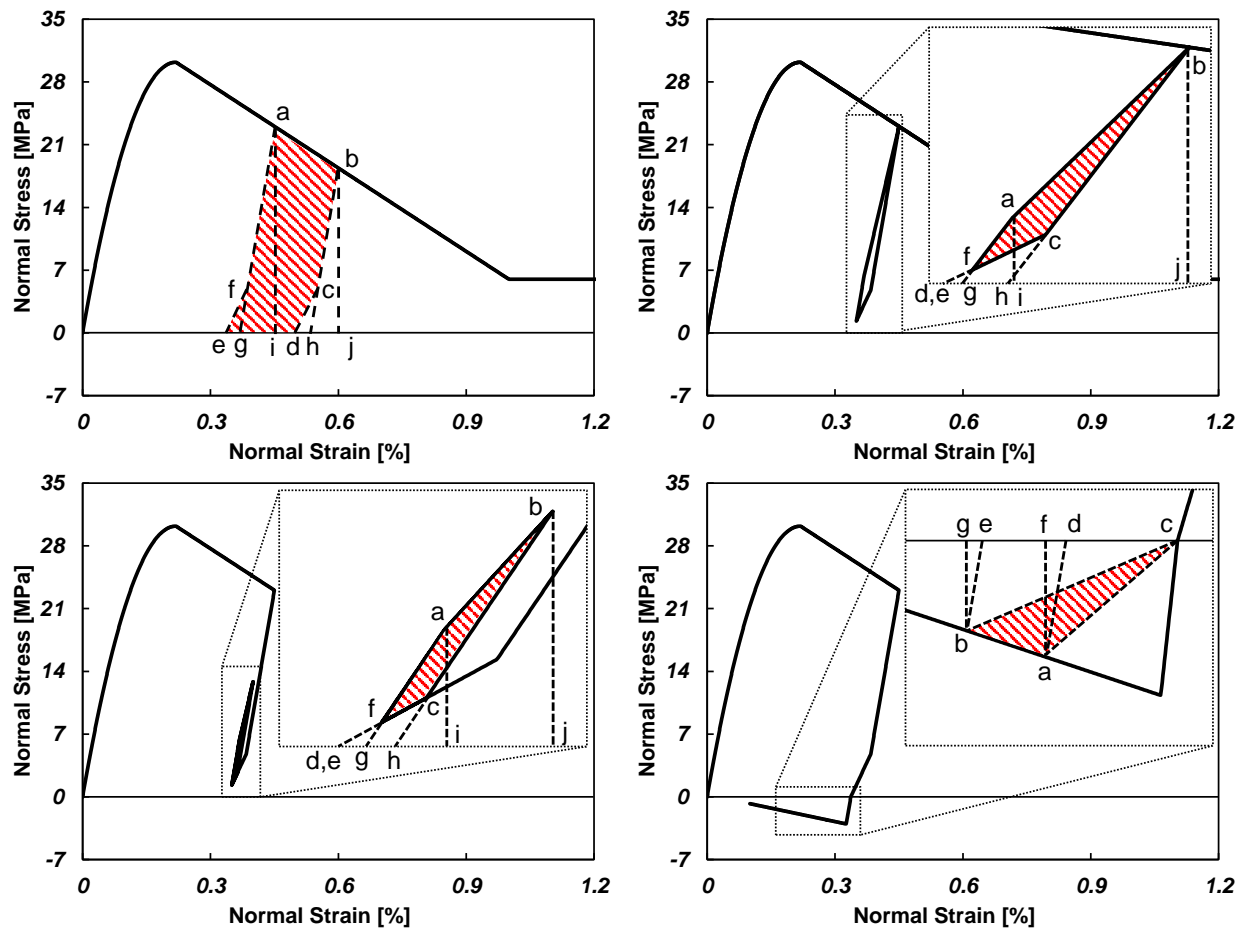


Figure 104.96: Energy computation of uniaxial concrete fiber: (a) Monotonic compression; (b) Single unloading-reloading cycle; (c) Unloading-reloading cycles within monotonic envelope; (d) Tension.

where the stress and strain at point *f* can be computed using the following expression:

$$\epsilon_f = \frac{\sigma + 0.5E_r\epsilon_t - E_c\epsilon}{0.5E_r - E_c} \quad \sigma_f = 0.5E_r(\epsilon_f - \epsilon_t) \quad (104.715)$$

Point *c* can be calculated using the same fashion, but with all variables evaluated at state *b*.

Note that the hexagon becomes quadrilateral in the cases of cyclic loading within the monotonic envelope, as can be observed in Figure 104.96 (b) and (c). But Equation 104.714 and 104.715 remains valid, obviously.

Plastic free energy  $E_P$  in this concrete material is calculated by taking the triangular area *fge* at state *a*:

$$E_P = \frac{1}{2} \left[ \left( \epsilon - \frac{\sigma}{E_c} - \epsilon_t \right) \sigma_f \right] \quad (104.716)$$

The incremental form of Equation 104.716 is obtained by taking the difference between the plastic free energy at state  $a$  and  $b$ :

$$dE_P = \frac{1}{2} \left[ \left( \sigma_c - \sigma_f - \frac{1}{E_c} \sigma \right) (\epsilon - \epsilon_t) - (d\epsilon - d\epsilon_t) \sigma_c - \frac{1}{E_c} \sigma c d\sigma \right] \quad (104.717)$$

Adding Equation 104.713, 104.714, and 104.717, the incremental form of energy balance is achieved:

$$dE_S + dE_P + dD_P = \sigma d\epsilon \quad (104.718)$$

where the increment of three energy components add up to the increment of stress power during any loading step.

### 104.12.3 Numerical Studies

Numerical examples presented in this section are performed using the Real-ESSI Simulator Jeremić et al. (1988-2025). Energy dissipation in numerical models consist of fiber section elements and uniaxial steel/concrete fibers are computed and analyzed.

First, numerical simulation of steel and plain concrete columns under various loading conditions are performed to study the energy behavior of uniaxial steel and concrete material models. Then, a model of reinforced concrete column, which consists of both concrete and steel fibers, is constructed and simulated to illustrate the energy dissipation in realistic structural elements. Finally, a bare steel frame structure is modeled with fiber section elements and loaded with seismic motion. Through these examples, it will be shown that the difference between plastic work and plastic energy dissipation can be significant.

External loads are applied incrementally using displacement-control scheme. System equations are solved using Newton-Raphson iteration algorithm and UMFPACK solver, which are available in Real-ESSI. Static integration algorithm is used for the column cases, while Newmark integration is used for the dynamic steel frame case. Note that viscous and numerical damping are excluded from all cases, in order to accurately evaluate energy dissipation due to material elastoplasticity.

#### 104.12.3.1 Steel Column

In order to verify the proposed energy computation approach for uniaxial steel material model, examples of steel columns are studied in this section. As shown in Figure 104.97, the one-meter-long column model is fixed at the bottom, and loads are applied at the top. The size of the cross section is 100 mm × 100 mm. The parameters for uniaxial steel material used in this section are summarized in Table 104.6.

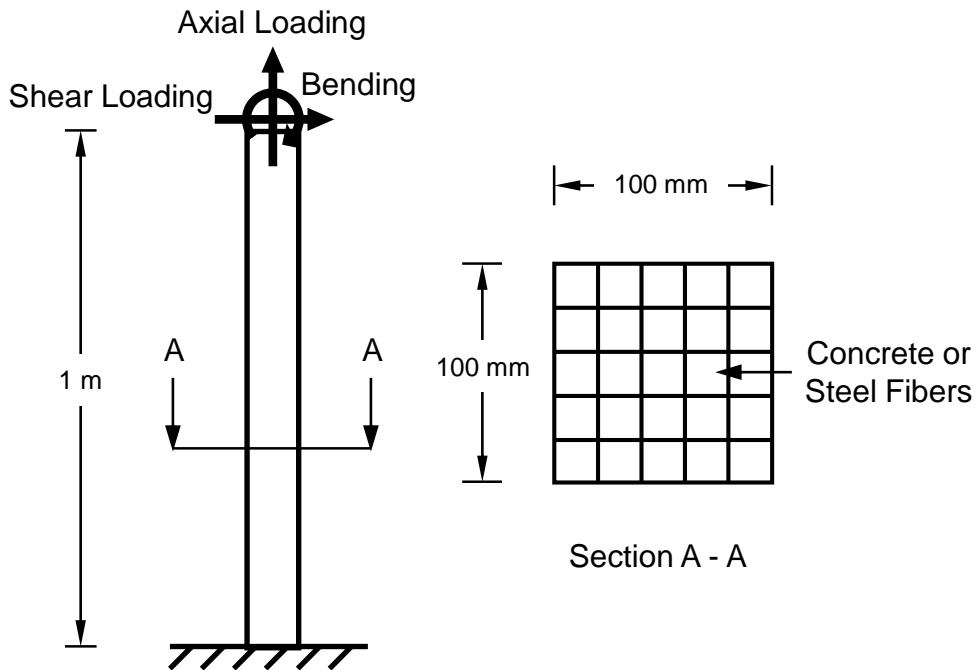


Figure 104.97: Schematic of the steel/plain-concrete column modeled with fiber sections and uniaxial steel/concrete materials.

Table 104.6: Material model parameters used in steel column examples.

$\sigma_y$ (MPa)	$E$ (GPa)	$b$	$R_0$	$c_{R_1}$	$c_{R_2}$	$a_1$	$a_2$	$a_3$	$a_4$
413.8	200.0	0.01	18.0	0.925	0.15	0.0	55.0	0.0	55.0

Cyclic Axial Loading. Since the fiber material model is uniaxial in nature, axial loading case is being investigated first. The evolution of energy parameters for uniaxial steel material are computed using Equation 507.10, 507.11, and 507.13. Figure 104.98 shows the stress-strain response as well as the energy results of the steel column under cyclic axial loading.

As expected, the stress-strain response shown in Figure 104.98 follows the constitutive model presented in Figure 104.93. Due to the choice of hardening parameters ( $a_1$ ,  $a_2$ ,  $a_3$ , and  $a_4$ ), isotropic hardening after first loading reversal is relatively small in this case. The evolution of plastic free energy, which is related to the hardening behavior of the constitutive model, is also observed to be insignificant after the first loading reversal. Energy balance in the steel material (Equation 507.14) is maintained during entire simulation.

In this particular case, the difference between plastic dissipation and plastic work is significant during initial loading (or monotonic loading), but then becomes less obvious during cyclic loading, which is

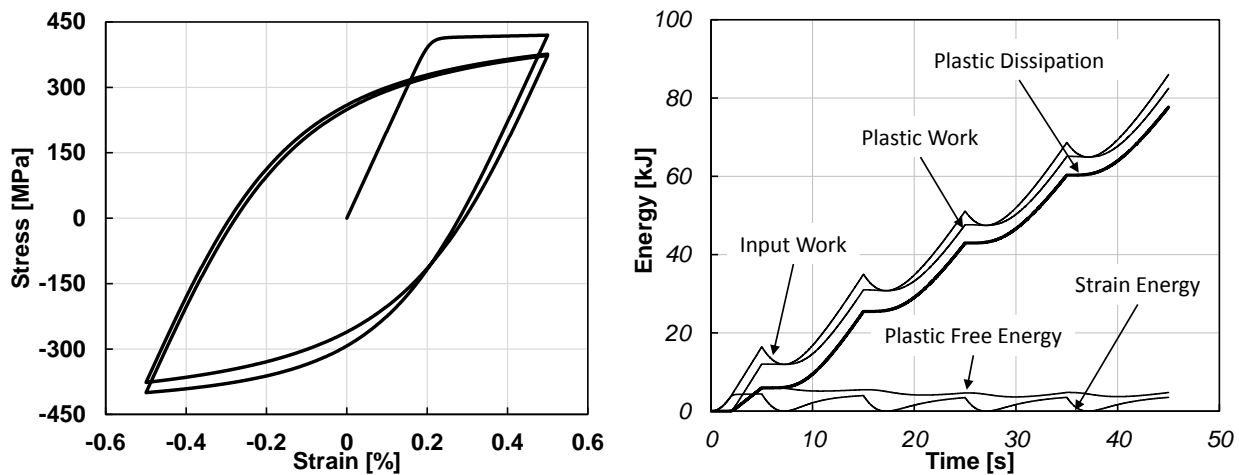


Figure 104.98: Energy analysis of steel column under cyclic axial loading: (a) Stress–strain response; (b) Plastic dissipation, plastic work, plastic free energy, strain energy, and input work.

probably the reason of ignorance of plastic free energy in many studies. It is important to point out that such difference could be significant if different hardening parameters are chosen or complex loading conditions (like seismic loading) are applied.

Another observation made in this example is that the ratio between plastic dissipation and plastic work (the Quinney–Taylor coefficient) changes from 0.5 to 0.9 in just a few loading cycles. Therefore, it is not accurate to prescribe a fixed number to be the Quinney–Taylor coefficient of a material during entire simulation, which is a common assumption made in a number of studies.

**Cyclic Bending Loading.** It has been proven that fiber section elements perform well under axial- and bending-dominant loading conditions. In this case, a cyclic bending moment is loaded on the top of the steel column. Figure 104.99 shows the moment–rotation response as well as the energy results of the steel column under cyclic bending loading.

Clearly, the moment–rotation response and energy results in this case are very similar to those in the axial loading case. When a beam element is under bending, half of the fibers will be under tension while the other half under compression, and the normal stress distribution on any cross section should be symmetric. Since the fiber material model used in this case has almost the same stress–strain response under tension and compression, the energy results in this bending case are expected to share the same pattern with those in the axial loading case.

Note that in both axial and bending cases, the strain energy accumulated in the material body is much smaller than the plastic dissipation. This means that most of the input work results in plastic

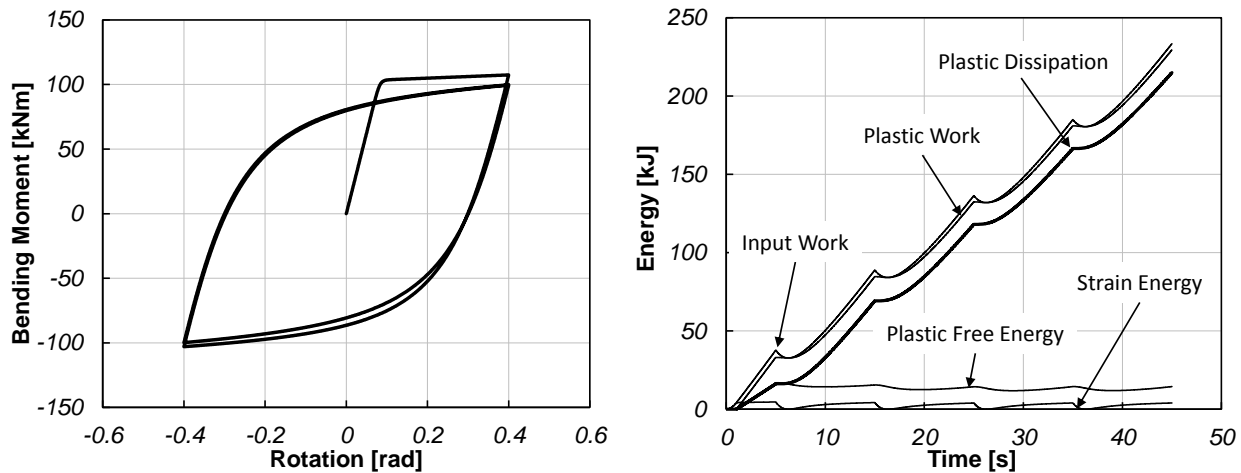


Figure 104.99: Energy analysis of steel column under cyclic bending loading: (a) Moment–rotation response; (b) Plastic dissipation, plastic work, plastic free energy, strain energy, and input work.

deformation of the material, which indicates high possibility of large deformation and material damage.

#### 104.12.3.2 Plain Concrete Column

In order to verify the proposed energy computation approach for uniaxial concrete material model, examples of plain concrete columns are studied in this section. The size and setup of the model are the same as those of the steel column, which has been shown in Figure 104.97. The parameters for uniaxial concrete material used in this section are summarized in Table 104.7.

Table 104.7: Material model parameters used in plain concrete column examples.

$f_{cs}$ (MPa)	$\epsilon_{cs}$	$f_{cu}$ (MPa)	$\epsilon_{cu}$	$\lambda$	$f_{ts}$ (MPa)	$E_t$ (GPa)
-30.2	-0.00219	-6.0	-0.00696	0.5	3.02	5.0

**Monotonic Axial Loading.** As stated in the assumptions for energy dissipation in the uniaxial concrete model, the amount of energy dissipated during monotonic loading is much larger than that during unloading/reloading. Such assumption is made based on the brittle nature of concrete materials, in which fracture is the main source of energy dissipation. In this case, the stress–strain response as well as the energy results of the plain concrete column model under monotonic axial compression is investigated and presented in Figure 104.100.

The stress–strain response shown in Figure 104.100 follows the constitutive model presented in

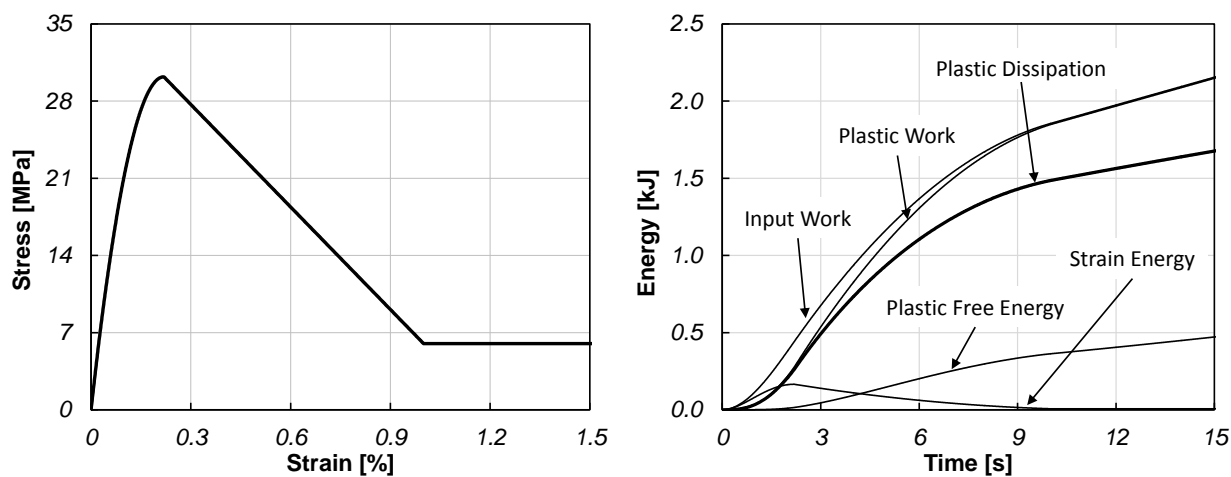


Figure 104.100: Energy analysis of plain concrete column under monotonic axial loading: (a) Stress–strain response; (b) Plastic dissipation, plastic work, plastic free energy, strain energy, and input work.

Figure 104.95, as expected. Energy balance in the model, which is expressed in Equation 507.8, is maintained during entire simulation.

As observed in Figure 104.100, large amount of the input work is dissipated during monotonic compression. It is important to point out that the difference between plastic dissipation and plastic work is significant. Plastic free energy starts to accumulate after maximum compressive strength is reached and continue to increase even after crushing. Such behavior can be explained by considering that the micro-structure of concrete continues to evolve as external loads continues to be applied on the material.

The strain energy starts to drop after maximum compressive strength and gradually decreases to almost zero after crushing. This observation is consistent with the fact that the micro-fractures expand rapidly after maximum strength is reached, which leads to the release of elastic strain energy and energy dissipation caused by fracture and crushing.

**Cyclic Axial Loading.** Due to the complex unloading–reloading rules of the model, the cyclic behavior of the uniaxial concrete material is much more complicated than that of the steel model. Figure 104.101 presents the stress–strain response as well as the energy results of the plain concrete column under cyclic axial loading.

As shown in Figure 104.101, the majority of plastic dissipation happens during monotonic loading branch. Notice that there are drops in plastic work during unloading, but plastic dissipation never decreases, which means that the second law of thermodynamics (Equation 504.8) is always obeyed.

It should be mentioned that there are certain amount of energy dissipation when the material is in

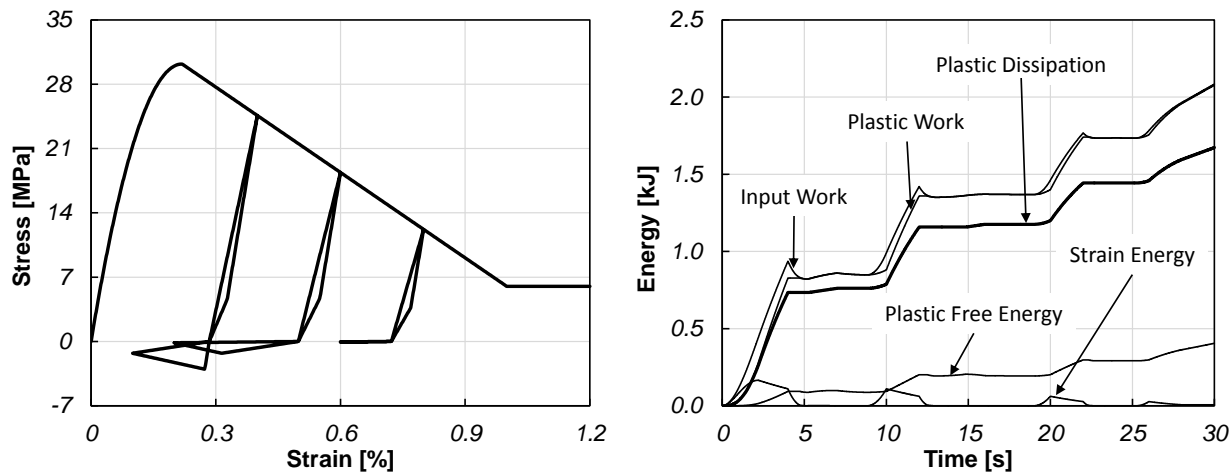


Figure 104.101: Energy analysis of plain concrete column under cyclic axial loading: (a) Stress–strain response; (b) Plastic dissipation, plastic work, plastic free energy, strain energy, and input work.

tension. But it is much smaller than that when the material is in monotonic compression, due to the low tensile strength of concrete material in general.

#### 104.12.3.3 Reinforced Concrete Column

To study the combined influence of concrete and steel fibers, a reinforced concrete column is modeled and tested in this section. The schematic of the model is shown in Figure 104.101, and the material model parameters are summarized in Table 104.8. The cross section of the column is modeled with unconfined concrete, confined concrete, and steel fibers with uniaxial material models discussed in earlier sections.

**Cyclic Axial Loading.** Figure 104.103 shows the force–displacement response as well as the energy results of the reinforced concrete column under cyclic axial loading.

Since concrete fibers have much higher compressive strength than tensile strength, the stress–strain response of the column is controlled by the concrete part when it is under compression, and by the steel part when under tension. In this case, the initial loading curve clearly resembles the stress–strain response of concrete fiber under monotonic compression. Then the unloading–reloading cycles have the same pattern as those of the steel fiber under cyclic axial loading.

By comparing the energy results shown in Figure 104.103 and those shown in Figure 104.98, it can be seen that the energy dissipation patterns in both cases are very close. This indicates that the majority of input work is dissipated in the steel fibers once the maximum strength of the concrete is exceeded. Again, it can be observed that the difference between plastic work and plastic dissipation is significant

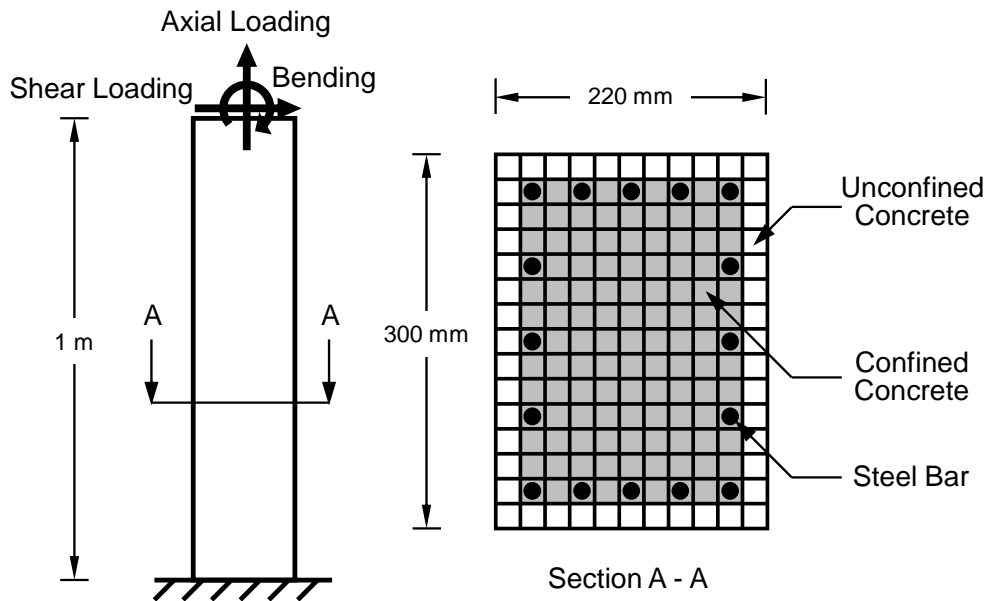


Figure 104.102: Schematic of the reinforced concrete column modeled with fiber sections and uniaxial steel/concrete materials.

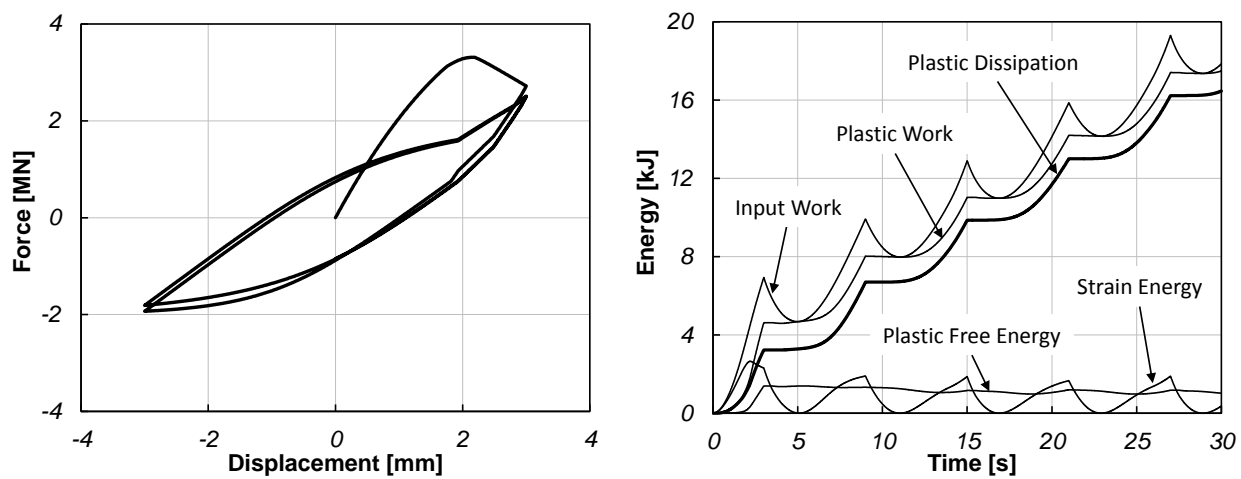


Figure 104.103: Energy analysis of reinforced concrete column under cyclic axial loading: (a) Force-displacement response; (b) Plastic dissipation, plastic work, plastic free energy, strain energy, and input work.

Table 104.8: Material model parameters used in reinforced concrete column examples.

Steel Fiber	Concrete Fiber		
	Confined	Unconfined	
$\sigma_y$ (MPa)	413.8	$f_{cs}$ (MPa)	-30.2
$E$ (GPa)	200.0	$\epsilon_{cs}$	-0.00219
$b$	0.01	$f_{cu}$ (MPa)	-6.0
$R_0$	18.0	$\epsilon_{cu}$	-0.00696
$c_{R_1}$	0.925	$\lambda$	0.5
$c_{R_2}$	0.15	$f_{ts}$ (MPa)	3.02
$a_1, a_3$	0.0	$E_t$ (GPa)	5.0
$a_2, a_4$	55.0		0.0

in this case.

Cyclic Bending Loading. Figure 104.104 shows the moment–rotation response as well as the energy results of the reinforced concrete column under cyclic bending loading.

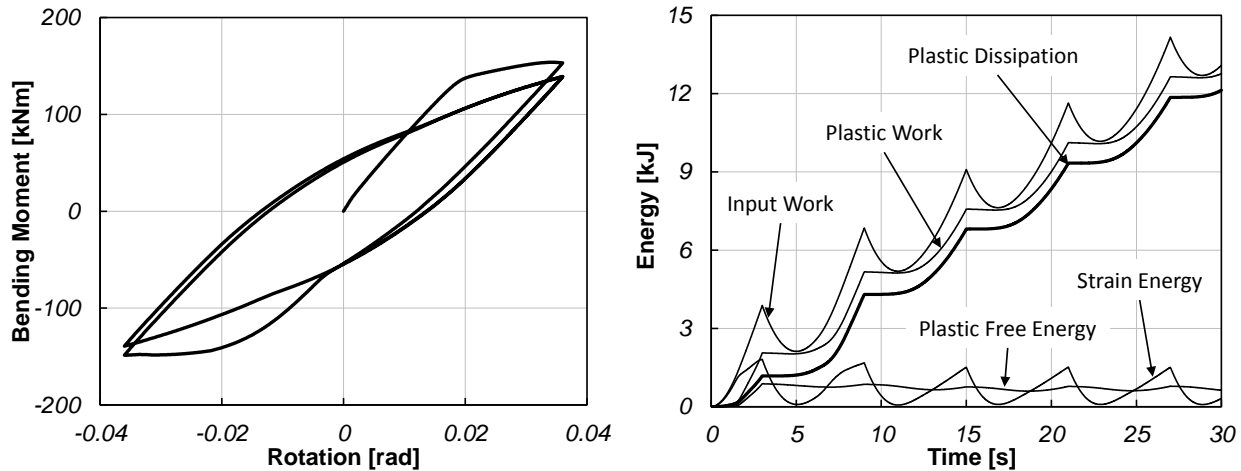


Figure 104.104: Energy analysis of reinforced concrete column under cyclic bending loading: (a) Moment–rotation response; (b) Plastic dissipation, plastic work, plastic free energy, strain energy, and input work.

During initial loading, the concrete fibers on the compressive side of the cross section take most of the compression, then during the first reverse loading, the concrete fibers on the other side of the

cross section are compressed and damaged. This process is indicated in the moment–rotation curve where a bump caused by the compressive strength of the concrete fibers during the first reverse loading is observed. The energy computation result also shows that the concrete fibers dissipate large amount of energy and get damaged during the first loading cycle. After that, the response of the reinforced concrete column is controlled by the steel bars.

According to the two cases of reinforced concrete column under cyclic loading, the concrete part of the column can dissipate the majority of the input work if the loading is mainly monotonic compression. For cyclic loading cases, if the loading does not exceed the maximum compressive strength of the concrete, which should not be significantly damaged, energy dissipation would be observed in both the concrete and steel. However, if the cyclic loading does exceed the maximum strength of the concrete, the majority of energy dissipation would be in the steel reinforcing bars after the concrete is damaged. This conclusion is consistent with the engineering experience that reinforcements are crucial to the performance of concrete structure during seismic events, when the beams and columns suffer from cyclic loadings.

#### 104.12.3.4 Steel Frame

All the previous cases are assumed to be static or quasi-static to investigate the energy dissipation on material level without the influence of dynamics. In other words, inertia and kinetic energy were not considered. In this example, a steel frame structure is model using fiber section element with uniaxial steel material, as shown in Figure 104.105, and loaded dynamically with a realistic seismic motion. The peak acceleration of the input motion is 0.76 g.

The energy computation results are shown in Figure 104.106. Strain energy, plastic free energy, and plastic dissipation in different stories are computed using Equation 507.10, 507.11, and 507.13. Input work is computed from the input motion and reaction forces at the base of model. Kinetic energy is computed indirectly by subtracting all other forms of energy from input work.

Note that the kinetic energy of the system is almost zero at certain times, and strain energy reaches a peak value. As can be observed from Figure 104.106, when kinetic energy becomes zero, the combination of strain energy, plastic free energy, and plastic dissipation of the system equals to the total input work. This observation proves that the energy balance of the system is maintained during entire simulation.

At the end of simulation, more than 80% of the total input work is dissipated due to material elasto-plasticity, while about 13% is transformed into plastic free energy which does not result in heating or material damage. In some cases, it might be reasonable to use input work (or energy demand in some literature) as a parameter to evaluate structure safety. However, as shown in this example, correctly computed energy dissipation is more appropriate for evaluation of material damage and structure performance in general.

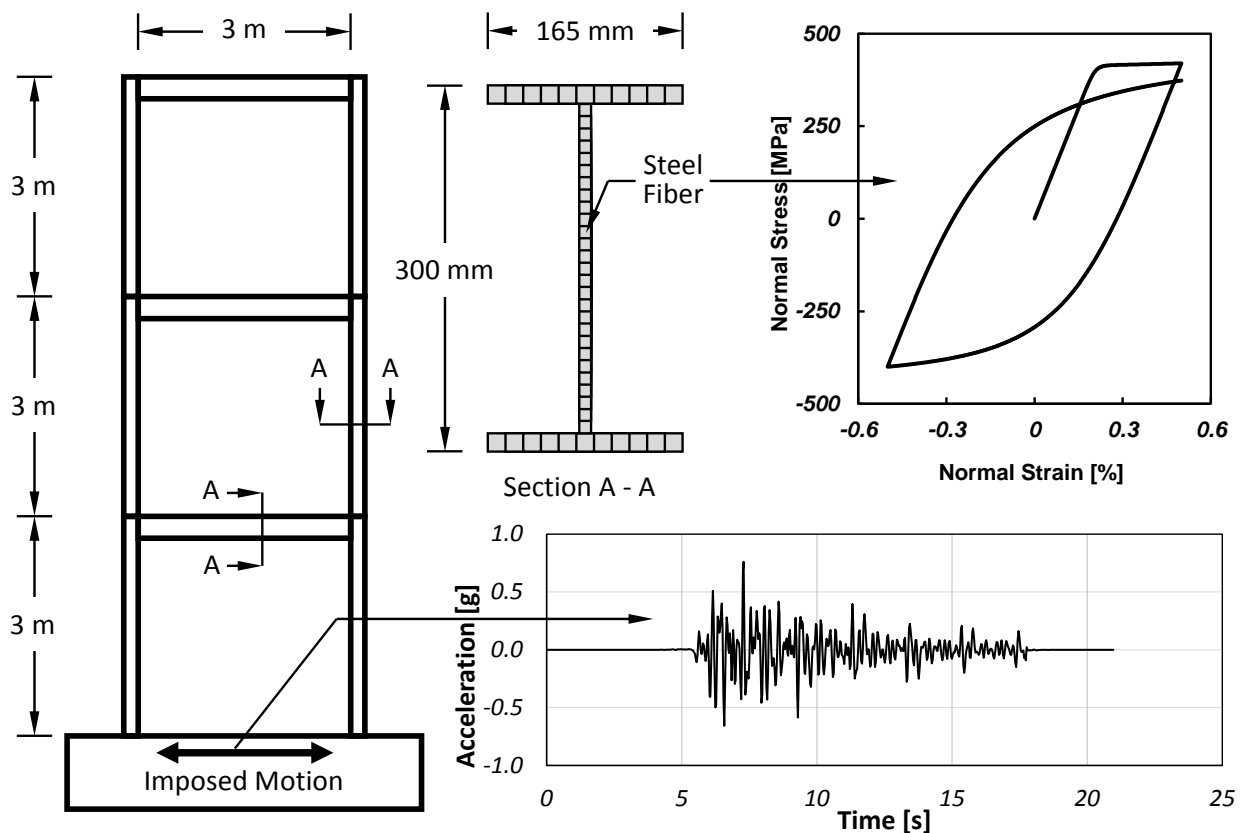


Figure 104.105: Schematic of the steel frame modeled with fiber section elements and uniaxial steel material.

#### 104.12.4 Conclusions

Presented in this section was a thermodynamic-based methodology for (correct) computation of energy dissipation in nonlinear structural elements modeled with fiber section and uniaxial material models. Two popular material models for steel and concrete were examined with focus on their nonlinear cyclic behaviors. Formulations for the energy storage and dissipation in these two material models were derived from the basic principles of thermodynamics, in combination with a few reasonable assumptions. The proposed methodology has been illustrated using a series of numerical simulations on columns and frame modeled with fiber section elements.

The misconception between plastic work and plastic dissipation, which leads to the violation of principles of thermodynamics, was addressed. Theoretical derivation and experimental observation have both proven that plastic free energy is a basic form of energy that should not be neglected without proper reasoning. By taking into account of all possible energy forms, including kinetic energy, strain energy, plastic free energy, and plastic dissipation, the first law of thermodynamics (energy balance) was

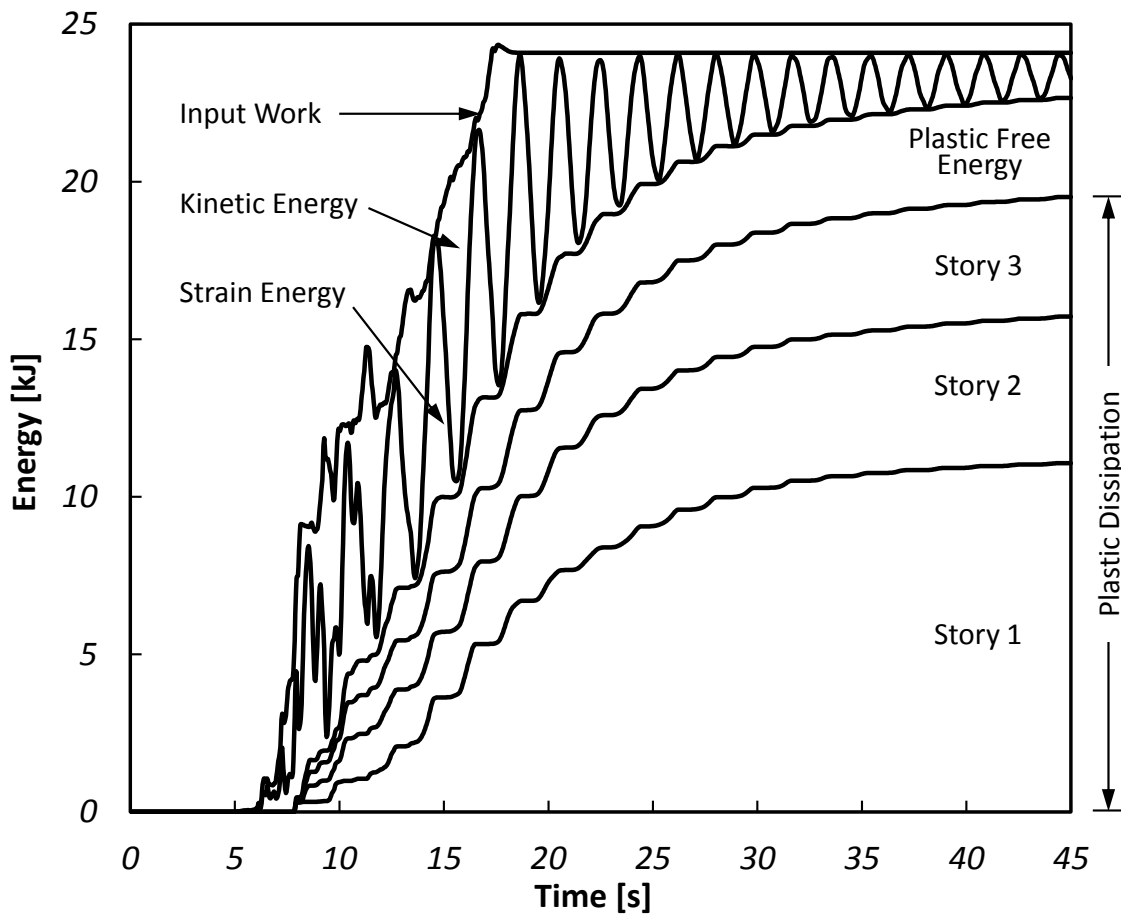


Figure 104.106: Energy analysis of steel frame model under imposed seismic motion.

ensured in the proposed methodology.

Physically, plastic free energy is related to the evolution of material micro-structure, which is not represented by specific parameters (like the internal variables in some elastoplasticity models). According to the experimental behavior of the material models, a few assumptions that ensure their energy behavior to follow the proposed thermomechanical framework were made. Equations for energy computation were derived and implemented in Real-ESSI, which was used to perform numerical simulations in this study.

Presented approach was illustrated and tested using several column and frame models with different loading conditions. As expected, energy balance was maintained during entire simulation in all tested cases. It was shown that plastic work could drop but plastic dissipation always maintained nonnegative during any time period, which is expressed in the second law of thermodynamics. It was also observed that the difference between plastic work and plastic dissipation could be significant in most cases. The ratio between them (Quinney–Taylor coefficient) evolved with time and thus should not be assumed to

be constant in general.

## 104.13 Localization of Deformation

(Rudnicki and Rice, 1975), (Lu et al., 2009)

## Chapter 105

# Probabilistic Elasto-Plasticity and Stochastic Elastic-Plastic Finite Element Method

(2004-2006-2009-2014-2016-2017-2019-2021-)

(In collaboration with Prof. Kallol Sett, Dr. Hexiang Wang, and Dr. Katarzyna Staszewska)

## 105.1 Chapter Summary and Highlights

For more details on work in this area, please consult the following papers:

[Jeremić et al. \(2007a\)](#),

[Sett et al. \(2007a\)](#),

[Sett et al. \(2007b\)](#),

[Jeremić and Sett \(2007\)](#),

[Jeremić and Sett \(2006\)](#),

[Sett and Jeremić \(2007\)](#),

[Jeremić and Sett \(2009a\)](#),

[Sett and Jeremić \(2010\)](#),

[Sett et al. \(2011b\)](#),

[Sett et al. \(2011a\)](#),

[Jeremić and Sett \(2010\)](#).

Material from (some of) the above papers is presented below.

## 105.2 Probabilistic Elasto-Plasticity, 1D FPK Formulation

A second-order exact expression for evolution of Probability Density Function (PDF) of stress is derived for general, one dimensional (1-D) elastic-plastic constitutive rate equations with uncertain material parameters. The Eulerian–Lagrangian (EL) form of Fokker–Planck–Kolmogorov (FPK) equation is used for this purpose. It is also shown that by using EL form of FPK, the so called "closure problem" associated with regular perturbation methods used so far, is resolved too. The use of EL form of FPK also replaces repetitive and computationally expensive deterministic elastic-plastic computations associated with Monte Carlo technique.

The derived general expression are specialized to the particular cases of point location scale linear elastic and elastic–plastic constitutive equations, related to associated Drucker-Prager with linear hardening

In a companion paper, the solution of FPK equations for 1D is presented, discussed and illustrated through a number of examples.

### 105.2.1 Probabilistic Elasto-Plasticity: Introduction

Advanced elasto–plasticity constitutive models, when properly calibrated, are very accurate in capturing important aspects of material behavior. However, all materials', and in particular geomaterials' (soil, rock,

concrete, powder, bone etc.) behavior is uncertain due to inherent spatial and point-wise uncertainties. These uncertainties in material properties could outweigh the advantages gained by using advanced constitutive models. For example, Fig. 105.1 shows a schematic of anticipated influence of material uncertainties on a bi-linear elastic-plastic stress-strain behavior. Depending on uncertainties in material properties and interaction between them, the behavior of the same material could be very different.

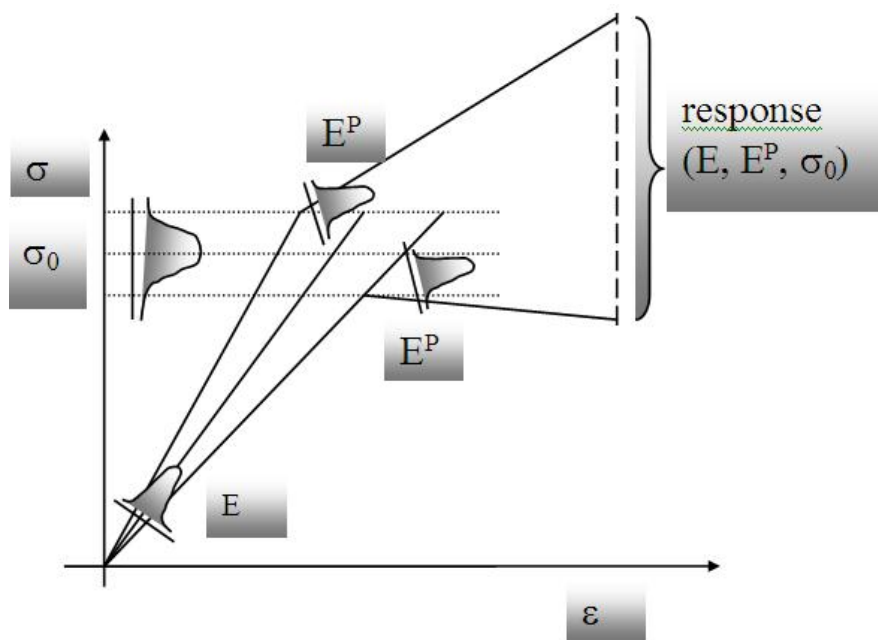


Figure 105.1: Anticipated Influence of Material Fluctuations on Stress-Strain Behavior

The uncertainties in material properties are inevitable in real materials and it is best to account for them in modeling and simulation. In traditional deterministic constitutive modeling, material models are calibrated against set of experimental data. Although those experimental data sets generally exhibit statistical distribution, the models are usually calibrated against the mean of the data and all the information about uncertainties is neglected.

The modeling and simulation of solids and structures with uncertain material properties involves two steps: (a) classification and quantification of uncertainties and (b) propagation of uncertainties through governing differential equations.

The uncertainties can be broadly classified into aleatory and epistemic types. Aleatory uncertainties are associated with the inherent variabilities of nature. This type of uncertainty can not be reduced. Highly developed mathematical theory is available for dealing with aleatory uncertainty. On the other hand, epistemic uncertainties arise due to our lack of knowledge. This type of uncertainty can be reduced by collecting more data but the mathematical tools to deal with them are not highly developed

(e.g. fuzzy logic [Zadeh \(1983\)](#), convex models [Ben-Haim and Elishakoff \(1990\)](#), interval arithmetic [Moore \(1979\)](#) etc.). Hence, it proves useful to trade epistemic uncertainties for aleatory uncertainties in order to facilitate their propagation through the governing equations using advanced mathematical tools. It is important to note that in trading-off epistemic uncertainties for aleatory uncertainties, one doesn't reduce the total uncertainties in the system, but assumes that the uncertainties in the system are irreducible. Under the framework of probability theory, uncertain material parameters are modeled as random variables or random fields ([Vanmarcke, 1983](#)) depending on whether they are specialized to a fixed location in their continuum or a function of location in their continuum. We note recent works in quantifying the uncertainties in material (soil) properties for geotechnical engineering applications, [Lumb \(1966\)](#), [Vanmarcke \(1977\)](#), [Mayerhoff \(1993\)](#), [DeGroot and Baecher \(1993\)](#), [Popescu \(1995\)](#), [Lacasse and Nadim \(1996\)](#), [Popescu et al. \(1998\)](#), [Phoon and Kulhawy \(1999a,b\)](#), [Fenton \(1999a,b\)](#), [Duncan \(2000b\)](#), [Rackwitz \(2000\)](#), [Marosi and Hiltunen \(2004\)](#), and [Stokoe II et al. \(2004\)](#). The issue of uncertain material properties becomes very pronounced when one starts dealing with the boundary value problems with uncertain material properties (elastic or elastic–plastic).

In mechanics, the equilibrium equation,  $A\sigma = \phi(t)$ , together with the strain compatibility equation,  $Bu = \epsilon$ , and the constitutive equation,  $\sigma = D\epsilon$ , are sufficient<sup>1</sup> to describe the behavior of the solid. Rigorous mathematical theory has been developed for problems where the only random parameter is the external force  $\phi(t)$ . In this case, the probability distribution function (PDF) of the response variable will satisfy FPK partial differential equation ([Soize, 1994](#)). With appropriate initial and boundary conditions the FPK PDE can be solved for PDF of response variable. The numerical solution method for FPK equation by finite element method (FEM) is described by number of researchers e.g. [Langtangen \(1991\)](#), [Masud and Bergman \(2005\)](#).

The other extreme case, which is of interest in this work, is when the stochasticity of the system is purely due to operator uncertainty. Exact solution of the problems with stochastic operator was attempted by [Hopf \(1952\)](#) using characteristic functional approach. Later, [Lee \(1974\)](#) applied the methodology to the problem of wave propagation in random media and derived a FPK equation satisfied by the characteristic functional of the random wave field. This characteristic functional approach is very complicated for linear problems and becomes even more intractable (and possibly unsolvable) for nonlinear problems and problems with irregular geometries and boundary conditions.

Monte Carlo simulation technique is an alternative to analytical solution of partial differential equation with stochastic coefficient. Nice descriptions of different aspects of formulation of Monte Carlo technique for stochastic mechanics problem is described by [Schüeller \(1997\)](#). Monte Carlo method is very popular

---

<sup>1</sup>Generalized stress is  $\sigma$ ,  $\phi(t)$  is generalized forces that can be time dependent,  $u$  is generalized displacements,  $\epsilon$  is generalized strain and  $A$ ,  $B$ , and  $D$  are operators which could be linear or non-linear.

tool with the advantage that accurate solution can be obtained for any problem whose deterministic solution (either analytical or numerical) is known. Monte Carlo technique has been used by a number of researchers in obtaining probabilistic solution of geotechnical boundary value problems, e.g. Paice et al. (1996); Griffiths et al. (2002); Fenton and Griffiths (2003, 2005). Popescu et al. (1997), Mellah et al. (2000), De Lima et al. (2001), Koutsourelakis et al. (2002), Nobahar (2003). The major disadvantage of Monte Carlo analysis is the repetitive use of the deterministic model until the solution variable become statistically significant. The computational cost associated with it could be very high especially for non-linear problems with multiple uncertain material properties.

Various difficulties in finding analytical solutions and the high computational cost associated with Monte Carlo technique instigated development of numerical method for the solution of stochastic differential equation with random coefficient. For stochastic boundary value problems Stochastic Finite Element Method (SFEM) is the most popular such method. There exist several formulations of SFEM, among which perturbation (Kleiber and Hien (1992); Der Kiureghian and Ke (1988); Mellah et al. (2000); Gutierrez and De Borst (1999)) and Spectral (Ghanem and Spanos (1991); Keese and Matthies (2002); Xiu and Karniadakis (2003); Debusschere et al. (2003); Anders and Hori (2000)) methods are very popular. A nice review on advantages and disadvantages of different formulations of SFEM was provided by Matthies et al. (1997). Mathematical issues regarding different formulations of SFEM was addressed by Deb et al. (2001) and Babuska and Chatzipantelidis (2002). It is important to note that most of the formulations described in the above mentioned references are for linear elastic problems.

A limited number of references is also available related to geometric non-linear problems, Liu and Der Kiureghian (1991); Keese and Matthies (2002) and Keese (2003)). Similarly, there exist only few published references related to material non-linear (elastic-plastic) problems with uncertain material parameters. The major difficulty in extending the available formulations of SFEM to general elastic-plastic problem is the high non-linear coupling in the elastic-plastic constitutive rate equation. First attempt to propagate uncertainties through elastic-plastic constitutive equations considering random Young's modulus was published only recently, e.g. Anders and Hori (1999, 2000). The perturbation expansion at the stochastic mean behavior (considering only the first term of the expansion) was used in the above mentioned references. In computing the mean behavior the Authors took the advantage of bounding media approximation. Although this method doesn't suffer from computational difficulty associated with Monte Carlo method for problems having no closed-form solution, it inherits "closure problem" and the "small coefficient of variation" requirements for the material parameters. Closure problem refers to the need for higher order statistical moments in order to calculate lower order statistical moments Kavas (2003). The small COV requirement claims that the perturbation method can be used (with reasonable accuracy) for probabilistic simulations of solids and structures with uncertain properties

only if their COV < 20 % (Sudret and Der Kiureghian, 2000). For soils and other natural materials, COVs are rarely below 20 % (Lacasse and Nadim (1996); Phoon and Kulhawy (1999a,b)). Furthermore, with bounding media approximation, difficulty arises in computing the mean behavior when one considers uncertainties in internal variable(s) and/or direction(s) of evolution of internal variable(s).

The focus of present work is on development of methodology for the probabilistic simulation of constitutive behavior of elastic–plastic materials with uncertain properties. Recently, Kavvas (2003) obtained a generic Eulerian–Lagrangian (EL) form of FPK equation, exact to second-order, corresponding to any non-linear ordinary differential equation with random coefficients and random forcing. The approach using EL form of the FPK equation doesn't suffer from the drawbacks of Monte Carlo method and perturbation technique. In this paper the authors applied developed EL form of the FPK equation to obtain probabilistic formulation for a general, one-dimensional incremental elastic–plastic constitutive equation with random coefficient. The solution methodology is designed with several applications in mind, namely to

- obtain probabilistic stress–strain behavior from spatial average form (upscaled form) of constitutive equation, when input uncertain material properties to the constitutive equation are random fields; and
- obtain probabilistic stress-strain behavior from point-location scale constitutive equation, when input uncertain material properties to the constitutive equation are random variables.

Application of the developed methodology is demonstrated on a particular point-location scale one-dimensional constitutive equation, namely Drucker–Prager associative linear hardening elastic–plastic material model. In this paper, derivation is made of the EL form of FPK equation that govern the 1D probabilistic elastic–plastic material models with uncertain material parameters. This general formulation is then specialized to a particular 1D Drucker–Prager associative linear hardening material model. In the companion paper the solution methodology of the FPK equation corresponding to Drucker–Prager associative linear hardening material model is described, along with illustrative examples. The methodology is general enough that it allows extension to three-dimensions and incorporation into a general stochastic finite element framework. This work is underway and will be reported in future publications.

### 105.2.2 Probabilistic Elasto-Plasticity: General Formulation

The incremental form of spatial-average elastic-plastic constitutive equation can be written as

$$\frac{d\sigma_{ij}(x_t, t)}{dt} = D_{ijkl}(x_t, t) \frac{d\epsilon_{kl}(x_t, t)}{dt} \quad (105.1)$$

where the continuum stiffness tensor  $D_{ijkl}(x_t, t)$  can be either elastic or elastic-plastic

$$D_{ijkl} = \begin{cases} D_{ijkl}^{el} & ; f < 0 \vee (f = 0 \wedge df < 0) \\ D_{ijkl}^{el} - \frac{D_{ijmn}^{el} \frac{\partial U}{\partial \sigma_{mn}} \frac{\partial f}{\partial \sigma_{pq}} D_{pqkl}^{el}}{\frac{\partial f}{\partial \sigma_{rs}} D_{rstu}^{el} \frac{\partial U}{\partial \sigma_{tu}} - \frac{\partial f}{\partial q_*} r_*} & ; f = 0 \vee df = 0 \end{cases} \quad (105.2)$$

and where  $D_{ijkl}^{el}$  is the elastic stiffness tensor,  $D_{ijkl}^{ep}$  is the elastic-plastic continuum stiffness tensor,  $f$  is the yield function, which is a function of stress ( $\sigma_{ij}$ ) and internal variables ( $q_*$ ),  $U$  is the plastic potential function (also a function of stress and internal variables). The internal variables ( $q_*$ ) could be scalar(s) (for perfectly-plastic and isotropic hardening models), second-order tensor (for translational and rotational kinematic hardening) or fourth-order tensor (for distortional hardening). Therefore, the most general form of incremental constitutive equation in terms of its parameters can be written as

$$\frac{d\sigma_{ij}(x_t, t)}{dt} = \beta_{ijkl}(\sigma_{ij}, D_{ijkl}, q_*, r_*, x_t, t) \frac{d\epsilon_{kl}(x_t, t)}{dt} \quad (105.3)$$

Due to randomness in elastic constants ( $D_{ijkl}^{el}$ ) and internal variables ( $q_*$ ) and/or rate of evolution of internal variables ( $r_*$ ) the material stiffness operator  $\beta_{ijkl}$  in Eq. (105.3) becomes stochastic. It follows that the Equation (105.1) becomes a linear/non-linear ordinary differential equations with stochastic coefficients. Similarly, randomness in the forcing term ( $\epsilon_{kl}$ ) of Equation (105.3) results in Equation (105.3) becoming linear/non-linear ordinary differential equations with stochastic forcing. This can be generalized, so that randomness in material properties and forcing function of Equation (105.3) results in Equation (105.3) becoming a linear/non-linear ordinary differential equation with stochastic coefficients and stochastic forcing.

In order to gain better understanding of the effects of random material parameters and forcing on response, focus is shifted from a general 3D case to a 1D case. In what follows, the probabilistic formulation for 1-D constitutive elastic-plastic incremental equation with stochastic coefficient and stochastic forcing is derived. In addition to that, the probabilistic formulation for 1-D elastic linear constitutive equation is obtained as a special case of non-linear general derivation.

Focusing on 1-D behavior, the Eq. (105.3) is written as

$$\frac{d\sigma(x_t, t)}{dt} = \beta(\sigma, D, q, r; x_t, t) \frac{d\epsilon(x_t, t)}{dt} \quad (105.4)$$

which is a non-linear ordinary differential equation with stochastic coefficient and stochastic forcing. The right hand side of Eq. (105.4) is replaced with the function  $\eta$  as

$$\eta(\sigma, D, q, r, \epsilon; x, t) = \beta(\sigma, D, q, r; x_t, t) \frac{d\epsilon(x_t, t)}{dt} \quad (105.5)$$

so that now Eq. (105.4) can be written as

$$\frac{\partial \sigma(x_t, t)}{\partial t} = \eta(\sigma, D, q, r, \epsilon; x, t) \quad (105.6)$$

with initial condition,

$$\sigma(x, 0) = \sigma_0 \quad (105.7)$$

In the above Eq. (105.6)  $\sigma$  can be considered to represent a point in the  $\sigma$ -space and hence, the Eq. (105.6) determines the velocity for the point in that  $\sigma$ -space. This may be visualized, from the initial point, and given initial condition  $\sigma_0$ , as a trajectory that describes the corresponding solution of the non-linear stochastic ordinary differential equation (ODE) (Eq. (105.6)). Considering now a cloud of initial points (refer to Fig. 105.2), described by a density  $\rho(\sigma, 0)$  in the  $\sigma$ -space.

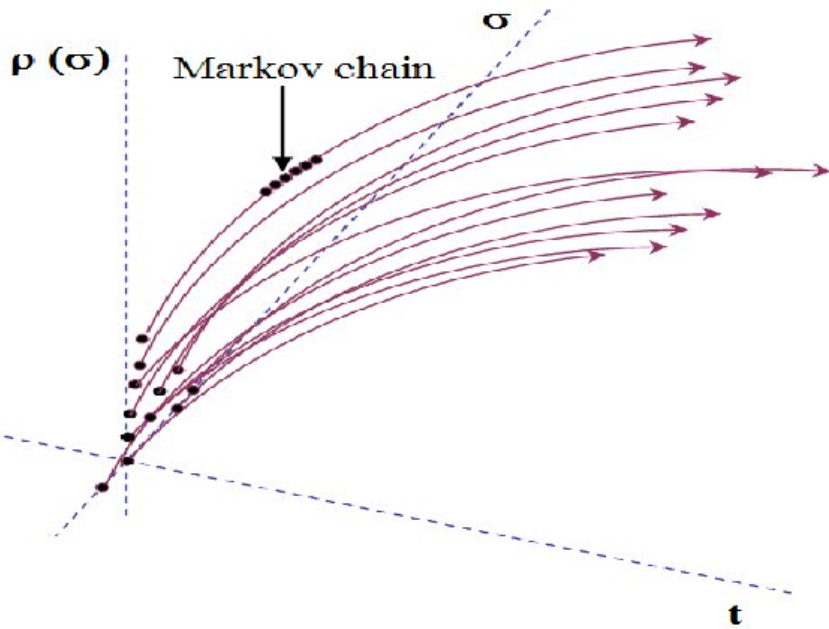


Figure 105.2: Movements of Cloud of Initial Points, described by density  $\rho(\sigma, 0)$ , in the  $\sigma$ -space

The phase density  $\rho$  of  $\sigma(x, t)$  (movement of any point dictated by Eq. (105.6)) varies in time according to a continuity equation which expresses the conservation of all these points in the  $\sigma$ -space. This continuity equation can be expressed in mathematical terms, using Kubo's stochastic Liouville equation (Kubo, 1963):

$$\frac{\partial \rho(\sigma(x, t), t)}{\partial t} = -\frac{\partial}{\partial \sigma} \eta[\sigma(x, t), D(x), q(x), r(x), \epsilon(x, t)].\rho[\sigma(x, t), t] \quad (105.8)$$

with an initial condition,

$$\rho(\sigma, 0) = \delta(\sigma - \sigma_0) \quad (105.9)$$

where  $\delta$  is the Dirac delta function and Eq. (105.9) is the probabilistic restatement in the  $\sigma$ -phase space of the original deterministic initial condition (Eq. (105.7)). Here it proves useful to recall Van Kampen's Lemma (Van Kampen, 1976), which states that the ensemble average of a phase density is the probability density

$$\langle \rho(\sigma, t) \rangle = P(\sigma, t) \quad (105.10)$$

where, the symbol  $\langle \cdot \rangle$  denotes the expectation operation, and  $P(\sigma, t)$  denotes evolutionary probability density of the state variable  $\sigma$  of the constitutive rate equation (Eq. (105.4)).

In order to obtain the deterministic probability density function (PDF)  $(\sigma, t)$  of the state variable,  $\sigma$ , it is necessary to obtain the deterministic partial differential equation (PDE) of the  $\sigma$ -space mean phase density  $\langle \rho(\sigma, t) \rangle$  from the linear stochastic PDE system (Eqs. (105.8) and (105.9)). This necessitates the derivation of the ensemble average form of Eq. (105.8) for  $\langle \rho(\sigma, t) \rangle$ . This ensemble average was recently derived by (Kavvas and Karakas, 1996; Kavvas, 2003) as

$$\begin{aligned} & \frac{\partial \langle \rho(\sigma(x_t, t), t) \rangle}{\partial t} = \\ & - \frac{\partial}{\partial \sigma} \left\{ \left[ \left\langle \eta(\sigma(x_t, t), D(x_t), q(x_t), r(x_t), \epsilon(x_t, t)) \right\rangle \right. \right. \\ & - \int_0^t d\tau \text{Cov}_0 \left[ \eta(\sigma(x_t, t), D(x_t), q(x_t), r(x_t), \epsilon(x_t, t)); \right. \\ & \left. \left. \frac{\partial \eta(\sigma(x_{t-\tau}, t-\tau), D(x_{t-\tau}), q(x_{t-\tau}), r(x_{t-\tau}), \epsilon(x_{t-\tau}, t-\tau))}{\partial \sigma} \right] \right] \langle \rho(\sigma(x_t, t), t) \rangle \right\} \\ & + \frac{\partial}{\partial \sigma} \left\{ \left[ \int_0^t d\tau \text{Cov}_0 [\eta(\sigma(x_t, t), D(x_t), q(x_t), r(x_t), \epsilon(x_t, t)); \right. \right. \\ & \left. \left. \eta(\sigma(x_{t-\tau}, t-\tau), D(x_{t-\tau}), q(x_{t-\tau}), r(x_{t-\tau}), \epsilon(x_{t-\tau}, t-\tau))] \right] \frac{\partial \langle \rho(\sigma(x_t, t), t) \rangle}{\partial \sigma} \right\} \end{aligned} \quad (105.11)$$

to exact second order (to the order of the covariance time of  $\eta$ ). In Eq. (105.11),  $\text{Cov}_0[\cdot]$  is the time ordered covariance function defined by

$$\text{Cov}_0 [\eta(x, t_1), \eta(x, t_2)] = \langle \eta(x, t_1) \eta(x, t_2) \rangle - \langle \eta(x, t_1) \rangle \cdot \langle \eta(x, t_2) \rangle \quad (105.12)$$

By combining Eqs. (105.11) and (105.10) and rearranging the terms yields the following Fokker-Planck equation (FPE, also known as Forward–Kolmogorov Equation or Fokker–Planck–Kolmogorov

FPK Equation) ([Riskin \(1989\)](#), [Gardiner \(2004\)](#), [Schüeller \(1997\)](#)):

$$\begin{aligned}
 & \frac{\partial P(\sigma(x_t, t), t)}{\partial t} = \\
 & - \frac{\partial}{\partial \sigma} \left[ \left\{ \left\langle \eta(\sigma(x_t, t), D(x_t), q(x_t), r(x_t)\epsilon(x_t, t)) \right\rangle \right\} \right. \\
 & + \int_0^t d\tau Cov_0 \left[ \frac{\partial \eta(\sigma(x_t, t), D(x_t), q(x_t), r(x_t)\epsilon(x_t, t))}{\partial \sigma} ; \right. \\
 & \quad \left. \eta(\sigma(x_{t-\tau}, t-\tau), D(x_{t-\tau}), q(x_{t-\tau}), r(x_{t-\tau}), \epsilon(x_{t-\tau}, t-\tau)) \right] \left. \right\} P(\sigma(x_t, t), t) \\
 & + \frac{\partial^2}{\partial \sigma^2} \left[ \left\{ \int_0^t d\tau Cov_0 \left[ \eta(\sigma(x_t, t), D(x_t, t), q(x_t, t), r(x_t, t), \epsilon(x_t, t)); \right. \right. \right. \\
 & \quad \left. \eta_1(\sigma(x_{t-\tau}, t-\tau), D(x_{t-\tau}), q(x_{t-\tau}), r(x_{t-\tau}), \epsilon(x_{t-\tau}, t-\tau)) \right] \left. \right\} P(\sigma(x_t, t), t) \quad (105.13)
 \end{aligned}$$

to exact second order. This is the most general relation for probabilistic behavior of inelastic (non-linear, elastic-plastic) 1-D stochastic incremental constitutive equation. The solution of this deterministic linear FPE (Eq. (105.13)), in terms of the probability density  $P(\sigma, t)$ , under appropriate initial and boundary conditions will yield the PDF of the state variable  $\sigma$  of the original 1-D non-linear stochastic constitutive rate equation (Eq. (105.4)). It is important to note that while the original equation (Eq. (105.4)) is non-linear, the FPE (Eq. (105.13)) is linear in terms of its unknown, the probability density  $P(\sigma, t)$  of the state variable  $\sigma$ . This linearity, in turn, provides significant advantages in the solution of the probabilistic behavior of the incremental constitutive equation (Eq. (105.4)).

One should also note that Eq. (105.13) is a mixed Eulerian-Lagrangian equation. This stems from the fact that while the real space location  $x_t$  at time  $t$  is known, the location  $x_{t-\tau}$  is an unknown. If one assumes small strain theory, one can relate the unknown location  $x_{t-\tau}$  from the known location  $x_t$  by using the strain rate,  $\dot{\epsilon}$  ( $=d\epsilon/dt$ ) as,

$$x_{t-\tau} = (1 - \dot{\epsilon}\tau)x_t \quad (105.14)$$

Once the probability density function  $P(\sigma, t)$  is obtained it can be used to obtain the mean of state variable ( $\sigma$ ) by usual expectation operation

$$\langle \sigma(t) \rangle = \int \sigma(t)P(\sigma(t))d\sigma(t) \quad (105.15)$$

Another possible way to obtain the mean of state variable is to use the equivalence between FPE and Itô stochastic differential equation ([Gardiner, 2004](#)). In this case Itô stochastic differential equation

equivalent to Eq. (105.13) is

$$\begin{aligned} d\sigma(x, t) &= \left\{ \left\langle \eta(\sigma(x_t, t), D(x_t), q(x_t), r(x_t), \epsilon(x_t, t)) \right\rangle \right. \\ &+ \int_0^t d\tau Cov_0 \left[ \frac{\partial \eta(\sigma(x_t, t), D(x_t), q(x_t), r(x_t), \epsilon(x_t, t))}{\partial \sigma} ; \right. \\ &\quad \left. \left. \eta(\sigma(x_{t-\tau}, t-\tau), D(x_{t-\tau}), q(x_{t-\tau}), r(x_{t-\tau}), \epsilon(x_{t-\tau}, t-\tau)) \right] \right\} dt \\ &+ b(\sigma, t) dW(t) \end{aligned} \quad (105.16)$$

where,

$$\begin{aligned} b^2(\sigma, t) &= 2 \int_0^t d\tau Cov_0 \left[ \eta(\sigma(x_t, t), D(x_t), q(x_t), r(x_t), \epsilon(x_t, t)); \right. \\ &\quad \left. \eta(\sigma(x_{t-\tau}, t-\tau), D(x_{t-\tau}), q(x_{t-\tau}), r(x_{t-\tau}), \epsilon(x_{t-\tau}, t-\tau)) \right] \end{aligned} \quad (105.17)$$

and,  $dW(t)$  is an increment of Wiener process  $W$  with  $\langle dW(t) \rangle = 0$ . It is also interesting to note that all the stochasticity of the original equation (Eq. (105.4)) are lumped together in the last term (Wiener increment term) of the right-hand-side of Eq. (105.16). By taking advantage of the independent increment property of the Wiener process ( $\langle dW(t) \rangle = 0$ ), one can derive the differential equation which describes the evolution of mean of state variable ( $\sigma$ ) of the nonlinear constitutive rate equation in time and space as, (e.g. (Kavvas, 2003))

$$\begin{aligned} \frac{\langle d\sigma(x, t) \rangle}{dt} &= \left\langle \eta(\sigma(x_t, t), D(x_t), q(x_t), r(x_t), \epsilon(x_t, t)) \right\rangle \\ &+ \int_0^t d\tau Cov_0 \left[ \frac{\partial \eta(\sigma(x_t, t), D(x_t), q(x_t), r(x_t), \epsilon(x_t, t))}{\partial \sigma} ; \right. \\ &\quad \left. \eta(\sigma(x_{t-\tau}, t-\tau), D(x_{t-\tau}), q(x_{t-\tau}), r(x_{t-\tau}), \epsilon(x_{t-\tau}, t-\tau)) \right] \end{aligned} \quad (105.18)$$

Eq. (105.18) is a nonlocal integro-differential equation in Eulerian-Lagrangian form, since, although the location  $x_t$  at time  $t$  is known, the Lagrangian location  $x_{t-\tau}$  is an unknown which is determined by Eq. (105.14). It is important to note that the state variable appearing within  $\eta(\cdot)$  on the right-hand-side of Eq. (105.18) is random and needs to be treated accordingly.

This concludes the development of relation for probabilistic behavior of 1-D elastic-plastic constitutive incremental equation with stochastic coefficients and stochastic forcing in most general form. In the following section the developed general relation is specialized to two particular types of point-location scale constitutive modeling: a) 1-D (shear) linear elastic constitutive behavior, and b) 1-D (shear) elastic-plastic Drucker-Prager associative linear hardening constitutive behavior.

### 105.2.3 Probabilistic Elasto-Plasticity: Elastic–Plastic Probabilistic 1-D Constitutive Incremental Equation

For materials obeying Drucker-Prager yield criteria (without cohesion), the yield surface can be written as:

$$f = \sqrt{J_2} - \alpha I_1 \quad (105.19)$$

where  $J_2 = \frac{1}{2}S_{ij}s_{ij}$  is the second invariant of the deviatoric stress tensor  $s_{ij} = \sigma_{ij} - 1/3\delta_{ij}\sigma_{kk}$ , and  $I_1 = \sigma_{ii}$  is the first invariant of the stress tensor, and  $\alpha$ , an internal variable, is a function of friction angle ( $\alpha = 2 \sin(\phi)/(\sqrt{3}(3 - \sin\phi))$ ), where  $\phi$  is the friction angle (e.g. (Chen and Han, 1988b)).

By assuming associative flow rule, so that the yield function has the same derivatives as the plastic flow function

$$\frac{\partial f}{\partial \sigma_{ij}} = \frac{\partial U}{\partial \sigma_{ij}} \quad (105.20)$$

one can expand parts of the tangent constitutive tensor given in Eq. (105.2) (from Page 424), to read<sup>2</sup>

$$\begin{aligned} A_{kl} = \frac{\partial f}{\partial \sigma_{pq}} D_{pqkl} = & A_{kl} \frac{\partial f}{\partial I_1} \left( 2G \left( \frac{\partial I_1}{\partial \sigma_{11}} \delta_{1l} \delta_{1k} + \frac{\partial I_1}{\partial \sigma_{22}} \delta_{2l} \delta_{2k} + \frac{\partial I_1}{\partial \sigma_{33}} \delta_{3l} \delta_{3k} \right) \right. \\ & + \left( K - \frac{2}{3}G \right) \frac{\partial I_1}{\partial \sigma_{cd}} \delta_{cd} \delta_{kl} \\ & \left. + \frac{\partial f}{\partial \sqrt{J_2}} \left( 2G \frac{\partial \sqrt{J_1}}{\partial \sigma_{ij}} \delta_{ik} \delta_{jl} + \left( K - \frac{2}{3}G \right) \frac{\partial \sqrt{J_2}}{\partial \sigma_{ab}} \delta_{ab} \delta_{kl} \right) \right) \end{aligned} \quad (105.21)$$

and,

$$\begin{aligned} B = & \frac{\partial f}{\partial \sigma_{rs}} D_{rstu} \frac{\partial f}{\partial \sigma_{tu}} = \\ & \left( \frac{\partial f}{\partial I_1} \right)^2 \left( 2G \left( \left( \frac{\partial I_1}{\partial \sigma_{11}} \right)^2 + \left( \frac{\partial I_1}{\partial \sigma_{22}} \right)^2 + \left( \frac{\partial I_1}{\partial \sigma_{33}} \right)^2 \right) \right. \\ & + \left( K - \frac{2}{3}G \right) \left( \frac{\partial I_1}{\partial \sigma_{ij}} \delta_{ij} \right)^2 \\ & \left. + \left( \frac{\partial f}{\partial \sqrt{J_2}} \right)^2 \left( 2G \frac{\partial \sqrt{J_2}}{\partial \sigma_{ij}} \frac{\partial \sqrt{J_2}}{\partial \sigma_{ij}} + \left( K - \frac{2}{3}G \right) \left( \frac{\partial \sqrt{J_2}}{\partial \sigma_{ij}} \delta_{ij} \right)^2 \right) \right) \end{aligned} \quad (105.22)$$

where,  $K$  and  $G$  are the elastic bulk modulus and the elastic shear modulus respectively.

---

<sup>2</sup>A more detailed derivation of this probabilistic differentiation is given in the Appendix.

By further assuming that the evolution of internal variable is a function of equivalent plastic strain<sup>3</sup>,  $e_{eq}^p = 2/3 e_{ij}^p e_{ij}^p$  then one can write

$$K_P = -\frac{\partial f}{\partial q_n} r_n = -\frac{1}{\sqrt{3}} \frac{\partial f}{\partial \alpha} \frac{d\alpha}{de_{eq}^p} \frac{\partial f}{\partial \sqrt{J_2}} \quad (105.23)$$

It should be noted that since material properties are assumed to be random, the resulting stress tensor will also become random and hence the derivatives of the stress invariants with respect to stress tensor ( $\sigma_{ij}$ ) will become random. Therefore, differentiations appearing in Eqs. (105.21), (105.22), and (105.23) can not be carried out in a deterministic sense.

The parameter tensor in Eq. (105.1) then becomes

$$D_{ijkl}^{ep} = \begin{cases} 2G\delta_{ik}\delta_{jl} + \left(K - \frac{2}{3}G\right)\delta_{ij}\delta_{kl} & ; f < 0 \vee (f = 0 \wedge df < 0) \\ 2G\delta_{ik}\delta_{jl} + \left(K - \frac{2}{3}G\right)\delta_{ij}\delta_{kl} - \frac{A_{ij}A_{kl}}{B + K_P} & ; f = 0 \vee df = 0 \end{cases} \quad (105.24)$$

where tensor  $A_{ij}$  and scalars  $B$  and  $K_P$  are defined by Eqs. (105.21), (105.22), and (105.23) respectively. The above equation (Eq. 105.24) represents a probabilistic continuum stiffness tensor for an elastic–plastic material model, in this case Drucker-Prager isotropic linear hardening material with associated plasticity. By focusing our attention on one dimensional point-location scale shear constitutive relationship between  $\sigma_{12}$  and  $\epsilon_{12}$  for Drucker-Prager material model, one can simplify the function  $\eta(\sigma, D, q, r, \epsilon; x, t)$  as defined in Eq. (105.5) (on Page 424) to read

$$\eta = \begin{cases} 2G \frac{d\epsilon_{12}}{dt} & ; f < 0 \vee (f = 0 \wedge df < 0) \\ \left( 2G - \frac{4G^2 \left( \frac{\partial f}{\partial \sqrt{J_2}} \frac{\sqrt{J_2}}{\partial \sigma_{12}} \right)^2}{B + K_P} \right) \frac{d\epsilon_{12}}{dt} & ; f = 0 \vee df = 0 \end{cases} \quad (105.25)$$

By considering both the material properties (shear modulus  $G$ , bulk modulus  $K$ , friction angle  $\alpha$ , and rate of change of friction angle (linear hardening)  $\alpha'$ ) and the strain rate ( $d\epsilon_{12}/dt(t)$ ) as random, one can substitute  $\eta$  as derived in Eq. (105.13) to obtain the particular FPK equation for the probabilistic behavior of Drucker-Prager associative linear hardening, 1-D point-location scale elastic-plastic shear constitutive rate equation. In particular, two cases are recognized, one for elastic (pre-yield) behavior of

<sup>3</sup>This is a fairly common assumption, e.g. (Chen and Han, 1988b)

material ( $f < 0 \vee (f = 0 \wedge df < 0)$ )

$$\begin{aligned} \frac{\partial P(\sigma_{12}(t), t)}{\partial t} = & \\ - \frac{\partial}{\partial \sigma_{12}} & \left[ \left\langle 2G \frac{d\epsilon_{12}}{dt}(t) \right\rangle P(\sigma_{12}(t), t) \right] \\ + \frac{\partial^2}{\partial \sigma_{12}^2} & \left[ \left\{ \int_0^t d\tau Cov_0 \left[ 2G \frac{d\epsilon_{12}}{dt}(t); 2G \frac{d\epsilon_{12}}{dt}(t-\tau) \right] \right\} P(\sigma_{12}(t), t) \right] \end{aligned} \quad (105.26)$$

noting that this is the same equation as Eq. (??). In addition to that, the case of elastic–plastic behavior ( $f = 0 \vee df = 0$ ) is described by the following probabilistic equation

$$\begin{aligned} \frac{\partial P(\sigma_{12}(t), t)}{\partial t} = & - \frac{\partial}{\partial \sigma_{12}} \left[ \left\{ \left\langle (G^{ep}(t)) \frac{d\epsilon_{12}}{dt}(t) \right\rangle \right. \right. \\ + \int_0^t d\tau Cov_0 & \left[ \frac{\partial}{\partial \sigma_{12}} \left( G^{ep}(t) \frac{d\epsilon_{12}}{dt}(t) \right); G^{ep}(t-\tau) \frac{d\epsilon_{12}}{dt}(t-\tau) \right] \left. \right\} P(\sigma_{12}(t), t) \\ + \frac{\partial^2}{\partial \sigma_{12}^2} & \left[ \left\{ \int_0^t d\tau Cov_0 \left[ G^{ep}(t) \frac{d\epsilon_{12}}{dt}(t); G^{ep}(t-\tau) \frac{d\epsilon_{12}}{dt}(t-\tau) \right] \right\} P(\sigma_{12}(t), t) \right] \end{aligned} \quad (105.27)$$

where  $G^{ep}(a)$  is defined as probabilistic elastic–plastic kernel and is introduced to shorten the writing (but will also have other uses later)

$$G^{ep}(a) = \left( 2G - \frac{4G^2 \left( \frac{\partial f}{\partial \sqrt{J_2}(a)} \frac{\partial \sqrt{J_2}(a)}{\partial \sigma_{12}(a)} \right)^2}{B(a) + K_P(a)} \right) \quad (105.28)$$

and  $a$  assumes values  $t$  or  $t - \tau$ .

It is important to note that the differentiations appearing in the coefficient terms of the FPK PDE (Eq. (105.27)), within the probabilistic elastic–plastic kernel  $G^{ep}(a)$  (i.e. Eq. (105.28)), are for fixed values of  $\sigma_{12}$  and hence those differentiations can be carried out in a deterministic sense. After carrying out the differentiations, the probabilistic elastic–plastic kernel becomes

$$G^{ep}(a)|_{\sigma_{12} \rightarrow const.} = \left( 2G - \frac{G^2}{G + 9K\alpha^2 + \frac{1}{\sqrt{3}}I_1(a)\alpha'} \right) \quad (105.29)$$

which, after substitution, result in simplification of the FPK equation (105.27). Further simplification is possible by noting that the first random process in the covariance term of the first coefficient on the r.h.s of the equation (105.27) is independent of  $\sigma_{12}$ . Furthermore, since the covariance of zero with any

random process is zero, the FPK equation (105.27) is further simplified to read

$$\begin{aligned} \frac{\partial P(\sigma_{12}(t), t)}{\partial t} = & \\ - \frac{\partial}{\partial \sigma_{12}} & \left[ \left\langle G^{ep}(t) \frac{d\epsilon_{12}}{dt}(t) \right\rangle P(\sigma_{12}(t), t) \right] \\ + \frac{\partial^2}{\partial \sigma_{12}^2} & \left[ \left\{ \int_0^t d\tau Cov_0 \left[ G^{ep}(t) \frac{d\epsilon_{12}}{dt}(t); G^{ep}(t-\tau) \frac{d\epsilon_{12}}{dt}(t-\tau) \right] \right\} P(\sigma_{12}(t), t) \right] \end{aligned} \quad (105.30)$$

where the probabilistic elastic-plastic kernel  $G^{ep}(a)$  is given by the Eq. (105.29).

The evolution of a mean value of shear stress  $\sigma_{12}$  is obtained by substituting  $\eta$  (derived for Drucker-Prager material in Eq. (105.18)) as

$$\begin{aligned} \frac{d\langle \sigma_{12}(t) \rangle}{dt} = & \left\langle G^{ep}(t) \frac{d\epsilon_{12}}{dt}(t) \right\rangle \\ + \int_0^t d\tau Cov_0 & \left[ \frac{\partial}{\partial \sigma_{12}} \left( G^{ep}(t) \frac{d\epsilon_{12}}{dt}(t) \right); G^{ep}(t-\tau) \frac{d\epsilon_{12}}{dt}(t-\tau) \right] \end{aligned} \quad (105.31)$$

It is important to note that the derivatives appearing in the mean and covariance term of the above Eulerian-Lagrangian integro-differential equation (Eq. (105.31) with the probabilistic elastic-plastic kernel defined through the Eq. (105.29)) are random differentiations and need to be treated accordingly. One possible approach to obtaining these differentiations could be perturbation with respect to mean (Anders and Hori, 2000) but the "closure problem" will appear. Hence, in this study the evolution of mean of  $\sigma_{12}$  will be obtained by the expectation operation on the PDF (Eq. (105.15)).

#### 105.2.4 Probabilistic Elasto-Plasticity: Initial and Boundary Conditions for the Probabilistic Elastic-Plastic PDE

The PDE describing the probabilistic behavior of constitutive rate equations can be written in the following general form:

$$\begin{aligned} \frac{\partial P(\sigma_{12}, t)}{\partial t} = & -\frac{\partial}{\partial \sigma_{12}} \left\{ P(\sigma_{12}, t) N_{(1)} \right\} + \frac{\partial^2}{\partial \sigma_{12}^2} \left\{ P(\sigma_{12}, t) N_{(2)} \right\} \\ = & -\frac{\partial}{\partial \sigma_{12}} \left[ P(\sigma_{12}, t) N_{(1)} - \frac{\partial}{\partial \sigma_{12}} \left\{ P(\sigma_{12}, t) N_{(2)} \right\} \right] \\ = & -\frac{\partial \zeta}{\partial \sigma_{12}} \end{aligned} \quad (105.32)$$

where,  $N_{(1)}$  and  $N_{(2)}$  are coefficients<sup>4</sup> of the PDE and represent the expressions within the curly braces of the first and second terms respectively on the right-hand-side of Eqs. ( ??), (105.26), and (105.27). These terms are called the advection ( $N_{(1)}$ ) and diffusion ( $N_{(2)}$ ) coefficients as the form of Eq. (105.32)

<sup>4</sup>Indices in brackets are not used in index summation convention.

closely resembles advection–diffusion equation (Gardiner, 2004). The symbol  $\zeta$  in Eq. (105.32) can be considered to be the probability current. This follows from Eq. (105.32), which is a continuity equation and the state variable of the equation is probability density.

After introducing initial and boundary conditions, one can solve Eq. (105.32) for probability densities of  $\sigma_{12}$  with evolution of time. The initial condition could be deterministic or stochastic depending on the type of problem. For probabilistic behavior of linear elastic constitutive rate equation (Eq. (??)), one can assume that all the probability mass at time  $t = 0$  is concentrated at  $\sigma_{12} = 0$  or at some constant value of  $\sigma_{12}$  if there were some initial stresses to begin with (e.g. overburden pressure on a soil mass).

In mathematical term, this translates to,

$$P(\sigma_{12}, 0) = \delta(\sigma_{12}) \quad (105.33)$$

where,  $\delta(\cdot)$  is the Dirac delta function.

For the post–yield behavior of probabilistic elastic-plastic constitutive rate Equation<sup>5</sup> (105.30), there will be a distribution of  $\sigma_{12}$ , corresponding to the solution of the pre-yield probabilistic behavior (Eq. (105.26)), to begin with. This probability mass ( $P(\sigma_{12}(t), t)$ ), dictated by Eq. (105.13), will advect and diffuse into the domain ( $\sigma_{12}, t$  space) of the system throughout the evolution (in time/strain) of the simulation. Since it is required that the probability mass within the system is conserved i.e. no leaking is allowed at the boundaries, a reflecting barrier at the boundaries will be the preferred choice. In mathematical term, one can express this condition as (Gardiner, 2004)

$$\zeta(\sigma_{12}, t)|_{At\, Boundaries} = 0 \quad (105.34)$$

In theory, the stress domain could extend from  $-\infty$  to  $\infty$  so that boundary conditions are then

$$\zeta(-\infty, t) = \zeta(\infty, t) = 0 \quad (105.35)$$

With these initial and boundary conditions, the probabilistic differential equation (with random material properties and random strain) for elasto–plasticity, specialized in this case to associated Drucker–Prager material model with linear hardening, and by using FPK transform described above, can be solved for probability densities of shear stress ( $\sigma_{12}$ ) as it evolves with time/shear strain ( $\epsilon_{12}$ ).

### 105.2.5 Probabilistic Elasto-Plasticity: Fokker–Planck–Kolmogorov Equation for Probabilistic Elasticity and Elasto–Plasticity in 1-D

By focusing attention to the randomness of material properties only (i.e. assuming the forcing function (strain rate) as deterministic), partial differential equation (PDE) describing the evolution of probability

---

<sup>5</sup>Specialized to Drucker-Prager associated linear hardening model.

density function (PDF) of stress can be simplified. In particular, for 1D case, and for linear elastic material (but still with probabilistic material properties, in this case shear modulus  $G$ ) one can write the following PDE

$$\begin{aligned} \frac{\partial P(\sigma_{12}(t))}{\partial t} = & - \left\langle 2G \frac{d\epsilon_{12}}{dt} \right\rangle \frac{\partial P(\sigma_{12}(t))}{\partial \sigma_{12}} \\ & + \left\{ \int_0^t d\tau Cov_0 \left[ 2G \frac{d\epsilon_{12}}{dt}; 2G \frac{d\epsilon_{12}}{dt} \right] \right\} \frac{\partial^2 P(\sigma_{12}(t))}{\partial \sigma_{12}^2} \end{aligned} \quad (105.36)$$

Similarly, for elastic–plastic state, again by neglecting the randomness in strain rate, one can write the PDE for evolution of PDF of stress in 1D as

$$\begin{aligned} \frac{\partial P(\sigma_{12}(t))}{\partial t} = & - \left\langle (G^{ep}(t)) \frac{d\epsilon_{12}}{dt} \right\rangle \frac{\partial P(\sigma_{12}(t))}{\partial \sigma_{12}} \\ & + \left\{ \int_0^t d\tau Cov_0 \left[ G^{ep}(t) \frac{d\epsilon_{12}}{dt}; G^{ep}(t-\tau) \frac{d\epsilon_{12}}{dt} \right] \right\} \frac{\partial^2 P(\sigma_{12}(t))}{\partial \sigma_{12}^2} \end{aligned} \quad (105.37)$$

where  $G^{ep}(a)$  is the probabilistic elastic–plastic tangent stiffness, (given in [Jeremić et al. \(2007a\)](#))

$$G^{ep}(a) = 2G - \frac{G^2}{G + 9K\alpha^2 + \frac{1}{\sqrt{3}}I_1(a)\alpha'} \quad (105.38)$$

where in the previous equation (105.38),  $a$  assumes values  $t$  or  $t - \tau$ . With appropriate initial and boundary conditions as described in [Jeremić et al. \(2007a\)](#), one can solve Eqs. (105.36) and (105.37) for evolution of PDF of shear stress with shear strain.

### 105.2.6 Probabilistic Elasto-Plasticity: Example Problem Statements

The applicability of proposed FPK equations (Eqs. (105.36) and (105.37)) in describing probabilistic elasto-plastic behavior, is verified using the following three example problems.

**Problem I.** Assume the material is linear elastic, probabilistic, with probabilistic shear modulus ( $G$ ) given by a normal distribution at a point–location scale with mean of 2.5 MPa and standard deviation of 0.707 MPa. The aim is to calculate the evolution of PDF of shear stress ( $\sigma_{12}$ ) with shear strain ( $\epsilon_{12}$ ) for a displacement-controlled test with deterministic shear strain increment. The other parameters are considered deterministic and are as follows: Poisson's ratio ( $\nu = 0.2$ , and confining pressure  $I_1 = 0.03$  MPa).

**Problem II.** Assume elastic–plastic material model, composed of linear elastic component and Drucker–Prager associative isotropic linear hardening elastic–plastic component. The probabilistic shear modulus

( $G$ ) is given through a normal distribution at a point–location scale with mean of 2.5 MPa and standard deviation of 0.707 MPa. The aim is to calculate the evolution of the PDF of shear stress ( $\sigma_{12}$ ) with shear strain ( $\epsilon_{12}$ ) for a displacement-controlled test with deterministic shear strain increment. The other parameters are considered deterministic and are as follows: Poisson's ratio  $\nu = 0.2$ , confining pressure  $I_1 = 0.03$  MPa, yield parameter<sup>6</sup>  $\alpha = 0.071$ , plastic slope<sup>7</sup>  $\alpha' = 5.5$ .

Problem III. Assume elastic–plastic material model, with linear elastic component and Drucker–Prager associative isotropic linear hardening elastic–plastic component. The probabilistic yield parameter ( $\alpha$ ) is given through a normal distribution at a point–location scale with mean of 0.52 and standard deviation of 0.1. The aim is to calculate the evolution of the PDF of shear stress ( $\sigma_{12}$ ) with shear strain ( $\epsilon_{12}$ ) for a displacement-controlled test with deterministic shear strain increment. The other parameters are considered deterministic and are as follows: shear modulus  $G = 2.5$  MPa, Poisson's ratio  $\nu = 0.2$ , confining pressure  $I_1 = 0.03$  MPa, and the plastic slope  $\alpha' = 5.5$ .

The above three problems will be solved using the proposed FPK equation approach. In addition to that, the solution will be verified using either variable transformation method, for linear elastic case or repetitive Monte Carlo type simulations for elastic-plastic case.

### 105.2.7 Probabilistic Elasto-Plasticity: Determination of Coefficients for Fokker–Planck–Kolmogorov Equation

To solve Problems I, II, and III, the advection and diffusion coefficients  $N_{(1)}$  and  $N_{(2)}$  must be determined for all three problems. For sake of simplicity, a constant strain rate is assumed and hence, terms containing  $d\epsilon_{12}/dt$  in coefficients of Eqs. (105.36) and (105.37) can be substituted by a constant numerical value for the entire simulation of the evolution of PDF. It should be noted that the FPK equation (Eqs. (105.36) or (105.37)) describes the evolution of PDFs of stress with time, while, similarly, strain rate describes the evolution of strain with time. Combining the two, the evolution of PDF of stress with strain can be obtained. Time has been brought in this simulation as an intermediate dimension to help in solution process, and hence, the numerical value of strain rate could be any arbitrary value, which will cancel out once the time evolution of PDF of stress is converted to strain evolution of PDF of stress. For simulation of all the three example problems, an arbitrary value of strain rate of  $d\epsilon_{12}/dt = 0.0541/s$  is assumed.

It should also be noted that since the material properties are assumed as random variables at a point–location scale, the covariance terms appearing within the advection and diffusion coefficients become variances of random variables. For estimations of means and variances of functions of random variables

---

<sup>6</sup>The yield parameter  $\alpha$  is an internal variable and is a function of friction angle  $\phi$  given by ( $\alpha = 2 \sin(\phi)/(\sqrt{3}(3 - \sin\phi))$ ) (e.g. (Chen and Han, 1988b))

<sup>7</sup>The plastic slope  $\alpha'$  is a rate of change of friction angle governing linear hardening.

(e.g. for Problems II and III) from basic random variables, commercially available statistical software mathStatica Rose and Smith (2002) was used.

Substituting the values of deterministic and random material properties and the strain rate, coefficients  $N_{(1)}$  and  $N_{(2)}$  of the FPK equations can be obtained for all problems:

### Problem I

$$\begin{aligned} N_{(1)} &= \left\langle 2G \frac{d\epsilon_{12}}{dt} \right\rangle \\ &= 2 \frac{d\epsilon_{12}}{dt} \langle G \rangle \\ &= 0.27 \text{ MPa/s} \end{aligned}$$

$$\begin{aligned} N_{(2)} &= \int_0^t d\tau \text{Var} \left[ 2G \frac{d\epsilon_{12}}{dt} \right] \\ &= 4t \left( \frac{d\epsilon_{12}}{dt} \right)^2 \text{Var}[G] \\ &= 0.0058t \text{ (MPa/s)}^2 \end{aligned}$$

### Problem II

For pre-yield linear elastic case, the coefficients  $N_{(1)}$  and  $N_{(2)}$  will be the same as those for Problem I.

I. For post-yield elastic-plastic case the coefficients are

$$\begin{aligned} N_{(1)} &= \left\langle \left( 2G - \frac{G^2}{G + 9K\alpha^2 + \frac{1}{\sqrt{3}}I_1\alpha'} \right) \frac{d\epsilon_{12}}{dt} \right\rangle \\ &= \frac{d\epsilon_{12}}{dt} \left\langle 2G - \frac{G^2}{G + 9K\alpha^2 + \frac{1}{\sqrt{3}}I_1\alpha'} \right\rangle \\ &= 0.147 \text{ MPa/s} \end{aligned}$$

$$\begin{aligned} N_{(2)} &= t \left( \frac{d\epsilon_{12}}{dt} \right)^2 \text{Var} \left[ 2G - \frac{G^2}{G + 9K\alpha^2 + \frac{1}{\sqrt{3}}I_1\alpha'} \right] \\ &= 0.00074t \text{ (MPa/s)}^2 \end{aligned}$$

### Problem III

For post-yield elastic-plastic simulation the coefficients  $N_{(1)}$  and  $N_{(2)}$  are

$$\begin{aligned} N_{(1)} &= \left\langle \left( 2G - \frac{G^2}{G + 9K\alpha^2 + \frac{1}{\sqrt{3}}I_1\alpha'} \right) \frac{d\epsilon_{12}}{dt} \right\rangle \\ &= \frac{d\epsilon_{12}}{dt} \left\langle 2G - \frac{G^2}{G + 9K\alpha^2 + \frac{1}{\sqrt{3}}I_1\alpha'} \right\rangle \\ &= 0.2365 \text{ MPa/s} \end{aligned}$$

$$\begin{aligned} N_{(2)} &= t \left( \frac{d\epsilon_{12}}{dt} \right)^2 \text{Var} \left[ 2G - \frac{G^2}{G + 9K\alpha^2 + \frac{1}{\sqrt{3}}I_1\alpha'} \right] \\ &= 0.0001t \text{ (MPa/s)}^2 \end{aligned}$$

It should be noted that for Problem III, since the shear modulus is deterministic, the pre-yield elastic case is deterministic.

#### 105.2.8 Probabilistic Elasto-Plasticity: Results and Verifications of Example Problems

In this section results are presented for elastic and elastic–plastic probabilistic 1D problem. The results are obtained by using FPK equation approach described in previous sections and in the companion paper ([Jeremić et al., 2007a](#)). In addition to that, the Monte Carlo based verification of developed solutions (results) is presented. The effort to verify developed solutions (that are based on FPK approach) plays a crucial role in presented development of probabilistic elasto–plasticity as there are no previously published solutions which could have been used for verification. In addition to that, verification and validation efforts should always be included in any modeling and simulations work ([Oberkampf et al., 2002](#)).

For linear elastic constitutive rate equations (Problem-I and pre-yield case of Problem-II) the verification is performed by comparing solutions obtained through the use of FPK equation approach with high accuracy (exact) solution, using a transformation method of random variables ([Montgomery and Rungar, 2003](#)). This method is applicable as for rate-independent linear elastic case the 1D shear constitutive equation simplify to a linear algebraic equation of the form,

$$\sigma_{12} = 2G\epsilon_{12} = u(G, \epsilon_{12}) \quad (105.39)$$

Using the definition of strain rate, the above equation can be written in terms of time  $t$  as,

$$\sigma_{12} = 2G(0.054t) = v(G, t) \quad (105.40)$$

where, 0.054 1/s is the arbitrary strain-rate assumed for this example problem. According to the transformation method of random variables (Montgomery and Rungar, 2003), and, given the continuous random variable (shear modulus)  $G$ , with PDF  $g(G)$  and Eqs. (105.39) or (105.40) as one-to-one transformations between the values of random variables of  $G$  and  $\sigma_{12}$ , one can obtain the PDF of shear stress ( $\sigma_{12}$ ),  $P(\sigma_{12})$  as,

$$P(\sigma_{12}) = g(u^{-1}(\sigma_{12}, \epsilon_{12})) |J| \quad (105.41)$$

which will allow for predicting the evolution of PDF of  $\sigma_{12}$  with  $\epsilon_{12}$  or,

$$P(\sigma_{12}) = g(v^{-1}(\sigma_{12}, t)) |J| \quad (105.42)$$

Eq. (105.42) will predict the evolution of PDF of  $\sigma_{12}$  with  $t$ . In Eqs. (105.41) and (105.42), functions  $G = u^{-1}(\sigma_{12}, \epsilon_{12})$  or  $G = u^{-1}(\sigma_{12}, t)$  are the inverse of functions  $\sigma_{12} = u(G, \epsilon_{12})$  or  $\sigma_{12} = v(G, t)$  respectively and  $J = du^{-1}(\sigma_{12}, \epsilon_{12})/d\sigma_{12}$  and  $J = dv^{-1}(\sigma_{12}, t)/d\sigma_{12}$  are their respective Jacobians of transformations.

For non-linear elastic-plastic constitutive rate equations (post-yield cases of Problems II and III) the verification is done using Monte-Carlo simulation technique by generating sample data for material properties from standard normal distribution and by repeating solution of the deterministic elastic-plastic constitutive rate equation for each data generated above. The probabilistic characteristics of resulting random stress variable for each time (or strain) step are then easily computed. A relatively large number of data points (1,000,000) were generated for each material constant random variable for this simulation purpose.

### 105.2.9 Problem I

The evolution of PDF of shear stress with time and shear strain is shown in Figures 105.3 and 105.4. Presented PDFs are for linear elastic material with random shear modulus, and were obtained using *FPE approach* (Fig. reffigure:ElasticPDF) and *transformation method* (Fig. 105.4).

The contours of evolution of PDFs are compared in Fig. 105.5. Similarly, comparison of the evolution of mean and standard deviations are shown in Fig. 105.6. It can be seen from the comparison figure that even-though the FPK approach predicted the mean behavior exactly, it slightly over-predicted the standard deviation. This is because of the approximation used to represent the Dirac delta function, which was used as the initial condition for the FPK. One may note that at  $\epsilon_{12} = 0$ , the probability of shear stress  $\sigma_{12}$  should theoretically be 1 i.e. all the probability mass should theoretically be concentrated at  $\sigma_{12} = 0$ . As such, it would be best described by the Dirac delta function. However, for numerical simulation of FPK, Dirac delta function as initial condition was approximated with a Gaussian function of

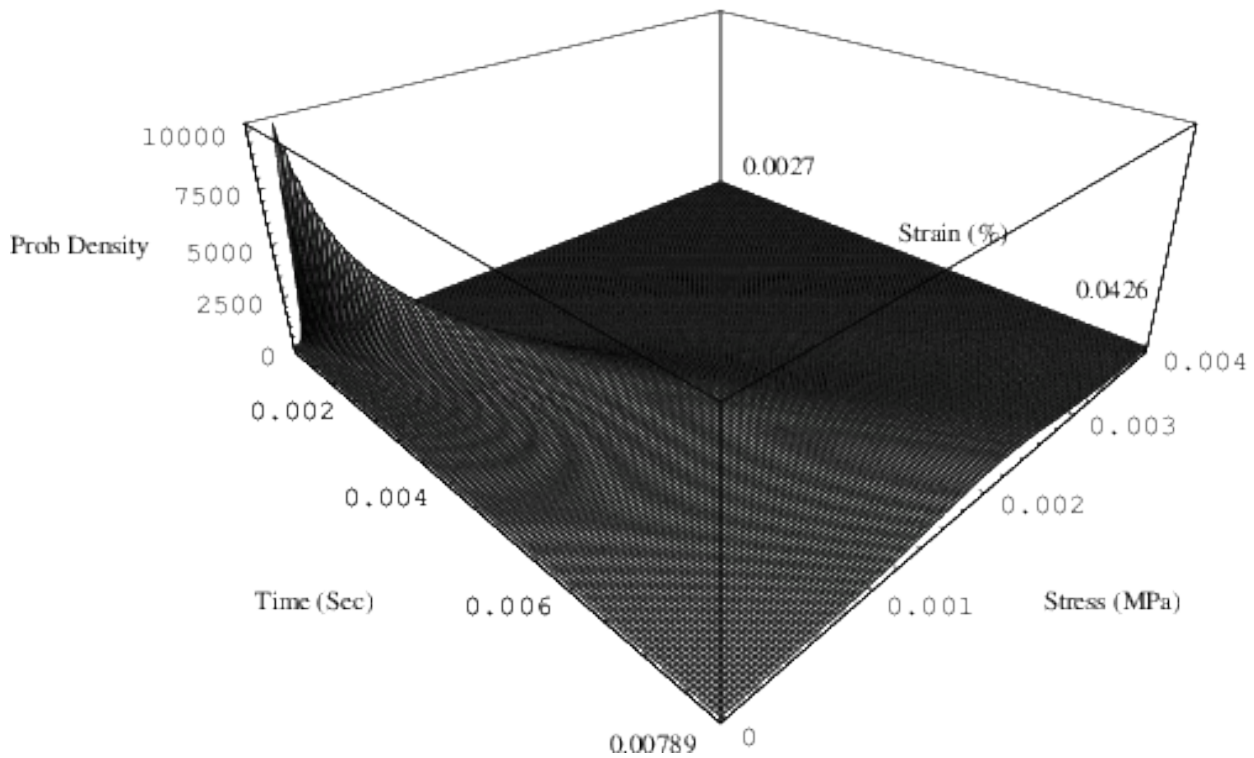


Figure 105.3: Evolution of PDF of shear stress versus strain (or time) for linear elastic material model with random shear modulus (Problem I) obtained using FPK equation approach.

mean zero and standard deviation of 0.00001 MPa, as shown in Fig. ???. This error in the initial condition advected and diffused into the domain with the simulation of the evolution process. This error could be minimized by better approximating the Dirac delta initial condition (but at higher computational cost). The effect of approximating the initial condition of the PDF of shear stress at  $\epsilon_{12} = 0.0426 \%$  is shown in Fig. 105.7. In this figure the actual PDF at  $\epsilon_{12} = 0.0426 \%$  obtained using the transformation method was compared with the PDFs at  $\epsilon_{12} = 0.0426 \%$  obtained using the FPK approach with three different approximate initial conditions - all having zero mean but standard deviations of 0.01 MPa, 0.005 MPa and 0.00001 MPa.

One may also note that finer approximation of initial condition necessitates finer discretization of stress domain close to (or at)  $\sigma_{12} = 0$ . The finite difference discretization scheme adopted here uses the same fine discretization uniformly all throughout the entire domain. It is noted that that fine, uniform discretization is not needed (and is quite expensive) in later stages of calculation of evolution of PDF, but is kept the same for simplicity sake. In presented examples, to properly capture the approximate initial condition (as shown in Fig. ??), the stress domain between  $-0.1$  MPa and  $+0.1$  MPa was discretized with a uniform step size of 0.000005 MPa and hence there is a total of 40,000 nodes. This not only requires

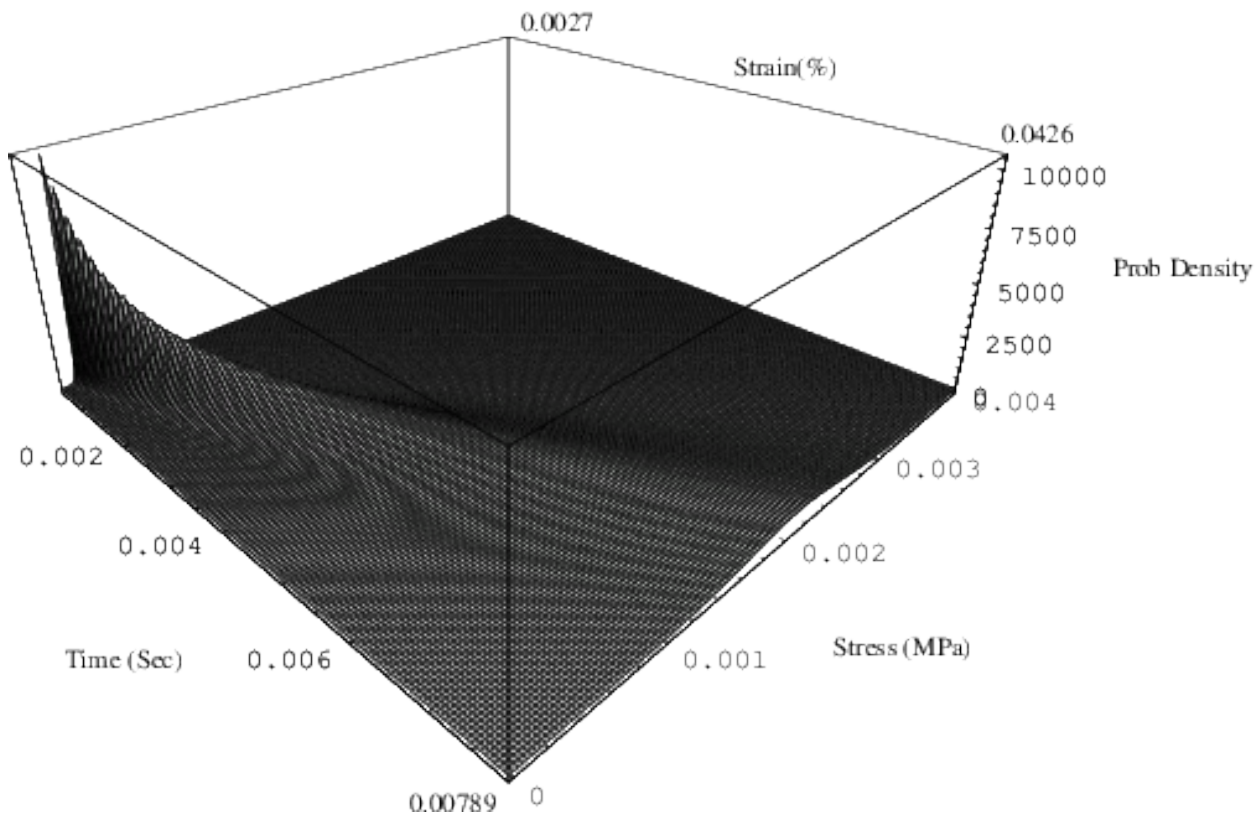


Figure 105.4: Evolution of PDF of shear stress versus strain (or time) for linear elastic material model with random shear modulus (Problem I) obtained using transformation method.

large computational effort but is also very memory sensitive. An adaptive discretization technique will be a much better approach to solving this problem. Current work is going on in formulating an adaptive algorithm for the solution of this type of problem.

#### 105.2.10 Problem II

The solution to this problem involves the solving two FPK equations, one corresponding to the pre-yield elastic part and the other corresponding to the post-yield elastic-plastic part. The elastic part of this problem is identical to Problem-I. The initial condition for the post-yield elastic-plastic part of the problem is random and is shown in Fig. 105.8. It may be noted that this initial condition corresponds to the PDF of shear stress ( $P(\sigma_{12})$ ) at yield obtained from the solution of FPK equation of the pre-yield elastic part. A view of the surface of evolution of the PDF of shear stress versus shear strain (time) is shown in Fig. 105.9. Another view to the PDF of stress-strain surface is shown in Fig. 105.10. It is noted that the yielding of this material occurred at  $t=0.00789$  second (which is equivalent to  $\epsilon_{12}=$

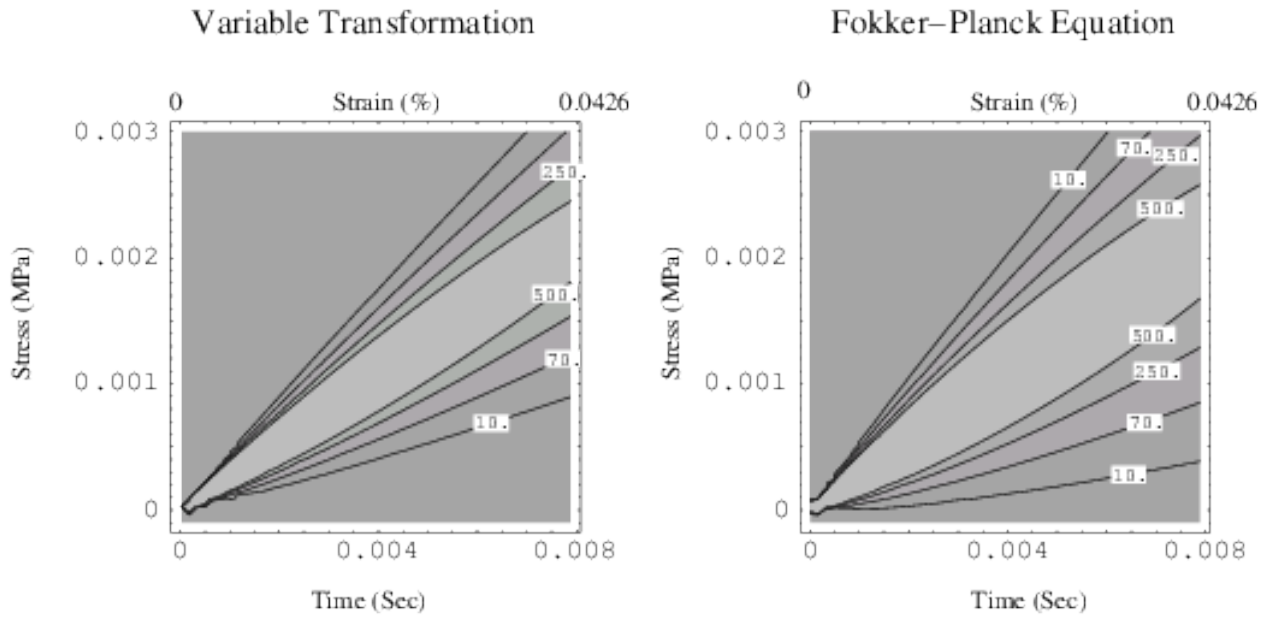


Figure 105.5: Comparison of Contours of Time (or Strain) Evolution of Probability Density Function for Shear Stress for Elastic Constitutive Rate Equation with Random Shear Modulus (Problem-I) for FPE Solution and Variable Transformation Method Solution.

0.0426 %). The evolution contours for PDF of shear stress versus strain (time) along with the mean and standard deviations are shown in Fig. 105.11. It can be seen from that figure that, as expected, the evolution of mean of shear stress changes slope after the material yielded. Another interesting aspect to note is the relative slope of the evolution of standard deviation with respect to the evolution of mean. The relative slope in the pre-yield elastic zone increases at a higher rate during the evolution process when compared with that in the post-yield elastic-plastic zone. In other words, in the evolution process the post-yield elastic-plastic constitutive rate equation did not amplify the initial uncertainty as much as the pre-yield elastic constitutive rate equation did. This can be easily viewed from Fig. 105.12 where the post-yield elastic-plastic evolution of PDF of shear stress was compared with fictitious extension of elastic evolution of PDF. Comparing the PDF of shear stress at  $\epsilon_{12} = 0.0804\%$  (which is equivalent to  $t = 0.01489s$ ), one can conclude that the variance of predicted elastic-plastic shear stress is much smaller (i.e. prediction is less uncertain) as compared to the same if the material were modeled as completely elastic.

Fig. 105.13 compares the evolution of means and standard deviations of predicted shear stress obtained using FPK equation approach and transformation method (pre-yield behavior)/Monte-Carlo approach (post-yield behavior). Although in the pre-yield response the FPK equation approach overpredicted the evolution of standard deviations because of reasons discussed earlier, in the post-yield

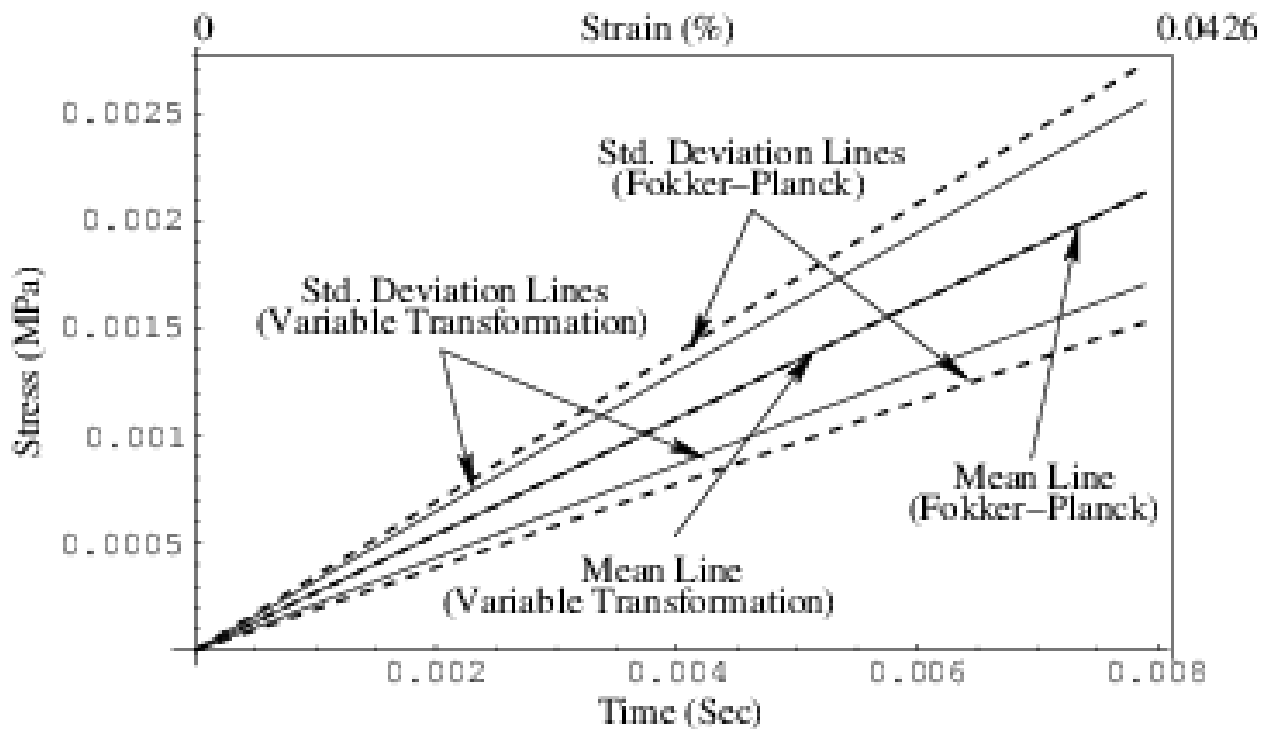


Figure 105.6: Comparison of Mean and Standard Deviation of Shear Stress for Elastic Constitutive Rate Equation with Random Shear Modulus (Problem-I) for FPE Solution and Variable Transformation Method Solution.

response it matched closely at regions further from the yielding region. The somewhat larger difference between FPK equation solution and the verification one (Monte Carlo solution) close to the yielding region is attributed to the fact that the initial condition for solution of post-yield elastic-plastic FPK equation was obtained from the solution of pre-yield elastic FPK equation. One way to better predict the overall probabilistic elastic-plastic behavior, would probably be to obtain the pre-yield elastic behavior through the transformation method and then use the FPK approach to predict post-yield elastic-plastic behavior.

### 105.2.11 Problem III

In this problem, the pre-yield linear elastic part is deterministic, however, at yield there is a distribution (with very small standard deviation) in shear stress due to assumed distribution in yield parameter  $\alpha$ . The distribution in shear stress corresponds to the PDF of the random variable  $\alpha I_1$  (first invariant of the stress tensor or mean confining stress) and is assumed to be deterministic. This PDF of shear stress at yield was assumed to be the initial condition for the solution of post-yield elastic-plastic FPK equation

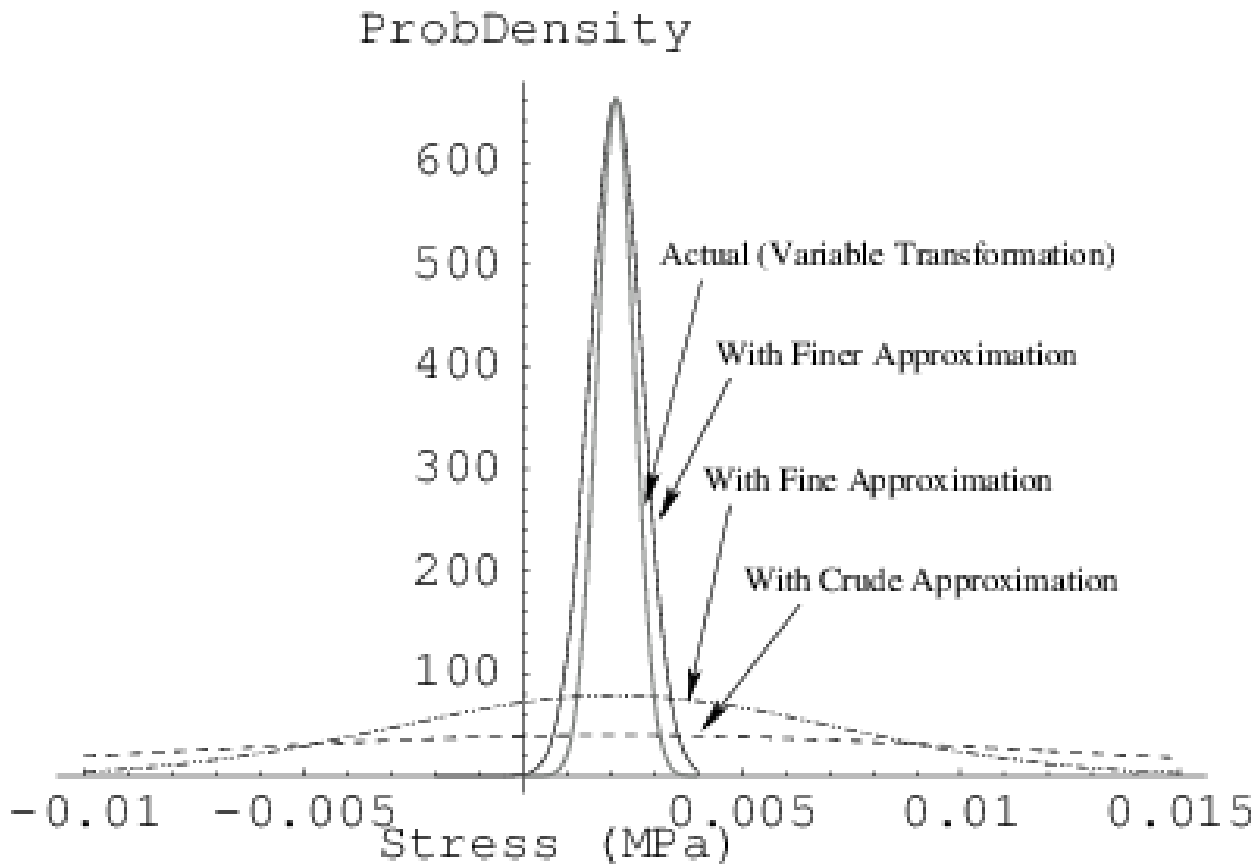


Figure 105.7: Effect of Approximating Function of Dirac Delta Initial Condition : PDF of Stress at Yield for Different Approximation of Initial Condition with Actual (Variable Transformation Method) Solution).

and is shown in Fig. 105.14.

The evolution of PDF for shear stress versus strain (time) is shown in Fig. 105.15. In addition to that the contours (including mean and standard deviation) of the evolution of PDF for shear stress versus strain (time) are shown in Fig. 105.16.

Looking at Fig. 105.16 and comparing the slopes of evolution of mean and standard deviation, one can conclude that the elastic-plastic evolution process didn't amplify the initial uncertainty in yield strength significantly. The initial (at yield) probability density function of shear stress just advected into the domain during the elastic–plastic evolution process without diffusing much. Fig. 105.15 clearly shows this advection process. The evolution of mean and standard deviations of shear stress obtained from the FPK equation approach was compared with those obtained from the Monte Carlo simulation and is shown in Fig. 105.17.

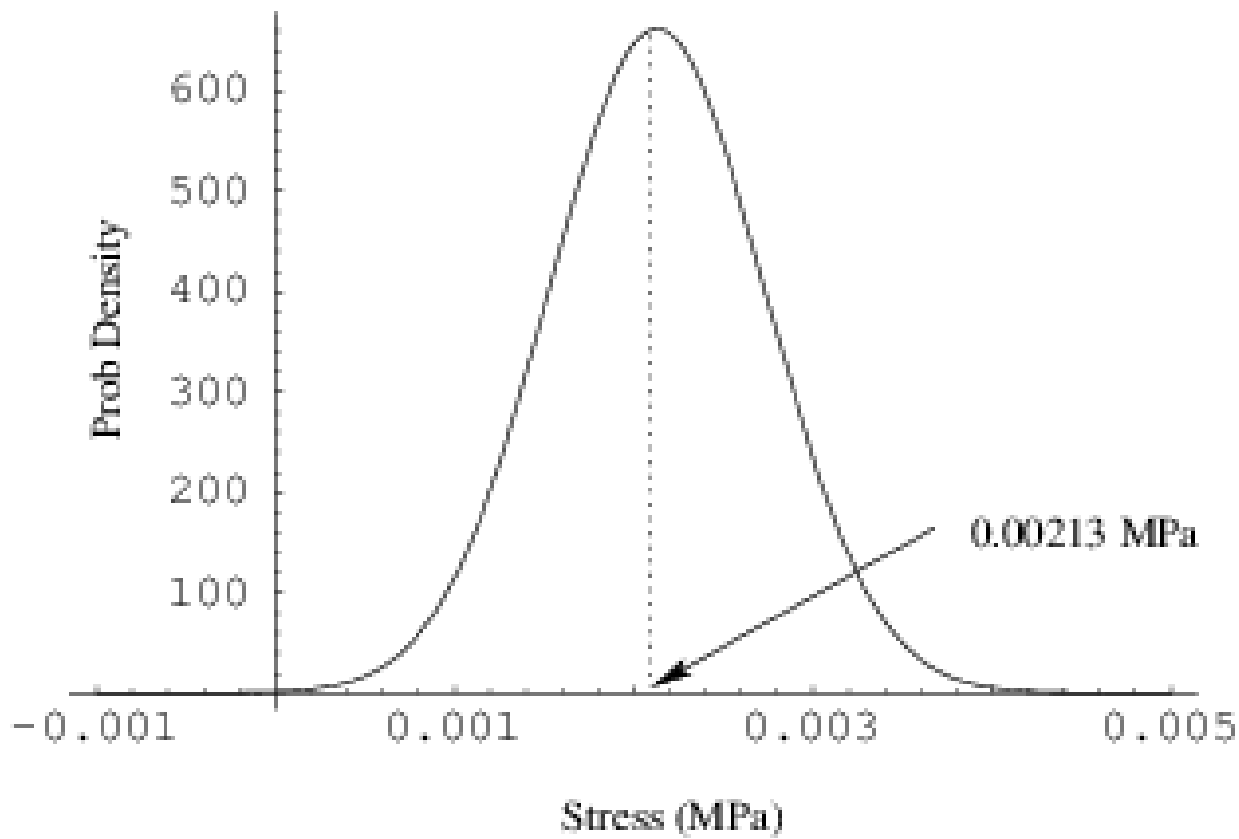


Figure 105.8: Initial condition for FPK equation for elastic–plastic zone (Problem-II).

### 105.3 Probabilistic Yielding and Cyclic Loading, 1D FPK Formulation

Modeling of geomaterials is inherently uncertain. These uncertainties stem from natural variability of geomaterials (spatial uncertainty), and testing and transformation errors (point uncertainty) (Lacasse and Nadim [Lacasse and Nadim \(1996\)](#), Phoon and Kulhawy [Phoon and Kulhawy \(1999a\)](#)). These uncertainties not only affect the failure characteristics of geomaterials, but also the behavior of geostructures, made with geomaterials. Traditionally, geotechnical engineering community deals with uncertainties in geomaterial by applying (large) factor of safety. However, use of large factors of safety results not only in over-expensive design, but also, sometimes, in unsafe structures (cf. Duncan [Duncan \(2000b\)](#)). Hence, in recent years, the geotechnical community has seen an increasing emphasis on probabilistic characterization of soil and subsequent reliability-based design.

One of the important aspects of probabilistic geomechanics simulation that has received less attention is the probabilistic constitutive problem. Among the few published papers were those by Fenton and Griffiths ([Fenton and Griffiths \(2002\)](#), [Fenton and Griffiths \(2003\)](#), [Fenton and Griffiths \(2005\)](#)) on

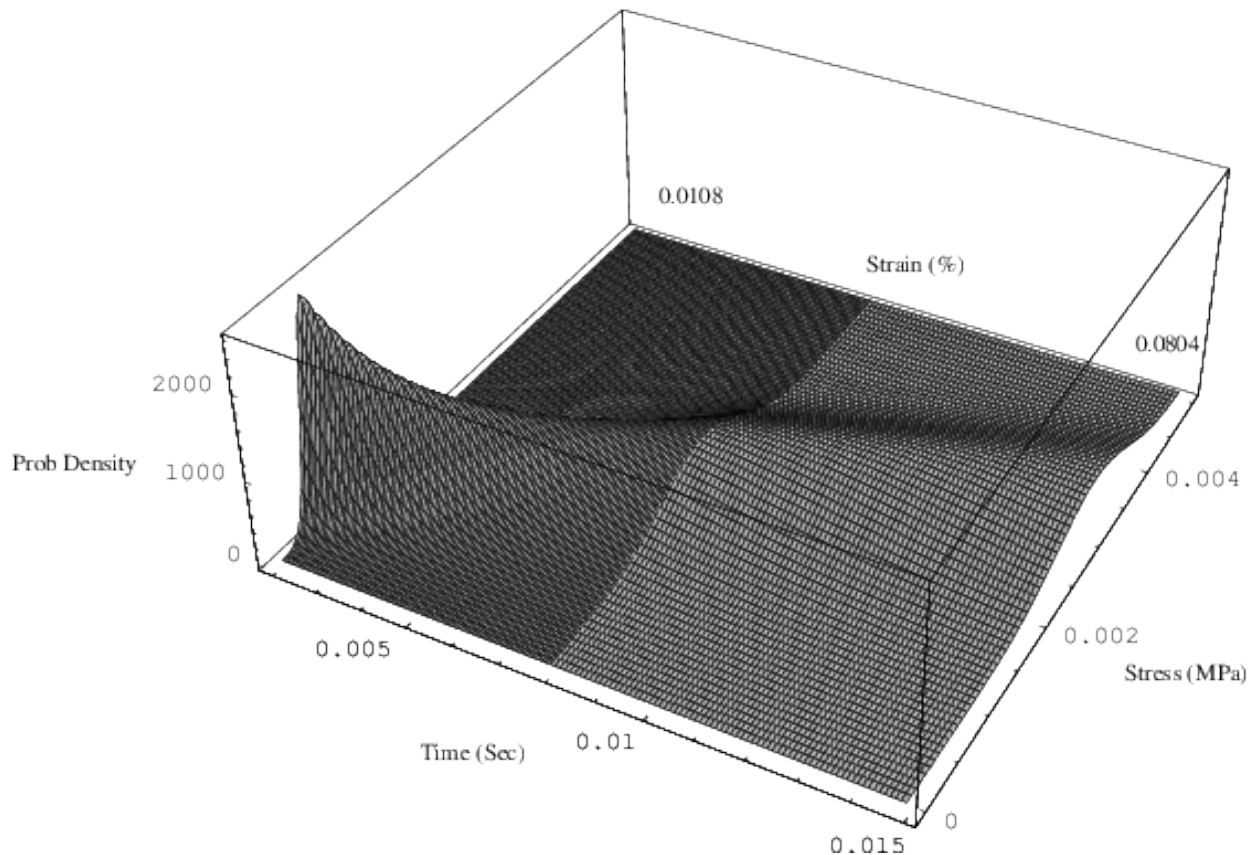


Figure 105.9: Evolution of PDF of shear stress versus strain (time) for elastic-plastic material with random shear modulus (Problem-II). View 1.

probabilistic simulation of spatially random  $c-\phi$  soil using Monte Carlo technique, and those by Anders and Hori ([Anders and Hori \(1999\)](#), [Anders and Hori \(2000\)](#)) on probabilistic simulation of von Mises elastic-perfectly plastic material using perturbation technique. Both Monte Carlo and perturbation techniques have their inherent drawbacks ([Matthies et al. Matthies et al. \(1997\)](#), [Keese Keese \(2003\)](#)) and in dealing with those, recently, Jeremić et al. [Jeremić et al. \(2007b\)](#) proposed Eulerian–Lagrangian form of Fokker–Planck–Kolmogorov equation (FPKE) approach (cf. [Kavvas Kavvas \(2003\)](#)) to modeling and simulation for probabilistic elasto–plasticity. FPKE approach to probabilistic elasto–plasticity not only overcomes the drawbacks associated with other probabilistic simulation techniques, but also is fully compatible with the incremental theory of elasto–plasticity, and hence can easily be applied to probabilistic modeling and simulation of different elastic–plastic constitutive models. Solution strategies for FPK partial differential equation, corresponding to elastic–plastic constitutive rate equation and simulated probabilistic stress-strain responses under monotonic loading, assuming mean stress yielding, were discussed by Sett et al. ([Sett et al. \(2007c\)](#), [Sett et al. \(2007d\)](#)) for both linear and non-linear

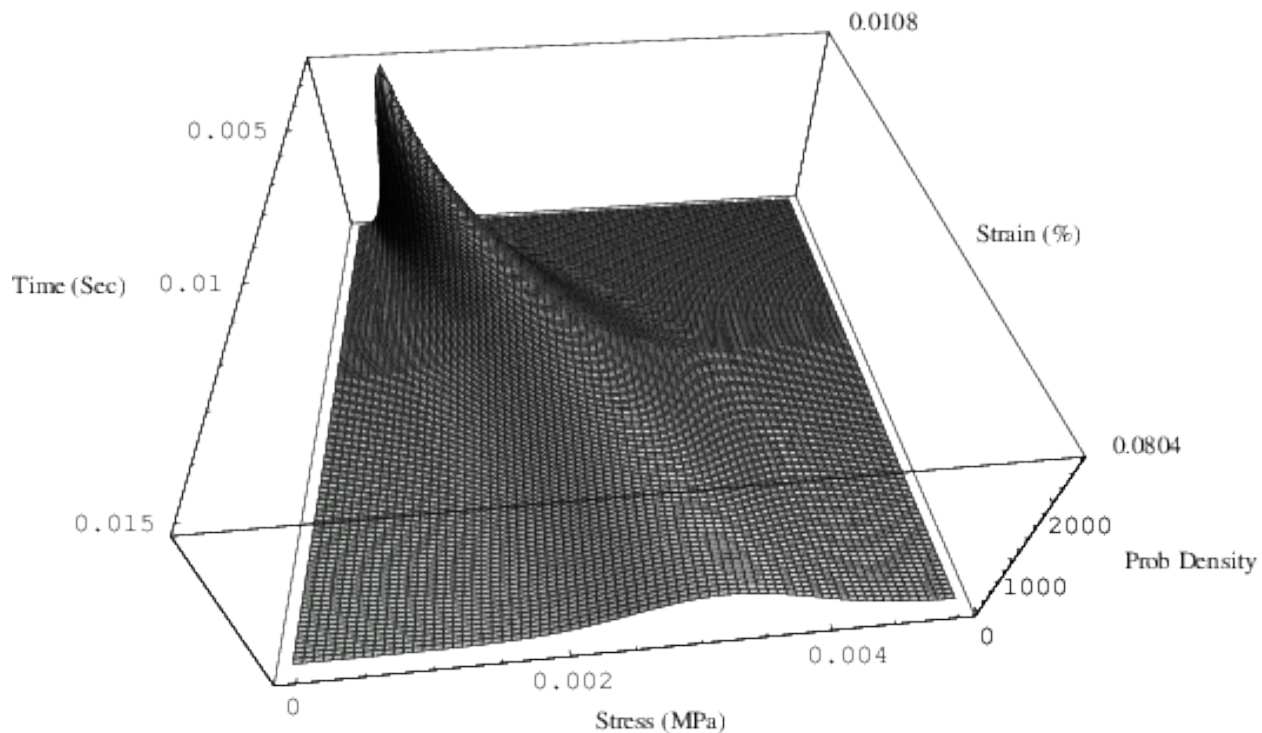


Figure 105.10: Evolution of PDF of shear stress versus strain (time) for elastic-plastic material with random shear modulus (Problem-II). View 2.

hardening models. The concept of probabilistic yielding was introduced and its effect on constitutive simulation under monotonic loading was discussed by Jeremić and Sett [Jeremić and Sett \(2009b\)](#). It was shown that due to uncertainty in yield function (stress), there is always a possibility, depending upon the magnitude of uncertainty, that plastic behavior starts at very very low strain and influence of elastic behavior continues far into plastic domain (at large strains) and hence, the ensemble average (mean) of all the possibilities or the most probable (mode) possibility differ from deterministic behavior. In addition to that, a very realistic, smooth transition between elastic and plastic domains was observed even for elastic perfectly plastic models. Further, nonlinear behavior was observed even for linear hardening models.

In this paper, the concept of probabilistic yielding is extended to 1-D cyclic simulations of geomaterials. Both elastic–perfectly plastic and hardening-type material model are considered. The numerical technique of solving FPKE cyclically with probabilistic yielding is discussed. Simulated responses were discussed in terms of probability density function (PDF) and its statistical moments.

Modeling of geomaterials is inherently uncertain. This uncertainty stems from natural variability of geomaterials (spatial uncertainty), and testing and transformation errors (point uncertainty) (Lacasse

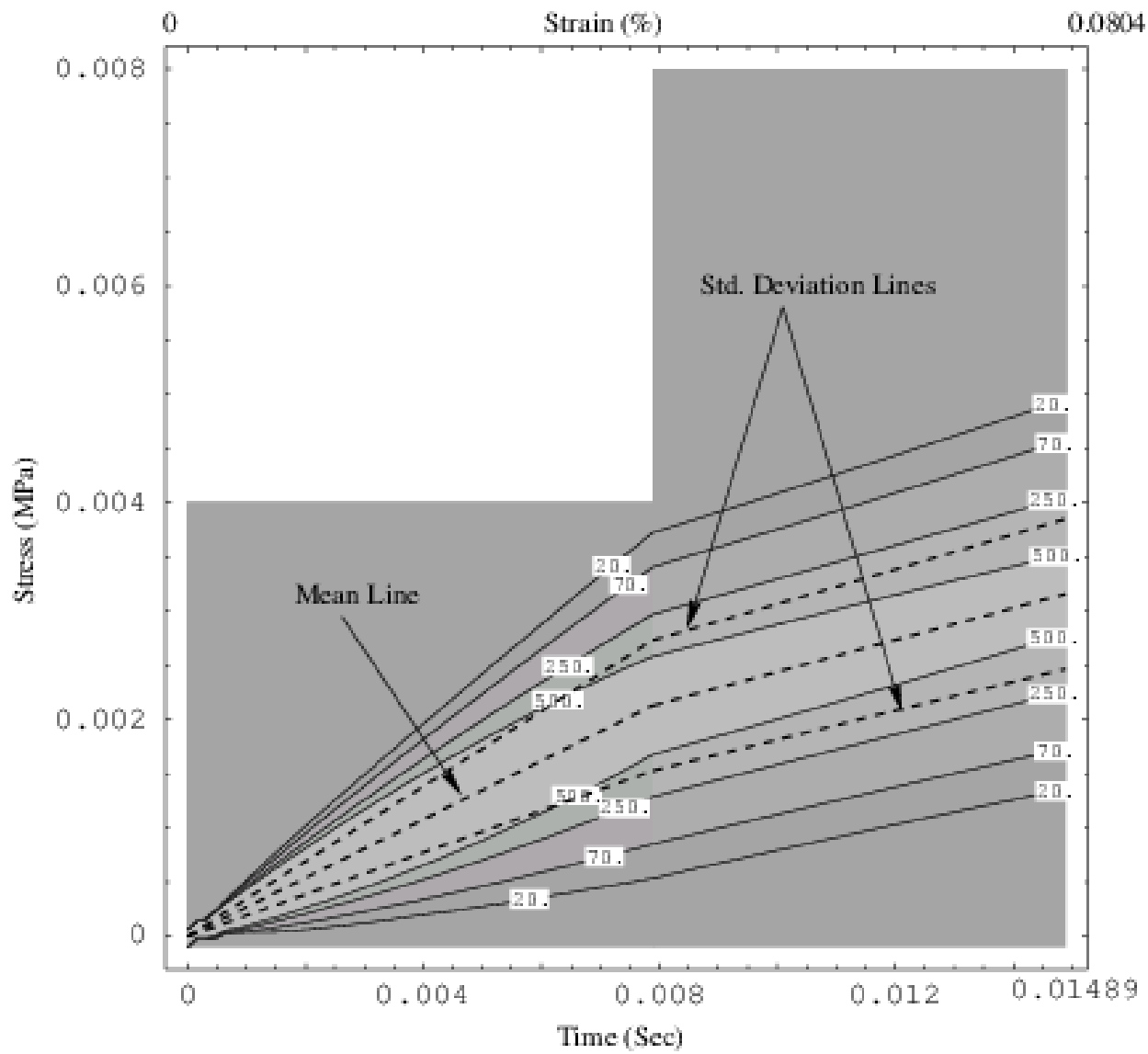


Figure 105.11: Contour of evolution of PDF for shear stress versus strain (time) for elastic-plastic material with random shear modulus (Problem-II).

and Nadim [Lacasse and Nadim \(1996\)](#), Phoon and Kulhawy [Phoon and Kulhawy \(1999a\)](#)). These uncertainties not only affect the failure characteristics of geomaterials, but also the behavior of geostructures, made with geomaterials. Traditionally, geotechnical engineering community deals with uncertainties in geomaterial by applying (large) factor of safety. However, use of large factors of safety results not only in over-expensive design, but also, sometimes, in unsafe structures (cf. Duncan [Duncan \(2000b\)](#)). Hence, in recent years, the geotechnical community has seen an increasing emphasis on probabilistic characterization of soil and subsequent reliability-based design.

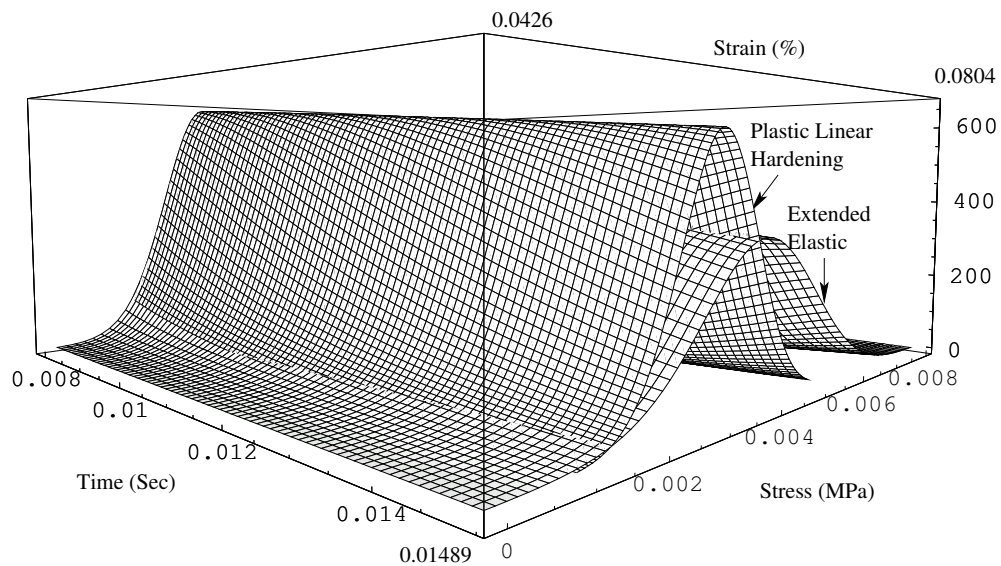


Figure 105.12: Comparison of evolution of PDF for elastic-plastic material and extended elastic material cases for random shear modulus.

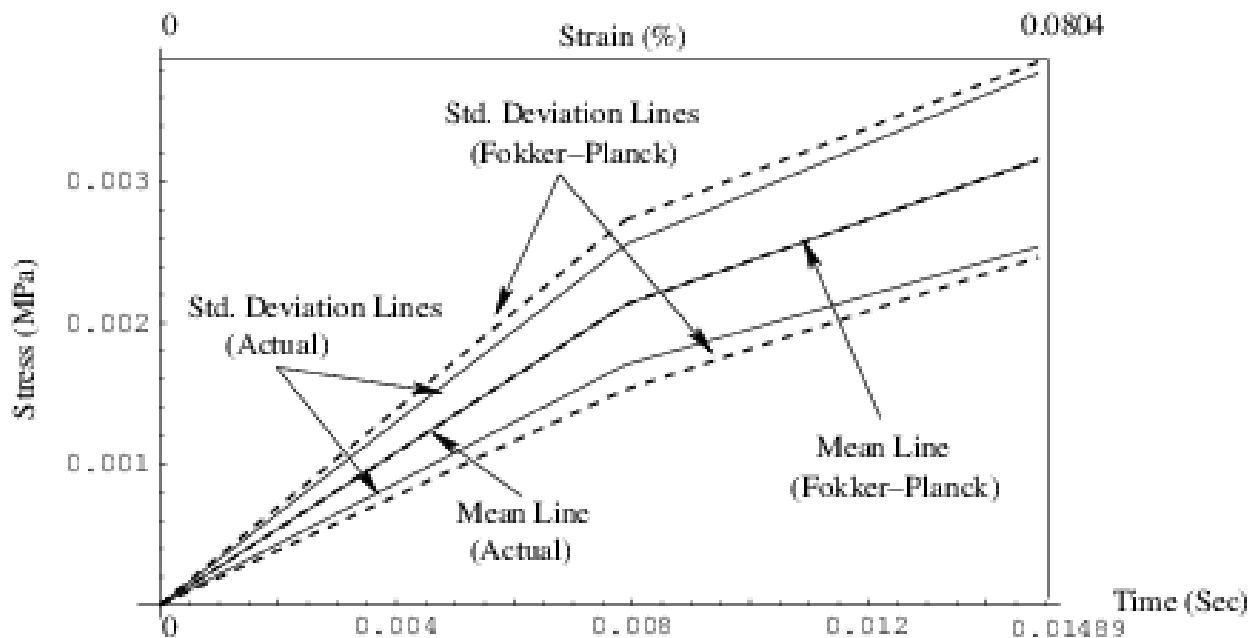


Figure 105.13: Comparison of mean and standard deviation of shear stress for plastic constitutive rate equation with random shear modulus (problem-ii) for FPK equation solution and Monte Carlo simulation solution.

One of the important aspects of probabilistic geomechanics simulation that has received less attention is the probabilistic constitutive problem. Among the few published papers were those by Fenton and Griffiths ([Fenton and Griffiths \(2002\)](#), [Fenton and Griffiths \(2003\)](#), [Fenton and Griffiths \(2005\)](#)) on probabilistic simulation of spatially random  $c-\phi$  soil using Monte Carlo technique, and those by Anders and Hori ([Anders and Hori \(1999\)](#), [Anders and Hori \(2000\)](#)) on probabilistic simulation of von Mises elastic-perfectly plastic material using perturbation technique. Both Monte Carlo and perturbation techniques have their inherent drawbacks ([Matthies et al. Matthies et al. \(1997\)](#), [Keese Keese \(2003\)](#)) and in dealing with those, recently, Jeremić et al. [Jeremić et al. \(2007b\)](#) proposed Eulerian–Lagrangian form of Fokker–Planck–Kolmogorov equation (FPKE) approach (cf. [Kavvas Kavvas \(2003\)](#)) to modeling and simulation for probabilistic elasto–plasticity. FPKE approach to probabilistic elasto–plasticity not only overcomes the drawbacks associated with other probabilistic simulation techniques, but also is fully compatible with the incremental theory of elasto–plasticity, and hence can easily be applied to probabilistic modeling and simulation of different elastic–plastic constitutive models. Solution strategies for FPK partial differential equation, corresponding to elastic–plastic constitutive rate equation and simulated probabilistic stress-strain responses under monotonic loading, assuming mean stress yielding, were discussed by Sett et al. ([Sett et al. \(2007c\)](#), [Sett et al. \(2007d\)](#)) for both linear and non-linear

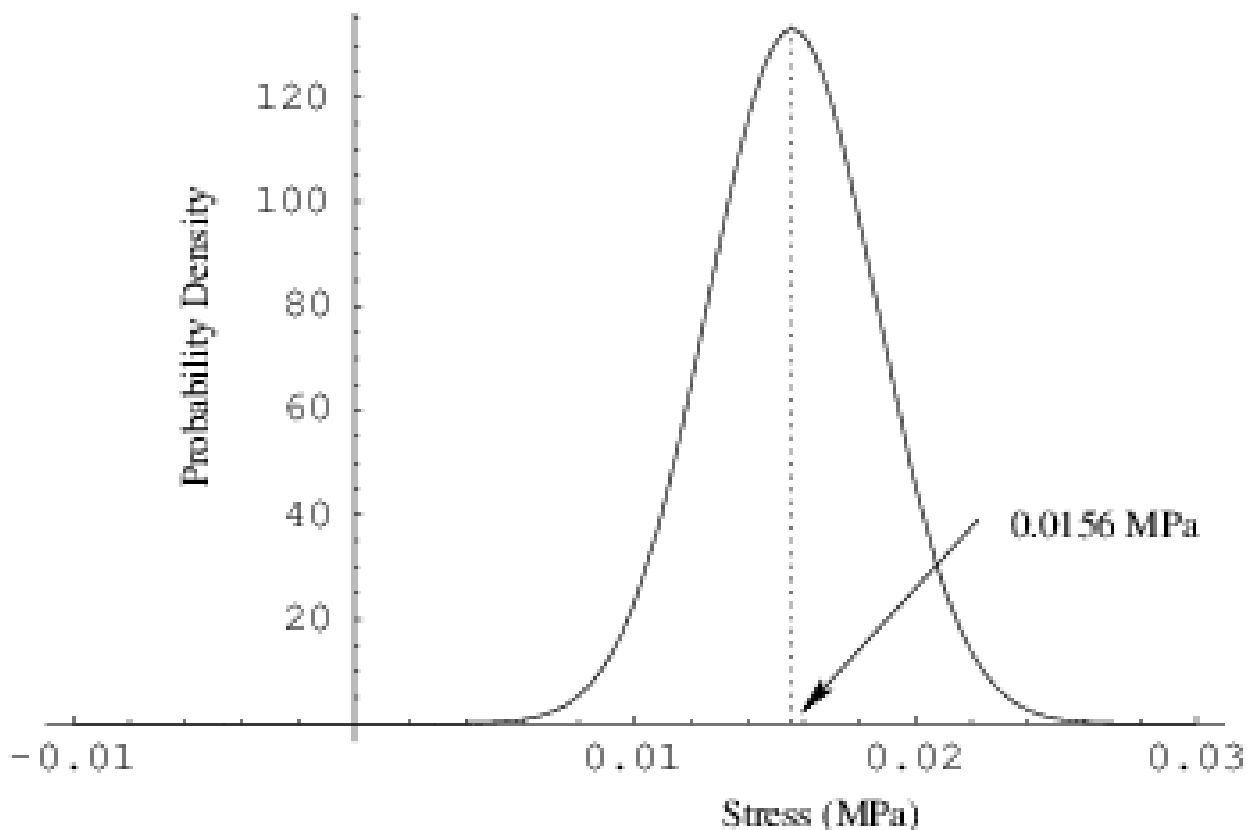


Figure 105.14: Initial condition for FPK equation for elastic–plastic material with random yield strength (Problem–III).

hardening models. The concept of probabilistic yielding was introduced and its effect on constitutive simulation under monotonic loading was discussed by Jeremić and Sett [Jeremić and Sett \(2009b\)](#). It was shown that due to uncertainty in yield function (stress), there is always a possibility, depending upon the magnitude of uncertainty, that plastic behavior starts at very very low strain and influence of elastic behavior continues far into plastic domain (at large strains) and hence, the ensemble average (mean) of all the possibilities or the most probable (mode) possibility differ from deterministic behavior. In addition to that, a very realistic, smooth transition between elastic and plastic domains was observed even for elastic perfectly plastic models. Further, nonlinear behavior was observed even for linear hardening models.

In this paper, the concept of probabilistic yielding is extended to 1-D cyclic simulations of geomaterials. Both elastic–perfectly plastic and hardening-type material model are considered. The numerical technique of solving FPKE cyclically with probabilistic yielding is discussed. Simulated responses were discussed in terms of probability density function (PDF) and its statistical moments.

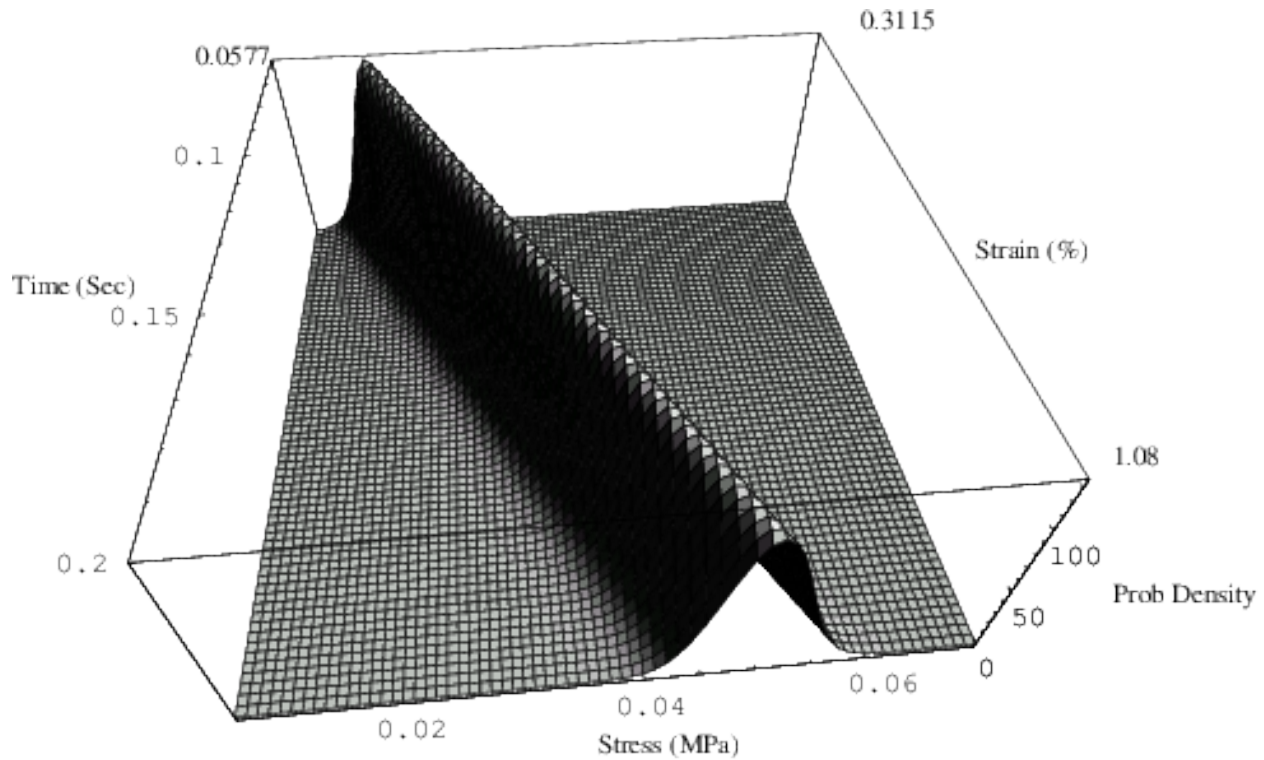


Figure 105.15: Evolution of PDF for shear stress for elastic–plastic material with random yield strength (Problem–III) (only plastic zone is shown).

### 105.3.1 Fokker–Planck–Kolmogorov Approach to Probabilistic Elasto–Plasticity

The Eulerian–Lagrangian form Fokker–Planck–Kolmogorov equation (cf. Kavvas [Kavvas \(2003\)](#)) corresponding to generalized 1–D constitutive rate equation can be written as ([Jeremić et al. Jeremić et al. \(2007b\)](#)):

$$\begin{aligned} \frac{\partial P(\sigma(x_t, t), t)}{\partial t} = & \\ & \frac{\partial}{\partial \sigma} \left[ \left\{ \left\langle \eta(\sigma, D, \epsilon; x_t, t) \right\rangle + \int_0^t d\tau \text{Cov}_0 \left[ \frac{\partial \eta(\sigma, D, \epsilon; x_t, t)}{\partial \sigma}; \eta(\sigma, D, \epsilon; x_{t-\tau}, t-\tau) \right] \right\} P(\sigma(x_t, t), t) \right] \\ & + \frac{\partial^2}{\partial \sigma^2} \left[ \left\{ \int_0^t d\tau \text{Cov}_0 \left[ \eta(\sigma, D, \epsilon; x_t, t); \eta(\sigma, D, \epsilon; x_{t-\tau}, t-\tau) \right] \right\} P(\sigma(x_t, t), t) \right] \end{aligned} \quad (105.43)$$

where,  $P(\sigma(x_t, t), t)$  is the probability density of stress ( $\sigma$ ) at (pseudo) time  $t$ , and  $\eta$  is the operator variable, obtained by collecting together all the operators and variables on the r.h.s of the generalized constitutive rate equation:

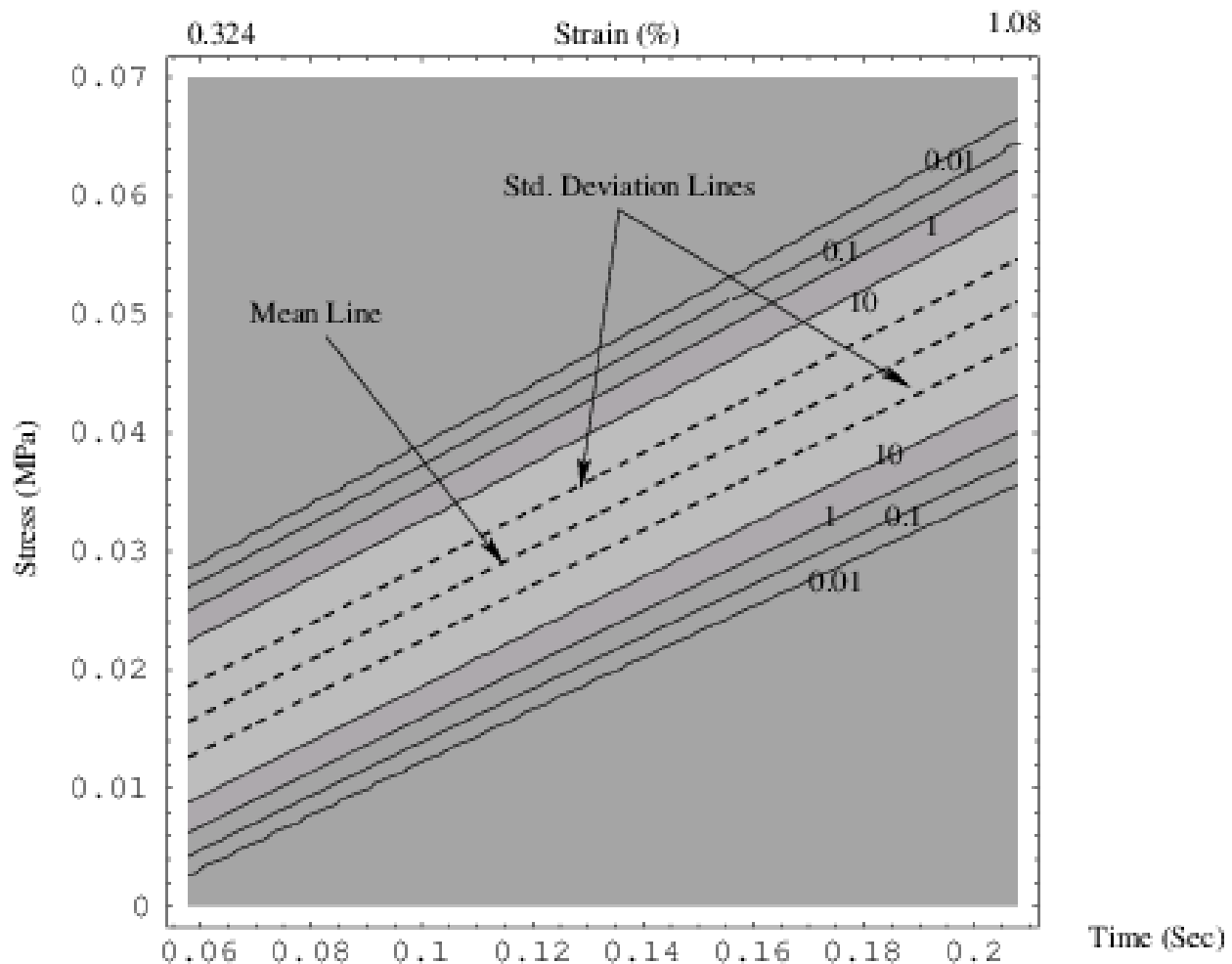


Figure 105.16: Contour PDF for shear stress versus strain (time) for elastic–plastic material with random yield strength (Problem-III).

$$\frac{d\sigma(x_t, t)}{dt} = \eta(\sigma, D, \epsilon; x_t, t) \quad (105.44)$$

In Eq. (105.66),  $\epsilon$  is the strain, and  $D$  is the tangent modulus, which could be elastic or elastic–plastic:

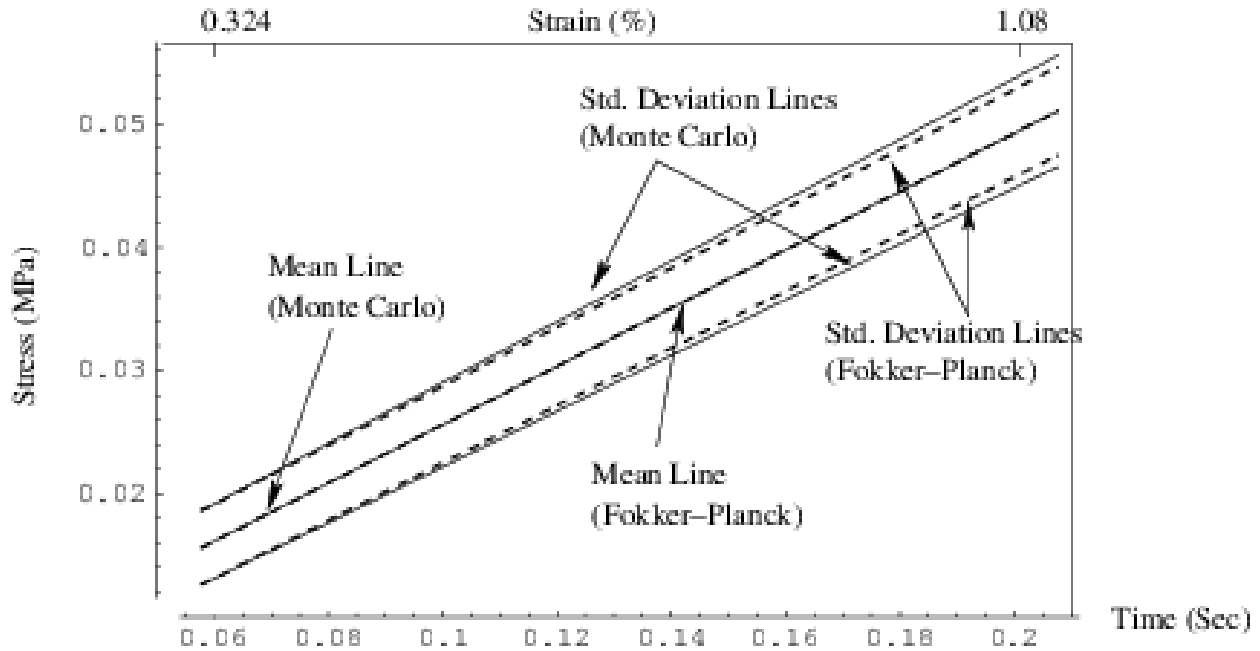


Figure 105.17: Comparison of Mean and Standard Deviation of Shear Stress for Elastic-Plastic Constitutive Rate Equation with Random Yield Strength (Problem-III) for FPE Solution and Monte Carlo Simulation Solution

$$D = \begin{cases} D^{el} & \text{elastic} \\ D^{el} - \frac{D^{el} \frac{\partial U}{\partial \sigma} \frac{\partial f}{\partial \sigma} D^{el}}{\frac{\partial f}{\partial \sigma} D^{el} \frac{\partial U}{\partial \sigma} - \frac{\partial f}{\partial q_*} r_*} & \text{elastic-plastic} \end{cases} \quad (105.45)$$

where,  $D^{el}$ ,  $f$ ,  $U$ ,  $q_*$ , and  $r_*$  are elastic modulus, yield surface, plastic potential surface, internal variable(s), and rate(s) of evolution of internal variable(s) respectively.

Eq. (105.65) is the most general form of elastic–plastic constitutive rate equation, written in probability density space. This equation (Eq. (105.65)) can be written in a more compact form:

$$\frac{\partial P(\sigma(x_t, t), t)}{\partial t} = \frac{\partial}{\partial \sigma} \{N_{(1)}P(\sigma(x_t, t), t)\} + \frac{\partial^2}{\partial \sigma^2} \{N_{(2)}P(\sigma(x_t, t), t)\} \quad (105.46)$$

where,  $N_{(1)}$  and  $N_{(2)}$  are advection and diffusion coefficients respectively, and are material model specific. By specializing Eq. (105.46) to (any) particular constitutive model, the resulting FPKE can be

solved to obtain the probability density function of stress response, given uncertainties in material properties and driving strain. However, difference in material behavior in elastic and elastic-plastic regions necessitates solution of FPKE twice - one corresponding to elastic constitutive equation (with  $N_{(1)}^{el}$  and  $N_{(2)}^{el}$ , the advection and diffusion coefficients corresponding to elastic constitutive equation) and the other corresponding to elastic–plastic constitutive equation (with  $N_{(1)}^{ep}$  and  $N_{(2)}^{ep}$ , the advection and diffusion coefficients corresponding to elastic–plastic constitutive equation). The switch from elastic to elastic–plastic region (solution) can be controlled using mean stress yielding:

$$\begin{aligned} \text{if } & \langle f \rangle < 0 \vee (\langle f \rangle = 0 \wedge d \langle f \rangle < 0) && \text{use elastic FPKE} \\ \text{or, if } & \langle f \rangle = 0 \vee d \langle f \rangle = 0 && \text{use elastic–plastic FPKE} \end{aligned} \quad (105.47)$$

However, difficulty arises if the material yield parameter(s) are uncertain, as the mean yield criteria then does not account for the complete probabilistic yielding of material. For example, such mean yielding will neglect the possibilities of elastic–plastic behavior in the elastic region and vice versa. The concept of probabilistic yielding overcomes this limitation, as it solves Eq. (105.46) once, with equivalent advection and diffusion coefficients,  $N_{(1)}^{eq}$  and  $N_{(2)}^{eq}$  (Jeremić and Sett Jeremić and Sett (2009b)):

$$\begin{aligned} N_{(1)}^{eq}(\sigma) &= (1 - P[\Sigma_y \leq \sigma])N_{(1)}^{el} + P[\Sigma_y \leq \sigma]N_{(1)}^{ep} \\ N_{(2)}^{eq}(\sigma) &= (1 - P[\Sigma_y \leq \sigma])N_{(2)}^{el} + P[\Sigma_y \leq \sigma]N_{(2)}^{ep} \end{aligned} \quad (105.48)$$

where  $(1 - P[\Sigma_y \leq \sigma])$  represents the probability of material being elastic, while  $P[\Sigma_y \leq \sigma]$  represents the probability of material being elastic–plastic. The probabilities of material being elastic and the probabilities of material being elastic–plastic can easily be calculated from the cumulative density function of yield function (stress).

It is worth noting that the probabilistic yield criterion (Eq. (105.48)) represents probabilistic restatement of the deterministic yield criteria. The probabilistic yield criteria is introduced (or, the deterministic yield criteria is written in probability space) in order to properly model uncertain (probabilistic) yield strength.

It is also very interesting to note that proposed approach for calculating equivalent advection and diffusion coefficients is similar to the solution strategy of famous Black–Scholes Black and Scholes (1973) equation in financial engineering modeling of European option, where probabilities of exercise of the (European) option, obtained from cumulative density functions, are multiplied with stock price and present value of option strike price to calculate the option price.

### 105.3.2 Elastic–Perfectly Plastic Material

In this section, the FPKE–approach, along with the concept of probabilistic yielding, is applied to simulate 1-D (shear stress–shear strain) cyclic behavior of elastic–perfectly plastic material. Only von Mises material model has been considered. It may, however, be noted that presented development is general enough to be used with any material model and that von Mises is just one such model we use for illustration purposes.

The von Mises yield criteria can be written as:

$$\sqrt{J_2} - k = 0 \quad (105.49)$$

where,  $k$  is a material parameter (yield strength like) and  $J_2 = 3/2s_{ij}s_{ij}$  is the second invariant of deviatoric stress tensor  $s_{ij} = \sigma_{ij} - 1/3\sigma_{kk}\delta_{ij}$ . For 1-D shear, Eq. (105.49) becomes:

$$|\sigma| - \sigma_y = 0 \quad \text{or} \quad \sigma = \pm\sigma_y \quad (105.50)$$

The yielding occurs at a yield stress of  $\pm\sigma_y$ . It, however, is important to note that both  $\sigma_y$  and  $\sigma$  are uncertain and are described by their respective probability density functions. For elastic–perfectly plastic material, the distribution of yield stress ( $\sigma_y$ ) is given by its experimentally measured initial distribution, and remains constant. The stress ( $\sigma$ ), however, evolves according to the governing FPKE (Eq. (105.46)) and its distribution is given by the solution of the governing FPKE (Eq. (105.46)). For 1-D von Mises elastic–perfectly plastic shear constitutive model, the elastic and the elastic–plastic advection and diffusion coefficients of the governing FPKE (Eq. (105.46)), becomes:

$$\begin{aligned} N_{(1)}^{el} &= \frac{d\epsilon_{xy}}{dt} \langle G \rangle \quad ; \quad N_{(2)}^{el} = t \left( \frac{d\epsilon_{xy}}{dt} \right)^2 \text{Var}[G] \\ N_{(1)}^{ep} &= 0 \quad ; \quad N_{(1)}^{ep} = 0 \end{aligned} \quad (105.51)$$

where,  $G$  is the shear modulus,  $d\epsilon_{xy}$  is the (deterministic) incremental shear strain,  $t$  is the pseudo time,  $\langle \cdot \rangle$  represents expectation operation and  $\text{Var}[\cdot]$  represents variance operation. The equivalent advection and diffusion coefficients (refer Eq. (105.48)) for von Mises elastic–perfectly plastic material, then, becomes:

$$\begin{aligned} N_{(1)}^{eq}(\sigma) &= (1 - P[\Sigma_y \leq \sigma]) \frac{d\epsilon_{xy}}{dt} \langle G \rangle \\ N_{(2)}^{eq}(\sigma) &= (1 - P[\Sigma_y \leq \sigma]) t \left( \frac{d\epsilon_{xy}}{dt} \right)^2 \text{Var}[G] \end{aligned} \quad (105.52)$$

One may note that, in deriving the elastic and elastic–plastic advection and diffusion coefficients (Eq. (105.51)), it was assumed that spatial random field material properties ( $G$ , and  $\sigma_y$ ) would be

first discretized into random variables, for example at Gauss points, by appropriate tools, for example Karhunen–Loève expansion (Karhunen [Karhunen \(1947\)](#), Loève [Loève \(1948\)](#), Ghanem and Spanos [Ghanem and Spanos \(1991\)](#)). In other words, the solution of FPKE, with advection and diffusion coefficients given by Eq. (105.52), represents point–location scale von Mises elastic–perfectly plastic material behavior, and not the local–average material behavior. The local–average material behavior, if sought for, can then be assembled using polynomial chaos expansion (Wiener [Wiener \(1938\)](#), Ghanem and Spanos [Ghanem and Spanos \(1991\)](#)).

#### 105.3.2.1 Probability Density Function

The FPKE (Eq. (105.46)), with advection and diffusion coefficients given by Eq. (105.52), was solved incrementally with pseudo time steps using method of lines. The stress domain of the Fokker–Planck–Kolmogorov PDE was discretized first on a uniform grid by central differences, and thereby obtaining a series of ODE. The series of ODEs was then solved, after incorporating boundary conditions, simultaneously and incrementally, with  $n$  pseudo time steps, using a standard open–source ODE solver, SUNDIALS [Hindmarsh et al. \(2005\)](#), which utilizes ADAMS method and functional iteration.

The yield shear strength ( $\sigma_y$ ) of the material was assumed to have a mean value of 60 kPa with a COV of 30%, values typical for clay (Federal Highway Administration [Federal Highway Administration \(2002\)](#), Lacasse and Nadim [Lacasse and Nadim \(1996\)](#)). Also, the yield shear strength was assumed to be either normal or Weibull (with shape parameter of 3.31 and scale parameter of 0.067) distribution as shown in Fig. 105.18. The shear modulus ( $G$ ) was also assumed to be either normal or Weibull distribution, but

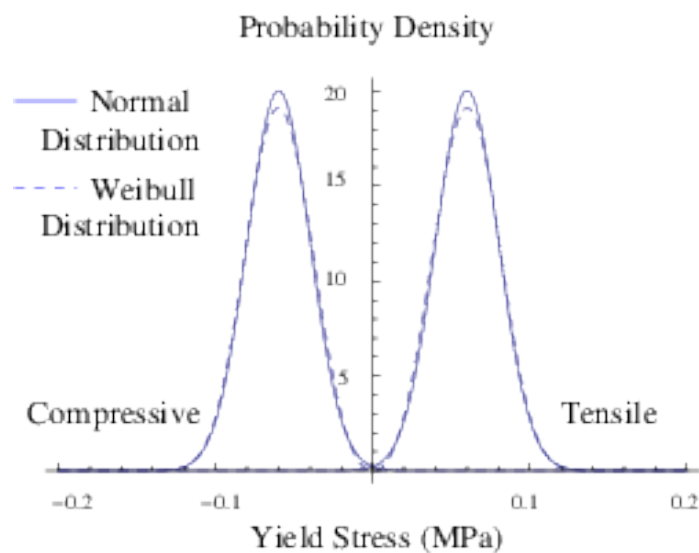


Figure 105.18: Elastic–perfectly plastic probabilistic model: PDF of yield stress

with a mean value of 100 MPa and a COV of 25%. The cyclic probabilistic von Mises, elastic–perfectly plastic shear stress–shear strain response (evolutionary probability density function (PDF) of shear stress), for the case where both yield shear strength ( $\sigma_y$ ) and shear modulus ( $G$ ) are normally distributed, is shown in Fig. 105.19. Two different views of the loading–unloading–reloading cycle are shown, focusing on the

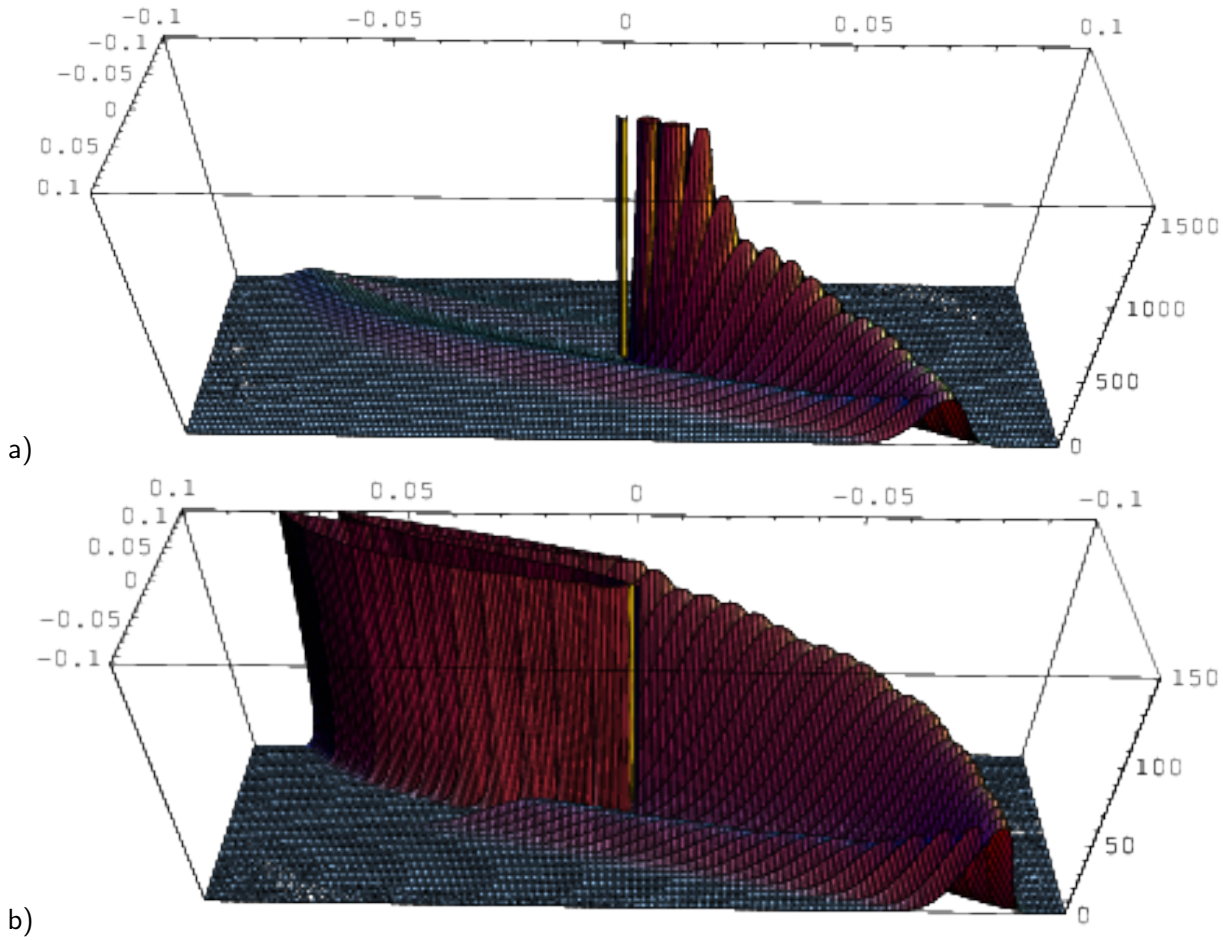


Figure 105.19: Elastic–perfectly plastic probabilistic model under cyclic loading: evolutionary PDF of shear stress (a) view from the junction of loading and unloading branches (probability densities of shear stress are truncated at a value 1500 for clarity of the plot) and (b) view from the junction of unloading and reloading branches (probability densities of shear stress are truncated at a value of 150 for clarity of the plot)

transition between loading and unloading, and unloading and reloading branches. As can be seen from Fig. 105.19, PDF for initial stress (a deterministic Dirac delta function at stress–strain origin) advected and diffused into the domain, governed by the advection and diffusion coefficients (Eq. (105.52)). It is very important to also note that, even–though the deterministic response for von Mises elastic–perfectly

plastic material is bi-linear, due to introduced uncertainties in yielding, the probabilistic response is non-linear from the beginning. That is, due to uncertainty in yield strength, there is a (small) possibility that the material becomes elasto-plastic from the very beginning of loading. This possibility has been quantified from the PDF of the yield strength and taken into consideration implicitly during simulation using the equivalent advection and diffusion coefficients ( $N_{(1)}^{eq}$  and  $N_{(2)}^{eq}$ , refer Eq. (105.52)). Those coefficients assigns probability weights to the realizations of stress response based on the probability of material being elastic or elastic-plastic. Initially, in the loading branch, at small strains, the probability of material being elastic-plastic is very small and hence, the initial probabilistic stress response (ensemble of all realizations) is closer (but not fully) to linear, elastic response. However, as strain increases, the probability of elastic-plastic material behaving increases and the probabilistic stress response gradually becomes more elastic-plastic (Fig. 105.19(a)).

Upon unloading, the material behaves as (mostly) elastic since elastic-plastic probability weights from the governing PDF of mirror image (negative) of shear strength (Fig. 105.18) are initially very small. During later stages of unloading (loading in the opposite direction), and similar to the loading branch, the elastic-plastic probability weights increase and gradually transition the response toward elasto-plasticity (Fig. 105.19(b)). Similar to this, in the subsequent reloading branch, the probability weights are again governed the PDF of (positive, loading branch of) shear strength (Fig. 105.18), and hence the probabilistic response is again initially more linear, elastic, while gradually it transitions to full elasto-plasticity.

#### 105.3.2.2 Case of Increasing Strain Loops

In Fig. 105.20, the evolutionary PDF of shear stress for von Mises elastic-perfectly plastic material (refer Fig. 105.19) is plotted in terms of its statistical moments – the evolutionary mean (Fig. 105.20(a)), and standard deviation (Fig. 105.20(b)) of shear stress – for the first couple of cycles with increasing strain loops. The mean response, when both the yield shear strength ( $\sigma_y$ ) and the shear modulus ( $G$ ) are modeled as Weibull distribution, is also shown in Fig. 105.20(a). The oscillations in the evolution of standard deviation of shear stress with shear strain are due to step size issue, inherent to the forward Euler method that has been used in solving the FPKE. Work is underway to implement linearly implicit mid-point rule for solving the FPKE corresponding to elastic-plastic constitutive rate equation.

The very important observation that can be made using Fig. 105.20(a) is that, if one consider uncertainties in geomaterial properties, even the simplest elastic-perfectly model, captures some of the very important features of geomaterial behaviors. For example, reduction of (secant) modulus with cyclic strain, commonly observed in soil (cf. Vucetic and Dobry [Vucetic and Dobry \(1991\)](#)), is fairly nicely captured. If using deterministic models, this feature can only be somewhat successfully modeled with

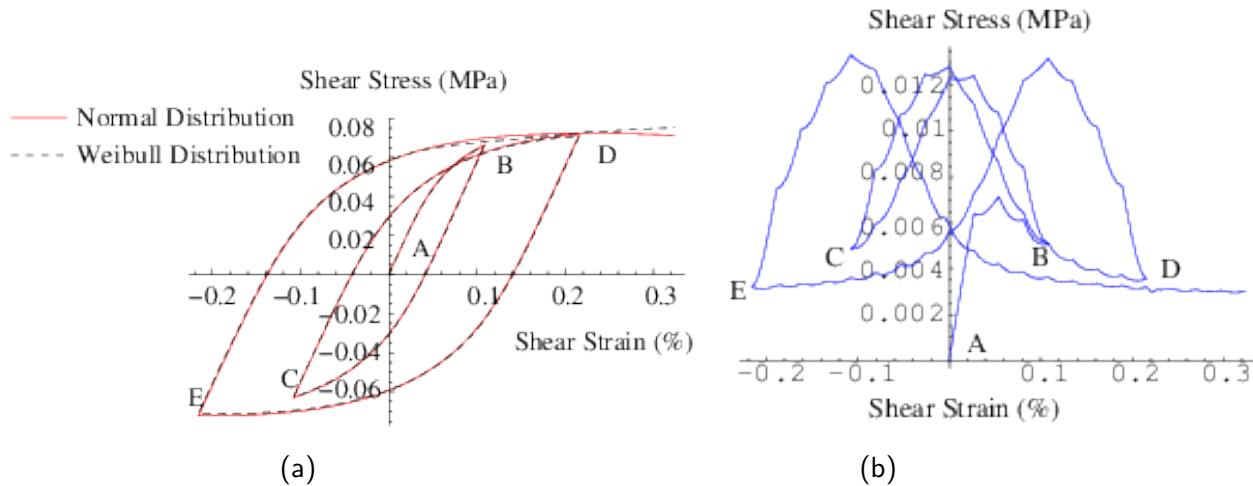


Figure 105.20: Elastic–perfectly plastic probabilistic model under cyclic loading with increasing strain loops: evolution of (a) mean and (b) standard deviation of shear stress

fairly complex models, which require many more parameters. It is important to remark that for our probabilistic modeling, (only) statistical distributions (probability density functions) of shear modulus ( $G$ ) and shear strength ( $\sigma_y$ ), are needed. Expansion of elastic–plastic modeling into probability space seems to have added significant new capabilities to modeling.

#### 105.3.2.3 Case of Constant Strain Loops

This von Mises elastic–plastic material, however, didn't exhibit (secant) modulus degradation, commonly observed in clay (cf. Vucetic and Dobry [Vucetic and Dobry \(1988\)](#)), when the material is cycled repeatedly at the same strain. Fig. 105.21(a) shows such probabilistic response (mean of shear stress). The material was cycled repeatedly up to 0.2% strain. Only first three cycles are shown. It is important to note that the von Mises mean elastic–plastic material behavior is function of both the mean and standard deviation of both shear modulus ( $G$ ) and yield shear strength ( $\sigma_y$ ). The same von Mises elastic–perfectly plastic model with a different set of material properties could, however, be able to capture the degradation of mean (secant) shear modulus. For example, Japanese stiff clay, when modeled as von Mises elastic–perfectly plastic material, exhibited modulus degradation with number of cycles (Sett et al. [Sett et al. \(2008\)](#))

#### 105.3.2.4 Monotonic Loading

For completeness of comparison, the monotonic behavior of this probabilistic von Mises perfectly plastic material is also shown (refer Fig. 105.22). As can be observed from Fig. 105.22(a), the mean shear

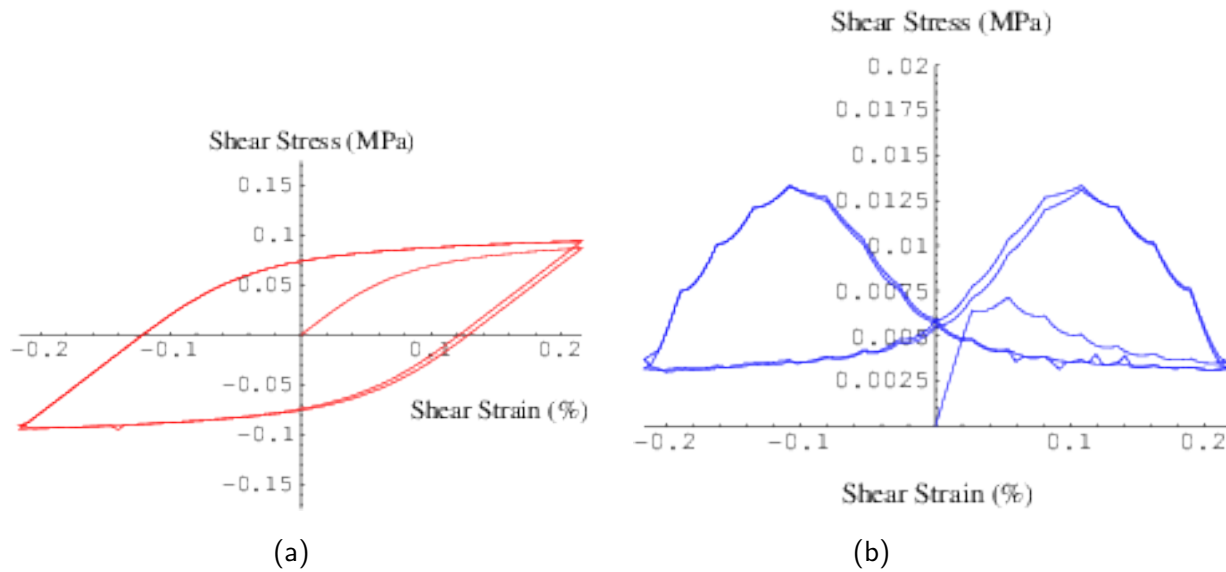


Figure 105.21: Elastic–perfectly plastic probabilistic model under cyclic loading with all equal loops: evolution of (a) mean and (b) standard deviation of shear stress

stress non-linearly increases with shear strain before reaching the perfectly plastic state.

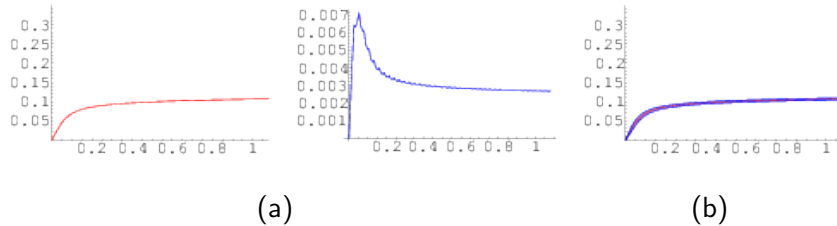


Figure 105.22: Elastic–perfectly plastic probabilistic model under monotonic loading: evolution of (a) mean, (b) standard deviation, and (c) mean  $\pm$  standard deviation of shear stress

Physically, one may visualize the probabilistic soil constitutive response as an ensemble of the behaviors of infinite number of soil particles in a representative volume element (RVE), for example, a laboratory soil specimen. The behavior of an individual soil particle in a RVE is governed, in case of elastic–perfectly plastic material, by its modulus and strength. However, if the modulus and strength of each particle are different, for example, governed by their respective PDF, then each particle would behave differently. The PDF of the response behavior then represents the ensemble of all such behaviors, with their respective probability weights. The mean, on the other hand, represents the ensemble average of all such behaviors. In this context, it is important to note that the behaviors presented in this paper do not take into account the correlation between soil particles (scale effect). The scale effect

can be accounted for, among others, using stochastic elastic–plastic finite element technique. Sett (2007) proposed one such finite element method by extending the spectral approach to stochastic finite element (cf. Ghanem and Spanos Ghanem and Spanos (1991)) to elastic–plastic problems by updating the material properties at Gauss integration points using the FPKE approach, as the material plastifies.

Further to the promise of an alternate approach to geomaterial modeling, probabilistic approach also quantifies our confidence in the simulated behavior of geomaterials. FPKE based probabilistic elasto–plasticity solves for second-order accurate evolutionary PDF of shear stress (Fig. 105.19). Ability to obtain the PDF of stress accurately is very important in failure simulation of geomaterials, as they often fail at low probabilities (tails of PDF). A full PDF contains enormous amount of information. From the PDF, other than the statistical moments, other useful engineering information, for example, the probability of exceedance, most probable solution, as well as some derivative application like sensitivity analysis can be easily obtained or derived. Figs. 105.20(b) and 105.21(b) show one of the important confidence measuring parameters, the evolutionary standard deviation of shear stress (square-root of second moment of the evolutionary PDF of shear stress (Fig. 105.19)), for cyclic responses with increasing loops and all equal loops, respectively. As can be observed from the above figures (Figs. 105.20(b) and 105.21(b)), inside any branch (loading, unloading, re-loading, re-unloading, ...), as well as in Fig. 105.22(b), where the monotonic response is shown, the standard deviation, first increases and then decreases. This is because, initially, when the material is mostly elastic, both the uncertainties in shear modulus ( $G$ ) and yield strength ( $\sigma_y$ ) are governing. As material becomes mostly elastic–plastic, the influence of uncertainty in shear modulus ( $G$ ) decreases. However, it is important to note that this type of standard deviation response is not generic to all von Mises elastic–perfectly plastic material. The standard deviation response is very much dependent on the amount uncertainties present in both shear modulus ( $G$ ) and yield strength ( $\sigma_y$ ). For example, Fig. 105.23(b), shows probabilistic response of cyclic behavior of the same material model, except that COV of yield strength ( $\sigma_y$ ), is now assumed to be 300%. The standard deviation response shown here is always increasing which is completely different from what was observed in previous case (Figs. 105.20(b), 105.21(b) and 105.22(b))). This is because, for this material, the COV of shear modulus (assumed 30%) is non-significant, compared to the COV of yield strength (assumed 300%), and hence, the standard deviation response (Fig. 105.23(b)) is predominantly influenced by the uncertainty in yield strength ( $\sigma_y$ ). Similar standard deviation response can be observed in Fig. 105.24(b), where the material with large COV of yield strength was subjected to monotonic loading.

It is also interesting to compare Figs. 105.21(a) and 105.23(a). Both are mean responses of von Mises elastic–perfectly plastic material model with same material parameters, except with different COV of yield strength. COV of yield strength for simulation in Fig. 105.21(a) was 30% and that for simulation in Fig. 105.23(a) was 300%. It is observed that a completely different responses were obtained. The effect

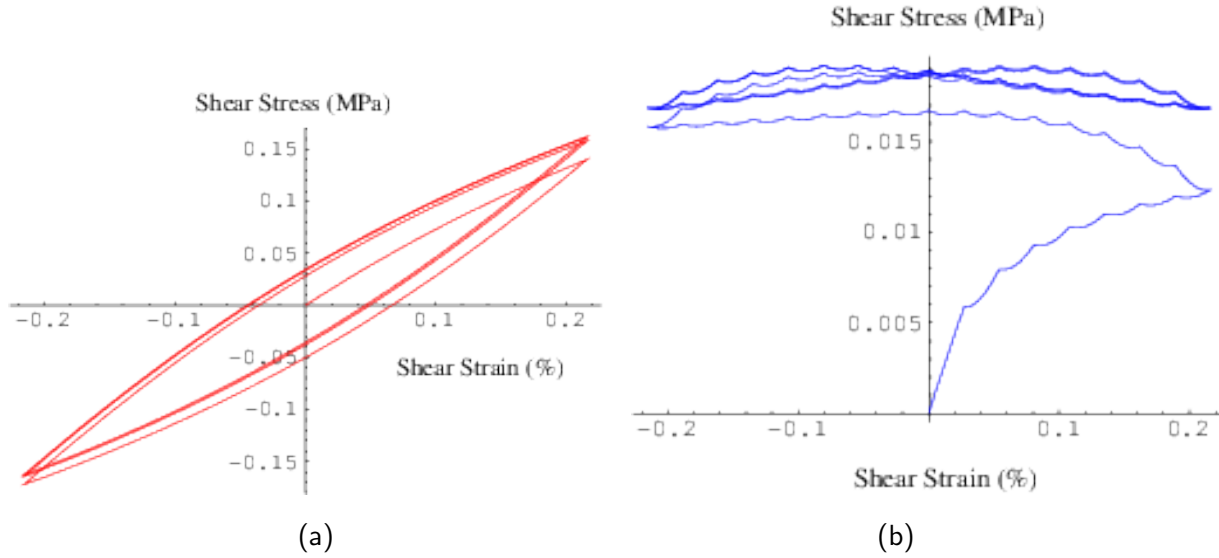


Figure 105.23: Elastic–perfectly plastic probabilistic model under cyclic loading with all equal loops (probabilistic model parameters are exactly the same as used for simulation in Fig. 105.21, but with very large yield uncertainty): evolution of (a) mean and (b) standard deviation of shear stress

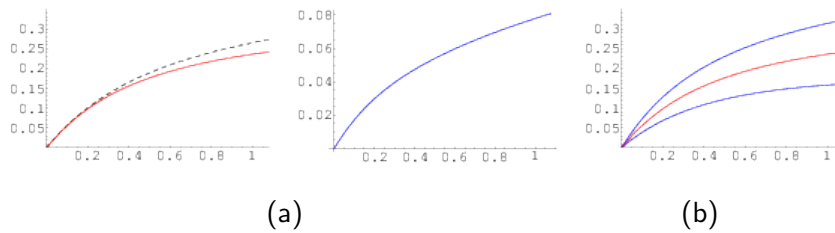


Figure 105.24: Elastic–perfectly plastic probabilistic model under monotonic loading (model parameters are exactly the same as used for simulation in Fig. 105.22, but with very large yield uncertainty): evolution of (a) mean, mode, (b) standard deviation, and (c) mean  $\pm$  standard deviation of shear stress

of COV of yield strength on monotonic mean behavior can, similarly, be compared in Figs. 105.22(a) and 105.24(a).

### 105.3.2.5 Hardening Material

In this section, the influence of probabilistic yielding is evaluated on cyclic responses of isotropic and kinematic hardening materials. To this end, the same example, as discussed in the previous section (Section 105.3.2) is used but with appropriate hardening rule – isotropic or kinematic.

The main difference between the simulations shown in Section 105.3.2 for elastic–perfectly plastic

material is that for a hardening material the internal variables ( $q_*$ , refer Eq. (105.45)) will evolve as the material plastifies. Such evolution (change) of internal variables is here assumed to be a function of plastic strain. The FPKE that govern the probabilistic evolution of internal variable ( $q$ ) can be written, in most the general form, as:

$$\frac{\partial P(q(x_t, t), t)}{\partial t} = \frac{\partial}{\partial q} \left\{ N_{(1)IV}^{eq} P(q(x_t, t), t) \right\} + \frac{\partial^2}{\partial q^2} \left\{ N_{(2)IV}^{eq} P(q(x_t, t), t) \right\} \quad (105.53)$$

where,  $N_{(1)IV}^{eq}$  and  $N_{(2)IV}^{eq}$  are the equivalent advection and diffusion coefficients, respectively, for the internal variable. As explained for the case of probabilistic stress response for elastic–perfectly plastic material (refer Section 105.3.2), since point–location scale FPKE will be solved, the equivalent advection and diffusion coefficients for the internal variable,  $N_{(1)IV}^{eq}$  and  $N_{(2)IV}^{eq}$ , can be written as:

$$\begin{aligned} N_{(1)IV}^{eq}(q) &= P[\Sigma_y \leq \sigma(q)] \frac{d\epsilon_{xy}}{dt} \left\langle \frac{Gr}{G + \frac{1}{\sqrt{3}}r} \right\rangle \\ N_{(2)IV}^{eq}(q) &= P[\Sigma_y \leq \sigma(q)] t \left( \frac{d\epsilon_{xy}}{dt} \right)^2 \text{Var} \left[ \frac{Gr}{G + \frac{1}{\sqrt{3}}r} \right] \end{aligned} \quad (105.54)$$

where,  $r$  is the rate of evolution of internal variable ( $q$ ) with plastic strain. One may note that in the above equivalent advection and diffusion coefficients (Eq. (105.54)), the contributions of probability weights that the material being elastic are absent. This is because the evolution rule of internal variable is governed by the plastic component of strain only. The equivalent advection and diffusion coefficients for shear stress ( $N_{(1)}^{eq}$  and  $N_{(2)}^{eq}$ ) for hardening–type materials, will have contributions from both elastic and plastic components, just like the elastic–perfectly plastic case. However, unlike the elastic–perfectly plastic case, those ( $N_{(1)}^{eq}$  and  $N_{(2)}^{eq}$ ) will contain the hardening terms:

$$\begin{aligned} N_{(1)}^{eq}(\sigma) &= \frac{d\epsilon_{xy}}{dt} \left[ (1 - P[\Sigma_y \leq \sigma]) \langle G \rangle + P[\Sigma_y \leq \sigma] \left\langle G - \frac{G^2}{G + \frac{1}{\sqrt{3}}r} \right\rangle \right] \\ N_{(2)}^{eq}(\sigma) &= t \left( \frac{d\epsilon_{xy}}{dt} \right)^2 \left[ (1 - P[\Sigma_y \leq \sigma]) \text{Var}[G] + P[\Sigma_y \leq \sigma] \text{Var} \left[ G - \frac{G^2}{G + \frac{1}{\sqrt{3}}r} \right] \right] \end{aligned} \quad (105.55)$$

To obtain the probabilistic response of von Mises hardening material, the FPKE for probabilistic evolution of internal variable (Eq. (105.53), with advection and diffusion coefficients given by Eq. (105.54)) needs to be solved incrementally. This solution needs to be done simultaneously with the FPKE for probabilistic evolution of shear stress (Eq. (105.46), with advection and diffusion coefficients given by Eq. (105.55)). Those, in turn, need also to be solved incrementally, with the yield strength random variable ( $\Sigma_y$ ) in Eqs. (105.54) and (105.55) being updated after each incremental step.

### 105.3.2.6 Isotropic Hardening

For von Mises isotropic hardening material, the yield strength ( $\sigma_y$ ) is the internal variable. Yield strength will evolve probabilistically with plastic strain, following Eq. (105.53), with advection and diffusion coefficients given by Eq. (105.54). The shear stress, on the other hand, evolves in accordance with Eq. (105.46), with advection and diffusion coefficients given by Eq. (105.55).

Fig. 105.25 shows the evolutionary mean and standard deviation of shear stress during first couple of loading–unloading cycles for von Mises isotropic hardening material with a non-dimensional rate of evolution of internal variable (yield strength, in this case) of 10. All other material parameters are assumed to be the same as used for simulation of elastic–perfectly plastic material in the previous section (Section 105.3.2).

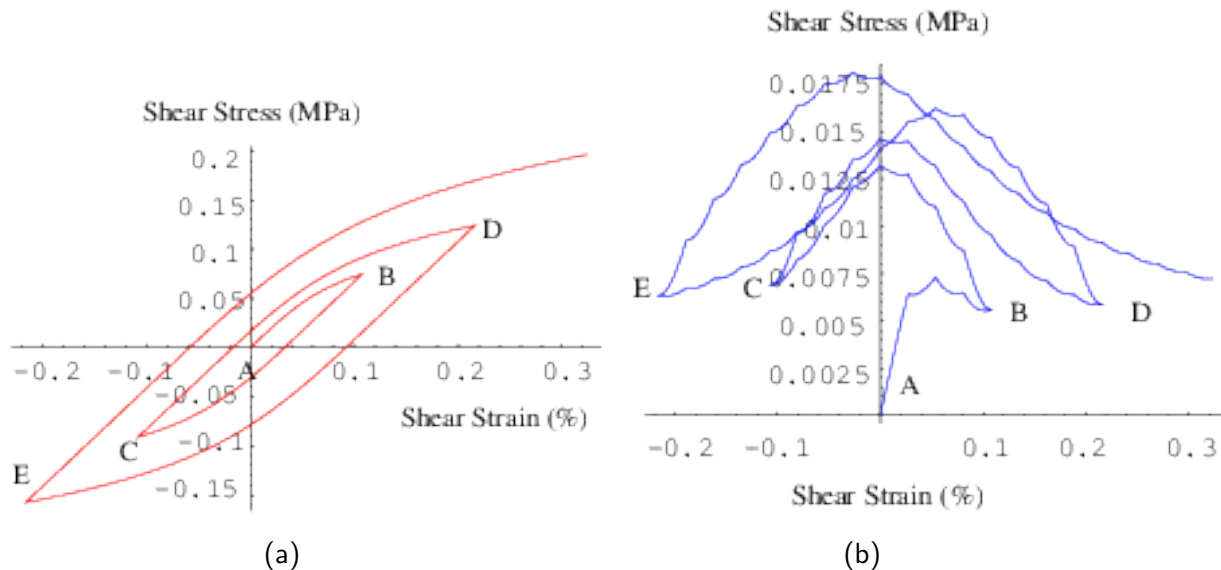


Figure 105.25: Isotropic hardening probabilistic model under cyclic loading with increasing loops: evolution of (a) mean and (b) standard deviation of shear stress

The evolved PDFs of yield strength after each branch (loading, unloading, re-loading, and re-unloading) are shown in Fig. 105.26. The initial PDFs of yield strength (positive for loading branch and negative for unloading branch) are the same as assumed for elastic–perfectly plastic material in Section 105.3.2 (refer Fig. 105.18). As expected (and prescribed by the isotropic hardening model), the yield strength evolved (grew) isotropically. However, it is interesting to note the change in probability distributions of yield strength. The normally distributed initial PDFs of yield strength (Fig. 105.18) evolved into much dispersed non-Gaussian distributions having low kurtosis. In other words, when the material is cycled through loading–unloading cycles, the uncertainty in yield strength increases.

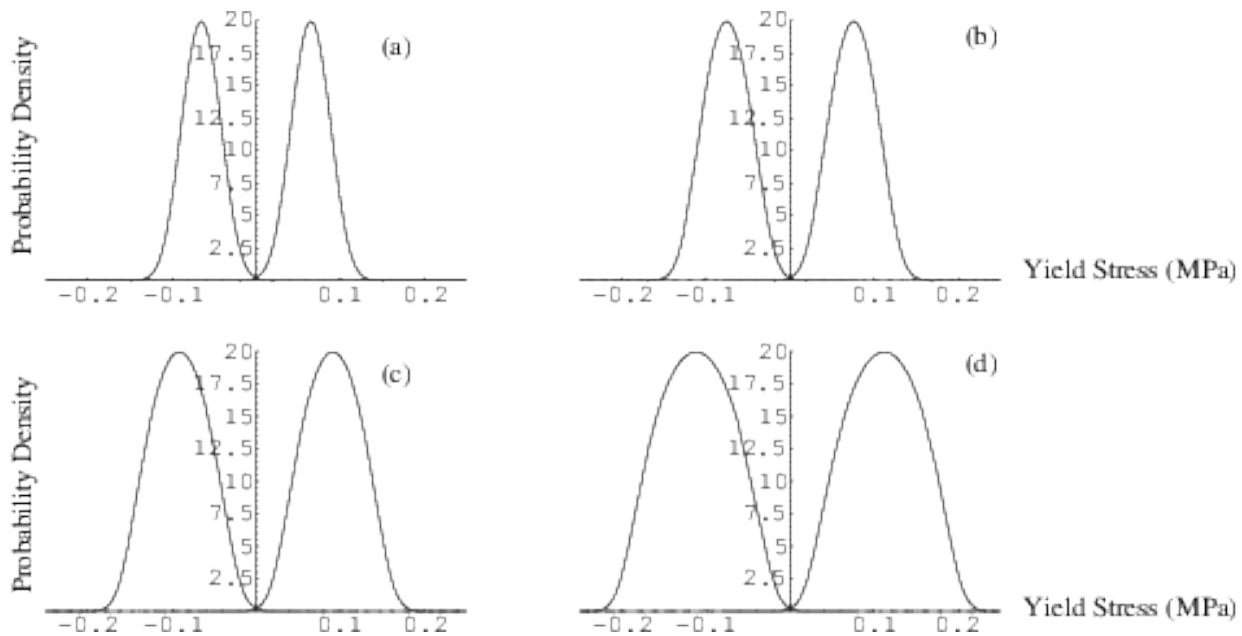


Figure 105.26: Isotropic hardening probabilistic model under cyclic loading with increasing loops: evolved PDF of yield stress after (a) loading branch, (b) unloading branch, (c) re-loading branch, and (d) re-unloading branch

Mathematically, increase in uncertainty of shear strength is due to the nonlinearity in formulation of probabilistic yielding , that is, the state variable  $q$  appears in both advection and diffusion equations (refer Eq. (105.54)), and in the evolution equation for internal variable (Eq. (105.53)).

When comparison is made between Figs. 105.25 and 105.20, one can clearly see that, in simulating cyclic behaviors of geomaterials, isotropic hardening model (Fig. 105.25) performed, as expected, poorly. That is, the elastic–perfectly plastic probabilistic model (Fig. 105.20) captures (PDF of) stress–strain loops in a much more realistic way. However, for completeness of comparison, the behavior of isotropic hardening material, when it was cycled to same level (Fig. 105.27) and when loaded monotonically (Fig. 105.28) are also shown.

It is noted that monotonic loading curves for both perfectly plastic probabilistic model (Fig. 105.22) and linear isotropic hardening probabilistic model (Fig. 105.28) do look similar (with a noted difference of more pronounced hardening for a hardening model), but the real difference in stress–strain predictions with both probabilistic models becomes obvious in the case of cyclic loading.

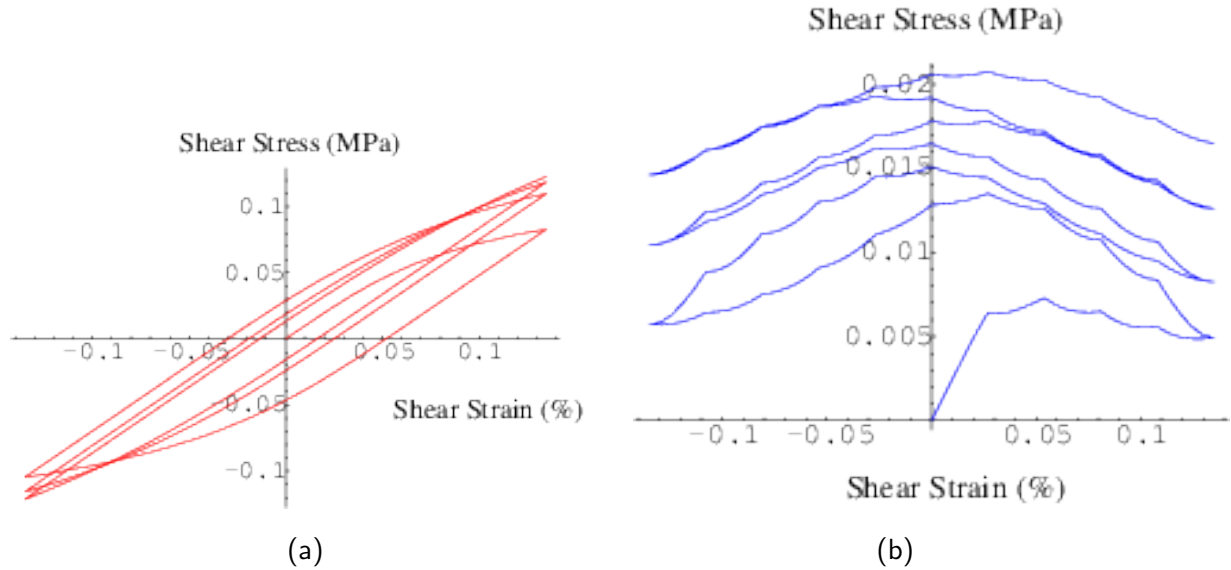


Figure 105.27: Isotropic hardening probabilistic model under cyclic loading with equal loops: evolution of (a) mean and (b) standard deviation of shear stress

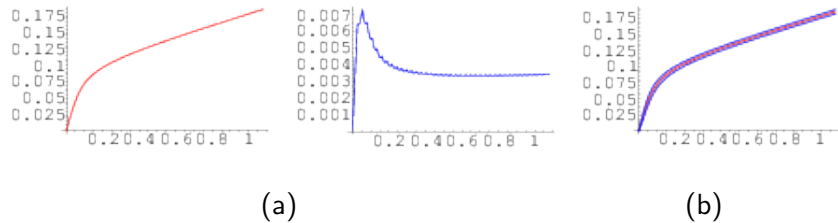


Figure 105.28: Isotropic hardening probabilistic model under monotonic loading: evolution of (a) mean, (b) standard deviation, and (c) mean  $\pm$  standard deviation of shear stress

#### 105.3.2.7 Kinematic Hardening

Expanding on elastic–plastic hardening probabilistic models, we now focus on a simple linear kinematic hardening rule based on evolution of back stress ( $\alpha$ ). By introducing back stress ( $\alpha$ ) to von Mises yield criteria, one can write:

$$\sqrt{J_\alpha} - k = 0 \quad (105.56)$$

where,  $k$  is again material parameter (yield strength like) and  $J_\alpha = 3/2(s_{ij} - \alpha_{ij})(s_{ij} - \alpha_{ij})$  is the  $\alpha$ –modified second invariant of deviatoric stress tensor ( $s_{ij}$ ). For 1-D shear, Eq. (105.56) becomes:

$$|\sigma - \alpha| - \sigma_y = 0 \quad \text{or} \quad \sigma = \alpha \pm \sigma_y \quad (105.57)$$

Hence, for kinematic hardening material, the yielding occurs at a stress of  $\alpha \pm \sigma_y$ , termed in the following as the equivalent yield stress. Initially,  $\alpha$  is zero, and  $\sigma_y$  is assumed to have a mean value of 60 kPa with a standard deviation of 20 kPa, resulting in equivalent yield stress of 60 kPa with a COV of 30%, same as the assumed yield stress for the elastic–perfectly plastic material in Section 105.3.2 and isotropic hardening material in Section 105.3.2.6. However, the same distribution of equivalent yield stress will be obtained, if one transfers the initial uncertainty from  $\sigma_y$  to  $\alpha$ . In other words, a deterministic  $\sigma_y$  of 60 kPa, and an uncertain  $\alpha$  of zero mean and a standard deviation of 20 kPa will result in the same equivalent yield stress. The advantage of keeping  $\sigma_y$  deterministic is that it will simplify the probabilistic addition/subtraction in Eq. (105.57), while estimating the equivalent yield stress after each incremental step of the governing FPKEs, once the back stress ( $\alpha$ ), the internal variable for kinematic hardening material, starts evolving.

In this study, the back stress ( $\alpha$ ) is assumed to evolve with plastic strain and hence, it would evolve probabilistically similar to probabilistic evolution of the yield strength for isotropic hardening material. Probabilistic evolution of the back stress will occur according to Eq. (105.53), with advection and diffusion coefficients given by Eq. (105.54). Shear stress evolves according to Eq. (105.46), with advection and diffusion coefficients given by Eq. (105.55). One may note that the yield strength random variable ( $\Sigma_y$ ), appearing in Eqs. (105.54) and (105.55), is the equivalent yield strength and is given by Eq. (105.57). Fig. 105.29 shows the probabilistic evolution of shear stress in terms of mean, mode, and standard deviation, when a kinematic hardening material<sup>8</sup>, was cycled couple of times with increasing strain loops. All other material parameters are assumed to be the same as for the elastic–perfectly plastic material in Section 105.3.2. The evolved PDFs of the back stress ( $\alpha$ ) at the beginning and end of each branch (loading, unloading, re-loading, and re-unloading) are shown in Fig. 105.30. The evolved PDFs of equivalent yield stress (refer Eq. (105.57)) after each loading branch are shown in Fig. 105.31. Similar to the isotropic hardening case the uncertainty in (equivalent) yield strength increased as the material was cycled through, but unlike the isotropic hardening model, kinematic hardening model resulted in high kurtosis PDFs of (equivalent) yield strength. It is noted that the cyclic shear stress response of kinematic hardening material (Fig. 105.29), was more realistic than isotropic hardening material (Fig. 105.25), however, it didn't differ much from elastic–perfectly plastic material response (Fig. 105.20). Qualitatively, those, the elastic–perfectly plastic and the kinematic hardening responses, are similar. Like the elastic–perfectly plastic material, for kinematic hardening material, the mean and mode of the evolutionary shear stress (refer Fig. 105.29) are different, although not significantly.

Similarly, when one compares response (mean and standard deviation of shear stress) for loading cycles to the same strain level, for (i) elastic–perfectly plastic, (Fig. 105.21), (ii) isotropic linear hardening

<sup>8</sup>with non-dimensional rate of evolution of back stress with plastic strain of 10.

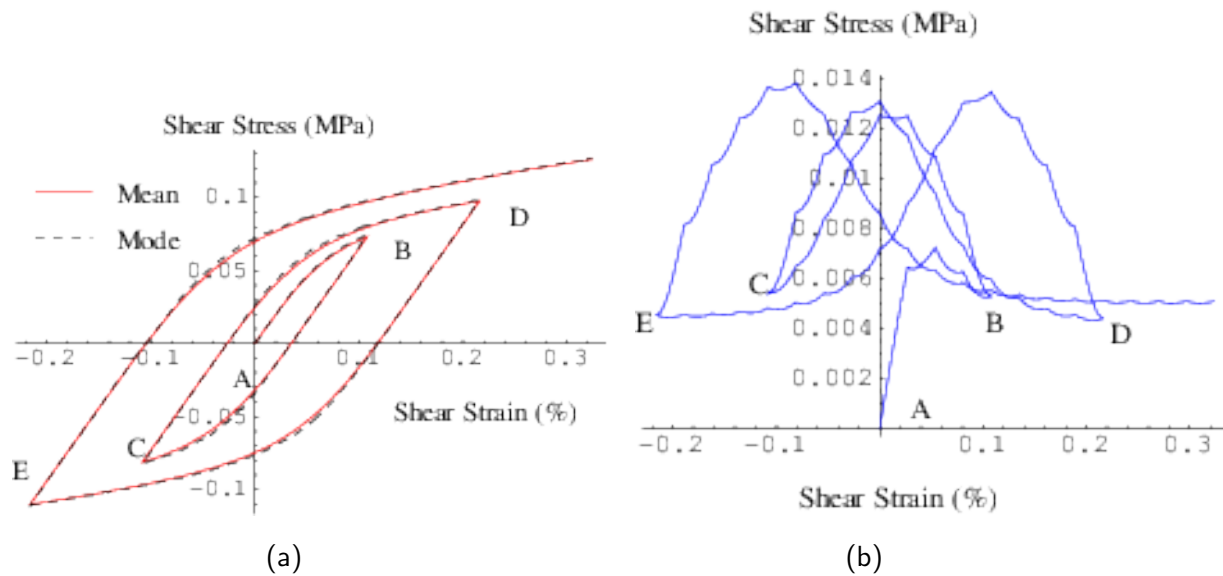


Figure 105.29: Kinematic hardening probabilistic model under cyclic loading with increasing loops: evolution of (a) mean, mode and (b) standard deviation of shear stress

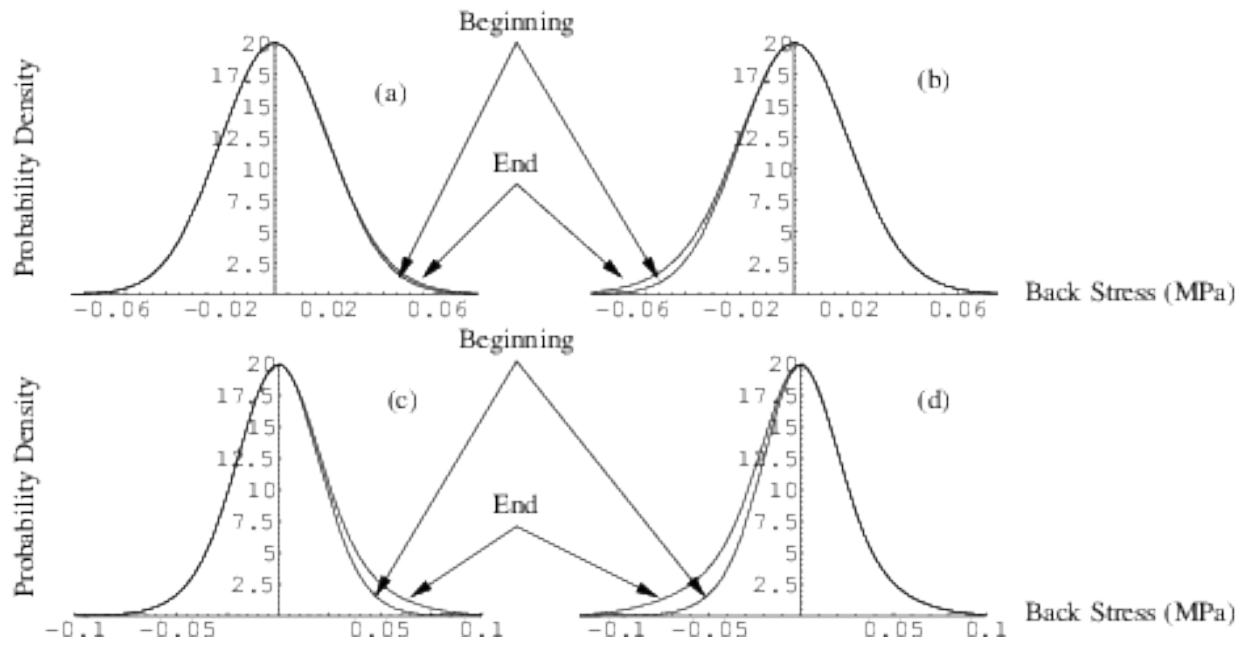


Figure 105.30: Kinematic hardening probabilistic model under cyclic loading with increasing loops: evolved PDF of back stress at the beginning and end of (a) loading branch, (b) unloading Branch, (c) re-loading branch, and (d) re-unloading branch

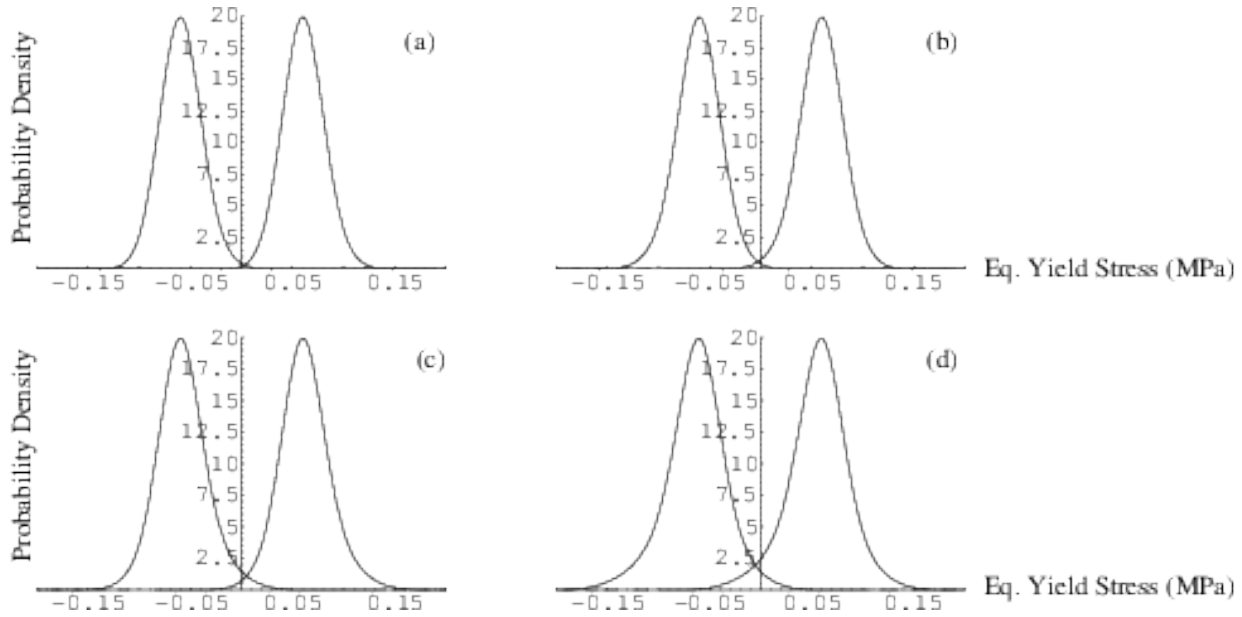


Figure 105.31: Kinematic hardening probabilistic model under cyclic loading with increasing loops: evolved PDF of equivalent yield stress after (a) loading branch, (b) unloading branch, (c) re-loading branch, and (d) re-unloading branch

(Fig. 105.27), and (iii) linear kinematic hardening (Fig. 105.32), probabilistic material models, one can easily observe the qualitative similarity between elastic–perfectly plastic (i) and kinematic hardening responses (iii).

Monotonic loading cases, however, for all probabilistic material models ((i) elastic–perfectly plastic, (Fig. 105.22), (ii) isotropic linear hardening (Fig. 105.28), and (iii) linear kinematic hardening (Fig. 105.33)), are qualitatively similar, with expected differences in rate of hardening.

## 105.4 Hermite Polynomial Chaos Karhunen-Loève Expansion

Hermite polynomial chaos Karhunen-Loève (PC-KL) expansion is formulated for the general heterogeneous random field  $H(\mathbf{x}, \theta)$  of arbitrary marginal distributions. Here  $\theta$  denotes the uncertainties and  $\mathbf{x}$  is the general coordinate that can be either temporal as in the case of uncertain random process motions or spatial as in the case of random field material parameters.

Random field  $H(\mathbf{x}, \theta)$  with any type of marginal distributions can be discretized with orthogonal Hermite polynomial chaos  $\Omega_i(\gamma(\mathbf{x}, \theta))$  up to a certain order  $P$  [Sakamoto and Ghanem \(2002\)](#):

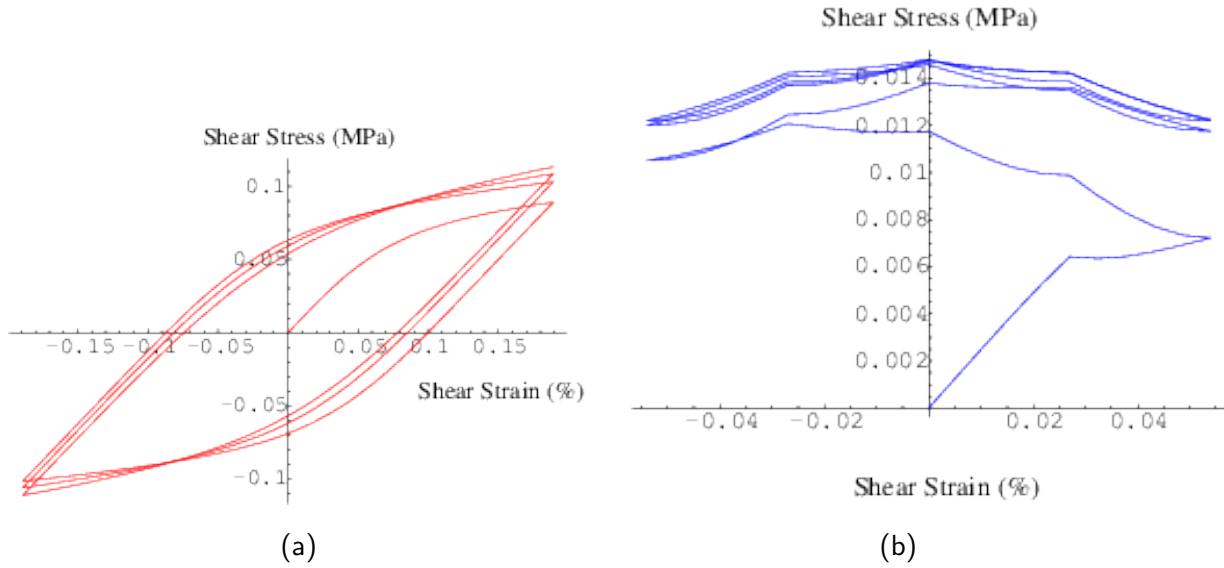


Figure 105.32: Kinematic hardening probabilistic model under cyclic loading with equal loops: evolution of (a) mean and (b) standard deviation of shear stress

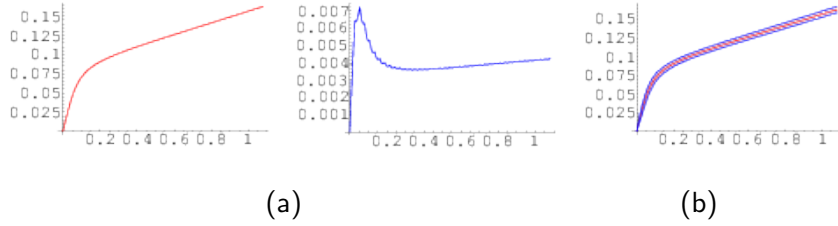


Figure 105.33: Kinematic hardening probabilistic model under monotonic loading: evolution of (a) mean, (b) standard deviation, and (c) mean  $\pm$  standard deviation of shear stress

$$H(\mathbf{x}, \theta) = \sum_{i=0}^P H_i(\mathbf{x}) \Omega_i(\gamma(\mathbf{x}, \theta)) \quad (105.58)$$

where random functions  $\{\Omega_i\}$  are Hermite polynomials constructed from a zero mean, unit variance kernel Gaussian random field  $\gamma(\mathbf{x}, \theta)$ . Random functions  $\{\Omega_i\}$  are determined by the initial condition  $\Omega_0 = 1$  and the recursive relation:

$$\Omega_{i+1}(\gamma) = \gamma \Omega_i(\gamma) - \Omega'_i(\gamma) \quad (105.59)$$

The deterministic PC coefficient field  $H_i(\mathbf{x})$  can be calculated by projecting random field  $H(\mathbf{x}, \theta)$  onto PC basis  $\Omega_i$ . Given the input covariance structure  $Cov_H(x_1, x_2)$  of the original random field, the underlying

Gaussian covariance kernel  $Cov_{\gamma}(x_1, x_2)$  can then be determined by solving:

$$Cov_H(x_1, x_2) = \sum_{i=1}^P H_i(x_1) H_i(x_2) i! Cov_{\gamma}(x_1, x_2)^i \quad (105.60)$$

Following Karhunen-Loëve (KL) theorem [Ghanem and Spanos \(1991\)](#), the underlying kernel Gaussian random field  $\gamma(\mathbf{x}, \theta)$  can be represented as:

$$\gamma(\mathbf{x}, \theta) = \sum_{i=1}^M \sqrt{\lambda_i} f_i(\mathbf{x}) \xi_i(\theta) \quad (105.61)$$

where eigenvalues  $\lambda_i$  and eigenvectors  $f_i(\mathbf{x})$  of the covariance kernel  $Cov_{\gamma}(x_1, x_2)$  have to satisfy Fredholm's integral equation of the second kind [Sakamoto and Ghanem \(2002\)](#). Zero mean and unit variance Gaussian random variables  $\{\xi_i(\theta)\}$  are represented in  $M$  independent dimensions.

By combining Equations [105.58](#) to [105.61](#), the ultimate PC-KL expansion of the general random field  $H(\mathbf{x}, \theta)$  into multi-dimensional orthogonal Hermite PC bases  $\{\Psi_i\}$  of order  $P$  and dimension  $M$  can be obtained as:

$$H(\mathbf{x}, \theta) = \sum_{i=0}^K h_i(\mathbf{x}) \Psi_i(\{\xi_j(\theta)\}) \quad (105.62)$$

$$h_i(\mathbf{x}) = \frac{p!}{\langle \Psi_i^2 \rangle} H_p(\mathbf{x}) \prod_{j=1}^p \frac{\sqrt{\lambda_{k(j)}} f_{k(j)}(\mathbf{x})}{\sqrt{\sum_{m=1}^M (\sqrt{\lambda_m} f_m(\mathbf{x}))^2}} \quad (105.63)$$

where  $K$  is the total number of multidimensional Hermite PC bases  $\{\Psi_i\}$  that depends on order  $P$  and dimension  $M$  as  $K = 1 + \sum_{s=1}^P \frac{1}{s!} \prod_{j=0}^{s-1} (M+j)$ . The upper product limit  $p$ , in equation [105.63](#) is the order of PC basis  $\Psi_i(\{\xi_j(\theta)\})$ . The marginal mean, marginal variance, correlation structure and any other statistics of the random field  $H(\mathbf{x}, \theta)$  can be synthesized from the above Hermite PC-KL expansion. The goodness of the PC-KL expansion can be checked by comparing the PC-synthesized statistics with the input statistics of the random field  $H(\mathbf{x}, \theta)$ .

## 105.5 Galerkin Stochastic Elastoplastic Finite Element Formulations

### 105.5.1 Stochastic Elastoplastic Finite Element Method

Within the developed time domain stochastic Galerkin formulations, the uncertain material parameters and the uncertain forcing are modeled as heterogeneous random fields and non-stationary random process, respectively. As a unified probabilistic discretization scheme, Hermite PC-KL expansion is applied to both input uncertainties and output uncertainties, e.g., probabilistic displacement and acceleration responses.

Stochastic Galerkin projection is performed to minimize the error for estimating response PC coefficients. The resulting PC coefficients are used to develop statistics and distributions of the probabilistic response.

The weak form of deterministic, dynamic finite elements Jeremić et al. (1989-2025) can be written as:

$$\int_{D_e} N_m(\mathbf{x})\rho(\mathbf{x})N_n(\mathbf{x})dV \ddot{u}_n(t) + \int_{D_e} \nabla N_m(\mathbf{x})E(\mathbf{x})\nabla N_n(\mathbf{x})dV u_n(t) - f_m(t) = 0 \quad (105.64)$$

where  $N_m$  are the finite element shape functions, and  $f_m(t)$  is the nodal force vector, while  $\rho(\mathbf{x})$  and  $E(\mathbf{x})$  are the deterministic density and deterministic stiffness fields in the deterministic FEM.

### 105.5.2 Stochastic Elastoplastic Finite Element Method, 1D Polynomial Chaos Formulation

Considering the tangential stiffness field,  $E(\mathbf{x})$  to be a heterogeneous random field, and the forcing function,  $f_m(t)$  to be a non-stationary random process, both are represented using multidimensional, Hermite PC expansions with known coefficients:

$$E(\mathbf{x}, \theta) = \sum_{i=0}^{P_1} E_i(\mathbf{x})\Psi_i(\{\xi_r(\theta)\}) \quad (105.65)$$

$$f_m(t, \theta) = \sum_{j=0}^{P_2} f_{mj}(t)\psi_j(\{\xi_r(\theta)\}) \quad (105.66)$$

When the system with uncertain properties is excited by uncertain forces, the results, displacement and acceleration responses also become uncertain and can be represented using Hermite PCs with unknown coefficients expanded up to order  $P_3$ :

$$u_n(t, \theta) = \sum_{k=0}^{P_3} u_{nk}(t)\phi_k(\{\xi_l(\theta)\}) \quad (105.67)$$

$$\ddot{u}_n(t, \theta) = \sum_{k=0}^{P_3} \ddot{u}_{nk}(t)\phi_k(\{\xi_l(\theta)\}) \quad (105.68)$$

By substituting Eqs. 105.65, 105.66, 105.67, and 105.68 into Eq. 105.64, and denoting the shape function gradients  $\nabla N_n(\mathbf{x})$  as  $B(\mathbf{x})$ , we obtain:

$$\begin{aligned} & \sum_{k=0}^{P_3} \int_{D_e} N_m(\mathbf{x})\rho(\mathbf{x})N_n(\mathbf{x})dV \phi_k \ddot{u}_{nk}(t) + \\ & \sum_{k=0}^{P_3} \sum_{i=0}^{P_1} \int_{D_e} B_m(\mathbf{x})E_i(\mathbf{x})B_n(\mathbf{x})dV \Psi_i \phi_k u_{nk}(t) - \sum_{j=0}^{P_2} f_{mj}(t)\psi_j = 0 \end{aligned} \quad (105.69)$$

Performing stochastic Galerkin projection by multiplying both sides of Eq. 105.69 with PC basis  $\phi_l$  and taking expectation Ghanem and Kruger (1996), we obtain the following system of ordinary differential equations (ODEs):

$$\begin{aligned} \sum_{k=0}^{P_3} \langle \phi_k \phi_l \rangle \int_{D_e} N_m(\mathbf{x}) \rho(\mathbf{x}) N_n(\mathbf{x}) dV \ddot{u}_{nk}(t) + \\ \sum_{k=0}^{P_3} \sum_{i=0}^{P_1} \langle \Psi_i \phi_k \phi_l \rangle \int_{D_e} B_m(\mathbf{x}) E_i(\mathbf{x}) B_n(\mathbf{x}) dV u_{nk}(t) = \sum_{j=0}^{P_2} \langle \psi_j \phi_l \rangle f_{mj}(t) \end{aligned} \quad (105.70)$$

with  $l = 0, 1, 2, \dots, P_3$  where  $P_3$  is the PC expansion order, while  $m = 1, 2, \dots, N$  where  $N$  is the number of finite element nodes, and the expectation operator is denoted as  $\langle \cdot \rangle$ . The expectations of double products  $\langle \phi_k \phi_l \rangle$ ,  $\langle \psi_j \phi_l \rangle$  and triple products  $\langle \Psi_i \phi_k \phi_l \rangle$  of Hermite PC bases can be analytically computed beforehand and looked up during the stochastic FEM analysis.

Eq. 105.70 can be written into a matrix-vector form as:

$$\mathbf{M}\ddot{\mathbf{u}} + \mathbf{K}\mathbf{u} = \mathbf{F} \quad (105.71)$$

where  $\mathbf{M}$ ,  $\mathbf{K}$  and  $\mathbf{F}$  are the stochastic expanded mass matrix, stiffness matrix and force vector, respectively. Vectors of unknown acceleration and displacement PC coefficients are denoted as  $\ddot{\mathbf{u}}$  and  $\mathbf{u}$ , respectively.

Equation 105.71 is written in index notation, using Einstein summation convention, as:

$$M_{mlnk} \ddot{u}_{nk} + K_{mlnk} u_{nk} = F_{ml} \quad (105.72)$$

where

$$M_{mlnk} = \bigcup_e \langle \phi_k \phi_l \rangle \int_{D_e} N_m(\mathbf{x}) \rho(\mathbf{x}) N_n(\mathbf{x}) dV \quad (105.73)$$

$$K_{mlnk} = \bigcup_e \sum_{i=0}^{P_1} \langle \Psi_i \phi_k \phi_l \rangle \int_{D_e} B_m(\mathbf{x}) E_i(\mathbf{x}) B_n(\mathbf{x}) dV \quad (105.74)$$

$$F_{ml} = \bigcup_e \sum_{j=0}^{P_2} \langle \psi_j \phi_l \rangle f_{mj} \quad (105.75)$$

and  $\bigcup_e$  is the assembly operator for elemental mass matrices, stiffness matrices and force vectors. Rayleigh damping can also be added into Eq. 105.71 as:

$$\mathbf{M}\ddot{\mathbf{u}} + \mathbf{C}\dot{\mathbf{u}} + \mathbf{K}\mathbf{u} = \mathbf{F} \quad (105.76)$$

The stochastic expanded damping matrix  $\mathbf{C}$  can be represented as:

$$\mathbf{C} = \alpha\mathbf{M} + \beta\mathbf{K} \quad (105.77)$$

where  $\alpha$  and  $\beta$  are Rayleigh damping parameters. The Rayleigh damping would produce the damping ratio  $\xi$  dependent on the response frequency  $\omega$  in a hyperbolic functional form as (Chopra Chopra (2000)):

$$\xi = \frac{1}{2} \left( \frac{\alpha}{\omega} + \beta \omega \right) \quad (105.78)$$

Due to the formulation of Rayleigh damping, its uncertainties are inherently considered and modeled through the uncertainties of the mass and stiffness matrix. In Eq. 105.77, both the matrix  $\mathbf{M}$  and the matrix  $\mathbf{K}$ , are stochastic expanded matrices that reflect the uncertainties from the material density and stiffness. Additional uncertainties could be included through uncertain Rayleigh damping parameters  $\alpha$  and  $\beta$ . However, these uncertainties are difficult to calibrate. Therefore, in this study, we consider both the damping parameters  $\alpha$  and  $\beta$  to be deterministic. As such, the damping uncertainties come directly as the combination of the mass uncertainties and the stiffness uncertainties. The same Galerkin projection scheme is inherently applied to propagate the damping uncertainties to the probabilistic system response.

The ordinary differential system of equations 105.71 or 105.76 may be solved using any time integration method, for example Newmark method Newmark (1959). Note that the size of the stochastic finite element system of equations is much larger when compared to corresponding deterministic finite element system of equations, depending upon the number of PC terms used to represent the probabilistic displacement and acceleration response. After solving for the unknown PC coefficients for displacements  $u_{nk}$  and accelerations  $\ddot{u}_{nk}$  from the stochastic FEM analysis, the complete probabilistic dynamic response of the system can be determined. Using the resulting PC coefficients for  $u_{nk}$  and  $\ddot{u}_{nk}$ , any probabilistic measure of the uncertain system response can be obtained. For example, the time-evolving mean and variance of the probabilistic displacement response at node  $n$  can be computed as:

$$\langle u_n(t, \theta) \rangle = u_{n0}(t) \quad (105.79)$$

$$\text{Var}(u_n(t, \theta)) = \sum_{k=1}^{P_3} \langle \phi_k^2 \rangle u_{nk}^2(t) \quad (105.80)$$

### 105.5.3 Probabilistic Elastoplastic Constitutive Modeling, 1D Polynomial Chaos Formulation

In the above stochastic elastoplastic FEM formulation, the probabilistic tangential stiffness  $E(\mathbf{x}, \theta)$  needs to be updated at each incremental step. Probabilistic elastoplastic constitutive modeling is performed at

each Gauss point to update the uncertain elastoplastic stiffness and stress. For the one dimensional (1D) stochastic site response analysis in this study, the constitutive behavior of the soil is represented by a 1D elastoplastic material model with a vanishing elastic region and Armstrong–Frederick nonlinear kinematic hardening [Armstrong and Frederick \(1966\)](#). Without considering uncertainties in material properties, the relationship between the stress increment  $d\sigma$  and the strain increment  $d\epsilon$ , in 1D, can be written in the incremental form as:

$$d\sigma = H_a d\epsilon - C_r \sigma |d\epsilon| \quad (105.81)$$

where  $H_a$  and  $C_r$  are model parameters. The shear strength  $S_u$  given by the model becomes  $S_u = H_a/C_r$ . The elastoplastic tangential stiffness is a function of the stress  $\sigma$  as:

$$E(\sigma) = \frac{d\sigma}{d\epsilon} = H_a - C_r \sigma \operatorname{sgn}(d\epsilon) \quad (105.82)$$

where  $\operatorname{sgn}(d\epsilon)$  is the sign function of the strain increment  $d\epsilon$ . This function returns  $\operatorname{sgn}(d\epsilon) = 1$  for the positive strain increment  $d\epsilon > 0$  and  $\operatorname{sgn}(d\epsilon) = -1$  otherwise, for  $d\epsilon < 0$ .

Here model parameters  $H_a$  and  $C_r$  are considered to be uncertain and modeled as random fields  $H_a(\mathbf{x}, \theta)$  and  $C_r(\mathbf{x}, \theta)$ . Representation of those two model parameters using Hermite PC bases  $\varphi_i(\{\xi_r(\theta)\})$  can be written as:

$$H_a(\mathbf{x}, \theta) = \sum_{i=0}^P H_{ai}(\mathbf{x}) \varphi_i(\{\xi_r(\theta)\}) \quad (105.83)$$

$$C_r(\mathbf{x}, \theta) = \sum_{i=0}^P C_{ri}(\mathbf{x}) \varphi_i(\{\xi_r(\theta)\}) \quad (105.84)$$

The strain increments  $d\epsilon(\mathbf{x}, \theta)$ , that represent input to the constitutive driver (Equation 105.81), are also uncertain, since  $\epsilon(\mathbf{x}, \theta) = B(\mathbf{x})u_n(t, \theta)$ :

$$d\epsilon(\mathbf{x}, \theta) = \sum_{i=0}^P d\epsilon_i(\mathbf{x}) \varphi_i(\{\xi_r(\theta)\}) \quad (105.85)$$

As a result, the probabilistic incremental stress  $d\sigma(\mathbf{x}, \theta)$  and the tangential stiffness  $E(\mathbf{x}, \theta)$  can be represented using unknown PC coefficients  $\{d\sigma_i(\mathbf{x})\}$  and  $\{E_i(\mathbf{x})\}$  as:

$$d\sigma(\mathbf{x}, \theta) = \sum_{i=0}^P d\sigma_i(\mathbf{x}) \varphi_i(\{\xi_r(\theta)\}) \quad (105.86)$$

$$E(\mathbf{x}, \theta) = \sum_{i=0}^P E_i(\mathbf{x}) \varphi_i(\{\xi_r(\theta)\}) \quad (105.87)$$

Substituting Equations 105.83 ~ 105.87 into Equations 105.81 and 105.82, and applying Galerkin projection on PC basis  $\varphi_i\{\xi_r(\theta)\}$  yields:

$$\sum_{m=0}^P d\sigma_m \langle \varphi_m \varphi_i \rangle = \sum_{j=0}^P \sum_{k=0}^P H_{aj} d\epsilon_k \langle \varphi_j \varphi_k \varphi_i \rangle \pm \sum_{l=0}^P \sum_{n=0}^P \sum_{s=0}^P C_{rl} \sigma_n d\epsilon_s \langle \varphi_l \varphi_n \varphi_s \varphi_i \rangle \quad (105.88)$$

$$\sum_{i=0}^P E_m \langle \varphi_m \varphi_i \rangle = \sum_{j=0}^P H_{aj} \langle \varphi_j \varphi_i \rangle \pm \sum_{l=0}^P \sum_{n=0}^P C_{rl} \sigma_n \langle \varphi_l \varphi_n \varphi_i \rangle \quad (105.89)$$

Solutions to the unknown PC coefficients of the incremental stress  $d\sigma(x, \theta)$  and the elastoplastic stiffness  $E(x, \theta)$  can be computed using the orthogonality of Hermite PC bases  $\langle \varphi_i \varphi_j \rangle = \delta_{ij}$ :

$$d\sigma_i = \frac{1}{\text{Var}[\varphi_i]} \left[ H_{ai} d\epsilon_k \langle \varphi_j \varphi_k \varphi_i \rangle \pm C_{rl} \sigma_n d\epsilon_s \langle \varphi_l \varphi_n \varphi_s \varphi_i \rangle \right] \quad (105.90)$$

$$E_i = H_{ai} \pm \frac{1}{\text{Var}[\varphi_i]} C_{rl} \sigma_n \langle \varphi_l \varphi_n \varphi_i \rangle \quad (105.91)$$

where  $\text{Var}[\varphi_i]$  is the scalar variance of PC basis  $\varphi_i\{\xi_r(\theta)\}$ , that equals to  $\langle \varphi_i^2 \rangle$ . The Einstein's summation convention is followed in equations 105.90 and 105.91 with index  $i$  as a free index. The above formulation for the probabilistic constitutive modeling is implemented in the context of the explicit, forward Euler algorithm Jeremić et al. (1989-2025).

To illustrate the above probabilistic constitutive model, Figure 105.34 shows the stress-strain behavior using uncertain material parameters  $H_a$  with mean 10MPa and coefficient of variation (CV) 25%, uncertain shear strength  $S_u = H_a/C_r$  with mean 150kPa and coefficient of variation 25%. The material is driven by an uncertain cyclic strain with a mean strain increment  $10^{-4}$  and coefficient of variation of 20%.

It is observed that the probabilistic material response obtained through the intrusive polynomial chaos modeling matches well with Monte Carlo analysis using 10,000 samples. It is noted that the intrusive probabilistic modeling is around 2,000 times more computationally efficient, faster than Monte Carlo simulations.

#### 105.5.4 Stochastic Elastoplastic Finite Element Method, 3D Polynomial Chaos Formulation

#### 105.5.5 Probabilistic Elastoplastic Constitutive Modeling, 3D Polynomial Chaos Formulation

### 105.6 Sobol' Indices Computation Using Polynomial Chaos Expansion

In global sensitivity analysis, the variance of model output is decomposed into a sum of contributions from individual random variable, or groups of random variables. Consider a general mathematical model

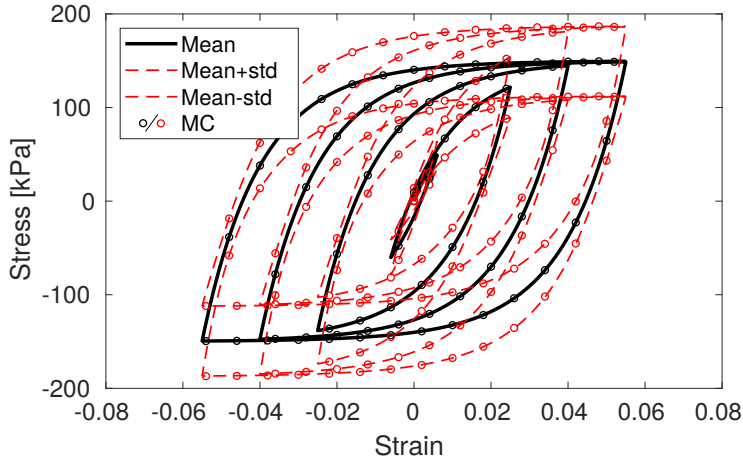


Figure 105.34: The hysteretic behavior of 1-D elastoplastic material with uncertain parameters  $H_a$  and  $H_a/C_r$ .

with  $n$  uncertain inputs represented by vector  $\mathbf{x}$  and scalar output  $y$  as:

$$y = f(\mathbf{x}) \quad \mathbf{x} \in I^n \quad (105.92)$$

where the input parameters  $\mathbf{x}$  are defined in  $n$  dimensional unit cube  $I^n$  without the loss of generality. The ANOVA (ANalysis Of VAriance) representation of  $f(\mathbf{x})$  can be written as [Sobol \(2001\)](#):

$$f(x_1, x_2, \dots, x_n) = f_0 + \sum_{i=1}^n f_i(x_i) + \sum_{1 \leq i < j \leq n} f_{ij}(x_i, x_j) + \dots + f_{1,2,\dots,n}(x_1, \dots, x_n) \quad (105.93)$$

There are  $2^n$  summands in total. Constant  $f_0$  is the mean value of the function:

$$f_0 = \int_{I^n} f(\mathbf{x}) d\mathbf{x} \quad (105.94)$$

The integral of each summand in Equation 105.93 over any of its independent variable is zero:

$$\int_0^1 f_{i_1, \dots, i_s}(x_{i_1}, x_{i_2}, \dots, x_{i_s}) dx_{i_k} = 0 \quad \text{for } 1 \leq k \leq s \quad (105.95)$$

From Equation 105.95, it can be seen that the summands are orthogonal to each other in the following sense:

$$\int_{I^n} f_{i_1, \dots, i_s}(x_{i_1}, x_{i_2}, \dots, x_{i_s}) f_{j_1, \dots, j_t}(x_{j_1}, x_{j_2}, \dots, x_{j_t}) d\mathbf{x} = 0 \quad \text{for } \{i_1, \dots, i_s\} \neq \{j_1, \dots, j_t\} \quad (105.96)$$

For given mathematical model  $f(\mathbf{x})$ , the above ANOVA representation is unique and can be derived analytically. For example, the univariate terms can be solved as:

$$f_i(x_i) = \int_{I^{n-1}} f(\mathbf{x}) \, d\mathbf{x}_{\sim i} - f_0 \quad (105.97)$$

where  $\int_{I^{n-1}} (\cdot) \, d\mathbf{x}_{\sim i}$  denotes the integration over all dimensions except  $x_i$ . Similarly, the bivariate terms can be derived as follows:

$$f_{ij}(x_i, x_j) = \int_{I^{n-2}} f(\mathbf{x}) \, d\mathbf{x}_{\sim [ij]} - f_i(x_i) - f_j(x_j) - f_0 \quad (105.98)$$

Following this procedure, any summand  $f_{i_1, \dots, i_s}(x_{i_1}, x_{i_2}, \dots, x_{i_s})$  can be constructed from some multidimensional integral of  $f(\mathbf{x})$ .

Considering uncertain input parameters  $\mathbf{X}$  to be independent random variables following uniform distribution in  $[0, 1]$ :

$$\mathbf{X} = [X_1, \dots, X_n], \quad X_i \sim U(0, 1), \quad \text{for } i = 1, \dots, n \quad (105.99)$$

Then the total variance of the probabilistic model response  $y = f(\mathbf{X})$  can be computed as:

$$D = \text{Var}[f(\mathbf{X})] = \int_I^n f^2(\mathbf{x}) \, d\mathbf{x} - f_0^2 \quad (105.100)$$

Using Equations 105.93 and 105.96, the total variance  $D$  can be decomposed as follows:

$$D = \sum_{i=1}^n D_i + \sum_{1 \leq i < j \leq n} D_{ij} + \dots + D_{1,2,\dots,n} = \sum_{s=1}^n \sum_{i_1 < \dots < i_s} D_{i_1 \dots i_s} \quad (105.101)$$

where the variance contribution from individual summand is given as follows:

$$D_{i_1 \dots i_s} = \int_{I^s} f_{i_1 \dots i_s}^2(x_{i_1}, \dots, x_{i_s}) \, dx_{i_1} \dots dx_{i_s}, \text{ with } 1 \leq i_1 < \dots < i_s \leq n, s = 1, \dots, n \quad (105.102)$$

The Sobol' indices  $S_{i_1 \dots i_s}$  are defined as:

$$S_{i_1 \dots i_s} = D_{i_1 \dots i_s} / D \quad (105.103)$$

The Sobol' indices  $S_{i_1 \dots i_s}$  quantifies the fractional contributions from random inputs  $\{X_{i_1}, \dots, X_{i_s}\}$  to the total variance  $D$ . The first order indices  $S_i$  gives the influence of each uncertain input parameter  $X_i$  when considered individually. The high order terms describe the mixed influence when a group of uncertain input parameters are considered collectively. Clearly, from Equation 105.101 we have:

$$\sum_{i=1}^n S_i + \sum_{1 \leq i < j \leq n} S_{ij} + \dots + S_{1,2,\dots,n} = 1 \quad (105.104)$$

The Sobol' indices for global sensitivity analysis can be used for the following purposes: (1) Ranking of input uncertain parameters  $X = [X_1, \dots, X_n]$ . (2) Neglect of inessential uncertain parameters and high order terms in Equation 105.93. The total sensitivity indices  $S_i^{\text{total}}$  is defined to evaluate the total influence of a certain input parameter  $X_i$  as:

$$S_i^{\text{total}} = \sum_{\mathcal{S}_i} D_{i_1 \dots i_s} \quad (105.105)$$

where set  $\mathcal{S}_i$  contains all the indexes involving index  $i$  defined as Equation 105.106 and Sobol' indices set  $\{D_{i_1 \dots i_s}\}$  is the collection of all partial sensitivity indices that are related to parameter  $X_i$ .

$$\mathcal{S}_i = \{(i_1, \dots, i_s) : \exists k, 1 \leq k \leq s, i_k = i\} \quad (105.106)$$

Using Hermite PC expansion Ghanem and Spanos (1991), the probabilistic model response  $y = f(X)$  can be represented as:

$$y = \sum_{j=0}^{P-1} y_j \Psi_j(\xi), \quad \xi = \{\xi_1, \dots, \xi_M\} \quad (105.107)$$

where  $\{\Psi_j\}$  are multi-dimensional, mutually orthogonal Hermite PC bases of order  $p$  constructed from  $M$  dimension, independent, standard Gaussian random vector  $\xi$ . The total number of PC bases  $P$  is related to the dimension  $M$  and order  $p$  as:

$$P = \binom{M+p}{p} = \frac{(M+p)!}{M!p!} \quad (105.108)$$

It is noted that the input random vector  $X$  of any prescribed joint PDF or any given marginal PDF and correlations can be approximately transformed to standard Gaussian random vector  $\xi$  using transformation techniques such as iso-probabilistic transform and Nataf transform Lebrun and Dutfoy (2009):

$$X = T(\xi) \quad (105.109)$$

Therefore, the probabilistic model response can be evaluated and represented with Hermite PC expansion as:

$$y = f(X) = f \circ T(\xi) = \sum_{j=0}^{P-1} y_j \Psi_j(\xi), \quad \xi = \{\xi_1, \dots, \xi_M\} \quad (105.110)$$

Here we transform the input random vector  $X$  into standard Gaussian random vector  $\xi$  and perform Hermite polynomial chaos expansion. We can also transform the input random vector  $X$  into other types

of basic random variables, e.g., uniform distribution, and represent model response  $y$  with associated generalized PC expansion [Xiu and Karniadakis \(2002\)](#).

Since the PC bases  $\{\Psi_j(\xi)\}$  are zero-mean ( $j \geq 1$ ) and mutually orthogonal, the mean  $\bar{y}$  and total variance of model response  $D_{PC}$  can be calculated from its PC representation:

$$\begin{aligned}\bar{y} &= E[f(X)] = y_0 \\ D_{PC} &= \text{Var} \left[ \sum_{j=0}^{P-1} y_j \Psi_j \right] = \sum_{j=1}^{P-1} y_j^2 E \left[ \Psi_j^2 \right]\end{aligned}\quad (105.111)$$

To compute the Sobol' indices, the above PC expansion of  $y$  should be organized into the ANOVA form [Sudret \(2008\)](#). The multi-dimensional polynomial chaos bases  $\{\Psi_j(\xi)\}$  can be decomposed into the multiplication of single dimension polynomial chaos bases of different orders:

$$\Psi_j(\xi) = \prod_{i=1}^n \phi_{\alpha_i}(\xi_i) \quad (105.112)$$

where  $\phi_{\alpha_i}(\xi_i)$  is the single dimensional, order  $\alpha_i$ , polynomial function of underlying basic random variable  $\xi_i$ . The functional form of the generalized polynomial chaos function  $\phi_{\alpha_i}(\xi_i)$  depends on the selected underlying basic random variable  $\xi_i$  [Xiu and Karniadakis \(2002\)](#). For example, when the basic random variable  $\xi_i$  follows standard Gaussian distribution, Hermite polynomial functions  $\phi_{\alpha_i}(\xi_i)$  should be constructed as follows:

$$\phi_0 = 1; \quad \phi_{k+1}(\xi_i) = \xi_i \phi_k(\xi_i) - \phi'_k(\xi_i) \quad \text{for all } k \geq 1 \quad (105.113)$$

Each multidimensional polynomial chaos basis can be uniquely characterized by vector  $\alpha = (\alpha_1, \dots, \alpha_n)$ . The connection between the PC expansion and the ANOVA representation of model response  $y$  can be established by defining set  $\mathcal{S}$  from  $\alpha$  as [Sudret \(2008\)](#):

$$\mathcal{S}_{i_1, \dots, i_s} = \{\alpha : \forall k = 1, \dots, n, \text{ when } k \in (i_1, \dots, i_s), \alpha_k > 0, \text{ otherwise, } \alpha_k = 0\} \quad (105.114)$$

For example,  $\mathcal{S}_i$  would correspond to the PC bases depending only on dimension  $\xi_i$ . Following Equation 105.114, the PC expansion shown in Equation 105.110 could be written into ANOVA representation:

$$\begin{aligned}y &= y_0 + \sum_{i=1}^n \sum_{\alpha \in \mathcal{S}_i} y_{\alpha} \Psi_{\alpha}(\xi_i) + \sum_{1 \leq i_1 < i_2 \leq n} \sum_{\alpha \in \mathcal{S}_{i_1, i_2}} y_{\alpha} \Psi_{\alpha}(\xi_{i_1}, \xi_{i_2}) + \dots \\ &\quad + \sum_{1 \leq i_1 < \dots < i_s \leq n} \sum_{\alpha \in \mathcal{S}_{i_1, \dots, i_s}} y_{\alpha} \Psi_{\alpha}(\xi_{i_1}, \dots, \xi_{i_s}) + \dots \\ &\quad + \sum_{\alpha \in \mathcal{S}_{1, 2, \dots, n}} y_{\alpha} \Psi_{\alpha}(\xi_1, \dots, \xi_n)\end{aligned}\quad (105.115)$$

where the term  $\sum_{\alpha \in \mathcal{S}_{i_1, \dots, i_s}} y_\alpha \Psi_\alpha(\xi_{i_1}, \dots, \xi_{i_s})$  denotes the summation of polynomial chaos expansions depending on all the basic random variables  $\{\xi_{i_1}, \dots, \xi_{i_s}\}$  and only on them. From the above ANOVA representation of probabilistic model response, the PC-based Sobol' indices  $S_{i_1 \dots i_s}^{PC}$  can be derived as:

$$S_{i_1 \dots i_s}^{PC} = \sum_{\alpha \in \mathcal{S}_{i_1, \dots, i_s}} y_\alpha^2 E[\Psi_\alpha^2] / D^{PC} \quad (105.116)$$

The total Sobol' indices  $S_{j_1 \dots j_t}^{PC, \text{total}}$  for any group of parameters  $\{\xi_{j_1}, \dots, \xi_{j_t}\}$  can then be computed as:

$$S_{j_1 \dots j_t}^{PC, \text{total}} = \sum_{(i_1, \dots, i_s) \in \mathcal{S}_{j_1, \dots, j_t}} S_{i_1 \dots i_s}^{PC} \quad (105.117)$$

where set  $\mathcal{S}_{j_1, \dots, j_t}$  is defined as:

$$\mathcal{S}_{j_1, \dots, j_t} = \{(i_1, \dots, i_s) : (j_1, \dots, j_t) \subset (i_1, \dots, i_s)\} \quad (105.118)$$

From the above formulations, it can be observed that once the PC representation of probabilistic model response is established, Sobol' sensitivity indices can be analytically evaluated with very small computational expense.

## Chapter 106

# Large Deformation Elasto-Plasticity

(1996-2004-)

(In collaboration with Dr. Zhao Cheng)

## 106.1 Chapter Summary and Highlights

## 106.2 Continuum Mechanics Preliminaries: Kinematics

### 106.2.1 Deformation

In modeling the material nonlinear behavior of solids, plasticity theory is applicable primarily to those bodies that can experience inelastic deformations considerably greater than the elastic deformation. If the resulting total deformation, including both translations and rotations, are small enough, we can apply small deformation theory in solving these problems. If, however strains and rotations are finite, one must resort to the theory of large deformations. In doing so, we will be using two sets of representations<sup>1</sup>, namely:

- *Material coordinates* in the undeformed configuration, also called *Lagrangian coordinates*,
- *Spatial coordinates* in the deformed configuration, also called *Eulerian coordinates*.

Figure 106.1 shows the displacement of a particle from its initial position  $X_I$  to the current position  $x_i$ , defined by the deformation equation:

$$x_i = x_i(X_1, X_2, X_3, t) \quad (106.1)$$

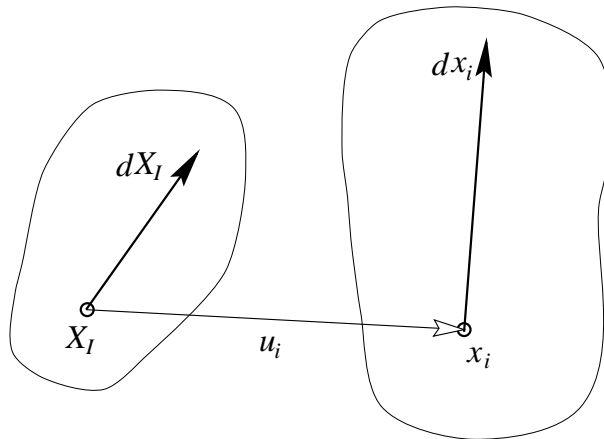


Figure 106.1: Displacement, stretch and rotation of material vector  $dX_I$  to new position  $dx_i$ .

The initial position  $X_I$  of the particle now occupying the position  $x_i$  is given by the *Eulerian equation*:

$$X_I = X_I(x_1, x_2, x_3, t) \quad (106.2)$$

<sup>1</sup>See Malvern (1969).

The two positions are connected by the displacement  $u_I$ :

$$x_i = X_I + u_i \quad ; \quad X_I = x_i - u_i \quad (106.3)$$

### 106.2.2 Deformation Gradient

The *deformation gradients* are the gradients of the functions on the right-hand side of equations (106.1) and (106.2). To emphasize the difference between the material, Lagrangian setting and the spatial, Eulerian setting, we will use capital letters for the material coordinate indices and lower case letters for the spatial coordinate indices. We limit our work to the rectangular Cartesian coordinates, thus simplifying the tensor notation to the covariant indices only.

The deformation gradient is defined as the *two-point tensor* whose rectangular Cartesian components are the partial derivatives:

$$F_{kK} = \frac{\partial x_k}{\partial X_K} = x_{k,K} \quad (106.4)$$

The deformation gradient  $F_{kK}$  transforms (convects) an arbitrary infinitesimal material vector  $dX_I$  at  $X_I$  to associate it with a vector  $dx_i$  at  $x_i$ :

$$dx_k = F_{kK} dX_K = \frac{\partial x_k}{\partial X_K} dX_K = x_{k,K} dX_K \quad (106.5)$$

The *the spatial deformation gradients* are tensors referred to the deformed, Eulerian configuration:

$$(F_{Kk})^{-1} = \frac{\partial X_K}{\partial x_k} = X_{K,k} \quad (106.6)$$

Similarly to the deformation gradient  $F_{kK}$ , *spatial deformation gradient*  $(F_{Kk})^{-1}$  operates on an arbitrary infinitesimal material vector  $dx_i$  at  $x_i$  to associate it with a vector  $dX_I$  at  $X_I$ :

$$dX_K = (F_{Kk})^{-1} dx_k = \frac{\partial X_K}{\partial x_k} dx_k = X_{K,k} dx_k \quad (106.7)$$

The *spatial deformation gradient*  $(F_{Kk})^{-1}$  at  $x_i$  is the inverse to the two-point tensor  $F_{kK}$  at  $X_I$ :

$$F_{iJ} (F_{Jk})^{-1} = \delta_{ik} \quad \text{and} \quad (F_{Ij})^{-1} F_{jk} = \delta_{IK} \quad (106.8)$$

The *Jacobian* of the mapping (106.4) can be represented as:

$$J = \det(F_{kK}) = \frac{1}{6} e_{ijk} e_{PQR} F_{iP} F_{jQ} F_{kR} \quad (106.9)$$

The relative deformation gradient  $f_{km}$  is the gradient for the relative motion function:

$$\xi = \chi_t(x_i, \tau) \quad (106.10)$$

and is defined as:

$$f_{km} = \xi_{k,m} \equiv \frac{\partial \xi_k}{\partial x_m} \quad (106.11)$$

If the fixed reference position  $X_I$ , the current position  $x_i$  and the variable position  $\xi_i$  are all referred to the rectangular Cartesian coordinate system, the chain rule of differentiation yields:

$$\frac{\partial \xi_k}{\partial X_I} = \frac{\partial \xi_k}{\partial x_m} \frac{\partial x_m}{\partial X_I} \quad \text{or} \quad F_{kl} = f_{km} F_{ml} \quad (106.12)$$

The polar decomposition theorem permits the unique representation<sup>2</sup>:

$$F_{ij} = R_{ik} U_{kj} = v_{ik} R_{kj} \quad (106.13)$$

where  $U_{kj}$ ,  $v_{ik}$  are positive definite symmetric tensors, called *right stretch tensors* and *left stretch tensors*, respectively, and  $R_{kj}$  is an *orthogonal tensor* such that:

$$R_{ik} R_{jk} = \delta_{ij} \quad \text{and also} \quad R_{ki} R_{kj} = \delta_{ij} \quad (106.14)$$

Equation (106.13), as well as Figure 106.2.2 demonstrate that the motion and deformation of an infinitesimal volume element at  $X_i$  consist of consecutive applications of:

- a stretch by  $U_{kj}$ ,
- a rigid body rotation by  $R_{ik}$ ,
- a rigid body translation to  $x_i$

or alternatively:

- a rigid body translation to  $x_i$
- a rigid body rotation by  $R_{kj}$ ,
- a stretch by  $v_{ik}$ ,

---

<sup>2</sup>referring  $x_i$  and  $X_i$  to the same reference axes and using lower case indices for both. This reference to the same coordinate system will be applied only for the polar decomposition example presented here.

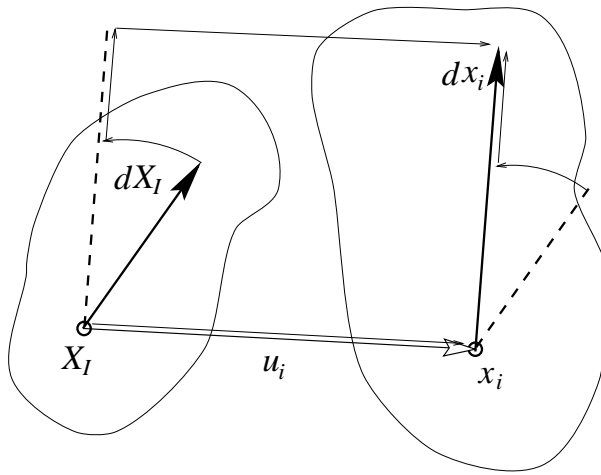


Figure 106.2: Illustration of the equation  $F_{ij} = R_{ik} U_{kj} = v_{ik} R_{kj}$ .

### 106.2.3 Strain Tensors, Deformation Tensors and Stretch

The strain tensors  $E_{IJ}$  and  $e_{ij}$  are defined so that they give the change in the square length of the material vector  $dX_I$ . For the Lagrangian formulation we write:

$$(ds)^2 - (dS)^2 = 2dX_I E_{IJ} dX_J \quad (106.15)$$

and for the Eulerian formulation:

$$(ds)^2 - (dS)^2 = 2dx_i e_{ij} dx_j \quad (106.16)$$

The deformation tensors  $C_{IJ}$  and  $c_{ij}$  are connecting the squared lengths in Lagrangian and Eulerian configurations. The Green deformation tensor<sup>3</sup>  $C_{IJ}$ , referred to the undeformed configuration, gives the new squared length  $(ds)^2$  of the element into which the given element  $dX_I$  is deformed:

$$(ds)^2 = dX_I C_{IJ} dX_J \quad (106.17)$$

The Cauchy deformation tensor  $c_{ij}$ , sometimes also denoted as<sup>4</sup>  $(b_{ij})^{-1}$ , gives the initial squared length  $(dS)^2$  of an element  $dx_i$  identified in the deformed configuration:

$$(dS)^2 = dx_i c_{ij} dx_j \quad (106.18)$$

<sup>3</sup>Also called *right Cauchy-Green tensor*.

<sup>4</sup>Another name for  $b_{ij}$  is *Finger deformation tensor* or *left Cauchy-Green tensor*.

Substituting equation (106.17) into (106.15) yield:

$$2E_{IJ} = C_{IJ} - \delta_{IJ} \quad (106.19)$$

and similarly, substituting equation (106.18) into (106.16) we obtain:

$$2e_{ij} = \delta_{ij} - c_{ij} \quad (106.20)$$

By using equation (106.5) we can express  $(ds)^2$  as:

$$\begin{aligned} (ds)^2 &= dx_k dx_k = (F_{kI} dX_I)(F_{kJ} dX_J) = \\ (x_{k,I} dX_I)(x_{k,J} dX_J) &= dX_I (F_{kI} F_{kJ}) dX_K = dX_I C_{IJ} dX_K \end{aligned} \quad (106.21)$$

so we have obtained the connection between the deformation tensor  $C_{IJ}$  and the deformation gradient  $F_{kI}$  in the form:

$$C_{IJ} = (F_{kI} F_{kJ}) = x_{k,I} dX_I x_{k,J} dX_J \quad (106.22)$$

Similarly, by using equation (106.7) and the expression for  $(dS)^2$  we can establish the connection between the deformation tensor  $c_{ij}$  and the deformation gradient  $F_{Ki}$  as:

$$\begin{aligned} (dS)^2 &= dS_K dX_K = (F_{Ki} dx_i)(F_{Kj} dx_j) = \\ (X_{K,i} dx_i)(X_{K,j} dx_j) &= dx_i (F_{Ki} F_{Kj}) dx_k = dx_i c_{ij} dx_k \Rightarrow \\ c_{ij} &= (F_{Ki})^{-1} F_{Kj}^{-1} \end{aligned} \quad (106.23)$$

The expressions for the strain tensors in Lagrangian and Eulerian description<sup>5</sup> is obtained from equations (106.19) and (106.20):

$$\text{L: } E_{IJ} = \frac{1}{2} ((F_{kI} F_{kJ}) - \delta_{IJ}) \quad ; \quad \text{E: } e_{ij} = \frac{1}{2} \left( \delta_{ij} - (F_{Ki})^{-1} (F_{Kj})^{-1} \right) \quad (106.24)$$

If one starts from the displacement equation (106.3), referenced to the same axes for both  $X_I$  and  $x_i$

$$x_I = X_I + u_I \quad ; \quad X_I = x_I - u_I$$

the general expression for the Lagrangian strain tensor  $E_{IJ}$  in terms of displacements is:

$$\begin{aligned} E_{IJ} &= \frac{1}{2} ((F_{KI} F_{KJ}) - \delta_{IJ}) = \\ \frac{1}{2} &\left( (\delta_{KI} + u_{K,I}) (\delta_{KJ} + u_{K,J}) - \delta_{IJ} \right) = \\ \frac{1}{2} &\left( \delta_{KI} \delta_{KJ} + \delta_{KI} u_{K,J} + u_{K,I} \delta_{KJ} + u_{K,I} u_{K,J} - \delta_{IJ} \right) = \\ \frac{1}{2} &\left( \delta_{IJ} + u_{I,J} + u_{J,I} + u_{K,I} u_{K,J} - \delta_{IJ} \right) = \\ \frac{1}{2} &\left( u_{I,J} + u_{J,I} + u_{K,I} u_{K,J} \right) \end{aligned} \quad (106.25)$$

<sup>5</sup>Lagrangian format will be denoted by L: while Eulerian format by E:.

Similarly, the general expression for the Eulerian strain tensor  $e_{ij}$  in terms of displacements is:

$$\begin{aligned}
 e_{ij} &= \frac{1}{2} \left( \delta_{ij} - (F_{ki})^{-1} (F_{kj})^{-1} \right) = \\
 &\frac{1}{2} (\delta_{ij} - (\delta_{ki} - u_{k,i}) (\delta_{kj} - u_{k,j})) = \\
 &\frac{1}{2} (\delta_{ij} - \delta_{ki}\delta_{kj} + \delta_{ki}u_{k,j} + u_{k,i}\delta_{kj} - u_{k,i}u_{k,j}) = \\
 &\frac{1}{2} (\delta_{ij} - \delta_{ij} + u_{i,j} + u_{j,i} - u_{k,i}u_{k,j}) = \\
 &\frac{1}{2} (u_{i,j} + u_{j,i} - u_{k,i}u_{k,j})
 \end{aligned} \tag{106.26}$$

It is worthwhile noting that equations (106.25) and (106.26) represent the complete finite strain tensor. They involve only linear and quadratic terms in the components of displacement gradients.

The stretch is a measure of extension of an infinitesimal element and is a function of direction of an element, in either deformed or undeformed configuration. By denoting  $N_I$  a unit vector in the undeformed configuration and  $n_i$  a unit vector in the deformed configuration, we denote material stretch as  $\Lambda_{(N)}$  of those elements with initial direction  $N_I$  and spatial stretch  $\lambda_{(n)}$  of those elements with initial direction  $n_i$ . By dividing equations (106.15) and (106.16) by  $(ds)^2$  and  $(dS)^2$  respectively and by using:

$$N_I = \frac{dX_I}{dS} \quad \text{and} \quad n_i = \frac{dx_i}{ds} \tag{106.27}$$

we obtain the Cartesian form of stretch in the Lagrangian and Eulerian descriptions:

$$\text{L: } \Lambda_{(N)}^2 = \frac{dX_I}{dS} C_{IJ} \frac{dX_J}{dS} \quad \text{and} \quad \text{E: } \lambda_{(n)}^2 = \frac{dx_i}{ds} c_{ij} \frac{dx_j}{ds} \tag{106.28}$$

General strain tensors can be defined by considering a scale function (Hill, 1978) for the stretch. Scale function is any smooth, monotonic function of stretch  $f(\lambda)$  such that:

$$f(\lambda) ; \lambda \in [0, \infty) \text{ subject to } f(1) = 0, f'(1) = 1 \tag{106.29}$$

Scale function is often taken in the form  $(\lambda^{2m} - 1)/2m$ , where  $m$  may have any value. If we choose  $m$  to be an integer, the corresponding strain tensor is:

$$E_{IJ} = \frac{(U_{IJ}^{2m} - \delta_{IJ})}{2m} \quad \text{where} \quad F_{IJ} = R_{IK} U_{KJ} = v_{IK} R_{KJ} \tag{106.30}$$

Table 106.1 shows different Lagrangian strain measures obtained for a particular choice of parameter  $m$ .

In the Eulerian setting, generalized strain tensor is defined as

$$e_{ij} = \frac{(\delta_{ij} - v_{ij}^{2m})}{2m} ; F_{IJ} = R_{IK} U_{KJ} = v_{IK} R_{KJ} \tag{106.31}$$

Table 106.1: Different Lagrangian strain measures.

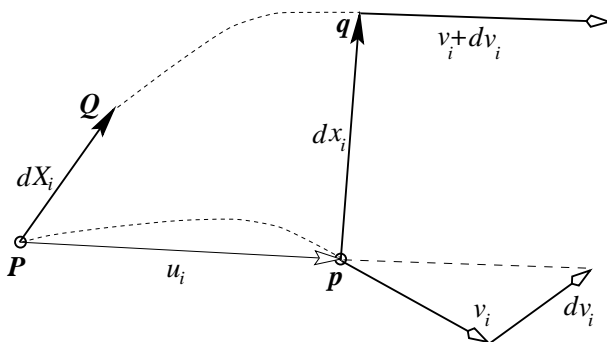
Strain measure name	parameter $m$	expression for $E_{IJ}^m$
Green–Lagrange	1	$E_{IJ}^{GL} = (U_{IJ}^2 - \delta_{IJ})/2$
Almansi	-1	$E_{IJ}^A = (\delta_{IJ} - U_{IJ}^{-2})/2$
Biot	1/2	$E_{IJ}^B = (U_{IJ} - \delta_{IJ})$
Hencky	0	$E_{IJ}^H = \ln(U_{IJ})$

#### 106.2.4 Rate of Deformation Tensor

The *rate of deformation tensor*<sup>6</sup> describes the *tangent motion* in terms of velocity components  $v_i = dx_i/dt$ .

The spatial coordinates are:

$$v_i = v_i(x_1, x_2, x_3, t) \quad (106.32)$$

Figure 106.3: Relative velocity  $dv_i$  of particle  $Q$  at point  $q$  relative to particle  $P$  at point  $p$ .

In Figure 106.3 the dashed lines represents the trajectories of particles  $P$  and  $Q$ . The velocity vectors  $v_i$  at  $p$  and  $v_i + dv_i$  at  $q$  are tangent to the two trajectories. The relative velocity components  $dv_i$  of particle at  $q$  relative to the particle at  $p$  are given by:

$$dv_k = \frac{\partial v_k}{\partial x_m} dx_m = v_{k,m} dx_m = L_{km} dx_m \quad (106.33)$$

<sup>6</sup>Also called *stretch tensor* or *velocity strain*.

The spatial gradient of the velocity  $L_{km}$  can be decomposed as the sum of the symmetric, rate of deformation tensor  $D_{km}$ , and a skew symmetric spin tensor  $W_{km}$  as follows:

$$L_{km} = \frac{1}{2}(L_{km} + L_{mk}) + \frac{1}{2}(L_{km} - L_{mk}) = D_{km} + W_{km} \quad (106.34)$$

where:

$$D_{km} = \frac{1}{2}(L_{km} + L_{mk}) = D_{mk} \quad \text{and} \quad W_{km} = \frac{1}{2}(L_{km} - L_{mk}) = -W_{mk} \quad (106.35)$$

An alternate way of deriving the rate of deformation tensor goes as follows. The rate of change of squared length  $(ds)^2$  is given as:

$$\frac{d(ds)^2}{dt} = 2 \frac{d(ds)}{dt} ds \quad (106.36)$$

since  $(ds)^2 = dx_k dx_k$  it follows:

$$\frac{d(ds)^2}{dt} = 2 \frac{d(dx_k)}{dt} dx_k \quad (106.37)$$

and with  $dx_k = (\partial x_k / \partial X_m) dX_m$  it follows:

$$\frac{d(dx_k)}{dt} = \frac{d\left(\frac{\partial x_k}{\partial X_m} dX_m\right)}{dt} = \frac{d\left(\frac{\partial x_k}{\partial X_m}\right)}{dt} dX_m + \frac{d(dX_m)}{dt} \frac{\partial x_k}{\partial X_m} = \frac{d\left(\frac{\partial x_k}{\partial X_m}\right)}{dt} dX_m \quad (106.38)$$

since  $d(dX_m)/dt \equiv 0$ , because the initial relative position vector  $dX_m$  does not change with time. By interchanging the order of differentiation we get:

$$\frac{d(dx_k)}{dt} = dv_k = \frac{d\left(\frac{\partial x_k}{\partial X_m}\right)}{dt} dX_m = \frac{\partial v_k}{\partial X_m} dX_m \quad \text{where} \quad v_k = \frac{\partial x_k}{\partial t} \quad (106.39)$$

From equation (106.33)  $dv_k = L_{km} dx_m$  and equation (106.39) it follows that:

$$\frac{\partial v_k}{\partial X_m} dX_m = L_{km} dx_m \Rightarrow \frac{d(dx_k)}{dt} = dv_k = L_{km} dx_m = v_{k,m} dx_m \quad (106.40)$$

and then the equation (106.37) becomes:

$$\begin{aligned} \frac{d(ds)^2}{dt} &= 2 \frac{d(dx_k)}{dt} dx_k = 2 dx_k v_{k,m} dx_m dx_k = 2 dx_k L_{km} dx_m dx_k = \\ &= 2 dx_k D_{km} dx_m dx_k + 2 dx_k W_{km} dx_m dx_k = 2 dx_k D_{km} dx_m dx_k \end{aligned} \quad (106.41)$$

since  $dx_k dx_m \equiv dx_m dx_k$  and  $W_{km}$  is skew symmetric such that  $W_{km} = -W_{mk}$ . Finally we obtain:

$$\frac{d(ds)^2}{dt} = 2 dx_k D_{km} dx_m \quad (106.42)$$

and thus it follows that the rate of change of the squared length  $(ds)^2$  of the material instantaneously occupying any infinitesimal relative position  $dx_k$  at point  $p$  is determined by the tensor  $D_{km}$  at point  $p$ .

In order to compare the strain rate to the rate of deformation, we differentiate equation (106.15) with respect to time:

$$\begin{aligned} \frac{d((ds)^2 - (dS)^2)}{dt} &= 2 \frac{d(dX_I E_{IJ} dX_J)}{dt} = \\ &= \frac{d((ds)^2)}{dt} = 2dX_I \frac{d(E_{IJ})}{dt} dX_J \end{aligned} \quad (106.43)$$

since  $(dS)^2$  and  $dX_I$  are constant through time. From the equations (106.42) and (106.43) it follows that:

$$\frac{d(ds)^2}{dt} = 2dx_k D_{km} dx_m d = 2(dX_I F_{Ik}) D_{km} (F_{mJ} dX_J) = 2dX_I (F_{Ik} D_{km} F_{mJ}) dX_J \quad (106.44)$$

and from equations (106.43) and (106.44) it follows that:

$$\frac{dE_{IJ}}{dt} = F_{Ik} D_{km} F_{mJ} \quad (106.45)$$

or inversely:

$$D_{km} = (F_{Ik})^{-1} \frac{dE_{IJ}}{dt} (F_{mJ})^{-1} \quad (106.46)$$

To obtain the rate of change of the deformation gradient we start from equations (106.4) and differentiate it with respect to time:

$$\begin{aligned} \frac{dF_{kK}}{dt} &= \frac{d\left(\frac{\partial x_k}{\partial X_K}\right)}{dt} = \frac{\partial\left(\frac{dx_k}{dt}\right)}{\partial X_K} = \frac{\partial v_k}{\partial X_K} = \frac{\partial v_k}{\partial x_m} \frac{\partial x_m}{\partial X_K} = v_{k,m} x_{m,K} = \frac{dx_{k,K}}{dt} = \\ &= L_{km} F_{mK} = \dot{F}_{kK} \end{aligned} \quad (106.47)$$

or inversely:

$$\begin{aligned} v_{k,m} &= \frac{dx_{k,K}}{dt} X_{K,m} = \frac{dF_{kK}}{dt} (F_{Km})^{-1} = \\ &= \dot{F}_{kK} (F_{Km})^{-1} = L_{km} \end{aligned} \quad (106.48)$$

## 106.3 Constitutive Relations: Hyperelasticity

### 106.3.1 Introduction

A material is called *hyperelastic* or *Green elastic*, if there exists an *elastic potential function*  $W$ , also called the *strain energy function per unit volume of the undeformed configuration*, which represents a scalar function of strain of deformation tensors, whose derivatives with respect to a strain component determines the corresponding stress component. The most general form of the elastic potential function, is described in equation 106.49, with restriction to pure mechanical theory, by using the *axiom of locality* and the *axiom of entropy production*<sup>7</sup>:

$$W = W(X_K, F_{kK}) \quad (106.49)$$

By using the *axiom of material frame indifference*<sup>8</sup>, we conclude that  $W$  depends only on  $X_K$  and  $C_{IJ}$ , that is:

$$W = W(X_K, C_{IJ}) \quad \text{or:} \quad W = W(X_K, c_{ij}) \quad (106.50)$$

By assuming hyperelastic response, the following are the constitutive equations for the material stress tensors:

- 2. Piola–Kirchhoff stress tensor:

$$S_{IJ} = 2 \frac{\partial W}{\partial C_{IJ}} \quad (106.51)$$

- Mandel stress tensor:

$$T_{IJ} = C_{IK} S_{KJ} = 2C_{IK} \frac{\partial W}{\partial C_{KJ}} \quad (106.52)$$

- 1. Piola–Kirchhoff stress tensor

$$P_{iJ} = S_{IJ}(F_{il})^t = 2 \frac{\partial W}{\partial C_{IJ}}(F_{il})^t \quad (106.53)$$

and the spatial, Kirchhoff stress tensor is defined as:

- Kirchhoff stress tensor

$$\tau_{ij} = 2 \frac{\partial W}{\partial b_{ij}} = 2 F_{iA}(F_{jB})^t \frac{\partial W}{\partial C_{AB}} = F_{iA}(F_{jB})^t S_{AB} \quad (106.54)$$

<sup>7</sup>See Marsden and Hughes (1983) pp. 190.

<sup>8</sup>See Marsden and Hughes (1983) pp. 194.

Material tangent stiffness relation is defined from:

$$dS_{IJ} = 2 \frac{\partial^2 W}{\partial C_{IJ} \partial C_{KL}} dC_{KL} = \frac{1}{2} \mathcal{L}_{IJKL} dC_{KL} \quad (106.55)$$

where

$$\mathcal{L}_{IJKL} = 4 \frac{\partial^2 W}{\partial C_{IJ} \partial C_{KL}} \quad (106.56)$$

The spatial tangent stiffness tensor  $\mathcal{E}_{ijkl}$  is obtained by the following *push-forward* operation with the deformation gradient:

$$\mathcal{E}_{ijkl} = F_{il} F_{lj} (F_{kk})^t (F_{ll})^t \mathcal{L}_{IJKL} \quad (106.57)$$

### 106.3.2 Isotropic Hyperelasticity

In the case of material isotropy, the strain energy function  $W(X_K, C_{IJ})$  belongs to the class of isotropic, invariant scalar functions. It satisfies the relation:

$$W(X_K, C_{KL}) = W(X_K, Q_{KI} C_{IJ} (Q_{JL})^t) \quad (106.58)$$

where  $Q_{KI}$  is the proper orthogonal transformation. If we choose  $Q_{KI} = R_{KI}$ , where  $R_{KI}$  is the orthogonal rotation transformation, defined by the polar decomposition theorem in equation (106.13), then:

$$W(X_K, C_{KL}) = W(X_K, U_{KL}) = W(X_K, v_{kl}) \quad (106.59)$$

Right and left stretch tensors,  $U_{KL}$ ,  $v_{kl}$  have the same principal values<sup>9</sup>  $\lambda_i$  ;  $i = \overline{1,3}$  so the strain energy function  $W$  can be represented in terms of principal stretches, or similarly in terms of principal invariants of deformation tensor:

$$W = W(X_K, \lambda_1, \lambda_2, \lambda_3) = W(X_K, I_1, I_2, I_3) \quad (106.60)$$

where:

$$\begin{aligned} I_1 &\stackrel{\text{def}}{=} C_{II} \\ I_2 &\stackrel{\text{def}}{=} \frac{1}{2} (I_1^2 - C_{IJ} C_{JI}) \\ I_3 &\stackrel{\text{def}}{=} \det(C_{IJ}) = \frac{1}{6} e_{IJK} e_{PQR} C_{IP} C_{IQ} C_{KR} = J^2 \end{aligned} \quad (106.61)$$

Left and right Cauchy–Green tensors were defined by equations (106.22) and (106.23), respectively as:

$$C_{IJ} = (F_{kI})^t F_{kj} \quad ; \quad (c^{-1})_{ij} = b_{ij} = F_{iK} (F_{jk})^t \quad (106.62)$$

---

<sup>9</sup>Principal stretches.

The spectral<sup>10</sup> decomposition theorem for symmetric positive definite tensors<sup>11</sup> states that:

$$C_{IJ} = \lambda_A^2 \left( N_I^{(A)} N_J^{(A)} \right)_A \quad \text{where} \quad A = \overline{1, 3} \quad (106.63)$$

and  $N_I$  are the eigenvectors<sup>12</sup> of  $C_{IJ}$ . Values  $\lambda_A^2$  are the roots of the characteristic polynomial

$$P(\lambda_A^2) \stackrel{\text{def}}{=} -\lambda_A^6 + I_1 \lambda_A^6 - I_2 \lambda_A^4 + I_3 = 0 \quad (106.64)$$

It should be noted that no summation is implied over indices in parenthesis<sup>13</sup>.

The mapping of the eigenvectors can be deduced from equation (106.5) and is given by

$$\lambda_{(A)} n_i^{(A)} = F_{iJ} N_J^{(A)} \quad (106.65)$$

where  $\|n_i^{(A)}\| \equiv 1$ . The spectral decomposition of  $F_{iJ}$ ,  $R_{iJ}$  and  $b_{ij}$  is then given by

$$F_{iJ} = \lambda_A \left( n_i^{(A)} N_J^{(A)} \right)_A \quad (106.66)$$

$$R_{iJ} = \sum_{A=1}^3 n_i^{(A)} N_J^{(A)} \quad (106.67)$$

$$b_{ij} = \lambda_A^2 \left( n_i^{(A)} n_j^{(A)} \right)_A \quad (106.68)$$

Spectral decomposition from equation (106.63) is valid for the case of non-equal principal stretches, i.e.  $\lambda_1 \neq \lambda_2 \neq \lambda_3$ . If two or all three principal stretches are equal, we shall introduce a small perturbation to the numerical values for principal stretches in order to make them distinct. The case of two or all three values of principal stretches being equal is theoretically possible and results for example from standard triaxial tests or isotropic compression tests. However, we are never certain about equivalence of two numerical numbers, because of the finite precision arithmetics involved in calculation of these numbers. From the numerical point of view, two number are equal if the difference between them is smaller than the machine precision (*macheps*) specific to the computer platform on which computations are performed. Our perturbation will be a function of the *macheps*.

The characteristic polynomial  $P(\lambda_A^2)$  from equation (106.64) can be solved<sup>14</sup> for  $\lambda_A$ :

$$\lambda_A = \frac{1}{\sqrt{3}} \sqrt{I_1 + 2\sqrt{I_1^2 - 3I_2} \cos\left(\frac{\Theta + 2\pi A}{3}\right)} \quad (106.69)$$

---

<sup>10</sup>See Simo and fTaylor (1991).

<sup>11</sup>Cauchy–Green tensor  $C_{IJ}$  for example.

<sup>12</sup>So that  $\|N_I\| = 1$ .

<sup>13</sup>For example, in the present case  $N_I^{(A)}$  is the  $A$ th eigenvector with members  $N_1^{(A)}$ ,  $N_2^{(A)}$  and  $N_3^{(A)}$ , so that the actual equation  $C_{IJ} = \lambda_A^2 \left( N_I^{(A)} N_J^{(A)} \right)_A$  can also be written as  $C_{IJ} = \sum_{A=1}^{A=3} \lambda_A^2 N_I^{(A)} N_J^{(A)}$ . In order to follow the consistency of indicial notation in this work, we shall make an effort to represent all the tensorial equations in indicial form.

<sup>14</sup>See also Morman (1986) and Schellekens and Schellekens and Parisch (1994).

where

$$\Theta = \arccos \frac{2I_1^3 - 9I_1I_2 + 27I_3}{2\sqrt{(I_1^2 - 3I_2)^3}} \quad (106.70)$$

Recently, Ting (1985) and Morman (1986) have used Serrin's representation theorem in order to devise a useful representation for generalized strain tensors<sup>15</sup>  $E_{IJ}$  and  $e_{ij}$  through  $C_{IJ}^m$  and  $b_{ij}^m$ . Morman (1986) has shown that  $b_{ij}^m$  can be stated as

$$b_{ij}^m = \lambda_A^{2m} \left( \frac{(b^2)_{ij} - (I_1 - \lambda_{(A)}^2) b_{ij} + I_3 \lambda_{(A)}^{-2} \delta_{ij}}{2\lambda_{(A)}^4 - I_1 \lambda_{(A)}^2 + I_3 \lambda_{(A)}^{-2}} \right)_A \quad (106.71)$$

By comparing equations (106.71) and (106.68) it follows that the Eulerian eigendiad  $n_i^{(A)} n_j^{(A)}$  can be written as

$$n_i^{(A)} n_j^{(A)} = \frac{(b^2)_{ij} - (I_1 - \lambda_{(A)}^2) b_{ij} + I_3 \lambda_{(A)}^{-2} \delta_{ij}}{2\lambda_{(A)}^4 - I_1 \lambda_{(A)}^2 + I_3 \lambda_{(A)}^{-2}} \quad (106.72)$$

The Lagrangian eigendiad  $N_I^{(A)} N_J^{(A)}$ , from equation (106.63), can be derived, if one substitutes mapping of the eigenvectors, (106.65), into equation (106.72) to get:

$$N_I^{(A)} N_J^{(A)} = \lambda_{(A)}^2 \frac{C_{IJ} - (I_1 - \lambda_{(A)}^2) \delta_{IJ} + I_3 \lambda_{(A)}^{-2} (C^{-1})_{IJ}}{2\lambda_{(A)}^4 - I_1 \lambda_{(A)}^2 + I_3 \lambda_{(A)}^{-2}} \quad (106.73)$$

where it was used that:

$$C_{IJ} = (F_{iI})^{-1} (b^2)_{ij} (F_{jJ})^{-t} \quad (106.74)$$

$$\delta_{IJ} = (F_{iI})^{-1} b_{ij} (F_{jJ})^{-t} \quad (106.75)$$

$$(C^{-1})_{IJ} = (F_{iI})^{-1} \delta_{ij} (F_{jJ})^{-t} \quad (106.76)$$

It should be noted that the denominator in equations (106.72) and (106.73) can be written as:

$$2\lambda_{(A)}^4 - I_1 \lambda_{(A)}^2 + I_3 \lambda_{(A)}^{-2} = (\lambda_{(A)}^2 - \lambda_{(B)}^2) (\lambda_{(A)}^2 - \lambda_{(C)}^2) \stackrel{\text{def}}{=} D_{(A)} \quad (106.77)$$

where indices  $A, B, C$  are cyclic permutations of 1, 2, 3. It follows directly from the definition of  $D_{(A)}$  in equation (106.77) that  $\lambda_1 \neq \lambda_2 \neq \lambda_3 \Rightarrow D_{(A)} \neq 0$  for equations (106.72) and (106.73) to be valid. Similarly to equations (106.63) and (106.68) we can obtain:

$$(C^{-1})_{IJ} = \lambda_A^{-2} \left( N_I^{(A)} N_J^{(A)} \right)_A \quad (106.78)$$

$$(b^{-1})_{ij} = \lambda_A^{-2} \left( n_i^{(A)} n_j^{(A)} \right)_A \quad (106.79)$$

<sup>15</sup>Defined by equations (106.30) and (106.31).

### 106.3.3 Volumetric–Isochoric Decomposition of Deformation

It proves useful to separate deformation in volumetric and isochoric parts by a multiplicative split of a deformation gradient as

$$F_{il} = \tilde{F}_{i\beta} {}^{vol}F_{\beta I} \quad \text{where} \quad \tilde{F}_{i\beta} = F_{il} J^{-\frac{1}{3}} \quad ; \quad {}^{vol}F_{\beta I} = J^{\frac{1}{3}} \delta_{\beta I} \quad (106.80)$$

where  $x_\beta$  represents an intermediate configuration such that deformation  $X_I \rightarrow x_\beta$  is purely volumetric and  $x_\beta \rightarrow x_i$  is purely isochoric. It also follows from equation (106.80) that  $\tilde{F}_{\beta I}$  and  $F_{il}$  have the same eigenvectors.

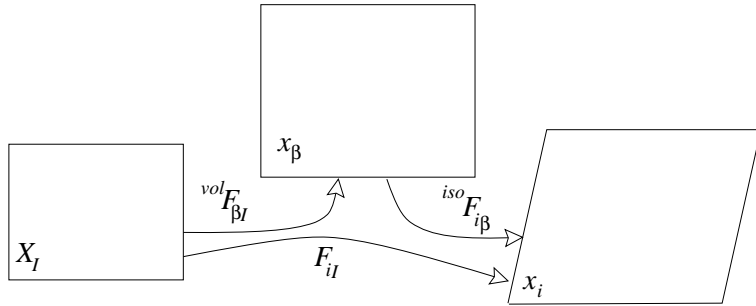


Figure 106.4: Volumetric isochoric decomposition of deformation.

The isochoric part of the Green deformation tensor  $C_{IJ}$ , defined in equation (106.63) can be defined as

$$\tilde{C}_{IJ} = J^{-\frac{2}{3}} C_{IJ} = \tilde{\lambda}_A^2 \left( N_I^{(A)} N_J^{(A)} \right)_A \quad (106.81)$$

while the isochoric part of the Finger deformation tensor  $b_{ij}$  can be defined similarly as

$$\tilde{b}_{ij} = J^{-\frac{2}{3}} b_{ij} = \tilde{\lambda}_A^2 \left( n_i^{(A)} n_j^{(A)} \right)_A \quad (106.82)$$

where the isochoric principal stretches are defined as

$$\tilde{\lambda}_A = J^{-\frac{1}{3}} \lambda_A = (\lambda_1 \lambda_2 \lambda_3)^{-\frac{1}{3}} \lambda_A \quad (106.83)$$

The free energy  $W$  is then decomposed additively as:

$$W(X_K, \lambda_{(A)}) = {}^{iso}W(X_K, \tilde{\lambda}_{(A)}) + {}^{vol}W(X_K, J) \quad (106.84)$$

### 106.3.4 Simo–Serrin's Formulation

In Section (106.3.2) we have presented the most general form of the isotropic strain energy function  $W$  in terms of principal stretches:

$$W = W(X_K, \lambda_1, \lambda_2, \lambda_3, ) \quad (106.85)$$

It was also shown in Section (106.3.1) that it is necessary to calculate the gradient  $\partial W / \partial C_{IJ}$  in order

to obtain 2. Piola–Kirchhoff stress tensor  $S_{IJ}$  and accordingly other stress measures. Likewise, it was shown that the material tangent stiffness tensor  $\mathcal{L}_{IJKL}$  (as well as the spatial tangent stiffness tensor  $\mathcal{E}_{ijkl}$ ) requires second order derivatives of strain energy function  $\partial^2 W/(\partial C_{IJ} \partial C_{KL})$ . In order to obtain these quantities we introduce<sup>16</sup> a second order tensor  $M_{IJ}^{(A)}$

$$\begin{aligned} M_{IJ}^{(A)} &\stackrel{\text{def}}{=} \lambda_{(A)}^{-2} N_I^{(A)} N_J^{(A)} & (106.86) \\ &= (F_{il})^{-1} \left( n_i^{(A)} n_j^{(A)} \right) (F_{jl})^{-t} \\ &= \frac{1}{D_{(A)}} \left( C_{IJ} - \left( I_1 - \lambda_{(A)}^2 \right) \delta_{IJ} + I_3 \lambda_{(A)}^{-2} (C^{-1})_{IJ} \right) \quad \text{from (106.73)} \end{aligned}$$

where  $D_{(A)}$  was defined by equation (106.77). With  $M_{IJ}^{(A)}$  defined by equation (106.86), we get from equation (106.63) that:

$$C_{IJ} = \lambda_A^4 \left( M_{IJ}^{(A)} \right)_A \quad (106.87)$$

and also from equation (106.78) it follows that:

$$(C^{-1})_{IJ} = M_{IJ}^{(1)} + M_{IJ}^{(2)} + M_{IJ}^{(3)} \quad (106.88)$$

It can also be concluded that:

$$\delta_{IJ} = \lambda_{(1)}^2 M_{IJ}^{(1)} + \lambda_{(2)}^2 M_{IJ}^{(2)} + \lambda_{(3)}^2 M_{IJ}^{(3)} = \lambda_A^2 \left( M_{IJ}^{(A)} \right)_A \quad (106.89)$$

since, from the orthogonal properties of eigenvectors

$$\delta_{IJ} = \sum_{A=1}^3 N_I^{(A)} N_J^{(A)} = \left( N_I^{(A)} \right)_A \left( N_J^{(A)} \right)_A \quad (106.90)$$

We are now in a position to define the *Simo–Serrin* fourth order tensor  $\mathcal{M}_{IJKL}$  as:

$$\begin{aligned} \mathcal{M}_{IJKL}^{(A)} &\stackrel{\text{def}}{=} \frac{\partial M_{IJ}^{(A)}}{\partial C_{KL}} = \\ &= \frac{1}{D_{(A)}} \left( I_{IJKL} - \delta_{KL} \delta_{IJ} + \lambda_{(A)}^2 \left( \delta_{IJ} M_{KL}^{(A)} + M_{IJ}^{(A)} \delta_{KL} \right) + \right. \\ &+ I_3 \lambda_{(A)}^{-2} \left( (C^{-1})_{IJ} (C^{-1})_{KL} + \frac{1}{2} \left( (C^{-1})_{IK} (C^{-1})_{JL} + (C^{-1})_{IL} (C^{-1})_{JK} \right) \right) - \\ &- \lambda_{(A)}^{-2} I_3 \left( (C^{-1})_{IJ} M_{KL}^{(A)} + M_{IJ}^{(A)} (C^{-1})_{KL} \right) - D'_{(A)} M_{IJ}^{(A)} M_{KL}^{(A)} \end{aligned} \quad (106.91)$$

Complete derivation of  $\mathcal{M}_{IJKL}$  is given in Appendix (704.2).

---

<sup>16</sup>See Runesson (1996).

### 106.3.5 Stress Measures

In Section (106.3.1) we have defined various stress measures in terms of derivatives of the free energy function  $W$ . With the free energy function decomposition, as defined in equation (106.84) we can appropriately decompose all the previously defined stress measures:

- 2. Piola–Kirchhoff stress tensor:

$$\begin{aligned} S_{IJ} &= 2 \frac{\partial W}{\partial C_{IJ}} = 2 \frac{\partial^{iso}W}{\partial C_{IJ}} + 2 \frac{\partial^{vol}W}{\partial C_{IJ}} \\ &= {}^{iso}S_{IJ} + {}^{vol}S_{IJ} \end{aligned} \quad (106.92)$$

- Mandel stress tensor:

$$\begin{aligned} T_{IJ} &= C_{IK}S_{KJ} = 2C_{IK}\frac{\partial W}{\partial C_{KJ}} = 2C_{IK}\frac{\partial^{iso}W}{\partial C_{KJ}} + 2C_{IK}\frac{\partial^{vol}W}{\partial C_{KJ}} \\ &= {}^{iso}T_{IJ} + {}^{vol}T_{IJ} \end{aligned} \quad (106.93)$$

- 1. Piola–Kirchhoff stress tensor

$$\begin{aligned} P_{iJ} &= S_{IJ}(F_{il})^t = 2 \frac{\partial W}{\partial C_{IJ}}(F_{il})^t = 2 \frac{\partial^{iso}W}{\partial C_{IJ}}(F_{il})^t + 2 \frac{\partial^{vol}W}{\partial C_{IJ}}(F_{il})^t \\ &= {}^{iso}P_{iJ} + {}^{vol}P_{iJ} \end{aligned} \quad (106.94)$$

- Kirchhoff stress tensor

$$\begin{aligned} \tau_{ab} &= 2 \frac{\partial W}{\partial e_{ij}} = F_{al}(F_{bj})^t S_{IJ} = 2F_{al}(F_{bj})^t \frac{\partial^{iso}W}{\partial C_{IJ}} + 2F_{al}(F_{bj})^t \frac{\partial^{vol}W}{\partial C_{IJ}} \\ &= F_{al}(F_{bj})^t {}^{iso}S_{IJ} + F_{al}(F_{bj})^t {}^{vol}S_{IJ} \\ &= {}^{iso}\tau_{ab} + {}^{vol}\tau_{ab} \end{aligned} \quad (106.95)$$

The derivative of the volumetric part of the free energy function is

$$\frac{\partial^{vol}W(J)}{\partial C_{IJ}} = \frac{\partial^{vol}W(J)}{\partial J} \frac{\partial J}{\partial C_{IJ}} = \frac{1}{2} \frac{\partial^{vol}W(J)}{\partial J} J (C^{-1})_{IJ} \quad (106.96)$$

where equation (704.9) was used, while the derivative of the isochoric part of the free energy function yields

$$\frac{\partial^{iso}W(\tilde{\lambda}_{(A)})}{\partial C_{IJ}} = \frac{\partial^{iso}W(\tilde{\lambda}_{(A)})}{\partial \lambda_{(A)}} \frac{\partial \lambda_{(A)}}{\partial C_{IJ}} = \frac{1}{2} \frac{\partial^{iso}W(\lambda_{(A)})}{\partial \lambda_{(A)}} \lambda_{(A)} (M_{IJ}^{(A)})_A = \frac{1}{2} w_A (M_{IJ}^{(A)})_A \quad (106.97)$$

where equation (704.7) was used and  $w_A$  is derived in Appendix 704.5 as:

$$w_A = \frac{\partial^{iso}W(\lambda_{(A)})}{\partial \tilde{\lambda}_B} \frac{\partial \tilde{\lambda}_B}{\partial \lambda_{(A)}} \tilde{\lambda}_{(A)} = -\frac{1}{3} \frac{\partial^{iso}W(\tilde{\lambda}_{(A)})}{\partial \tilde{\lambda}_B} \tilde{\lambda}_B + \frac{\partial^{iso}W(\tilde{\lambda}_{(A)})}{\partial \tilde{\lambda}_{(A)}} \tilde{\lambda}_{(A)} \quad (106.98)$$

The decomposed 2. Piola–Kirchhoff stress tensor is

$$\begin{aligned} S_{IJ} &= {}^{vol}S_{IJ} + {}^{iso}S_{IJ} \\ &= \frac{\partial^{vol}W(J)}{\partial J} J (C^{-1})_{IJ} + w_A (M_{IJ}^{(A)})_A \end{aligned} \quad (106.99)$$

The derivative of the free energy is then:

$$\begin{aligned} \frac{\partial W(\lambda_{(A)})}{\partial C_{IJ}} &= \frac{\partial^{vol}W(\lambda_{(A)})}{\partial C_{IJ}} + \frac{\partial^{iso}W(\lambda_{(A)})}{\partial C_{IJ}} \\ &= \frac{1}{2} \frac{\partial^{vol}W(J)}{\partial J} J (C^{-1})_{IJ} + \frac{1}{2} w_A (M_{IJ}^{(A)})_A \end{aligned} \quad (106.100)$$

It is obvious that the only material dependent parts are derivatives in the form  $\partial^{vol}W/\partial J$  and  $w_A$ , while the rest is independent of which hyperelastic material model we choose.

### 106.3.6 Tangent Stiffness Operator

The free energy function decomposition (106.84) is used together with the appropriate definitions made in section (106.3.1) toward the tangent stiffness operator decomposition

$$\mathcal{L}_{IJKL} = {}^{vol}\mathcal{L}_{IJKL} + {}^{iso}\mathcal{L}_{IJKL} = 4 \frac{\partial^2({}^{vol}W)}{\partial C_{IJ} \partial C_{KL}} + 4 \frac{\partial^2({}^{iso}W)}{\partial C_{IJ} \partial C_{KL}} \quad (106.101)$$

The volumetric part  $\partial^2({}^{vol}W)/(\partial C_{IJ} \partial C_{KL})$  can be written as:

$$\begin{aligned} \frac{\partial^2{}^{vol}W}{\partial C_{IJ} \partial C_{KL}} &= \\ \frac{1}{4} \left( J^2 \frac{\partial^2({}^{vol}W)}{\partial J \partial J} + J \frac{\partial({}^{vol}W)}{\partial J} \right) (C^{-1})_{KL} (C^{-1})_{IJ} + \frac{1}{2} J \frac{\partial({}^{vol}W)}{\partial J} I_{IJKL}^{(C^{-1})} & \end{aligned} \quad (106.102)$$

and the complete derivation is again given in appendix 704.3.

The isochoric part  $\partial^2 ({}^{iso}W)/(\partial C_{IJ} \partial C_{KL})$  can be written in the following form:

$$\frac{\partial^2 {}^{iso}W(\lambda_{(A)})}{\partial C_{IJ} \partial C_{KL}} = \frac{1}{4} Y_{AB} (M_{KL}^{(B)})_B (M_{IJ}^{(A)})_A + \frac{1}{2} w_A (\mathcal{M}_{IJKL}^{(A)})_A \quad (106.103)$$

and the complete derivation is given in the appendix (704.4).

Finally, one can write the volumetric and isochoric parts of the tangent stiffness tensors as:

$${}^{vol}\mathcal{L}_{IJKL} =$$

$$J^2 \frac{\partial^2 {}^{vol}W(J)}{\partial J \partial J} (C^{-1})_{KL} (C^{-1})_{IJ} + J \frac{\partial {}^{vol}W(J)}{\partial J} (C^{-1})_{KL} (C^{-1})_{IJ} + 2J \frac{\partial {}^{vol}W(J)}{\partial J} I_{IJKL}^{(C^{-1})} \quad (106.104)$$

$$\mathcal{L}_{IJKL}^{iso} = Y_{AB} (M_{KL}^{(B)})_B (M_{IJ}^{(A)})_A + 2 w_A (\mathcal{M}_{IJKL}^{(A)})_A \quad (106.105)$$

In a similar manner to the stress definitions it is clear that the only material model dependent parts are  $Y_{AB}$  and  $w_A$ . The remaining second and fourth order tensors  $M_{IJ}^{(A)}$  and  $\mathcal{M}_{IJKL}^{(A)}$  are independent of the choice of the material model. This observation has a practical consequence in that it is possible to create a *template derivations* for various hyperelastic isotropic material models. Only first and second derivatives of strain energy function with respect to isochoric principal stretches ( $\tilde{\lambda}_A$ ) and Jacobian ( $J$ ) are needed in addition to the independent tensors, for the determination of various stress and tangent stiffness tensors.

### 106.3.7 Isotropic Hyperelastic Models

The strain energy function for isotropic solid in terms of principal stretches is represented as:

$$W = W(\lambda_1, \lambda_2, \lambda_3) \quad (106.106)$$

The only restriction is that  $W$  is a symmetric function of  $\lambda_1, \lambda_2, \lambda_3$ , although an appropriate natural configuration condition requires that:

$$W(1, 1, 1) = 0 \quad \text{and} \quad \frac{\partial W(1, 1, 1)}{\partial \lambda_i} = 0 \quad (106.107)$$

The strain energy function  $W$  can either be regarded as a function of principal stretches or the principal invariants of stretches<sup>17</sup>:

$$\begin{aligned} I_1 &= \lambda_1^2 + \lambda_2^2 + \lambda_3^2 \\ I_2 &= \lambda_2^2 \lambda_3^2 + \lambda_3^2 \lambda_1^2 + \lambda_1^2 \lambda_2^2 \\ I_3 &= \lambda_1^2 \lambda_2^2 \lambda_3^2 \end{aligned} \quad (106.108)$$

<sup>17</sup>See also equation (106.61).

A slightly more general formulation is obtained by using principal stretches in the strain energy function definition. A widely exploited family of compressible hyperelastic models<sup>18</sup> are defined (Ogden, 1984) as an infinite series in powers of  $(I_1 - 3)$ ,  $(I_2 - 3)$  and  $(I_3 - 1)$  as:

$$W = \sum_{p,q,r=0}^{N \rightarrow \infty} c_{pqr} (I_1 - 3)^p (I_2 - 3)^q (I_3 - 1)^r \quad (106.109)$$

The regularity condition that  $W$  is continuously differentiable an infinitely number of times is satisfied. The requirement that energy vanishes in the reference configuration is met provided  $c_{000} = 0$ . Reference configuration is stress free iff  $c_{100} + 2c_{010} + c_{001} = 0$ . Isochoric deviatoric decoupling is possible by setting  $c_{pqr} = 0$  ( $r = 1, 2, 3, \dots$ ) and  $c_{pqr} = 0$  ( $p, q = 1, 2, 3, \dots$ ) to obtain:

$$W = {}^{iso}W + {}^{vol}W \quad (106.110)$$

where:

$$\begin{aligned} {}^{iso}W &= \sum_{p,q=0}^{N \rightarrow \infty} c_{pq0} (I_1 - 3)^p (I_2 - 3)^q \\ {}^{vol}W &= \sum_{r=0}^{N \rightarrow \infty} c_{00r} (I_3 - 1)^r \end{aligned} \quad (106.111)$$

In what follows, we will present a number of widely used strain energy functions for isotropic elastic solids.

#### 106.3.7.1 Ogden Model

A very general set of hyperelastic models was defined by Ogden (1984). The strain energy is expressed as a function of principal stretches as:

$$W = \sum_{r=1}^{N \rightarrow \infty} \frac{c_r}{\mu_r} (\lambda_1^{\mu_r} + \lambda_2^{\mu_r} + \lambda_3^{\mu_r} - 3) \quad (106.112)$$

The isochoric strain energy function can be written as:

$${}^{iso}W = \sum_{r=1}^{N \rightarrow \infty} \frac{c_r}{\mu_r} (\tilde{\lambda}_1^{\mu_r} + \tilde{\lambda}_2^{\mu_r} + \tilde{\lambda}_3^{\mu_r} - 1) \quad (106.113)$$

where the following was used  $\tilde{\lambda}_i = J^{-\frac{1}{3}} \lambda_i$ .

Derivatives needed for building tensors  $w_A$  and  $Y_{AB}$  are given by the following formulae:

$$\frac{\partial {}^{iso}W}{\partial \tilde{\lambda}_A} = \sum_{r=1}^{N \rightarrow \infty} c_r (\tilde{\lambda}_A)^{\mu_r - 1} \quad (106.114)$$

---

<sup>18</sup>Used mainly for rubber-like materials.

$$\frac{\partial^2 (\text{iso}W)}{\partial \tilde{\lambda}_A^2} = \sum_{r=1}^{N \rightarrow \infty} c_r (\mu_r - 1) \left( \tilde{\lambda}_A \right)^{\mu_r - 2} \quad (106.115)$$

$$\frac{\partial^2 (\text{iso}W)}{\partial \tilde{\lambda}_A \partial \tilde{\lambda}_B} = 0 \quad (106.116)$$

### 106.3.7.2 Neo-Hookean Model

The general isotropic hyperelastic model defined in terms of invariants of principal stretches contains the Neo-Hookean model as special cases. The isochoric part of Neo-Hookean isotropic elastic model can be obtained by selecting  $N = 1$ ,  $q = 0$ ,  $c_{p00} = G/2$ , to get:

$$\text{iso}W = \frac{G}{2} \left( \tilde{\lambda}_1^2 + \tilde{\lambda}_2^2 + \tilde{\lambda}_3^2 - 3 \right) \quad (106.117)$$

while the volumetric part can be defined by choosing  $N = 2$ ,  $c_{001} = 0$ ,  $c_{002} = K_b/2$ , as:

$$\text{vol}W = \frac{K_b}{2} \left( \lambda_1^2 \lambda_2^2 \lambda_3^2 - 1 \right)^2 = \frac{K_b}{2} \left( J^2 - 1 \right)^2 \quad (106.118)$$

where  $G$  and  $K_b$  are the shear and bulk moduli respectively.

Derivatives needed for building tensors  $w_A$  and  $Y_{AB}$  are given by the following formulae:

$$\frac{\partial \text{iso}W}{\partial \tilde{\lambda}_A} = G \tilde{\lambda}_A \quad (106.119)$$

$$\frac{\partial^2 (\text{iso}W)}{\partial \tilde{\lambda}_A^2} = G \quad (106.120)$$

$$\frac{\partial^2 (\text{iso}W)}{\partial \tilde{\lambda}_A \partial \tilde{\lambda}_B} = 0 \quad (106.121)$$

### 106.3.7.3 Mooney–Rivlin Model

Mooney proposed a strain energy function for isochoric behavior of the form:

$$\begin{aligned} \text{iso}W &= \sum_{n=0}^{N \rightarrow \infty} \left( a_n \left( \tilde{\lambda}_1^{2n} + \tilde{\lambda}_2^{2n} + \tilde{\lambda}_3^{2n} - 3 \right) + b_n \left( \tilde{\lambda}_1^{-2n} + \tilde{\lambda}_2^{-2n} + \tilde{\lambda}_3^{-2n} - 3 \right) \right) \\ &= \sum_{n=0}^{N \rightarrow \infty} \left( a_n \left( \tilde{\lambda}_1^{2n} + \tilde{\lambda}_2^{2n} + \tilde{\lambda}_3^{2n} - 3 \right) \right. \\ &\quad \left. + b_n \left( \left( \tilde{\lambda}_2 \tilde{\lambda}_3 \right)^{-2n} + \left( \tilde{\lambda}_3 \tilde{\lambda}_1 \right)^{-2n} + \left( \tilde{\lambda}_1 \tilde{\lambda}_2 \right)^{-2n} - 3 \right) \right) \end{aligned} \quad (106.122)$$

with  $a_n$  and  $b_n$  being the material parameters and a volume preserving constrain  $\lambda_a = 1/(\lambda_b \lambda_c)$ , and  $a, b, c$  are cyclic permutations of  $(1, 2, 3)$ . A more general form was proposed by Rivlin:

$$\text{iso}W = \sum_{p,q=0}^{N \rightarrow \infty} c_{pq} (I_1 - 3)^p (I_2 - 3)^q \quad (106.123)$$

which is actually quite similar to the isochoric part of the general isotropic representation from equation (106.111). Both Mooney and Rivlin strain energy functions become similar, if one chooses to set  $N = 1$  and  $c_{10} = C_1$  and  $c_{01} = C_2$  to obtain:

$$\begin{aligned} {}^{iso}W &= \left( C_1 \left( \tilde{\lambda}_1^2 + \tilde{\lambda}_2^2 + \tilde{\lambda}_3^2 - 3 \right) + C_2 \left( \tilde{\lambda}_1^{-2} + \tilde{\lambda}_2^{-2} + \tilde{\lambda}_3^{-2} - 3 \right) \right) \\ &= (C_1 (\tilde{I}_1 - 3) + C_2 (\tilde{I}_2 - 3)) \end{aligned} \quad (106.124)$$

Derivatives needed for building tensors  $w_A$  and  $Y_{AB}$  are given by the following formulae:

$$\frac{\partial {}^{iso}W}{\partial \tilde{\lambda}_A} = 2 C_1 \tilde{\lambda}_A - 2 C_2 \tilde{\lambda}_A^{-3} \quad (106.125)$$

$$\frac{\partial^2 {}^{iso}W}{\partial \tilde{\lambda}_A^2} = 2 C_1 + 6 C_2 \tilde{\lambda}_A^{-4} \quad (106.126)$$

$$\frac{\partial^2 {}^{iso}W}{\partial \tilde{\lambda}_A \partial \tilde{\lambda}_B} = 0 \quad (106.127)$$

#### 106.3.7.4 Logarithmic Model

By choosing an alternative set of isochoric principal stretch invariants in the form:

$$\begin{aligned} \tilde{I}_1^{ln} &= 2 \left( \ln \tilde{\lambda}_1 \right)^2 + 2 \left( \ln \tilde{\lambda}_2 \right)^2 + 2 \left( \ln \tilde{\lambda}_3 \right)^2 \\ &= \left( \tilde{\lambda}_1^{ln} \right)^2 + \left( \tilde{\lambda}_2^{ln} \right)^2 + \left( \tilde{\lambda}_3^{ln} \right)^2 \\ \tilde{I}_2^{ln} &= 4 \left( \ln \tilde{\lambda}_2 \right)^2 \left( \ln \tilde{\lambda}_3 \right)^2 + 4 \left( \ln \tilde{\lambda}_3 \right)^2 \left( \ln \tilde{\lambda}_1 \right)^2 + 4 \left( \ln \tilde{\lambda}_1 \right)^2 \left( \ln \tilde{\lambda}_2 \right)^2 \\ &= \left( \tilde{\lambda}_2^{ln} \right)^2 \left( \tilde{\lambda}_3^{ln} \right)^2 + \left( \tilde{\lambda}_3^{ln} \right)^2 \left( \tilde{\lambda}_1^{ln} \right)^2 + \left( \tilde{\lambda}_1^{ln} \right)^2 \left( \tilde{\lambda}_2^{ln} \right)^2 \end{aligned} \quad (106.128)$$

where the isochoric logarithmic stretch  $\tilde{\lambda}_i^{ln}$  was used:

$$\tilde{\lambda}_i^{ln} = \sqrt{2} \ln \tilde{\lambda}_i = \frac{1}{\sqrt{2}} \ln \tilde{\lambda}_i^2 \quad (106.129)$$

The general representation of the isochoric part of the strain energy function in terms of  $\tilde{I}_1^{ln}$  and  $\tilde{I}_2^{ln}$  was proposed by Simo and Miehe (1992). A somewhat simpler isochoric strain energy function can be presented in the form:

$${}^{iso}W = G \left( \left( \ln \tilde{\lambda}_1 \right)^2 + \left( \ln \tilde{\lambda}_2 \right)^2 + \left( \ln \tilde{\lambda}_3 \right)^2 \right) \quad (106.130)$$

while the volumetric part is suggested in the form:

$$volW = \frac{K_b}{2} (\ln J)^2 \quad (106.131)$$

Derivatives needed for building tensors  $w_A$  and  $Y_{AB}$  are given by the following formulae:

$$\frac{\partial^{iso}W}{\partial \tilde{\lambda}_A} = 2 G \left( \tilde{\lambda}_A \right)^{-1} \quad (106.132)$$

$$\frac{\partial^2 (isoW)}{\partial \tilde{\lambda}_A^2} = -2 G \left( \tilde{\lambda}_A \right)^{-2} \quad (106.133)$$

$$\frac{\partial^2 (isoW)}{\partial \tilde{\lambda}_A \partial \tilde{\lambda}_B} = 0 \quad (106.134)$$

$$\frac{d \left( volW \right)}{dJ} = K_b J^{-1} \ln J \quad (106.135)$$

$$\frac{d^2 \left( volW \right)}{dJ^2} = K_b J^{-2} - K_b J^{-2} \ln J \quad (106.136)$$

### 106.3.7.5 Simo–Pister Model

Another form or a volumetric part of strain energy function was proposed by [Simo and Pister \(1984\)](#) in the form:

$$W_{vol}(J) = \frac{1}{4} K_b \left( J^2 - 1 - 2 \ln J \right) \quad (106.137)$$

The first and second derivatives with respect to  $J$  are then given as:

$$\frac{d^{vol}W(J)}{dJ} = \frac{\left( \frac{-2}{J} + 2J \right) K_b}{4} \quad (106.138)$$

$$\frac{d^2^{vol}W(J)}{dJ^2} = \frac{\left( 2 + \frac{2}{J^2} \right) K_b}{4} \quad (106.139)$$

## 106.4 Finite Deformation Hyperelasto–Plasticity

### 106.4.1 Introduction

The mathematical structure and numerical analysis of classical small deformation elasto–plasticity is generally well established. However, development of large deformation elastic–plastic algorithms for isotropic and anisotropic material models is still a research area. Here, we present a new integration algorithm, based on the multiplicative decomposition of the deformation gradient into elastic and plastic parts. The algorithm is novel in that it is designed to be used with isotropic as well as anisotropic material

models. Consistent derivation is based on the idea from the infinitesimal strain algorithm developed earlier by [Jeremić and Sture \(1997\)](#). The algorithm is not an extension of earlier developments, but rather a novel development which consistently utilizes Newton's method for numerical solution scheme for integrating pertinent constitutive equations. It is also shown that in the limit, the proposed algorithm reduces to the small strain counterpart.

In what follows, we briefly introduce the multiplicative decomposition of the deformation gradient and pertinent constitutive relations. We then proceed to present the numerical algorithm and the algorithmic tangent stiffness tensor consistent with the presented algorithm.

#### 106.4.2 Kinematics

An appropriate generalization of the additive strain decomposition is the multiplicative decomposition of displacement gradient. The motivation for the multiplicative decomposition can be traced back to the early works of [Bilby et al. \(1957\)](#), and [Kröner \(1960\)](#) on micromechanics of crystal dislocations and application to continuum modeling. In the context of large deformation elastoplastic computations, the work by [Lee and Liu \(1967\)](#), [Fox \(1968\)](#) and [Lee \(1969\)](#) stirred an early interest in multiplicative decomposition.

The appropriateness of multiplicative decomposition technique for soils may be justified from the particulate nature of the material. From the micromechanical point of view, plastic deformation in soils arises from slipping, crushing, yielding and plastic bending<sup>19</sup> of granules comprising the assembly<sup>20</sup>. It can certainly be argued that deformations in soils are predominantly plastic, however, reversible deformations could develop from the elasticity of soil grains, and could be relatively large when particles are locked in high density specimens.

The reasoning behind multiplicative decomposition is a rather simple one. If an infinitesimal neighborhood of a body  $x_i, x_i + dx_i$  in an inelastically deformed body is cut-out and unloaded to an unstressed configuration, it would be mapped into  $\hat{x}_i, \hat{x}_i + d\hat{x}_i$ . The transformation would be comprised of a rigid body displacement<sup>21</sup> and purely elastic unloading. The elastic unloading is a fictitious one, since materials with a strong Baushinger's effect, unloading will lead to loading in an other stress direction, and, if there are residual stresses, the body must be cut-out in small pieces and then every piece relieved of stresses. The unstressed configuration is thus incompatible and discontinuous. The position  $\hat{x}_i$  is arbitrary, and we may assume a linear relationship between  $dx_i$  and  $d\hat{x}_i$ , in the form<sup>22</sup>:

<sup>19</sup>For plate like clay particles.

<sup>20</sup>See also [Lambe and Whitman \(1979\)](#) and [Sture \(1993\)](#).

<sup>21</sup>Translation and rotation.

<sup>22</sup>referred to same Cartesian coordinate system.

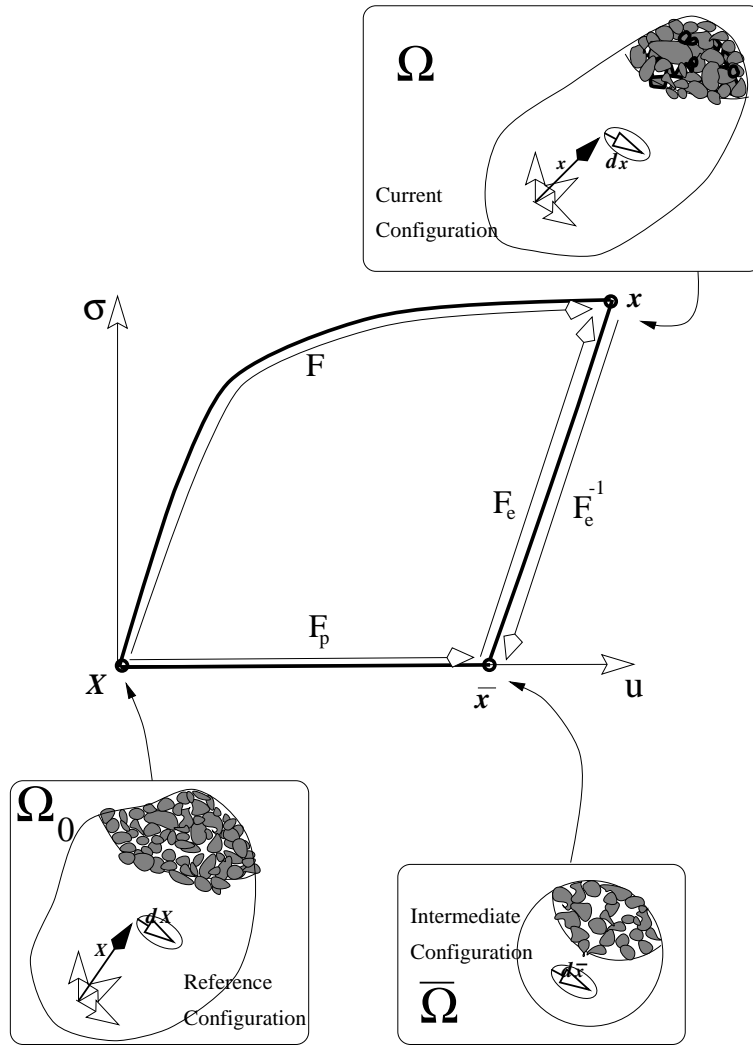


Figure 106.5: Multiplicative decomposition of deformation gradient: schematics.

$$d\hat{x}_k = (F_{ik}^e)^{-1} dx_i \quad (106.140)$$

where  $(F_{ik}^e)^{-1}$  is not to be understood as a deformation gradient, since it may represent the incompatible, discontinuous deformation of a body. By considering the reference configuration of a body  $dX_i$ , then the connection to the current configuration is<sup>23</sup>:

$$dx_k = F_{ki} dX_i \Rightarrow d\hat{x}_k = (F_{ik}^e)^{-1} F_{ij} dX_j \quad (106.141)$$

<sup>23</sup>See section 106.2.2.

so that one can define:

$$F_{kj}^p \stackrel{\text{def}}{=} (F_{ik}^e)^{-1} F_{ij} \Rightarrow F_{ij} \stackrel{\text{def}}{=} F_{ki}^e F_{kj}^p \quad (106.142)$$

The plastic part of the deformation gradient,  $F_{kj}^p$  represents micro-mechanically, the irreversible process of slipping, crushing dislocation and macroscopically the irreversible plastic deformation of a body. The elastic part,  $F_{ki}^e$  represents micro-mechanically a pure elastic reversal of deformation for the particulate assembly, macroscopically a linear elastic unloading toward a stress free state of the body, not necessarily a compatible, continuous deformation but rather a fictitious elastic unloading of small cut outs of a deformed particulate assembly or continuum body.

### 106.4.3 Constitutive Relations

We propose the free energy density  $W$ , which is defined in  $\bar{\Omega}$ , as follows

$$\rho_0 W(\bar{C}_{ij}^e, \kappa_\alpha) = \rho_0 W^e(\bar{C}_{ij}^e) + \rho_0 W^p(\kappa_\alpha) \quad (106.143)$$

where  $W^e(\bar{C}_{ij}^e)$  represents a suitable hyperelastic model in terms of the elastic right deformation tensor  $\bar{C}_{ij}^e$ , whereas  $W^p(\kappa_\alpha)$  represents the hardening. It has been shown elsewhere (Runesson, 1996), that the pertinent dissipation inequality becomes

$$D = \bar{T}_{ij} \bar{L}_{ij}^p + \sum_\alpha \bar{K}_\alpha \dot{\kappa}_\alpha \geq 0 \quad (106.144)$$

where  $\bar{T}_{ij}$  is the Mandel stress<sup>24</sup> and  $\bar{L}_{ij}^p$  is the plastic velocity gradient defined on  $\bar{\Omega}$ .

We now define elastic domain  $\mathcal{B}$  as

$$\mathcal{B} = \{\bar{T}_{ij}, \bar{K}_\alpha \mid \Phi(\bar{T}_{ij}, \bar{K}_\alpha) \leq 0\} \quad (106.145)$$

When  $\Phi$  is isotropic in  $\bar{T}_{ij}$  (which is the case here) in conjunction with elastic isotropy, we can conclude that  $\bar{T}_{ij}$  is symmetrical and we may replace  $\bar{T}_{ij}$  by  $\tau_{ij}$  in  $\Phi$ .

As to the choice of elastic law, it is emphasized that this is largely a matter of convenience since we shall be dealing with small elastic deformations. Here, the Neo-Hookean elastic law is adopted. The generic situation is  $\bar{T}_{ij} = \bar{T}_{ij}(\tilde{U}_{kl}^e, \bar{J}^e)$ , where we have used the isochoric/volumetric split of the elastic right stretch tensor as  $\bar{U}_{kl}^e = \tilde{U}_{kl}^e (\bar{J}^e)^{1/3}$ .

The constitutive relations can now be written as

$$\bar{T}_{ij} = \bar{T}_{ij}(\tilde{U}_{kl}^e, \bar{J}^e) \quad (106.146)$$

$$\bar{L}_{ij}^p := \dot{F}_{ik}^p \left( F_{jk}^p \right)^{-1} = \dot{\mu} \frac{\partial \Phi^*}{\partial \bar{T}_{ij}} = \dot{\mu} \bar{M}_{ij} \quad (106.147)$$

---

<sup>24</sup>See section 106.3.1.

$$\bar{K}_\alpha = \bar{K}_\alpha(\kappa_\beta) \quad (106.148)$$

$$\dot{\bar{\kappa}}_\beta = \dot{\mu} \frac{\partial \Phi^*}{\partial K_\beta} \quad , \quad \kappa_\beta(0) = 0 \quad (106.149)$$

where  $F_{ik}^p = (\bar{F}_{li}^e)^{-1} F_{lk}$  is the plastic part of the deformation gradient.

#### 106.4.4 Implicit Integration Algorithm

The incremental deformation and plastic flow are governed by the system of evolution equations (106.147) and (106.149):

$$\dot{F}_{ik}^p \left( F_{jk}^p \right)^{-1} = \dot{\mu} \bar{M}_{ij} \quad (106.150)$$

$$\dot{\bar{\kappa}}_\beta = \dot{\mu} \frac{\partial \Phi^*}{\partial K_\beta} \quad , \quad \kappa_\beta(0) = 0 \quad (106.151)$$

The flow rule from equation (106.150) can be integrated to give

$${}^{n+1}F_{ij}^p = \exp \left( \Delta \mu {}^{n+1}\bar{M}_{ik} \right) {}^nF_{kj}^p \quad (106.152)$$

By using the multiplicative decomposition

$$F_{ij} = \bar{F}_{ik}^e F_{kj}^p \Rightarrow \bar{F}_{ik}^e = F_{ij} \left( F_{kj}^p \right)^{-1} \quad (106.153)$$

and equation (106.152) we obtain

$$\begin{aligned} {}^{n+1}\bar{F}_{ij}^e &= {}^{n+1}F_{im} \left( {}^nF_{mk}^p \right)^{-1} \exp \left( -\Delta \mu {}^{n+1}\bar{M}_{kj} \right) \\ &= {}^{n+1}\bar{F}_{ik}^{e,tr} \exp \left( -\Delta \mu {}^{n+1}\bar{M}_{kj} \right) \end{aligned} \quad (106.154)$$

where we used that

$${}^{n+1}\bar{F}_{ik}^{e,tr} = {}^{n+1}F_{im} \left( {}^nF_{km}^p \right)^{-1} \quad (106.155)$$

The elastic deformation is then

$$\begin{aligned} {}^{n+1}\bar{C}_{ij}^e &\stackrel{\text{def}}{=} \left( {}^{n+1}\bar{F}_{im}^e \right)^T {}^{n+1}\bar{F}_{mj}^e \\ &= \exp \left( -\Delta \mu {}^{n+1}\bar{M}_{ir}^T \right) \left( {}^{n+1}\bar{F}_{rk}^{e,tr} \right)^T {}^{n+1}\bar{F}_{kl}^{e,tr} \exp \left( -\Delta \mu {}^{n+1}\bar{M}_{lj} \right) \\ &= \exp \left( -\Delta \mu {}^{n+1}\bar{M}_{ir}^T \right) {}^{n+1}\bar{C}_{rl}^{e,tr} \exp \left( -\Delta \mu {}^{n+1}\bar{M}_{lj} \right) \end{aligned} \quad (106.156)$$

By recognizing that the exponent of a tensor can be expanded in Taylor series<sup>25</sup>

$$\exp \left( -\Delta \mu {}^{n+1}\bar{M}_{lj} \right) = \delta_{lj} - \Delta \mu {}^{n+1}\bar{M}_{lj} + \frac{1}{2} \left( \Delta \mu {}^{n+1}\bar{M}_{ls} \right) \left( \Delta \mu {}^{n+1}\bar{M}_{sj} \right) + \dots \quad (106.157)$$

<sup>25</sup>See for example Pearson (1974).

and by using the first order expansion in the equation (106.156), we obtain

$$\begin{aligned}
 {}^{n+1}\bar{C}_{ij}^e &= \left( \delta_{ir} - \Delta\mu^{n+1}\bar{M}_{ir} \right) {}^{n+1}\bar{C}_{rl}^{e,tr} \left( \delta_{lj} - \Delta\mu^{n+1}\bar{M}_{lj} \right) \\
 &= \left( {}^{n+1}\bar{C}_{il}^{e,tr} - \Delta\mu^{n+1}\bar{M}_{ir} {}^{n+1}\bar{C}_{rl}^{e,tr} \right) \left( \delta_{lj} - \Delta\mu^{n+1}\bar{M}_{lj} \right) \\
 &= {}^{n+1}\bar{C}_{ij}^{e,tr} - \Delta\mu^{n+1}\bar{M}_{ir} {}^{n+1}\bar{C}_{rj}^{e,tr} - \Delta\mu {}^{n+1}\bar{C}_{il}^{e,tr} {}^{n+1}\bar{M}_{lj} \\
 &\quad + \Delta\mu^2 {}^{n+1}\bar{M}_{ir} {}^{n+1}\bar{C}_{rl}^{e,tr} {}^{n+1}\bar{M}_{lj}
 \end{aligned} \tag{106.158}$$

**Remark 106.4.1** The Taylor's series expansion from equation (106.157) is a proper approximation for the general nonsymmetric tensor  $\bar{M}_{lj}$ . That is, the approximate solution given by equation (106.158) is valid for a general anisotropic solid. This contrasts with the spectral decomposition family of solutions<sup>26</sup> which are restricted to isotropic solids.

**Remark 106.4.2** Taylor's series expansion<sup>27</sup> is proper for "small" values of plastic flow tensor  $\Delta\mu^{n+1}\bar{M}_{lj}$ . This is indeed the case for small increments, when  $\Delta\mu \rightarrow 0$  which are required for following the equilibrium path for path-dependent solids.

**Remark 106.4.3** In the limit, when the displacements are sufficiently small, the solution (106.158) collapses to

$$\begin{aligned}
 \lim_{F_{ij} \rightarrow \delta_{ij}} \delta_{ij} + 2^{n+1}\epsilon_{ij} &= + \delta_{ij} + 2^{n+1}\epsilon_{ij}^{e,tr} \\
 &\quad - \Delta\mu^{n+1}\bar{M}_{ir} \left( \delta_{rj} + 2^{n+1}\epsilon_{rj}^{e,tr} \right) \\
 &\quad - \Delta\mu \left( \delta_{il} + 2^{n+1}\epsilon_{il}^{e,tr} \right) {}^{n+1}\bar{M}_{lj} \\
 &\quad + \Delta\mu^2 {}^{n+1}\bar{M}_{ir} \left( \delta_{rl} + 2^{n+1}\epsilon_{rl}^{e,tr} \right) {}^{n+1}\bar{M}_{lj} \\
 &= + \delta_{ij} + 2^{n+1}\epsilon_{ij}^{e,tr} \\
 &\quad - \Delta\mu^{n+1}\bar{M}_{ij} - 2\Delta\mu {}^{n+1}\bar{M}_{ir} {}^{n+1}\epsilon_{rj}^{tr} \\
 &\quad - \Delta\mu {}^{n+1}\bar{M}_{ij} - 2\Delta\mu {}^{n+1}\epsilon_{il}^{tr} {}^{n+1}\bar{M}_{lj} \\
 &\quad + \Delta\mu^2 {}^{n+1}\bar{M}_{il} {}^{n+1}\bar{M}_{lj} + 2\Delta\mu^2 {}^{n+1}\bar{M}_{ir} {}^{n+1}\epsilon_{rl}^{trn+1} {}^{n+1}\bar{M}_{lj} \\
 &= \delta_{ij} + 2^{n+1}\epsilon_{ij}^{e,tr} - 2\Delta\mu {}^{n+1}\bar{M}_{ij} \\
 \Rightarrow {}^{n+1}\epsilon_{ij} &= {}^{n+1}\epsilon_{ij}^{tr} - \Delta\mu {}^{n+1}\bar{M}_{ij}
 \end{aligned} \tag{106.159}$$

which is a small deformation elastic predictor–plastic corrector equation in strain space. In working out

---

<sup>26</sup>See Simo (1992).

<sup>27</sup>It should be called MacLaurin's series expansion, since expansion is about zero plastic flow state (no incremental plastic deformation).

the small deformation counterpart (106.159) it was used that

$$\begin{aligned} \lim_{F_{ij} \rightarrow \delta_{ij}} {}^{n+1}\bar{C}_{ij}^e &= \delta_{ij} + 2{}^{n+1}\epsilon_{ij} \\ 2\Delta\mu {}^{n+1}\epsilon_{il}^{tr} {}^{n+1}\bar{M}_{lj} &\ll {}^{n+1}\bar{M}_{ij} \\ \Delta\mu &\ll 1 \end{aligned} \quad (106.160)$$

By neglecting the higher order term with  $\Delta\mu^2$  in equation (106.158), the solution for the right elastic deformation tensor  ${}^{n+1}\bar{C}_{ij}^e$  can be written as

$${}^{n+1}\bar{C}_{ij}^e = {}^{n+1}\bar{C}_{ij}^{e,tr} - \Delta\mu \left( {}^{n+1}\bar{M}_{ir} {}^{n+1}\bar{C}_{rj}^{e,tr} + {}^{n+1}\bar{C}_{il}^{e,tr} {}^{n+1}\bar{M}_{lj} \right) \quad (106.161)$$

The hardening rule (106.151) can be integrated to give

$${}^{n+1}\kappa_\alpha = {}^n\kappa_\alpha + \Delta\mu \left. \frac{\partial \Phi^*}{\partial K_\alpha} \right|_{n+1} \quad (106.162)$$

**Remark 106.4.4** It is interesting to note that equation (106.161) resembles the *elastic predictor–plastic corrector* equation for small deformation elastic–plastic incremental analysis. That resemblance will be used to build an iterative solution algorithm in the next section.

The incremental problem is defined by equations (106.161), (106.162), and the constitutive relations

$${}^{n+1}\bar{S}_{IJ} = 2 \left. \frac{\partial W}{\partial C_{IJ}} \right|_{n+1} \quad (106.163)$$

$${}^{n+1}K_\alpha = - \left. \frac{\partial W}{\partial \kappa_\alpha} \right|_{n+1} \quad (106.164)$$

and the Karush–Kuhn–Tucker (KKT) conditions

$$\Delta\mu < 0 \quad ; \quad {}^{n+1}\Phi \leq 0 \quad ; \quad \Delta\mu {}^{n+1}\Phi = 0 \quad (106.165)$$

where

$$\Phi = \Phi(\bar{T}_{ij}, K_\alpha) \quad (106.166)$$

**Remark 106.4.5** The Mandel stress tensor  $\bar{T}_{ij}$  can be obtained from the second Piola–Kirchhoff stress tensor  $\bar{S}_{kj}$  and the right elastic deformation tensor  $\bar{C}_{ik}^e$  as

$$\bar{T}_{ij} = \bar{C}_{ik}^e \bar{S}_{kj} \quad (106.167)$$

This set of nonlinear equations will be solved with a Newton type procedure, described in the next section. For a given  ${}^{n+1}F_{ij}$ , or  ${}^{n+1}\bar{C}_{ij}^{e,tr}$ , the upgraded quantities  ${}^{n+1}\bar{S}_{IJ}$  and  ${}^{n+1}K_\alpha$  can be found, then the appropriate pull-back to  $B_0$  or push-forward to  $B$  will give  ${}^{n+1}S_{IJ}$  and  ${}^{n+1}\tau_{ij}$

$${}^{n+1}S_{IJ} = \left( {}^{n+1}F_{il}^p \right)^{-1} {}^{n+1}\bar{S}_{IJ} \left( {}^{n+1}F_{jJ}^p \right)^{-T} \quad (106.168)$$

$${}^{n+1}\tau_{ij} = {}^{n+1}\bar{F}_{il}^e {}^{n+1}\bar{S}_{IJ} \left( {}^{n+1}F_{jJ}^e \right)^{-1} \quad (106.169)$$

The elastic predictor, plastic corrector equation

$$\begin{aligned} {}^{n+1}\bar{C}_{ij}^e &= {}^{n+1}\bar{C}_{ij}^{e,tr} - \Delta\mu \left( {}^{n+1}\bar{M}_{ir} {}^{n+1}\bar{C}_{rj}^{e,tr} + {}^{n+1}\bar{C}_{il}^{e,tr} {}^{n+1}\bar{M}_{lj} \right) \\ &= {}^{n+1}\bar{C}_{ij}^{e,tr} - \Delta\mu {}^{n+1}Z_{ij} \end{aligned} \quad (106.170)$$

is used as a starting point for a Newton iterative algorithm. In previous equation, we have introduced tensor  $Z_{ij}$  to shorten writing. The trial right elastic deformation tensor is defined as

$$\begin{aligned} {}^{n+1}\bar{C}_{ij}^{e,tr} &= \left( {}^{n+1}\bar{F}_{ri}^{e,tr} \right)^T \left( {}^{n+1}\bar{F}_{rj}^{e,tr} \right) \\ &\quad \left( {}^{n+1}\bar{F}_{rM} \left( {}^n F_{iM}^p \right)^{-1} \right)^T \left( {}^{n+1}\bar{F}_{rS} \left( {}^n F_{jS}^p \right)^{-1} \right) \end{aligned} \quad (106.171)$$

We introduce a tensor of deformation residuals

$$R_{ij} = \underbrace{\bar{C}_{ij}^e}_{\text{current}} - \underbrace{\left( {}^{n+1}\bar{C}_{ij}^{e,tr} - \Delta\mu {}^{n+1}Z_{ij} \right)}_{\text{BackwardEuler}} \quad (106.172)$$

Tensor  $R_{ij}$  represents the difference between the current right elastic deformation tensor and the Backward Euler right elastic deformation tensor. The trial right elastic deformation tensor  ${}^{n+1}\bar{C}_{ij}^{e,tr}$  is maintained fixed during the iteration process. The first order Taylor series expansion can be applied to the equation (106.172) in order to obtain the iterative change, the new residual  $R_{ij}^{new}$  from the old  $R_{ij}^{old}$

$$R_{ij}^{new} = R_{ij}^{old} + d\bar{C}_{ij}^e + d(\Delta\mu) {}^{n+1}Z_{ij} + \Delta\mu \frac{\partial {}^{n+1}Z_{ij}}{\partial \bar{T}_{mn}} d\bar{T}_{mn} + \Delta\mu \frac{\partial {}^{n+1}Z_{ij}}{\partial K_\alpha} dK_\alpha \quad (106.173)$$

By using that

$$\bar{T}_{mn} = \bar{C}_{mk}^e \bar{S}_{kn} \Rightarrow (\bar{C}_{sk}^e)^{-1} \bar{T}_{sn} = \bar{S}_{kn} \quad (106.174)$$

we can write

$$\begin{aligned} d\bar{T}_{mn} &= d\bar{C}_{mk}^e \bar{S}_{kn} + \bar{C}_{mk}^e d\bar{S}_{kn} \\ &= d\bar{C}_{mk}^e \bar{S}_{kn} + \frac{1}{2} \bar{C}_{mk}^e \bar{L}_{knpq}^e d\bar{C}_{pq}^e \quad \text{from (106.55)} \\ &= d\bar{C}_{mk}^e (\bar{C}_{sk}^e)^{-1} \bar{T}_{sn} + \frac{1}{2} \bar{C}_{mk}^e \bar{L}_{knpq}^e d\bar{C}_{pq}^e \quad \text{from (106.174)} \end{aligned} \quad (106.175)$$

and the equation (106.173) can be rewritten as

$$\begin{aligned}
 R_{ij}^{new} = & R_{ij}^{old} + d\bar{C}_{ij}^e + d(\Delta\mu)^{n+1}Z_{ij} + \\
 & + \Delta\mu \frac{\partial^{n+1}Z_{ij}}{\partial \bar{T}_{mn}} \left( d\bar{C}_{mk}^e (\bar{C}_{sk}^e)^{-1} \bar{T}_{sn} + \frac{1}{2} \bar{C}_{mk}^e \bar{\mathcal{L}}_{knpq}^e d\bar{C}_{pq}^e \right) + \\
 & + \Delta\mu \frac{\partial^{n+1}Z_{ij}}{\partial K_\alpha} dK_\alpha \\
 = & R_{ij}^{old} + d\bar{C}_{ij}^e + d(\Delta\mu)^{n+1}Z_{ij} + \\
 & + \Delta\mu \frac{\partial^{n+1}Z_{ij}}{\partial \bar{T}_{mn}} d\bar{C}_{mk}^e (\bar{C}_{sk}^e)^{-1} \bar{T}_{sn} + \\
 & + \frac{1}{2} \Delta\mu \frac{\partial^{n+1}Z_{ij}}{\partial \bar{T}_{mn}} \bar{C}_{mk}^e \bar{\mathcal{L}}_{knpq}^e d\bar{C}_{pq}^e + \\
 & + \Delta\mu \frac{\partial^{n+1}Z_{ij}}{\partial K_\alpha} dK_\alpha \\
 = & R_{ij}^{old} + d\bar{C}_{ij}^e + d(\Delta\mu)^{n+1}Z_{ij} + \\
 & + \Delta\mu \frac{\partial^{n+1}Z_{mn}}{\partial \bar{T}_{ik}} (\bar{C}_{sj}^e)^{-1} \bar{T}_{sk} d\bar{C}_{ij}^e + \quad \text{dummy indices rearrangement} \\
 & + \frac{1}{2} \Delta\mu \frac{\partial^{n+1}Z_{pq}}{\partial \bar{T}_{mn}} \bar{C}_{mk}^e \bar{\mathcal{L}}_{knij}^e d\bar{C}_{ij}^e + \quad \text{dummy indices rearrangement} \\
 & + \Delta\mu \frac{\partial^{n+1}Z_{ij}}{\partial K_\alpha} dK_\alpha
 \end{aligned} \tag{106.176}$$

The goal is to have  $R_{ij}^{new} = 0$  so one can write

$$\begin{aligned}
 0 &= R_{ij}^{old} + d\bar{C}_{ij}^e + d(\Delta\mu)^{n+1}Z_{ij} + \\
 &+ \Delta\mu \frac{\partial^{n+1}Z_{mn}}{\partial\bar{T}_{ik}} \left(\bar{C}_{sj}^e\right)^{-1} \bar{T}_{sk} d\bar{C}_{ij}^e + \\
 &+ \frac{1}{2} \Delta\mu \frac{\partial^{n+1}Z_{pq}}{\partial\bar{T}_{mn}} \bar{C}_{mk}^e \bar{\mathcal{L}}_{knij}^e d\bar{C}_{ij}^e + \\
 &+ \Delta\mu \frac{\partial^{n+1}Z_{ij}}{\partial K_\alpha} dK_\alpha \\
 \\ 
 &= R_{ij}^{old} + d(\Delta\mu)^{n+1}Z_{ij} \\
 &+ \Delta\mu \frac{\partial^{n+1}Z_{ij}}{\partial K_\alpha} dK_\alpha + \\
 &+ d\bar{C}_{ij}^e + \\
 &+ \Delta\mu \frac{\partial^{n+1}Z_{mn}}{\partial\bar{T}_{ik}} \left(\bar{C}_{sj}^e\right)^{-1} \bar{T}_{sk} d\bar{C}_{ij}^e + \\
 &+ \frac{1}{2} \Delta\mu \frac{\partial^{n+1}Z_{pq}}{\partial\bar{T}_{mn}} \bar{C}_{mk}^e \bar{\mathcal{L}}_{knij}^e d\bar{C}_{ij}^e \\
 \\ 
 &= R_{ij}^{old} + d(\Delta\mu)^{n+1}Z_{ij} + \Delta\mu \frac{\partial^{n+1}Z_{ij}}{\partial K_\alpha} dK_\alpha + \\
 &+ (\delta_{im}\delta_{nj} + \Delta\mu \frac{\partial^{n+1}Z_{mn}}{\partial\bar{T}_{ik}} \left(\bar{C}_{sj}^e\right)^{-1} \bar{T}_{sk} + \frac{1}{2} \Delta\mu \frac{\partial^{n+1}Z_{mn}}{\partial\bar{T}_{pq}} \bar{C}_{pk}^e \bar{\mathcal{L}}_{kqij}^e) d\bar{C}_{ij}^e
 \end{aligned} \tag{106.177}$$

Upon introducing notation

$$\mathcal{T}_{mnij} = \delta_{im}\delta_{nj} + \Delta\mu \frac{\partial^{n+1}Z_{mn}}{\partial\bar{T}_{ik}} \left(\bar{C}_{sj}^e\right)^{-1} \bar{T}_{sk} + \frac{1}{2} \Delta\mu \frac{\partial^{n+1}Z_{mn}}{\partial\bar{T}_{pq}} \bar{C}_{pk}^e \bar{\mathcal{L}}_{kqij}^e \tag{106.178}$$

we can solve (106.177) for  $d\bar{C}_{ij}^e$

$$d\bar{C}_{ij}^e = (\mathcal{T}_{mnij})^{-1} \left( -R_{mn}^{old} - d(\Delta\mu)^{n+1}Z_{mn} - \Delta\mu \frac{\partial^{n+1}Z_{mn}}{\partial K_\alpha} dK_\alpha \right) \tag{106.179}$$

or, by rearranging indices

$$d\bar{C}_{pq}^e = (\mathcal{T}_{mnpq})^{-1} \left( -R_{mn}^{old} - d(\Delta\mu)^{n+1}Z_{mn} - \Delta\mu \frac{\partial^{n+1}Z_{mn}}{\partial K_\alpha} dK_\alpha \right) \tag{106.180}$$

By using that

$$dK_\alpha = \frac{\partial K_\alpha}{\partial \kappa_\beta} d\kappa_\beta = -d(\Delta\mu) \frac{\partial K_\alpha}{\partial \kappa_\beta} \frac{\partial Q}{\partial K_\beta} = -d(\Delta\mu) H_{\alpha\beta} \frac{\partial Q}{\partial K_\beta} \tag{106.181}$$

it follows from (106.180)

$$d\bar{C}_{pq}^e = (\mathcal{T}_{mnpq})^{-1} \left( -R_{mn}^{old} - d(\Delta\mu)^{n+1} Z_{mn} + \Delta\mu \frac{\partial^{n+1} Z_{mn}}{\partial K_\alpha} d(\Delta\mu) H_{\alpha\beta} \frac{\partial Q}{\partial K_\beta} \right) \quad (106.182)$$

A first order Taylor series expansion of a yield function yields

$$\begin{aligned} {}^{new} \Phi(\bar{T}_{ij}, K_\alpha) &= {}^{old} \Phi(\bar{T}_{ij}, K_\alpha) + \\ &+ \frac{\partial \Phi(\bar{T}_{ij}, K_\alpha)}{\partial \bar{T}_{mn}} d\bar{T}_{mn} \\ &+ \frac{\partial \Phi(\bar{T}_{ij}, K_\alpha)}{\partial K_\alpha} dK_\alpha \\ &= {}^{old} \Phi(\bar{T}_{ij}, K_\alpha) + \\ &+ \frac{\partial \Phi(\bar{T}_{ij}, K_\alpha)}{\partial \bar{T}_{mn}} \left( d\bar{C}_{mk}^e (\bar{C}_{sq}^e)^{-1} \bar{T}_{sn} + \frac{1}{2} \bar{C}_{mk}^e \bar{\mathcal{L}}_{knpq}^e d\bar{C}_{pq}^e \right) \\ &+ \frac{\partial \Phi(\bar{T}_{ij}, K_\alpha)}{\partial K_\alpha} dK_\alpha \\ &= {}^{old} \Phi(\bar{T}_{ij}, K_\alpha) + \\ &+ \frac{\partial \Phi(\bar{T}_{ij}, K_\alpha)}{\partial \bar{T}_{pn}} \left( \bar{C}_{sq}^e \right)^{-1} \bar{T}_{sn} d\bar{C}_{pq}^e \quad \text{dummy indices rearrangement} \\ &+ \frac{1}{2} \frac{\partial \Phi(\bar{T}_{ij}, K_\alpha)}{\partial \bar{T}_{mn}} \bar{C}_{mk}^e \bar{\mathcal{L}}_{knpq}^e d\bar{C}_{pq}^e \\ &+ \frac{\partial \Phi(\bar{T}_{ij}, K_\alpha)}{\partial K_\alpha} dK_\alpha \\ &= {}^{old} \Phi(\bar{T}_{ij}, K_\alpha) + \\ &+ \left( \frac{\partial \Phi(\bar{T}_{ij}, K_\alpha)}{\partial \bar{T}_{pn}} \left( \bar{C}_{sq}^e \right)^{-1} \bar{T}_{sn} + \frac{1}{2} \frac{\partial \Phi(\bar{T}_{ij}, K_\alpha)}{\partial \bar{T}_{mn}} \bar{C}_{mk}^e \bar{\mathcal{L}}_{knpq}^e \right) d\bar{C}_{pq}^e \\ &+ \frac{\partial \Phi(\bar{T}_{ij}, K_\alpha)}{\partial K_\alpha} dK_\alpha \end{aligned} \quad (106.183)$$

By using (106.181), equation (106.183) becomes

$$\begin{aligned} {}^{new} \Phi(\bar{T}_{ij}, K_\alpha) &= {}^{old} \Phi(\bar{T}_{ij}, K_\alpha) + \\ &+ \left( \frac{\partial \Phi(\bar{T}_{ij}, K_\alpha)}{\partial \bar{T}_{pn}} \left( \bar{C}_{sq}^e \right)^{-1} \bar{T}_{sn} + \frac{1}{2} \frac{\partial \Phi(\bar{T}_{ij}, K_\alpha)}{\partial \bar{T}_{mn}} \bar{C}_{mk}^e \bar{\mathcal{L}}_{knpq}^e \right) d\bar{C}_{pq}^e \\ &- d(\Delta\mu) \frac{\partial \Phi(\bar{T}_{ij}, K_\alpha)}{\partial K_\alpha} H_{\alpha\beta} \frac{\partial \Phi^*}{\partial K_\beta} \end{aligned} \quad (106.184)$$

Upon introducing the following notation

$$\mathcal{F}_{pq} = \frac{\partial \Phi(\bar{T}_{ij}, K_\alpha)}{\partial \bar{T}_{pn}} \left( \bar{C}_{sq}^e \right)^{-1} \bar{T}_{sn} + \frac{1}{2} \frac{\partial \Phi(\bar{T}_{ij}, K_\alpha)}{\partial \bar{T}_{mn}} \bar{C}_{mk}^e \bar{\mathcal{L}}_{knpq}^e \quad (106.185)$$

and with the solution for  $d\bar{C}_{pq}^e$  from (106.182), (106.184) becomes

$$\begin{aligned} {}^{new}\Phi(\bar{T}_{ij}, K_\alpha) &= {}^{old}\Phi(\bar{T}_{ij}, K_\alpha) + \\ &+ \mathcal{F}_{pq} \left( (\mathcal{T}_{mnpq})^{-1} \left( -R_{mn}^{old} - d(\Delta\mu) {}^{n+1}Z_{mn} + d(\Delta\mu) \Delta\mu \frac{\partial^{n+1}Z_{mn}}{\partial K_\alpha} H_{\alpha\beta} \frac{\partial\Phi^*}{\partial K_\beta} \right) \right) \\ &- d(\Delta\mu) \frac{\partial\Phi(\bar{T}_{ij}, K_\alpha)}{\partial K_\alpha} H_{\alpha\beta} \frac{\partial\Phi^*}{\partial K_\beta} \end{aligned} \quad (106.186)$$

After setting  ${}^{new}\Phi(\bar{T}_{ij}, K_\alpha) = 0$  we can solve for the incremental inconsistency parameter  $d(\Delta\mu)$

$$d(\Delta\mu) = \frac{{}^{old}\Phi - \mathcal{F}_{pq} (\mathcal{T}_{mnpq})^{-1} R_{mn}^{old}}{\mathcal{F}_{pq} (\mathcal{T}_{mnpq})^{-1} {}^{n+1}Z_{mn} - \Delta\mu \mathcal{F}_{pq} (\mathcal{T}_{mnpq})^{-1} \frac{\partial^{n+1}Z_{mn}}{\partial K_\alpha} H_{\alpha\beta} \frac{\partial\Phi^*}{\partial K_\beta} + \frac{\partial\Phi}{\partial K_\alpha} H_{\alpha\beta} \frac{\partial\Phi^*}{\partial K_\beta}} \quad (106.187)$$

**Remark 106.4.6** In the perfectly plastic case, the increment inconsistency parameter  $d(\Delta\mu)$  is

$$d(\Delta\mu) = \frac{{}^{old}\Phi - \mathcal{F}_{pq} (\mathcal{T}_{mnpq})^{-1} R_{mn}^{old}}{\mathcal{F}_{pq} (\mathcal{T}_{mnpq})^{-1} {}^{n+1}Z_{mn}} \quad (106.188)$$

**Remark 106.4.7** In the limit, for small deformations, isotropic response, the increment inconsistency parameter  $d(\Delta\mu)$  becomes

$$d(\Delta\mu) = \frac{{}^{old}\Phi - (n_{mn} E_{mnpq}) \left( \delta_{pm} \delta_{nq} + \Delta\mu \frac{\partial m_{mn}}{\partial \sigma_{ij}} E_{ijpq} \right)^{-1} R_{mn}^{old}}{n_{mn} E_{mnpq} \left( \delta_{mp} \delta_{qn} + \Delta\mu \frac{\partial m_{pq}}{\partial \sigma_{ij}} E_{ijmn} \right)^{-1} {}^{n+1}m_{mn} + \frac{\partial\Phi}{\partial K_\alpha} H_{\alpha\beta} \frac{\partial\Phi^*}{\partial K_\beta}} \quad (106.189)$$

since in the limit, as deformations are getting small

$$\begin{aligned} \mathcal{T}_{mnpq} &\rightarrow \delta_{pm} \delta_{nq} + \Delta\mu \frac{\partial m_{mn}}{\partial \sigma_{ij}} E_{ijpq} \\ \mathcal{F}_{pq} &\rightarrow \frac{1}{2} \frac{\partial\Phi}{\partial \sigma_{mn}} E_{mnpq} \\ Z_{pq} &\rightarrow 2 m_{pq} \\ R_{pq} &\rightarrow 2 \epsilon_{pq} \end{aligned} \quad (106.190)$$

Upon noting that residual  $R_{pq}$  is defined in strain space, the increment inconsistency parameter  $d(\Delta\mu)$  compares exactly with it's small strain counterpart ([Jeremić and Sture, 1997](#)).

The procedure described below summarizes the implementation of the return algorithm.

**Trial State** Given the right elastic deformations tensor  ${}^n\bar{C}_{pq}^e$  and a set of hardening variables  ${}^nK_\alpha$  at a specific quadrature point in a finite element, compute the relative deformation gradient  ${}^{n+1}f_{ij}$  for a given displacement increment  $\Delta^{n+1}u_i$ , and the right deformation tensor

$${}^{n+1}f_{ij} = \delta_{ij} + u_{i,j} \quad (106.191)$$

$${}^{n+1}\bar{C}_{ij}^{e,tr} = \left( {}^{n+1}f_{ir} {}^nF_{rk}^e \right)^T \left( {}^{n+1}f_{kl} {}^nF_{lj}^e \right) = \left( {}^nF_{rk}^e \right)^T \left( {}^{n+1}f_{ir} \right)^T \left( {}^{n+1}f_{kl} {}^nF_{lj}^e \right) \quad (106.192)$$

Compute the trial elastic second Piola–Kirchhoff stress and the trial elastic Mandel stress tensor

$${}^{n+1}\bar{S}_{ij}^{e,tr} = 2 \frac{\partial W}{\partial {}^{n+1}\bar{C}_{ij}^{e,tr}} \quad (106.193)$$

$${}^{n+1}\bar{T}_{ij}^{e,tr} = {}^{n+1}\bar{C}_{il}^{e,tr} {}^{n+1}\bar{S}_{lj}^{e,tr} \quad (106.194)$$

Evaluate the yield function  ${}^{n+1}\Phi^{tr}(\bar{T}_{ij}^{e,tr}, K_\alpha)$ . If  ${}^{n+1}\Phi^{tr} \leq 0$  there is no plastic flow in current increment

$${}^{n+1}\bar{C}_{ij}^e = {}^{n+1}\bar{C}_{ij}^{e,tr}$$

$${}^{n+1}K_\alpha = {}^nK_\alpha$$

$${}^{n+1}T_{ij} = {}^nT_{ij}^{e,tr}$$

and exit constitutive integration procedure.

**Return Algorithm** If yield criteria has been violated ( ${}^{n+1}\Phi^{tr} > 0$ ) proceed to step 1.

step 1.  $k^{th}$  iteration. Known variables

$${}^{n+1}\bar{C}_{ij}^{e(k)} ; {}^{n+1}\kappa_\alpha^{(k)} ; {}^{n+1}K_\alpha^{(k)} ; {}^{n+1}T_{ij}^{(k)} ; {}^{n+1}\Delta\mu^{(k)}$$

evaluate the yield function and the residual

$$\begin{aligned} \Phi^{(k)} &= \Phi({}^{n+1}\bar{T}_{ij}^{e(k)}, {}^{n+1}K_\alpha^{(k)}) \\ R_{ij}^{(k)} &= {}^{n+1}\bar{C}_{ij}^{e,(k)} - \left( {}^{n+1}\bar{C}_{ij}^{e,tr} - {}^{n+1}\Delta\mu^{(k)} {}^{n+1}Z_{ij}^{(k)} \right) \end{aligned}$$

step 2. Check for convergence,  $\Phi^{(k)} \leq NTOL$  and  $\|R_{ij}^{(k)}\| \leq NTOL$ . If convergence criteria is satisfied set

$${}^{n+1}\bar{C}_{ij}^e = {}^{n+1}\bar{C}_{ij}^{e(k)}$$

$${}^{n+1}\kappa_\alpha = {}^{n+1}\kappa_\alpha^{(k)}$$

$${}^{n+1}K_\alpha = {}^{n+1}K_\alpha^{(k)}$$

$${}^{n+1}T_{ij} = {}^{n+1}T_{ij}^{(k)}$$

$${}^{n+1}\Delta\mu = {}^{n+1}\Delta\mu^{(k)}$$

Exit constitutive integration procedure.

step 3.<sup>28</sup> If convergence is not achieved, i.e.  $\Phi^{(k)} > NTOL$  or  $\|R_{ij}^{(k)}\| > NTOL$  then compute the elastic stiffness tensor  $\mathcal{L}_{ijkl}$

$$\bar{\mathcal{L}}_{ijkl}^{(k)} = 4 \frac{\partial^2 W}{\partial \bar{C}_{ij}^{e(k)} \partial \bar{C}_{kl}^{e(k)}} \quad (106.195)$$

step 4. Compute the incremental inconsistency parameter  $d(\Delta\mu^{(k+1)})$

$$d(\Delta\mu^{(k+1)}) = \frac{\Phi^{(k)} - \bar{\mathcal{F}}_{mn}^{(k)} R_{mn}^{(k)}}{\bar{\mathcal{F}}_{mn}^{(k)} Z_{mn}^{(k)} - \Delta\mu^{(k)} \bar{\mathcal{F}}_{mn}^{(k)} \frac{\partial Z_{mn}^{(k)}}{\partial K_\alpha} \bar{H}_\alpha^{(k)} + \frac{\partial \Phi^{(k)}}{\partial K_\alpha} \bar{H}_\alpha^{(k)}} \quad (106.196)$$

where

$$\bar{H}_\alpha^{(k)} = H_{\alpha\beta}^{(k)} \frac{\partial \Phi^{*,(k)}}{\partial K_\beta} \quad ; \quad \bar{\mathcal{F}}_{mn}^{(k)} = \mathcal{F}_{pq}^{(k)} \left( \mathcal{T}_{mnpq}^{(k)} \right)^{-1}$$

$$\mathcal{F}_{pq} = \frac{\partial \Phi(\bar{T}_{ij}^{(k)}, K_\alpha^{(k)})}{\partial \bar{T}_{pn}} \left( \bar{C}_{sq}^{e,(k)} \right)^{-1} \bar{T}_{sn}^{(k)} + \frac{1}{2} \frac{\partial \Phi(\bar{T}_{ij}^{(k)}, K_\alpha^{(k)})}{\partial \bar{T}_{mn}} \bar{C}_{mk}^{e,(k)} \bar{\mathcal{L}}_{kn}^{e,(k)}$$

$$\mathcal{T}_{mni} = \delta_{im} \delta_{nj} + \Delta\mu^{(k)} \frac{\partial Z_{mn}^{(k)}}{\partial \bar{T}_{ik}^{(k)}} \left( \bar{C}_{sj}^{e,(k)} \right)^{-1} \bar{T}_{sk}^{(k)} + \frac{1}{2} \Delta\mu^{(k)} \frac{\partial Z_{mn}^{(k)}}{\partial \bar{T}_{pq}^{(k)}} \bar{C}_{pk}^{e,(k)} \bar{\mathcal{L}}_{kqij}^{e,(k)}$$

step 5. Updated the inconsistency parameter  $\Delta\mu^{(k+1)}$

$$\Delta\mu^{(k+1)} = \Delta\mu^{(k)} + d(\Delta\mu^{(k+1)}) \quad (106.197)$$

step 6. Updated the right deformation tensor, the hardening variable and the Mandel stress

$$d\bar{C}_{pq}^{e,(k+1)} = \left( \mathcal{T}_{mnpq}^{(k)} \right)^{-1} \left( -R_{mn}^{(k)} - d(\Delta\mu^{(k+1)})^{n+1} Z_{mn}^{(k)} + \Delta\mu^{(k)} \frac{\partial Z_{mn}^{(k)}}{\partial K_\alpha} d(\Delta\mu^{(k+1)}) \bar{H}_\alpha^{(k)} \right) \quad (106.198)$$

$$d\kappa_\alpha^{(k+1)} = d(\Delta\mu^{(k+1)}) \frac{\partial \Phi^{*,(k)}}{\partial K_\beta} \quad (106.199)$$

$$dK_\alpha^{(k+1)} = -d(\Delta\mu^{(k+1)}) H_{\alpha\beta}^{(k)} \frac{\partial \Phi^{*,(k)}}{\partial K_\beta} \quad (106.200)$$

<sup>28</sup>From step 3. to step 9. all of the variables are in intermediate  $n + 1$  configuration. For the sake of brevity we are omitting superscript  $n + 1$ .

$$d\bar{T}_{mn}^{(k+1)} = d\bar{C}_{mk}^{e,(k+1)} \left( \bar{C}_{sk}^{e,(k)} \right)^{-1} \bar{T}_{sn}^{(k)} + \frac{1}{2} \bar{C}_{mk}^{e,(k)} \bar{\mathcal{L}}_{kn}^{e,(k)} d\bar{C}_{pq}^{e,(k+1)} \quad (106.201)$$

step 7. Update right deformation tensor  $\bar{C}_{pq}^{e,(k+1)}$ , hardening variable  $K_\alpha^{(k+1)}$  and Mandel stress  $\bar{T}_{mn}^{(k+1)}$

$$\begin{aligned} \bar{C}_{pq}^{e,(k+1)} &= \bar{C}_{pq}^{e,(k)} + d(\bar{C}_{pq}^{e,(k+1)}) \\ \kappa_\alpha^{(k+1)} &= \kappa_\alpha^{(k)} + d(\kappa_\alpha^{(k+1)}) \\ K_\alpha^{(k+1)} &= K_\alpha^{(k)} + d(K_\alpha^{(k+1)}) \\ \bar{T}_{mn}^{(k+1)} &= \bar{T}_{mn}^{(k)} + d(\bar{T}_{mn}^{(k+1)}) \end{aligned} \quad (106.202)$$

step 8. evaluate the yield function and the residual

$$\Phi^{(k+1)} = \Phi(\bar{T}_{ij}^{e,(k+1)}, K_\alpha^{(k+1)}) ; R_{ij}^{(k+1)} = \bar{C}_{ij}^{e,(k+1)} - \left( \bar{C}_{ij}^{e,tr} - \Delta\mu^{(k+1)} Z_{ij}^{(k+1)} \right) \quad (106.203)$$

step 9. Set  $k = k + 1$

$$\begin{aligned} \Delta\mu^{(k)} &= \Delta\mu^{(k+1)} \\ \bar{C}_{pq}^{e,(k)} &= \bar{C}_{pq}^{e,(k+1)} \\ \kappa_\alpha^{(k)} &= \kappa_\alpha^{(k+1)} \\ K_\alpha^{(k)} &= K_\alpha^{(k+1)} \\ \bar{T}_{mn}^{(k)} &= \bar{T}_{mn}^{(k+1)} \end{aligned} \quad (106.204)$$

and return to step 2.

#### 106.4.5 Algorithmic Tangent Stiffness Tensor

Starting from the elastic predictor–plastic corrector equation

$${}^{n+1}\bar{C}_{ij}^e = {}^{n+1}\bar{C}_{ij}^{e,tr} - \Delta\mu {}^{n+1}Z_{ij} \quad (106.205)$$

and taking the first order Taylor series expansion we obtain

$$\begin{aligned} d\bar{C}_{ij}^e &= d\bar{C}_{ij}^{e,tr} - d(\Delta\mu) Z_{ij} - \Delta\mu \frac{\partial Z_{ij}}{\partial \bar{T}_{mn}} d\bar{T}_{mn} - \Delta\mu \frac{\partial Z_{ij}}{\partial K_\alpha} dK_\alpha \\ &= d\bar{C}_{ij}^{e,tr} - d(\Delta\mu) Z_{ij} \\ &\quad - \Delta\mu \frac{\partial Z_{ij}}{\partial \bar{T}_{mn}} \left( d\bar{C}_{mk}^e (\bar{C}_{sk}^e)^{-1} \bar{T}_{sn} + \frac{1}{2} \bar{C}_{mk}^e \bar{\mathcal{L}}_{kn}^e d\bar{C}_{pq}^e \right) \text{ from (106.175)} \\ &\quad - \Delta\mu \frac{\partial Z_{ij}}{\partial K_\alpha} dK_\alpha \end{aligned} \quad (106.206)$$

Previous equation can be written as

$$\begin{aligned} d\bar{C}_{ij}^e + \Delta\mu \frac{\partial Z_{ij}}{\partial \bar{T}_{mn}} (\bar{C}_{sk}^e)^{-1} \bar{T}_{sn} d\bar{C}_{mk}^e + \Delta\mu d(\Delta\mu) \frac{\partial Z_{ij}}{\partial \bar{T}_{mn}} \frac{1}{2} \bar{C}_{mk}^e \bar{\mathcal{L}}_{kn}^e d\bar{C}_{pq}^e \\ = d\bar{C}_{ij}^{e,tr} - d(\Delta\mu) Z_{ij} + \Delta\mu d(\Delta\mu) \frac{\partial Z_{ij}}{\partial K_\alpha} H_{\alpha\beta} \frac{\partial \Phi^*}{\partial K_\beta} \end{aligned} \quad (106.207)$$

or as

$$d\bar{C}_{ij}^e (\mathcal{T}_{mnij}) = d\bar{C}_{ij}^{e,tr} - d(\Delta\mu) Z_{ij} + \Delta\mu d(\Delta\mu) \frac{\partial Z_{ij}}{\partial K_\alpha} H_{\alpha\beta} \frac{\partial\Phi^*}{\partial K_\beta} \quad (106.208)$$

where

$$\mathcal{T}_{mnij} = \delta_{im}\delta_{nj} + \Delta\mu^{(k)} \frac{\partial Z_{mn}^{(k)}}{\partial \bar{T}_{ik}^{(k)}} \left( \bar{C}_{sj}^{e,(k)} \right)^{-1} \bar{T}_{sk}^{(k)} + \frac{1}{2} \Delta\mu^{(k)} \frac{\partial Z_{mn}^{(k)}}{\partial \bar{T}_{pq}^{(k)}} \bar{C}_{pk}^{e,(k)} \bar{\mathcal{L}}_{kqij}^{e,(k)}$$

The solution for the increment in right elastic deformation tensor is then

$$d\bar{C}_{ij}^e = (\mathcal{T}_{mnij})^{-1} \left( d\bar{C}_{ij}^{e,tr} - d(\Delta\mu) Z_{ij} + \Delta\mu d(\Delta\mu) \frac{\partial Z_{ij}}{\partial K_\alpha} H_{\alpha\beta} \frac{\partial\Phi^*}{\partial K_\beta} \right) \quad (106.209)$$

We next use the first order Taylor series expansion of yield function  $d\Phi(\bar{T}_{ij}, K_\alpha) = 0$

$$\begin{aligned} \frac{\partial\Phi}{\partial \bar{T}_{mn}} d\bar{T}_{mn} + \frac{\partial\Phi}{\partial K_\alpha} dK_\alpha &= \\ \frac{\partial\Phi}{\partial \bar{T}_{mn}} \left( d\bar{C}_{mk}^e (\bar{C}_{sk}^e)^{-1} \bar{T}_{sn} + \frac{1}{2} \bar{C}_{mk}^e \bar{\mathcal{L}}_{knpq}^e d\bar{C}_{pq}^e \right) + \frac{\partial\Phi}{\partial K_\alpha} dK_\alpha &= \\ \frac{\partial\Phi}{\partial \bar{T}_{pn}} \left( \bar{C}_{sq}^e \right)^{-1} \bar{T}_{sn} d\bar{C}_{pq}^e + \frac{1}{2} \frac{\partial\Phi}{\partial \bar{T}_{mn}} \bar{C}_{mk}^e \bar{\mathcal{L}}_{knpq}^e d\bar{C}_{pq}^e + \frac{\partial\Phi}{\partial K_\alpha} dK_\alpha &= \\ \left( \frac{\partial\Phi}{\partial \bar{T}_{pn}} \left( \bar{C}_{sq}^e \right)^{-1} \bar{T}_{sn} + \frac{1}{2} \frac{\partial\Phi}{\partial \bar{T}_{mn}} \bar{C}_{mk}^e \bar{\mathcal{L}}_{knpq}^e \right) d\bar{C}_{pq}^e - \frac{\partial\Phi}{\partial K_\alpha} d(\Delta\mu) H_{\alpha\beta} \frac{\partial\Phi^*}{\partial K_\beta} &= \\ \mathcal{F}_{pq} d\bar{C}_{pq}^e - \frac{\partial\Phi}{\partial K_\alpha} d(\Delta\mu) H_{\alpha\beta} \frac{\partial\Phi^*}{\partial K_\beta} &= 0 \end{aligned} \quad (106.210)$$

where

$$\mathcal{F}_{pq} = \frac{\partial\Phi}{\partial \bar{T}_{pn}} \left( \bar{C}_{sq}^e \right)^{-1} \bar{T}_{sn} + \frac{1}{2} \frac{\partial\Phi}{\partial \bar{T}_{mn}} \bar{C}_{mk}^e \bar{\mathcal{L}}_{knpq}^e \quad (106.211)$$

By using solution for  $d\bar{C}_{ij}^e$  from 106.209 we can write

$$\begin{aligned} \mathcal{F}_{pq} (\mathcal{T}_{mnpq})^{-1} \left( d\bar{C}_{mn}^{e,tr} - d(\Delta\mu) Z_{mn} + \Delta\mu d(\Delta\mu) \frac{\partial Z_{mn}}{\partial K_\alpha} H_{\alpha\beta} \frac{\partial\Phi^*}{\partial K_\beta} \right) \\ - \frac{\partial\Phi}{\partial K_\alpha} d(\Delta\mu) H_{\alpha\beta} \frac{\partial\Phi^*}{\partial K_\beta} &= 0 \end{aligned} \quad (106.212)$$

We are now in the position to solve for the incremental inconsistency parameter  $d(\Delta\mu)$

$$d(\Delta\mu) = \frac{\mathcal{F}_{pq} (\mathcal{T}_{mnpq})^{-1} d\bar{C}_{mn}^{e,tr}}{\Gamma} \quad (106.213)$$

where we have used  $\Gamma$  to shorten writing

$$\Gamma = \mathcal{F}_{pq} (\mathcal{T}_{mnpq})^{-1} n+1 Z_{mn} - \Delta\mu \mathcal{F}_{pq} (\mathcal{T}_{mnpq})^{-1} \frac{\partial^{n+1} Z_{mn}}{\partial K_\alpha} H_{\alpha\beta} \frac{\partial\Phi^*}{\partial K_\beta} + \frac{\partial\Phi}{\partial K_\alpha} H_{\alpha\beta} \frac{\partial\Phi^*}{\partial K_\beta} \quad (106.214)$$

Since

$$d\bar{S}_{kn} = \frac{1}{2} \bar{\mathcal{L}}_{knpq}^e d\bar{C}_{pq}^e \quad (106.215)$$

and by using 106.209 we can write

$$\begin{aligned} d\bar{C}_{pq}^e = & \\ & (\mathcal{T}_{mnpq})^{-1} \left( \delta_{mv} \delta_{nt} - \frac{\mathcal{F}_{op} (\mathcal{T}_{rsop})^{-1} \delta_{rv} \delta_{st}}{\Gamma} Z_{mn} + \right. \\ & \left. \Delta\mu \frac{\mathcal{F}_{op} (\mathcal{T}_{rsop})^{-1} \delta_{rv} \delta_{st}}{\Gamma} \frac{\partial Z_{ij}}{\partial K_\alpha} H_{\alpha\beta} \frac{\partial \Phi^*}{\partial K_\beta} \right) d\bar{C}_{vt}^{e,tr} \end{aligned} \quad (106.216)$$

Then

$$d\bar{C}_{pq}^e = \bar{\mathcal{P}}_{pqvt} d\bar{C}_{vt}^{e,tr} \quad (106.217)$$

where

$$\begin{aligned} \bar{\mathcal{P}}_{pqvt} = & (\mathcal{T}_{mnpq})^{-1} \delta_{mv} \delta_{nt} - \frac{\mathcal{F}_{op} (\mathcal{T}_{rsop})^{-1} \delta_{rv} \delta_{st}}{\Gamma} Z_{mn} \\ & + \Delta\mu \frac{\mathcal{F}_{op} (\mathcal{T}_{rsop})^{-1} \delta_{rv} \delta_{st}}{\Gamma} \frac{\partial Z_{ij}}{\partial K_\alpha} H_{\alpha\beta} \frac{\partial \Phi^*}{\partial K_\beta} \\ = & (\mathcal{T}_{mnpq})^{-1} \left( \delta_{mv} \delta_{nt} - \frac{\mathcal{F}_{ab} (\mathcal{T}_{vtab})^{-1}}{\Gamma} \left( Z_{mn} - \Delta\mu \frac{\partial^{n+1} Z_{mn}}{\partial K_\alpha} H_{\alpha\beta} \frac{\partial \Phi^*}{\partial K_\beta} \right) \right) \end{aligned} \quad (106.218)$$

Algorithmic tangent stiffness tensor  $\bar{\mathcal{L}}_{ijkl}$  (in intermediate configuration  $\bar{\Omega}$ ) is then defined as

$$\bar{\mathcal{L}}_{knvt}^{ATS} = \bar{\mathcal{L}}_{knpq}^e \bar{\mathcal{P}}_{pqvt} \quad (106.219)$$

Pull-back to the reference configuration  $\Omega_0$  yields the algorithmic tangent stiffness tensor  $\mathcal{L}_{ijkl}$  in reference configuration  $\Omega_0$

$${}^{n+1}\mathcal{L}_{ijkl}^{ATS} = {}^{n+1}F_{im}^p {}^{n+1}F_{jn}^p {}^{n+1}F_{kr}^p {}^{n+1}F_{ls}^p {}^{n+1}\bar{\mathcal{L}}_{mnrs}^{ATS} \quad (106.220)$$

**Remark 106.4.8** In the limit, for small deformations, isotropic response, the Algorithmic Tangent Stiffness tensor  $\mathcal{L}_{ijkl}^{ATS}$  becomes

$$\begin{aligned} \lim \bar{\mathcal{L}}_{vtpq}^{ATS} = E_{vtpq}^{ATS} = & E_{knpq} \left( \Upsilon_{mnpq}^{-1} \left( \delta_{mv} \delta_{nt} - \frac{n_{cd} E_{cdab} \Upsilon_{vtab}^{-1} \mathcal{H}_{mn}}{\Gamma} \right) \right) \\ = & E_{knpq} \left( \Upsilon_{vtpq}^{-1} - \frac{\Upsilon_{mnpq}^{-1} n_{cd} E_{cdab} \Upsilon_{vtab}^{-1} \mathcal{H}_{mr}}{\Gamma} \right) \\ = & E_{knpq} \Upsilon_{vtpq}^{-1} - \frac{E_{knpq} \Upsilon_{mnpq}^{-1} n_{cd} E_{cdab} \Upsilon_{vtab}^{-1} \mathcal{H}_{mr}}{\Gamma} \\ = & \mathcal{R}_{knvt} - \frac{n_{cd} \mathcal{R}_{cdvt} \mathcal{R}_{kmnr} \mathcal{H}_{mr}}{\Gamma} \end{aligned} \quad (106.221)$$

since

$$\begin{aligned}\lim \bar{\mathcal{T}}_{mnpq} &= \Upsilon_{mnpq} = \delta_{pm}\delta_{nq} + \Delta\mu \frac{\partial Z_{mn}}{\partial \bar{T}_{pk}} \left( \bar{C}_{sq}^e \right)^{-1} \bar{T}_{sk} + \frac{1}{2} \Delta\mu \frac{\partial Z_{mn}}{\partial \bar{T}_{rs}} \bar{C}_{rk}^e \bar{\mathcal{L}}_{kspq} \\ &= \delta_{pm}\delta_{nq} + \Delta\mu \frac{\partial m_{mn}}{\partial \sigma_{rs}} E_{kspq}^e\end{aligned}\quad (106.222)$$

$$\begin{aligned}\lim \mathcal{F}_{ab} &= \lim \left( \frac{\partial \Phi}{\partial \bar{T}_{ad}} \left( \bar{C}_{sb}^e \right)^{-1} \bar{T}_{sd} + \frac{1}{2} \frac{\partial \Phi}{\partial \bar{T}_{cd}} \bar{C}_{ck}^e \bar{\mathcal{L}}_{kdab}^e \right) \\ &= \frac{1}{2} n_{cd} E_{cdab}^e\end{aligned}\quad (106.223)$$

$$\mathcal{H}_{mn} = m_{mn} - \Delta\mu \frac{\partial m_{mn}}{\partial K_\alpha} H_{\alpha\beta} \frac{\partial \Phi^*}{\partial K_\beta} \quad (106.224)$$

$$\begin{aligned}\lim \Gamma &= \lim \left( \mathcal{F}_{pq} \left( \mathcal{T}_{mnpq} \right)^{-1} n^{+1} Z_{mn} - \Delta\mu \mathcal{F}_{pq} \left( \mathcal{T}_{mnpq} \right)^{-1} \frac{\partial^{n+1} Z_{mn}}{\partial K_\alpha} H_{\alpha\beta} \frac{\partial \Phi^*}{\partial K_\beta} + \frac{\partial \Phi}{\partial K_\alpha} H_{\alpha\beta} \frac{\partial \Phi^*}{\partial K_\beta} \right) \\ &= n_{ab} E_{abpq} \Upsilon_{mnpq}^{-1} m_{mn} - \Delta\mu n_{ab} E_{abpq} \Upsilon_{mnpq}^{-1} \frac{\partial m_{mn}}{\partial K_\alpha} H_{\alpha\beta} \frac{\partial \Phi^*}{\partial K_\beta} + \frac{\partial \Phi}{\partial K_\alpha} H_{\alpha\beta} \frac{\partial \Phi^*}{\partial K_\beta} \\ &= n_{ab} E_{abpq} \Upsilon_{mnpq}^{-1} \left( m_{mn} - \Delta\mu \frac{\partial m_{mn}}{\partial K_\alpha} H_{\alpha\beta} \frac{\partial \Phi^*}{\partial K_\beta} \right) + \frac{\partial \Phi}{\partial K_\alpha} H_{\alpha\beta} \frac{\partial \Phi^*}{\partial K_\beta} \\ &= n_{ab} \mathcal{R}_{abmn} \mathcal{H}_{mn} + \frac{\partial \Phi}{\partial K_\alpha} H_{\alpha\beta} \frac{\partial \Phi^*}{\partial K_\beta}\end{aligned}\quad (106.225)$$

It is noted that the Algorithmic Tangent Stiffness tensor given by 106.221 compares exactly with it's small strain counterpart ([Jeremić and Sture, 1997](#)).

## Chapter 107

# Solution of Static Equilibrium Equations

(1994-2016-)

(In collaboration with Dr. Yuan Feng)

## 107.1 Chapter Summary and Highlights

## 107.2 The Residual Force Equations

This chapter is based on [Felippa \(1993\)](#).

In previous Chapters we have derived the basic equations for (material and/or geometric) nonlinear analysis of solids. Discretization of such problems by finite element methods results in a set of nonlinear algebraic equations called *residual force equations*:

$$\mathbf{r}(\mathbf{u}, \lambda) = \mathbf{f}_{int}(\mathbf{u}) - \lambda \mathbf{f}_{ext} = 0 \quad (107.1)$$

where  $\mathbf{f}_{int}(\mathbf{u})$  are the internal forces which are functions of the displacements,  $\mathbf{u}$ , the vector  $\mathbf{f}_{ext}$  is a fixed external loading vector and the scalar  $\lambda$  is a load-level parameter that multiplies  $\mathbf{f}_{ext}$ . Equation (107.1) describes the case of proportional loading in which the loading pattern is kept fixed.

All solution procedures of practical importance are strongly rooted in the idea of "advancing the solution" by *continuation*. Except in very simple problems, the continuation process is *multilevel* and involves hierarchical breakdown into stages, incremental steps and iterative steps. Processing a complex nonlinear problem generally involves performing a series of analysis stages. Multiple control parameters are not varied independently in each stage and may therefore be characterized by a single stage control parameter  $\lambda$ . Stages are only weakly coupled in the sense that end solution of one may provide the starting point for another.

## 107.3 Constraining the Residual Force Equations

Various forms of path following methods<sup>1</sup> have stemmed from the original work of [Riks \(1972\)](#), [Riks \(1979\)](#) and [Wempner \(1971\)](#). They aimed at finding the intersection of equation (107.1) with  $s = \text{constant}$  where  $s$  is the arc-length , defined as<sup>2</sup>:

$$s = \int ds \quad (107.2)$$

where:

$$ds = \sqrt{\frac{\psi_u^2}{u_{ref}^2} d\mathbf{u}^T \mathbf{S} d\mathbf{u} + d\lambda^2 \psi_f^2} \quad (107.3)$$

<sup>1</sup> also called arc-length methods with various methods of approximating the exact length of an arc.

<sup>2</sup>A bit different form in that it is scaled with scaling matrix  $\mathbf{S}$ , introduced by [Felippa \(1984\)](#).

Differential form (107.3) can be replaced with an incremental form:

$$a = (\Delta s)^2 - (\Delta l)^2 = \left( \frac{\psi_u^2}{u_{ref}^2} \Delta \mathbf{u}^T \mathbf{S} \Delta \mathbf{u} + \Delta \lambda^2 \psi_f^2 \right) - (\Delta l)^2 \quad (107.4)$$

where  $\Delta l$  is the radius of the desired intersection<sup>3</sup> and represents an approximation to the incremental arc length. Scaling matrix  $\mathbf{S}$  is usually diagonal non-negative matrix that scales the state vector  $\Delta \mathbf{u}$  and  $u_{ref}$  is a reference value with the dimension of  $\sqrt{\Delta \mathbf{u}^T \mathbf{S} \Delta \mathbf{u}}$ . It is important to note that the vector  $\Delta \mathbf{u}$  and scalar  $\Delta \lambda$  are incremental and not iterative values, and are starting from the last converged equilibrium state.

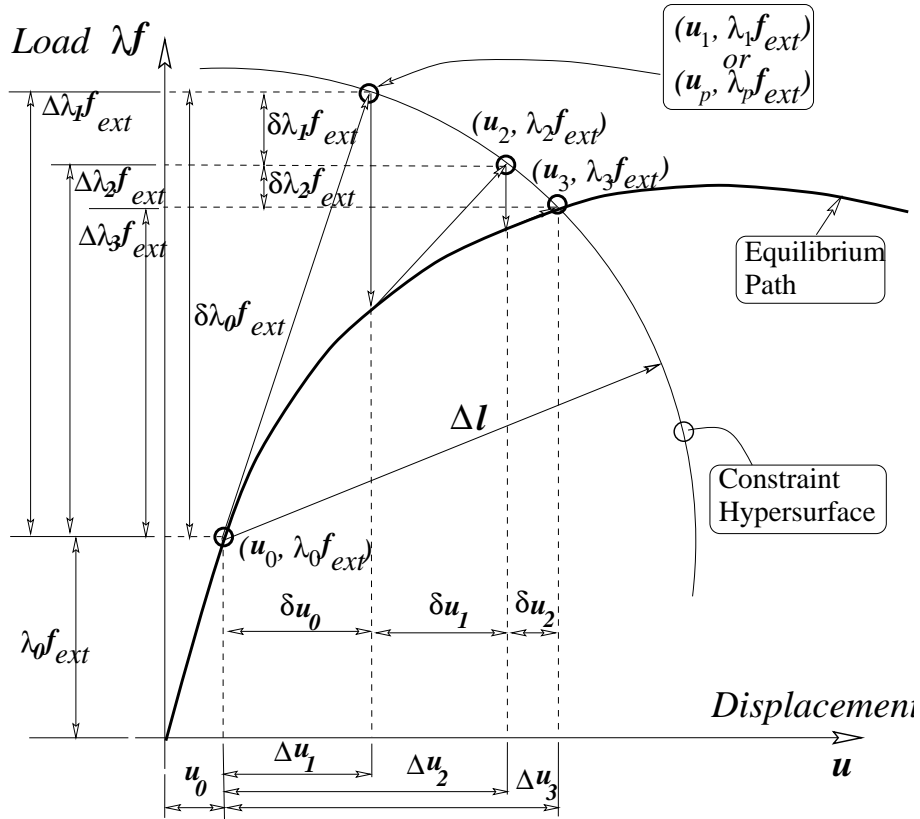


Figure 107.1: Spherical arc-length method and notation for one DOF system.

The main essence of the arc-length methods is that the load parameter  $\lambda$  becomes a variable. With load parameter  $\lambda$  variable we are dealing with  $n + 1$  unknowns<sup>4</sup>. In order to solve this problem we have  $n$  equilibrium equations (107.1) and the one constraint equation (107.4). We can solve the augmented

<sup>3</sup>See Figure (107.1).

<sup>4</sup> $n$  unknown displacement variables and one extra unknown in the form of load parameter.

system of  $n + 1$  equations by applying the Newton-Raphson<sup>5</sup> method to equations (107.1) and (107.4)

$$\begin{aligned}\mathbf{r}^{new}(\mathbf{u}, \lambda) &= \mathbf{r}^{old}(\mathbf{u}, \lambda) + \frac{\partial \mathbf{r}(\mathbf{u}, \lambda)}{\partial \mathbf{u}} \delta \mathbf{u} + \frac{\partial \mathbf{r}(\mathbf{u}, \lambda)}{\partial \lambda} \delta \lambda = \\ &= \mathbf{r}^{old}(\mathbf{u}, \lambda) + \mathbf{K}_t \delta \mathbf{u} - \mathbf{f}_{ext} \delta \lambda = \\ &= 0\end{aligned}\quad (107.5)$$

$$a^{new} = a^{old} + 2 \frac{\psi_u^2}{u_{ref}^2} \Delta \mathbf{u}^T \mathbf{S} \delta \mathbf{u} + 2 \Delta \lambda \delta \lambda \psi_f^2 = 0 \quad (107.6)$$

where  $\mathbf{K}_t = \frac{\partial \mathbf{r}(\mathbf{u}, \lambda)}{\partial \mathbf{u}}$  is the tangent stiffness matrix. The aim is to have  $\mathbf{r}^{new}(\mathbf{u}, \lambda) = 0$  and  $a^{new} = 0$  so the previous system can be written as:

$$\begin{bmatrix} \mathbf{K}_t & -\mathbf{f}_{ext} \\ 2 \frac{\psi_u^2}{u_{ref}^2} \Delta \mathbf{u}^T \mathbf{S} & 2 \Delta \lambda \psi_f^2 \end{bmatrix} \begin{bmatrix} \delta \mathbf{u} \\ \delta \lambda \end{bmatrix} = - \begin{bmatrix} \mathbf{r}^{old} \\ a^{old} \end{bmatrix} \quad (107.7)$$

One can solve previous system of two equations for  $\delta \mathbf{u}$  and  $\delta \lambda$ :

$$\begin{bmatrix} \delta \mathbf{u} \\ \delta \lambda \end{bmatrix} = - \begin{bmatrix} \mathbf{K}_t & -\mathbf{f}_{ext} \\ 2 \frac{\psi_u^2}{u_{ref}^2} \Delta \mathbf{u}^T \mathbf{S} & 2 \Delta \lambda \psi_f^2 \end{bmatrix}^{-1} \begin{bmatrix} \mathbf{r}^{old} \\ a^{old} \end{bmatrix} \quad (107.8)$$

or by defining the augmented stiffness matrix<sup>6</sup>  $\mathcal{K}$  as:

$$\mathcal{K} = \begin{bmatrix} \mathbf{K}_t & -\mathbf{f}_{ext} \\ 2 \frac{\psi_u^2}{u_{ref}^2} \Delta \mathbf{u}^T \mathbf{S} & 2 \Delta \lambda \psi_f^2 \end{bmatrix} \quad (107.9)$$

the equation (107.8) can be written as:

$$\begin{bmatrix} \delta \mathbf{u} \\ \delta \lambda \end{bmatrix} = -\mathcal{K}^{-1} \begin{bmatrix} \mathbf{r}^{old} \\ a^{old} \end{bmatrix} \quad (107.10)$$

It should be mentioned that the augmented stiffness matrix remains non-singular even if  $\mathbf{K}_t$  is singular.

<sup>5</sup>By using a truncated Taylor series expansion.

<sup>6</sup>Or augmented Jacobian.

## 107.4 Load Control

## 107.5 Displacement Control

## 107.6 Generalized, Hyper-Spherical Arc-Length Control

In section (107.3) we have introduced an constraining equation that is intended to reduce the so called drift error in the incremental nonlinear finite element procedure. The constraining equation was given in a rather general form. Some further comments and observations are in order. By assigning various numbers to parameters  $\psi_u$ ,  $\psi_f$ ,  $\mathbf{S}$  and  $u_{ref}$  one can obtain different constraining schemes from (107.4).

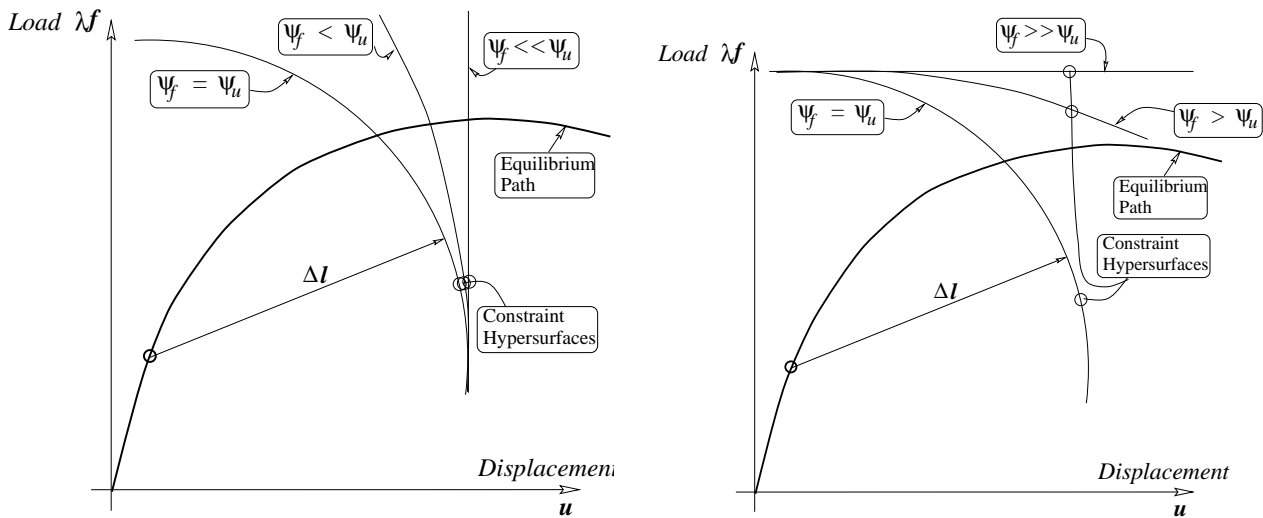


Figure 107.2: Influence of  $\psi_u$  and  $\psi_f$  on the constraint surface shape.

Coefficients  $\psi_u$  and  $\psi_f$  may not be simultaneously zero. Useful choices for  $\mathbf{S}$  are  $\mathbf{I}$ ,  $\mathbf{K}_t$  and  $diag(\mathbf{K}_t)$ . If  $\mathbf{S} = \mathbf{I}$  and  $u_{ref} = 1$  the method is called the arclength method<sup>7</sup>. If we choose  $\mathbf{S} = diag(\mathbf{K}_t)$  nice scaling is obtained<sup>8</sup> but otherwise no physical meaning can be attributed to this scaling type. With  $\mathbf{S} = \mathbf{K}_t$  and  $\psi_f \equiv 0$  one ends up with something very similar to the external work constraint of [Bathe and Dvorkin \(1983\)](#). A rather general equation (107.4) can be further specialized to load ( $\lambda$ ) control with  $\psi_u \equiv 0$ ;  $\psi_f \equiv 1$  and state control<sup>9</sup> with  $\psi_u \equiv 1$ ;  $\psi_f \equiv 0$  and  $\mathbf{S} = \mathbf{I}$ . In the finite element literature, the term displacement control has been traditionally associated with the case in which only one of the components of the displacement vector  $\mathbf{u}$ <sup>10</sup> is specified. This may be regarded either as a variant of state

<sup>7</sup>It actually reduces to the original work of [Riks \(1972\)](#), [Riks \(1979\)](#) and [Wempner \(1971\)](#).

<sup>8</sup>For example if FEM model includes both translational and rotational DOFs.

<sup>9</sup>That is the cylindrical constraint, or general displacement control.

<sup>10</sup>Say  $\mathbf{u}_i$ .

control, in which a norm that singles out the  $i$ th component is used, or as a variant of the  $\lambda$  control if the control parameter is taken as  $\lambda \mathbf{u}_i$ . It is, of course, possible to make the previous parameters variable, functions of different unknowns. For example if one defines  $u_{ref} = \Delta \mathbf{u}^T \mathbf{S} \Delta \mathbf{u}$  then close to the limit point  $\Delta \mathbf{u} \rightarrow 0 \Rightarrow \frac{\psi_u^2}{u_{ref}^2} \gg \psi_f^2$  that makes our constraint from equation (107.4) behave like state control. One important aspect of scaling constraint equations by using  $\mathbf{S} = diag(\mathbf{K}_t)$  or  $\mathbf{S} = \mathbf{K}_t$  is the possibility of non-positive definite stiffness matrix  $\mathbf{K}_t$ . It usually happens that after the limit point is passed, at least one of the eigenvalues of  $\mathbf{K}_t$  is non-positive, thus rendering the constraint hypersurface non-convex.

In order to get better control of the solution to the system of equations (107.10) one may directly introduce the constraint from equation (107.6) by following the approach proposed by [Batoz and Dhatt \(1979\)](#), as described by [Crisfield \(1991\)](#) and [Felippa \(1993\)](#).

The iterative displacement  $\delta \mathbf{u}$  is split into two parts, and with the Newton change at the new unknown load level:

$$\lambda^{new} = \lambda^{old} + \delta\lambda \quad (107.11)$$

becomes:

$$\begin{aligned} \delta \mathbf{u} &= -\mathbf{K}_t^{-1} \mathbf{r}(\mathbf{u}^{old}, \lambda) = -\mathbf{K}_t^{-1} (\mathbf{f}_{int}(\mathbf{u}^{old}) - \lambda^{new} \mathbf{f}_{ext}) \\ &= -\mathbf{K}_t^{-1} (\mathbf{f}_{int}(\mathbf{u}^{old}) - (\lambda^{old} + \delta\lambda) \mathbf{f}_{ext}) = -\mathbf{K}_t^{-1} ((\mathbf{f}_{int}(\mathbf{u}^{old}) - \lambda^{old} \mathbf{f}_{ext}) - \delta\lambda \mathbf{f}_{ext}) \\ &= -\mathbf{K}_t^{-1} (\mathbf{r}(\mathbf{u}^{old}, \lambda^{old}) - \delta\lambda \mathbf{f}_{ext}) = -\mathbf{K}_t^{-1} \mathbf{r}^{old} + \delta\lambda \mathbf{K}_t^{-1} \mathbf{f}_{ext} = \delta \bar{\mathbf{u}} + \delta\lambda \delta \mathbf{u}_t \end{aligned} \quad (107.12)$$

where  $\delta \mathbf{u}_t = \mathbf{K}_t^{-1} \mathbf{f}_{ext}$  is the displacement vector corresponding to the fixed load vector  $\mathbf{f}_{ext}$ , and  $\delta \bar{\mathbf{u}}$  is an iterative change that would stem from the standard load-controlled Newton-Raphson, at a fixed load level  $\lambda^{old}$ . With the solution<sup>11</sup> for the  $\delta \mathbf{u}$  from (107.12), the new incremental displacements are:

$$\Delta \mathbf{u}^{new} = \Delta \mathbf{u}^{old} + \delta \mathbf{u} = \Delta \mathbf{u}^{old} + \delta \bar{\mathbf{u}} + \delta\lambda \delta \mathbf{u}_t \quad (107.13)$$

where  $\delta\lambda$  is the only unknown. The constraint from equation (107.4) can be used here, and by rewriting it as:

$$\left( \frac{\psi_u^2}{u_{ref}^2} (\Delta \mathbf{u}^{new})^T \mathbf{S} (\Delta \mathbf{u}^{new}) + (\Delta \lambda^{new})^2 \psi_f^2 \right) = (\Delta l)^2 \quad (107.14)$$

<sup>11</sup>But having in mind that  $\delta\lambda$  is still unknown!

then by substituting  $\Delta\mathbf{u}^{new}$  from equation (107.13) into equation (107.14) and by recalling that  $\lambda^{new} = \lambda^{old} + \delta\lambda$  one ends up with the following quadratic scalar equation:

$$\left( \frac{\psi_u^2}{u_{ref}^2} (\Delta\mathbf{u}^{old} + \delta\bar{\mathbf{u}} + \delta\lambda\delta\mathbf{u}_t)^T \mathbf{S} (\Delta\mathbf{u}^{old} + \delta\bar{\mathbf{u}} + \delta\lambda\delta\mathbf{u}_t) + (\Delta\lambda^{old} + \delta\lambda)^2 \psi_f^2 \right) = (\Delta l)^2 \quad (107.15)$$

or, by collecting terms:

$$\begin{aligned} & \left( \frac{\psi_u^2}{u_{ref}^2} \delta\mathbf{u}_t^T \mathbf{S} \delta\mathbf{u}_t + \psi_f^2 \right) \delta\lambda^2 + \\ & + 2 \left( \frac{\psi_u^2}{u_{ref}^2} \delta\mathbf{u}_t^T \mathbf{S} (\Delta\mathbf{u}^{old} + \delta\bar{\mathbf{u}}) + \Delta\lambda^{old} \psi_f^2 \right) \delta\lambda + \\ & + \left( \frac{\psi_u^2}{u_{ref}^2} (\Delta\mathbf{u}^{old} + \delta\bar{\mathbf{u}})^T \mathbf{S} (\Delta\mathbf{u}^{old} + \delta\bar{\mathbf{u}}) - \Delta l^2 + (\Delta\lambda^{old})^2 \psi_f^2 \right) = 0 \end{aligned} \quad (107.16)$$

or:

$$a_1 \delta\lambda^2 + 2a_2 \delta\lambda + a_3 = 0 \quad (107.17)$$

where:

$$\begin{aligned} a_1 &= \frac{\psi_u^2}{u_{ref}^2} \delta\mathbf{u}_t^T \mathbf{S} \delta\mathbf{u}_t + \psi_f^2 \\ 2a_2 &= 2 \left( \frac{\psi_u^2}{u_{ref}^2} \delta\mathbf{u}_t^T \mathbf{S} (\Delta\mathbf{u}^{old} + \delta\bar{\mathbf{u}}) + \Delta\lambda^{old} \psi_f^2 \right) \\ a_3 &= \frac{\psi_u^2}{u_{ref}^2} (\Delta\mathbf{u}^{old} + \delta\bar{\mathbf{u}})^T \mathbf{S} (\Delta\mathbf{u}^{old} + \delta\bar{\mathbf{u}}) - \Delta l^2 + (\Delta\lambda^{old})^2 \psi_f^2 \end{aligned}$$

The quadratic scalar equation (107.17) can be solved for  $\delta\lambda$ :

$$\delta\lambda = \delta\lambda_1 = \frac{-a_2 + \sqrt{a_2^2 - a_1 a_3}}{a_1} ; \quad \delta\lambda = \delta\lambda_2 = \frac{-a_2 - \sqrt{a_2^2 - a_1 a_3}}{a_1} \quad (107.18)$$

or, if  $a_1 = 0$ , then:

$$\delta\lambda = -\frac{a_3}{2a_2} \quad (107.19)$$

and then the complete change is defined from equation (107.13):

$$\Delta \mathbf{u}^{new} = \Delta \mathbf{u}^{old} + \delta \bar{\mathbf{u}} + \delta \lambda \delta \mathbf{u}_t \quad (107.20)$$

An ambiguity is introduced in the solution for  $\delta\lambda$  from (107.18). The tangent at the regular point on the equilibrium path has two possible directions, which generally intersect the constraint hypersurface at two points. However, some exceptions from that rule are possible, so the solutions from (107.18) can be categorized as:

- Real roots of opposite signs. This occurs when the iteration process converges normally and there is no limit or turning point enclosed by the constraint hypersurface. The root is chosen by applying one of the schemes proposed below.
- Real roots of equal sign opposite to that of  $\Delta\lambda^{old}$ . This usually happens when going over a "flat" limit point.
- Real roots of equal sign same as that of  $\Delta\lambda^{old}$ . This is an unusual case. It may signal a turning point or be triggered by erratic iteration behavior.
- Complex roots. This is an unusual case too. It may signal a sharp turning point, a bifurcation point, erratic or divergent iterates.

For the first two cases, the correct  $\Delta\lambda$  can be chosen by applying one of the following schemes.

### 107.6.1 Traversing Equilibrium Path in Positive Sense

#### 107.6.1.1 Positive External Work

The simplest rule requires that the external work expenditure over the predictor step be positive:

$$\Delta W = \mathbf{f}_{ext}^T \Delta \mathbf{u} = \mathbf{f}_{ext}^T \mathbf{K}_t^{-1} \mathbf{f}_{ext} \delta \lambda > 0 \quad (107.21)$$

The simple conclusion is that  $\delta\lambda$  should have the sign of  $\mathbf{f}_{ext}^T \mathbf{K}_t^{-1} \mathbf{f}_{ext}$ . This condition is particularly effective at limit points. However, it fails when  $\mathbf{f}_{ext}$  and  $\mathbf{K}_t^{-1} \mathbf{f}_{ext}$  are orthogonal:

$$\mathbf{f}_{ext}^T \mathbf{K}_t^{-1} \mathbf{f}_{ext} = 0 \quad (107.22)$$

This can happen at:

- Bifurcation points,

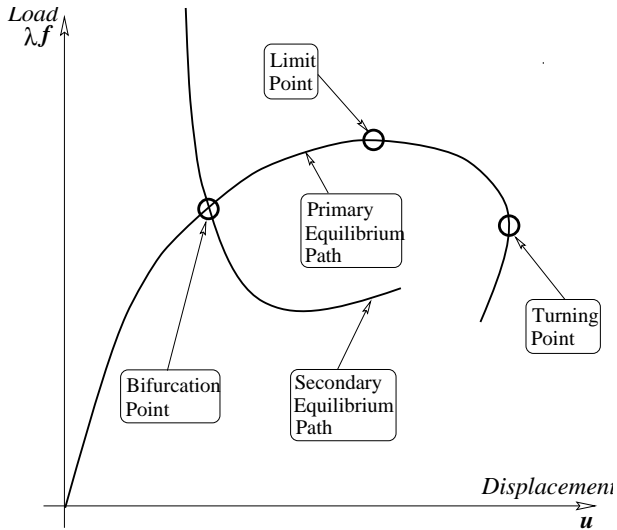


Figure 107.3: Simple illustration of Bifurcation and Turning point.

- Turning points,

The treatment of bifurcation points is of a rather special nature and is left for the near future. Turning points<sup>12</sup> can be traversed by a modification of a previous rule, as described in the next section.

#### 107.6.1.2 Angle Criterion

Near a turning point application of the positive work rule (107.21) causes the path to double back upon itself. When it crosses the turning point it reverses so the turning point becomes impassable. Physically, a positive work rule is incorrect because in passing a turning point the structure releases external work until another turning point is encountered.

To pass a turning point imposing a condition on the angle of the prediction vector proves more effective. The idea is to compute both solutions  $\delta\lambda_1$  and  $\delta\lambda_2$  and then both  $\Delta\mathbf{p}_1^{new}$  and  $\Delta\mathbf{u}_1^{new}$ :

$$\Delta\mathbf{u}_1^{new} = \Delta\mathbf{u}^{old} + \delta\bar{\mathbf{u}} + \delta\lambda_1\delta\mathbf{u}_t \quad (107.23)$$

$$\Delta\mathbf{u}_2^{new} = \Delta\mathbf{u}^{old} + \delta\bar{\mathbf{u}} + \delta\lambda_2\delta\mathbf{u}_t \quad (107.24)$$

<sup>12</sup>One might ask "why treating turning points in a material nonlinear analysis?". The answer is rather simple: "try to prevent all unnecessary surprises". For a good account of some of surprises in material nonlinear analysis one might take a look at some examples in Crisfield (1991) pp. 270.

The one that lies closest to the old incremental step direction  $\Delta\mathbf{u}^{old}$  is the one sought. This should prevent the solution from double backing. The procedure can be implemented by finding the solution with the minimum angle between  $\Delta\mathbf{u}^{old}$  and  $\Delta\mathbf{p}^{new}$ , and hence the maximum cosine of the angle:

$$\cos \phi = \frac{(\Delta\mathbf{u}^{old})^T (\Delta\mathbf{u}^{new})}{\|\Delta\mathbf{u}^{old}\| \|\Delta\mathbf{u}^{new}\|} = \frac{(\Delta\mathbf{u}^{old})^T (\Delta\mathbf{u}^{old} + \delta\bar{\mathbf{u}} + \delta\lambda\delta\mathbf{u}_t)}{\|\Delta\mathbf{u}^{old}\| \|\Delta\mathbf{u}^{old} + \delta\bar{\mathbf{u}} + \delta\lambda\delta\mathbf{u}_t\|} \quad (107.25)$$

where  $\delta\bar{\mathbf{u}} = -\mathbf{K}_t^{-1}\mathbf{r}^{old}$  and  $\delta\mathbf{u}_t = \mathbf{K}_t^{-1}\mathbf{f}_{ext}$ . Once the turning point has been crossed, the work criterion should be reversed so the external work is negative.

By directly introducing the constraint from equation (107.6) and following the method through equations (107.12) to (107.25) a limitation is introduced. Precisely at the limit point,  $\mathbf{K}_t$  is singular and the equations cannot be solved. However, Batoz and Dhatt (1979) and Crisfield (1991) report that no such problem has occurred, because one appears never to arrive precisely at limit point.

### 107.6.2 Predictor step

The predictor solution is achieved by applying one forward Euler, explicit step from the last obtained equilibrium point:

$$\Delta\mathbf{u}_p = \mathbf{K}_t^{-1}\Delta\mathbf{q}_e = \Delta\lambda_p \mathbf{K}_t^{-1}\mathbf{f}_{ext} = \Delta\lambda_p \delta\mathbf{u}_t \quad (107.26)$$

where  $\mathbf{K}_t$  is the tangent stiffness matrix at the beginning of increment. Substituting equation (107.26) into the constraint equation (107.14) one obtains:

$$\begin{aligned} \left( \frac{\psi_u^2}{u_{ref}^2} (\Delta\mathbf{u}^{new})^T \mathbf{S} (\Delta\mathbf{u}^{new}) + (\Delta\lambda^{new})^2 \psi_f^2 \right) &= \\ \left( \frac{\psi_u^2}{u_{ref}^2} \Delta\lambda_p^2 \delta\mathbf{u}_t^T \mathbf{S} \delta\mathbf{u}_t \right) + (\Delta\lambda_p)^2 \psi_f^2 &= \\ \Delta\lambda_p^2 \left( \frac{\psi_u^2}{u_{ref}^2} \delta\mathbf{u}_t^T \mathbf{S} \delta\mathbf{u}_t + \psi_f^2 \right) &= (\Delta l)^2 \end{aligned} \quad (107.27)$$

The solution for  $\Delta\lambda_p$  is readily found:

$$\Delta\lambda_p = \pm \frac{\Delta l}{\sqrt{\frac{\psi_u^2}{u_{ref}^2} |\delta\mathbf{u}_t^T \mathbf{S} \delta\mathbf{u}_t| + \psi_f^2}} \quad (107.28)$$

where  $\Delta l > 0$  is the given increment length. The absolute value of  $|\delta \mathbf{u}_t^T \mathbf{S} \delta \mathbf{u}_t|$  is needed if the stiffness matrix is chosen as a scaling matrix, i.e.  $\mathbf{S} = \mathbf{K}_t$ , since, after passing limit point, the stiffness matrix is non-positive definite so  $\delta \mathbf{u}_t^T \mathbf{S} \delta \mathbf{u}_t \leq 0$ . The question of choosing the right sign + or - in (107.28) is still a vigorous research topic. In the simplified procedure<sup>13</sup> the negative sign - is chosen with respect to the occurrence of one negative pivot during factorization of the tangent stiffness matrix  $\mathbf{K}_t$ . If more than one pivot happens to be negative, one is advised<sup>14</sup> to stop the analysis and try to restart from previously converged solution with smaller step size.

### 107.6.3 Automatic Increments

A number of workers have advocated different strategies for controlling the step length size. In this work we will follow the strategy advocated by Crisfield (1991). The idea is to find the new incremental length by applying:

$$\Delta l^{new} = \Delta l^{old} \left( \frac{I_{desired}}{I_{old}} \right)^n \quad (107.29)$$

where  $\Delta l^{old}$  is the old incremental factor for which  $I_{old}$  iterations were required,  $I_{desired}$  is the input, desired number of iterations<sup>15</sup> and the parameter  $n$  is set to  $\frac{1}{2}$  as suggested by Ramm (1982) Ramm (1981).

### 107.6.4 Convergence Criteria

Introduction of an iterative scheme calls for the introduction of an iteration termination test. There are several convergence criteria that can be applied.

- Absolute Displacement Convergence Criteria. The change in the last correction  $\delta \mathbf{u}$  of the state vector  $\mathbf{u}$ , measured in an appropriate norm, should not exceed a given tolerance  $\epsilon_u$ . For example, if we use Euclidean norm<sup>16</sup> the termination criteria can be written as:

$$\|\delta \mathbf{u}\|_{absolute} = \sqrt{(\delta \mathbf{u})^T \mathbf{S} (\delta \mathbf{u})} \leq \epsilon_u \quad (107.30)$$

Scaling matrix  $\mathbf{S}$  is used in order to ensure that for a problem involving mixed units<sup>17</sup>, all parameters have the same unit. Here, an obvious choice for the scaling matrix is  $\mathbf{S} = diag(\mathbf{K}_t^{-1})$ . If, on the

<sup>13</sup>Which is not guaranteed to work if one takes into account bifurcation phenomena.

<sup>14</sup>For more details see Crisfield (1991).

<sup>15</sup>Say  $I_{desired} \approx 3$ .

<sup>16</sup>The so called 2-norm.

<sup>17</sup>For example, if rotations and displacements are involved.

other hand we don't have mixed variables in state vector  $\mathbf{u}$  then the simplest choice for scaling matrix is  $\mathbf{S} = \mathbf{I}$ .

Currently used within FEB and the Real-ESSI program is an absolute convergence criteria with unit scaling matrix  $\mathbf{S} = \mathbf{I}$ . This means that absolute tolerance criteria mixes units for different Degrees of Freedom (DoFs). Supplied tolerance is converted to basic units of the system (meter and Newton) and that is used for comparison and convergence decisions.

- Relative Displacement Convergence Criteria. It is beneficial to use the relative convergence criteria in order to relax convergence criteria for problems where one or few displacements dominate. In order to do that, use of ratio of Euclidean norm of iterative displacement  $\|\delta\mathbf{u}\|_{scaled}$  and Euclidean norm of total displacement  $\|\mathbf{u}\|_{scaled}$  is recommended:

$$\frac{\|\delta\mathbf{u}\|_{relative}}{\|\mathbf{u}\|_{scaled}} \leq \epsilon_u \quad (107.31)$$

Again it is important to note that currently used within FEB and the Real-ESSI program is an absolute convergence criteria with unit scaling matrix  $\mathbf{S} = \mathbf{I}$ . This means that relative tolerance criteria mixes units for different Degrees of Freedom (DoFs). Supplied tolerance is converted to basic units of the system (meter and Newton) and that is used for comparison and convergence decisions.

- Average Displacement Convergence Criteria. The change in the last correction  $\delta\mathbf{u}$  of the state vector  $\mathbf{u}$ , measured in an appropriate norm, should not exceed a given tolerance  $\epsilon_u$ , divided by the total number of DoFs:

$$\|\delta\mathbf{u}\|_{average} = \frac{\sqrt{(\delta\mathbf{u})^T \mathbf{S} (\delta\mathbf{u})}}{nDoFs} \leq \epsilon_u \quad (107.32)$$

This is important in order to preserve objectivity of displacement convergence criteria for similar (same) models that are discretized with a different number of finite elements (and therefore feature different number of nodes and DoFs). For example, a cantilever (simplest model) can be discretized using 5 DoFs and 5,000,000 DoFs. Since equation 107.32 essentially sums up absolute values of all displacements, it is expected that in the case of larger number of DoFs, larger norm will be calculated. This will create a problem since specified tolerance will then be a function of a number of DoFs a model features. Hence, a norm of all iterative displacements is divided by the total number of DoFs.

One more time, it is important to note that currently used within FEB and the Real-ESSI program is an absolute convergence criteria with unit scaling matrix  $\mathbf{S} = \mathbf{I}$ . Therefore average tolerance criteria

mixes units. Supplied tolerance is converted to basic units of the system (meter and Newton) and that is used for comparison and convergence decisions.

- Absolute Residual Force Convergence Criteria. Since the residual  $\mathbf{r}(\mathbf{u}, \lambda)$  measures the departure from the equilibrium path, an appropriate convergence test would be to compare Euclidean norm of residual with some predefined tolerance:

$$\|\mathbf{r}(\mathbf{u}, \lambda)\|_{scaled} = \sqrt{(\mathbf{r})^T \mathbf{S}(\mathbf{r})} \leq \epsilon_r \quad (107.33)$$

Here, an obvious choice for scaling matrix is  $\mathbf{S} = diag(\mathbf{K}_t)$

Much the same as for displacement based convergence criteria, currently used within FEB and the Real-ESSI program is a convergence criteria with unit scaling matrix  $\mathbf{S} = \mathbf{I}$ . This means that absolute tolerance criteria mixes units for different Degrees of Freedom (DoFs). Supplied tolerance is converted to basic units of the system (meter and Newton) and that is used for comparison and convergence decisions.

- Relative Residual Force Convergence Criteria. In order to provide scaling of residual forces that are used to tolerance criteria, (previously defined) absolute residual force norm is divided (scaled) by a a norm of residual forces at the beginning of the iterative step:

$$\|\mathbf{r}(\mathbf{u}, \lambda)\|_{relative} = \frac{\sqrt{(\mathbf{r})^T \mathbf{S}(\mathbf{r})}}{\sqrt{(\mathbf{r}_0)^T \mathbf{S}(\mathbf{r}_0)}} \leq \epsilon_r \quad (107.34)$$

Here, an obvious choice for scaling matrix is  $\mathbf{S} = diag(\mathbf{K}_t)$ , however, within FEB and the Real-ESSI program, for this convergence criteria, a unit scaling matrix  $\mathbf{S} = \mathbf{I}$  is used, therefor relative tolerance criteria will feature mixed units.

- Average Residual Force Convergence Criteria. With the residual  $\mathbf{r}(\mathbf{u}, \lambda)$ , which measures the departure from the equilibrium path, there is a need to take into the account number of DoFs, in order to reduce the influence of a model discretization (number of DoFs) on norm of the residual force vector:

$$\|\mathbf{r}(\mathbf{u}, \lambda)\|_{scaled} = \frac{\sqrt{(\mathbf{r})^T \mathbf{S}(\mathbf{r})}}{nDoFs} \leq \epsilon_{average} \quad (107.35)$$

Here, an obvious choice for scaling matrix is  $\mathbf{S} = diag(\mathbf{K}_t)$  however, again, as noted above, within FEB and the Real-ESSI program, for this convergence criteria, a unit scaling matrix  $\mathbf{S} = \mathbf{I}$  is used, therefor relative tolerance criteria will feature mixed units.

- Energy Based Convergence Criteria. The previous convergence criteria can be combined in a single work change criterion:

$$\|(\delta\mathbf{u})^T(\mathbf{r})\| = \sqrt{(\delta\mathbf{u})^T(\mathbf{r})} \leq \epsilon_u \epsilon_r \quad (107.36)$$

A word of caution is appropriate at this point. As pointed out by Crisfield (1991), it follows that:

$$\|(\delta\mathbf{u})^T(\mathbf{r})\| = \|(\delta\mathbf{u})^T(\mathbf{K}_t^{-1}\mathbf{K}_t)(\mathbf{r})\| = \|-(\delta\mathbf{u})^T\mathbf{K}_t(\delta\mathbf{u})\| \leq \epsilon_u \epsilon_r \quad (107.37)$$

where the iterative change was  $(\delta\mathbf{u}) = -\mathbf{K}_t^{-1}\mathbf{r}$ . It should be noted that equations (107.37) give a measure of the "stiffness" of  $\mathbf{K}_t$ . This merely implies that a stationary energy position has been reached in the current iterative direction,  $\delta\mathbf{u}$ . This can occur when the solution is still far away from equilibrium.

Since  $\mathbf{u}$  and  $\mathbf{r}$  usually have physical unites, so do necessarily  $\epsilon_u$  and  $\epsilon_r$ . For a general purpose implementation of Newton–Raphson iteration this dependency on physical units is undesirable and it is more convenient to work with ratios that render the  $\epsilon_u$  and  $\epsilon_r$  dimensionless. Displacement Convergence Criteria can be rendered dimensionless by using ratio of scaled Euclidean norm of iterative displacement  $\|\delta\mathbf{u}\|_{scaled}$  and scaled Euclidean norm of total displacement  $\|\mathbf{u}\|_{scaled}$ :

$$\frac{\|\delta\mathbf{u}\|_{scaled}}{\|\mathbf{u}\|_{scaled}} \leq \epsilon_u \quad (107.38)$$

The similar approach can be used for Residual Convergence Criteria:

$$\frac{\|\mathbf{r}\|_{scaled}}{\|\mathbf{r}^{predictor}\|_{scaled}} \leq \epsilon_r \quad (107.39)$$

Another important thing to be considered is Divergence. The Newton–Raphson scheme is not guaranteed to converge. Some sort of divergence detection scheme is therefor necessary in order to interrupt an erroneous iteration cycle. Divergence can be diagnosed if either of following inequalities occur:

$$\frac{\|\delta\mathbf{u}\|_{scaled}}{\|\mathbf{u}\|_{scaled}} \geq g_u \quad (107.40)$$

$$\frac{\|\mathbf{r}\|_{scaled}}{\|\mathbf{r}^{predictor}\|_{scaled}} \geq g_r \quad (107.41)$$

where  $g_u$  and  $g_r$  are dangerous growth factors that can be set to, for example  $g_u = g_r = 100$ .

In some cases, the Newton–Raphson iteration scheme will neither diverge nor converge, but rather exhibit oscillatory behavior. To avoid excessive bouncing around, a good practice is to put upper limit to the number of iterations performed in one iteration cycle. Typical limits to the iteration number are 20 to 50.

### 107.6.5 The Algorithm Progress

The progress of the scheme will be briefly described, in relation with the Figure (107.1). The procedure starts from a previously converged solution  $(\mathbf{u}_0, \lambda_0 \mathbf{f}_{ext})$ . An incremental, tangential predictor step  $\Delta\mathbf{u}_1, \Delta\lambda_1$  is obtained<sup>18</sup> and the next point obtained is  $(\mathbf{u}_1, \lambda_1 \mathbf{f}_{ext})$ . The first iteration would then use quadratic equation 107.17 where constants  $a_1, a_2$  and  $a_3$  should be computed with  $\Delta\mathbf{u}^{old} = \Delta\mathbf{u}_1$  and  $\Delta\lambda^{old} = \Delta\lambda_1$ , to calculate  $\delta\lambda_1$  and<sup>19</sup>  $\delta\mathbf{u}_1 = -\mathbf{K}_t^{-1}\mathbf{r}(\mathbf{u}_1, \lambda_1) + \delta\lambda_1 \mathbf{K}_t^{-1}\mathbf{f}_{ext}$ . After these values are calculated, the updating procedure<sup>20</sup> would lead to:

$$\Delta\lambda_2 = \Delta\lambda_1 + \delta\lambda_1 \quad \text{and} \quad \Delta\mathbf{u}_2 = \Delta\mathbf{u}_1 + \delta\mathbf{u}_1 \quad (107.42)$$

When added to the displacements  $\mathbf{u}_0$  and load level  $\lambda_0$ , at the end of the previous increment this process would lead to the next point  $(\mathbf{u}_2, \lambda_2 \mathbf{f}_{ext})$ .

The next iteration would then again use quadratic equation 107.17 where constants  $a_1, a_2$  and  $a_3$  should be computed with  $\Delta\mathbf{u}^{old} = \Delta\mathbf{u}_2$  and  $\Delta\lambda^{old} = \Delta\lambda_2$ , to calculate  $\delta\lambda_3$  and  $\delta\mathbf{u}_3 = \delta\bar{\mathbf{u}} + \delta\lambda_2 \delta\mathbf{u}_t$ . After these values are calculated, the updating procedure would lead to:

$$\Delta\lambda_3 = \Delta\lambda_2 + \delta\lambda_2 \quad \text{and} \quad \Delta\mathbf{u}_3 = \Delta\mathbf{u}_2 + \delta\mathbf{u}_2 \quad (107.43)$$

When added to the displacements  $\mathbf{u}_0$  and load level  $\lambda_0$ , at the end of the previous increment this process would lead to the next point  $(\mathbf{u}_3, \lambda_3 \mathbf{f}_{ext})$ .

---

<sup>18</sup>As explained in Section (107.6.2).

<sup>19</sup>From equation (107.12).

<sup>20</sup>See (107.11) and (107.13)

## Chapter 108

# Solution of Dynamic Equations of Motion

(1989-2006-2016-2018-2019-)

(In collaboration with Dr. Nima Tafazzoli and Prof. José Abell)

## 108.1 Chapter Summary and Highlights

## 108.2 The Principle of Virtual Displacements in Dynamics

(see section 102.2 on page 100).

Great reading on this subject is a book by [Argyris and Mlejnek \(1991\)](#).

## 108.3 Direct Integration Methods for the Equations of Dynamic Equilibrium

This section follows [Argyris and Mlejnek \(1991\)](#) and [Hughes \(1987\)](#).

need to rewrite and improve! BJ

### 108.3.1 Newmark Integrator

The Newmark time integration method ([Newmark, 1959](#)) uses two parameters,  $\beta$  and  $\gamma$ , and is defined by the following two equations:

$${}^{n+1}x = {}^n x + \Delta t {}^n \dot{x} + \Delta t^2 [(\frac{1}{2} - \beta) {}^n \ddot{x} + \beta {}^{n+1} \ddot{x}] \quad (108.1)$$

$${}^{n+1} \dot{x} = {}^n \dot{x} + \Delta t [(\frac{1}{2} - \gamma) {}^n \ddot{x} + \gamma {}^{n+1} \ddot{x}] \quad (108.2)$$

These equations give relationship between knowns variables at time step  $n$  to the unknown variables at next time step  $n + 1$ . Method is in general an implicit one, except when  $\beta = 0$  and  $\gamma = 1/2$ .

There are several possible implementation methods for Newmark Integrator. One possible approach to integrating equations of motion using Newmark algorithm is to use displacement as the basic unknowns, and the following difference relations are used to relate  ${}^{n+1} \dot{x}$  and  ${}^{n+1} \ddot{x}$  to  ${}^{n+1} x$  and the response quantities are

$${}^{n+1} \dot{x} = \frac{\gamma}{\beta \Delta t} ({}^{n+1} x - {}^n x) + \left(1 - \frac{\gamma}{\beta}\right) {}^n \dot{x} + \left(1 - \frac{\gamma}{2\beta}\right) {}^n \ddot{x} \quad (108.3)$$

$${}^{n+1} \ddot{x} = \frac{1}{\beta \Delta t^2} ({}^{n+1} x - {}^n x) - \frac{1}{\beta \Delta t} {}^n \dot{x} + \left(1 - \frac{1}{2\beta}\right) {}^n \ddot{x} \quad (108.4)$$

The predictors are then:

$${}^{n+1} \dot{x}^\diamond = -\frac{\gamma}{\beta \Delta t} {}^n x + \left(1 - \frac{\gamma}{\beta}\right) {}^n \dot{x} + \Delta t \left(1 - \frac{\gamma}{2\beta}\right) {}^n \ddot{x} \quad (108.5)$$

$${}^{n+1} \ddot{x}^\diamond = -\frac{1}{\beta \Delta t^2} {}^n x - \frac{1}{\beta \Delta t} {}^n \dot{x} + \left(1 - \frac{1}{2\beta}\right) {}^n \ddot{x} \quad (108.6)$$

and the correctors:

$${}^{n+1} \dot{x} = {}^{n+1} \dot{x}^\diamond + \frac{\gamma}{\beta \Delta t} {}^{n+1} x \quad (108.7)$$

$${}^{n+1} \ddot{x} = {}^{n+1} \ddot{x}^\diamond + \frac{1}{\beta \Delta t^2} {}^{n+1} x \quad (108.8)$$

The Newton integration method becomes

$$\left[ \frac{M}{\beta \Delta t^2} + \frac{\gamma C}{\Delta t} + K \right] \Delta x = -^{n+1}R \quad (108.9)$$

Equation 108.5 to 108.9 constitute an iterative solving procedure (Argyris and Mlejnek, 1991).

If the parameters  $\beta$  and  $\gamma$  satisfy

$$\gamma \geq \frac{1}{2}, \quad \beta \geq \frac{1}{4}(\gamma + \frac{1}{2})^2 \quad (108.10)$$

the procedure is unconditionally stable and second-order accurate. Any  $\gamma$  value greater than 0.5 will introduce numerical damping. Well-known members of the Newmark time integration method family include: trapezoidal rule or average acceleration method for  $\beta = 1/4$  and  $\gamma = 1/2$ , linear acceleration method for  $\beta = 1/6$  and  $\gamma = 1/2$ , and (explicit) central difference method for  $\beta = 0$  and  $\gamma = 1/2$ . If and only if  $\gamma = 1/2$ , the accuracy is second-order Hughes (1987). For values of  $\beta = 1$  and  $\gamma = 2/3$ , the strongest numerical damping is obtained, as spectral ratio  $\rho_\infty = 0$  (Hughes (1987), page 502)

### 108.3.2 HHT Integrator

Numerical damping introduced in the Newmark time integration method will degrade the order of accuracy. The Hilber-Hughes-Taylor (HHT) time integration  $\alpha$ -method (Hilber et al., 1977), (Hughes and Liu, 1978a) and (Hughes and Liu, 1978b) using an alternative residual form by introducing an addition parameter  $\alpha$  to improve the performance:

$$^{n+1}R = M^{n+1}\ddot{x} + (1 + \alpha)F(^{n+1}\dot{x}, ^{n+1}x) - \alpha F(^n\dot{x}, ^n x) - ^{n+1}f \quad (108.11)$$

but retaining the Newmark finite-difference formulas 108.1 and 108.2 or 108.3 and 108.4. If  $\alpha = 0$ , the HHT time integration method becomes exactly the same Newmark time integration method. Decreasing  $\alpha$  value increase numerical dissipation (Hughes, 1987).

The iteration method for HHT time integration is similar to that of Newmark time integration. Due to the change of Equation 108.11, Equation 108.9 becomes

$$\left[ M + (1 + \alpha)\gamma \Delta t C + (1 + \alpha)\beta \Delta t^2 K \right] \Delta \ddot{x} = -^{n+1}R \quad (108.12)$$

for acceleration iteration and

$$\left[ \frac{1}{\beta \Delta t^2} M + \frac{(1 + \alpha)}{\gamma \Delta t} C + (1 + \alpha)K \right] \Delta x = -^{n+1}R \quad (108.13)$$

for displacement iteration.

If the parameters  $\alpha$ ,  $\beta$  and  $\gamma$  satisfy

$$-1/3 \leq \alpha \leq 0, \quad \gamma = \frac{1}{2}(1 - 2\alpha), \quad \beta = \frac{1}{4}(1 - \alpha)^2 \quad (108.14)$$

it is unconditionally stable and second-order accurate (Hughes, 1987).

## 108.4 Synthetic Viscous Damping for Solids and Structures

Presented here are commonly used, viscous damping methods for time domain analysis of solids and structures. These methods, Rayleigh and Caughey damping, are mimicking viscous damping of the solids and structures by generating the damping matrix  $\mathbf{C}$  using mass and stiffness matrices.

These synthetic viscous damping approaches should be distinguished from a natural viscous damping that is created during interaction of fluid and soil. For example, a natural viscous damping occurs when pore fluid and porous solid have differential displacements, as described in section [102.12.1.4](#) on page [143](#) (see for example equation ?? on page ??).

### 108.4.1 Synthetic Viscous Damping Approaches

There are different numerical methods available to simulate the seismic wave propagation through the soil-structure systems such as boundary elements, finite elements, finite differences, meshfree methods, and spectral elements. There are advantages of using methods such as finite elements or spectral elements for complex geometries or modeling the nonlinearities but also disadvantage such as numerical dispersion for low-order finite elements or reflection of the motions from the boundaries of the model ([Semblat et al. \(2010\)](#)).

Boundary element method can deal better with the issue of reflecting the motions from boundaries comparing to other numerical methods. Research has been done on coupling this method with other numerical methods for better applications. Domain reduction method is also available for large models implemented in finite element in order to reduce the problem of reflection ([Bielak et al. \(2003a\)](#)).

There are methods so called non-reflecting boundary conditions which directly can attenuate the reflections at the mesh boundaries. One of the commonly used method is absorbing boundary conditions. Absorbing boundary conditions have special conditions at the model boundaries in order to approximate the radiation condition for seismic waves ([Givoli \(1991\)](#)).

Another method applicable in finite element methods is so called infinite element method. These elements can absorb the waves using decaying laws at model boundaries at infinity ([Nenning and Schanz \(2010\)](#); [Kallivokas et al. \(1997\)](#)). In this method it is assumed that the element and nodes of the boundary are in infinity. In this case the seismic waves have enough distance to dissipate at the boundaries and not to reflect back to the model.

There has been a recently developed method to prevent reflection of the waves from boundaries called Perfectly Matched Layers (PML). This absorbing layer is based on attenuation laws with specific properties and finite thickness located at the model boundaries. There are several PML formulations proposed for finite element methods which allows the treatment of surface waves as well as body waves

(Festa and Nielsen (2003); Basu (2009)).

Bilbao et al. (2006) proposed two energy-based methods to model damping in structures with added viscoelastic dampers. these methods approximate the effects of the added viscoelastic dampers with a damping matrix in the form of Caughey damping matrix.

The method to be used here is so called Caughey Absorbing Layer Method. The 2<sup>nd</sup> order of this method is also known as a Rayleigh damping. Caughey damping is a classical method in which the damping matrix is built based on the mass and stiffness matrices. Since the stiffness and mass matrices of have to be created for solving the system of equations, they are used for creating the damping matrix as well.

Considering the relationship between internal friction and frequency for damping, it is possible to build a model involving the same attenuation/frequency dependence for Caughey damping (Semblat (1997)). The relation of the inverse of the quality factor  $Q^{-1}$  and the damping ratio  $\xi$  can be written as:

$$Q^{-1} \approx 2\xi \quad (108.15)$$

Caughey damping formulation in general can be expressed as

$$C = [M] \sum_{j=0}^{m-1} a_j ([M]^{-1} [K])^j \quad (108.16)$$

where the order to be used depends on number of modes to be considered for damping in the problem.

The way it is implemented in ESSI Simulator gives the opportunity to the user to use different types of damping for different elements. There might not be a need to use damping for all the elements of the model. In this case, damping could be used for particular elements and leave the rest of them with no physical Caughey damping. It can also be used for damping out the residual waves coming out of the domain reduction boundary layer.

#### 108.4.2 Caughey Damping 2<sup>nd</sup> Order, aka Rayleigh Damping

The second order Caughey damping, is also known as a Rayleigh damping, with  $j = 1$  in Equation (108.16). From dynamic parameters and formulation of the system following equations can be observed:

$$\xi_n = \frac{C_n}{2M_n\omega_n} \quad (108.17)$$

$$K_n = \omega_n^2 M_n \quad (108.18)$$

Considering the first two terms in Caughey damping formulation, if the damping matrix formulation is written separately for each term:

$$C = a_0 M \quad (108.19)$$

Based on Equation (108.17),  $a_0$  can be written as:

$$a_0 = 2\xi\omega \quad (108.20)$$

Writing the damping matrix based on the second coefficient:

$$C = a_1 K = a_1 \omega^2 M \quad (108.21)$$

Then  $a_1$  can be obtained as:

$$a_1 = \frac{2\xi}{\omega} \quad (108.22)$$

So the damping ratio of the  $n^{th}$  mode of the system is:

$$\xi_n = \frac{a_0}{2} \frac{1}{\omega_n} + \frac{a_1}{2} \omega_n \quad (108.23)$$

Presenting Equation (108.23) for first two modes in matrix form leads to:

$$\frac{1}{2} \begin{bmatrix} \frac{1}{\omega_i} & \omega_i \\ \frac{1}{\omega_j} & \omega_j \end{bmatrix} \begin{bmatrix} a_0 \\ a_1 \end{bmatrix} = \begin{bmatrix} \xi_i \\ \xi_j \end{bmatrix} \quad (108.24)$$

The following procedure given by Hall (2006) is useful to conveniently determine Rayleigh damping coefficients  $a_0$  and  $a_1$ . Select a desired amount of damping  $\xi$  and a frequency range from  $\hat{\omega}$  to  $R\hat{\omega}$ , where  $R > 1$ . Compute  $\Delta$  from:

$$\Delta = \xi \frac{1 + R - 2\sqrt{R}}{1 + R + 2\sqrt{R}} \quad (108.25)$$

where  $\Delta$  determines bounds on the damping ratios that are imparted to those modes within the specified frequency range. Any such mode will have a damping ratio bounded by  $\xi_{max} = \xi + \Delta$  and  $\xi_{min} = \xi - \Delta$ . If these bounds are satisfactorily narrow, the constants  $a_0$  and  $a_1$  are then calculated from:

$$a_0 = 2\xi\hat{\omega} \frac{2R}{1+R+2\sqrt{R}} \quad (108.26)$$

$$a_1 = 2\xi\frac{1}{\hat{\omega}} \frac{2}{1+R+2\sqrt{R}} \quad (108.27)$$

and can be used to compute an actual damping value  $\xi_n$  for mode  $n$  from Equation (108.23).

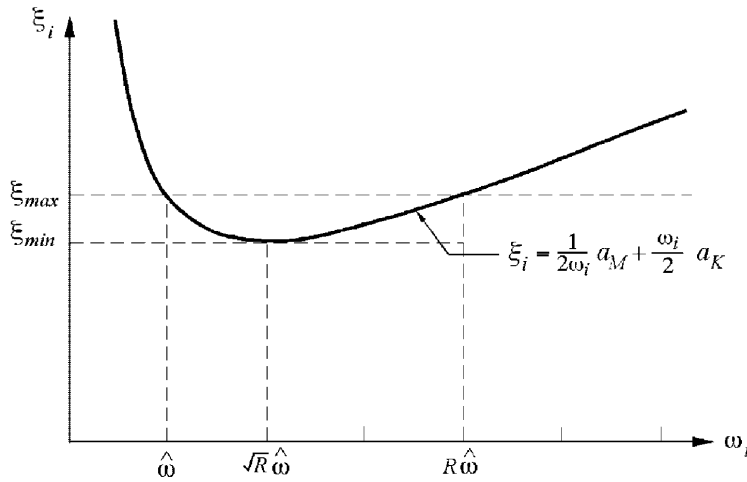


Figure 108.1: Actual damping ratio  $\xi_n$  of mode  $n$  as a function of frequency  $\omega_n$  of mode  $n$  when using Rayleigh damping (Hall (2006)).

Figure (108.1) shows that  $\xi_n = \xi_{max}$  if  $\omega_n = \hat{\omega}$  or  $\omega_n = R\hat{\omega}$ , and that  $\xi_n = \xi_{min}$  if  $\omega_n = \sqrt{R}\hat{\omega}$ . If  $\omega_n$  is outside the range  $\hat{\omega}$  to  $R\hat{\omega}$ , then  $\xi_n > \xi_{max}$ . Above  $R\hat{\omega}$ ,  $\xi_n$  increases with  $\omega_n$ , approaching a linear relation as the last term in Equation (108.23) dominates.

Note: It's worth pointing out that damping could be unrealistically high for motions outside the prescribed frequency range, if the frequency range is not well-chosen.

### 108.4.3 Caughey Damping 3<sup>rd</sup> Order

Following the same logic as the 2<sup>nd</sup> order, the last coefficient of the 3<sup>rd</sup> order Caughey damping formulation can be written as following:

$$C = a_2 KM^{-1} K = a_2 \omega^4 M \quad (108.28)$$

So  $a_2$  can be obtained as:

$$a_2 = \frac{2\xi}{\omega^3} \quad (108.29)$$

Considering the last coefficient in the formulation, the damping ratio of the system can now be shown as:

$$\xi_n = \frac{a_0}{2} \frac{1}{\omega_n} + \frac{a_1}{2} \omega_n + \frac{a_2}{2} \omega_n^3 \quad (108.30)$$

By solving the following set of equations, 3<sup>rd</sup> order Caughey damping coefficients can be found:

$$\frac{1}{2} \begin{bmatrix} \frac{1}{\omega_i} & \omega_i & \omega_i^3 \\ \frac{1}{\omega_j} & \omega_j & \omega_j^3 \\ \frac{1}{\omega_k} & \omega_k & \omega_k^3 \end{bmatrix} \begin{bmatrix} a_0 \\ a_1 \\ a_2 \end{bmatrix} = \begin{bmatrix} \xi_i \\ \xi_j \\ \xi_k \end{bmatrix} \quad (108.31)$$

#### 108.4.4 Caughey Damping 4<sup>th</sup> Order

The 4<sup>th</sup> coefficient of the Caughey damping formulation can be obtained as:

$$C = a_3 KM^{-1} KM^{-1} K = a_3 \omega^6 M \quad (108.32)$$

$$a_3 = \frac{2\xi}{\omega^5} \quad (108.33)$$

$$\xi_n = \frac{a_0}{2} \frac{1}{\omega_n} + \frac{a_1}{2} \omega_n + \frac{a_2}{2} \omega_n^3 + \frac{a_3}{2} \omega_n^5 \quad (108.34)$$

So the damping coefficients can be obtained by solving the following set of equations:

$$\frac{1}{2} \begin{bmatrix} \frac{1}{\omega_i} & \omega_i & \omega_i^3 & \omega_i^5 \\ \frac{1}{\omega_j} & \omega_j & \omega_j^3 & \omega_j^5 \\ \frac{1}{\omega_k} & \omega_k & \omega_k^3 & \omega_k^5 \\ \frac{1}{\omega_l} & \omega_l & \omega_l^3 & \omega_l^5 \end{bmatrix} \begin{bmatrix} a_0 \\ a_1 \\ a_2 \\ a_3 \end{bmatrix} = \begin{bmatrix} \xi_i \\ \xi_j \\ \xi_k \\ \xi_l \end{bmatrix} \quad (108.35)$$

## Chapter 109

# Earthquake Soil Structure Interaction, Theoretical Aspects

(1989-2001-2006-2016-2018-2019-2020-2021-)

(In collaboration with Dr. Nima Tafazzoli, Prof. José Abell, Dr. Yuan Feng, Dr. Hexiang Wang )

## 109.1 Chapter Summary and Highlights

### 109.2 Seismic Energy Propagation and Dissipation

[Jeremić \(2010\)](#)

#### 109.2.1 Seismic energy input into SSI system

Earthquakes release large amounts energy at the source<sup>1</sup> Part of released energy is radiated as mechanical waves ( $\approx 1.6 \times 10^{-5}$ ) and part of that energy makes it to the surface where SSI system is located.

Mechanical seismic wave energy enters the SSI system through a closed surface  $\Gamma$  that encompasses (significant) soil volume as well as foundation system and the structure (see Figure 109.7). Kinetic energy flux through closed surface  $\Gamma$  includes both incoming and outgoing waves and can be calculated using Domain Reduction Method ([Bielak et al., 2003a](#)) as:

$$E_{flux} = \\ [0; -M_{be}^{\Omega+} \ddot{u}_e^0 - K_{be}^{\Omega+} u_e^0; M_{eb}^{\Omega+} \ddot{u}_b^0 + K_{eb}^{\Omega+} u_b^0]_i \times u_i$$

where  $M_{be}^{\Omega+}$ ,  $M_{eb}^{\Omega+}$ ,  $K_{be}^{\Omega+}$ ,  $K_{eb}^{\Omega+}$  are mass and stiffness matrices, respectively for a single layer of elements just outside of the boundary  $\Gamma$ , while  $\ddot{u}_e^0$  and  $u_e^0$  are accelerations and displacements from a free field model for nodes belonging to that layer of elements. Alternatively, energy flux can be calculated using ([\(Aki and Richards, 2002\)](#), page 122):

$$E_{flux} = \rho A c \int_0^t \dot{u}_i^2 dt$$

Outgoing kinetic energy can be obtained from outgoing wave field  $w_i$ , (from DRM, [Bielak et al. \(2003a\)](#)), while the difference then represents the incoming kinetic energy that needs to be dissipated with SSI region.

#### 109.2.2 Seismic Energy Dissipation in SSI System

Seismic energy that enters the SSI system will be dissipated in a number of ways. Part of the energy that enters SSI system is reflected and radiated back into domain outside  $\Gamma$  by

- wave reflection from impedance boundaries (free surface, soil/rock layers, foundations, etc.).
- SSI system oscillates and emits, radiates waves back into the domain

---

<sup>1</sup>for example, some of the recent large earthquake energy releases are listed: Northridge, 1994,  $M_{Richter} = 6.7$ ,  $E_r = 6.8 \times 10^{16} J$ ; Loma Prieta, 1989,  $M_{Richter} = 6.9$ ,  $E_r = 1.1 \times 10^{17} J$ ; Sumatra-Andaman, 2004,  $M_{Richter} = 9.3$ ,  $E_r = 4.8 \times 10^{20} J$ ; Valdivia, Chile, 1960,  $M_{Richter} = 9.5$ ,  $E_r = 7.5 \times 10^{20} J$ ;

The rest of seismic energy is dissipated through one of the following mechanisms within SSI system:

- Inelastic, elasto-plastic behavior of soil and rock
- Inelastic, elasto-plastic, damage behavior of the foundation system
- Inelastic, elasto-plastic, damage behavior of the structure
- Viscous coupling of porous solid with pore fluid (air, water)
- Viscous coupling of structure with surrounding, internal and external fluids (air, water)

It is also important to note that in numerical simulations, part of the energy can be dissipated or produced by purely numerical means. That is, numerical energy dissipation (damping) or production (negative damping) has to be carefully controlled ([Argyris and Mlejnek, 1991](#)), ([Hughes, 1987](#)).

#### 109.2.2.1 Energy Dissipation by Plasticity

Elastic-plastic deformation of soil, foundation and structure is probably responsible for major part of the energy dissipation for large earthquakes. This, displacement proportional dissipation is a result of plastic dissipation and is present in all three components of the system (soil, foundation and the structure).

A note about plastic dissipation is important at this point. There is a misconception about plastic energy dissipation that is being widely used. Here are some details:

- Origins of the Misconception: The paper by [Uang and Bertero \(1990\)](#) has been considered the definitive work in using energy as a measure of structural demand by many researchers ([Léger and Dussault, 1992](#); [Cosenza et al., 1993](#); [Kalkan and Kunnath, 2007, 2008](#); [Symans et al., 2008](#); [Chopra, 2000](#); [Gajan and Saravanathiiban, 2011](#); [Moustafa, 2011](#); [Moustafa and Mahmoud, 2014](#); [Mezgebo and Lui, 2017](#); [Deniz et al., 2017](#)). An energy analysis methodology based on absolute input energy (or energy demand) was presented and discussed. Numerical analysis results were compared with experiments on a multi-story building. In this paper, hysteretic energy is calculated indirectly by taking the difference of absorbed energy and elastic strain energy. The term *absorbed energy* of each time step was simply defined as force times incremental displacement. It was stated that *hysteretic energy* is irrecoverable, which indicates that this parameter was considered the same as *hysteretic dissipation* or *plastic dissipation*. An equation for energy balance is given:

$$E_i = E_k + E_\xi + E_a = E_k + E_\xi + E_s + E_h \quad (109.1)$$

where  $E_i$  is the (absolute) input energy,  $E_k$  is the (absolute) kinetic energy,  $E_\xi$  is the viscous damping energy,  $E_a$  is the absorbed energy, which is composed of elastic strain energy  $E_s$  and hysteretic energy  $E_h$ .

The problem of this theory is the absence of plastic free energy, which is necessary to correctly evaluate energy dissipation of elastic-plastic materials and to uphold the second law of thermodynamics. There was no direct plot of plastic dissipation (hysteretic energy) in this paper, since it was not defined directly. There were plots of other energy components and plastic dissipation can be easily calculated or deducted from these plots. After doing this, indications of negative incremental energy dissipation, which violates the basic principles of thermodynamics, were found in various sections of the paper.

This misconception could be clarified by renaming hysteretic energy to *plastic work*, which is the combination of plastic dissipation and plastic free energy. Both plastic work and plastic free energy can be incrementally negative, but plastic dissipation (defined as the difference of plastic work and plastic free energy) must be incrementally non-negative during any time period. Unfortunately, this misconception has been inherited (if not magnified) by almost all following studies on energy analysis of earthquake soils and structures.

Besides, another issue regarding energy dissipation is found in this paper. *Viscous damping energy* (or viscous damping energy) was calculated directly using damping coefficient and velocity. The author stated that this term should always be non-negative. But it was ignored that the incremental viscous energy dissipation should also be non-negative. In fact, the equation used to compute viscous energy dissipation should be able to ensure that it remains non-negative incrementally. However, it appeared in one of the plots that (accumulated) viscous damping energy was clearly dropping during certain time periods, which was in contradiction with the equation derived in the same paper. Such result was also a violation of thermodynamics.

- Misconception in Other Studies: Although input energy was the key parameter used in [Uang and Bertero \(1990\)](#), the misconception of energy dissipation has been carried on in a vast number of studies on energy analysis of ESSI systems.

[Léger and Dussault \(1992\)](#) used Equation 109.1 from [Uang and Bertero \(1990\)](#) to perform energy response analysis of multi-story buildings under earthquake loading. It was stated that the total input energy at the end of ground motion is approximately equal to the total dissipated energy. This statement is only valid if plastic free energy remains constant, which is generally not true in elastic-plastic materials.

[Kalkan and Kunnath \(2007\)](#) calculated energy dissipation of a single-degree-of-freedom (SDOF) oscillator under earthquake loading. Inelastic material was used so plastic energy dissipation appeared in the results. Negative incremental hysteretic energy (plastic dissipation) was observed in the plots, which is a clear violation of thermodynamics. The change of plastic free energy was not

considered in this study. Several papers by the same authors performed energy analysis on various structures using the same theory, and similar misconceptions can be noticed in these publications.

[Symans et al. \(2008\)](#) summarized current practice and recent developments in the application of passive energy dissipation systems for seismic protection of structures. There was no consideration of plastic free energy in the energy balance equation, which was very close to the ones present by [Uang and Bertero \(1990\)](#) and [Léger and Dussault \(1992\)](#). It was stated that the cumulative hysteretic energy is equal to the energy demand (absolute input energy) at the end of earthquake. Although no direct violation of thermodynamics was observed, such statement clearly indicated the same misconception of plastic work and plastic dissipation appeared in other publications.

[Gajan and Saravanathiiban \(2011\)](#) performed both numerical simulations and centrifuge experiments on a rocking foundation system. Energy dissipation in foundation soil and structural elements were calculated. It can be observed that hysteretic energy dissipation in both the soil and the structure was decreasing during certain time periods, which is a direct violation of thermodynamics. Again, this was a misconception of plastic work and plastic energy dissipation. The change in plastic free energy of the system was significant in this case, since large drops of plastic work were noticed in the plots.

[Chopra \(2000\)](#) used similar set of equations in section 7.9, and equation 7.9.6 is clearly wrong!

A number of recent studies [Moustafa \(2011\)](#); [Moustafa and Mahmoud \(2014\)](#); [Mezgebo and Lui \(2017\)](#); [Deniz et al. \(2017\)](#) performed energy analysis on ESSI systems without considering plastic free energy. Misleading results were obtained using the wrong energy balance equation. This means that the misconception of plastic work and plastic energy dissipation is still not realized by many researchers. Note that the influence of this mistake could be negligible or significant, depending on the case analyzed. Nevertheless, plastic free energy should not be ignored without plausible reasoning or experimental evidences.

- Early Studies on Plastic Free Energy (Cold Work): This issue has been pointed out and studied extensively by researchers from mechanical engineering and material science. In the early 20th century, Taylor and his colleagues [Farren and Taylor \(1925\)](#), [Taylor and Quinney \(1934\)](#) performed experiments on metals and proved that a large part, but not all, of the input mechanical energy is converted into heat. The remaining part of the non-recoverable plastic work is known as the stored energy of cold work. The ratio of plastic work converted into heating (Quinney–Taylor coefficient), usually denoted as  $\beta$ , has been used in almost all later papers on this topic. Based on large amount of experimental data, this ratio was assumed to be a constant between 0.6 to 1.0 in many studies (e.g. [Clifton et al. \(1984\)](#), [Belytschko et al. \(1991\)](#), [Zhou et al. \(1996\)](#), [Dolinski](#)

et al. (2010), Ren and Li (2010), Osovski et al. (2013)). It has been realized that this assumption is not valid in all cases, but it's simply too complicated to involve the evolution of Quinney–Taylor coefficient in thermomechanical constitutive models.

Decades later, Mason et al. (1994) showed that the fraction of plastic work converted into heat is both strain and strain rate dependent. Infrared imaging was used in this study (and almost all future studies) to obtain temperature distribution in the material, because it is the only effective approach to directly measure energy dissipation (heat). In the recent 20 years, there has been many developments on this issue. Rittel (Rittel, 2000; Rittel and Rabin, 2000; Rittel et al., 2003) published several insightful papers on the energy dissipation (heat generation) of polymers during cyclic loading, presenting both experimental and theoretical works. Rosakis et al. (2000) presented a constitutive model based on thermoplasticity to model the evolution of in metal. This model is capable of calculating the evolution of energy dissipation and material properties, and is validated by sets of experiments. There are some follow-up papers by Rosakis and his colleagues (Hodowany et al., 2000; Ravichandran et al., 2002) on the same issue with some assumptions to simplify the problem. One widely used assumption is the adiabatic condition, since air conducts heat much slower than metal. This assumption is reasonable in rapid monotonic or cyclic loading (impact, vibration, earthquake). One application of this theory in geotechnical engineering is presented in papers of (Veveakis et al., 2007, 2012), in which thermoporomechanics is used to model the heating and pore pressure increase in large landslides, like the 1963 Vajont slide in Italy.

In the field of civil engineering, the basic principles of thermodynamics are frequently used to derive new constitutive models Dafalias and Popov (1975); Ziegler and Wehrli (1987); Collins and Houlsby (1997); Houlsby and Puzrin (2000); Collins (2002); Collins and Kelly (2002); Collins (2003); Feigenbaum and Dafalias (2007). to enforce the second law of thermodynamics for developed constitutive models. Note that plastic free energy is the same concept as cold work. The former term is more popular in solid physics and geotechnical engineering, while the latter is used in mechanical engineering. energy dissipation due to plasticity and plastic work, which is often a source of a confusion. through a conceptual example that is analyzed on particle scale. development of plastic free energy is caused by particle rearrangement in granular assembly under external loading.

Ideally, majority of the incoming energy would be dissipated in soil, before reaching foundation and structures. The possibility to direct energy dissipation to soil can be used in design by recognizing energy dissipation capacity for different soils. For example, simple elastic-plastic models of stiff and soft clay as well as dense and loose sand predict different energy dissipation capacities, as shown in Figure 109.1, for

single loading-unloading-reloading cycle. While Figure 109.1 shows that stiff clay and dense sand have

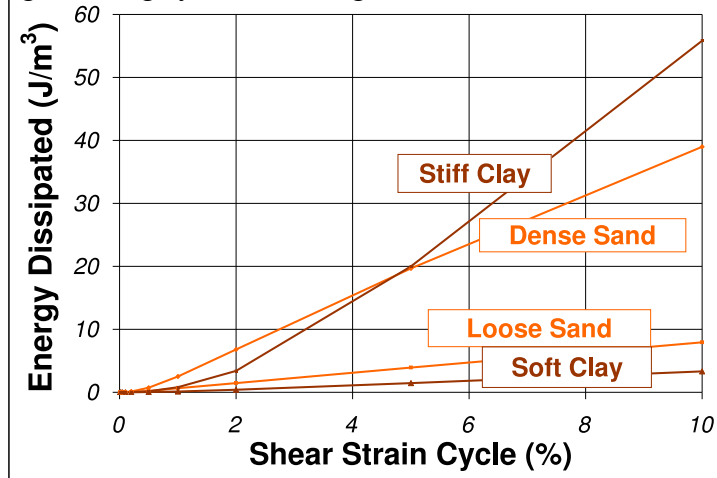


Figure 109.1: Energy dissipation capacity for one cycle at various strains for four generic soils.

much higher dissipation capacity, it is important to note that soft/loose soils can undergo much larger deformation/strain, thus offering increased energy dissipation capacity through flexibility.

#### 109.2.2.2 Energy Dissipation by Viscous Coupling

Viscous coupling of pore fluid (air, water...) and soil particles and/or foundation or structural components is responsible for velocity proportional energy dissipation. In particular, viscous coupling of porous solid and fluid results in  $E_{vc} = n^2 k^{-1} (\dot{U}_i - \dot{u}_i)^2$  energy loss per unit volume. It is noted that this type of dissipation is realistically modeled using  $u - p - U$  formulation (Jeremić et al., 2008).

#### 109.2.2.3 Numerical Energy Dissipation and Production

As noted above, numerical integration of nonlinear equations of motions affects calculated energy in various ways. Most common effect for nonlinear (elastic-plastic) systems is the positive (energy dissipation) and negative (energy production) damping. For example Newmark (N) (Newmark, 1959) and Hilber–Hughes–Taylor (HHT) (Hilber et al., 1977) are energy preserving for linear elastic system with proper choice of constants ( $\alpha = 0.0$ ;  $\beta = 0.25$ ,  $\gamma = 0.5$ ). Both methods can also be used to dissipate higher frequency modes for linear elastic models by changing constants so that for N:  $\gamma \geq 0.5$ ,  $\beta = 0.25(\gamma+0.5)^2$ , while for HHT:  $-0.33 \leq \alpha \leq 0$ ,  $\gamma = 0.5(1 - 2\alpha)$ ,  $\beta = 0.25(1 - \alpha)^2$ . However, for nonlinear problems it is impossible to maintain energy of the system throughout computations (Argyris and Mlejnek, 1991).

#### 109.2.2.4 Energy Dissipation by Nonlinearities in Soil/Rock

Elasto-plasticity of solid skeleton

Viscous (coupling) effects

### 109.2.2.5 Energy Dissipation by Nonlinearities in Soil/Rock – Foundation Interface Zone

Gap, Slip

Dry

Saturated

### 109.2.2.6 Energy Dissipation by Nonlinearities in Seismic Isolators

### 109.2.2.7 Energy Dissipation by Nonlinearities in Structures, Systems and Components

### 109.2.2.8 Numerical Energy Dissipation and Production

## 109.2.3 Seismic Motions: Empirical Models

### 109.2.4 1D/1C Wave Propagation Modeling

The theory of wave propagation is associated with vertical propagation of shear and/or comporessional waves through the linear viscoelastic system is described in this section. Developments shown here follow standard approach, as found by, for example, Kramer (1996a). Shown in Figure 109.2 is a 1C wave propagation setup. The model consists of  $N$  horizontal layers, that extend to infinity in the horizontal direction. At the bottom of layers is bedrock that represents a halfspace. Each layer is homogeneous and isotropic and is characterized by the thickness  $h$ , mass density  $\rho$ , shear wave velocity  $V_s^2$ , and compressional wave velocity  $V_p^3$  and damping factor,  $\beta$ .

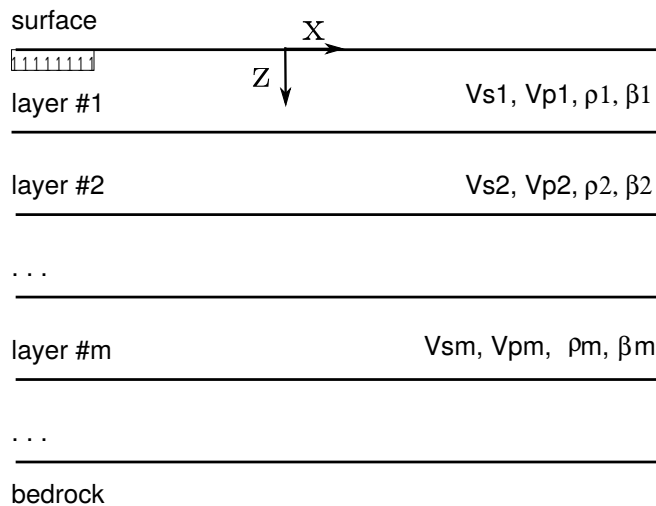


Figure 109.2: Problem Description: Wave Propagation

Vertical propagation of shear or compressional waves will cause only horizontal or vertical displacements respectively.

$$u = u(z, t) \quad (109.2)$$

Focusing on vertical propagation of shear waves, and with a presence of displacements in  $x$  direction only, a wave equation, that describes wave propagation in vertical,  $z$  directions can be written as

$$\rho \frac{\partial^2 u}{\partial t^2} = G \frac{\partial^2 u}{\partial z^2} + \eta \frac{\partial^3 u}{\partial z^2 \partial t} \quad (109.3)$$

<sup>2</sup>Shear Wave velocity is used to obtain shear shear modulus  $G$ ,  $V_s = \sqrt{G/\rho}$ ,  $G = V_s^2 \rho$ ,  $G = E/(2(1+\nu))$ ,  $E = (9KG)/(3K+g)$ ,  $E = (G(3M - 4G))/(M - G)$ .

<sup>3</sup>Compressional wave velocity is used to obtain constrained modulus  $M$   $V_p = \sqrt{M/\rho}$ ,  $M = V_p^2 \rho$ ,  $M = K + 4G/3$ ,  $M = E(1 - \nu)/((1 + \nu)(1 - 2\nu))$ .

Harmonic oscillation, displacements with frequency  $\omega$ , can be written in the as:

$$u(z, t) = U(z) \cdot e^{i\omega t} \quad (109.4)$$

Substituting Eq (109.4) into Eq (109.3) one obtains

$$(G + i\omega\eta) \frac{\partial^2 u}{\partial z^2} = \rho\omega^2 U \quad (109.5)$$

which has the general solution:

$$U(z) = Ee^{ikz} + Fe^{-ikz} \quad (109.6)$$

in which

$$k^2 = \frac{\rho\omega^2}{G + i\omega\eta} = \frac{\rho\omega^2}{G^*} \quad (109.7)$$

where  $k$  is the complex wave number and  $G^*$  is the complex shear modulus. The critical damping ratio,  $\beta$ , is related to the viscosity  $\eta$  by

$$\omega\eta = 2G\beta \quad (109.8)$$

For convenience, one can use use soil damping ratio  $\beta$  to represent the complex shear modulus.

$$G^* = G + i\omega\eta = G(1 + 2i\beta) \quad (109.9)$$

By combine Eq. (109.4) and Eq. (109.6) one obtains the wave equation for a harmonic motion of frequency  $\omega$ .

$$u(z, t) = Ee^{i(kz+\omega t)} + Fe^{-i(kz-\omega t)} \quad (109.10)$$

where the first term represents the incident wave traveling in the upward, in positive  $z$  direction and the second term represents the reflected wave traveling in the negative, downward  $z$ -direction.

This equation is valid for each of the soil and rock layers.

Introducing a local coordinate system  $Z$  for each layer, the displacements at the top and bottom of layer  $m$  are :

$$u_m(z = 0) = (E_m + F_m)e^{i\omega t} \quad (109.11)$$

$$u_m(z = h_m) = (E_m \cdot e^{ik_m h_m} + F_m e^{-ik_m h_m}) \cdot e^{i\omega t} \quad (109.12)$$

The shear stress on a horizontal plane is

$$\tau(z, t) = G \cdot \frac{\partial u}{\partial z} + \eta \frac{\partial u}{\partial z \partial t} = G^* \frac{\partial u}{\partial z} \quad (109.13)$$

In another form,

$$\tau(z, t) = ikG^*(Ee^{ikz} - Fe^{-ikz})e^{i\omega t} \quad (109.14)$$

and the shear stress at the top and bottom of layer  $m$  are respectively:

$$\tau_m(z = 0) = ik_m G_m^*(E_m - F_m)e^{i\omega t} \quad (109.15)$$

$$\tau_m(z = h_m) = ik_m G_m^*(E_m e^{ik_m h_m} - F_m e^{-ik_m h_m})e^{i\omega t} \quad (109.16)$$

Stresses and displacements must be continuous at all interfaces. Hence, by Eq (109.11), (109.12), (109.15) and (109.16), the coefficients are

$$E_{m+1} + F_{m+1} = E_m e^{ik_m h_m} + F_m e^{-ik_m h_m} \quad (109.17)$$

$$E_{m+1} - F_{m+1} = \frac{k_m G_m^*}{k_{m+1} G_{m+1}^*} (E_m e^{ik_m h_m} - F_m e^{-ik_m h_m}) \quad (109.18)$$

Subtraction and addition Eqs. 15 and 16 yield the following recursion formulas for the amplitudes,  $E_{m+1}$  and  $F_{m+1}$ , of the incident and reflected wave in layer  $m+1$ , expressed in terms of the amplitudes in layer  $m$ :

$$E_{m+1} = \frac{1}{2} E_m (1 + \alpha_m) e^{ik_m h_m} + \frac{1}{2} F_m (1 - \alpha_m) e^{-ik_m h_m} \quad (109.19)$$

$$F_{m+1} = \frac{1}{2} E_m (1 - \alpha_m) e^{ik_m h_m} + \frac{1}{2} F_m (1 + \alpha_m) e^{-ik_m h_m} \quad (109.20)$$

where  $\alpha_m$  is the complex impedance ratio

$$\alpha_m = \frac{k_m G_m^*}{k_{m+1} G_{m+1}^*} = \left( \frac{\rho_m G_m^*}{\rho_{m+1} G_{m+1}^*} \right)^{1/2} \quad (109.21)$$

At the free surface, the shear stresses must be zero. In addition, according to Eq. (109.15), it obtains  $E_1 = F_1$ . Namely, the amplitudes of the incident and reflected waves are always equal at the free surface. Beginning with the surface layer, repeated use of Eq (109.19) and Eq (109.20) to build the wave field:

$$E_m = e_m(\omega) E_1 \quad (109.22)$$

$$F_m = f_m(\omega)E_1 \quad (109.23)$$

The transfer function  $e_m$  and  $f_m$  are simply the amplitudes for the case  $E_1 = F_1 = 1$ , and can be determined by substituting this condition into the above recursion formulas. Other transfer functions are easily obtained from the  $e_m$  and  $f_m$  functions. The transfer function  $A_{n,m}$  between the displacements at level  $n$  and  $m$  is defined by:

$$A_{n,m}(\omega) = \frac{u_m}{u_n} \quad (109.24)$$

and can be represented by

$$A_{n,m}(\omega) = \frac{e_m(\omega) + f_m(\omega)}{e_n(\omega) + f_n(\omega)} \quad (109.25)$$

Based on these equations, the transfer function  $A(\omega)$  can be found between any two layers in the system. Hence, if the motion is known in any one layer in the system, the motion can be computed in any other layer.

In summary, after the  $E$  and  $F$  are computed for all layers in the system, the accelerations are expressed by the equation:

$$\ddot{u}(z, t) = \frac{\partial^2 u}{\partial t^2} = -\omega^2(E e^{i(kz+\omega t)} + F e^{-i(kz-\omega t)}) \quad (109.26)$$

### 109.2.5 Seismic Motions: 3D/3C Analytic Wave Propagation Modeling

[Thomson \(1950\); Haskell \(1953\)](#)

This is based in part on [Wang et al. \(2020a\)](#).

Considered is the inclined wave propagation in the layered ground as shown in Fig. 109.3. There are  $n$  layers with layer thickness  $d_m$ , density  $\rho_m$ , compressional velocity  $\alpha_m$  and shear wave velocity  $\beta_m$  ( $m = 1, 2, \dots, n$ ). Since the incidence of out-of-plane  $SH$  wave is simpler (no mode conversion), here we focus on the incidence of  $P$  and  $SV$  wave and account for the mode conversion between them. The wave potential formulations below are general and also applicable to incident  $SH$  wave ([Haskell, 1953](#)). Without loss of generality, incident waves are considered to be monochromatic with angular frequency  $\omega$  and horizontal phase velocity  $c$ . For incident waves with arbitrary time signal and multiple frequencies, free field motions can be Fourier synthesized from the monochromatic solutions.

According to Helmholtz decomposition theorem ([Arfken and Weber, 1999](#)), the displacement of wave propagation Eq. (109.27) in linear elastic media can be expressed with  $P$  wave scalar potential  $\phi$  and  $S$  wave vector potential  $\Psi$  as shown in Eq. 109.28, where  $\phi$  is the curl free part corresponding to volumetric deformation and  $\Psi$  is divergence free part corresponding to deviatoric deformation.

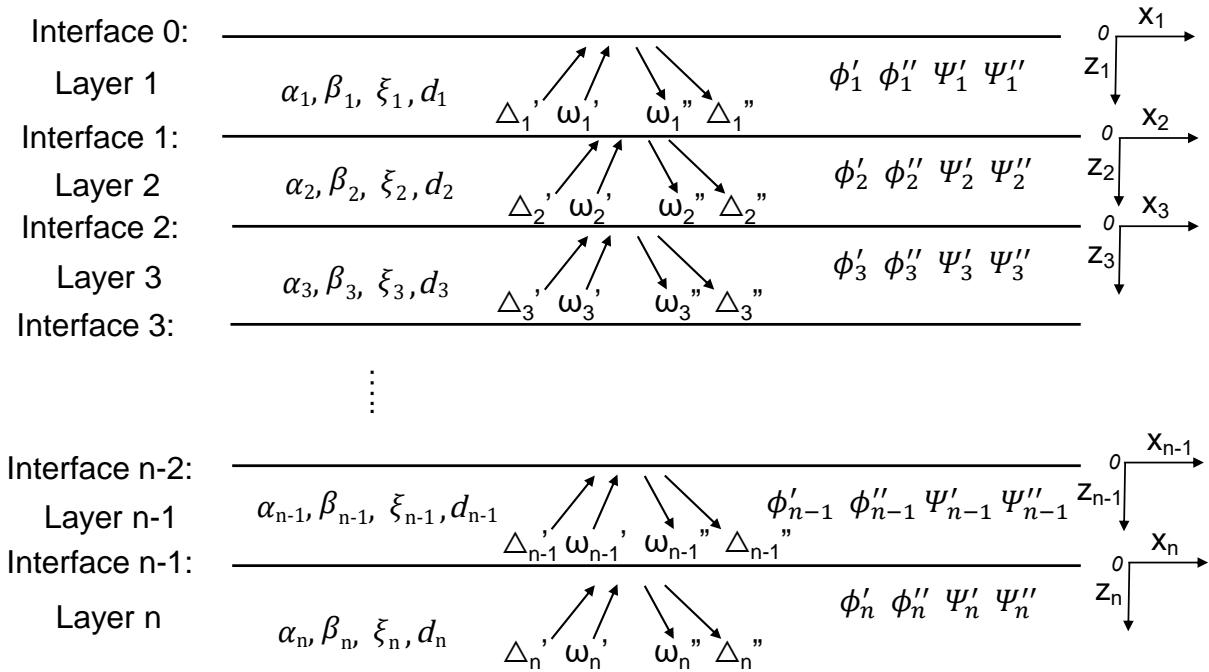


Figure 109.3: 2D layered ground and free field motion

$$\rho \ddot{\mathbf{u}} = (\lambda + 2\mu) \nabla \nabla \cdot \mathbf{u} - \mu \nabla \times \nabla \times \mathbf{u} \quad (109.27)$$

$$\mathbf{u} = \nabla \phi + \nabla \times \Psi \quad (109.28)$$

Therefore, the unknown variables for  $m^{th}$  layer are simplified into incident  $P$  wave potential magnitude  $\phi'_m$ , reflected  $P$  wave potential magnitude  $\phi''_m$ , incident  $SV$  wave potential magnitude  $\Psi'_m$  and reflected  $SV$  wave potential magnitude  $\Psi''_m$ .

$$\begin{aligned} \phi_m &= [\phi'_m e^{ik(x-\gamma_{\alpha m}z)} + \phi''_m e^{ik(x+\gamma_{\alpha m}z)}] e^{-iwt} \\ \Psi_m &= [\Psi'_m e^{ik(x-\gamma_{\beta m}z)} + \Psi''_m e^{ik(x+\gamma_{\beta m}z)}] e^{-iwt} \end{aligned} \quad (109.29)$$

The  $P$  and  $SV$  wave potential can be expressed as Eq. (109.29), where  $k$  is the horizontal wave number, equals to  $w/c$ . And  $\cot^{-1}\gamma_{\alpha m}$  and  $\cot^{-1}\gamma_{\beta m}$  are incident and reflected angles for  $P$  and  $SV$  wave, respectively. The harmonic nature of the potential field is characterized by the time factor  $e^{-iwt}$ . It will be understood and omitted hereafter.  $\gamma_{\alpha m}$  and  $\gamma_{\beta m}$  can be determined by Snell's law (equation ??). Note that when  $\alpha_m$  or  $\beta_m$  is greater than  $c$ , the incidence from  $P$  or  $SV$  wave is beyond the critical

angle.  $\gamma_{\alpha_m}$  and  $\gamma_{\beta_m}$  become complex numbers. The plane wave magnitude exponentially decays along the depth. To be consistent with the original formulation by Haskell (1953), dilatational wave solutions  $\Delta_m$  and rotational wave solutions  $\omega_m$  are first introduced as Eq. (109.30).

$$\begin{aligned}\Delta &= \frac{\partial u_x}{\partial x} + \frac{\partial u_z}{\partial z} \\ \omega &= \frac{1}{2} \left( \frac{\partial u_x}{\partial z} - \frac{\partial u_z}{\partial x} \right)\end{aligned}\quad (109.30)$$

$\phi_m$  and  $\Psi_m$  are related to  $\Delta_m$  and  $\omega_m$  as follows:

$$\begin{aligned}\phi_m &= -\left(\frac{\alpha_m}{w}\right)^2 \Delta_m \\ \Psi_m &= 2\left(\frac{\beta_m}{w}\right)^2 \omega_m\end{aligned}\quad (109.31)$$

The displacements ( $u_x, u_y$ ) and interfacial stresses ( $\sigma_{zz}, \tau_{zx}$ ) can be expressed in wave potential magnitudes  $\phi$  and  $\Psi$ .

From Eqs. (109.28)-(109.31), the displacement and stress field of  $m^{th}$  layer can be calculated from the dilatational wave and rotational wave solutions  $\Delta_m$  and  $\omega_m$  as follows:

$$\begin{aligned}u_x &= \left\{ -ik\left(\frac{\alpha_m}{\omega}\right)^2 [(\Delta'_m + \Delta''_m) \cos(k\gamma_{\alpha_m} z) - i(\Delta'_m - \Delta''_m) \sin(k\gamma_{\alpha_m} z)] \right. \\ &\quad \left. + 2ik\gamma_{\beta_m}\left(\frac{\beta_m}{\omega}\right)^2 [(\omega'_m - \omega''_m) \cos(k\gamma_{\beta_m} z) + i(\omega''_m + \omega'_m) \sin(k\gamma_{\beta_m} z)] \right\} e^{ikx}\end{aligned}\quad (109.32)$$

$$\begin{aligned}u_z &= \left\{ ik\gamma_{\alpha_m}\left(\frac{\alpha_m}{\omega}\right)^2 [(\Delta'_m - \Delta''_m) \cos(k\gamma_{\alpha_m} z) - i(\Delta''_m + \Delta'_m) \sin(k\gamma_{\alpha_m} z)] \right. \\ &\quad \left. + 2ik\left(\frac{\beta_m}{\omega}\right)^2 [(\omega'_m + \omega''_m) \cos(k\gamma_{\beta_m} z) - i(\omega'_m - \omega''_m) \sin(k\gamma_{\beta_m} z)] \right\} e^{ikx}\end{aligned}\quad (109.33)$$

$$\begin{aligned}\sigma_{zz} &= \rho_m \left\{ \alpha_m^2 (1 - 2\frac{\beta_m^2}{c^2}) [(\Delta'_m + \Delta''_m) \cos(k\gamma_{\alpha_m} z) - i(\Delta'_m - \Delta''_m) \sin(k\gamma_{\alpha_m} z)] \right. \\ &\quad \left. + 4\frac{\beta_m^4}{c^2} \gamma_{\beta_m} [(\omega'_m - \omega''_m) \cos(k\gamma_{\beta_m} z) - i(\omega''_m + \omega'_m) \sin(k\gamma_{\beta_m} z)] \right\} e^{ikx}\end{aligned}\quad (109.34)$$

$$\begin{aligned}\tau_{zx} &= 2\rho_m \beta_m^2 \left\{ -\gamma_{\alpha_m}\left(\frac{\alpha_m}{c}\right)^2 [(\Delta'_m - \Delta''_m) \cos(k\gamma_{\alpha_m} z) - i(\Delta''_m + \Delta'_m) \sin(k\gamma_{\alpha_m} z)] \right. \\ &\quad \left. + [1 - 2(\frac{\beta_m}{c})^2] [(\omega'_m + \omega''_m) \cos(k\gamma_{\beta_m} z) - i(\omega'_m - \omega''_m) \sin(k\gamma_{\beta_m} z)] \right\} e^{ikx}\end{aligned}\quad (109.35)$$

Define the displacement and stress solution at  $m^{th}$  interface as  $S^{(m)}$ , which is equal to  $[\dot{u}_x(z_m = d_m)/c, \dot{u}_z(z_m = d_m)/c, \sigma_{zz}(z_m = d_m), \tau_{zx}(z_m = d_m)]^T$ . Eqs. (109.32) - (??) can be reduced to the following matrix notations (Haskell, 1953):

$$S^{(m-1)} = \mathbf{E}_m [\Delta_m'' + \Delta_m', \Delta_m'' - \Delta_m', \omega_m'' - \omega_m', \omega_m'' + \omega_m']^T \quad (109.36)$$

$$S^{(m)} = \mathbf{D}_m [\Delta_m'' + \Delta_m', \Delta_m'' - \Delta_m', \omega_m'' - \omega_m', \omega_m'' + \omega_m']^T \quad (109.37)$$

where transformation matrix  $\mathbf{E}_m$  and  $\mathbf{D}_m$  are given in Appendix (Eqs. ?? and ??). The recurrence relation between  $S^{(m)}$  and  $S^{(m-1)}$  then can be established as Eq. 109.38, where  $\mathbf{G}_m = \mathbf{D}_m \mathbf{E}_m^{-1}$ .

$$S^{(m)} = \mathbf{D}_m \mathbf{E}_m^{-1} S^{(m-1)} = \mathbf{G}_m S^{(m-1)} \quad (109.38)$$

Recursively applying Eq. 109.38 leads to Eq. 109.39. Using the relation between  $S^{(m-1)}$  and  $\Delta_m$ ,  $\omega_m$ , Eq. 109.40 bridges the gap between the upper boundary (i.e., response at ground surface  $S^{(0)}$ ) and lower boundary (i.e., solutions of wave incident layer  $\Delta_n$  and  $\omega_n$ ), upon which specific boundary conditions can be imposed.

$$S^{(n-1)} = \prod_{i=1}^{n-1} \mathbf{G}_i S^{(0)} \quad (109.39)$$

$$\begin{aligned} S^{(0)} &= \mathbf{L} [\Delta_n'' + \Delta_n', \Delta_n'' - \Delta_n', \omega_n'' - \omega_n', \omega_n'' + \omega_n']^T \\ \mathbf{L} &= (\prod_{i=1}^{n-1} \mathbf{G}_i)^{-1} \mathbf{E}_n \end{aligned} \quad (109.40)$$

Following boundary conditions are incorporated: (1) At  $n^{th}$  layer, the incident in-plane  $P$  and  $SV$  wave potential magnitude  $\phi_n'$  and  $\Psi_n'$  are given as  $K_1$  and  $K_2$ ; (2) At the ground surface ( $z = 0$ ), the traction is free (i.e., the third and fourth component of  $S^{(0)}$  is 0). Therefore, the reflected dilatational wave magnitude and rotational wave magnitude can be solved by Eq. 109.41, where  $\Delta_n'$  is  $-K_1 \omega^2 / \alpha_n^2$  and  $\omega_n'$  is  $K_2 w^2 / (2\beta_n^2)$ .

$$\begin{bmatrix} \Delta_n'' \\ \omega_n'' \end{bmatrix} = \begin{bmatrix} L_{31} + L_{32} & L_{33} + L_{34} \\ L_{41} + L_{42} & L_{43} + L_{44} \end{bmatrix}^{-1} \begin{bmatrix} (L_{32} - L_{31})\Delta_n' + (L_{33} - L_{34})\omega_n' \\ (L_{42} - L_{41})\Delta_n' + (L_{43} - L_{44})\omega_n' \end{bmatrix} \quad (109.41)$$

Finally, recurrence relation Eq. 109.42 can be used to trace back dilatational wave magnitude  $\Delta_m$  and rotational wave magnitudes  $\omega_m$  for the rest  $n - 1$  layers. Based on these solved dilatational and rotational magnitudes of each layer, the whole displacement and stress field can be easily computed following Eqs. (109.32)-(??).

$$\begin{bmatrix} \Delta''_{m-1} + \Delta'_m \\ \Delta''_{m-1} - \Delta'_m \\ \omega''_{m-1} - \omega'_m \\ \omega''_{m-1} + \omega'_m \end{bmatrix} = D_{m-1}^{-1} E_m \begin{bmatrix} \Delta''_m + \Delta'_m \\ \Delta''_m - \Delta'_m \\ \omega''_m - \omega'_m \\ \omega''_m + \omega'_m \end{bmatrix} \quad (109.42)$$

In addition, viscosity can also be included with slight modification. Considering Kelvin-Voigt viscoelastic material (Chirita et al., 2008), viscosity can be handled with complex Lame modulus and wave velocities as shown in Eq. 109.43, where  $\xi$  is the damping ratio.

$$G^* = G(1 + 2\xi i) \quad \beta_m^* \simeq \beta_m(1 + \xi i) \quad \alpha_m^* \simeq \alpha_m(1 + \xi i) \quad (109.43)$$

## 109.2.6 Seismic Motions: Large Scale Geophysical Models

### 109.2.6.1 Regional Seismic Motion Modeling using Serpentine Wave Propagation, SW4

### 109.2.7 Site Response

Site response is ...

This is part of free field motions section and just uses free field motions for producing site response.

### 109.2.8 Seismic Motion Incoherence

Seismic motion incoherence (as it is called for frequency domain analysis, for time domain analysis it is called lack of correlation) is a phenomena that results in spatial variability of ground motions over small distances. Significant work has been done in researching seismic motion incoherence over the last few decades. The main sources of lack of spatial correlation, according to [Zerva \(2009\)](#) are due to:

- Attenuation effects,
- Wave passage effects,
- Scattering effects,
- Extended source effects

Figure 109.4 shows an illustration of main sources of lack of correlation.

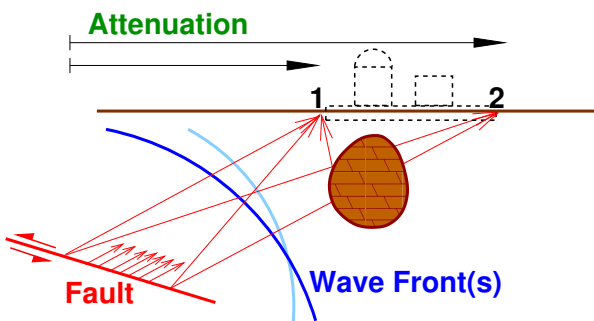


Figure 109.4: Four main sources contributing to the lack of correlation of seismic waves as measured at two observation points.

1. Attenuation effects are responsible for change in amplitude and phase of seismic motions due to the distance between observation points and losses (damping, energy dissipation) that seismic wave experiences along that distance. This is a significant source of lack of correlation for long structures (bridges), however for NPPSSS it is not of much significance.
2. Wave passage effects contribute to lack of correlation due to difference in recorded wave field at two location points as the (surface) wave travels, propagates from first to second point.

3. Scattering effects are responsible to lack of correlation by creating a scattered wave field. Scattering is due to (unknown or not known enough) subsurface geologic features that contribute to modification of wave field.
4. Extended source effects contribute to lack of correlation by creating a complex wave source field, as the fault ruptures, rupture propagates and generate seismic sources along the fault. Seismic energy is thus emitted from different points (along the rupturing fault) and will have different travel path and timing as it makes it observation points.

Early studies concluded that the correlation of motions increases as the separation distance between observation points decreases. In addition to that, correlation increased for decrease in frequency of observed motions. Moreover, there is a strong probabilistic nature of this phenomena, as significant uncertainty is present in relation to all four sources of lack of correlation, mentioned above. A number of excellent references are available on the subject of incoherent (or lacking correlation) seismic motions [Abrahamson et al. \(1991\)](#); [Roblee et al. \(1996\)](#); [Abrahamson \(1992a, 2005, 1992b\)](#); [Zerva and Zervas \(2002\)](#); [Liao and Zerva \(2006\)](#); [Zerva \(2009\)](#)

It is very important to note that all current models for modeling incoherent seismic motions make an ergodic assumption. That is all the models assume that a variability of seismic motions at a single site – source combination will be the same as variability in the ground motions from a data set that was collected over different site and source locations [Walling \(2009\)](#). Unfortunately, there does not exist a large enough data set for east North American seismic events that can be used to develop incoherence models. Rather, there are models that are used to model possible incoherent behavior for east North American seismic wave propagations.

#### 109.2.8.1 Lack of Correlation Modeling and Simulation

Incorporation of lack of correlation effects in seismic motions can be done using the following methods:

- along 1D, in one direction, usually one of the horizontal directions, where all the points that are the same distance (in 1D) from a control point, plane) share a single lack of correlation,
- along 2D, in two directions, usually in a vertical plane or in a horizontal plane, where all the points in a set of vertical planes or a set of horizontal planes, share same lack of correlation, and
- in full 3C, where every point of interest (in a 3D volume of soil/rock) has its own, specified, lack of correlation.

The method used here is using the so called seed motions, motions obtained through DRM in full 3C (inclined, body and surface waves), that are then enriched with appropriate uncorrelated (incoherent) components. It is important to note that only translational motions are used to model incoherence effects, while the rotational motions are not perturbed/made incoherent. This stems from the fact that currently vast majority of seismic recording stations only record translational motions and that only those translational motions are used to develop incoherent motions models. Code developed by [Abrahamson \(1992b\)](#) is used for this purpose.

### 109.2.9 Lack of Volume Change Data for Soil

Use of  $G/G_{max}$  and damping curves for describing and calibrating material behavior of soil is missing a very important (crucial) information about soil/rock volume change during shearing deformation. Volume change data is very important for soil behavior. It is important to emphasize that soil behavior is very much a function of volumetric response during shear. During shearing of soil there are two essential types of soil behavior:

- Dilative (dense) soils will increase volume due to shearing
- Compressive (loose) soils will decrease volume due to shearing

The soil volume response, that is not provided by  $G/G_{max}$  and damping curves data can significantly affect response due to volume constraints of soil. For example, for one dimensional site response (1C wave propagation, vertically propagating (SV) shear waves) the soil will try to change its volume (dilate if it is dense or compress if it is loose). However, such volume change can only happen vertically (since there is no constraint (foundation for example) on top, while horizontally the soil will be constraint by other soil. That means that any intended volume change in horizontal direction will be resisted by change in (increase for dense and decrease for loose soil) horizontal stress. For example for dilative (dense) soil, additional horizontal stress will contribute to the increase in mean pressure (confinement) of the soil, thus increasing the stiffness of that soil. It is the opposite for compressive soil where shearing will result in a reduction of confinement stress. Figure 109.5 shows three responses for no-volume change (left), compressive (middle) and dilative (right) soil with full volume constraint, resulting in changes in stiffness for compressive (reduction in stiffness), and dilative (increase in stiffness).

Changes in stiffness of soil during shearing deformation will influence wave propagation and amplification of different frequencies. Figure 109.6 shows response of no-volume change soil (as it is/should be assumed if only  $G/G_{max}$  and damping curves are available, with no volume change data) and a response of a dilative soil which stiffens up during shaking due to restricted intent to dilate. It is clear that dilative soil will show significant amplification of higher frequencies.

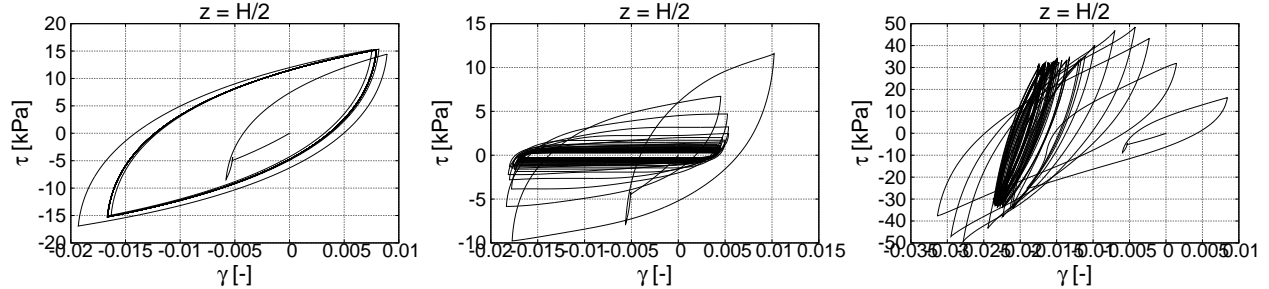


Figure 109.5: Constitutive Cyclic response of soils with constraint volumetric deformation: (left) no volume change (soil is at the critical state); (middle) compressive response with decrease in stiffness; (right) dilative response with increase in stiffness.

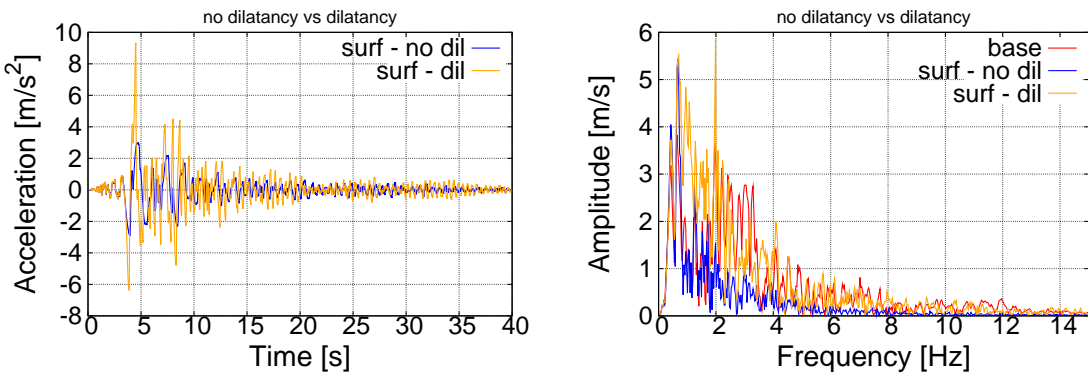


Figure 109.6: One dimensional seismic wave propagation through no-volume change and dilative soil. Please note the (significant) increase in frequency of motions for dilative soil. Left plot is a time history of motions, while the right plot shows amplitudes at different frequencies.

## 109.3 Earthquake Soil Structure Interaction

Current design practice for structures subject to earthquake loading regards dynamic SSII to be mainly beneficial to the behavior of structures ([Jeremić and Preisig, 2005](#)). Including the flexibility of the foundation reduces the overall stiffness of a system and therefore reduces peak loads caused by a given ground motion. Even if this is true in most cases there is the possibility of resonance occurring as a result of a shift of the natural frequencies of the SSI-system. This can lead to large inertial forces acting on a structure.

As a result of these large inertial forces caused by the structure oscillating in its natural frequency the structure as well as the soil surrounding the foundation can undergo plastic deformations. This in turn further modifies the overall stiffness of the SSI-system and makes any prediction on the behavior very difficult.

Dynamic SSII also becomes important in the design of large infrastructure projects. As authorities and insurance companies try to introduce the concept of performance based design to the engineering community more sophisticated models are needed in order to obtain the engineering demand parameters (EDP's). A good numerical model of a soil-foundation-structure system can therefore not only prevent the collapse or damage of a structure but also help to save money by optimizing the design to withstand an earthquake with a certain return period.

A variety of methods of different levels of complexity are currently being used by engineers. In the following an overview over the most important ones is presented. A more thorough discussion on methods and specific aspects of dynamic SSII is available in [Wolf \(1985\)](#) and more recently in [Wolf and Song \(2002\)](#).

- No SSII

The ground motion is applied directly to the base of the building. Alternatively, instead of applying the ground motion directly to the base of the structure, effective earthquake forces proportional to the base acceleration can be applied to the nodes.

This procedure is reasonable only for flexible structures on very stiff soil or rock. In this case the displacement of the ground doesn't get modified by the presence of the structure. For stiffer structures on soil the ground motion has to be applied to the soil. The model has to incorporate propagation of the motion through the soil, its interaction with the structure and the radiation away from the structure.

- Direct methods

Direct methods treat the SSI-system as a whole. The numerical model incorporates the spatial

discretization of the structure and the soil. The analysis of the entire system is carried out in one step. This method provides most generality as it is capable of incorporating all nonlinear behavior of the structure, the soil and also the interface between those two (sliding, uplift).

- Substructure methods

Substructure methods refer to the principle of superposition. The SSI-system is generally subdivided into a structure part and a soil part. Both substructures can be analyzed separately and the total displacement can be obtained by adding the contributions at the nodes on the interface.

This method reduces the size of the problem considerably. As the time needed for an analysis doesn't increase linearly with an increasing number of equations the substructure method is much faster than the direct method. The biggest drawback of the method however is the fact that linearity is assumed. For nonlinear systems the substructure method cannot be used.

For the direct method different levels of sophistication are possible:

- Foundation stiffness approach

The behavior of the soil is accounted for by simple mechanical elements such as springs, masses and dash pots. Different configurations of the subsoil can be taken into account by connecting several springs, masses and dash pots whose parameters have been determined by a curve fitting procedure [Wolf \(1994\)](#). This approach is very popular among structural engineers as it is relatively easy to be integrated in a commonly used finite element code.

Other methods use frequency dependent springs and dash pots and therefore require an analysis in frequency domain. Relatively complex configurations of layered subsoil and embedded foundations can be modeled with good accuracy by replacing the (elastic) soil with a sequence of conical rods [Wolf and Song \(2002\)](#) and [Wolf and Preisig \(2003\)](#).

- p-y methods

Attempts have been made to apply the static p-y approach for evaluating lateral loading on pile foundations to dynamic problems. [Mostafa and El Naggar \(2002\)](#) lists several references and provides a parametric study of single piles and pile groups in different soil types under simplified loading cases.

Even if p-y curves are widely used for estimating lateral loading on piles they are rarely used in full dynamic soil-structure interaction analysis. Current work trying to implement these methods into finite element codes is likely to make them more popular with the engineering community.

- Full 3d

Full nonlinear three-dimensional modeling of dynamic soil-foundation-structure interaction can be regarded as the 'brute force' approach. Displacements and forces can be obtained not only for the structure as in the above mentioned methods but also for the soil. In spite of the computational resources and modeling effort required for an analysis it is the only method that remains valid for all kinds of problems involving material nonlinearities, contact/interface problems, different loading cases and complex geometries.

## 109.4 Earthquake Soil Structure Interaction Modeling Details

### 109.4.1 Seismic Motions Input into Finite Element Model

A number of methods is used to input seismic motions into finite element model. Most of them are based on simple intuitive approaches, and as such are not based on rational mechanics. Most of those currently still widely used methods cannot properly model all three components of body waves as well as always present surface waves. There exist a method that is based on rational mechanics and can model both body and surface seismic waves input into finite element models with high accuracy. That method is called the Domain Reduction Method (DRM) (Bielak et al., 2003a; Yoshimura et al., 2003a)). The DRM aims to reduce the large computational domain, encompassing fault, rock, soil and the structure, to a much smaller domain, encompassing only local soil and the structure. The method was developed with earthquake ground motions in mind, with the main idea to replace the force couples at the fault with their counterpart acting on a continuous surface surrounding local feature of interest. The local feature can be any geologic or man made object that constitutes a difference from the simplified large domain, free field, for which displacements and accelerations are easier to obtain.

The DRM is applicable to a much wider range of problems. It is essentially a variant of global-local set of methods and as formulated can be used for any problems where the local feature can be bounded by a continuous surface (that can be closed or not). The local feature in general can represent a soil–foundation–structure system (bridge, building, dam, tunnel...), or it can be a crack in large domain, or some other type of inhomogeneity that is fairly small compared to the size of domain where it is found.

In what follow, the DRM is developed in a somewhat different way than it was done in original papers by Bielak et al. (2003a); Yoshimura et al. (2003a)). The main features of the DRM are then analyzed and appropriate practical modeling issues addressed.

### 109.4.1.1 The Domain Reduction Method (DRM) Development

A large physical domain is to be analyzed for dynamic behavior. The source of disturbance is a known time history of a force field  $P_e(t)$ . That source of loading is far away from a local feature which is dynamically excited by  $P_e(t)$  ( $P_e(t)$ ) (see Figure 109.7).

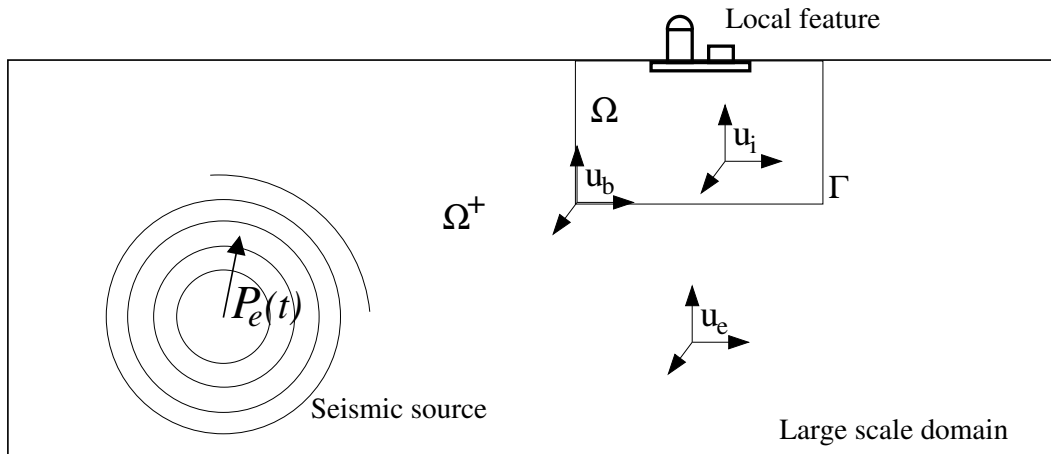


Figure 109.7: Large physical domain with the source of load  $P_e(t)$  and the local feature (in this case a soil-structure system).

The system to be analyzed can be quite large, for example earthquake hypocenter can be many kilometers away from the local feature of interest. Similarly, the small local feature in a machine part can be many centimeters away from the source of dynamic loading which influences this local feature. In this sense the term large domain is relative to the size of the local feature and the distance to the dynamic forcing source.

It would be beneficial not to analyze the complete system, as we are only interested in the behavior of the local feature and its immediate surrounding, and can almost neglect the domain outside of some relatively close boundaries. In order to do this, we need to somehow transfer the loading from the source to the immediate vicinity of the local feature. For example we can try to reduce the size of the domain to a much smaller model bounded by surface  $\Gamma$  as shown in Figure 109.7. In doing so we must ensure that the dynamic forces  $P_e(t)$  are appropriately propagated to the much smaller model boundaries  $\Gamma$ .

**DRM Formulation** In order to appropriately propagate dynamic forces  $P_e(t)$  one actually has to solve the large scale problem which will include the effects of the local feature. Most of the time this is impossible as it involves all the complexities of large scale computations and relatively small local feature. Besides, the main goal of presented developments is to somehow reduce the large scale domain as to be able to

analyze in details behavior of the local feature.

In order to propagate consistently the dynamic forces  $P_e(t)$  we will make a simplification in that we will replace a local feature with a simpler domain that is much easier to be analyzed. That is, we replace the local feature (bridge, building, tunnel, crack) with a much simpler geometry and material. For example, Figure 109.8 shows a simplified model, without a foundation–building system.

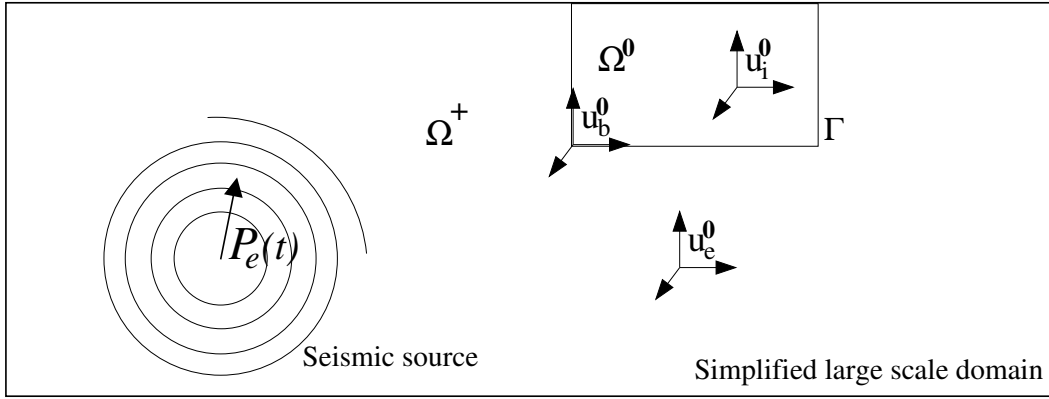


Figure 109.8: Simplified large physical domain with the source of load  $P_e(t)$  and without the local feature (in this case a soil–foundation–building system. Instead of the local feature, the model is simplified so that it is possible to analyze it and simulate the dynamic response as to consistently propagate the dynamic forces  $P_e(t)$

The idea is to simplify the model so that it is much easier to consistently propagate the dynamic forces to the boundary  $\Gamma$ . The notion that it is much easier to propagate those dynamic forces is of course relative. This is still a very complex problem, but at least the influence of local feature is temporarily taken out.

It is convenient to name different parts of domain. For example, the domain inside the boundary  $\Gamma$  is named  $\Omega_0$ . The rest of the large scale domain, outside boundary  $\Gamma$ , is then named  $\Omega^+$ . The outside domain  $\Omega^+$  is still the same as in the original model, while the change, simplification, is done on the domain inside boundary  $\Gamma$ . The displacement fields for exterior, boundary and interior of the boundary  $\Gamma$  are  $u_e$ ,  $u_b$  and  $u_i$ , respectively, on the original domain.

The equations of motions for the complete system can be written as

$$\begin{bmatrix} M \end{bmatrix} \begin{Bmatrix} \ddot{u} \end{Bmatrix} + \begin{bmatrix} K \end{bmatrix} \begin{Bmatrix} u \end{Bmatrix} = \begin{Bmatrix} P_e \end{Bmatrix} \quad (109.44)$$

or, if written for each domain (interior, boundary and exterior of  $\Gamma$ ) separately, the equations obtain the

following form:

$$\begin{bmatrix} M_{ii}^{\Omega} & M_{ib}^{\Omega} & 0 \\ M_{bi}^{\Omega} & M_{bb}^{\Omega} + M_{bb}^{\Omega+} & M_{be}^{\Omega+} \\ 0 & M_{eb}^{\Omega+} & M_{ee}^{\Omega+} \end{bmatrix} \begin{Bmatrix} \ddot{u}_i \\ \ddot{u}_b \\ \ddot{u}_e \end{Bmatrix} + \begin{bmatrix} K_{ii}^{\Omega} & K_{ib}^{\Omega} & 0 \\ K_{bi}^{\Omega} & K_{bb}^{\Omega} + K_{bb}^{\Omega+} & K_{be}^{\Omega+} \\ 0 & K_{eb}^{\Omega+} & K_{ee}^{\Omega+} \end{bmatrix} \begin{Bmatrix} u_i \\ u_b \\ u_e \end{Bmatrix} = \begin{Bmatrix} 0 \\ 0 \\ P_e \end{Bmatrix} \quad (109.45)$$

In these equations, the matrices  $\mathbf{M}$  and  $\mathbf{K}$  are mass and stiffness matrices respectively; the subscripts  $i$ ,  $e$ , and  $b$  are referencing nodes in either the interior ( $i$ ) or exterior ( $e$ ) domain or on their common boundary ( $b$ ), while the superscripts  $\Omega$  and  $\Omega^+$  reference domains to which matrices belong.

The previous equation can be separated provided that we maintain the compatibility of displacements and equilibrium. The resulting two equations of motion are

$$\begin{bmatrix} M_{ii}^{\Omega} & M_{ib}^{\Omega} \\ M_{bi}^{\Omega} & M_{bb}^{\Omega} \end{bmatrix} \begin{Bmatrix} \ddot{u}_i \\ \ddot{u}_b \end{Bmatrix} + \begin{bmatrix} K_{ii}^{\Omega} & K_{ib}^{\Omega} \\ K_{bi}^{\Omega} & K_{bb}^{\Omega} \end{bmatrix} \begin{Bmatrix} u_i \\ u_b \end{Bmatrix} = \begin{Bmatrix} 0 \\ P_b \end{Bmatrix}, \quad \text{in } \Omega \quad (109.46)$$

and

$$\begin{bmatrix} M_{bb}^{\Omega+} & M_{be}^{\Omega+} \\ M_{eb}^{\Omega+} & M_{ee}^{\Omega+} \end{bmatrix} \begin{Bmatrix} \ddot{u}_b \\ \ddot{u}_e \end{Bmatrix} + \begin{bmatrix} K_{bb}^{\Omega+} & K_{be}^{\Omega+} \\ K_{eb}^{\Omega+} & K_{ee}^{\Omega+} \end{bmatrix} \begin{Bmatrix} u_b \\ u_e \end{Bmatrix} = \begin{Bmatrix} -P_b \\ P_e \end{Bmatrix}, \quad \text{in } \Omega^+ \quad (109.47)$$

Compatibility of displacements is maintained automatically since both equations contain boundary displacements  $u_b$  (on boundary  $\Gamma$ ), while the equilibrium is maintained through action–reaction forces  $P_b$ .

In order to simplify the problem, the local feature is removed from the interior domain. Thus, the interior domain is significantly simplified. In other words, the exterior region and the material therein are identical to those of the original problem as the dynamic force source. On the other hand, the interior domain (denoted as  $\Omega_0$ ), is simplified, the localized features is removed (as seen in figure 109.8).

For this simplified model, the displacement field (interior, boundary and exterior, respectively) and action–reaction forces are denoted by  $u_i^0$ ,  $u_b^0$ ,  $u_e^0$  and  $P_b^0$ . The entire simplified domain  $\Omega_0$  and  $\Omega^+$  is now easier to analyze.

The equations of motion in  $\Omega^+$  for the auxiliary problem can now be written as:

$$\begin{bmatrix} M_{bb}^{\Omega+} & M_{be}^{\Omega+} \\ M_{eb}^{\Omega+} & M_{ee}^{\Omega+} \end{bmatrix} \begin{Bmatrix} \ddot{u}_b^0 \\ \ddot{u}_e^0 \end{Bmatrix} + \begin{bmatrix} K_{bb}^{\Omega+} & K_{be}^{\Omega+} \\ K_{eb}^{\Omega+} & K_{ee}^{\Omega+} \end{bmatrix} \begin{Bmatrix} u_b^0 \\ u_e^0 \end{Bmatrix} = \begin{Bmatrix} -P_b^0 \\ P_e \end{Bmatrix} \quad (109.48)$$

Since there was no change to the exterior domain  $\Omega^+$  (material, geometry and the dynamic source are still the same) the mass and stiffness matrices and the nodal force  $P_e$  are the same as in Equations (109.46) and (109.47).

Previous equation 109.48 can be used to obtain the dynamic force  $P_e$ :

$$P_e = M_{eb}^{\Omega+} \ddot{u}_b^0 + M_{ee}^{\Omega+} \ddot{u}_e^0 + K_{eb}^{\Omega+} u_b^0 + K_{ee}^{\Omega+} u_e^0 \quad (109.49)$$

The total displacement,  $u_e$ , can be expressed as the sum of the free field  $u_e^0$  (from the background, simplified model) and the residual field  $w_e$  (coming from the local feature) as following:

$$u_e = u_e^0 + w_e \quad (109.50)$$

It is important to note that this is just a change of variables and not an application of the principle of superposition. The residual displacement field,  $w_e$  is measured relative to the reference free field  $u_e^0$ .

By substituting Equation 109.50 in Equation 109.45 one obtains:

$$\begin{bmatrix} M_{ii}^\Omega & M_{ib}^\Omega & 0 \\ M_{bi}^\Omega & M_{bb}^\Omega + M_{bb}^{\Omega+} & M_{be}^{\Omega+} \\ 0 & M_{eb}^{\Omega+} & M_{ee}^{\Omega+} \end{bmatrix} \begin{Bmatrix} \ddot{u}_i \\ \ddot{u}_b \\ \ddot{u}_e^0 + \ddot{w}_e \end{Bmatrix} + \begin{bmatrix} K_{ii}^\Omega & K_{ib}^\Omega & 0 \\ K_{bi}^\Omega & K_{bb}^\Omega + K_{bb}^{\Omega+} & K_{be}^{\Omega+} \\ 0 & K_{eb}^{\Omega+} & K_{ee}^{\Omega+} \end{bmatrix} \begin{Bmatrix} u_i \\ u_b \\ u_e^0 + w_e \end{Bmatrix} = \begin{Bmatrix} 0 \\ 0 \\ P_e \end{Bmatrix} \quad (109.51)$$

which, after moving the free field motions  $u_e^0$  to the right hand side, becomes

$$\begin{bmatrix} M_{ii}^\Omega & M_{ib}^\Omega & 0 \\ M_{bi}^\Omega & M_{bb}^\Omega + M_{bb}^{\Omega+} & M_{be}^{\Omega+} \\ 0 & M_{eb}^{\Omega+} & M_{ee}^{\Omega+} \end{bmatrix} \begin{Bmatrix} \ddot{u}_i \\ \ddot{u}_b \\ \ddot{w}_e \end{Bmatrix} + \begin{bmatrix} K_{ii}^\Omega & K_{ib}^\Omega & 0 \\ K_{bi}^\Omega & K_{bb}^\Omega + K_{bb}^{\Omega+} & K_{be}^{\Omega+} \\ 0 & K_{eb}^{\Omega+} & K_{ee}^{\Omega+} \end{bmatrix} \begin{Bmatrix} u_i \\ u_b \\ w_e \end{Bmatrix} = \begin{Bmatrix} 0 \\ -M_{be}^{\Omega+}\ddot{u}_e^0 - K_{be}^{\Omega+}u_e^0 \\ -M_{ee}^{\Omega+}\ddot{u}_e^0 - K_{ee}^{\Omega+}u_e^0 + P_e \end{Bmatrix} \quad (109.52)$$

By substituting Equation 109.49 in previous Equation 109.52, the right hand side can now be written as

$$\begin{bmatrix} M_{ii}^\Omega & M_{ib}^\Omega & 0 \\ M_{bi}^\Omega & M_{bb}^\Omega + M_{bb}^{\Omega+} & M_{be}^{\Omega+} \\ 0 & M_{eb}^{\Omega+} & M_{ee}^{\Omega+} \end{bmatrix} \begin{Bmatrix} \ddot{u}_i \\ \ddot{u}_b \\ \ddot{w}_e \end{Bmatrix} + \begin{bmatrix} K_{ii}^\Omega & K_{ib}^\Omega & 0 \\ K_{bi}^\Omega & K_{bb}^\Omega + K_{bb}^{\Omega+} & K_{be}^{\Omega+} \\ 0 & K_{eb}^{\Omega+} & K_{ee}^{\Omega+} \end{bmatrix} \begin{Bmatrix} u_i \\ u_b \\ w_e \end{Bmatrix} = \begin{Bmatrix} 0 \\ -M_{be}^{\Omega+}\ddot{u}_e^0 - K_{be}^{\Omega+}u_e^0 \\ M_{eb}^{\Omega+}\dot{u}_b^0 + K_{eb}^{\Omega+}u_b^0 \end{Bmatrix} \quad (109.53)$$

The right hand side of equation 109.53 is a dynamically consistent replacement force, the so called effective force,  $P^{eff}$  for the dynamic source forces  $P_e$ . In other words, the dynamic force  $P_e$  was consistently

replaced by the effective force  $P^{eff}$ :

$$P^{eff} = \begin{Bmatrix} P_i^{eff} \\ P_b^{eff} \\ P_e^{eff} \end{Bmatrix} = \begin{Bmatrix} 0 \\ -M_{be}^{\Omega+}\ddot{u}_e^0 - K_{be}^{\Omega+}u_e^0 \\ M_{eb}^{\Omega+}\ddot{u}_b^0 + K_{eb}^{\Omega+}u_b^0 \end{Bmatrix} \quad (109.54)$$

### DRM Discussion

Single Layer of Elements used for  $P^{eff}$ . The Equation (109.54) shows that the effective nodal forces  $P^{eff}$  involve only the sub-matrices  $M_{be}$ ,  $K_{be}$ ,  $M_{eb}$ ,  $K_{eb}$ . These matrices vanish everywhere except the single layer of finite elements in domain  $\Omega^+$  adjacent to  $\Gamma$ . The significance of this is that the only wave-field (displacements and accelerations) needed to determine effective forces  $P^{eff}$  is that obtained from the simplified (auxiliary) problem at the nodes that lie on and between boundaries  $\Gamma$  and  $\Gamma_e$ , as shown in Figure 109.9.

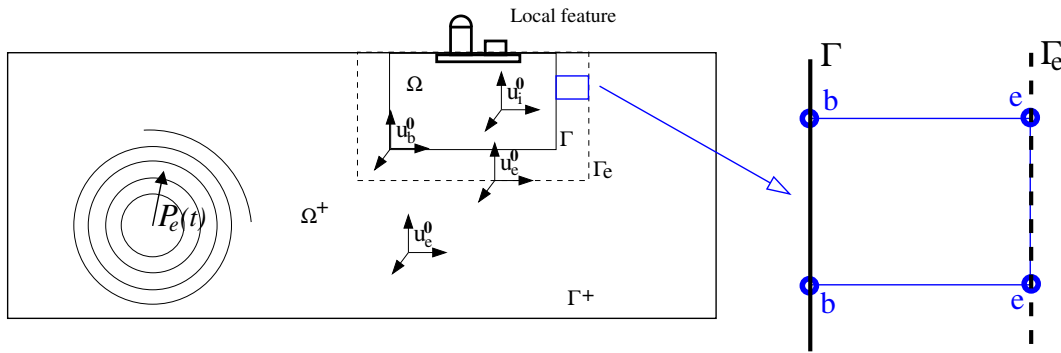


Figure 109.9: DRM: Single layer of elements between  $\Gamma$  and  $\Gamma_e$  is used to create  $P^{eff}$ , for a section of 8 node brick.

Figure 109.10 show boundary and external nodes for a section of a 27 node brick. Please note that for a 20, 20-17 and 27 node bricks, boundary nodes are nodes that belong to  $\Gamma$  surface, so for 27 node brick there are 9 nodes on that face, while the external nodes are all the nodes that are not boundary nodes, there will be 18 of those nodes.

Only residual waves outgoing. Another interesting observation is that the solution to problem described in Equation (109.53) comprises full unknowns (displacements and accelerations) inside and on the boundary  $\Gamma$  ( $\mathbf{u}_i$  and  $\mathbf{u}_b$  respectively). On the other hand, the solution for the domain outside single layer of finite elements (outside  $\Gamma_e$ ) is obtained for the residual unknown (displacement and accelerations) field,

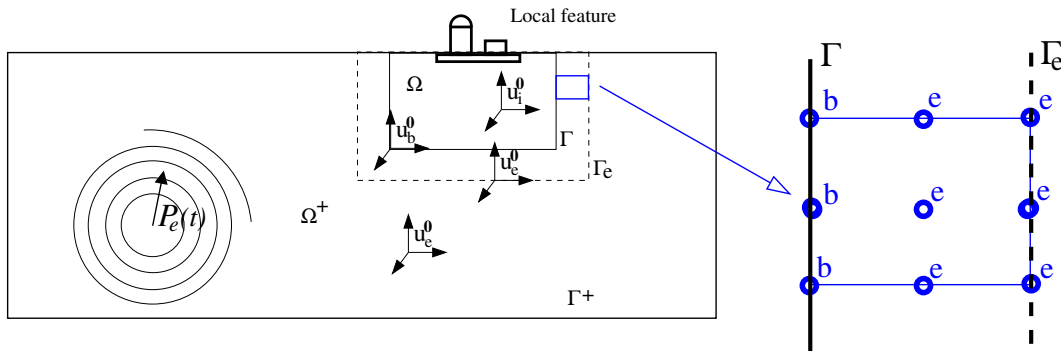


Figure 109.10: DRM: Single layer of elements between  $\Gamma$  and  $\Gamma_e$  is used to create  $P^{eff}$ , for 20, 20-17 and 27 node Brick.

$w_e$  only. This residual unknown field is measured relative to the reference free field of unknowns (see comments on page 572). That effectively means that the solution to the equation Equation (109.53) outside the boundary  $\Gamma_e$  will only contain additional waves field resulting from the presence of a local feature. This in turn means that if the interest is in behavior of local feature and the surrounding media (all within boundary  $\Gamma$ ) one can neglect the behavior of the full model (outside  $\Gamma_e$  in  $\Omega^+$ ) and provide appropriate supports (including fixity and damping) at some distance from the boundary  $\Gamma_e$  into region  $\Omega^+$ . This is significant for a number of reasons:

- large models can be reduced in size to encompass just a few layers of elements outside boundary  $\Gamma_e$  (significant reduction for, say earthquake problems where the size of a local feature is orders of magnitudes smaller than the distance to the dynamic source force  $P_e$  (earthquake hypocenter)).
- the residual unknown field can be monitored and analyzed for information about the dynamic characteristics of the local feature. Since the residual wave field is  $w_e$  is measured relative to the reference free field  $u_0^e$ , the solution for  $w_e$  has all the characteristics of the additional wave field stemming from the local feature.

Inside domain  $\Omega$  can be inelastic. In all the derivations in section 109.4.1.1 no restriction was made on the type of material inside the plastic bowl (inside  $\Gamma_e$ ). That is, the assumption that the material inside is linear elastic is not necessary as the DRM is not relying on principle of superposition. The Equation 109.50 was only describing the change of variables, and clearly there was no use of the principle of superposition, which is only valid for linear elastic solids and structures. It is therefore possible to assume that the derivations will still be valid with any type of material (linear or nonlinear, elastic

or inelastic) inside  $\Gamma_e$ . With this in mind, the DRM becomes a very powerful method for analysis of soil–foundation–structure systems.

All types of realistic seismic waves are modeled. Since the effective forcing  $P_{eff}^{eff}$  consistently replaces the effects of the seismic source, all appropriate (real) seismic waves are properly (analytically) modeled, including body (SV, SH, P) and surface (Rayleigh, Love, etc...) waves.

Properties of finite elements inside the DRM Layer. The DRM layers, a single layer of finite elements just outside  $\Gamma$  surfaces, where effective DRM forces  $P_{eff}$  are applied, needs to be carefully modeled. A number of conditions regarding the DRM layer need to be taken into account:

- The finite elements within the DRM layer need to be linear elastic.
- Material models for the finite elements within the DRM layer need to have same, or very similar material properties as the elastic part of material properties as the material inside the DRM layer. Although material inside the DRM layer can be elastic-plastic, it is beneficial if the linear elastic portion of material properties, for example for nonlinear elastic material at zero strain or for elastic-plastic material, elastic properties inside yield surface, for the DRM layer, is same, similar to the material used inside the DRM layer. All of the used elastic material properties need to be same as elastic material properties used for free field analysis in order to have consistent wave field.
- Dimensions of the DRM layer finite elements (thickness of the DRM layer) need to follow the same rule for element size (depending on chosen stiffness) so that there is no artificial (mesh dependent) filtering above certain frequencies. That means that 10 linear interpolation finite elements (8 node bricks) or 2 quadratic interpolation elements (27 node bricks) are needed per wave length ([Bathe and Wilson, 1976](#); [Hughes, 1987](#); [Argyris and Mlejnek, 1991](#)). For example if maximum modeling frequency is  $f_{max} = 20$  Hz, and wave length is given as  $\lambda_{min} = v/f_{max}$ , where  $v$  is the wave velocity, maximum grid spacing (element size) for linear interpolation elements  $\Delta h^{LE}$  should not exceed

$$\Delta h^{LE} \leq \frac{\lambda}{10} = \frac{v}{10f_{max}} = \frac{v}{10 \times 20 \text{ Hz}} = \frac{v}{200 \text{ Hz}}$$

while for quadratic interpolation elements such grid spacing (element size)  $\Delta h^{QE}$  is limited to

$$\Delta h^{QE} \leq \frac{\lambda}{2} = \frac{v}{2f_{max}} = \frac{v}{2 \times 20 \text{ Hz}} = \frac{v}{40 \text{ Hz}}$$

The wave velocity  $v$  is the lowest wave velocity that is of interest in the simulation, usually the shear wave velocity.

Properties of the finite elements outside of the DRM Layer. Finite elements outside DRM layer need special considerations as well.

- Material outside the DRM layer needs to be linear elastic with addition of viscous damping, Caughey, Rayleigh, etc.
- At least one layer of finite elements outside DRM layer needs to be provided. If damping of outgoing waves, the so called radiation damping, is to be modeled, then more than one layer of finite elements outside DRM needs to be provided.
- If radiation damping is modeled, it is recommended to have more than just two layers, outside DRM layer. For example 4 or 5 additional layers work quite well.
- First layer outside DRM layer needs to be linear elastic, of similar/same properties as material inside DRM layer, and with NO viscous damping. The reason for this requirement, is explained by the fact that  $P^{eff}$  force, see equation 109.54 on page 573, is applied to finite elements within DRM layer. If finite elements that are outside/adjacent to the DRM layer have large viscous damping, then  $P^{eff}$  forces will be producing potentially significant reaction forces from large viscous damping that is placed on nodes of elements that are shared with DRM finite element nodes, and nodes of finite elements just outside DRM layer, and are connected to DRM finite elements. These reaction, viscous forces, will affects, change  $P^{eff}$  forces in a way that will not be consistent with seismic wave field that was used to develop  $P^{eff}$ .
- Viscous damping, Caughey, Rayleigh, should be placed on finite elements outside this first layer of elements, that is outside, adjacent to DRM layer, in order to damp out outgoing waves, the differential wave field, the " $w_e$ " waves, see equation 109.50 on page 572. Additional viscous damping layers are added to damp out any additional waves, the so called radiation damping from structural oscillations. Damping in those additional layers is to be progressively larger, much larger than physical viscous damping. Values of equivalent damping of 20%, then 30%, then 50%, or higher have been used in order to damp outgoing waves, to model radiation damping.

A Note on Input Motions for DRM. Seismic motions (free field) that are used for input into a DRM model need to be consistent. In other words, a free field seismic wave that is used needs to fully satisfy equations of motion. For example, if free field motions are developed using a tool (SHAKE, or EDT or SW4, or fk, &c.) using time step  $\Delta t = 0.01s$  and then you decide that you want to run your analysis with a time step of  $\Delta t = 0.001s$ , simple interpolation (10 additional steps for each of the original steps) might create problems. Simple linear interpolation actually might (will) not satisfy wave propagation

equations and if used will introduce additional, high frequency motions into the model. It is a very good idea to generate free field motions with the same time step as it will be used in ESSI simulation.

Similar problem might occur if spacial interpolation is done, that is if location of free field model nodes is not very close to the actual DRM nodes used in ESSI model. Spatial interpolation problems are actually a bit less acute, however one still has to pay attention and test the ESSI model for free conditions and only then add the structure(s) on top.

Input motions for the DRM are based on Free Field motions, that can be developed by a number of methods, as described in section [502.2.3](#) on page [2266](#).

### DRM in Action, 1C vs 6C Free Field Motions

- One component of motions, 1C from 6C
- Excellent fit, however wrong physics



Figure 109.11: 6C real and 1C "horizontal motions fit" seismic motions. (Figure is a link to mp4 animation).

DRM in Action, 6C Free Field Motions, Variation in Input Frequency, Inclinded wave at  $\theta = 60^\circ$ .

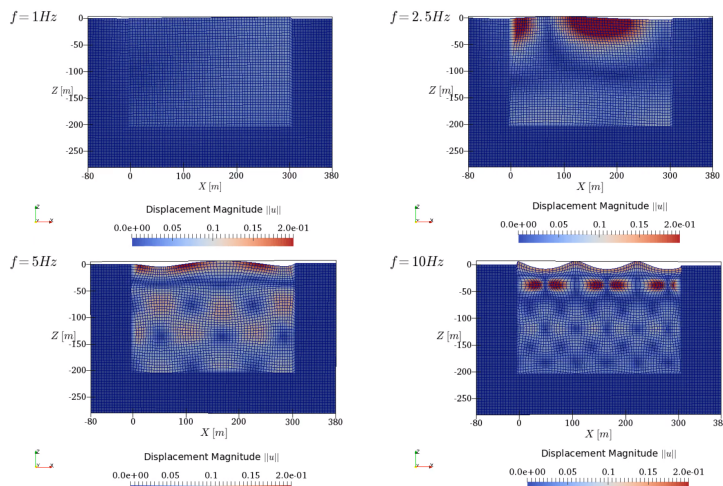


Figure 109.12: 6C real motions, variation in input frequency, inclined wave at  $\theta = 60^\circ$ .

## Chapter 110

# Parallel Computing in Computational Mechanics

(1998-2000-2005-2015-2016-2017-2018-2019-2021-)

(In collaboration with Dr. Guanzhou Jie and Dr. Yuan Feng, and Prof. Han Yang)

## 110.1 Chapter Summary and Highlights

### 110.2 Introduction

#### 110.2.1 High Performance Computing on DMPs, SMPs, GPGPUs, FPGA

##### 110.2.1.1 Distributed Memory Parallel (SMP) Computations

##### 110.2.1.2 Shared Memory Parallel (SMP) Computations

##### 110.2.1.3 General Purpose Graphical Processing Units (GPGPUs)

##### 110.2.1.4 Fast Programmable Gate Arrays (FPGAs)

#### 110.2.2 Parallel Computing for Elastic-Plastic Solids and Structures

#### 110.2.3 Problem Requirements

##### Stages, Increments, Iterations

For many classes of scientific simulations, an initial (static) decomposition of a finite element mesh needs to be computed such that the number of mesh elements assigned to each processor is roughly equal and the number of mesh elements that are adjacent to elements assigned to other processors (i.e., the size of the subdomain boundary) is minimized. Ensuring that the number of mesh elements is balanced will result in a load-balanced computation, while minimizing the size of the subdomain boundary will minimize the inter-processor communications overhead. Such a decomposition is usually obtained by a graph partitioning algorithm. Recently, a number of multilevel graph partitioning algorithms (e.g. [Hendrickson and Leland \(1995\)](#), [Karypis and Kumar \(1998b,a\)](#), [Monien et al. \(1999\)](#), [Walshaw and Cross \(1999\)](#)) have been developed that are able to compute excellent static decompositions for a wide range of scientific simulations.

##### 110.2.3.1 Finite Element Computations in Geomechanics

The distinct feature of elasto–plastic finite element computations is the presence of two iteration levels. In a standard displacement based finite element implementation, constitutive driver at each Gauss point iterates in stress and internal variable space, computes the updated stress state, constitutive stiffness tensor and delivers them to the finite element functions. Finite element functions then use the updated stresses and stiffness tensors to integrate new (internal) nodal forces and element stiffness matrix. Then, on global level, nonlinear equations are iterated on until equilibrium between internal and external forces is satisfied within some tolerance. In more details:

Elastic computations. In the case of elastic computations constitutive driver has a simple task of computing increment in stresses ( $\Delta\sigma_{ij}$ ) for a given deformation increment ( $\Delta\epsilon_{kl}$ ), through a closed form equation ( $\Delta\sigma_{ij} = E_{ijkl}\Delta\epsilon_{kl}$ ) (Jeremić and Sture, 1997). It is important to note that in this case the amount of work per Gauss point is known in advance. The amount of computational work is the same for every integration point. If we assume the same number of integration points per element, it follows that the amount of computational work is the same for each element and it is known in advance.

Elasto–plastic computations. On the other hand, for elasto–plastic problems, for a given incremental deformation the constitutive driver is iterating in stress and internal variable space until consistency condition is satisfied ( $F = 0$ ). The number of iterations is not known in advance. Initially, all Gauss points are in elastic range, but as we incrementally apply loads, the plastic zones develop. For Gauss points still in elastic range, there are no iterations, the constitutive driver just computes incremental stresses from closed form solution. Computational load will increase significantly for integration of constitutive equations in plastic range. In particular, constitutive level integration algorithms (Jeremić et al., 1998, 1999; Jeremić and Yang, 2002) for soils are very computationally demanding. From the experience of the PI, more than 70% of wall clock time during an elasto–plastic finite element analysis is spent in constitutive level iterations. This is in sharp contrast with elastic computations where the dominant part is solving the system of equations which consumes about 80% of run time. The extent of additional, constitutive level iterations is not known before the actual computations are over. In other words, the extent of elastic-plastic domain is not known ahead of time.

The traditional preprocessing type of DD method (also known as topological DD) splits domain based on the initial geometry and assigns roughly the same number of elements to every computational node and minimizes the size of subdomain boundaries. This approach might result in serious computational load imbalance for elasto–plastic problems. For example one domain might be assigned all of the elasto–plastic elements and spend large amount of time in constitutive level iterations. The other domains will have elements in elastic state and thus spend far less computational time in computing stress increments. This results in program having to wait for the slowest domain (the one with large number of elasto–plastic finite elements) to complete constitutive level iterations and only proceed with global system iterations after that.

This illustrates a two–fold challenge with computational load balancing for elastic–plastic simulations in geomechanics.

### 110.2.3.2 Adaptive Computation

First, these computations are dynamic in nature. That is, the structure of elastic and elastic–plastic domains changes dynamically and unpredictably during the course of the computation. For this reason, a static decomposition computed as a pre-processing step is not sufficient to ensure the computational load-balance of the entire computation. Instead, periodic computational load-balancing is required during the course of the computation. The problem of computing a dynamic decomposition shares the same requirements as that of computing the initial decomposition (i.e., balance the mesh elements and minimize the inter-processor communications), while also requiring that the cost associated with redistributing the data in order to balance the computational load is minimized. This last requirement prevents us from simply computing a whole new static partitioning from scratch each time computational load-balancing is required.

Often, the objective of minimizing the data redistribution cost is at odds with the objective of minimizing the inter-processor communications. For applications in which the computational requirements of different regions of the domain change rapidly, or the amount of state associated with each element is relatively high, minimizing the data redistribution cost is preferred over minimizing the communications incurred during parallel processing.

For applications in which computational load-balancing occurs very infrequently, the key objective of a load-balancing algorithm is in obtaining the minimal inter-processor communications. For many application domains, it is straightforward to select a primary objective to minimize (i.e., minimize whichever cost dominates). However, one of the key issues concerning the elastic-plastic computation is that the number of iterations between computational load-balancing phases is both unpredictable and dynamic. For example, in the case of static problems, zones in the 3D solid may become plastic and then unload to elastic (during increments of loading) so that the extent of plastic zone is changing. The change can be both slow and rapid. Slow change usually occurs during initial loading phases, while the later deformation tends to localize in narrow zones rapidly and the rest of the solid unloads rapidly (becomes elastic again). The narrow, localized zone has heavy computational load on the constitutive level (in each integration point within elements). Similar phenomena is observed in seismic soil–structure interaction computations where stiff structure interacts with soft soil and elastic and elastic–plastic zones change significantly during loading cycles. In this type of computation, it is extremely difficult to select the type of computational load-balancing algorithm to employ. Furthermore, the preferred computational load-balancing algorithm is liable to change during the course of the computation, and so the selection must be made dynamically.

### 110.2.3.3 Multi-phase Computation

The second challenge associated with computational load-balancing elastic-plastic computations in geomechanics is that these are two-phase computations. That is, plastic computations follow up the elastic computations. There is a synchronization phase between the computations, as only after the elastic computation is finished is it possible to check if the plastic computation is required for a given integration (Gauss) point within an element. For regions of the mesh in which this check indicates that the plastic computation is necessary, lengthy plastic computations are then performed. The existence of the synchronization step between the two phases of the computation requires that each phase be individually load balanced. That is, it is not sufficient to simply sum up the relative times required for each phase and to compute a decomposition based on this sum. Doing so may lead to some processors having too much work during the elastic computation (and so, these may still be working after other processors are idle), and not enough work during the plastic computation, (and so these may be idle while other processors are still working), and vice versa. Instead, it is critical that every processor have an equal amount of work from both of the phases of the computation.

### 110.2.4 Parallel Computing Hardware

#### 110.2.4.1 DMPs and SMPs

Scalability issues for SMPs Cache coherence

Compute Nodes, CPUs, Cores,

GPUs (band-with and latency with the main memory)

Networks (band-with and latency) 10, 100, 1,000, 10,000, Infiniband,

Large parallel supercomputers

small, user owned parallel machines (clusters of clusters)

ESSI Computer

- 208 (784) CPU cores,
- 288GB (1056GB) of distributed RAM,
- 24TB (48TB) of distributed disk space, and
- dual network, InfiniBand for MPI, and GigaBit for file system

Small ESSI Computer

- 32 CPU cores (AMD), 24 CPU cores (Intel)

- 64GB RAM,
- 4TB
- on-board network

### 110.2.5 Parallel Computing Software

#### 110.2.5.1 Amdahl's Law

$n$  is a number of parallel processes

$B$  is the fraction of algorithm that is serial

Total time to finish (wall clock time) with  $n$  parallel processes  $T(n)$

$$T(n) = T(1)(B + \frac{1}{n}(1 - B)) \quad (110.1)$$

Theoretical speedup

$$S(n) = \frac{T(1)}{T(n)} = \frac{T(1)}{T(1)(B + \frac{1}{n}(1 - B))} = \frac{1}{(B + \frac{1}{n}(1 - B))} \quad (110.2)$$

#### 110.2.5.2 Static and Dynamic Graph Partitioning

google search, data mining etc.

#### 110.2.5.3 Real parallel and embarrassingly parallel

Finite Element matrices computations (elastic and elastic-plastic)

System of equation solvers (non-iterative and iterative)

Examples for

elastic (elements (Seq) + solver(P))

elastic (elements (P) + solver (Seq))

elastic (elements (P) + solver (P))

elastic-plastic (Seq) + solver (P)

elastic-plastic (P) + solver (Seq)

elastic-plastic (P) + solver (P)

#### 110.2.5.4 Parallel Computing for Elastic-Plastic FEM

- Current Parallel FEM are
  - Well developed for elastic FEM
  - Undeveloped for elastic-plastic FEM
  - Well developed for homogeneous distributed memory parallel (DMP) computers,
  - Undeveloped for multiple performance (multi-generation) DMPs (example MOOSE, ESSI...)
- Need: dynamic computational load balancing for
  - multiple element types,
  - multiple material models
  - multiple compute node performances
  - multiple network performance performances

#### 110.2.5.5 Plastic Domain Decomposition

- Multi-objective optimization problem (minimize both the inter-processor communications, the data redistribution costs and create balanced partitions)
- computational load balancing adds overhead  $T_{overhead} := T_{comm} + T_{regen}$ 
  - $T_{comm}$  data communication load depending on network conditions.
  - $T_{regen}$  model regeneration for new partitioning, application (model) dependent
- Computational load among CPUs  $T_j := \sum_{i=1}^{nel} ElemCompLoad[i], j = 1, ..., nCPU$
- Goal: minimize maximum compute time (slowest CPU)  $T_{max} := \max(T_j) j = 1, ..., nCPU$
- Total compute time (not wall clock time)  $T_{sum} := \text{sum}(T_j)$
- Best execution time (perfect load balancing)  $T_{best} := T_{sum}/nCPU, \Rightarrow T_j \equiv T_{best}$  for each  $j = 1, ..., nCPU$
- Best performance gain  $T_{gain} := T_{max} - T_{best}$
- Computational load balancing is beneficial iff  $T_{gain} \geq T_{overhead} = T_{comm} + T_{regen}$
- Scalability (saturation, superlinear ...)

#### 110.2.5.6 Template Meta-programs

Fine grained parallelism

### 110.3 Plastic Domain Decomposition Algorithm

#### 110.3.1 Introduction

Domain Decomposition approach is the most popular and effective method to implement parallel finite element method. The underlying idea is to physically divide the problem domain into subdomains and finite element calculations will be performed on each individual domain in parallel. Domain Decomposition can be overlapping or non-overlapping. The overlapping domain decomposition method divides the problem domain into several slightly overlapping subdomains. Non-overlapping domain decomposition is extensively used in continuum finite element modeling due to the relative ease to program and organize computations and is the one that will be examined in this chapter.

In general, a good non-overlapping decomposition algorithm should be able to

- handle irregular mesh of arbitrarily shaped domain.
- minimize the interface problem size by delivering minimum boundary connectivity, which will help reducing the communication overheads.

The well-known idea of domain decomposition method can be found in a 1870 paper by the father of domain decomposition, H.A. Schwarz ([Rixena and Magoulès, 2007](#)). Domain decomposition method is also the underlying paradigm of substructuring methods developed in the sixties, which aim at reducing the dimension of models in structural analysis by applying static condensation-type techniques to subdomains.

Other than static condensation, [Farhat and Roux \(1991a\)](#); [Farhat \(1991\)](#); [Farhat and Geradin \(1992\)](#) proposed FETI (Finite Element Tearing and Interconnecting) method for domain decomposition analysis. In FETI method, Lagrange multipliers are introduced to enforce compatibility at the interface nodes. Rigid body modes are eliminated in parallel from each local problem and a direct scheme is applied concurrently to all subdomains in order to recover each partial local solution. The contributions of these modes are then related to the Lagrange multipliers through an orthogonality condition. This FETI method has been shown that it can deliver high efficiency for parallel implicit transient simulations in structural mechanics ([Crivelli and Farhat, 1993](#)).

Domain decomposition itself has become a active topic as parallel processing techniques receive much more attention in mathematics and engineering world during recent years. Domain decomposition

was revived as a natural paradigm for parallel solvers (Rixena and Magoulès, 2007). Many papers have discussed two algorithms that are currently receiving much research effort, namely the FETI-DP (or Dual Primal Finite Element Tearing and Interconnecting) method and the even more recent BDDC (or Balancing Domain Decomposition by Constraints).

FETI-DP is the third generation FETI method (Bavestrello et al., 2007) developed for the fast, scalable, and domain-decomposition-based iterative solution of symmetric systems of equations arising from the finite element (FE) discretization of static, dynamic, structural and acoustic problems (Farhat et al., 2001, 2000).

BDDC, on the other hand, derives its formulation from substructuring method by enforcing constraints associated with disjoint sets of nodes on substructure boundaries using constrained energy minimization concepts (Dohrmann, 2003; Mandel and Dohrmann, 2003).

An early endeavor on dynamic computational load balancing was presented by McKenna (1997). Limited number of examples show that run time, dynamic computational load balancing can indeed improve parallel program performance in some cases, particularly when nonlinearities are involved.

Although many works have been presented on domain decomposition methods, the most popular methods such as FETI-type and BDDC all stem from the root of subdomain interface constraints handling. The merging of iterative solving with domain decomposition-type preconditioning is promising as shown by many researchers (Pavarino, 2007; Li and Widlund, 2007). Schwartz-type preconditioners for parallel domain decomposition system solving have also shared part of the spotlight (Hwang and Cai, 2007; Sarkis and Szyld, 2007).

In solid finite element methods, it has been assumed that the equation solving is the most computational expensive part so it is totally reasonable that all focus has been set on equation solver during the past decades.

Work presented in this chapter, however, has originated from the observation that for highly nonlinear materials, the constitutive level computation can be at least equally costly as equation solving, if not more expensive. The novelty of this chapter is to break out of the existing substructuring or FETI frameworks to further address the fundamental load balance issue of parallel computing. Namely, in order to achieve better parallel performance, we want to keep all processors equally busy. Load imbalance issue resulted from nonlinear constitutive level computations is too important to be neglected. This chapter proposes the Plastic Domain Decomposition algorithm which focuses on adaptive load balancing operation for nonlinear finite elements.

From the implementation point of view, for mesh-based scientific computations, domain decomposition corresponds to the problem of mapping a mesh onto a set of processors, which is well defined as a graph partitioning problem (Schloegel et al., 1999).

Formally, the graph partitioning problem is as follows. Given a weighted, undirected graph  $G = (V; E)$  for which each vertex and edge has an associated weight, the  $k$ -way graph partitioning problem is to split the vertices of  $V$  into  $k$  disjoint subsets (or subdomains) such that each subdomain has roughly an equal amount of vertex weight (referred to as the balance constraint), while minimizing the sum of the weights of the edges whose incident vertices belong to different subdomains (i. e., the edge-cut).

In computational solid mechanics, the element graph is naturally used in parallel finite element method due to the fact that elemental operation forms the basis of finite element method. On the other hand, for material nonlinearity simulations, the element calculations represent the most computationally expensive part. In order to facilitate consistent interfaces for computational load measuring and data migration, element graph has been utilized as fundamental graph structure in this chapter, although it has been shown that the node-graph can be used as well for structure dynamics problem and the element-cut partitioning can make certain algorithms simpler (Krysl and Bittnar, 2001).

The graph partitioning problem is known to be NP-complete<sup>1</sup>. Therefore, generally it is not possible to compute optimal partitioning for graphs of interesting size in a reasonable amount of time. Various heuristic approaches have been developed, which can be classified as either geometric, combinatorial, spectral, combinatorial optimization techniques, or multilevel methods (Dongarra et al., 2003).

In finite element simulations involving nonlinear material response, static graph partitioning mentioned above does not guarantee even load distribution among processors. Plastification introduces work load that is much heavier than pure elastic computation. So for this kind of multiphase simulation, adaptive computational load balancing scheme has to be considered to keep all processing units equally busy as much as possible. Traditional static graph partitioning algorithm is not adequate to do multiphase partition/repartitioning. A parallel multilevel graph partitioner has been introduced in this research to achieve dynamic load balancing for inelastic finite element simulations.

In this chapter, the algorithm of Plastic Domain Decomposition (PDD) is proposed. The adaptive multi-level graph partitioning kernel of the PDD algorithm is implemented through the ParMETIS interface. Studies are performed to extract optimal algorithmic parameters for our specific applications.

### 110.3.2 Inelastic Parallel Finite Element

The distinct feature of inelastic (elastic-plastic) finite element computations is the presence of two iteration levels. In a standard displacement based finite element implementation, constitutive driver

---

<sup>1</sup>The complexity class NP is the set of decision problems that can be solved by a non-deterministic Turing machine in polynomial time. the NP-complete problems are the most difficult problems in NP ("non-deterministic polynomial time") in the sense that they are the smallest subclass of NP that could conceivably remain outside of P, the class of deterministic polynomial-time problems, <http://en.wikipedia.org/wiki/NP-complete>

at each Gauss point iterates in stress and internal variable space, computes the updated stress state, constitutive stiffness tensor and delivers them to the finite element functions. Finite element functions then use the updated stresses and stiffness tensors to integrate new (internal) nodal forces and element stiffness matrix. Then, on global level, nonlinear equations are iterated on until equilibrium between internal and external forces is satisfied within some tolerance.

- Elastic Computations

In the case of elastic computations constitutive driver has a simple task of computing increment in stresses ( $\Delta\sigma_{ij}$ ) for a given deformation increment ( $\Delta\epsilon_{kl}$ ), through a closed form equation ( $\Delta\sigma_{ij} = E_{ijkl}\Delta\epsilon_{kl}$ ) It is important to note that in this case the amount of work per Gauss point is known in advance. The amount of computational work is the same for every integration point. If we assume the same number of integration points per element, it follows that the amount of computational work is the same for each element and it is known in advance.

- Elastic-Plastic Computations

On the other hand, for elastic-plastic problems, for a given incremental deformation the constitutive driver is iterating in stress and internal variable space until consistency condition is satisfied ( $F = 0$ ). The number of iterations is not known in advance. Initially, all Gauss points are in elastic range, but as we incrementally apply loads, the plastic zones develop. For Gauss points still in elastic range, there are no iterations, the constitutive driver just computes incremental stresses from closed form solution. Computational load will increase significantly for integration of constitutive equations in plastic range. In particular, constitutive level integration algorithms for soils, concrete, rocks, foams and other granular materials are very computationally demanding. More than 70% of wall clock time during an elastic-plastic finite element analysis is spent in constitutive level iterations. This is in sharp contrast with elastic computations where the dominant part is solving the system of equations which consumes about 80% of run time. The extent of additional, constitutive level iterations is not known before the actual computations are over. In other words, the extent of elastic-plastic domain is not known ahead of time.

The traditional preprocessing type of Domain Decomposition method (also known as topological DD) splits domain based on the initial geometry and assigns roughly the same number of elements to every computational node and minimizes the size of subdomain boundaries. This approach might result in serious computational load imbalance for elastic-plastic problems. For example one domain might be assigned all of the elastic-plastic elements and spend large amount of time in constitutive level iterations. The other domains will have elements in elastic state and thus spend far less computational time in computing stress increments. This results in program having to wait

for the slowest domain (the one with large number of elastic-plastic finite elements) to complete constitutive level iterations and only proceed with global system iterations after that.

This illustrates a two-fold challenge with computational load balancing for inelastic simulations in mechanics. These two challenges is described below in some more detail.

#### 110.3.2.1 Adaptive Computation

First, these computations are dynamic in nature. That is, the structure of elastic and elastic-plastic domains changes dynamically and unpredictably during the course of the computation. For this reason, a static decomposition computed as a pre-processing step is not sufficient to ensure the computational load-balance of the entire computation. Instead, periodic computational load-balancing is required during the course of the computation. The problem of computing a dynamic decomposition shares the same requirements as that of computing the initial decomposition (i.e., balance the mesh elements and minimize the inter-processor communications), while also requiring that the cost associated with redistributing the data in order to balance the computational load is minimized. This last requirement prevents us from simply computing a whole new static partitioning from scratch each time computational load-balancing is required.

Often, the objective of minimizing the data redistribution cost is at odds with the objective of minimizing the inter-processor communications. For applications in which the computational requirements of different regions of the domain change rapidly, or the amount of state associated with each element is relatively high, minimizing the data redistribution cost is preferred over minimizing the communications incurred during parallel processing.

For applications in which computational load-balancing occurs very infrequently, the key objective of a load-balancing algorithm is in obtaining the minimal inter-processor communications. For many application domains, it is straightforward to select a primary objective to minimize (i.e., minimize whichever cost dominates). However, one of the key issues concerning the elastic-plastic computation is that the number of iterations between computational load-balancing phases is both unpredictable and dynamic. For example, in the case of static problems, zones in the 3D solid may become plastic and then unload to elastic (during increments of loading) so that the extent of plastic zone is changing. The change can be both slow and rapid. Slow change usually occurs during initial loading phases, while the later deformation tends to localize in narrow zones rapidly and the rest of the solid unloads rapidly (becomes elastic again). The narrow, localized zone has heavy computational load on the constitutive level (in each integration point within elements). Similar phenomena is observed in seismic soil-structure interaction computations where stiff structure interacts with soft soil and elastic and elasto-plastic zones change

significantly during loading cycles. In this type of computation, it is extremely difficult to select the type of computational load-balancing algorithm to employ. Furthermore, the preferred computational load-balancing algorithm is liable to change during the course of the computation, and so the selection must be made dynamically.

#### 110.3.2.2 Multiphase Computation

The second challenge associated with computational load-balancing elastic-plastic computations in geomechanics is that these are two-phase computations. That is, elastic-plastic computations follow up the elastic computations. There is a synchronization phase between the computations, as only after the elastic computation is finished is it possible to check if the elastic-plastic computation is required for a given integration (Gauss) point within an element. For regions of the mesh in which this check indicates that the elastic-plastic computation is necessary, lengthy elastic-plastic computations are then performed. The existence of the synchronization step between the two phases of the computation requires that each phase be individually load balanced. That is, it is not sufficient to simply sum up the relative times required for each phase and to compute a decomposition based on this sum. Doing so may lead to some processors having too much work during the elastic computation (and so, these may still be working after other processors are idle), and not enough work during the elastic-plastic computation, (and so these may be idle while other processors are still working), and vice versa. Instead, it is critical that every processor have an equal amount of work from both of the phases of the computation.

#### 110.3.2.3 Multiconstraint Graph Partitioning

Elastic-plastic FE computation can be understood as a two-phase calculation, which is also dynamic in nature. Traditional graph partitioning formulations are not adequate to ensure its efficient execution on high performance parallel computers. In this chapter very recent progresses from the graph partitioning algorithm research will be investigated. We need new adaptive graph partitioning formulations, which can compute adaptive partitioning-repartitionings that can satisfy an arbitrary number of balance constraints.

- Static Graph Partitioning

Given a weighted, undirected graph  $G = (V, E)$ , for which each vertex and edge has an associated weight, the  $k$ -way graph partitioning problem is to split the vertices of  $V$  into  $k$  disjoint subsets (or subdomains) such that each subdomain has roughly an equal amount of vertex weight (referred to as the balance constraint), while minimizing the sum of the weights of the edges whose incident vertices belong to different subdomains (i.e., the edge-cut).

### 1. Geometric Techniques

Compute partitioning based solely on the coordinate information of the mesh nodes, without considering edge-cut. Popular methods include, Coordinate Nested Dissection (CND or Recursive Coordinate Bisection), Recursive Inertial Bisection (RIB), Space-Filling Curve techniques and Sphere-Cutting approach.

### 2. Combinatorial Techniques

Attempt to group together highly connected vertices whether or not these are near each other in space. That is combinatorial partitioning schemes compute a partitioning based only on the adjacency information of the graph; they do not consider the coordinates of the vertices. They tend to have lower edge-cuts but generally slower. Popular methods include, Levelized Nested Dissection (LND) and Kernighan-Lin/Fiduccia-Mattheyses (KL/FM) partitioning refinement algorithm, which needs an initial partition input to do swapping refinement.

### 3. Multilevel Schemes

The multilevel paradigm consists of three phases: graph coarsening, initial partitioning, and multilevel refinement. Firstly, we form coarse graph by collapsing together selected vertices of the input graph. After rounds of coarsening, we get coarsest graph, on which an initial bisection will be performed. Then the KL/FM algorithm can be used to refine the partition back to the finest graph.

The multilevel paradigm works well for two reasons. First, a good coarsening scheme can hide a large number of edges on the coarsest graph, which makes the task of computing high-quality partitioning easier. Second reason, incremental refinement schemes such as KL/FM become much more powerful in the multilevel context.

Popular algorithms include Multilevel Recursive Bisection and Multilevel  $k$ -Way Partitioning.

- Adaptive Graph Partitioning

For large scale elasto-plastic FE simulations, it is necessary to dynamically load-balance the computations as the analysis progresses due to unpredictable plastification inside the domain. This dynamic load balancing can be achieved by using a graph partitioning algorithm.

Adaptive graph partitioning shares most of the requirements and characteristics of static graph partitioning but also adds an additional objective. That is, the amount of data that needs to be redistributed among the processors in order to balance the load should be minimized. If the vertex weight represents the computational cost of the work carried by the vertex, another metric, size of the vertex needs to be considered as well, which reflects distribution cost of the vertex. Thus, the repartitioner should attempt to balance the partitioning with respect to vertex weight while

minimizing vertex migration with respect to vertex size.

Different approaches are available. One can simply compute a new graph from scratch, so called Scratch-Remap Repartitioner, which expectedly introduces more data redistribution than necessary. Diffusion-Based Repartitioner attempt to minimize the difference between the original partitioning and the final repartitioning by making incremental changes in the partitioning to restore balance. This method has been a very active topic during recent years, [Dongarra et al. \(2003\)](#) gives up-to-date review.

- Multiconstraint Graph Partitioning

We can see traditional graph partitioning typically balances only a single constraint (i.e., the vertex weight) and minimizes only a single objective (i.e., the edge-cut). If we replace the vertex weight, which is a single number, with a weight vector of size  $m$ , then the problem becomes that of finding a partitioning that minimizes the edge-cuts subject to the constraints that each of the  $m$  weights is balanced across subdomains.

Multilevel graph partitioning algorithms for solving multiconstraint/multiobjective problems have been very successful [Schloegel et al. \(1999\)](#). The software libraries METIS and ParMETIS are widely used in computational mechanics research.

#### 110.3.2.4 Adaptive PDD Algorithm

In this chapter, the Plastic Domain Decomposition (PDD) has been developed using multi-level, multi-objective graph partitioning algorithm. This algorithm automatically monitors load balancing condition and updates element graph structure accordingly as the simulation progresses. Element redistribution will be triggered to achieve load balance when nonlinearity of materials brings down the parallel performance.

#### 110.3.3 Adaptive Multilevel Graph Partitioning Algorithm

[Karypis and Kumar \(1998\)](#) present a  $k$ -way multilevel partitioning algorithm whose run time is linear in the number of edges  $|E|$  (i.e.,  $O(|E|)$ ); whereas the run time of multilevel recursive bisection schemes is  $O(|E|\log k)$  for  $k$ -way partitioning. [Karypis and Kumar \(1998\)](#) show that the proposed multilevel partitioning scheme produces partitioning that are of comparable or better quality than those produced by multilevel recursive bisection, while requiring substantially less time. This paradigm consists of three phases: graph coarsening, initial partitioning, and multilevel refinement. In the graph coarsening phase, a series of graphs is constructed by collapsing together selected vertices of the input graph in order to form a related coarser graph. This newly constructed graph then acts as the input graph for another round of graph coarsening, and so on, until a sufficiently small graph is obtained. Computation of the initial

bisection is performed on the coarsest (and hence smallest) of these graphs, and so is very fast. Finally, partition refinement is performed on each level graph, from the coarsest to the nest (i.e., original graph) using a KL/FM-type algorithm Dongarra et al. (2003). Figure 110.1 illustrates the multilevel paradigm. This algorithm is available in METIS Karypis and Kumar (1998d) which is used in this research to provide initial static partitioning.

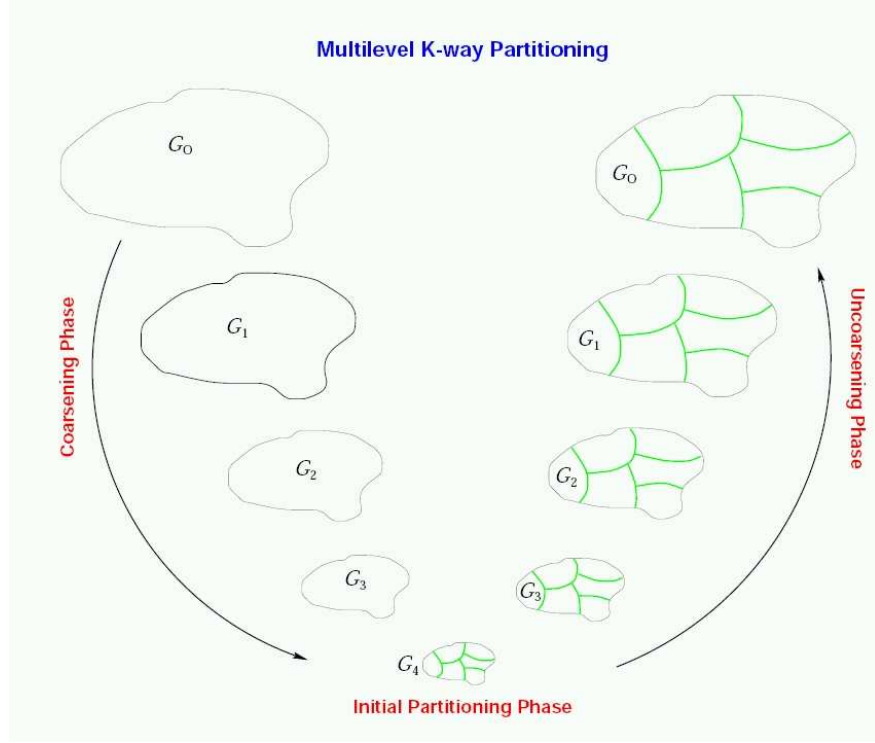


Figure 110.1: Multilevel Graph Partitioning Scheme Karypis et al. (2003)

Adaptive graph repartitioning algorithm can be used to achieve dynamic load balancing of multiphase elastic-plastic finite element simulations. Adaptive graph partitioning differs from static graph partitioning algorithm in the sense that one additional objective has to be targeted. That is, the amount of data the needs to be redistributed among the processors in order to balance the load should be minimized. In order to measure this redistribution cost, not only does the weight of a vertex, but also its size have to be considered. In our implementation for the purpose of this research, the vertex weight represents the computational load of each finite element, while the size reflects its redistribution cost. Thus, the application of adaptive graph partitioning algorithm aims at balancing the partitioning with respect to vertex weight while minimizing vertex migration with respect to vertex size.

A repartitioning of a graph can be obtained simply by partitioning a new graph from a scratch, which tends to bring much more unnecessary communications because the old distribution has not been taken

into account. Diffusion-based Repartitioner is more popular in which one attempts to minimize the difference between the original partitioning and the final repartitioning by making incremental changes in the partitioning to restore balance. Dongarra et al. (2003) gives a comprehensive review on this subject. Adaptive repartitioning is available in ParMETIS Karypis et al. (2003) and Jostle Warshaw (1998). The former is chosen in this research considering the fact that ParMETIS provides seamless interface for METIS 4.0 which makes the comparison between static and adaptive partitioning schemes more consistent.

PARMETIS is an MPI-based parallel library that implements a variety of algorithms for partitioning and repartitioning unstructured graphs and for computing fill-reducing orderings of sparse matrices Karypis et al. (2003). PARMETIS is particularly suited for parallel numerical simulations involving large unstructured meshes. In this type of computation, PARMETIS dramatically reduces the time spent in communication by computing mesh decompositions such that the numbers of interface elements are minimized. The algorithms in PARMETIS are based on the multilevel partitioning and fill-reducing ordering algorithms that are implemented in the widely-used serial package METIS Karypis and Kumar (1998c). However, PARMETIS extends the functionality provided by METIS and includes routines that are especially suited for parallel computations and large-scale numerical simulations. In particular, PARMETIS provides the following functionality Karypis et al. (2003):

- Partition unstructured graphs and meshes.
- Repartition graphs that correspond to adaptively refined meshes.
- Partition graphs for multi-phase and multi-physics simulations.
- Improve the quality of existing partitioning.
- Compute fill-reducing orderings for sparse direct factorization.
- Construct the dual graphs of meshes.

Both METIS and PARMETIS are used in this research. METIS routines are called to construct static partitioning for commonly used one-step static domain decomposition, while adaptive load-balancing is achieved by calling PARMETIS routines regularly during the progress of nonlinear finite element simulations.

Adaptive load-balancing through domain repartitioning is a multi-objective optimization problem, in which repartitionings should minimize both the inter-processor communications incurred in the iterative mesh-based computation and the data redistribution costs required to balance the load. PARMETIS

provides the routine [ParMETIS\\_V3\\_AdaptiveRepart](#) for repartitioning the previous unbalanced computational domain. This routine assumes that the existing decomposition is well distributed among the processors, but that (due to plastification of certain nonlinear elements) this distribution is poorly load balanced.

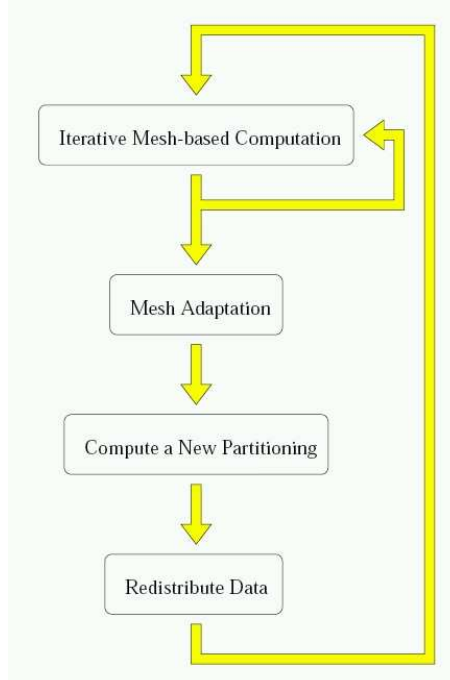


Figure 110.2: A diagram illustrating the execution of adaptive scientific simulations on high performance parallel computers [Schloegel et al. \(1999\)](#)

Figure 110.2 [Schloegel et al. \(2000\)](#) shows common steps involved in the execution of adaptive mesh-based simulations on parallel computers. Initially, the mesh is equally distributed on different processors. As all elements are elastic at the very beginning (carrying the same amount of elemental calculation work), computation load balance can be guaranteed with a even distribution. A number of iterations of the simulation are performed in parallel, after which plasticity occurs in certain nonlinear elements thus introducing some amount of load imbalance. A new partitioning based on the unbalanced domain is computed to re-balance the load, and then the mesh is redistributed among the processors, respectively. The simulation can then continue for another number of iterations until either more mesh adaptation is required or the simulation terminates.

If we consider each round of executing a number of iterations of the simulation, mesh adaptation, and load-balancing to be an epoch, then the run time of an epoch can be described by, [Schloegel et al.](#)

(2000)

$$(t_{comp} + f(|E_{cut}|))n + t_{repart} + g(|V_{move}|) \quad (110.3)$$

where  $n$  is the number of iterations executed,  $t_{comp}$  is the time to perform the computation for a single iteration of the simulation,  $f(|E_{cut}|)$  is the time to perform the communications required for a single iteration of the simulation, and  $t_{repart}$  and  $g(|V_{move}|)$  represent the times required to compute the new partitioning and to redistribute the data. Here, the inter-processor communication time is described as a function of the edge-cut of the partitioning and the data redistribution time is described as a function of the total amount of data that is required to be moved in order to realize the new partitioning. Adaptive repartitioning affects all of terms in Equation 110.3. How well the new partitioning is balanced influences  $t_{comp}$ . The inter-processor communications time is dependent on the edge-cut of the new partitioning. The data redistribution time is dependent on the total amount of data that is required to be moved in order to realize the new partitioning. It is critical for adaptive partitioning schemes to minimize both the edge-cut and the data redistribution when computing the new partitioning. Viewed in this way, adaptive graph partitioning is a multi-objective optimization problem.

There are various approaches how to handle this dual-objective problem. In general, two approaches have primarily been taken when designing adaptive partitioners. Schloegel et al. (2000) gives a comprehensive review on this topic. The first approach is to attempt to focus on minimizing the edge-cut and to minimize the data redistribution only as a secondary objective. This family of methods can be called scratch-remap repartitioner. These use some type of state-of-the-art graph partitioner to compute a new partitioning from scratch and then attempt to intelligently remap the subdomain labels to those of the original partitioning in order to minimize the data redistribution costs. Since a state-of-the-art graph partitioner is used to compute the partitioning, the resulting edge-cut tends to be extremely good. However, since there is no guarantee as to how similar the new partitioning will be to the original partitioning, data redistribution costs can be high, even after remapping. The second approach is to focus on minimizing the data redistribution cost and to minimize the edge-cut as a secondary objective, or so-called diffusion-based repartitioner. These schemes attempt to perturb the original partitioning just enough so as to balance it. This strategy usually leads to low data redistribution costs, especially when the partitioning is only slightly imbalanced. However, it can result in higher edge-cuts than scratch-remap methods because perturbing a partitioning in order to balance it also tends to adversely affect its quality.

These two types of repartitioner allow the user to compute partitioning that focus on minimizing either the edge-cut or the data redistribution costs, but give the user only a limited ability to control the tradeoffs among these objectives. This control of the tradeoffs is sufficient if the number of iterations

that a simulation performs between load-balancing phases (i.e. the value of  $n$  in Equation 110.3 ) is either very high or very low. However, when  $n$  is neither very high nor very low, neither type of scheme precisely minimizes the combined costs of  $f(E_{cut}|n)$  and  $g(|V_{move}|)$ . Another disadvantage exists for applications in which  $n$  is difficult to predict or those in which  $n$  can change dynamically throughout the course of the computation. As an example, one of the key issues concerning the elastic-plastic soil-structure interaction computations required for earthquake simulation is that the number of iterations between load-balancing phases is both unpredictable and dynamic. Here, zones in the 3D solid may become plastic and then unload (during increments of loading) so that the extent of the plastic zone is changing. The change can be both slow and rapid. Slow change usually occurs during initial loading phases, while the later deformation tends to localize in narrow zones rapidly and the rest of the solid unloads rapidly (becomes elastic again) Jeremić and Xenophontos (1999).

Schloegel et al. (2000) presents a parallel adaptive repartitioning scheme (called the Unified Repartitioning Algorithm) for the dynamic load-balancing of scientific simulations that attempts to solve the precise multi-objective optimization problem. By directly minimizing the combined costs of  $f(E_{cut}|n)$  and  $g(|V_{move}|)$ , the proposed scheme is able to gracefully tradeoff one objective for the other as required by the specific application. The paper shows that when inter-processor communication costs are much greater in scale than data redistribution costs, the proposed scheme obtains results that are similar to those obtained by an optimized scratch-remap repartitioner and better than those obtained by an optimized diffusion-based repartitioner. When these two costs are of similar scale, the scheme obtains results that are similar to the diffusive repartitioner and better than the scratch-remap repartitioner. When the cost to perform data redistribution is much greater than the cost to perform inter-processor communication, the scheme obtains better results than the diffusive scheme and much better results than the scratch-remap scheme. They also show in the paper that the Unified Repartitioning Algorithm is fast and scalable to very large problems.

#### 110.3.3.1 Unified Repartitioning Algorithm

A key parameter used in Unified Repartitioning Algorithm (URA) is the Relative Cost Factor (RCF). This parameter describes the relative times required for performing the inter-processor communications incurred during parallel processing and to perform the data redistribution associated with balancing the load. Using this parameter, it is possible to unify the two minimization objectives of the adaptive graph partitioning problem into the unified cost function

$$|E_{cut}| + \alpha |V_{move}| \quad (110.4)$$

where  $\alpha$  is the Relative Cost Factor,  $|E_{cut}|$  is the edge-cut of the partitioning, and  $|V_{move}|$  is the total amount of data redistribution. The Unified Repartitioning Algorithm attempts to compute a repartitioning while directly minimizing this cost function.

The Unified Repartitioning Algorithm is based upon the multilevel paradigm that is illustrated in Figure 110.1, which can be described as three phases: graph coarsening, initial partitioning, and uncoarsening/refinement Schloegel et al. (2000). In the graph coarsening phase, coarsening is performed using a purely local variant of heavy-edge matching. That is, vertices may be matched together only if they are in the same subdomain on the original partitioning. This matching scheme has been shown to be very effective at helping to minimize both the edge-cut and data redistribution costs and is also inherently more scalable than global matching schemes.

#### 110.3.3.2 Study of ITR in ParMETIS

The RCF in the URA implementation controls the tradeoff between two objectives, minimizing data redistribution cost or edge-cut. In our application, ParMETIS library has been linked to a MOSS (Modified OpenSees Services) analysis model to facilitate the partitioning/adaptive repartitioning scheme. The RCF is defined as a single parameter ITR in ParMETIS Karypis et al. (2003). This parameter describes the ratio between the time required for performing the inter-processor communications incurred during parallel processing compared to the time to perform the data redistribution associated with balancing the load. As such, it allows us to compute a single metric that describes the quality of the repartitioning, even though adaptive repartitioning is a multi-objective optimization problem. As recommended by Karypis et al. (2003), appropriate values to pass for the ITR Factor parameter can be determined depending on the times required to perform

1. all inter-processor communications that have occurred since the last repartitioning, and
2. the data redistribution associated with the last repartitioning/load balancing phase.

Simply divide the first time measurement by the second time measurement. The result is the correct ITR Factor. In case these times cannot be ascertained (e.g., for the first repartitioning/load balancing phase), Karypis et al. (2003) suggests that values between 100 and 1000 work well for a variety of situations. By default ITR is between 0.001 and 1000000. If ITR is set high, a repartitioning with a low edge-cut will be computed. If it is set low, a repartitioning that requires little data redistribution will be computed.

## 110.4 Performance Studies on PDD Algorithm

### 110.4.1 Introduction

In this chapter, parallel performance of the proposed PDD algorithm is thoroughly investigated. There are two major focuses for the timing analysis. Firstly we want to see how much performance gain we can have by introducing the PDD algorithm into inelastic finite element calculations. Secondly, we also want to show how scalable the proposed PDD algorithm is.

As our final objective is to apply PDD in large scale SFSI finite element simulations, finite element models of SFSI have been set up to study the parallel performance of the PDD based parallel program. Implicit constitutive integration scheme Jeremić and Sture (1997) has been used to expose the load imbalance by plasticity calculation. Only continuum element has been studied due to the fact they can be easily visualized to obtain partition and/or repartition figures.

Distributed memory Linux/Unix clusters are major platforms used in this chapter for speed up analysis.

### 110.4.2 Parallel Computers

Performance measurement has been carried out on two SMP-based clusters.

- IBM eServer p655

The DataStar IBM eServer p655 cluster consists of 176 8-way P655+ nodes at San Diego Supercomputer Center. System configuration is shown in Fig 110.3. The network benchmark is shown in Table 110.1.

Table 110.1: Latency and Bandwidth Comparison (as of August 2004)

	MPI Latencies ( $\mu$ sec)	Bandwidth (MBs)
Intra-node	3.9	3120.4
Inter-node	7.65	1379.1

- TeraGrid IA-64 Intel-Based Linux Cluster

The TeraGrid project was launched by the National Science Foundation with \$53 million in funding to four sites: the National Center for Supercomputing Applications (NCSA) at the University of Illinois, Urbana-Champaign, the San Diego Supercomputer Center (SDSC) at the University of California, San Diego, Argonne National Laboratory in Argonne, IL, and Center for Advanced Computing Research (CACR) at the California Institute of Technology in Pasadena.